

ISSN: 2249-6645

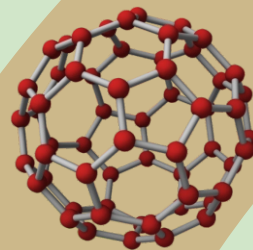


International Journal of Modern Engineering Research (IJMER)

Volume 4

Issue 1

January 2014



International Journal of Modern Engineering Research (IJMER)

Editorial Board

Executive Managing Editor

Prof. Shiv Kumar Sharma
India

Editorial Board Member

Dr. Jerry Van
Department of Mechanical, USA

Dr. George Dyrud
Research centre dy. Director of Civil Engineering, New Zealand

Dr. Masoud Esfal
R& D of Chemical Engineering, Australia

Dr. Nouby Mahdy Ghazaly
Minia University, Egypt

Dr. Stanley John
Department of Textile Engineering, United Kingdom

Dr. Valfitaf Rasoul
Professor and HOD of Electromechanical, Russian

Dr. Mohammed Ali Hussain
HOD, Sri Sai Madhavi Institute of Science & Technology, India

Dr. Manko dora
Associate professor of Computer Engineering, Poland

Dr. Ahmed Nabih Zaki Rashed
Menoufia University, Egypt

Ms. Amani Tahat
Ph.D physics Technical University of Catalonia-Spain

Associate Editor Member

Dr. Mohd Nazri Ismail
University of Kuala Lumpur (UniKL), Malaysia

Dr. Kamaljit I. Lakhtaria
Sir Padmapat Singhaniya University, Udaipur

Dr. Rajesh Shrivastava
Prof. & Head Mathematics & computer Deptt. Govt. Science & commerce College Benazir. M.P

Dr. Asoke Nath
Executive Director, St. Xavier's College, West Bengal, India

Prof. T. Venkat Narayana Rao
Head, CSE, HITAM Hyderabad

Dr. N. Balasubramanian
Ph. D (Chemical Engg), IIT Madras

Jasvinder Singh Sadana
M. TECH, USIT/GGSIPU, India

Dr. Bharat Raj Singh

Associate Director, SMS Institute of Technology, Lucknow

DR. RAVINDER RATHEE

C. R. P, Rohtak, Haryana

Dr. S. Rajendran

Research Supervisor, Corrosion Research Centre Department of Chemistry, GTN Arts College, Dindigul

Mohd Abdul Ahad

Department of Computer Science, Faculty of Management and Information Technology, Jamia Hamdad, New Delhi

Kunjai Mankad

Institute of Science & Technology for Advanced Studies & Research (ISTAR)

NILANJAN DEY

JIS College of Engineering, Kalyani, West Bengal

Dr. Hawz Nwayu

Victoria Global University, UK

Prof. Plewin Amin

Crewe and Alsager College of Higher Education, UK

Dr. (Mrs.) Annifer Zalic

London Guildhall University, London

Dr. (Mrs.) Malin Askiy

Victoria University of Manchester

Dr. ABSALOM

Sixth form College, England

Dr. Nimrod Nivek

London Guildhall University, London

Health Monitoring of Reinforcement In Concrete Piers In A Barrage Project

S. N. Sharma¹, Pankaj Sharma², R. P. Pathak³, Sameer Vyas⁴, N. V. Mahure⁵,
S. L. Gupta⁶

(Central Soil and Materials Research Station, New Delhi, India)

ABSTRACT: Useful life of any barrage project depends on functional stability of the concrete piers. The piers are constructed using concrete of different grades. Its durability is dependent on various factors viz. speed of running water, its aggressiveness, temperatures fluctuations etc. The endurance capacity of these piers against these adverse conditions is goes on reducing with passage of time. Gradually permeability of concrete increases which causes corrosion of reinforcement thus weakening of concrete. Once such a phenomenon is observed in any such structures a vigilant periodic monitoring approach becomes mandatory. The suitable remedial measure to be adopted will depend on the observed degree of deterioration. In this paper effort has been made to diagnose degree of corrosion of reinforcement in the piers of a barrage project using Half Cell Potentiometer.

Keywords: Corrosion. Half cell potentiometer. Piers. Rebar. Reinforcement.

I. INTRODUCTION

Corrosion problems are very common in almost all aspects of technology resulting in cropping of variety of problems. Corrosion damage in the reinforcement is an enormous economic liability. In a barrage project piers are constructed using concrete of different grades. The permeated water causes corrosion of reinforcement leading to weakening of structure [1] and spalling of cover (Fig. 1.1).



Fig. 1.1 Exposed reinforcement in piers due to spalling of cover

Diagnosis of the intensity of corrosion and its constant monitoring will provide useful information for adopting suitable preventive measures [2]. In this paper effort has been made to diagnose degree of corrosion of reinforcement in the piers of a barrage project using Half Cell Potentiometer.

II. METHOD ADOPTED

2.1. Half – Cell Electrical Potential Method to Measure Corrosion of Reinforcement in Concrete (ASTM C 876-91)

The Half Cell Potential Testing method is a technique, used for assessment of the durability of reinforced concrete and helps in diagnosing reinforcement corrosion [2, 3]. The method of half cell potential measurements normally involves measuring the potential of an embedded reinforcing bar relative to a reference half cell placed on the concrete surface. The half cell is usually Copper/ Copper Sulphate or Silver/ Silver Chloride cell but other combinations are used. The concrete functions as an electrolyte and the risk of corrosion

of reinforcement in immediate region of the test location may be related empirically to the measured potential difference. The typical layout of the equipment is shown Fig. 2.1.

The half cell consist a rigid tube composed of dielectric material that is non-reactive with copper or copper sulphate, a porous wooden or plastic plug that remains wet by capillary action, and a copper rod that is immersed within the tube in a saturated solution of copper sulphate. The solution is prepared using reagent grade copper sulphate dissolved to saturation in distilled or deionized water. An electrical junction device is used to provide a low electrical resistance liquid bridge between the surface and the half cell is normally a sponge. Electrical contact solution is made from normal house hold detergent.

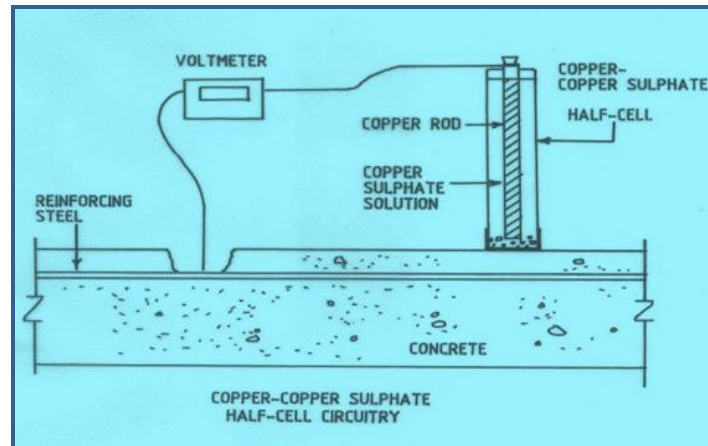


Fig 2.1 Copper- Copper Sulphate Half- Cell

Measurements are made in either a grid or random pattern. The potential risks of corrosion based on potential difference readings [3] are presented in Table I.

Table I: The potential risks of corrosion based on potential difference readings

Potential difference levels (mv)	Chance of re-bar being corroded
less than -500mv	Visible evidence of Corrosion
-350 to -500 mv	95%
-200 to -350 mv	50%
More than -200 mv	5%

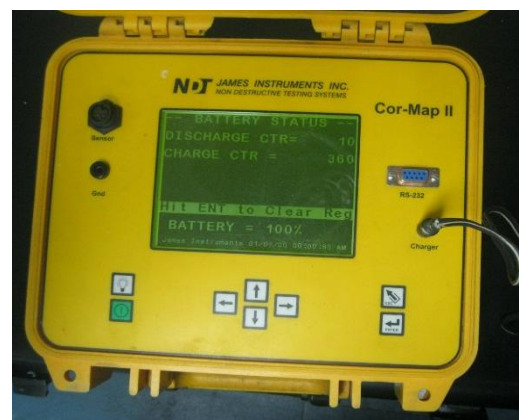
III. EQUIPMENT USED

Following equipments were deployed for the corrosion monitoring of reinforcement in concrete (Fig. 3.1)

- Micro cover meter- R Meter MKIII
- Half Cell Surveyor- CORMAP II



Micro Cover Meter



Half Cell Surveyor

Fig 3.1. Equipments Deployed for Investigation

The micro cover meter has been used to locate the rebar [4]. The concrete surface was examined for the exposed rebars/or got exposed to get a reference point. Surface was made wet and observation locations were marked on the surface [5]. The pre-activated Cu-CuSO₄ Half Cell was used to take observation.

The test results are categorized in 7 categories from A to G category in the typical map recorded on CORMAP II, their interpretation is given in Table II.

Table II: Categories of Corrosion Activity

A = - 0.420, B = - 0.350	A & B – 90% chance corrosion is occurring in this area
C = - 0.280 D = - 0.210	C & D – Corrosion activity over this area is uncertain
E = - 0.140 F = - 0.070	E –G – 90% chance that no corrosion activity is present over this area
G = - 0.00	

IV. TEST LOCATIONS

Detailed location of different piers and grid patterns are given in Table III.

Table III: Details of locations for corrosion monitoring

Pier	Location	Grid pattern
1	D/S RHS FACE, 3.2m from gate.	10'x5' (column x row)
2	D/S RHS FACE, 2.5m inside from nose of the pier	10'x5' (column x row)
3	D/S RHS FACE	10'x5' (column x row)
4	D/S LHS FACE	10'x5' (column x row)
5	D/S RHS FACE	10'x5' (column x row)
6	D/S RHS FACE, mid of the face, 20.5m apart from gate, lower end of the grid ended at 10.3m from top.	10'x5' (column x row)
7	D/S RHS FACE, mid of the face, 19.5m apart from gate, 4.7m from top.	10'x5' (column x row)
8 A	D/S RHS, 10.7m from top, 1.0 m above water level, 29.0 m apart from gate	10'x5' (column x row)
8 B	D/S RHS, 10.9 m from top & 27.0 m apart from gate. 0 m above water level	10'x5' (column x row)
9	RHS, 11.55m from top and 1.0 m above water level, 23.4 m apart from gate	10'x5' (row x column)
10	LHS, 11.5m from top and 1.0 m above water level, 13.7 m apart from gate	20' x 10' (10 x 10)

V. OBSERVATIONS

The investigation work of corrosion monitoring of the identified concrete piers was restricted to the area which could be accessed using a boat (Table 3). The observed values for the tests done on different piers are presented in Fig. 6.1 to Fig. 6.22 in the form of contour map and pie chart [6, 7, 8].

VI. RESULTS AND DISCUSSION

6.1. Pier 1

Only 2% region falls in 'D' category depicting uncertain corrosion activity while remaining 98% (6% in 'E', 70% in 'F' and 22% in 'G') area falls in categories which are indicative of no noticeable corrosion activity in the scanned area of the pier.

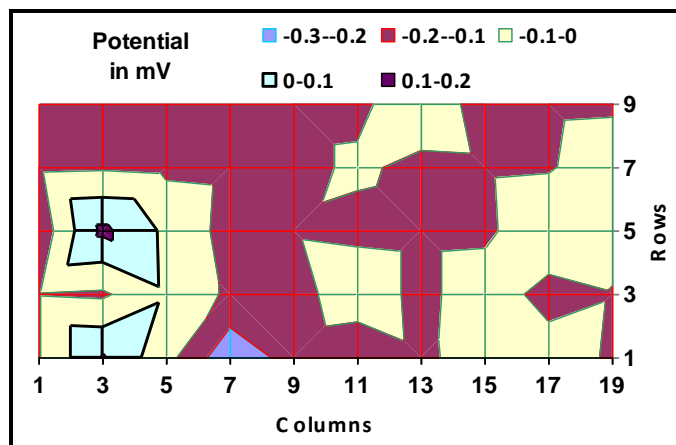


Fig. 6.1 Contour Map Showing Corrosion Status

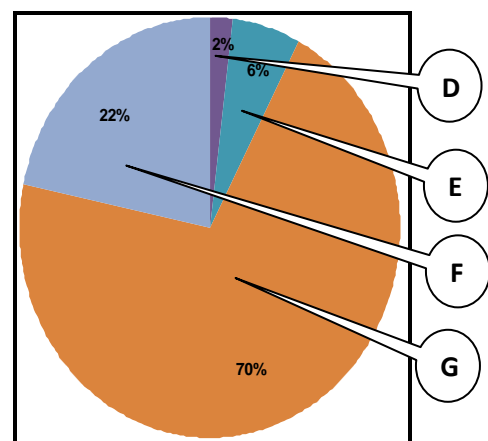


Fig. 6.2 Pie Chart of Scanned Area

6.2. Pier 2

Only 33% region falls in 'D' category depicting uncertain corrosion activity while remaining 67% (20% in 'E', 16% in 'F' and 31% in 'G') area falls in categories which are indicative of no noticeable corrosion activity in the scanned area of the pier.

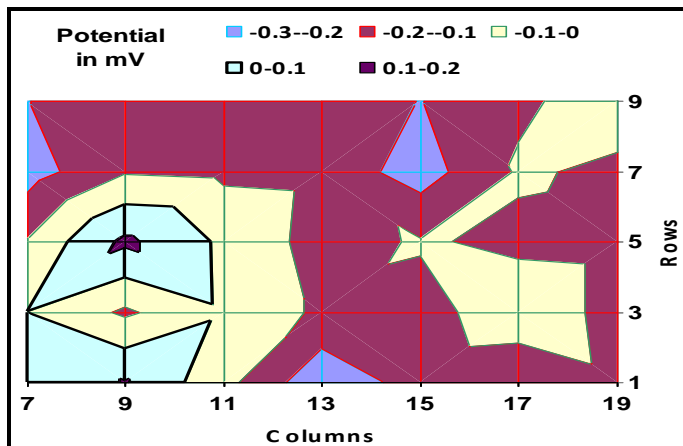


Fig. 6.3 Contour Map Showing Corrosion Status

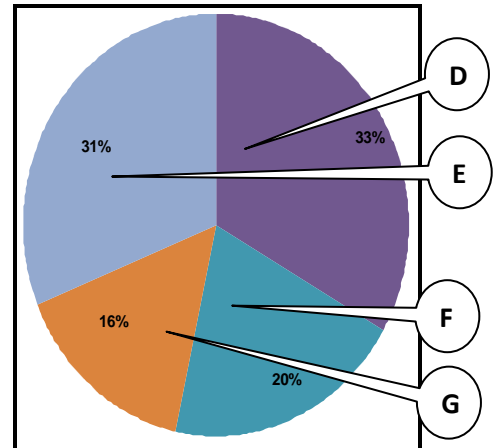


Fig. 6.4 Pie Chart of Scanned Area

6.3. Pier 3

Only 2% region falls in D category depicting uncertain corrosion activity while remaining 98% (6% in 'E', 42% in 'F' and 50% in 'G') area falls in categories which are indicative of no noticeable corrosion activity in the scanned area of the pier.

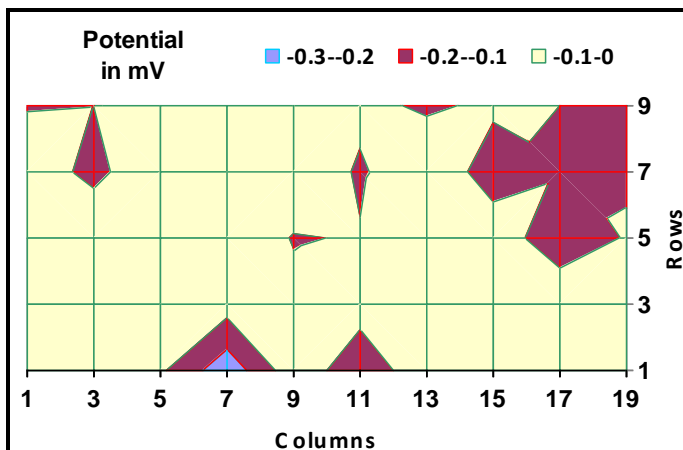


Fig. 6.5 Contour Map Showing Corrosion Status

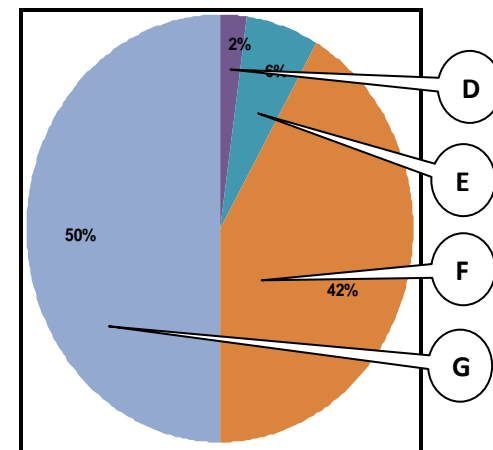


Fig. 6.6 Pie Chart of Scanned Area

6.4. Pier 4

100% area (43% in 'F' and 57% in 'G') falls in categories which are indicative of no noticeable corrosion activity in the scanned area of the pier.

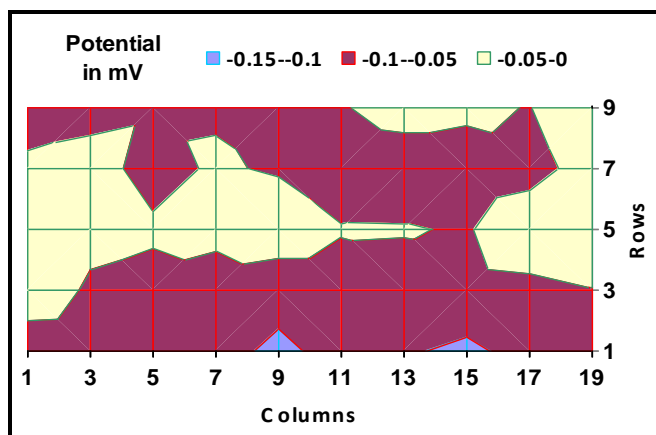


Fig. 6.7 Contour Map Showing Corrosion Status

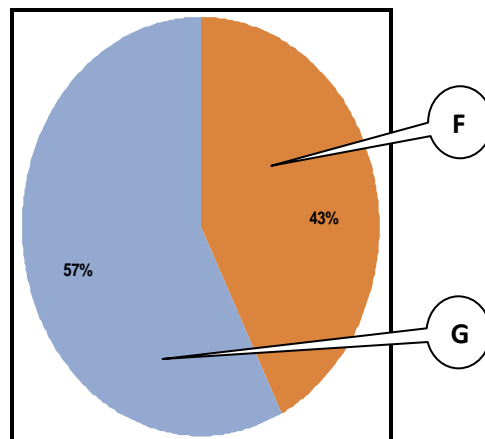


Fig. 6.8 Pie Chart of Scanned Area

6.5. Pier 5

100% area (18% in 'F' and 82% in 'G') falls in categories which are indicative of no noticeable corrosion activity in the scanned area of the pier.

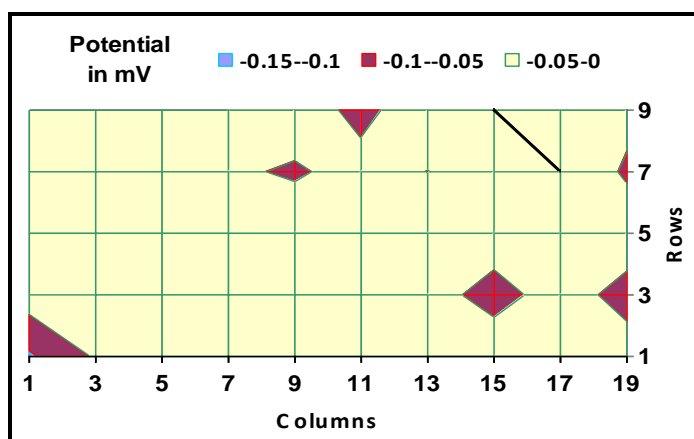


Fig. 6.9 Contour Map Showing Corrosion Status

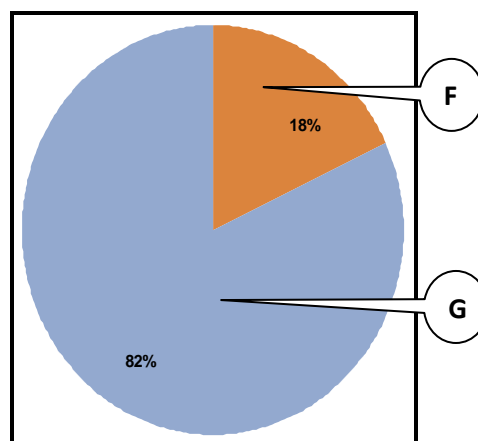


Fig. 6.10 Pie Chart of Scanned Area

6.6. Pier 6

Only 14% region (2% in 'C' and 12% in 'D' category) depicts uncertain corrosion activity while remaining 86% (46% in 'E' and 40% in 'F') area falls in categories which are indicatives of no noticeable corrosion activity in the scanned area of the pier.

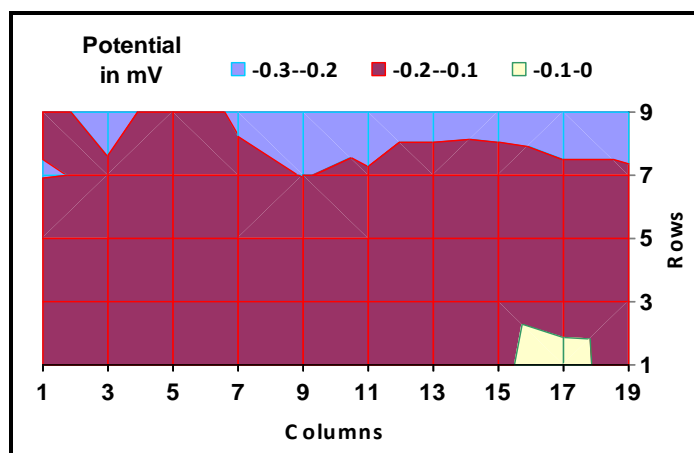


Fig. 6.11 Contour Map Showing Corrosion Status

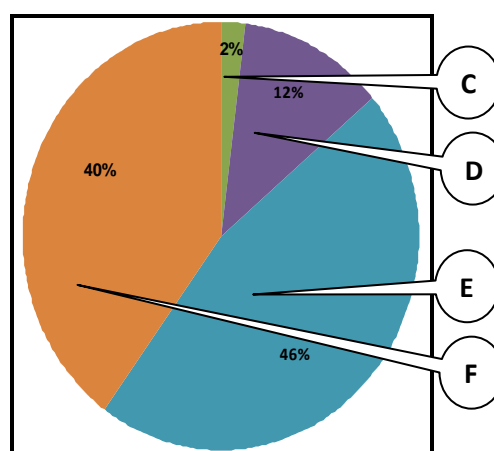


Fig. 6.12 Pie Chart of Scanned Area

6.7 Pier 7

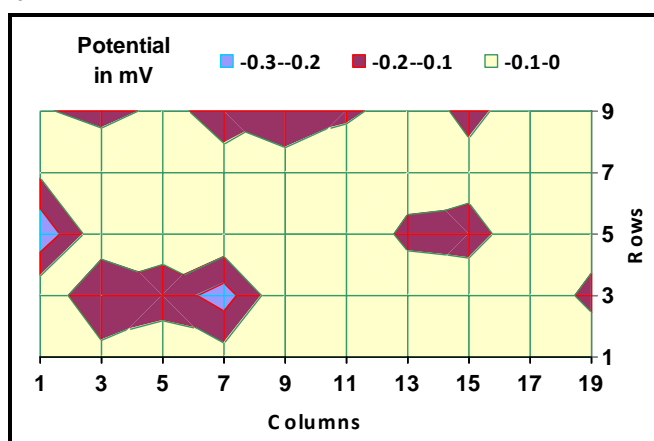


Fig. 6.13 Contour Map Showing Corrosion Status

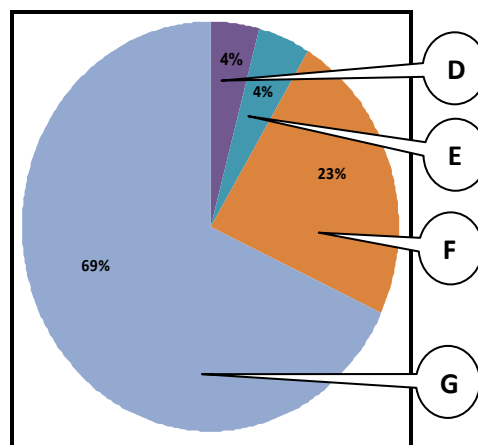


Fig. 6.14 Pie Chart of Scanned Area

Only 4% region falls in ‘D’ category depicting uncertain corrosion activity while remaining 96% (4% in ‘E’, 23% in ‘F’ and 69% in ‘G’) area falls in categories which are indicative of no noticeable corrosion activity in the scanned area of the pier.

6.8. Pier 8 A

100% area (28% in ‘E’, 56% in ‘F’ and 16% in ‘G’) falls in categories which are indicative of no noticeable corrosion activity in the scanned area of the pier.

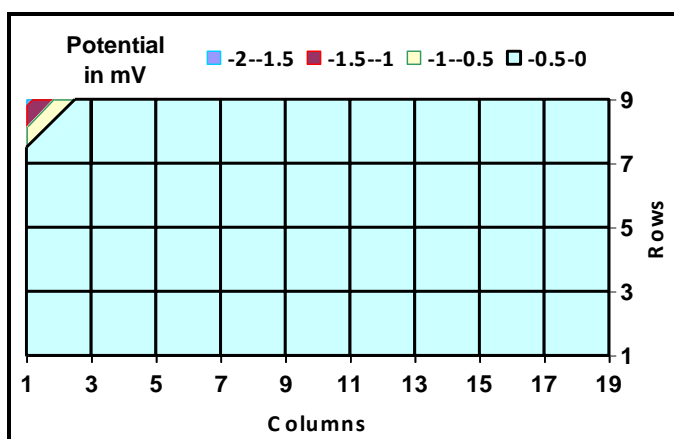


Fig. 6.15 Contour Map Showing Corrosion Status

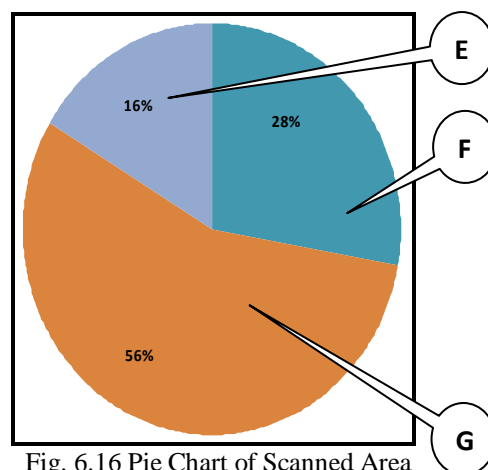


Fig. 6.16 Pie Chart of Scanned Area

6.9. Pier 8 B

100% area falls in ‘G’ category which indicates no noticeable corrosion activity in the scanned area of the pier.

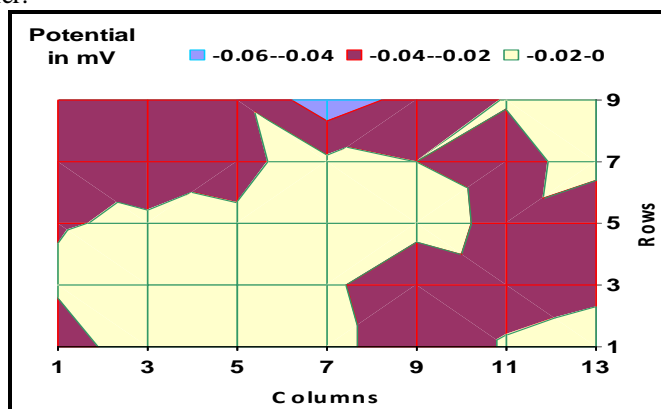


Fig. 6.17 Contour Map Showing Corrosion Status

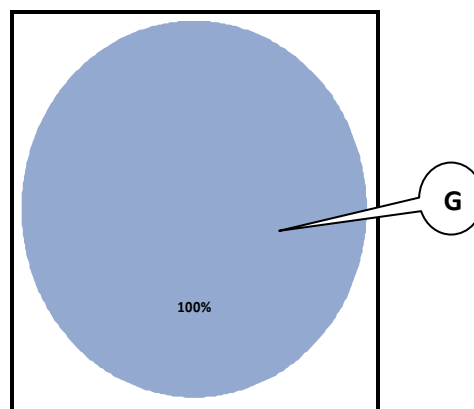


Fig. 6.18 Pie Chart of Scanned Area

6.10. Pier 9

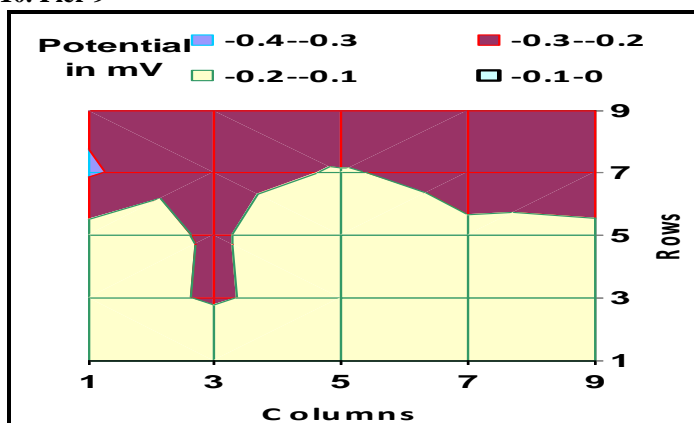


Fig. 6.19 Contour Map Showing Corrosion Status

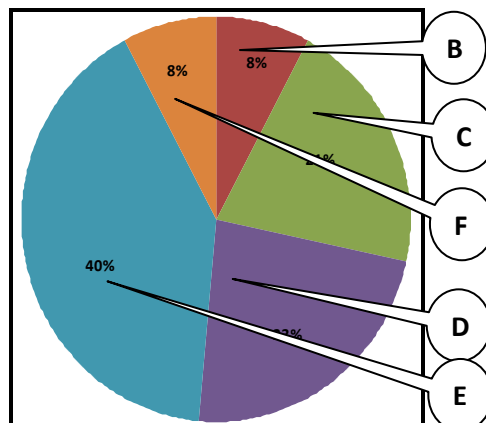


Fig. 6.20 Pie Chart of Scanned Area

6.11. Pier 10

5% scanned area fall under categories 'A' & 'B', depicting , 90% chance of corrosion is occurring in this area whereas 27% area fall under categories 'C' & 'D' showing uncertain corrosion activity. 68% area (49% in 'E', 16% in 'F' and 3% in 'G' categories) falls in area which are indicatives of no noticeable corrosion activity in the scanned area of the pier. The general look of exposed rebar shown in figure 1 is also evident of vigorous corrosion activities in the area.

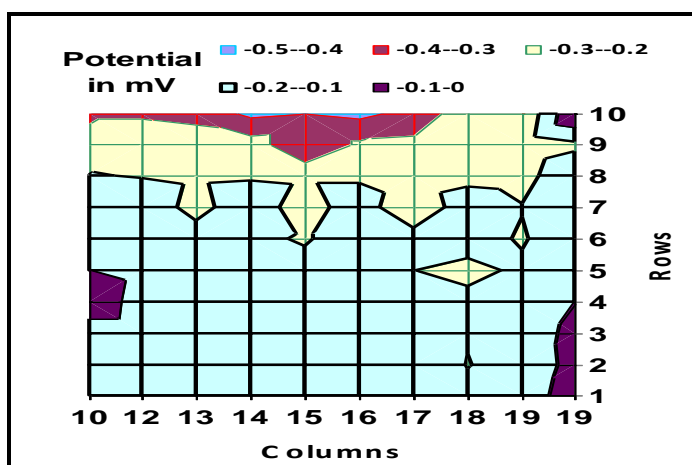


Fig. 6.21 Contour Map Showing Corrosion Status

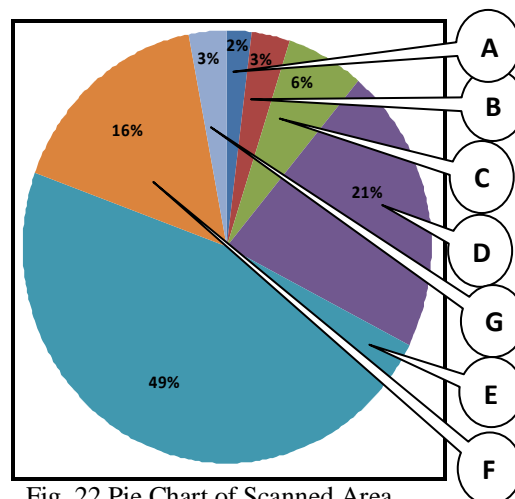


Fig. 22 Pie Chart of Scanned Area

VII. CONCLUSION

The Half Cell Potential Testing method is a technique, used for assessment of the durability of reinforced concrete and helps in diagnosing reinforcement corrosion. As per standard practices stated above, the test results shows that

- No corrosion activity is detected on pier no 4, 5, 8A and 8B.
- Corrosion activity has already initiated on the piers 1, 2, 3, 6, 7.
- Scanning result on pier no. 9 and 10 shows high degree of corrosion.

Since indications of deterioration of concrete and reinforcement have been observed a strict vigil through periodic monitoring of these piers should be kept using Non Destructive Tests.

Acknowledgements

The authors extend their sincere thanks to Director CSMRS for his constant inspiration. We also extend our sincere gratitude to Sh. Sohan Singh of CSMRS for his valuable efforts. We also extend our sincere gratitude to all the authors whose publications provided us directional information from time to time.

REFERENCES

- [1] Diagnosis of Deterioration of Concrete Structures- Identification of Defects, Evaluation and Development of Remedial Actions, *Concrete Society Camberley, UK, Technical Report 54*, (2000)
- [2] ASTM C 876-91 (Reapproved 1999), "Standard Test Method for Half-cell Potentials of Uncoated Reinforcing Steel in Concrete," *Annual Book of ASTM Standards, 03.02* (2006), 11-16.
- [3] RILEM TC 154-EMC, "Electrochemical Techniques for Measuring Metallic Corrosion" Recommendations, "Half-cell potential measurements – Potential mapping on reinforced concrete structures," *Materials and Structures*. 36 August - September (2003), 461-471.
- [4] Elsener, B. and Bohni, H., "Potential Mapping and Corrosion of Steel in Concrete," in "Corrosion Rates of Steel in Concrete," ASTM STP 1065, N.S. Berke, V. Chaker, D. Whiting eds. *American Society for Testing and Materials, Philadelphia* (1990), 143-156.
- [5] Stratfull, R. F., Jurkovich, and W. J., Spellman, D. L., "Corrosion Testing of Bridge Decks," *Highway Research Record 539, Washington, D. C., Transportation Research Board* (1975).
- [6] Clemena, G. G., "Benefits of Measuring Half-cell Potentials and Rebar Corrosion Rates in Condition Surveys of Concrete Bridge Decks," *Virginia Transportation Research Council* (1992).
- [7] JSCE-E 601-2000, "Test Method for Half-cell Potentials of Uncoated Rebars in Concrete Structures," Standard Specifications for Concrete Structures – 2002, Test Methods and Specifications, *Japan Society of Civil Engineers* (2002).
- [8] Pankaj Sharma et al, "Corrosion Monitoring Of Reinforcement in Underground Galleries of Hydro Electric Project" *Int. Journal of Engineering Research and Application*, Vol. 3, Issue 5, Sep-Oct 2013, pp.1087-1090.

Continuum Modeling Techniques to Determine Mechanical Properties of Nanocomposites

Sonali Gholap¹, Dr. Dhananjay R. Panchagade¹, Vinay Patil²

¹Mechanical Engg. Dept, D.Y.Patil College of Engineering, Akurdi, Pune, University of Pune, India

²Vaftsya CAE, Pune-411028, India, University of Pune, India

ABSTRACT: Nanotechnology offers fundamentally new capabilities to architect a broad array of novel materials, composites and structures on a molecular scale. A review of modeling techniques for predicting the mechanical behavior of nanocomposites is presented. A detailed discussion of Computational Chemistry and Computational Mechanics modeling techniques is given. The specific molecular-based and continuum based modeling approaches are described in terms of assumptions and theory. The analytical models discussed include Voigt and Reuss bounds, Hashin and Shtrikman bounds, Halpin-Tsai model, Cox model, and various Mori and Tanaka models. These micromechanics models predict stiffness of nanocomposites with both aligned and randomly oriented fibers. Three different approaches are discussed in finite element modeling, i.e. multiscale representative volume element (RVE) modeling, unit cell modeling, and object-oriented modeling.

Keywords: Finite element analysis (FEA), Nanocomposite, Mechanical properties, Multiscale modeling, Nanocomposite, Object-oriented modeling.

I. INTRODUCTION

Nanoscience and nanotechnology refer to the understanding and control of matter at the atomic, molecular or macromolecular levels, at the length scale of approximately 1 to 100 nanometers, where unique phenomena enable novel applications. Although experimental based research can ideally be used to determine structure-property relationships of nanostructured composites, experimental synthesis and characterization of nanostructured composites demands the use of sophisticated processing methods and testing equipment; which could result in exorbitant costs. To this end, computational modeling techniques for the determination of mechanical properties of nanocomposites have proven to be very effective. Computational modeling of nanocomposite mechanical properties renders the flexibility of efficient parametric study of nanocomposites to facilitate the design and development of nanocomposite structures for engineering applications. This review article will discuss the major modeling tools that are available for predicting the mechanical properties of nanostructured materials. Analytical and computational approaches to continuum-mechanics based modeling are discussed.

II. MODELING METHOD OVERVIEW

The importance of modeling in understanding of the behavior of matter is illustrated in Fig. 1. The earliest attempt to understanding material behavior is through observation via experiments. Careful measurements of observed data are subsequently used for the development of models that predict the observed behavior under the corresponding conditions. The models are necessary to develop the theory. The theory is then used to compare predicted behavior to experiments via simulation. This comparison serves to either validate the theory, or to provide a feedback loop to improve the theory using modeling data. Therefore, the development of a realistic theory of describing the structure and behavior of materials is highly dependent on accurate modeling and simulation techniques

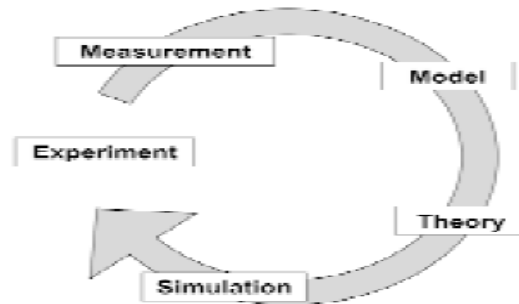


Fig. 1: Schematic of the process of developing theory and the validation of experimental data

Mechanical properties of nanostructured materials can be determined by a select set of computational methods. These modeling methods span a wide range of length and time scales, as shown in Fig. 2.

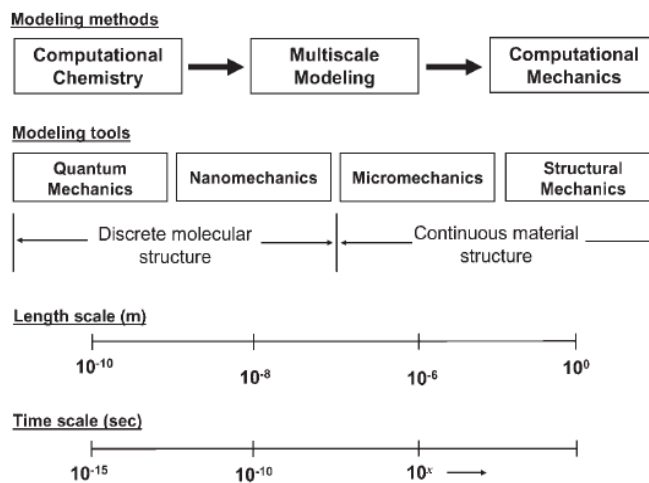


Fig. 2. Various length and time scales used in determining mechanical properties of polymer nanocomposites.

As indicated in Fig. 3, each modeling method has broad classes of relevant modeling tools. The continuum-based methods primarily include techniques such as the Finite Element Method (FEM), the Boundary Element Method (BEM), and the micromechanics approach developed for composite materials. Specific Micromechanical techniques include Eshelby approach, Mori-Tanaka method, Halpin-Tsai method.

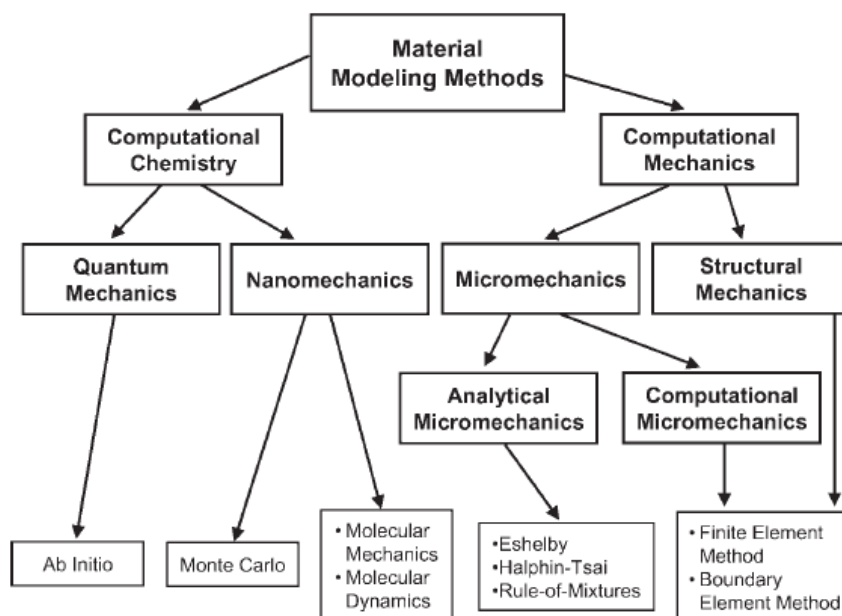


Fig. 3. Diagram of material modeling techniques.

III. CONTINUUM METHODS

3.1. Analytical continuum modeling

The popular micromechanical models for prediction of modulus of elasticity are summarized and discussed in the following:

3.1.1 Voigt upper bound and Reuss lower bound (V-R model)

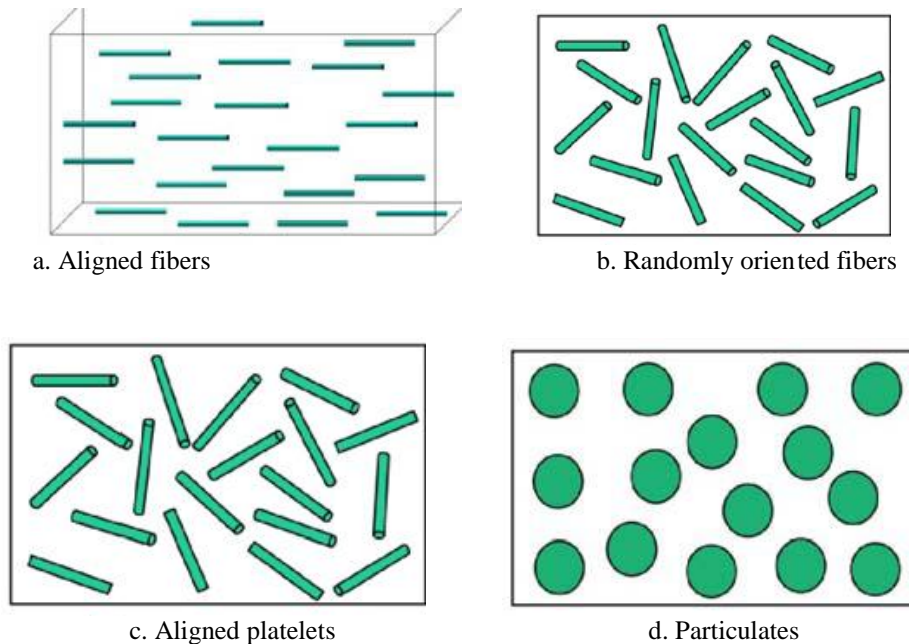
Assumed aligned fibers, and fibers and matrix are subjected to the same uniform strain in the fiber direction, Voigt got the effective modulus in the fiber direction as:

$$E_l = \varphi E_f + (1 - \varphi) E_m \quad (3.1)$$

Reuss applied the same uniform stress on the fiber and matrix in the transverse direction (normal to the fiber direction), and got the effective modulus in the transverse direction as:

$$\frac{1}{E_t} = \frac{\varphi}{E_f} + \frac{1 - \varphi}{E_m} \quad (3.2)$$

Where φ is the volume fraction of fiber in the two-phase composite system, and subscripts “f” and “m” respectively refer to the fiber and matrix, whereas the subscripts “L” and “T” refer to the longitudinal and transverse directions, respectively. Equation (3.1) is the parallel coupling, and it is also called the “rule of mixtures”, whereas (3.2) is the series coupling formula, and it is also called the “inverse rule of mixtures”.



a. Aligned fibers

b. Randomly oriented fibers

c. Aligned platelets

d. Particulates

Fig 4. Schematics of nanocomposites: (a) with aligned fibers; (b) with randomly oriented fibers; (c) with aligned platelets; and (d) with randomly oriented particulates

Equations (3.1) and (3.2) can be extended to any two-phase composites regardless the shape of

the filler, and E_L and E_T represent the upper and lower bounds of the modulus of the composite, respectively. Note that in these formulas, only three parameters are involved, i.e. modulus of the fiber and the matrix, and the fiber volume fraction.

3.1.2 Hashin and Shtrikman upper and lower bounds (H-S model)

Hashin and Shtrikman assumed macroscopical isotropy and quasi-homogeneity of the composite where the shape of the filler is not a limiting factor, and estimated the upper and lower bounds of the composite based on variational principles of elasticity. Depending on whether the stiffness of the matrix is more or less than that of the filler, the upper and lower bounds of the bulk moduli, *Kupper* and *Klower*, and shear moduli, *Gupper* and *Glower*, of the composite are given as

$$\begin{aligned}
 K_{upper} &= K_f + (1 - \phi) \left[\frac{1}{K_m - K_f} + \frac{3\phi}{3K_f + 4G_f} \right]^{-1} \\
 K_{lower} &= K_m + \phi \left[\frac{1}{K_f - K_m} + \frac{3(1 - \phi)}{3K_m + 4G_m} \right]^{-1} \\
 G_{upper} &= G_f + (1 - \phi) \left[\frac{1}{G_m - G_f} + \frac{6\phi(K_f + 2G_f)}{5G_f(3K_f + 4G_f)} \right]^{-1} \\
 G_{lower} &= G_m + \phi \left[\frac{1}{G_f - G_m} + \frac{6(1 - \phi)(K_m + 2G_m)}{5G_m(3K_m + 4G_m)} \right]^{-1}
 \end{aligned}
 \tag{3.3}$$

Where the subscripts “f” and “m” refer to the filler (fiber) and matrix, respectively. The upper and lower bounds of the elastic modulus can then be calculated using the following relation:

$$E = \frac{9K}{1 + 3K/G}
 \tag{3.4}$$

Similar to Voigt and Reuss models, H-S model only involves three parameters.

3.1.3 Halpin-Tsai model (H-T model)

For aligned fiber-reinforced composite materials, Halpin and Tsai developed the equations for prediction of elastic constants based on the work of Hermans and Hill. The H-T model is a semi-empirical model, and the longitudinal and transverse moduli are given by:

$$E_L = \frac{1 + 2(l/d)\phi\eta_L}{1 - \phi\eta_L} E_m
 \tag{3.5}$$

$$E_T = \frac{1 + 2\phi\eta_T}{1 - \phi\eta_T} E_m
 \tag{3.6}$$

where l and d are the length and diameter of the fiber, and η_L and η_T take the following expressions:

$$\begin{aligned}
 \eta_L &= \frac{E_f - E_m}{E_f + 2(l/d)E_m} \\
 \eta_T &= \frac{E_f - E_m}{E_f + 2E_m}
 \end{aligned}
 \tag{3.7}$$

For aligned nanoplatelets as shown in Fig.4 (c), equations (3.7) may still be used by replacing (l/d) with (D/t), where D and t are respectively the diameter and thickness of the platelet. H-T model takes the consideration of the fiber geometry, and has five independent parameters

3.1.4 Hui-Shia model (H-S model)

Mori and Tanaka developed analytical expressions for elastic constants based on the equivalent inclusion model of Eshelby. Taya and Mura and Taya and Chou used Mori-Tanaka approach to predict the longitudinal modulus of fiber-reinforced composites, Weng and Tandon and Weng further developed equations for the complete set of elastic constants of composite materials with aligned spheroidal isotropic inclusions. Based upon the results of Tandon and Weng, Hui and Shia and Shia et al. derived simplified formulas for predicting the overall moduli of composites with aligned reinforcements with emphases on fiber-like and flake-like reinforcements, and found that their theoretical predictions agree well with experimental results. The H-S model presents the Young’s modulus as follows:

$$E_L = E_m \left[1 - \frac{\phi}{\xi} \right]^{-1}$$

$$E_T = E_m \left[1 - \frac{\phi}{4} \left(\frac{1}{\xi} + \frac{3}{\xi + \Lambda} \right) \right]^{-1}$$

(3.8)

where

$$\xi = \phi + \frac{E_m}{E_f - E_m} + 3(1 - \phi) \left[\frac{(1 - g)\alpha^2 - g/2}{\alpha^2 - 1} \right]$$

$$\Lambda = (1 - \phi) \left[\frac{3(\alpha^2 + 0.25)g - 2\alpha^2}{\alpha^2 - 1} \right]$$

$$g = \begin{cases} \frac{\alpha}{(\alpha^2 - 1)^{3/2}} [\alpha\sqrt{\alpha^2 - 1} - \cosh^{-1} \alpha] & \alpha \geq 1 \\ \frac{\alpha}{(1 - \alpha^2)^{3/2}} [-\alpha\sqrt{1 - \alpha^2} + \cos^{-1} \alpha] & \alpha \leq 1 \end{cases}$$

(3.9)

and α is the aspect ratio of the filler, defined as the ratio of the filler's longitudinal (with Young's modulus EL) length to its transverse (with Young's modulus ET) length.

3.1.5 Wang-Pyrz model (W-P model)

For a composite material composed of an isotropic matrix and randomly oriented transversely isotropic spheroids, Qiu and Weng and Chen et al. gave the formulas for the overall bulk and shear moduli using the Mori-Tanaka method. These formulas are expressed in terms of the Eshelby tensor, thus are not final. Wang and Pyrz further gave the closed and concise formulas for the overall bulk modulus and shear modulus as follows:

$$K = K_m + K_m \frac{\phi\varphi}{1 - \phi(1 - \alpha)}$$

$$\mu = \mu_m + \mu_m \frac{\phi\psi}{1 - \phi(1 - \beta)}$$

(3.10)

The expressions for ϕ , ψ , α and β are given in the Appendix.

Note that W-P model is based on the Mori-Tanaka approach, and deals with the composite materials reinforced with randomly oriented and transversely isotropic spheroids. By varying the aspect ratio, the oblate spheroids can be approximate to platelets, and the prolate spheroids can be approximate to fibers.

3.1.6 Cox model (Shear lag model)

Shear lag model was the first micro-mechanics model for fiber-reinforced composites. Cox analyzed a single fiber of length l and radius r_f , which is encased in a concentric cylindrical shell of matrix having radius R . He derived the longitudinal modulus as

$$E_L = \eta_L \phi E_f + (1 - \phi) E_m$$

(3.11)

where η_L is a length-dependent efficiency factor,

$$\eta_L = 1 - \frac{\tanh(\beta l / 2)}{\beta l / 2}$$

(3.12)

With

$$\beta^2 = \frac{4\mu_m}{r_f^2 E_f \ln(K_R / \phi)}$$

(3.13)

K_R is a constant that depends on the fiber packing arrangements. For some typical fiber packing arrangements, the values of K_R are given in Table 1

Table 1. Values for K_R in Eq. (3.13)

FIBER PACKING	K_R
Cox	$2\pi / \sqrt{3} = 3.628$
Composite cylinders	1.000
Hexagonal	$\pi / 2\sqrt{3} = 0.907$
Square	$\pi / 4 = 0.785$

It is well known that the orientation of the dispersed phase has a dramatic effect on the composite modulus. It is apparent from their geometry that flake-like platelets can provide equal reinforcement in two directions, if appropriately oriented, while fibers provide primary reinforcement in one direction. If the longitudinal modulus E_L and the transverse modulus E_T are known, then the effective modulus of the composite with randomly oriented fibers and platelets in all three orthogonal directions are given by,

$$E_{3D}^{fiber} = 0.184E_L + 0.816E_T$$

$$E_{3D}^{platelet} = 0.49E_L + 0.51E_T$$

(3.14)

3.2. Computational continuum modeling

Continuum-based computational modeling techniques include FEM and BEM. While these approaches do not always supply exact solutions, they can provide very accurate estimates for a wide range of assumptions. These approaches are described in detail below.

3.2.1. Finite element method: FEM can be used for numerical computation of bulk properties based on the geometry, properties, and volume fraction of constituent phases. In the following, three finite element modeling approaches will be discussed. They are multiscale representative volume element (RVE) modeling, unit cell modeling, and object-oriented modeling.

Multiscale RVE modeling: FEM involves discretization of a material representative volume element (RVE) into elements for which the elastic solutions lead to determination of stress and strain field. The coarseness of the discretization determines the accuracy of the solution. Nanoscale RVEs of different geometric shapes can be chosen for simulation of mechanical properties. However, high complexity of models, expensive software, and time-consuming simulations limit the utility of this method.

Unit cell modeling: The conventional unit cell concept is the same as the RVE. Here we define a unit cell as a special RVE that it has a relatively big size (usually in micrometers) and contains a significant number of fillers (usually in tens to hundreds or more). Such defined unit cell is still the building block of the composite, but as it gets more complicated, analytical models are difficult to establish or too complicated to solve, and numerical modeling and simulation become a necessity.

Object-oriented modeling: The object-oriented modeling which is able to capture the actual microstructure morphology of the nanocomposites becomes necessary in order to accurately predict the overall properties. It incorporates the microstructure images such as scanning electron microscopy (SEM) micrographs into finite element grids. Thus the mesh reproduces exactly the original microstructure, namely the inclusions size, morphology, spatial distribution, and the respective volume fraction of the different constituents. An object-oriented finite element code, developed by National Institute of Standards and Technology (NIST), has been extensively used in analyzing fracture mechanisms and material properties of heterogeneous materials and mechanical properties of nanocomposites.

3.2.2 Boundary element method

BEM is a continuum mechanics approach which involves solving boundary integral equations for the evaluation of stress and strain fields. This method uses elements only along the boundary, unlike FEM, which involves elements throughout the volume; thus making BEM less computationally exhaustive than FEM. BEM

can be applied from micro to macro scale modeling . In BEM, it is assumed that a material continuum exists, and therefore, the details of molecular structure and atomic interactions are ignored.

IV. CONCLUSION

The modeling and simulation of polymer-based nanocomposites has become an important topic in recent times because of the need for the development of these materials for engineering applications. A review of the most widely used modeling techniques used for prediction of mechanical properties of polymer nanocomposites has been presented in this paper. Because of the complex interactions between constituent phases at the atomic level, a combination of modeling techniques is often required to simulate the bulk-level behavior of these composites. The Computational Chemistry techniques assume the presence of a discrete molecular structure, and are primarily used to predict the atomic structure of a material. Computational Mechanics techniques assume that the matter is composed of one or more continuous constituents, and are used to predict the mechanical behavior of materials and structures. These two types of modeling techniques must be combined to an overall multiscale mode that is capable of predicting the structure and properties of polymer nanocomposites based on fundamental and scientific principles.

REFERENCES

- [1] Hurang Hu, Landon Onyebueke, Ayo Abatan “Characterizing and Modeling Mechanical Properties of Nanocomposites- Review and Evaluation”, *Journal of Minerals & Materials Characterization & Engineering*, Vol. 9, No.4, pp.275-319, 2010.
- [2] P.K. Valavala and G.M. Odegard “Modeling Techniques for Determination of Mechanical Properties of Polymer Nanocomposites” , *Revised Advanced Material.Science*, 9 (2005) 34-44.
- [3] Leon L. Mishnaevsky Jr and Siegfried Schmauder “Continuum mesomechanical finite element modeling in materials development: A state-of-the-art review”, *ASME Reprint No AMR301, Appl Mech Rev* vol. 54, no 1, January 2001
- [4] T.S. Gates, G.M. Odegard, S.J.V. Frankland, T.C. Clancy, “Computational materials: Multi-scale modeling and simulation of nanostructured materials”, *Composites Science and Technology*, 65, 2416–2434, 2005

A New Method Based On the Comparison of the Unique Chain Code to Detect Isomorphism among Kinematic Chains

Syed Shane Haider Rizvi¹, Dr. Ali Hasan², Prof.R.A.Khan³

¹Research Scholar Mech Engg Deptt, F/o Engg & Tech Jamia Millia Islamia, New Delhi.

²Assistant Professor Mech Engg Deptt, F/o Engg & Tech Jamia Millia Islamia, New Delhi.

³Professor, Mech Engg Deptt, Galgotia University, G.Noida

ABSTRACT: This paper presents a new method for the detection of isomorphism in kinematic chains which plays an important role in structural synthesis of kinematic chains. The proposed method uses a new invariant i.e. a unique chain codec based on the degree of links and used as an identifier of a kinematic chain (KC). The proposed method is easy to compute, reliable and capable of detecting isomorphism in all types of KC, i.e. chains of single or multi degree of freedom with simple joints. This study will help the designer to select the best KC and mechanisms to perform the specified task at conceptual stage of

Keywords: Degree of freedom, Isomorphism, Invariant, Mechanisms, Kinematic chain (KC)

I. INTRODUCTION

One of the most difficult tasks in structural synthesis of kinematic chain is to check the isomorphism among two chains. The two kinematic chains KC1 and KC2 are said to be isomorphic, if there exists a one to one correspondence between the links of KC1 and KC2.

The detection of isomorphism among two kinematic chains with same link assortment is necessary to prevent duplication and omission of a potential useful chain. A lot of time and effort had been devoted in developing a reliable and computationally efficient technique; therefore a wealth of literature pertaining with this topic is available. However, there is a scope for an efficient, simple and reliable method and this paper is an attempt in this direction. Heuristic and visual methods [1] were only suitable for kinematic chains with a small number of links. Characteristic polynomial method [2] has the disadvantage of dealing with cumbersome calculations and later counter examples were also reported [3]. Quist and Soni presented a method of loops of a chain [4]. A unique index for isomorphism i.e. characteristic polynomial of structural matrix was proposed by Yan and Hwang [5], however this method is computationally uneconomical. Mruthyunjaya proposed the computerized method of structural synthesis which works on binary coding of chains [6]. Agarwal and Rao proposed Variable permanent function to identify multi loop kinematic chains [7]. Ambekar and Agarwal presents a method of Canonical coding of kinematic chains [8] but it becomes computationally uneconomical when applied to large kinematic chain. Hamming number technique [9] is very reliable and computationally efficient, however when the primary Hamming string fails, the time consuming computation of the secondary Hamming string is needed. Shin and Krishna Murthy presents some rules for relabeling its vertices canonically for a given kinematic chain [10]. However it tends to become computationally inefficient where a higher number of symmetry group elements in the kinematic chain are present. The degree code [11] of the contracted link adjacency matrix of a chain was also proposed to test the isomorphism. Yadav and Pratap present a method of link distance for the detection of isomorphism [12]. A method based on artificial neural network theory by Kong et al. was presented [13]. A method based on loop formations of a kinematic chain was proposed by Rao and Prasad [14]. A new method based on eigenvalues and eigenvectors of adjacent matrices of chains was also proposed [15]. The reliability of the existing spectral techniques for isomorphism detection was challenged by Sunkari, R.P., and Schmidt [16]. Huafeng Ding and Zhen Huang [17] shows that the characteristic polynomial and eigen value approach fails and proposed a method based on the perimeter topological graph and some rules for relabeling its vertices canonically and one-to-one descriptive method for the canonical adjacency matrix set of kinematic chains Hasan and Khan [18] presented a method based on degrees of freedom of kinematic pairs. All the above methods developed so far only uses the graphs of the KC or their adjacency matrices in one or the other way. The method presented in this paper uses 'connection string' to detect isomorphism in KCs.

II. PRELIMINARIES

The following definitions are to be understood clearly before applying this method.

(i) **Degree of link:** Degree of a particular link depends upon its type the degree of a binary link is 2, the degree of a ternary link is 3, and the degree of a quaternary link is 4 and so on.

(ii) **Adjacency Matrix:** A matrix which reveals the connectivity pattern of the kinematic chain is known as adjacency matrix and can be formed in the following manner

$$A=[a_{ij}] \tag{1}$$

$a_{ii} = 0$, since a link- i cannot connect to itself.

$a_{ij} = 1$, if link- i is directly connected to link- j .

$a_{ij} = 0$, if the vertices i and j are not directly connected.

(iii) **Instantaneous Centre:** The combined motion of rotation and translation of the link may be assumed to be a motion of pure rotation about some centre, known instantaneous centre of rotation. The number of instantaneous centres of a mechanism is given by the relation given below

$$\text{Number of I Centers} = \frac{N(N-1)}{2} \tag{2}$$

Where N is the number of links in the chain

(iv) **Unique Chain Code:** The unique chain code is a number rounded off to the nearest whole number which can be calculated by the formula given in the equation below

$$\text{Unique Chain Code} = N \sum_{i=1}^{i=N} \frac{\text{Number of I centers of the chain}}{S_i} \tag{3}$$

S_i is the sum of the degrees of the links connected to the i^{th} link

III. ISOMORPHISM DEFINITION

Two kinematic chains are said to be isomorphic if there is a one-to-one correspondence between the links of one chain to those of the other chain. If there is no such correspondence between the links of the two chains they are considered to be non-isomorphic.

IV. IDENTIFICATION OF ISOMORPHISM

If the unique codes and the sum of the characteristics polynomial of the adjacency matrices of the two kinematic chains are same then it is said that the two chains has one to one correspondence then the two chains are isomorphic or otherwise. Although no mathematical proof of this method is being offered but no counter example has been found by the author among the known cases of planar kinematic chains. If in any case the unique codes are same but the sum of the characteristics polynomial of the adjacency matrices are not same then both the chains will be coded with the same numerical code followed by the '-1' and '-2'. For example if the code for two chains is 345 then they will be coded as 345-1 and 345-2

V. APPLICATION TO KINEMATIC CHAINS

The proposed method for isomorphism detection in this paper is tested on several kinematic chains available in the literature and found that it works well in all cases. Three examples of ten links kinematic chains are shown below to reveal the reliability of the method

Example 1:- The two Kinematic chains with 10 links, single-degree of freedom shown in Fig 1(a) and (b). The aim is to examine whether these two KC are isomorphic as reported in the literature [13].

The value of unique chain code for both the chains shown in Fig 1(a) and (b) comes out to be 638 as determined by the relation (3), and the sum of the absolute characteristic polynomials of the adjacency matrices A_1 and B_1 is 146 which reveals that the two chains are isomorphic which is already proved by other researchers and now our method also gives the same result.

Example 2:- The two Kinematic chains with 10 links, single degree of freedom having same characteristic polynomials for their adjacency matrices are shown in Fig 2(a) and 2(b) The aim is to examine whether these two KC are non-isomorphic as reported in the literature [3].

The value of unique chain code for both the chain shown in Fig 2(a) is 775 and Fig 2(b) is 770 as determined by the relation (3), the sum of the absolute characteristic polynomials of the adjacency matrices A_2 and B_2 is 238 which reveals that the two chains are nonisomorphic because one of two the necessary conditions for isomorphism proposed in this paper is not satisfied hence our method also gives the same result as already proved by other researchers.

$$\begin{matrix}
 A1= & \begin{pmatrix} 0 & 1 & 0 & 0 & 0 & 0 & 1 & 1 & 1 & 0 \\ 1 & 0 & 1 & 0 & 0 & 0 & 0 & 0 & 0 & 0 \\ 0 & 1 & 0 & 1 & 0 & 0 & 0 & 0 & 1 & 0 \\ 0 & 0 & 1 & 0 & 1 & 0 & 0 & 0 & 0 & 1 \\ 0 & 0 & 0 & 1 & 0 & 1 & 0 & 0 & 0 & 1 \\ 0 & 0 & 0 & 0 & 1 & 0 & 1 & 0 & 0 & 0 \\ 1 & 0 & 0 & 0 & 0 & 1 & 0 & 1 & 0 & 0 \\ 1 & 0 & 0 & 0 & 0 & 1 & 0 & 0 & 0 & 0 \\ 1 & 0 & 0 & 0 & 0 & 1 & 0 & 0 & 0 & 0 \\ 1 & 0 & 1 & 0 & 0 & 0 & 0 & 0 & 0 & 1 \\ 0 & 0 & 0 & 1 & 0 & 0 & 0 & 0 & 1 & 0 \end{pmatrix} & B1= & \begin{pmatrix} 0 & 1 & 0 & 0 & 0 & 0 & 1 & 1 & 1 & 0 \\ 1 & 0 & 1 & 0 & 0 & 0 & 0 & 0 & 0 & 1 \\ 0 & 1 & 0 & 1 & 0 & 0 & 0 & 0 & 0 & 0 \\ 0 & 0 & 1 & 0 & 1 & 0 & 0 & 0 & 0 & 1 \\ 0 & 0 & 0 & 1 & 0 & 1 & 0 & 0 & 0 & 1 \\ 0 & 0 & 0 & 0 & 1 & 0 & 1 & 0 & 0 & 0 \\ 1 & 0 & 0 & 0 & 0 & 1 & 0 & 1 & 0 & 0 \\ 1 & 0 & 0 & 0 & 0 & 1 & 0 & 0 & 0 & 0 \\ 1 & 0 & 0 & 0 & 0 & 1 & 0 & 0 & 0 & 0 \\ 1 & 0 & 1 & 0 & 0 & 0 & 0 & 0 & 0 & 1 \\ 0 & 1 & 0 & 1 & 0 & 0 & 0 & 0 & 1 & 0 \end{pmatrix} & A2= & \begin{pmatrix} 0 & 1 & 0 & 1 & 1 & 0 & 0 & 1 & 0 & 0 \\ 1 & 0 & 1 & 0 & 0 & 0 & 0 & 0 & 1 & 0 \\ 0 & 1 & 0 & 1 & 0 & 0 & 0 & 0 & 0 & 1 \\ 0 & 0 & 0 & 1 & 0 & 1 & 0 & 0 & 0 & 1 \\ 1 & 0 & 1 & 0 & 0 & 0 & 0 & 0 & 0 & 1 \\ 1 & 0 & 0 & 0 & 0 & 1 & 0 & 0 & 0 & 1 \\ 0 & 0 & 0 & 0 & 0 & 1 & 0 & 1 & 0 & 0 \\ 1 & 0 & 0 & 0 & 0 & 1 & 0 & 1 & 0 & 0 \\ 0 & 0 & 0 & 0 & 0 & 1 & 0 & 1 & 0 & 0 \\ 1 & 0 & 0 & 0 & 0 & 1 & 0 & 0 & 0 & 0 \\ 0 & 1 & 0 & 0 & 0 & 1 & 0 & 0 & 0 & 0 \\ 0 & 0 & 1 & 0 & 1 & 0 & 0 & 0 & 0 & 0 \end{pmatrix} & B2= & \begin{pmatrix} 0 & 1 & 0 & 1 & 1 & 0 & 0 & 0 & 0 & 0 \\ 1 & 0 & 1 & 0 & 0 & 0 & 0 & 1 & 0 & 1 \\ 0 & 1 & 0 & 0 & 0 & 1 & 1 & 0 & 0 & 0 \\ 1 & 0 & 0 & 0 & 0 & 1 & 0 & 0 & 0 & 0 \\ 1 & 0 & 0 & 0 & 0 & 1 & 0 & 0 & 0 & 0 \\ 0 & 0 & 1 & 0 & 1 & 0 & 0 & 0 & 0 & 0 \\ 0 & 0 & 0 & 1 & 0 & 1 & 0 & 0 & 0 & 0 \\ 0 & 0 & 0 & 1 & 0 & 0 & 0 & 0 & 1 & 0 \\ 0 & 0 & 0 & 0 & 0 & 1 & 1 & 0 & 1 & 1 \\ 0 & 1 & 0 & 0 & 0 & 0 & 0 & 1 & 0 & 1 \end{pmatrix}
 \end{matrix}$$

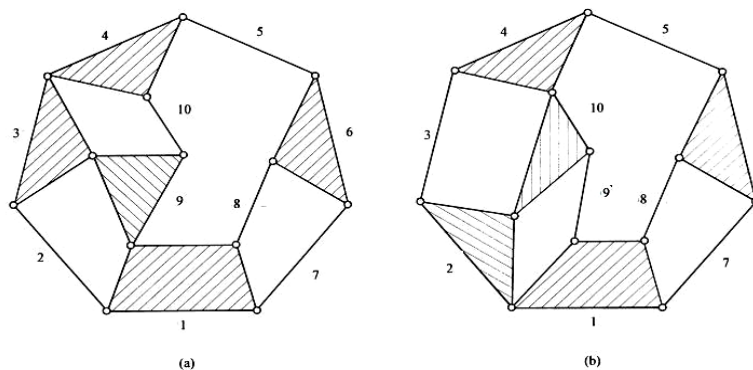


Fig. 1(a) and 1(b): The two ten link chains with single degree of freedom

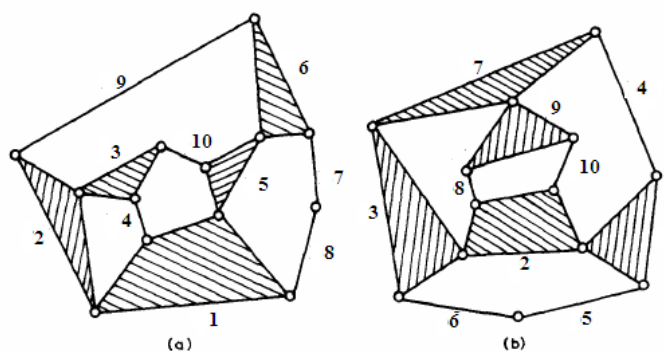


Fig. 2(a) and 2(b): The two ten link chains with single degree of freedom having same characteristic polynomial for their adjacency matrix.

Example 3:- The two Kinematic chains with two 10 link three degree of freedom, having same characteristic polynomials for their adjacency matrices are shown in Figs 3(a) and 3(b). The aim is to examine whether these two KC are non-isomorphic as reported in the literature [3].

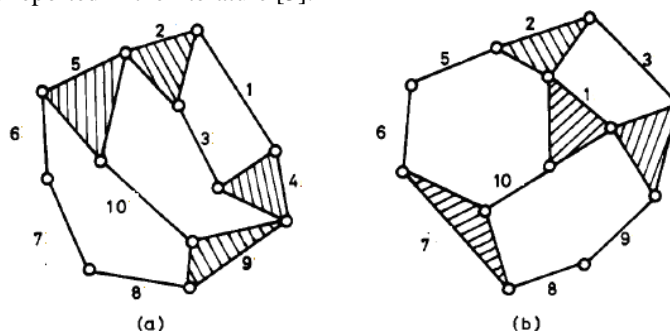


Fig. 3(a) and (b): The two ten link chains with three degree of freedom having same characteristic polynomial for their adjacency matrix.

$$A3 = \begin{pmatrix} 0 & 1 & 0 & 1 & 1 & 0 & 0 & 1 & 0 & 0 \\ 1 & 0 & 1 & 0 & 0 & 0 & 0 & 0 & 1 & 0 \\ 0 & 1 & 0 & 1 & 0 & 0 & 0 & 0 & 0 & 1 \\ 1 & 0 & 1 & 0 & 0 & 0 & 0 & 0 & 0 & 0 \\ 1 & 0 & 0 & 0 & 0 & 1 & 0 & 0 & 0 & 1 \\ 0 & 0 & 0 & 0 & 1 & 0 & 1 & 0 & 1 & 0 \\ 0 & 0 & 0 & 0 & 0 & 1 & 0 & 1 & 0 & 0 \\ 1 & 0 & 0 & 0 & 0 & 0 & 1 & 0 & 0 & 0 \\ 0 & 1 & 0 & 0 & 0 & 1 & 0 & 0 & 0 & 0 \\ 0 & 0 & 1 & 0 & 1 & 0 & 0 & 0 & 0 & 0 \end{pmatrix} \quad B3 = \begin{pmatrix} 0 & 1 & 0 & 1 & 1 & 0 & 0 & 0 & 0 & 0 \\ 1 & 0 & 1 & 0 & 0 & 0 & 0 & 0 & 1 & 0 \\ 0 & 1 & 0 & 0 & 0 & 1 & 1 & 0 & 0 & 0 \\ 1 & 0 & 0 & 0 & 0 & 1 & 0 & 0 & 0 & 0 \\ 1 & 0 & 0 & 0 & 0 & 1 & 0 & 0 & 0 & 0 \\ 0 & 0 & 1 & 0 & 1 & 0 & 0 & 0 & 0 & 0 \\ 0 & 0 & 1 & 1 & 0 & 0 & 0 & 0 & 1 & 0 \\ 0 & 1 & 0 & 0 & 0 & 0 & 0 & 0 & 1 & 0 \\ 0 & 0 & 0 & 0 & 0 & 0 & 1 & 1 & 0 & 1 \\ 0 & 1 & 0 & 0 & 0 & 0 & 0 & 0 & 1 & 0 \end{pmatrix}$$

The value of unique chain code for the chain shown in Fig 3(a) is 653 and Fig 3(b) is 655 as determined by the relation (3), and the sum of the absolute characteristic polynomials of the adjacency matrices A3 and B3 is 238 reveals that the two chains are nonisomorphic because one of two the necessary conditions for isomorphism proposed in this paper is not satisfied hence our method also gives the same result as already proved by other researchers.

Example 4:- The two Kinematic chains having 8 links single degree of freedom, were proven isomorphic by cubllio[19], are shown in Figs 4(a) and 4(b). The aim is to examine whether these two KC are non-isomorphic as reported in the literature.

The value of unique chain code for the chain shown in Fig 3(a) & 3(b) is 284 as determined by the relation (3) and the sum of the absolute characteristic polynomials of the adjacency matrices A4 and B4 is 74 hence the necessary conditions for isomorphism proposed in this paper is are satisfied so the two chains are isomorphic which shows the reliability our method as the proposed gives the same result that is available in the literature.

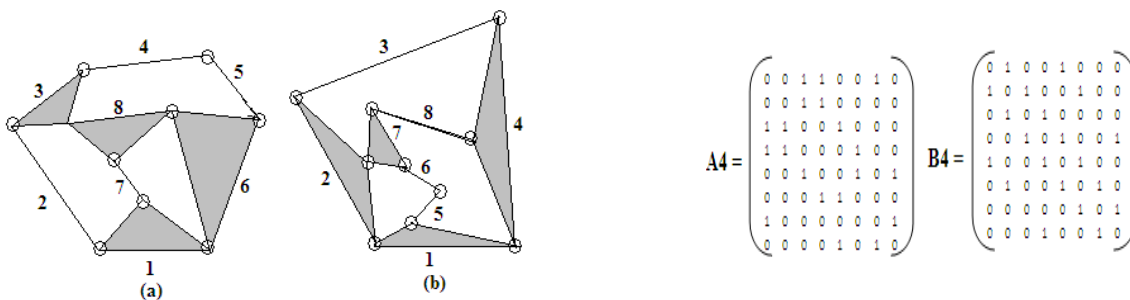


Fig-4(a) & (b): eight link isomorphic chains

Table-I: 16 Different Possible Combinations for 8 Link Single Degree of Freedom Chain.

S.No	KINEMATIC GRAPH OF THE CHAIN	SUM OF ABS CHAR POLY	CHAIN CODE	S.No	KINEMATIC GRAPH OF THE CHAIN	SUM OF ABS CHAR POLY	CHAIN CODE
1		12	379	9		45	291-2
2		72	279	10		51	268

3		52	277	11		70	270
4		74	284	12		38	283
5		12	1045	13		59	279
6		43	293	14		45	280
7		56	285	15		68	261
8		87	291-1	16		52	269

VI. RESULTS

The proposed method can detect isomorphism among all kinematic chains of single or multi degree of freedom having simple joints, up to 10-links. All 16 eight-bar single-DOF kinematic chains which are shown in 'Table-I' with their unique codes, 40 nine-bar two-DOF kinematic chains, 98 ten-bar three DOF kinematic chains and 230 ten-bar single-DOF kinematic chains have been tested with this method and no counterexamples have been found.

VII. CONCLUSIONS

The reliability of this method is based on the fact it has been found to be successful in not only distinguishing all known 16 kinematic chains of 8-links, 230 kinematic chains of 10-links having 1-degree of freedom and 40 kinematic chains of 9-links 2-degree of freedom but also on all the counter examples reported earlier literature. The method is so simple that one can detect isomorphism without computer program, whereas most of the methods developed so far requires sophisticated algorithms.

REFERENCES

- [1] T.H. Davies and F.E. Crossley; "Structural analysis of plane linkages by Franke's condensed notation", J. Mech., Vol. 1(2), pp. 171-183, 1966.
- [2] J.N. Yadav and C.R. Pratap; "Computer aided detection of isomorphism among kinematic chains and mechanisms using the link-link multiplicity distance concept", Mech. Mach. Theory, Vol. 31(4), pp. 873-877, 1996. DOI:0094-114X(95)0078X
- [3] T.S. Mruthyunjaya and H.R. Balasubramanian; "In quest of reliable and efficient computational test for detection of isomorphism in kinematic chains", Mech. Mach. Theory, Vol. 22(2), pp. 131-139, 1987. DOI:0094-114X/87
- [4] F.F. Quist and A.H. Soni; "Structural synthesis and analysis of kinematic chains using path matrices", In. Proceedings of the 3rd World Congress for Theory of Machines and Mechanisms, pp. D161-D176, 1971.
- [5] H.S. Yan and W.M. Hwang; "A method for identification of planar linkage Chains", J. Mech. Tran. Auto. Des. ASME Trans., Vol. 105(4), pp. 658-662, 1983.

- [6] T.S. Mruthyunjaya; "A computerized methodology for structural synthesis of kinematic chains: Part 1- formulation", *Mech. Mach. Theory*, Vol. 19(6), pp. 487–495, 1984.
- [7] V.P. Agarwal and J.S. Rao; "Identification of multi-loop kinematic chains and their paths", *J. Int. Eng. (I) ME*, Vol. 66, pp. 6-11, 1985.
- [8] A.G. Ambekar and V.P. Agarwal; "Canonical numbering of kinematic chains, mechanisms, path generators and function generators using min codes", *Mech. Mach. Theory*, Vol. 22(5), pp. 453-461, 1987.
- [9] A.C. Rao and D. Raju Varda; "Application of the hamming number technique to detect isomorphism among kinematic chains and inversions", *Mech. Mach. Theory*, Vol. 26(1), pp. 55-75, 1991.
- [10] J.K. Shin and S. Krishna Murthy; "On identification and conical numberings of pin jointed kinematic chains", *J. Mech. Des ASME*, Vol. 116(1), pp. 182-188, 1994. <http://dx.doi.org/10.1115/1.2919344>
- [11] W.M. Hwang and Y.W. Hwang; "Computer aided structural synthesis of planar kinematic chains with simple joints", *Mech. Mach. Theory*, Vol. 27(2), pp. 189–199, 1992.
- [12] J.N. Yadav, C.R. Pratap and V.P. Agrawal; "Computer aided detection of isomorphism among kinematic chains and mechanisms using the link-link multiplicity distance concept", *Mech. Mach. Theory*, Vol. 31(7), pp. 873–877, 1996.
- [13] F.G. Kong, Q. Li and W.J. Zhang; "An artificial neural network approach to mechanism kinematic chain isomorphism identification", *Mech. Mach. Theory*, Vol. 34(2), pp. 271–283, 1999. DOI:S0094-114X(01)00084-2
- [14] A.C. Rao and V.V.N. Raju Prasad; "Loop based detection of isomorphism among chains, inversions and type of freedom in multi degree of freedom chain", *J. Mech. Des.*, Vol. 122(1), pp. 31-41, 2000. DOI:S1050-0472-00!70801-4
- [15] Z. Chang, C. Zhang, Y. Yang and Y. Wang; "A new method to mechanism kinematic chain isomorphism Identification", *Mech. Mach. Theory*, Vol. 37(4), pp. 411–417, 2002. DOI:S0094-114X(01)00084-2
- [16] R.P. Sunkari and L.C. Schmidt; "Reliability and efficiency of the existing spectral methods for isomorphism detection", *J. Mech. Des.*, Vol. 128(6), pp. 1246–1252, 2006. DOI: 10.1115/1.2336253
- [17] H. Ding and Z. Huang; "The establishment of the canonical perimeter topological graph of kinematic chains and isomorphism identification", *J. Mech. Des.*, Vol. 129(9), pp. 915–923, 2007. DOI: 10.1115/1.2748451
- [18] A. Hasan and R.A. Khan; "Isomorphism and inversions of kinematic chains up to ten links using degrees of freedom of kinematic pairs", *Int. J. Comp. Methods*, Vol. 5(2), pp. 329–339, 2008. DOI: 10.1142/S0219876208001492
- [19] J.P. Cubillo and Jinbao Wan; "Comments on mechanism kinematic chain isomorphism identification using adjacent matrices" *Mech. Mach. Theory*, Vol. 40(2), pp. 131–139, 2005.

Turnstile S-Shaped Dipole and Swastika Wire Antennas for VHF and UHF Applications

Dr. Mustafa H. Abu Nasr¹, Prof. Samy S. Abu Naser²

¹Engineering Department, Faculty of Engineering and Information Technology, Al- Azhar University, Gaza, Palestine.

²Information Technology Department, Faculty of Engineering and Information Technology, Al- Azhar University, Gaza, Palestine.

ABSTRACT: New wire antennas are proposed, namely turnstile S -Shaped dipole and Swastika wire antenna. The radiation characteristics are obtained using the method of moments (MoM) with one-volt delta gap source and suitable dimensions for these antennas. From the obtained characteristics these antenna are considered of wide bandwidth. The proposed Swastika antenna and turnstile S-Shaped dipole antenna radiate left circularly polarized (LCP) waves. Right circularly polarized (RCP) waves are obtained using the inverted Swastika antenna and inverted turnstile S-Shaped dipole antenna. Swastika antenna and turnstile S-Shaped dipole antenna with comparison with turnstile dipole with the same absolute length have superiority performance of radiation characteristics in addition to save up to 75% of the area that the antennas can occupy. The given discussions proved the feasibility of using such antennas in a wide range of applications in the VHF and UHF frequency ranges both in free space and with a perfect grounded conducting plane. In this paper commercial software (NEC-win professional) is used to obtain all the radiation characteristics of the proposed antennas.

Keywords: The method of moments (MoM), Turnstile arrangement, Wire antennas

I. INTRODUCTION

Wire antennas are of spread use in the HF, VHF and UHF frequency ranges. They can be made from either solid wire or tubular conductors. They are relatively simple in concept, easy to construct and inexpensive. They are most widely used antennas for wireless mobile communication systems. Arrays of dipoles-the famous form of the wire antennas- are commonly used as base-station antennas in mobile systems. They have attractive features such as simple construction, relatively broadband characteristics, and small dimensions at high frequencies. The Loop antennas form another wire antenna type, which features simplicity, low cost and versatility. Loop antennas can have various shapes, namely circular, triangular, square, elliptical, etc. They are widely used in applications up to the UHF band. [1, 4]

The S-Shaped wire antenna-new form of wire antennas- which can radiate left elliptically polarized (LEP) waves. Right elliptically polarized (REP) waves are obtained using the inverted S-Shaped wire antenna. Also circular polarization of both senses is obtained using the turnstile arrangement and the Swastika antenna. The MoM solution is a numerical procedure for solving the electric field integral equation. Basis functions are chosen to represent the unknown currents (i.e., triangular basis functions). Testing functions are chosen to enforce the integral equation on the surface of the wires. With the choice of basis and testing functions, a matrix approximating the integral equation is derived. If this matrix is inverted and multiplied by the local sources of electric field, the complex magnitudes of the current basis functions are derived. All antenna performance parameters can be determined from the derived current distribution. In this paper commercial software (NEC-win professional) is used to obtain all the radiation characteristics of the proposed S-shaped antennas and Swastika antenna. [5,6]

II. METHOD OF MOMENTS

The Method of Moments (MoM) is a well-known technique for solving linear equations. In antenna analysis, the MoM is used to convert the electric field integral equation into a matrix equation or system of linear equations. The matrix equation can then be solved for the current coefficients by LU decomposition, Gaussian elimination, or other techniques of linear algebra. The following development is based on the work by [5,6]

The basic form of the equation to be solved by the MoM is

$$L(u) = f \tag{1}$$

where L is the linear operator, u is the unknown function, and f is the source or forcing function. In order to create the matrix equation, the unknown function is defined to be the sum of a set of known independent functions, u_n called basis or expansion functions with unknown amplitudes α_n ,

$$u = \sum_n \alpha_n u_n \tag{2}$$

Using the linearity of the operator, L the unknown amplitudes can be brought out of the operator giving

$$\sum_n \alpha_n L(u_n) = f \tag{3}$$

The unknown amplitudes cannot yet be determined because there are n unknowns, but one functional equation. A fixed set of equations are found by defining independent weighting or testing functions, w_m , which are integrated with (3) to give m different linear equations. The integration of the weighting functions with (3) may be written symbolically as the inner product of the two functions, giving

$$\sum_n \alpha_n \langle w_m, L(u_n) \rangle = \langle w_m, f \rangle, \tag{4}$$

Where the inner product $\langle a, b \rangle$ is defined to be the integral of the two functions over the domain of the linear operator. Now there are an equal number of unknowns and independent equations, which allow for the solution of the unknown amplitudes α_n .

For antenna problems, the matrix equation of (4) is usually written in a form similar to Ohm's law as

$$[Z_{m,n}][I_n] = [V_m]. \tag{5}$$

The generalized impedance matrix is given by $[Z_{m,n}] = [\langle w_m, L(u_n) \rangle]$, the generalized current matrix is given by $[I_n] = [\alpha_n]$, and the generalized voltage matrix is given by $[V_m] = [\langle w_m, f \rangle]$. The generalized matrices may need to be scaled to obtain the same units as the counterparts in Ohm's law.

III. TURNSTILE S-SHAPED ANTENNA

Antenna Description and Simulation Results: The turnstile arrangement of S-and inverted S-Shaped dipole antennas is energized with currents of equal magnitude but in phase quadrature. S-shaped dipole antenna was introduced in [7]. This arrangement, as shown in figures 1 and 2, are made of thin solid wire, and produce circular polarization wave of both senses.

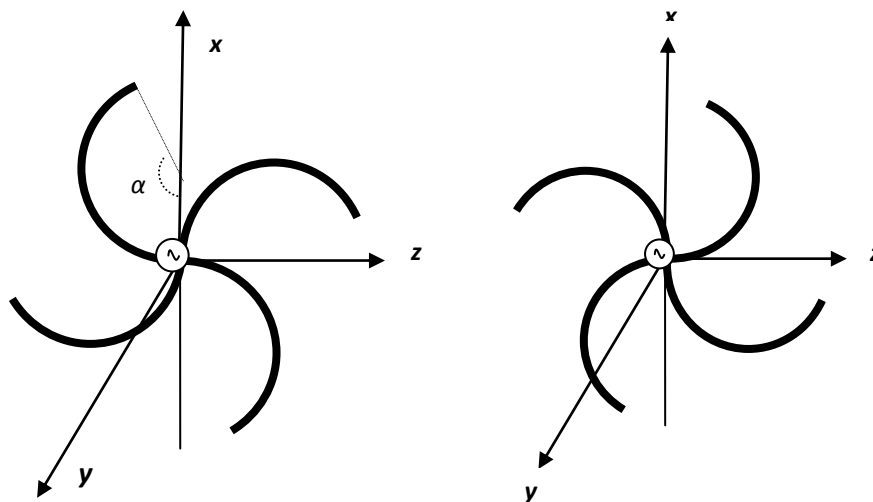


Figure 2 : Turnstile S-shaped antenna Figure 2: Turnstile Inverted S-shaped antenna

The input impedance and the VSWR for $\alpha = 180^\circ$ at different wire lengths ($L_s = 50$ cm, 100 cm and 200 cm) are shown in figures 3, 4 and 5. It is clear that after 600 MHz the input resistances vary between small

values and the antenna has capacitive reactance. The VSWR for $L_s=50$ cm is approximately ≤ 2 at $f > 600$ MHz.

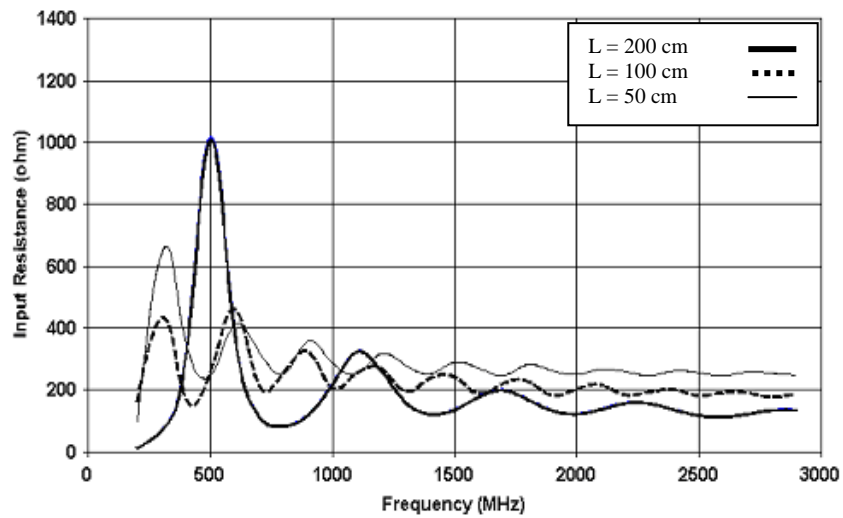


Figure 3: The input resistance at different values of wire length for S-Shaped turnstile antenna ($\alpha = 180^\circ$)

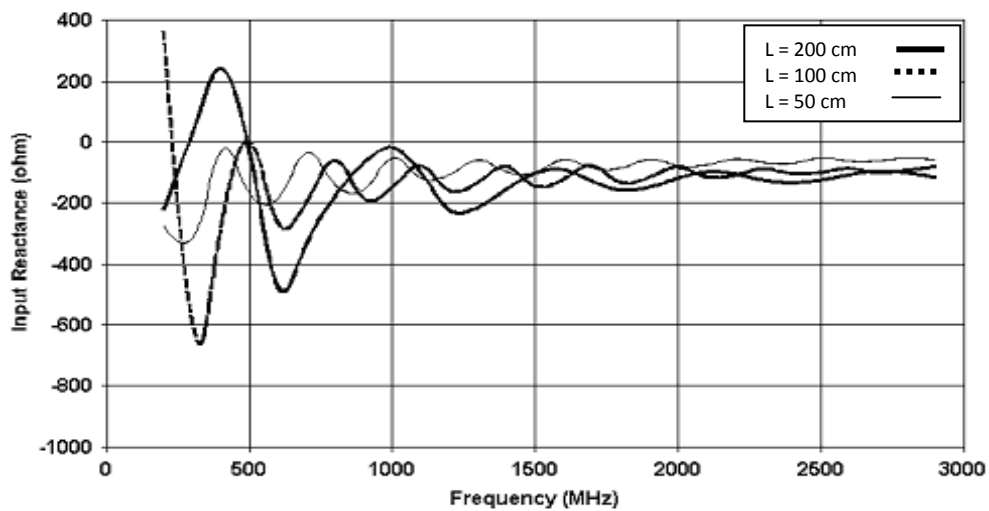


Figure 4: The input reactance at different values of wire length for S-Shaped turnstile antenna ($\alpha = 180^\circ$)

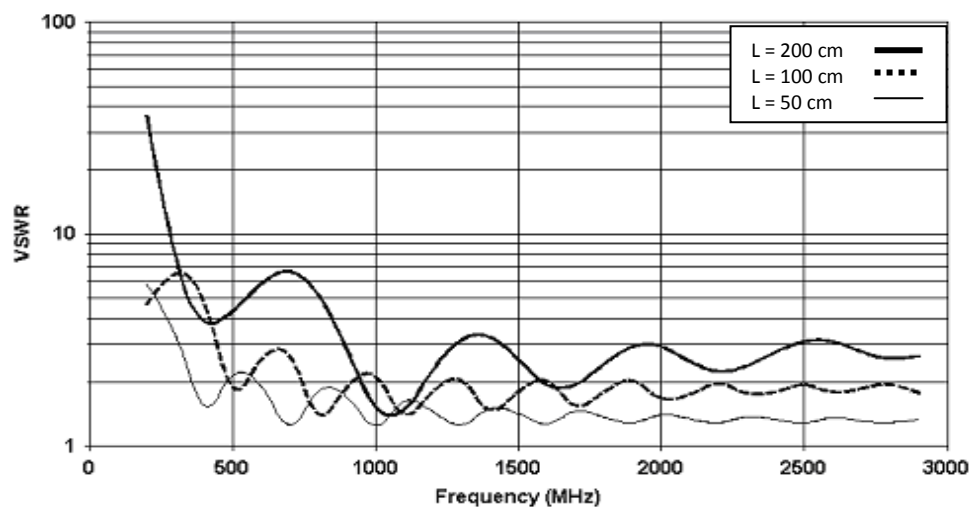


Figure 5: The VSWR at different values of wire length for S-Shaped turnstile antenna ($\alpha = 180^\circ$)

The gain in dB as a function of frequency for ($L_S = 50$ cm and $\alpha = 180^\circ$) when it is located in free space and over PCGP is shown in figure 6.

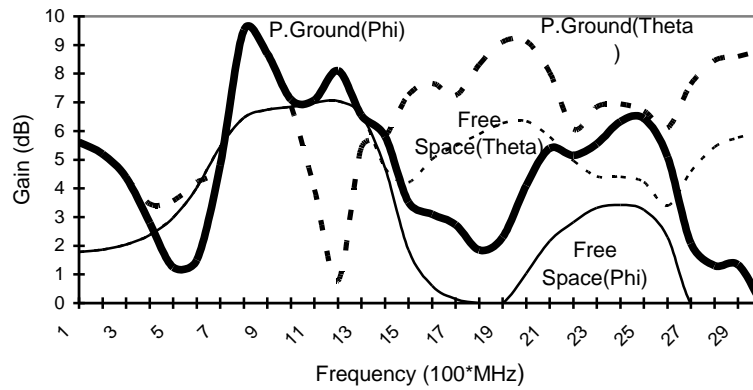


Figure 6: Gain relative to isotropic source for the turnstile S-Shaped dipole antenna ($L_S = 50$ cm and $\alpha = 180^\circ$) Typical power radiation patterns at 800 MHz and 1400 MHz for normal and inverted turnstile S-Shaped dipole antenna ($L_S, \alpha = (50$ cm, $180^\circ)$ in the free space and over a PCGP are given in figures 7 to 10.

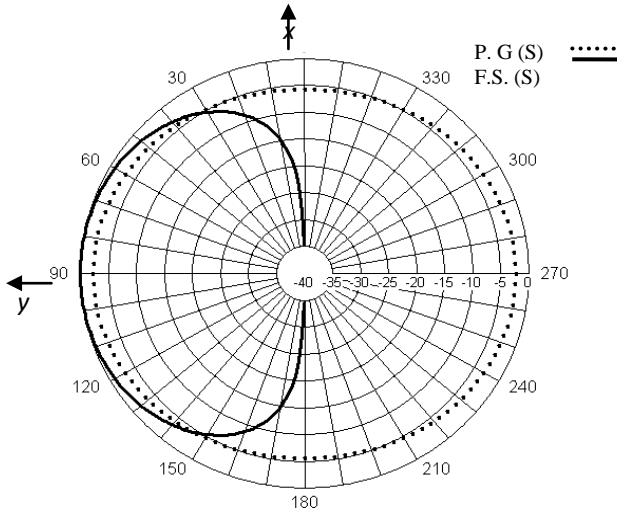


Figure 7: Total power radiation pattern in yz-plane at 800 MHz ($L_S = 50$ cm and $\alpha = 180^\circ$)

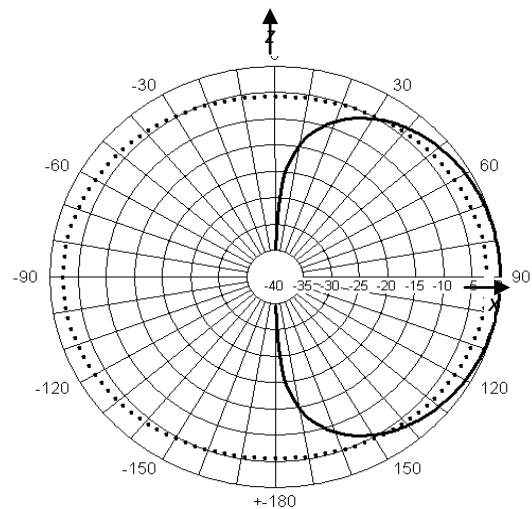


Figure 8: Total power radiation pattern in xy-plane at 800 MHz ($L_S = 50$ cm and $\alpha = 180^\circ$)

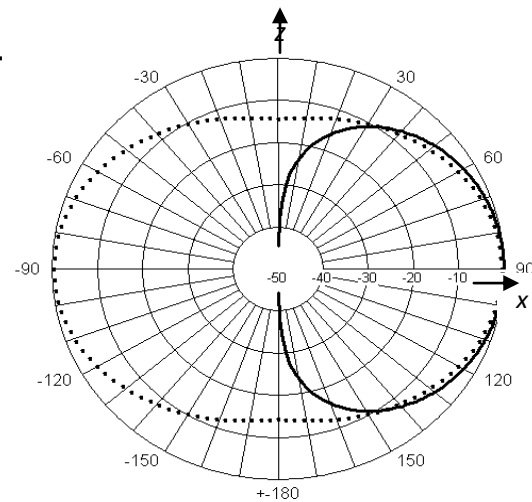
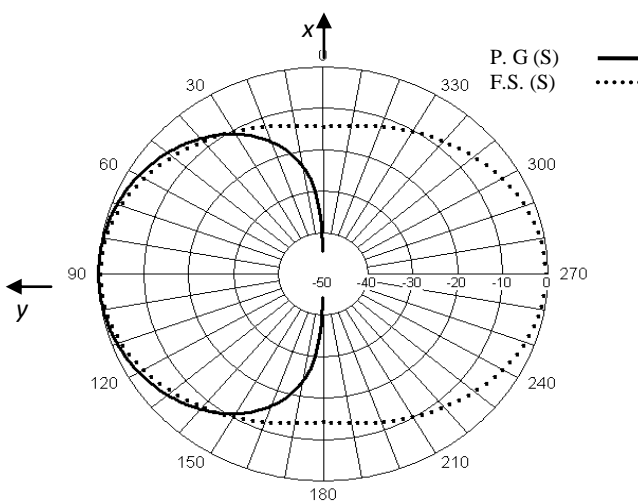


Figure 9: Total power radiation pattern in yz-plane at 1400 MHz ($L_s = 50$ cm and $\alpha = 180^\circ$)

Figure 10: Total power radiation pattern in xy-plane at 1400 MHz ($L_s = 50$ cm and $\alpha = 180^\circ$)

From figure 6 it is clear that the antenna over PCGP has high gain compared to that in free space case. For both cases the power radiation pattern becomes narrower as the frequency increase.

IV. SWASTIKA ANTENNA

The Swastika antennas which form by turnstile arrangement of clockwise and counter clockwise-Inverted swastika- 90° angle bent dipole antenna are energized with currents of equal magnitude but in phase quadrature. This arrangement, shown in Figures.11 and 12, made of thin solid wire, produce circular polarization wave of both senses. The antenna is located in the xz-plane. The MoM with one-volt delta gap source is applied to this antenna

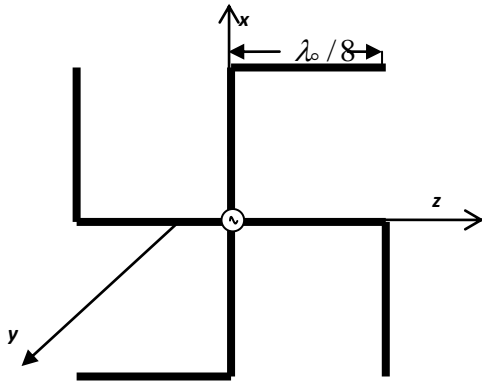


Figure 11: Swastika Antenna

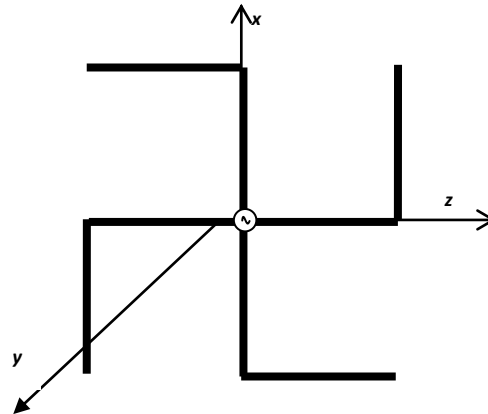


Figure 12: Inverted Swastika Antenna

The input resistance and reactance for the Swastika antenna with the same absolute length of turnstile half wavelength dipole ($\lambda_0/2$) are shown in Figures. 13 and 14. The variety of the input resistance of Swastika antenna after $2 f_0$ is less than that of turnstile dipole and the input reactance is capacitive after this frequency.

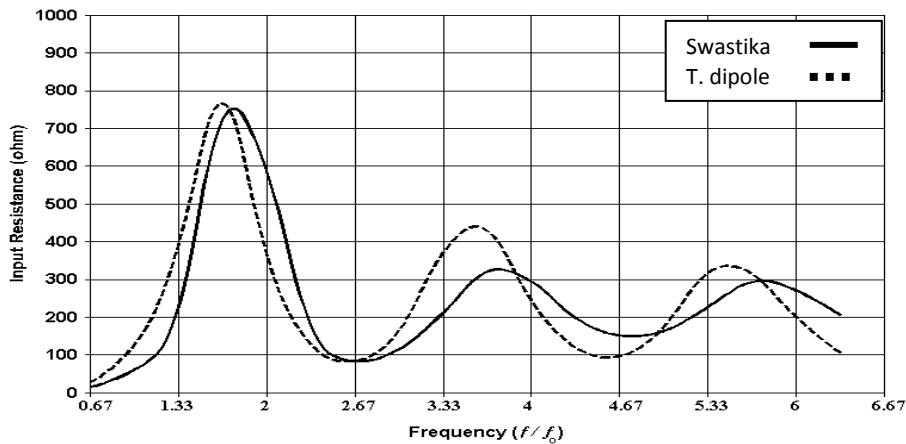


Figure 13: The input resistance as function of frequency for the Swastika antenna and the same length turnstile dipole

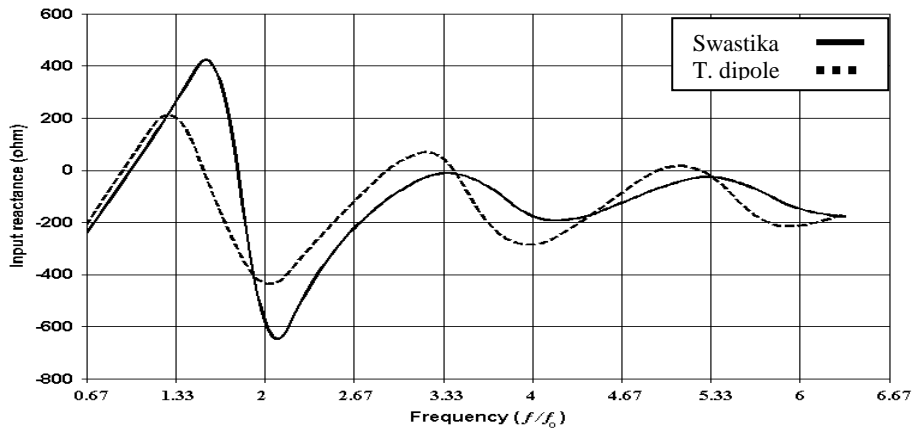


Figure 14: The input reactance as function of frequency for the swastika antenna and the same length turnstile dipole

The VSWR at $Z_o=300 \Omega$ for the same previous antennas is shown in Figure 15. From Figure 15 it's clear that Swastika antenna has superiority performance on the turnstile dipole.

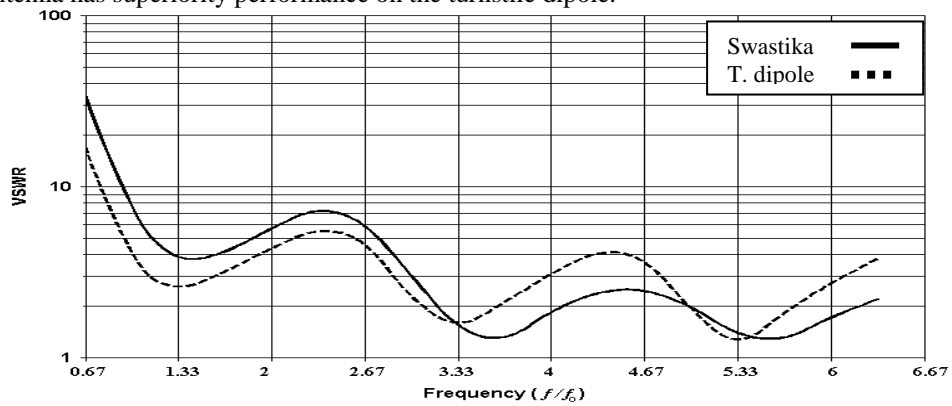


Figure 15: The VSWR as function of frequency for the Swastika antenna and the same length turnstile dipole

The current distribution over one side of the Swastika antenna and the current distribution over the same length dipole at the frequencies f_o , $2 f_o$ and $3 f_o$ are shown in Figures.16, 17 and 18.

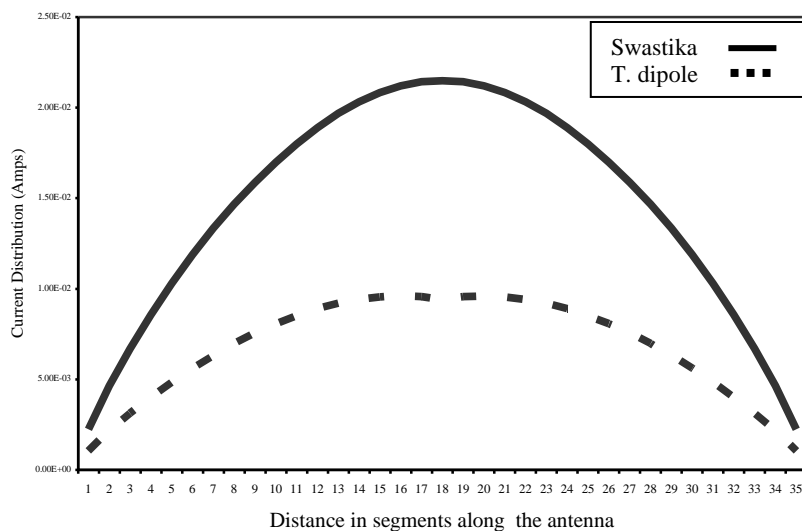


Figure 16: The Current distribution on the Swastika antenna and the same length turnstile dipole at f_o

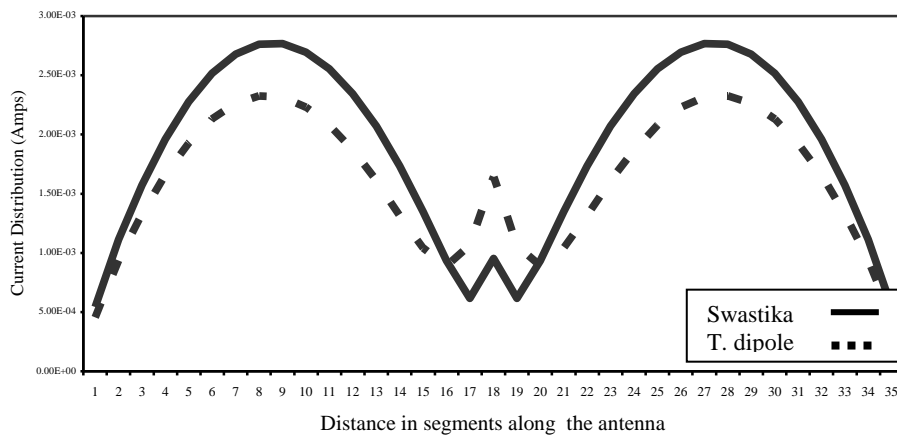


Figure 17: The Current distribution on the Swastika antenna and the same length turnstile dipole at $2 f_0$.

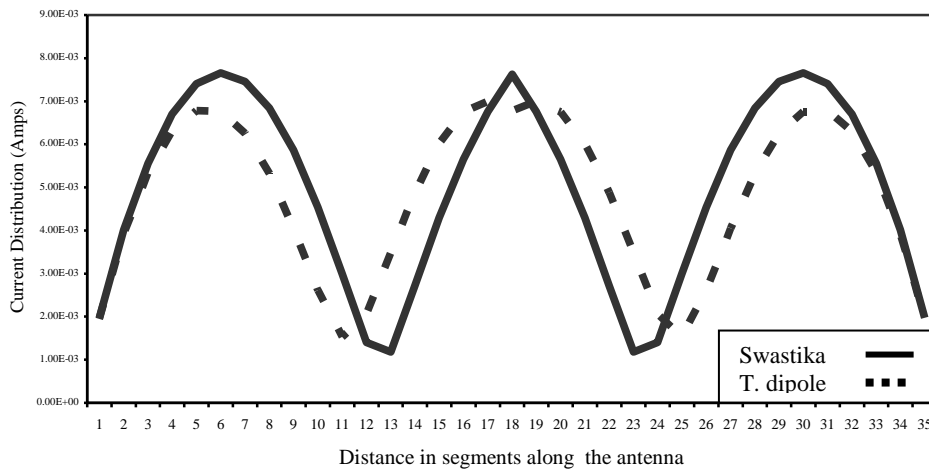


Figure 18: The Current distribution on the Swastika antenna and the same length turnstile dipole at $3 f_0$.

The gain in dB over an isotropic source as function of frequency for Swastika antenna when it is located in free space and over a perfectly conducting ground plane are shown in Figure 19. It is clear that the antenna over a perfectly conducting ground plane has superior performance.

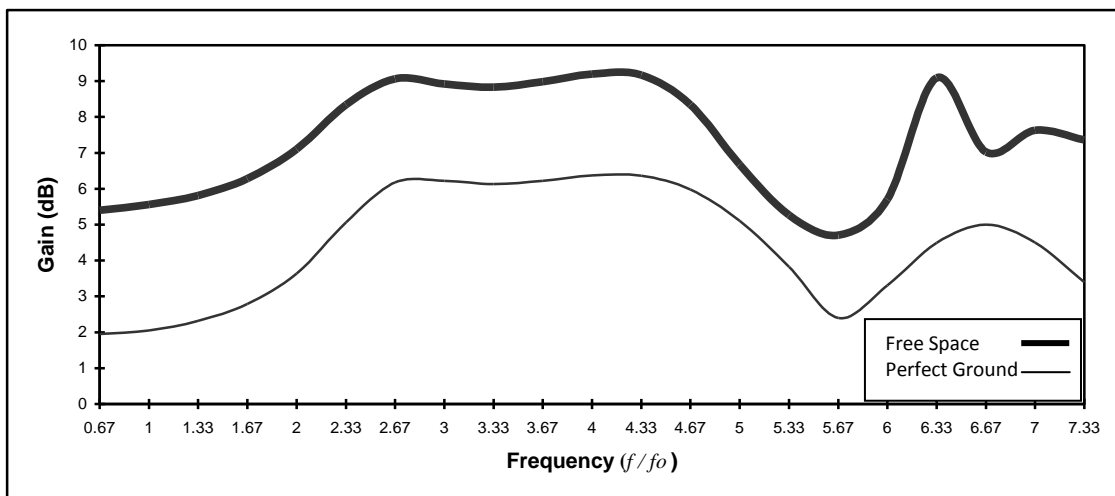


Figure 19: Gain relative to isotropic source for the Swastika antenna and the same length turnstile dipole

Typical power radiation patterns at f_0 and $3f_0$ for normal and inverted Swastika antenna in the free space and over perfectly conducting ground plane are given in Figures 20 and 21.

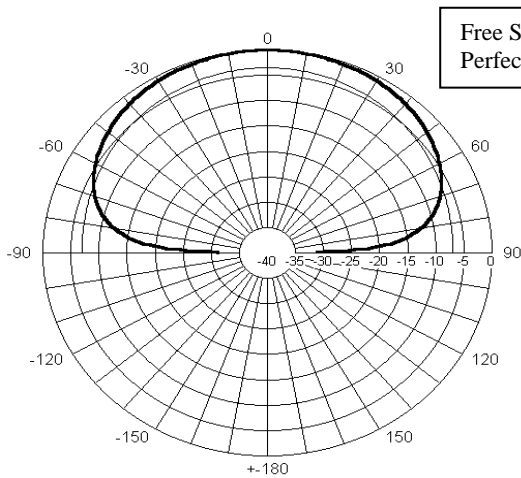


Figure 20: Power radiation pattern in at f_0 .

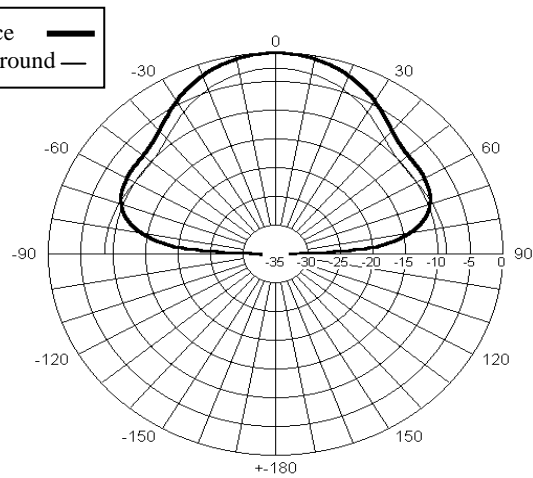


Figure 21: Power radiation Pattern in at $3f_0$.

V. COMPARISON BETWEEN SWASTIKA ANTENNA AND THE TURNSTILE S-SHAPED DIPOLE ANTENNA

In fact the idea of construction of Swastika antenna arises after finishing simulation and testing the S-Shaped dipole antenna[7] and its turnstile arrangements (Figure1).

By choosing the turnstile S-Shaped dipole with ($L_S = 50$ cm and $\alpha = 180^\circ$) and Swastika antenna with length side also 50 cm, the input impedance and the VSWR are shown in Figures 22, 23 and 24. The previous radiation characteristics are nearly the same for both antennas.

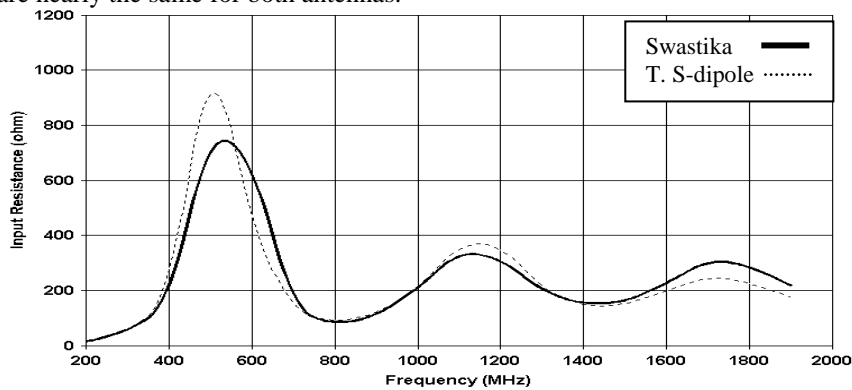


Figure 22: The input resistances for turnstile S-Shaped with $L_S = 50$ cm and $\alpha = 180^\circ$ and the same length Swastika antenna

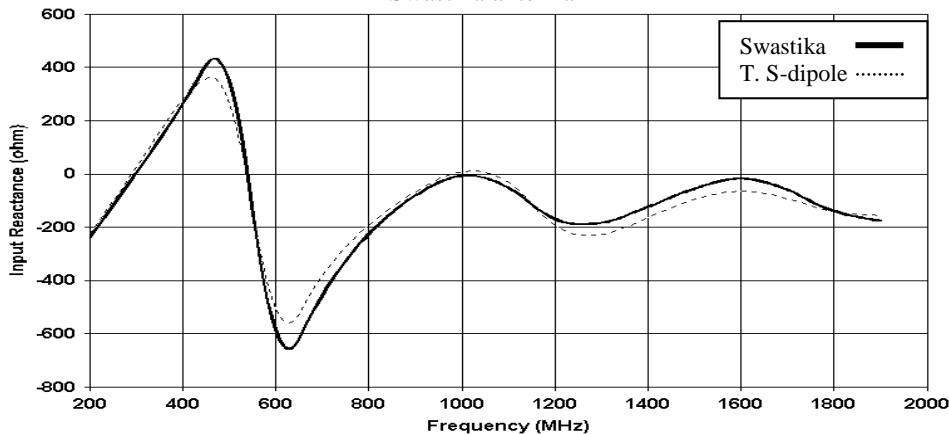


Figure 23: The input reactance for turnstile S-Shaped with $L_s = 50$ cm and $\alpha = 180^\circ$ and the same length Swastika antenna

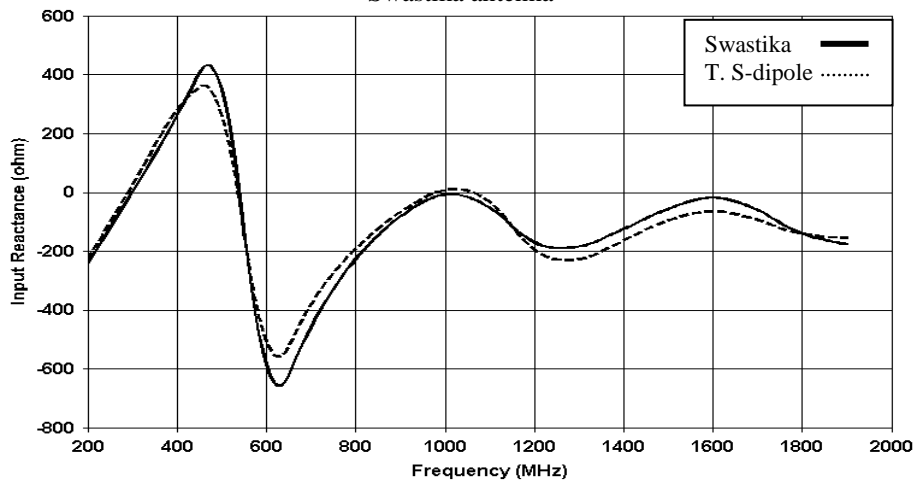


Figure 24: The VSWR for turnstile S-Shaped with $L_s = 50$ cm and $\alpha = 180^\circ$ and the same length Swastika antenna

The radiation pattern at 300MHz and 900MHz are shown in the Figures 25 and 26 and the gain as function of frequency for both antennas is shown in Figure 27.

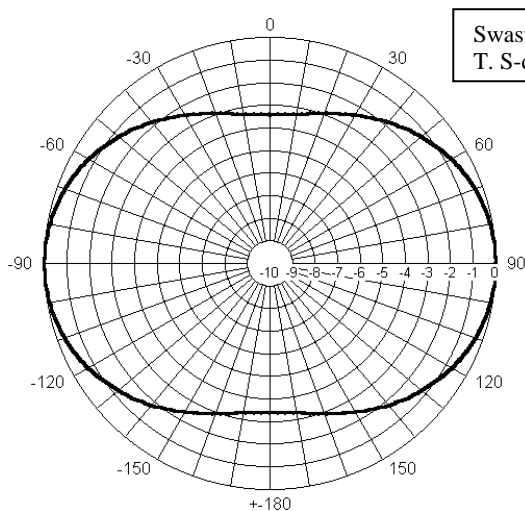


Figure 25: Power radiation pattern in at 300 MHz

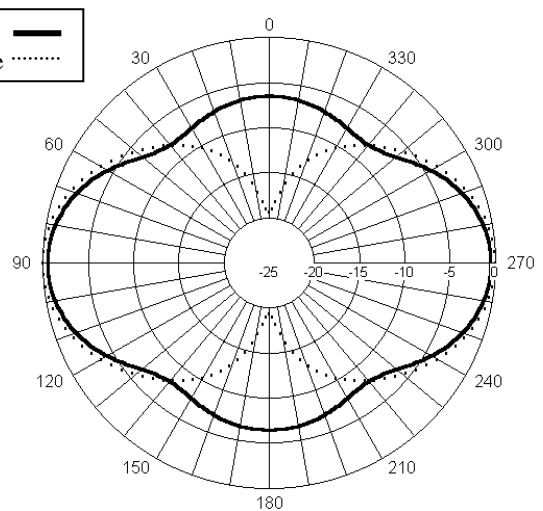


Figure 26: Power radiation pattern in at 900 MHz

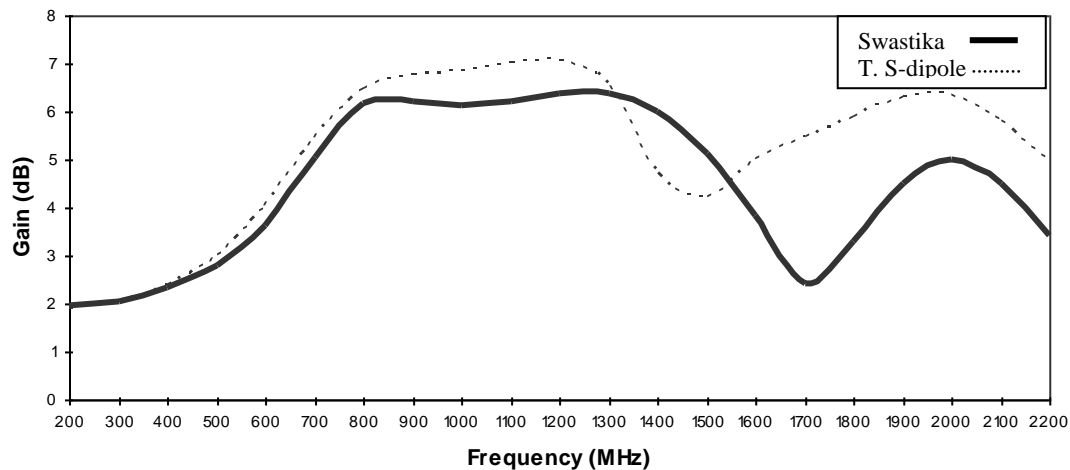


Figure 27: Gain relative to isotropic source for the turnstile S-Shaped with $L_s = 50$ cm and $\alpha = 180^\circ$ and the same length Swastika antenna

The pattern at 300 MHz the same for both antennas but at the 900 MHz some differences in the pattern and from Figure 44 cleared that after 600 MHz the gain has different shapes and values

VI. CONCLUSIONS

New simple wire antennas are proposed and analyzed, namely the S-Shaped and the inverted S-Shaped dipoles and its turnstile arrangements and Swastika antenna. The field patterns and gains in the principal planes over a range of frequencies are obtained for the mentioned arrangements. The other radiation characteristics such as input resistance, reactance and the VSWR as functions of frequency, for different antenna dimensions, are reported. The measurements of the power radiation patterns in the principal planes for the S-Shaped antenna are performed and proved theoretically. The results show that the proposed antennas can radiate linearly or circularly polarized waves and are promising to be used in the VHF and UHF frequency ranges. Wire antennas are still attractive due to their simple, rigid, cheap wide varieties and reliable constructions.

REFERENCES

- [1] Warren L. Stutzman and Gray A. Thiele, *Antenna Theory and Design* (second edition) (John Wiley & Sons 1998).
- [2] C.A. Balanis, *Antenna Theory Analysis and Design* (third edition, John Wiley & Sons, 2005).
- [3] Kraus, J. D., *Antennas For All Application* (third edition, McGraw-Hill companies Inc., New York, 2003).
- [4] Yi Huang and Kevin Boyle, *Antennas from Theory to Practice* (first edition, John Wiley & Sons, 2008).
- [5] ROGER F. HARRINGTON, *FIELD COMPUTATION BY MOMENT METHOD*, (Wiley-IEEE Press, 1993).
- [6] Bruke, G.J. and Poggio, A. J., "Numerical Electromagnetic Code (NEC)-Method of Moments." Part II. Program Description-Code, Lawrence Livermore Laboratory, 1981.
- [7] Mustafa Abu Nasr and H. Elkamchouchi (2004). The S-shaped Dipole Antenna, *ICMMT 2004, the Fourth International Conference on Microwave and Millimeter Wave Technology*, Beijing, CHINA, August, 18-21.

GIS based Decision Support System for Crime Mapping, Analysis and identify Hotspot in Ahmedabad City

Krunal Patel, Paru Thakkar, Leena Patel, Chandresh Parekh

ABSTRACT: *The rate of crime incidents is increasing in all developing countries due to change of technology and materialistic way of life and also due to poor socio, political, economic and environmental conditions. The distribution of incidents across the landscape is not geographically random since incidents are human phenomena. For incidents to occur, offenders and their targets - the victims and/or property - be required to exist at the same location for a period of time. Several factors, including the lure of potential targets and simple geographic convenience for an offender, influence where people choose to break the law.*

GIS based Decision Support System (DSS) uses geography and analysis as an interface for integrating and accessing massive amounts of location-based information. GIS based DSS allows police personnel to plan effectively for emergency response, determine mitigation priorities, analyze historical events, and predict future events. GIS based DSS can also be used to get critical information to emergency responders upon dispatch or while en route to an incident to assist in tactical planning and response. GIS helps identify potential suspects to increase investigators suspect base when no leads are evident.

I. INTRODUCTION

Naturally crime does not disappear on its own. Police departments are on the duty of protecting the citizen's safety and taking precautions to minimize the risk of crime. It has long been common practice for the police to identify locations and times that are more prone to criminal activity. To reduce or completely eliminate the crime, some actions, such as crime prevention methods, should be taken. Crime prevention can be signified as a set of ideas for combating incident and includes the activities taken by individuals and groups, both public and private.

The first step of crime prevention is to analyze the current status of incidents such as determining the density or pattern of the incidents. To identify highest incident concentration areas as hotspots which are useful for prompt analysis to uncover what factors make a location a good spot for crime. Normally, three criteria that affect the occurrence of the incident are; a suitable target, a motivated offender and an absence of guardians. Besides these criteria the suitable land use and appropriate time could be added into the reasons of incidents. There is a strong relationship between land use, time and incidents. Particular areas may be devoted to different types of land use (residential development, retailing, industry, leisure, open space) and based on its land use type the activities and population profile of an area may vary considerably according to the day of the week or time of day. Social and geographic factors, such as location of schools or neighborhoods with different socioeconomic status within an area, can influence the patterns and rate of crime incidents in that area.

II. RATIONALE OF THE MODEL

A **geographic information system (GIS)** integrates hardware, software, and data for capturing, managing, analyzing, and displaying all forms of geographically referenced information. GIS allows us to view, understand, question, interpret, and visualize data in many ways that reveal relationships, patterns, and trends in the form of maps, globes, reports, and charts. A GIS helps you answer questions and solve problems by looking at your data in a way that is quickly understood and easily shared. The usage of Geographic Information Systems (GIS) in data storage, manipulation and display makes incident prevention process more manageable, more realistic and case specific. The results of GIS give an idea about the current status of incident pattern. Due to its spatial operation capability, GIS helps police and also other people who are interested in incidents, to visualize and analyze the spatial relationships between different data layers such as incidents and land use, to forecast and take precautions for future incidents. Crime analysis and crime maps, achieved by GIS, have a major role in reducing crime and improving the effective police activities.

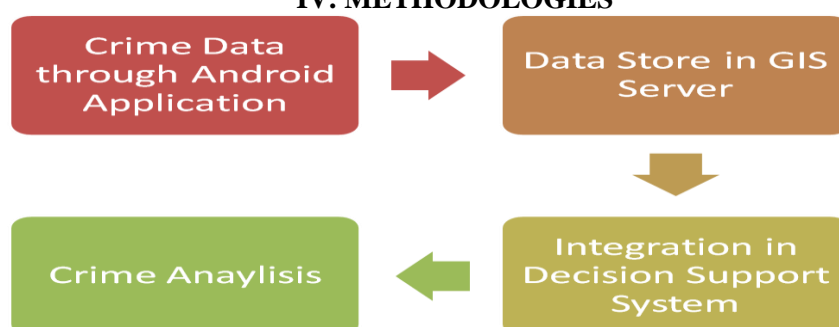
With GIS, police department is able to produce more versatile electronic maps by combining their databases of reported incident locations with digitized maps of the areas they serve. GIS opens new opportunities for the use of digital mapping in incident control and prevention programs. GIS allows police personnel to make plans effectively for emergency response, determine mitigation priorities, analyze historical events, and predict future events; it helps crime officers to determine potential incident sites and facilitates to explore the relationship between incident and land use.

III. OBJECTIVES

Main objective of this project is to apply spatial data analysis integrated with GIS and analyze what land uses are prone to incident and why incident is higher in one area than another. Following analysis may be generated in order to identify the incident pattern.

- **Identify** areas that may likely be targeted by an offender.
- **Determine** whether common attributes exists among a group of reported cases.
- **Explore** relationships between incident and other geographic features such as land use and the built environment.
- **Study** the movement of offenders to predict the location of future targets to establish interdiction locations along escape routes
- **Detect** whether the incident locations are clustered.
- **Determine** if incidents tend to be located close to a specific location such as taverns or gang territories or the periphery of a county or in the center.

IV. METHODOLOGIES



1. **To get** Operational Knowledge/Skill of GIS Software.
 2. **To collect** Crime Data from part of Ahmedabad City.
 3. **To use** collected data in the GIS software as pilot run.
 4. **To Develop and implement** different analysis methods to achieve valuable information for crime prevention and provide to police department.
 5. **To see and analyze** the effect of Process no. 4.
 6. **To repeat** the process 2 to 4 for whole Ahmedabad city.
- To provide/conduct** training to officers of police department

V. APPLICATION

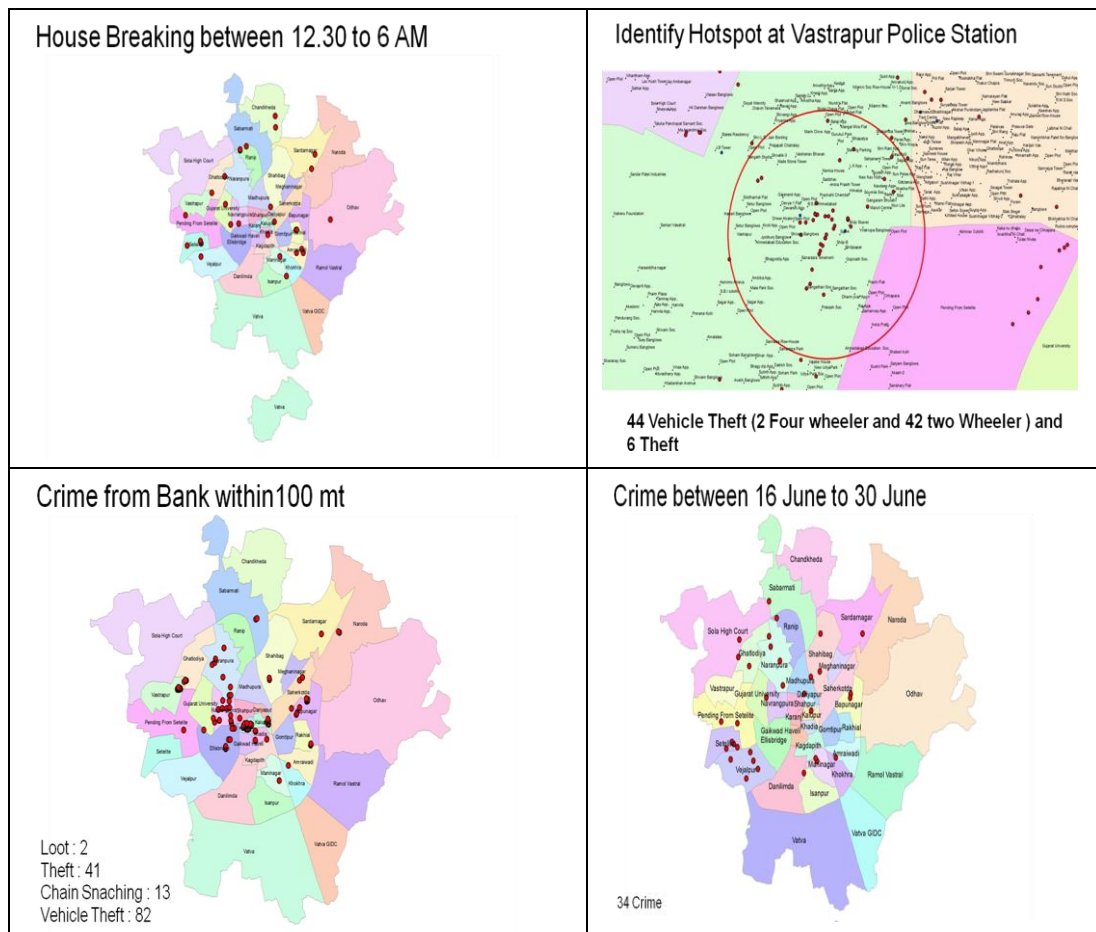
Crime data of property offenses for the period 1st July, 2011 to 31st December, 2011 were considered in the project and the same was received in the specified format. The following parameters were considered for the crime map.

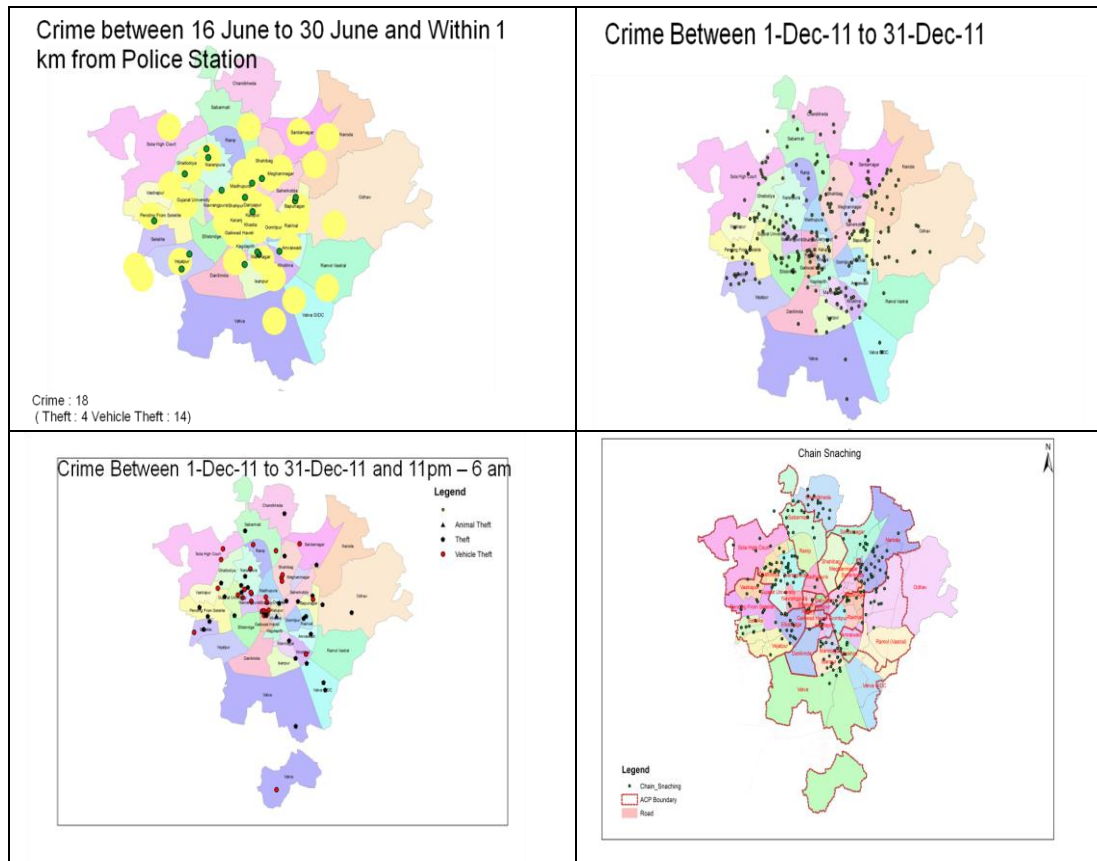
1.	Name of Complainant	10.	Name of accused
2.	Address of Complainant	11.	Address of accused
3.	Date of Crime Occurrence	12.	Number of Sector
4.	Time of Crime Occurrence	13.	Name of Police Station
5.	Date of Declaration	14.	Name of Police Choki
6.	Time of Declaration	15.	M.O.
7.	Place of Crime	16.	Type of Vehicle
8.	Type of Crime	17.	Make of Vehicle
9.	IPC Used	18.	Amount in theft

Crime data received from various police stations were not with latitude and longitude information of crime place without which crime mapping in GIS platform is not possible. To get latitude and longitude information of all crime places was very challenging and this was done with the help of detection staff of police department. In this project following all police station of Ahmedabad city were taken.

GIS based crime mapping for any objective needs the mapping of related information also which is useful always for making conclusion. All above maps include the related information for crime mapping such as sectors, zones and police station boundaries.

Following are few maps showing the results of Vejalpur Police Station crime mapping. Depending upon requirements, maps can be generated for study and analysis. Project is based on property offences only, and accordingly maps are designed. Figures show total crime map, maps with only particular IPC, map with only vehicle theft, map with type of vehicle and map with vehicle theft of particular company make etc.,. It also shows the theft with particular amount or more than particular amount and crimes in area centered particular point such as police station, school, temple, railway station etc.,.





VI. CONCLUSIONS

The proposed solution is scalable to enterprise level. GIS based DSS is crucial for Public Safety and financial growth of any nation. Geo spatial technology can not only be useful for better planning but also useful for better management of assets in industries. Convergence of MIS and GIS technologies can provide near real time information resulting in efficient and effective decision support system (DSS) to help multiple areas like Health, Defense, and Disaster etc.

Groundwater Quality Evaluation in Thal Doab of Indus Basin of Pakistan

D. Khan¹, Mona A. Hagra², Naveed Iqbal³

¹Director (GIS/GWM), Pakistan Council of Research in Water Resources, Islamabad, Pakistan

²Assistant Professor, Faculty of Engineering, Ain Shams University, Cairo, Egypt

³Assistant Director (GIS/RS), Pakistan Council of Research in Water Resources, Islamabad, Pakistan,

ABSTRACT: Indus Basin is typical model of conjunctive use of surface and groundwater. A well transmissive continuous and deep alluvium Indus Plain Aquifer (IPA) is underlain by world's largest contiguous Indus Basin Irrigation System (IBIS). Currently the overall Indus aquifer is supplementing more than 40 percent in total water resources of Pakistan. Pressure on groundwater is increasing and groundwater withdrawal has crossed the limit of safe yield in many parts of IPA. Groundwater mining is creating detrimental environmental issues like lowering of water table, saline water upconing and intrusion. Management of groundwater through regulation is difficult to implement in the absence of required updated hydrogeological information about the aquifer. A program of evaluation of national aquifers is under implementation by Pakistan Council of Research in Water Resource (PCRWR). Investigations program was initiated in Thal Doab of Indus Basin where 56 exploratory wells were drilled at a regular grid of 25 Km x 25 Km. Water as well as soil samples were collected and analyzed for seven important parameters of water quality. The mapping of water quality indicated large vertical and spatial variations in water quality of the study area. Hydrogeological facies were worked out by developing Piper and Durov Diagrams. The evolution of groundwater quality was worked out in the context of geological framework of the area. The study yielded that most of the groundwater in Thal Doab is fresh because of extensive seepage and recharge of aquifer from rivers, precipitation and irrigation network.

Keywords: Groundwater quality, groundwater evolution, Hydrogeological facies, Indus Plain Aquifer, Thal Doab

I. INTRODUCTION

Groundwater is one of the nation's most valuable natural resource and playing important role in agri-based economy of Pakistan. The sole groundwater potential exists in Upper part of IPA which comprises of four doabs (the land in between two rivers); Thal, Bari, Rechna, Chaj and riverian lands along Indus River. Variation in quality of water in this alluvium aquifer is dependent on the availability of recharge source. The management of this aquifer and associated environmental problems remained challenge since the middle of nineteenth century when natural groundwater equilibrium was disturbed with the onset of canal irrigation system in the Indus Basin. Environmental issues related to groundwater became a serious concern for sustainability of irrigated agriculture in Indus Basin. Research studies for remedial measures were initiated in 1870 when observation wells were installed in irrigated areas to monitor environmental hazards of rising water table. Later, in 1933, Taylor, Malhotra and Mehta [1] worked on water logging and salinity and related its cause to the monsoon precipitation. Wilsdon and Bose [2] conducted geophysical survey to assess vertical extent of alluvium aquifer in Upper Indus Plain. Tipton and Kalmbach [3] prepared feasibility report for Water and Power Development Authority (WAPDA) for implementation of Salinity Control and Reclamation Project (SCARP III) in Lower Thal Doab. Greenman et al. [4] described in detail the chemical quality of the native ground water of the Punjab region including Thal Doab through hundreds of exploratory wells. In 1970, Mundorff et al. [5] conducted analog modeling study to evaluate the aquifer characteristics and remedial measure of water logging and salinity in Thal Doab. In 1999 numerical groundwater simulation was applied as management tool under Punjab Private Sector Development Project of Punjab Irrigation and Power Department [6] to establish groundwater management areas in Lower Thal Doab. Tahir and Hifza [7] worked out distribution of nitrate in the water resources of the area to explore the possible risk of crippling fluorosis in Upper Thal Doab. Shaheen and Baig [8] assessed drought

severity in Thal Doab by using Remote Sensing and GIS techniques. They computed Standardized Precipitation Index on six monthly bases.

Exploitation of aquifer at large scale requires proper management based on updated knowledge of groundwater chemistry. The chemistry of a groundwater sample is signature that reflects main physical processes and chemical reactions in an aquifer. It gives the sum of effects of all processes starting from dilution of precipitation, infiltration to the soil and the water table. Many researchers used hydrochemical characteristics to evaluate the groundwater quality of river basins. Adonis[9] analyzed the hydrochemical characteristics of the groundwater in the Incomati Estuary, Maputo, Mozambique to work out the groundwater chemistry. The purpose of study was to assess spatial and temporal variations in water quality and to evaluate the suitability of the groundwater for drinking and irrigation purposes. El-Fiky[10] examined the hydrogeochemical and isotopic data of groundwater of the different aquifers of the RasSudr-Abu Zenima area, southwest Sinai, Egypt to determine the main factors controlling the groundwater chemistry and salinity as well as its hydrogeochemical process. Zhang et al.[11] applied hydrochemical characteristics to assess the water quality of surface water and groundwater in Songnen Plain, Northeast China by using fuzzy membership analysis and multivariate statistics. Hagrais[12] assessed the usability of groundwater for drinking and irrigation purpose using hydrochemical characteristics in Punjab, Pakistan. This study aims to investigate the groundwater quality in Thal part of IPA in Pakistan.

II. DESCRIPTION OF STUDY AREA

2.1 Geography

Thal Doab is one of the main parts of IPA which occupies an area of about 3.3 mha, spreading over seven districts of Punjab Province; Mianwali, Khoshab, Sargodha, Jhang/ Bakkhar and Muzaffargarh. The area is a triangular shape with base in north in foothills of the Salt Range Mountains and apex in south and is located between latitudes 28° 57' 46.3" to 32° 58' 49" north and longitudes 70° 30' 04" to 72° 55' 30" east as shown in the location map given in Fig.1. Thal area is bounded by hills in north, Indus River in west and Jhelum and Chenab Rivers in east. This doab is one of the hottest areas of Pakistan. The mean average annual temperature at Mianwali is 24°C with the maximum value of 30°C during June and average minimum of 4°C during January. The average minimum temperature during the year is 17°C. The average annual maximum rainfall is 500 mm in north which is highest throughout the Thal Doab. The construction of a network of irrigation canals and development of tubewell technology during 20th century has converted a major part of this desert into irrigated land. The southern part of Lower Thal is under extensive agricultural practices where different types of crops and orchards are contributing in national economy and benefiting the Indus Civilization.

2.2 Geology

The major rock units of Thal Doab, which constitutes the aquifer, are Quaternary alluvial and aeolian deposits. The alluvium consists dominantly of unconsolidated fine to coarse sand, with minor, generally localized lenses of clay and silt. The sediments were deposited in a subsiding trough by Indus River and its tributaries; Jhelum and Chenab Rivers. Surficial aeolian sand forms an extensive deposit over the alluvium in central Thal Doab. The thickness of the alluvium varies widely, with less in marginal areas along hills and greater in central part of Thal Doab. The whole adjacent boundary in north is dominated by Salt Range Mountains. Strata of the Salt Range are composed of highly fractured and folded, fossiliferous rocks of Cambrian to Pleistocene age. The Salt Range Formation (SRF) consists of an un-metamorphosed sequence of salt, marl, gypsum and dolomite with dominant red gypsiferous claystone. The top of the formation is a gypsum layer containing high-grade oil shale or at places a highly altered volcanic rock known as Khewra Trap or Khewra. Piedmont alluvial deposits flank the Salt Range, foothills [13]. The consolidated rocks on western boundary of Thal Doab are also of sedimentary origin and are extension of Suleman and Kirther Ranges. These rocks are of Carboniferous to Recent age and consist of sandstone, limestone shale and conglomerates [14].

2.3 Hydrology

The groundwater reservoir is available in the form of alluvium; and replenishment is based on hydrology in terms of source and extent of recharge. The Indus River controls hydrology in Upper Thal Doab mainly as it is at higher elevation and its depositions contains coarse grained sediments making it feasible for groundwater recharges. Due to favorable natural gradient several offtakes from mighty Indus with its travel through Thal Doab feed the irrigation network and replenish the underlying alluvium aquifer.

Because of high transmissivity of geological formation of Indus deposits the replenishment of aquifer is rapid along its course. The coefficient of permeability is in the range of 0.05 to 1.2 m/sec. Greenman et al.,[4]. Depth to water table in most of area is shallow and is in the range of 0.5 to 9 m from general ground surface. The groundwater exploitation in this area started in early 1980s and now about 0.18 million shallow

tubewells are pumping about 18 BCM of groundwater in ThalDoab[15].

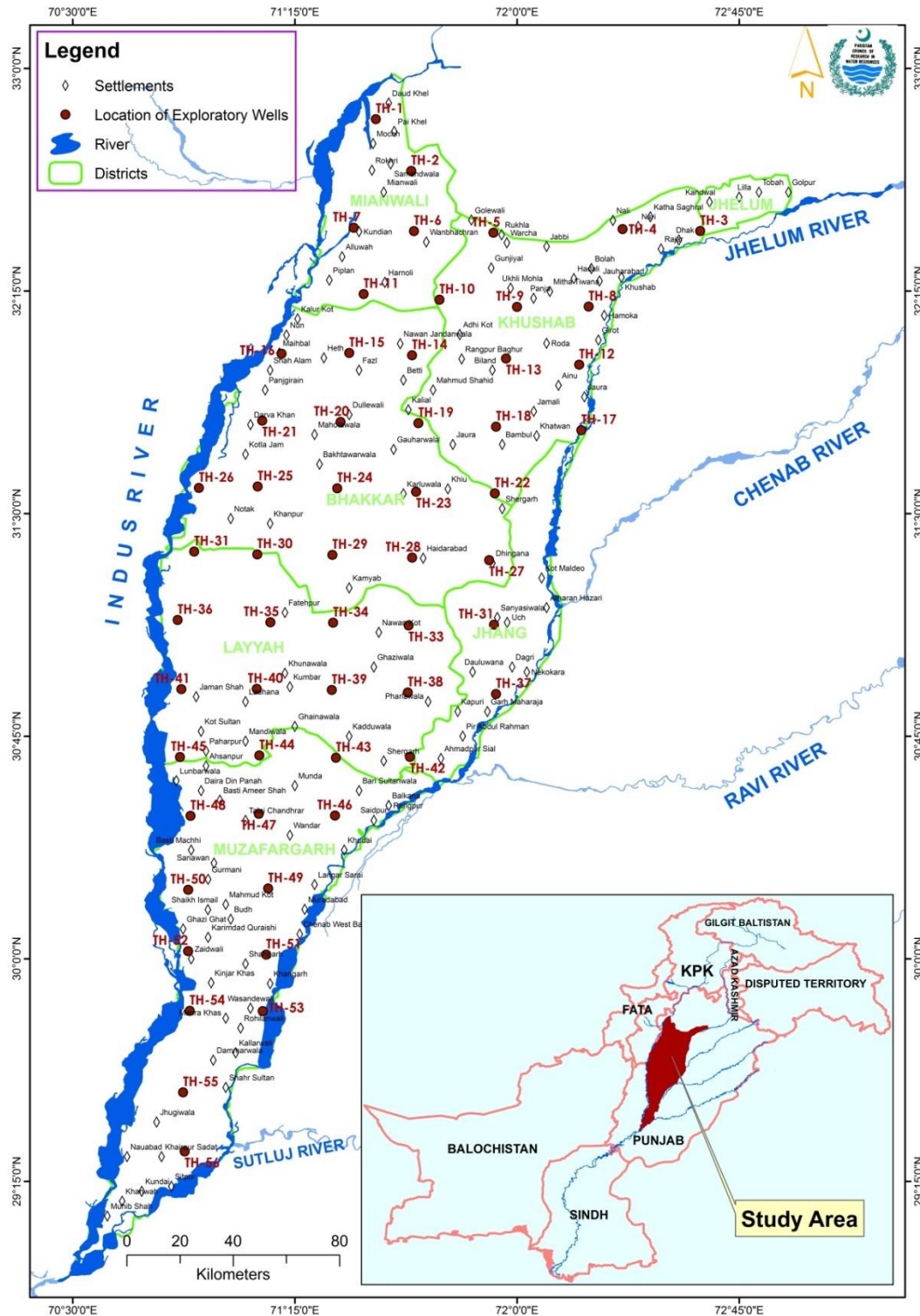


Figure 1: location map showing exploratory wells in Thal Doab

III. MATERIALS AND METHODS

Extensive water quality sampling of aquifer with large spatial and vertical coverage was necessary to understand geochemical process and evaluate water quality for irrigation, drinking and industrial use. The complete procedure consisted of well drilling, sample collection, transportation and analysis and then use of

existing graphical techniques and analytical procedures for description of groundwater quality and its evolution in the context of geology and recharge sources.

3.1 Exploratory Well Drilling and Water Quality Sampling

Comprehensive assessment of aquifer required extensive groundwater sampling which could cover spatial and vertical variations in quality. Total 56 exploratory wells (TH-1 to TH-56) of 450 mm diameter were drilled at regular grid of 25km x 25km over the area of about 3.3 mha by using Percussion Rigs. The location of exploratory wells is shown in Fig. 1. Percussion is useful for investigation purposes though it takes more time as compare to the rotary method of drilling. It gives accurate water quality and lithological sampling. All these exploratory wells were drilled to the constant depth of 90 meters for uniform vertical coverage. Water samples were collected at regular vertical interval of 3 m starting from watertable. In this way total 1860 water samples were collected and analyzed for evaluation of groundwater in study area. Similarly, the lithological sampling was carried out at 3 m depth interval for information on vertical changes in geological formation.

3.2 Water Samples Preservation and Laboratory Analysis

Collected water samples were analyzed for seven elements which make up nearly 95 percent of all water solutes; calcium, magnesium, sodium, potassium, chloride, sulfate and bicarbonate [16, 17]. Electrical conductivity (EC), total dissolved salts (TDS) and pH of these samples were also measured in laboratory at room temperature. Sodium Adsorption Ratio (SAR) and residual sodium carbonate (RSC) of each sample were calculated for assessment of use of water in irrigation. Standard protocols [18] as given in Table 1 were followed for sampling, preservation, transportation, field and laboratory testing of water samples. A blank sample of known standard and previously analyzed was reanalyzed after every ten samples to check the reproducibility of methods for the analyzed parameters and their results were found in the acceptable range of 5 % deviation from the actual samples.

Table 1: Methods Used for Water Samples Preservation and Analysis

Sr. #	PARAMETERS	ANALYTICAL METHOD
1.	Bicarbonate(mg/l)	2320, Standard method (1992)
2.	Calcium (mg/l)	3500-Ca-D, Standard Method (1992)
3.	Chloride (mg/l)	Titration (Silver Nitrate), Method 4500- B Standard Method (1992)
4.	Magnesium (mg/l)	2340-C, Standard Method (1992)
5.	Ph	4500-B, Standard Method (1992)
6.	Potassium (mg/l)	3500-B, Standard Method (1992)
7.	Sodium (mg/l)	3500-B, Standard Method (1992)
8.	Sulfate (mg/l)	SulfaVer4 (Hach-8051) by Spectrophotometer Method-4500-B, Standard Method (1992)
9.	TDS (mg/l)	2540C, Standard method (1992)

3.3 Statistical Analysis of Samples

The summary of statistical analysis for water quality parameters as generated in AquChem9.1 is given in Table 2. The table shows minimum, maximum, mean, standard deviation, skewness and t-statistic. All parameters are positively skewed with t-statistics in the range of absolute value of 1.7 to 1.8 which is little less than required value of 2. It is acceptable in field study of regional groundwater system. The variance has outcome for Na, Cl, TDS, SO₄ and EC due to large spatial variation in these parameters representing true extreme values of a distribution.

Table 2: Summary of Statistical Analysis of water quality parameters in 56 exploratory wells

Parameter	Minimum	Maximum	Arithmetic Mean	Standard deviation	Skewness	Variance	t-statistics
Ca(meq/l)	0.40	18.00	2.63	2.88	0.0025	8.30	-1.7
Na(meq/l)	0.00	53.60	8.14	10.14	0.0025	102.90	-1.7
K(meq/l)	0.04	4.10	0.53	0.59	0.0025	0.35	-1.7
Mg(meq/l)	0.40	17.00	3.53	3.45	0.0026	11.92	-1.8
Cl(meq/l)	0.00	41.50	3.67	6.36	0.0025	40.40	-1.7

SO ₄ (meq/l)	0.00	280.0	8.62	37.90	0.0025	1434	-1.7
HCO ₃ (meq/l)	2.20	20.00	6.21	3.27	0.0025	10.70	-1.7
EC(μS/cm)	300.00	7500	1401.60	1456.50	0.0025	2.1E+06	-1.7
TDS(ppm)	213.00	5361	993.90	1047.80	0.0026	1.1 E+06	-1.8

IV. RESULTS AND DISCUSSIONS

In an alluvium unconfined aquifer the groundwater moves in all directions from recharge zone with the velocity depending upon hydraulic conductivity and hydraulic heads. This movement is expressed by tensor which covers multi-dimensional variations in solute composition; therefore both spatial and vertical components have been mapped for valuable outcome of the current study.

4.1 Vertical Variation in Water Quality

The EC of water samples was plotted against depth in AquaChem for assessment of vertical variation in water quality as shown in Fig.2. The plot indicates that most of the exploratory wells are falling in freshwater zone with little variations in EC with depth, especially along Indus River. Plot in Fig. 2 indicates that 37 wells are falling in freshwater and show negligible changes in EC with depth. The variation in EC with depth in remaining 19 wells indicates following three trends in water quality with depth;

- I. Seven wells indicate decrease in EC with the depth: (TH-5, TH-1, TH-19, TH21, TH-25, TH-32 TH-37).
- II. Ten wells indicate increase in EC with depth: (TH-9, TH-10, TH -12, TH-20, TH-21, TH30 TH-41, TH-43, TH-39, TH-40).
- III. Two wells are having low EC at top and bottom but high in middle: (TH-2 and TH-26)

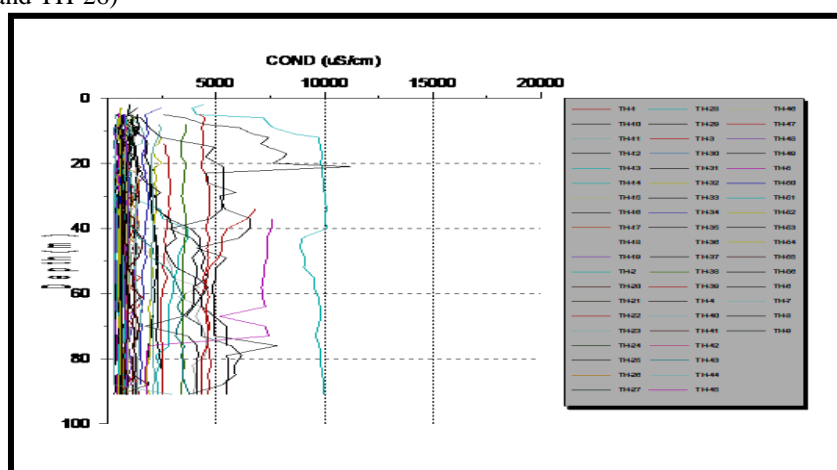


Figure 2: vertical variations in groundwater quality

4.2 Spatial variation in groundwater quality

For assessment of spatial variation in water quality, water sample from the top of aquifer were processed and plotted in ArcGIS 9.1. Separate maps were prepared for cations, anions and EC. Plotted EC in Fig. 3 indicates low values in recharge zones along Indus River in Upper Thal Doab. The area along river Jhelum, near Salt Range is found with highest salt concentration. This is because of the low permeability in formation along Jhelum River due to higher presence of clay lenses which retard the recharge. The recharge source in eastern side of Lower Thal is Chenab and Indus Rivers and dense irrigation network, therefore the groundwater is mostly fresh in Lower Thal. However a small patch of saline water at confluence of the two rivers is because of deep clay deposits in this area. The variation in cations and anions in the study area is depicted in Fig.4. Generally, the cations and anions variations follow the trend of EC. In anions, the Na varies from nil to 54 meq/l. Ca varies from 0.40 to 18 meq/l and Mg varies from 0.4 to 17 meq/l. In cations the SO₄ varies from 0.0 to 288 meq/l, Cl varies from 0 to 51.5 meq/l followed by the bicarbonates which varies from 2.20 to 20 meq/l. SO₄ are high in Upper Thal just below the Salt Range Mountain exposed with gypsum (CaSO₄H₂O) and anhydrite (CaSO₄).

4.3 Hydrogeochemical Facies and Water Typology

The idea of "hydrogeochemical facies" is the classification of waters according to the relative proportions of major ions [19]. Different graphical representation has been developed by researcher to classify water according to percentage of cations and anions in water sample. Most widely graphically methods for determination of water type and hydrogeological facies are Piper and Durov Diagrams. Developed diagrams for classification of groundwater in study area are disused in the following sections.

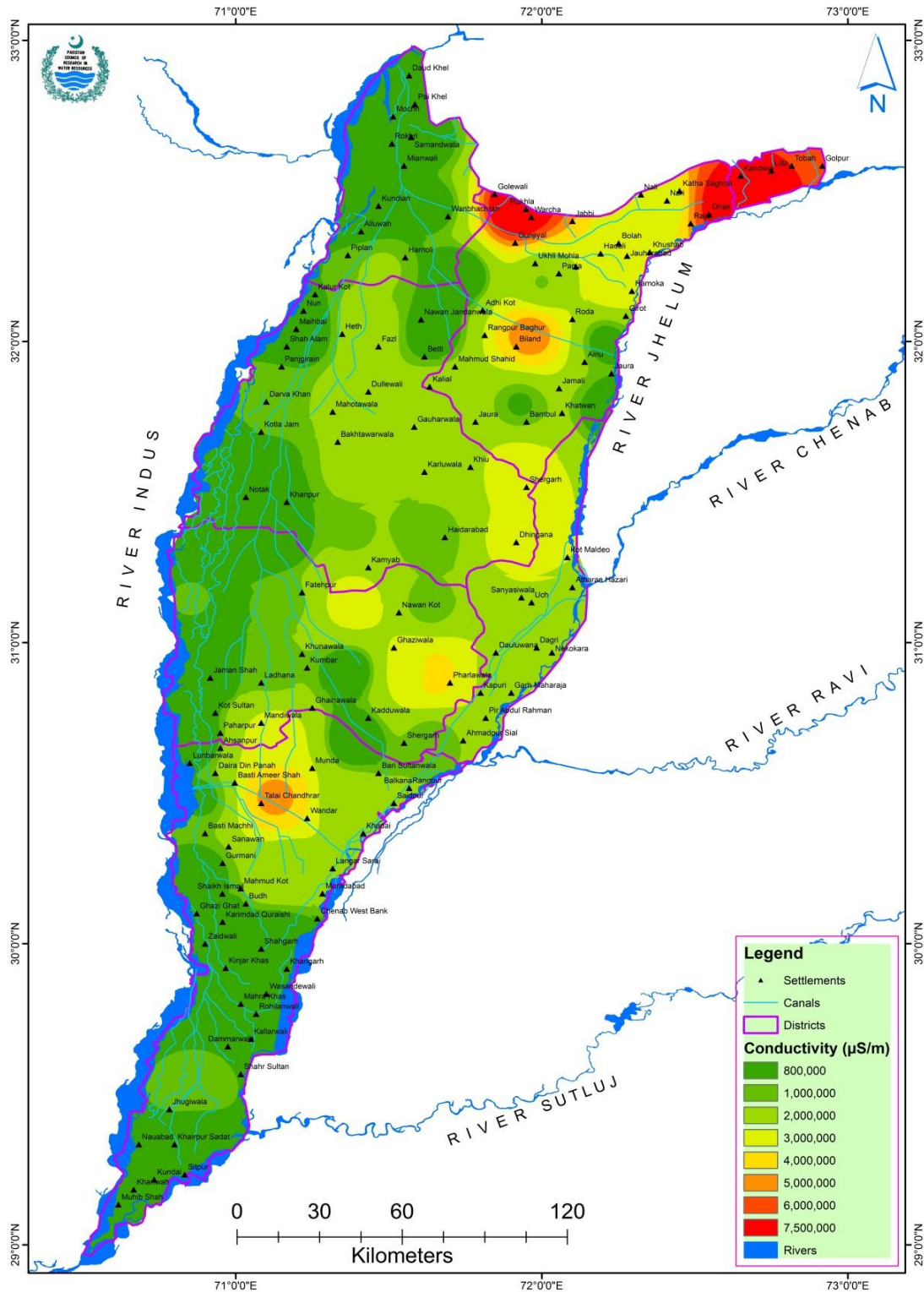


Figure 3: Electrical Conductivity Plot

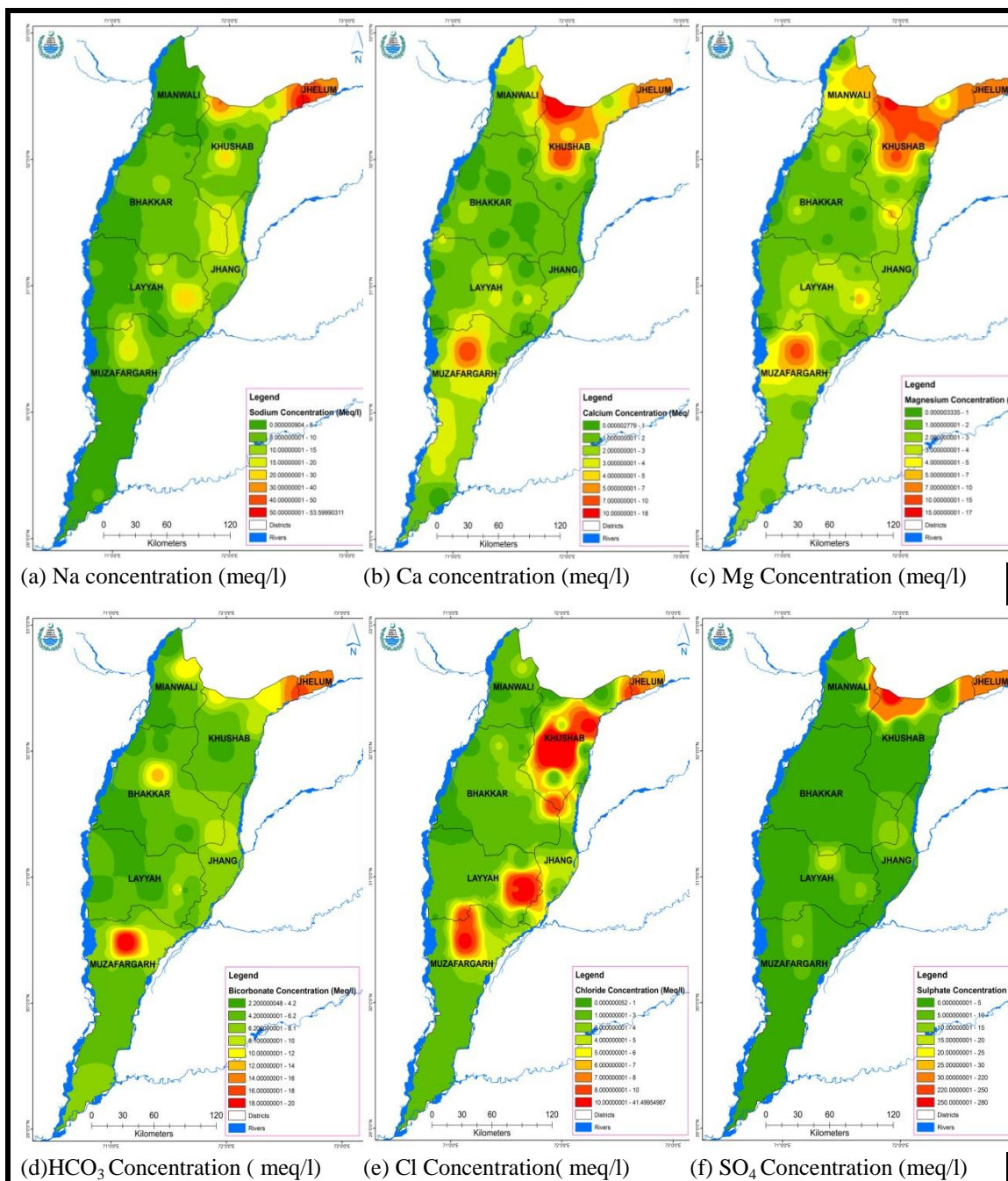


Figure 4: Spatial Variation of Major Anions and Cations Concentration in Thal Doab Groundwater

4.3.1 Piper Plot

The most commonly used graphical diagram which helps in classification of “water type” or “hydrochemicalfacies”; and mixing between two types of waters is Piper Diagram. In Piper Diagram the cations, expressed as percentages of total cations in milliequivalents per liter, are plotted as a single point on the left triangle; while anions, similarly expressed as percentages of total anions, appear as a point to the right triangle. These two points are then projected into the central diamond-shaped area parallel to the upper edges of the central area. This single point is thus uniquely related to the total ionic distribution; a circle can be drawn at this point with its area proportional to the total dissolved solids [20]. The trilinear diagram conveniently reveals similarities and differences among groundwater samples because those with similar qualities will tend to plot together as a groups. Further, simple mixtures of two source waters can be identified. The water quality data of Thal Doab was plotted in Piper Diagram by AquaChem to identify hydrogeochemicalfacies and mixing of groundwater.

The output of Piper as shown in Fig.5 and Table 3 indicates that prominent hydrogeological facies in Thal Doab Aquifer are; CaHCO₃ type followed by NaCl type whereas the mixing of water forms hydrogeological facies like; Ca Na HCO₃ and Ca Mg Cl, Ca, Mg, and HCO₃ type.

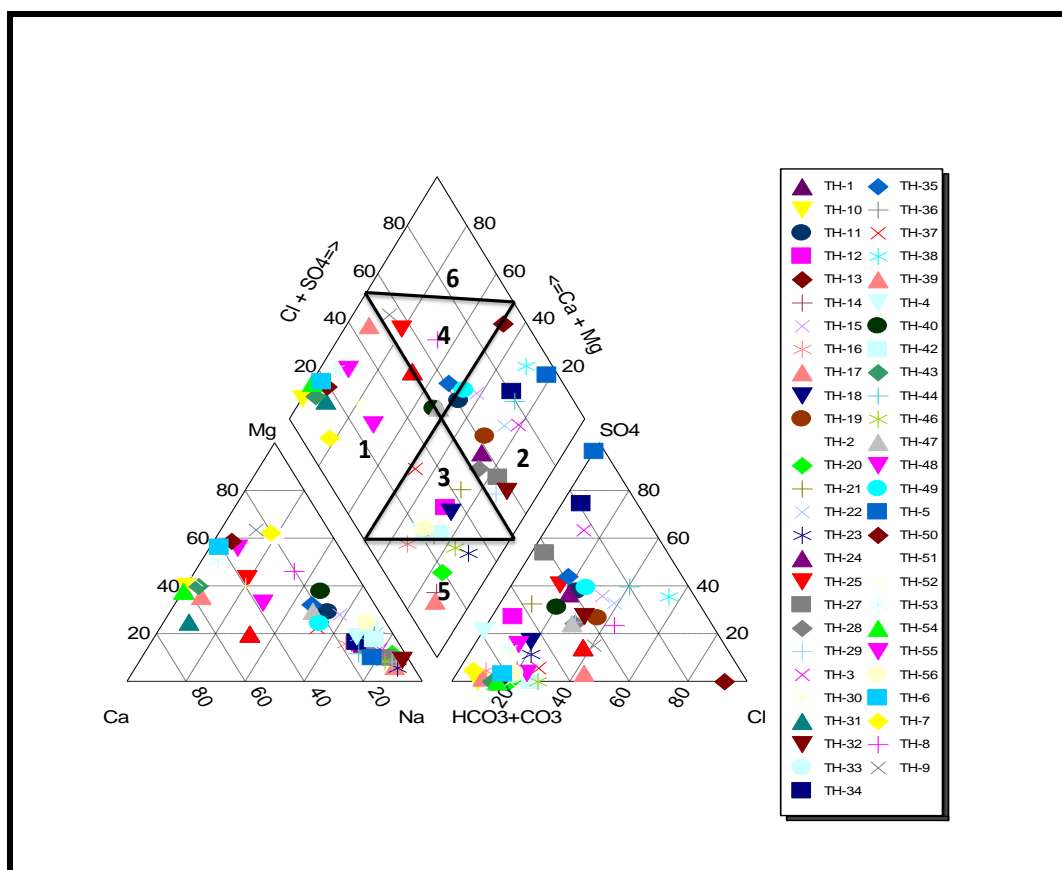


Figure 5: Piper Diagram depicting hydrogeological facies in Thal groundwater

Table 3: hydrogeological Facies as worked out by Piper Diagram

Facies Type	Exploratory Wells No	Number of Samples	Percentage
CaHCO ₃	TH-55,TH-39,TH-46,TH-43, TH-54,TH-6,TH-7,TH-48,TH-18, TH-31	10	22
NaCl	TH-13, TH-16, TH-34, TH-40, TH-19, TH-24, TH-28, TH-29, TH-11, TH-2, TH-32,TH-3, TH-22, TH-15	14	31
Mixed Ca Na HCO ₃	TH-56, Th-42,TH-18, TH-12, TH-21, TH-22, TH-16	7	16
Mixed Ca Mg Cl	TH-49, TH-47, TH-1, Th-25, TH-35, TH-2, TH-22, TH-29	8	18
CaCl	TH-17, TH-20, TH-46, TH-23, TH-14	6	13
Na HCO ₃	NILL		
Total		45	100

4.3.2 Durov Diagram

In Piper Diagram some information are lost during transformation from triangular to diamond-shaped part of the diagram. In this plot magnesium and calcium are combined in cations whereas chloride and sulfate are combined in anions. Durov[21] introduced another diagram which provides more information on the hydrochemical facies by helping to identify the water types. The advantage of this diagram is that it can display some possible geochemical processes that could help in understanding quality of groundwater and its evolution. In Durov it is possible to depict pH and EC in addition to cations and anions. The Durov Diagram for the major cations and anions was plotted using AquaChem software as given in Fig.6. The description of water quality by

marked fields yields that most of the water is along ion- exchange line in zone 3 and along mixing,dissolution line. Few wells are falling along reverse ion exchange and endpoint of aquifer (discharge zone). Durov Diagram indicates that Thal Doab is hydrogeologically active due to extensive pumping for irrigation, rapid replenishment because of transmissive alluvium, source in the form of IBIS and direct precipitation. On pH plot the concentration of wells reveals acidic groundwater as pH of most of the samples is below 7.5.

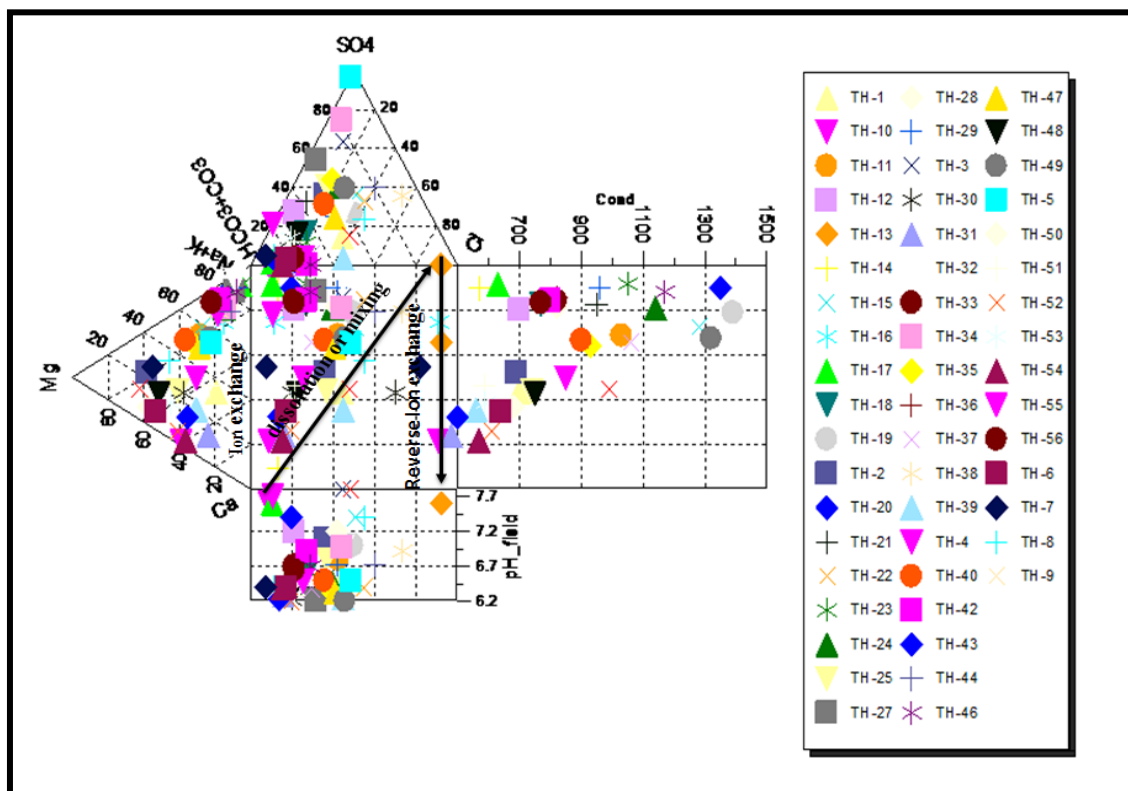


Figure 6: Durov Diagram depicting geochemical processes in Thal groundwater

4.4 Water Quality Assessment for Irrigation

The assessment of the water for irrigation is complex exercise due to interaction of soil-water- crop-climate during plant growth. The salt tolerant crop can give production by using water having 10 years salinity than usual agriculture based on soil and management practices. Soluble salts are present in all natural waters and its concentration and composition determines the suitability for irrigation. The amount of salts in water may be small but may be quite significant to affect yield of crops. Suitability of water for irrigation is based on its salinity, sodicity and toxicity.

The soil salinity problem due to application of water occurs when soluble salts accumulate in the root zone to extent that crops are injured. Salt accumulation increases the osmotic pressure and crop yield are reduced due to effect of osmotic pressure in reducing water uptake by plant.

Another consideration in evaluating irrigation water quality is sodicity (the potential for an excess concentration of sodium) in the soil leading to a deterioration of soil structure. The accumulation of sodium in soils results most often from the use of high Sodium Absorption Ratio (SAR) irrigation water or water with high level of HCO₃ and CO₃ ions. When calcium and magnesium are the predominant cations adsorbed on soil, exchange occurs and soil tends to have a granular structure. On the other hand the proportion of sodium tends to deflocculated soil, disperses the clay and may cause reduction of permeability when the amount of adsorbed sodium increases 10 % of the total cations.

There is long list of toxic element in water in which Boron is important in natural water. Though Boron is essential to plant growth but exceedingly toxic at concentration only slightly higher above optimum i.e. > 1 can become Toxic for crops [22]. However the Boron is a seldom problem in Indus Basin, therefore it is not analyzed in present study. The criteria followed by Provincial Irrigation Drainage Authority (PIDA) in Indus Basin is given in Table 4.

Table 4: Guideline for Interpretations of Water quality for irrigation adopted by PIDA in Pakistan

Parameter	Units	Usability		
		Usable	Marginal	Hazardous
Salinity	S/cm	<1500	1500-3000	>3000
Sodicity(SAR)	-	<10	10-1	>18
RSC	Meq	<2.5	2.5-5	>5
T oxicity(Boron)	Ppm	<1		

The combination of EC and SAR have also been used to determine the suitability of water for irrigation. Wilcox Diagram [23] was used to classify the groundwater samples for irrigation. In this diagram, EC is taken as salinity hazard and SAR as alkalinity hazard as shown in Fig. 7. The Fig. Indicates that out of 56 wells, five wells fall in the hazardous and thirteen wells fallen in marginal groundwater quality zones. In this way 68 % wells are falling in freshusable groundwater under normal cultural practices. The groundwater in 23 percent wells is indicating marginal groundwater which is being successfully utilized by local population as the soils of the area are sandy. Many farmers are using water of more than 4000µS/cm in areas along Jhelum River. However the groundwater in 9 % of wells is found unusable under conventional irrigation practices.

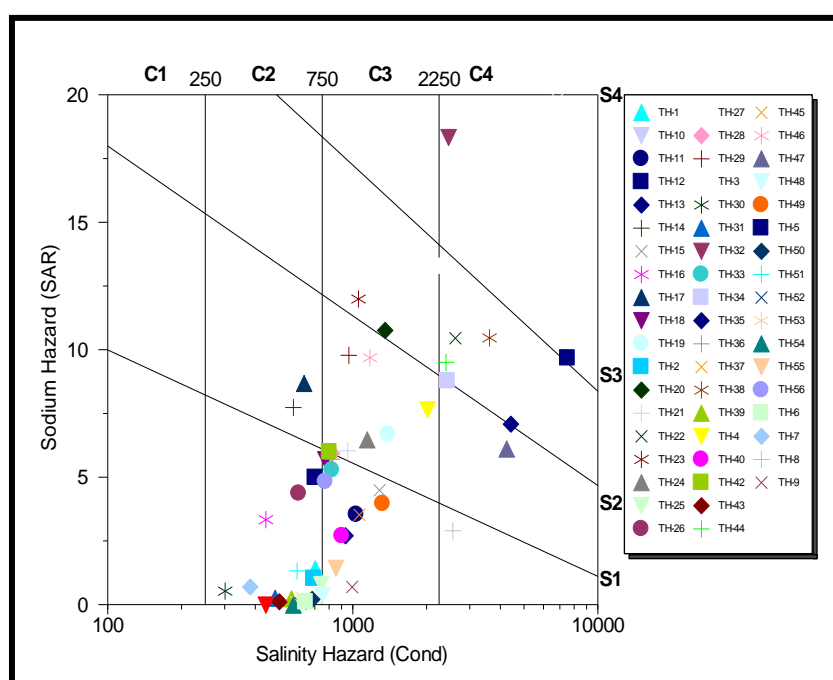


Figure 7: Wilcox diagram illustrating the groundwater quality for irrigation use

V. GROUNDWATER QUALITY EVOLUTION

The source of chemical and reactions that influenced the concentrations of solutes in groundwater of Thal Doab are expected to be: (1) the dissolution of limestone (calcite, CaCO₃) and dolomite (CaMg(CO₃)₂) for Ca, Mg, and HCO₃, (2) the dissolution of gypsum (CaSO₄H₂O) and anhydrite (CaSO₄) for Ca and SO₄, (3) the dissolution of halite (NaCl) for Na and Cl in the SRF. The possible source of ion exchange in Lower Thal might be reactions on the surfaces of some clay minerals whereby sodium is released to the water in exchange for calcium or magnesium. Sodium also is derived from the dissolution of silicate minerals such as plagioclase feldspars fills in this part of Doab. Potassium is most probably derived from the dissolution of silicate in some clay minerals However, some minerals, such as calcite CaCO₃, are expected to be precipitated from solution to form a solid.

In flood plains of Indus where sub-surface geological formation is transmissive and hydraulic gradient is favorable for groundwater recharge is found with low salt concentration up to entire depth of 90 meters. This is main recharge zone in Thal Doab. Away from the flood plains in eastern part of Upper and Middle Thal where the recharge source is mainly precipitation the salt concentration is low in shallow horizons and high in deep groundwater. Fig. 5 shows that anions are low in therecharge area and increasing towards the discharge

area in aquifer. In general the increase in EC and anions dominance evaluation sequence; $\text{HCO}_3 \rightarrow \text{SO}_4 \rightarrow \text{Cl}$ as suggested by Chebotarev[24] holds loosely by reflecting the change from oxidizing to reduction in alluvium aquifer of Thal Doab. This sequence might hold completely for crystalline or pure silicious sedimentary terrain. The cation evaluation sequence in the groundwater system is though difficult to hold, however the zonation identified by Matthes [25]; Ca- Ca+Mg-Na holds good in study area as the freshwater in recharge area has high concentration of Ca as indicted in Fig. 5.

VI. CONCLUSIONS

- I. Alluviums of Indus Plains are well transmissive and replenishment is rapid along rivers as recharge sources is available throughout the year. Water quality mapping revealed that about 1.81 mha constituting about 54percent of Thal Dab is underlain by freshwater of EC less than $1500\mu\text{S}/\text{cm}$.
- II. About 0.45Mha constituting 13 percent of study area is underlain by marginal quality water of EC 1500 to $2500\mu\text{S}/\text{cm}$. This is zone between active flood plains and Bar uplands. Remaining 33 percent area with water relatively higher salt concentration is central part called bar deposits.
- III. The area along Indus is with little vertical variation in water quality and groundwater is fresh upto greater depths(up to 90 meters) which form a huge groundwater reservoir.
- IV. The groundwater of Thal Doab is alkaline type with pH above 7 which is often preferred for drinking purpose.
- V. Thal Doab is hydrogeologically active as indicated by process like dissolution mixing, and ionic exchange in Duorv Diagram.
- VI. Most prominent hydrogeological facies are CaHCO_3 type followed by NaCl type.
- VII. Ca, Mg, and HCO_3 are produced by dissolution of limestone and dolomite and SO_4 is from Gypsum and Anhydrite of Khewrite whereas the Na and Cl are produced from dissolution of rock salt(NaCl) of SRF.

VII. RECOMMENDATIONS

- I. The monitoring network of SCARP Monitoring Organization (SMO) needs to be expanded to entire Thal Doab area and groundwater monitoring data be maintained in proper database system.
- II. Solute transport model should be developed for prediction of saline water intrusions and for different scenarios of pumping of aquifer at different depths

REFERENCES

- [1] Taylor E.M, Malhotra, J.K. and Metha M.I. (1933). An Investigation of Water Table in Upper Chenab Canal Area Punjab. Punjab Irrig. Research Inst., vol no.439 p.
- [2] Wilsdon, B. H, and Bose, N.K (1934). A Gravity Survey of Sub- alluvium of Jhelum-Chenab-Ravi –Doabs and its Application to Problem of Waterlogging; Punjab Irrig. Research Inst., Memv.6, V.1, 44 p.
- [3] Tipton and Kalmbatch. Inc (1963). Feasibility Report for Salinity Control and Reclamation Propjet: 3. in Lower Thal Doab. West Pakistan Water and Power Development Authority, Lahore.
- [4] Greenman, D.W. Swarzenski, W.V., and Bennet, G.D., (1967). The groundwater hydrology of the Punjab, West Pakistan, with emphasis on problems caused by canal irrigation: U.S. Geol. survey water supply paper 1608-H, iv, 66 P.
- [5] Mundorff, M.J. et al (1970). Electric Analog Studies of Flow to Wells in the Punjab Aquifer of West Pakistan. Geological Survey water-Supply Paper 1608-N
- [6] P I & P (Punjab Irrigation and Power Department) (1999). Database for Groundwater Management in Rangpur and Muzaffargarh Canal Commands of Thal Doab (SCARP –III Rangpur Unit)
- [7] Tahir M. A and Hifza Rashid (2008). Distribution of Nitrate in The water Resources of Pakistan. African Journal of Environmental Science and Technology Vol. 2 (11).
- [8] Shaheen A and M. A .Baig (2011). Drought Severity Assessment in Arid Area of Thal Doab, Using Remote Sensing and GIS. Journal of Water Resources and Arid Environments 1(2): 92-101
- [9] Adonis, S. (2007). The Hydrochemical Characteristics of Groundwater in the Incomati Estuary. Master Thesis, Department of Chemistry Faculty of Science University of the Western Cape, Republic of South Africa.
- [10] El-Fiky, A. A. (2010) Hydrogeochemical Characteristics and Evolution of Groundwater at the Ras Sudr- Abu Zenima Area, Southwest Sinai, Egypt. JKAU: Earth Sci., Vol. 21, No. 1, pp: 79-109 (2010 A.D. / 1431 A.H.) DOI: 10.4197 / Ear. 21-1.4.
- [11] Zhang, B. et al., (2012) Hydrochemical Characteristics and Water Quality Assessment of Surface Water and Groundwater in Songnen Plain, Northeast China. Water Research Journal (46) 2737-2748.
- [12] Hagra, M. A. (2013). Water Quality Assessment and Hydrochemical Characteristics of Groundwater in Punjab, Pakistan. IJRRAS, under press August 2013. Volume 16, Issue 2 (August 2013 Issue).
- [13] Kazmi, H. A. and Jan, M. Q. (1997). Geology and Tectonics of Pakistan. Graphic Publisher, Pakistan. 528 p
- [14] WAPDA (1989). Booklet on Hydrogeological Map of Pakistan scale 1:2,000,000 First edition

- [15] Kahlown. M. A. and Majeed A. (2004) Pakistan Water Resources Development and Management. Pakistan Council of Research in Water Resources, Islamabad, Pakistan.209 p.
- [16] Runnells, D.D. (1993). Inorganic Chemical Processes and Reactions, in Alley, W.M.,ed., Regional Groundwater Quality :New York, Van Nostrand Reinhold, 31-153.
- [17] Herczeg, A.L, and Edmunds, W.M., (1999). Environmental Tracers in Subsurface Hydrology: Boston, Kluwer Academic Publishers, 31-77.<http://www.academicjournals.org/AJest>
- [18] APHA, A WW A and WEF, D.E .(1992). Standard Methods for the Examination of Water and Wastewater.American Public Health Association, American Water Works Association and Water Environment Federation, 18th Edition, Washington, DC.
- [19] Kehew, A.E., (2001). Applied Chemical Hydrogeology. Prentice-Hall, Inc., 368 p.
- [20] Piper, A. M., (1944) A Graphical Procedure in the Geochemical Interpretation of Water Analysis. Am. Geophys Union Trans. V. 25, 914-928.
- [21] Durov, S. A. (1948). Natural Waters and Graphical Representation of Their Composition.Dokl.Akad.Nauk. USSR 59, 87-90.
- [22] FAO/ UNESCO (1973). Irrigation, Drainage and Salinity.An International Source Book. Paris, Unesco/Hutchinson (Publishers), London. 510 p.
- [23] Wilcox, L.V. (1955). Classification and use of irrigation waters.U.S.Dept. Agriculture Circular.
- [24] Chebotarev, I., (1955). Metamorphism of Natural Waters in The Crust of Weathering. Geochim.Cosmochim.Act, Vol. 8, London, New York, 23-48, 13-170,198-212.
- [25] Matthes, G. (1981). Properties of groundwater.AWiely –IntersciencePublication.New York, Chichester, Brisbane, Toronto, Singapore, 406 p.

Study the Effect of Different SHPB Test Parameters Using Numerical Simulation Technique

S. K. Gupta¹, S. K. Moulick²

¹Mechanical, BIT Durg/ CSVTU, bhilai, india

²Department of Mechanical Engineering, BIT Durg, India

ABSTRACT: Numerical simulation of split Hopkinson pressure bar (SHPB) test used for material characterization under high strain rates is presented. Finite element model is developed to simulate the dynamic compression response at high strain rates. A series of numerical simulations of SHPB tests using cylindrical specimens are conducted with ANSYS/LS-DYNA and validated with already published results. This dynamic analysis is performed to characterize the foam at higher strain rates (greater than 1000/s). In the present work, attempt has been made to numerically simulate the SHPB to study the effect of various test parameters and also to optimize these parameters so that the need of the repetitive testing can be reduced which ultimately results in cost and time saving.

Keywords: Hopkinson bar, High strain rates, FE modeling, Syntactic foam.

I. INTRODUCTION

Split Hopkinson bar test is a standard method to investigate the mechanical properties of materials under high strain rates (Hopkinson, 1914; Kolsky, 1949). The conventional Hopkinson bar shown in Figure 1. It consists of a striker bar, an incident bar, the specimen, and a transmitted bar. In this setup, when the striker bar hits the incident bar, a compression wave with a specific amplitude moves through the length of bars and sample. The compressive wave is a function of the velocity and length of the striker. When the wave reaches the end of the incident bar, (i.e. at interface of incident and sample) a fraction of this wave is transmitted to the specimen and part of it is reflected as shown in the Figure 2. These reflected and transmitted waves are recorded using data acquisition system and then converted into stress-strain curves based on one dimensional wave propagation theory (Goel et al., 2012). The split Hopkinson bar is one of the most common experimental methods used to characterize material at high strain rates. This technique is used to measure stress-strain response of materials at high strain rates, typically in the range of 10^3 - 10^6 /s (Goel et al., 2013). Recent advancements in the field of lightweight materials necessitated the need of high strain rate testing of the materials. This is required to understand the materials properties which to predict the behavior of the materials at different strain rates. In the present investigation, focus is on light weight metal foam. Hence, to use these foams for various applications in aviation and automotive sector, this investigation is essential (Goel et al., 2012). When these light weight metal foams are used in aircraft and automotive components or in shock-absorbing applications, it is necessary to understand the dynamic foam properties under impact loading conditions. To test these materials it requires a large experimental setup and extensive labor. Instead it can be easily done with the help of numerical simulation (Goel et al., 2013). A standard such as numerical simulations would enable data comparison and would facilitate the development of analytical models which eliminates the need for repetitive testing. Due to the lack of material properties under impact loading conditions, it is highly desirable to obtain dynamic stress-strain curves at higher strain rates directly from carefully controlled parameters. Such data are essential for conducting realistic numerical simulations for the safety design of structures. Hence, in this investigation a detailed simulation of SHPB is presented.

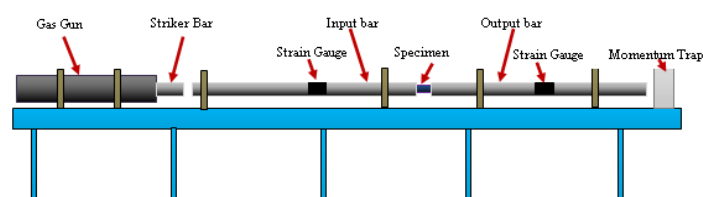


Fig 1: Conventional split Hopkinson pressure bar.

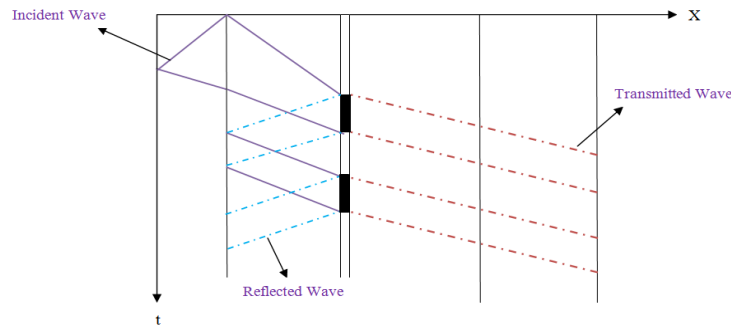
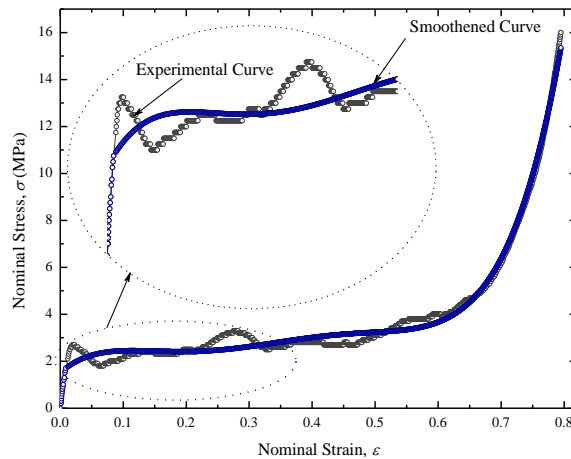


Fig 2: Wave propagation in SHPB.

II. NUMERICAL SIMULATION

The finite element code LS-DYNA is employed to model and analyze the SHPB test setup. A three dimensional model is developed to simulate the SHPB system. Several numerical simulations are carried to study the effect of the various parameters on SHPB measurements.

Both incident and transmitter bar are modeled with a radius of 11 mm and a length of 1 m. whereas the specimen is 14 mm in diameter and 7 mm in length. Instead of modeling a striker bar, the stress wave pulse corresponding to striker length and velocity is directly applied at the end of the incident bar. The bars are modeled as elastic materials with density $\rho = 1190 \text{ kg/m}^3$, Young's Modulus $E = 3.4 \text{ GPa}$ and Poisson's ratio $\nu = 0.35$. The foam specimen properties are $\rho = 270 \text{ kg/m}^3$, Young's Modulus $E = 1.1 \text{ GPa}$ and plastic Poisson's ratio $\nu = 0$. Figure 3 shows the typical quasi-static stress strain curve of the metal foam used in the present investigation. The finite element model includes the incident bar, specimen and the transmitted bar. Figure 4 (a) shows the finite element model for SHPB used in LS-DYNA.



2.1 Assumptions

- The incident, transmission, and the striker bar remain elastic during the testing.
- Wave propagation within the pressure bar is one-dimensional.
- Specimen undergoes homogeneous deformation.

2.2 Formulation

$$\frac{d\varepsilon_s(t)}{dt} = -\frac{2C_0}{L} \varepsilon_R(t)$$

$$\varepsilon_s(t) = -\frac{2C_0}{L} \int_0^t \varepsilon_R(t) dt$$

$$\sigma_s(t) = E \frac{A_0}{A} \varepsilon_T(t)$$

where,

C_0 = Wave propagation Velocity.

L = Length of the pressure Bar.

A_0 = Cross sectional Area.

$\varepsilon_T(t)$ = Transmitted strain.

$\varepsilon_R(t)$ = Reflected strain.

An assembly containing all parts (bars and specimen) is modeled using three dimensional solid constant stress element (LS DYNA). The bars have 90 elements in their cross section and 80 along the length, whereas the specimen has 300 elements and 7 mm along the length. Structured meshing is applied in both the bars with a little refinement in mesh of the specimen. The butterfly mesh configuration in LS-DYNA has been considered for modeling. Mesh configuration of the metal foam specimen is shown in Figure 4 (b), whereas Figure 4 (a) presents a detail of the model assembly in the region of contact between the specimen and both the bars. The effect of the meshing is also been discussed in the later part of the paper. The surface in contact is defined as frictionless. The contact between the bars and the specimen are defined as automatic surface to surface (LS-DYNA). Initial boundary conditions are applied to the input bars and specimen such that only movement in one direction is allowed. The end of output bars is constrained.

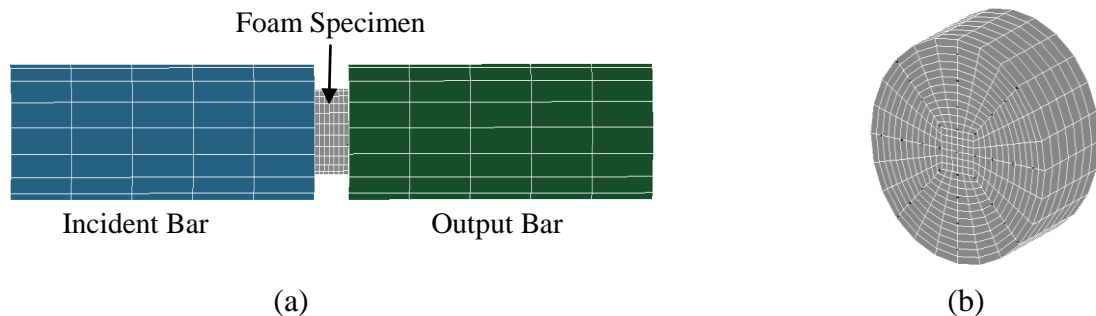


Fig 4 (a): Detail of the model assembly in the region of contact between the specimen and bars, **4 (b):** Mesh configuration of the metal foam specimen.

III. MODEL VALIDATION

This section presents the validation of the numerical scheme with already published results. This is presented to show that the numerical simulation technique used in the present investigation is valid and accurate. For validation purpose, results reported by Irausquín et al. (2010) are used. In the present investigation, the SHPB bar and specimen geometry are exactly same as those reported by Irausquín et al. (2010). The Figure 5 shows the results obtained from the present simulation of SHPB using LS-DYNA and those reported by Irausquín et al. (2010). It can be observed that the results are in good agreement with the results reported by Irausquín et al. (2010), hence validating the present FE approach.

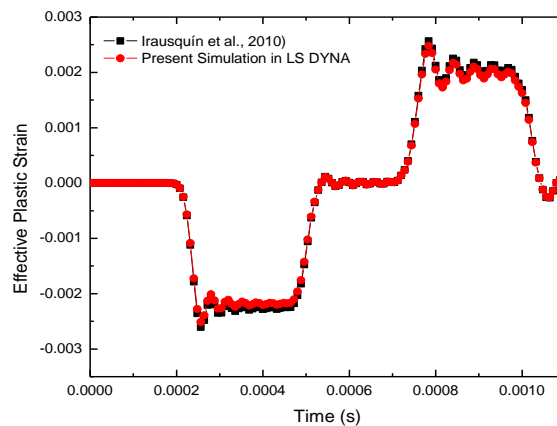


Fig 5: Validation of the present numerical scheme with the results reported by Irausquín et al., 2010

IV. RESULT AND DISCUSSIONS

Present investigation is carried with an aim of studying the effect of different SHPB test parameters on the wave propagation in metal foam and also to predict the optimal value of these parameters which governs the numerical simulation of SHPB. Figure 6 shows the typical incident reflected and transmitted wave time history obtained from numerical simulation. There are several aspects about the split Hopkinson pressure bar that can be varied in order to test different materials. Out of these many parameters, there are two parameters (i.e. the striker bar length and velocity) those have a significant impact on the split Hopkinson pressure bar results.

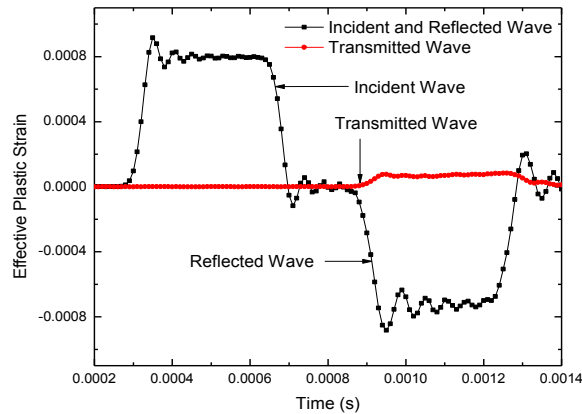


Fig 6: Incident reflected and transmitted wave obtained from simulation.

4.1. Effect of Length of Striker Bar

Figure 7 shows the effect of length of striker bar on the reflected and transmitted wave for three different striker lengths. It can be observed that as the striker length increases, the wave duration also increases. The trend of striker bar length to wave duration is linear. This shows that the wave duration is proportional to striker bar length. However, with the increase in length of striker, the peak pulse is unaffected for the scenario considered in the present investigation.

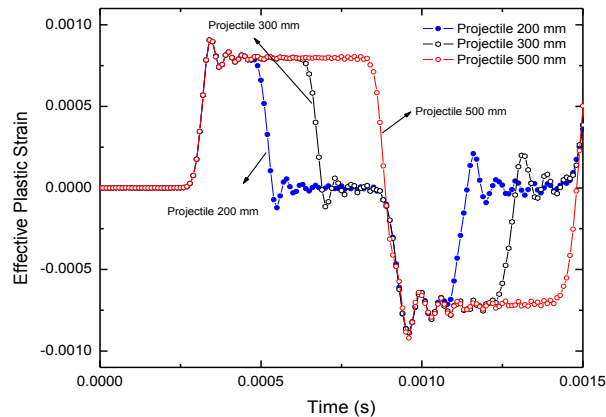


Fig 7: Effect on the wave pulse with different striker length.

4.2 Effect of Striker bar Velocity

Figure 8 shows the effect of striker velocity on the incident and reflected wave. It can be observed from the results that the amplitude of the wave is directly proportional to the striker bar velocity as the velocity increase the amplitude of the wave increases for the parameters considered in the present investigation. It can also be seen that there is little variation in amplitude in case of 12 m/s and 18 m/s as compared to the amplitude of 9 m/s and 25 m/s obtained from simulation. Hence, striker velocities govern the peak pulse

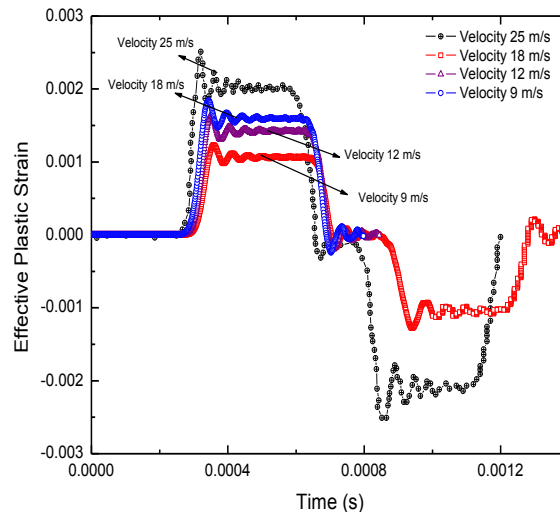


Fig 8: Incident and reflected wave of input bar with different striker bar velocity.

4.3 Effect on the Wave with Different Foam Material Models

Selecting a material model is a complex task as it requires in-depth knowledge of the behavior of the materials. However, this is not always possible in case of newly developed materials. A wide variety of material models are available for different types of foams in LS DYNA proposed by different researchers (LS DYNA). Some of these are designed to capture the important characteristics for particular types of foams and may not be applicable to other type of foam. Hence, it becomes important to understand these material models before applying them to newly developed foam materials. Furthermore, it is important to reproduce these behaviors in simulation; an effort must be made to calibrate such material models for the best results. Hence effective choice must be made while selective the material model depending upon the types of the materials to be used. Two material model MAT- 63 Crushable Foam Material Model and MAT 154 - Deshpande and Fleck Foam Model is considered in the present investigation which incorporates the effect of the strain rate (LS-DYNA). Figure 9 shows the effect of the different material model on the incident and reflected wave of the input bar. It can be seen from this figure that there is little variation in the wave pulse while considering the different material model. Hence, for modeling the present foam material either of the material models available in LS DYNA can be used.

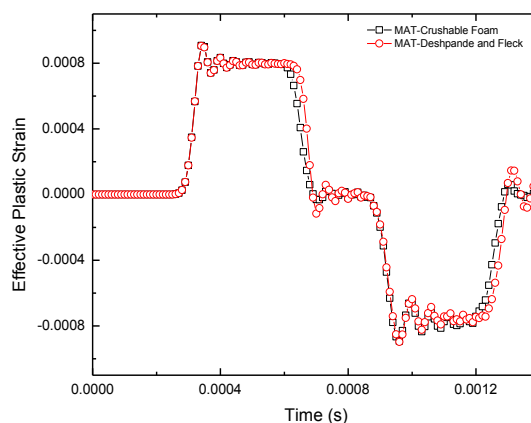


Fig 9: Effect of different material models on the incident and reflected wave of input bar.

4.4 Effect of the Modeling Parameters on the Waves

Figure 10 (a) shows the effect of mesh size on the incident and reflected wave of the input bar. Finer mesh (Incident and transmitter bar with 90 elements in radial direction and 80 elements along length whereas for specimen, 300 elements along radial direction and 7 elements along length) gives fewer oscillations compared to the coarse mesh (Incident and transmitter bar with 8 elements in radial direction and 80 elements along length whereas for specimen, 15 elements along radial direction and 7 elements along length) but with more computation time. It can also be seen from the figure that with the coarser mesh the wave shows more oscillations compared to the finer mesh. Figure 10 (b) depicts the effect of different element formulation taken

into consideration during modeling. The element formulation 1 is constant stress solid element and element formulation 2 is fully integrated solid element, while comparing the result obtained from above two formulation it is observed that there is no significant difference in the results, so we can take either of the elements formulation during modeling in case of metal foam.

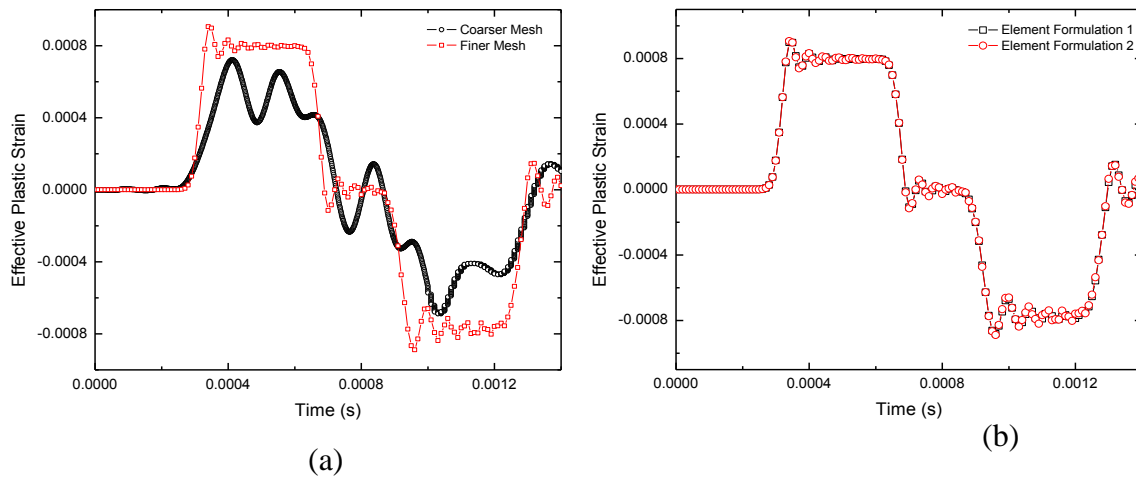


Fig 10 (a): Incident and reflected wave from numerical simulation of fine and coarser mesh, **10 (b):** Incident and reflected wave of input bar with different element formulation.

Figure 11 shows the simulated model of the split Hopkinson pressure bar. This figure shows the deformation of the specimen when the stress wave travels through the bars and reaches the interface between the incident bar and specimen. Striker generates a compressive stress waves in the incident bar which travels in a uniaxial direction to hit the test specimen. At this instance, generated compressive stress wave by the incident bar is partially transmitted into the transmitted bar through the test specimen. However, some of the compressive stress waves in the incident bar would reflect back into it as a tensile stress wave. Strains are recorded from both incident and transmitted bars with the help of the numerical strain gauges mounted on the bars using reference point. Figure 12 (a) 12 (b) show the stress wave pulse travelling from one end of the incident bar to the other end of the transmitter bar at different time intervals. The Figure 12 (a) shows that stress wave starts traveling from the incident bar at the time interval of about 0.0007 s and as the time reaches 0.00033 s the stress wave has travelled about half the distance of the incident bar. As further the time increases and become equal to about 0.0003 s the wave reaches the interface of the incident bar and specimen and the deformation of the specimen take place. At the time interval of about 0.0011 seconds the wave reaches at the end of the transmitter bar and some of the wave are transmitted back which is shown in Figure 12 (b).

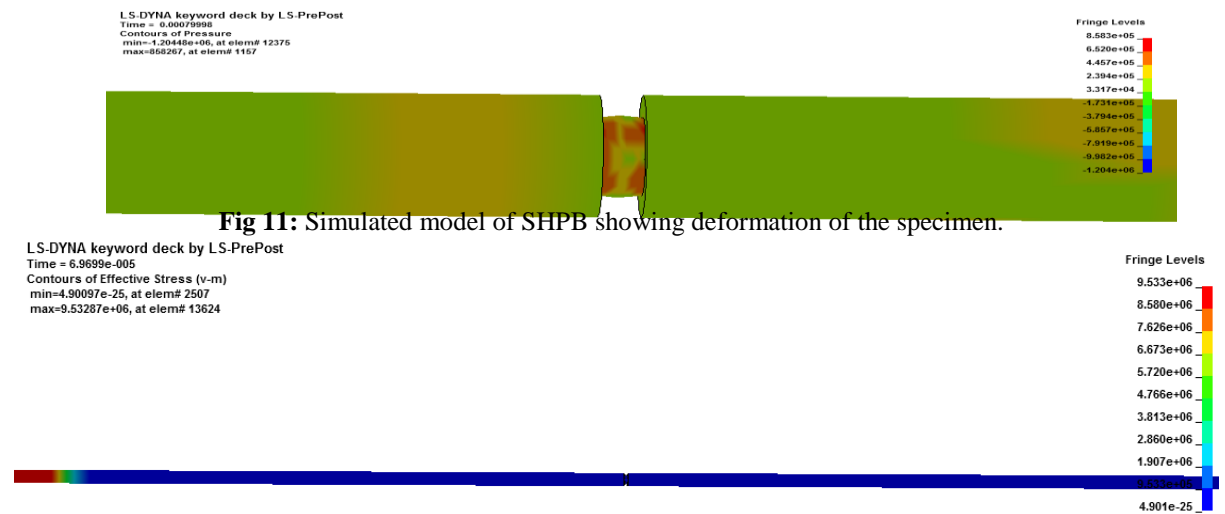


Fig 11: Simulated model of SHPB showing deformation of the specimen.

LS-DYNA keyword deck by LS-PrePost
Time = 0.0011996
Contours of Effective Stress (v-m)
min=2401.14, at elem# 6914
max=957756, at elem# 4221

Fringe Levels
9.578e+05
8.622e+05
7.667e+05
6.711e+05
5.756e+05
4.801e+05
3.845e+05
2.890e+05
1.935e+05
9.794e+04
7.401e+04



Fig 12: Wave propagation and effective stress at different time intervals.

V. CONCLUSION

Numerical simulation is an effective tool for carrying out the study of the wave on the behavior of metal foam. Parametric studies show the effects of the various parameters on the behavior of foam, which can effectively be used to carry out the studies and model the SHPB with ease. Using LS DYNA, a three dimensional split Hopkinson pressure bar is modeled and following conclusions are drawn from the simulation:

1. As the striker bar length increases the wave duration increases. The trend of striker bar length to wave duration is linear.
2. Amplitude of the wave is directly proportional to the striker bar velocity as the velocity increase the amplitude of the pulse increases.
3. Materials model play an important role while studying the behavior of any metal foam, accurate materials model is must to accurately predict the behavior of metal foam during simulation.
4. The meshing play an important role during the modeling so optimized meshing should be chosen to get the best result with minimum computational time. The meshing is related to computational time as the meshing become finer the computational time also increases.
5. An important criterion for SHPB test could be impact velocity, as maximum allowable impact velocity depends upon the specific materials.
6. Effect of friction between bars and specimen may play an important role for material's behavior under dynamic loading in the case of large plastic strain, even if lubricant is used, effect of which is not considered in the simulation.

REFERENCES

- [1] Hopkinson, B. (1914). "A method of measuring the pressure produced in the detonation of high explosive or by the impact of bullets", *Philosophical Transactions of the Royal Society of London*, pp. 497-508.
- [2] Kolsky, H. (1949). "An Investigation of the mechanical properties of materials at very high rates of strain", *Proceedings of Royal Physical Society*, B 62, pp. 676-700.
- [3] Goel, M.D., Peroni, M., Solomos, G., Mondal, D.P., Matsagar, V.A., Gupta, A.K., Larcher, M. and Marburg, S. (2012). "Dynamic compression behavior of cenosphere aluminum alloy syntactic foam." *Materials and Design*, 42, 418-423.
- [4] Goel, M.D., Matsagar, V.A., Gupta, A.K. and Marburg, S. (2012). "Strain rate sensitivity of closed cell aluminum fly ash foam." *Transactions of Nonferrous Metals Society of China*, Vol. 23, pp. 1080-1089.
- [5] Iraisquin, F. Teixeira-Dias, V. Miranda, J.L. Pérez-Castellanos (2010) "Numerical modeling of the dynamic compression of a closed cell aluminum foam." *Iberian Conference on Fracture and Structural Integrity*, Porto, Portugal.
- [6] LS-DYNA keyword User's Manual, Version 971.

Design and Implementation of OFDM Trans-Receiver for IEEE 802.11(WLAN)

Soham Bhavsar, Harshit Pandey, Prithviraj Chouhan

Department of Electronics & Communication, Shankersinh Vaghela Babu Institute of Technology,
Gujarat Technological University, Gujarat, India

ABSTRACT: Orthogonal Frequency Division Multiplexing (OFDM) is a multi-carrier modulation technique. OFDM provides high bandwidth efficiency because the carriers are orthogonal to each other's and multiple carriers share the data among themselves. The main advantage of this transmission technique is their robustness to channel fading in wireless communication environment. Orthogonally placed sub carriers are used to carry the data from the transmitter end to the receiver end. Presence of guard band in this system deals with the problem of ISI and noise is minimized by larger number of sub carriers. This paper present transmission of an OFDM System using the software tool MATLAB and have undertaken various methods to reduce the errors in the system so that this system can be used more commonly and effectively.

Keywords: FFT, IFFT, MATLAB

I. INTRODUCTION

With the ever growing demand of this generation, need for high speed communication has become an utmost priority. Various multicarrier modulation techniques have evolved in order to meet these demands, few notable among them being Code Division Multiple Access (CDMA) and Orthogonal Frequency Division Multiplexing (OFDM) [1]. Orthogonal Frequency Division Multiplexing is a frequency division multiplexing (FDM) scheme utilized as a digital multi carrier modulation method. A large number of closely spaced orthogonal sub carriers is used to carry data. The data is divided into several parallel streams of channels, one for each sub carriers. Each sub carrier is modulated with a conventional modulation scheme (such as BPSK) at a low symbol rate, maintaining total data rates similar to the conventional single carrier modulation schemes in the same bandwidth. OFDM is being used because of its capability to handle with multipath interference at the receiver. Due to multipath it faces the problem of inter symbol interference (ISI) and inter channel interference (ICI). Hence, the two main drawbacks of OFDM are the large dynamic range of the signals being transmitted and the sensitivity to frequency errors. Using a MATLAB simulation we can implement an OFDM transmission. Using this simulation we can see the amount of errors coming in the transmission by using different conventional modulation schemes. Then we can analyze the results of each transmission and see how these errors can be reduced.

II. OFDM DETAIL OVERVIEW

This section covers the details regarding the development of OFDM system and important terminologies.

A. Development of OFDM System

The development of OFDM systems can be divided into three parts. This comprises of Frequency Division Multiplexing, Multicarrier Communication and Orthogonal Frequency Division Multiplexing. Frequency Division Multiplexing is a form of signal multiplexing which involves assigning non overlapping frequency ranges or channels to different signals or to each user of a medium. A gap or guard band is left between each of these channels to ensure that the signal of one channel does not overlap with the signal from an adjacent one. Due to lack of digital filters it was difficult to filter closely packed adjacent channels [2]. As it is ineffective to transfer a high rate data stream through a channel, the signal is split to give a number of signals over that frequency range. Each of these signals are individually modulated and transmitted over the channel. At the receiver end, these signals are fed to a de-multiplexer where it is demodulated and recombined to obtain the original signal.

B. OFDM Theory

Orthogonal Frequency Division Multiplexing is a special form of multicarrier modulation which is particularly suited for transmission over a dispersive channel [2].

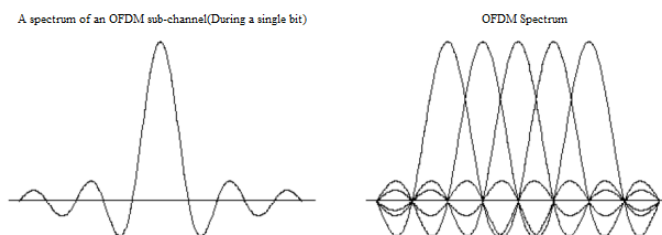


Figure 1. OFDM Spectrum

a) Orthogonality: Two periodic signals are orthogonal when the integral of their product over one period is equal to zero.

For The case of continuous time:

$$\int_0^T \cos(2\pi n f_0 t) \cos(2\pi m f_0 t) dt = 0,$$

For the case of Discrete Time:

$$\sum_{k=0}^{N-1} \cos\left(\frac{2\pi k n}{N}\right) \cos\left(\frac{2\pi k m}{N}\right) dt = 0,$$

Where $m \neq n$ in both cases.

b) Sub-Carriers: Each sub-carrier in an OFDM system is a sinusoid with a frequency that is an integer multiple of a fundamental frequency. Each sub-carrier is like a Fourier series component of the composite signal, an OFDM symbol.

$$\begin{aligned} s(t) &= \cos(2\pi f_c t + \theta_k) \\ &= a_n \cos(2\pi n f_0 t) + b_n \sin(2\pi n f_0 t) \\ &= \sqrt{a_n^2 + b_n^2} \cos(2\pi n f_0 t + \varphi_n), \end{aligned}$$

The sum of the sub – carriers is then the baseband OFDM signal:

$$s_B(t) = \sum_{n=0}^{N-1} \{a_n \cos(2\pi n f_0 t) - b_n \sin(2\pi n f_0 t)\}$$

c) Inter Symbol Interference: Inter symbol interference (ISI) is a form of distortion of a signal in which one symbol interferes with subsequent symbols. This is an unwanted phenomenon as the previous symbols have similar effect as noise, thus making the communication less reliable. ISI is usually caused by multipath propagation or the inherent nonlinear frequency response of a channel causing successive symbols to blur together. The presence of ISI in the system introduces error in the decision device at the receiver output [3].

d) Inter Carrier Interference: Presence of Doppler shifts and frequency and phase offsets in an OFDM system causes loss in orthogonality of the sub carriers. As a result, interference is observed between sub-carriers. This phenomenon is known as inter carrier interference (ICI).

e) Cyclic Prefix: The Cyclic Prefix or Guard Interval is a periodic extension of the last part of an OFDM symbol that is added to the front of the symbol in the transmitter, and is removed at the receiver before demodulation. The cyclic prefix has important benefits that, the cyclic prefix acts as a guard interval. It eliminates the inter symbol interference from the previous symbol.

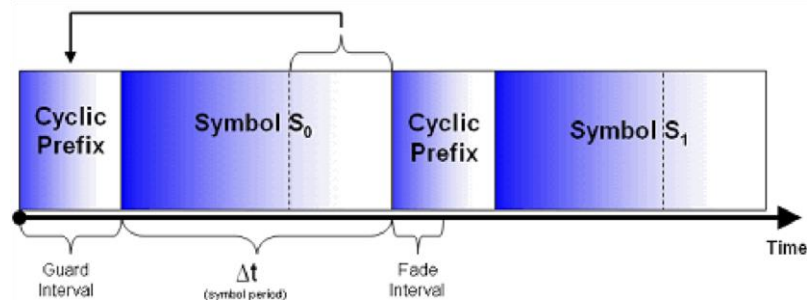


Figure 2. Cyclic Prefix

f) Modulation: Modulation is the technique by which the signal wave is transformed in order to send it over the communication channel in order to minimize the effect of noise. This is done in order to ensure that the received data can be demodulated to give back the original data. In an OFDM system, the high data rate information is divided into small packets of data which are placed orthogonal to each other. This is achieved by modulating the data by a desirable modulation technique (QPSK). After this, IFFT is performed on the modulated signal which is further processed by passing through a parallel to serial converter. In order to avoid ISI we provide a cyclic prefix to the signal.

g) Communication Channel: This is the channel through which the data is transferred. Presence of noise in this medium affects the signal and causes distortion in its data content.

h) Demodulation: Demodulation is the technique by which the original data (or a part of it) is recovered from the modulated signal which is received at the receiver end. In this case, the received data is first made to pass through a low pass filter and the cyclic prefix is removed. FFT of the signal is done after it is made to pass through a serial to parallel converter. A demodulator is used, to get back the original signal.

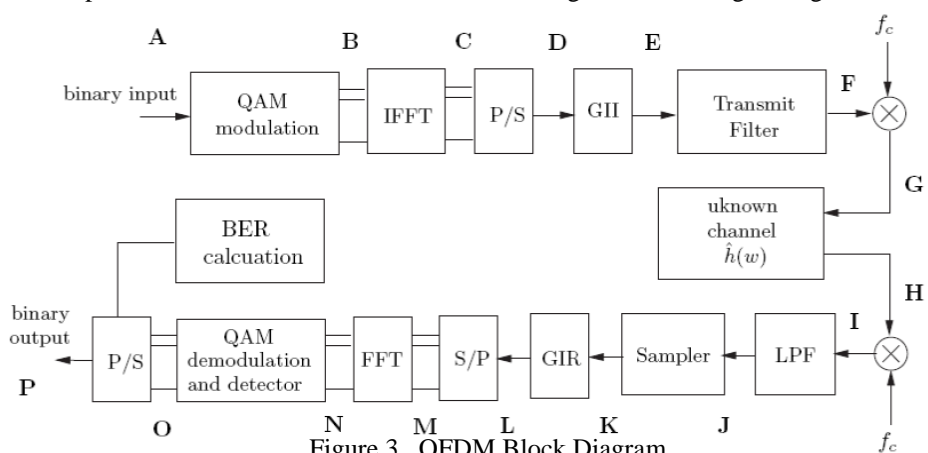


Figure 3. OFDM Block Diagram

III. DESIGN AND IMPLEMENTATION

A. Overview

Figure 3 shows a block diagram of an OFDM system. ADC, DAC, and RF front-ends (Amplification, RF up conversion/down conversion, etc.) are not simulated in this project. This MATLAB simulation program consists of six files. The MATLAB code used in this paper was developed by Paul Guanming Lin [4]. This implementation is used to transmit a computer file in binary data form modulated by OFDM [5].

OFDM_SIM.m shall be run while other m-files will be invoked accordingly. Source data for this simulation is taken from an 8-bit bitmap image file based on the user's choice. The image data will then be converted to the symbol size (bits/symbol) determined by the choice of MPSK from four variations provided by this simulation. The converted data will then be separated into multiple frames by the OFDM transmitter. The OFDM modulator modulates the data frame by frame.

Before the exit of the transmitter, the modulated frames of time signal are cascaded together along with frame guards inserted in between as well as a pair of identical headers added to the beginning and end of the data stream. The communication channel is modeled by adding Gaussian white noise and amplitude clipping effect.

The receiver detects the start and end of each frame in the received signal by an envelope detector. Each detected frame of time signal is then demodulated into useful data. The modulated data is then converted

back to 8-bit word size data used for generating an output image file of the simulation. Error calculations are performed at the end of the program. Representative plots are shown throughout the execution of this simulation

B. System Configuration and Parameters

At the beginning of this simulation MATLAB program, a script file ofdm_parameters.m is invoked, which initializes all required OFDM parameters and program variables to start the simulation. Some variables are entered by the user [4].The rest are either fixed or derived from the user-input and fixed variables. The user input variables include:

- 1) Input file:an 8-bit grayscale (256 gray levels) bitmap file
- 2) IFFT size: an integer of a power of two;
- 3) Number of carriers: not greater than [(IFFT size)/2 – 2];
- 4) Digital modulation method: BPSK, QPSK, 16-PSK
- 5) Signal peak power clipping in dB
- 6) Signal-to-Noise Ratio in dB

All user-inputs are checked for validity and the program will request the user to correct any incorrect fields with brief guidelines provided. An example is shown in Figure 4. This script also determines how the carriers and conjugate carriers are allocated into the IFFT bins, based on the IFFT size and number of carriers defined by the user. Figure 5 shows an example of 120 carriers and 120 conjugate carriers spreading out on 256 IFFT bins.

```
#####
#***** OFDM Simulation *****#
#####

source data filename: abc
"abc" does not exist in current directory.
source data filename: cat.bmp
Output file will be: cat_OFDM.bmp
IFFT size: 1200
IFFT size must be at least 8 and power of 2.
IFFT size: 1024
Number of carriers: 1000
Must NOT be greater than ("IFFT size"/2-2)
Number of carriers: 500
Modulation(1=BPSK, 2=QPSK, 4=16PSK, 8=256PSK): 3
Only 1, 2, 4, or 8 can be choosen
Modulation(1=BPSK, 2=QPSK, 4=16PSK, 8=256PSK): 4
Amplitude clipping introduced by communication channel (in dB): 6
```

Figure 4. User Input Panel

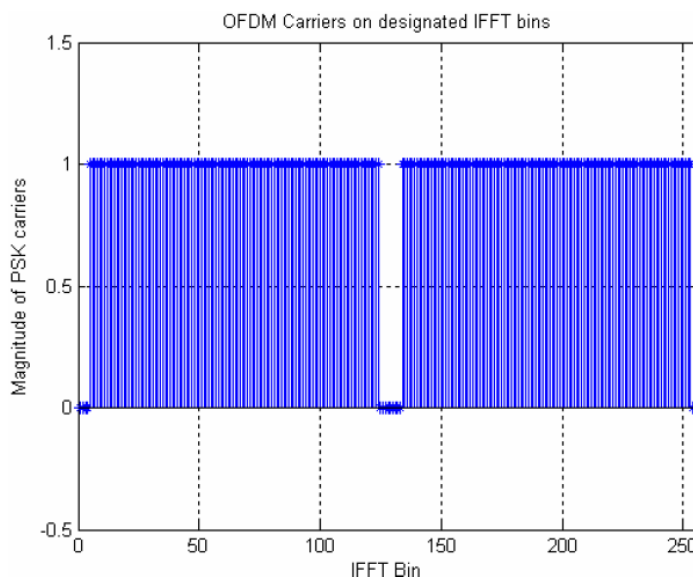


Figure 5. OFDM carriers allocated to IFFT bins

C. OFDM Transmitter

Frame Guards:

The core of the OFDM transmitter is the modulator, which modulates the input data stream frame by frame. Data is divided into frames based on the variable `symb_per_frame`, which refers to the number of symbols per frame per carrier. It is defined by: $\text{symb_per_frame} = \text{ceil}(2^{13}/\text{carrier_count})$. This limits the total number of symbols per frame ($\text{symb_per_frame} * \text{carrier_count}$) within the interval of $[2^{13}, 2*(2^{13}-1)]$, or [8192, 16382]. However, the number of carriers typically would not be much greater than 1000 in this simulation, thus the total 14 number of symbols per frame would typically be under 10,000. This is an experimentally reasonable number of symbols that one frame should keep under for this MATLAB program to run efficiently; thereby `symb_per_frame` is defined by the equation shown above. As shown in Figure 6, even if the data stream is not sufficiently long to be divided into multiple frames, two frame guards with all zero values and in a length of one symbol period are still added to both ends of the modulated time signal. This is to assist the receiver to locate the beginning of the substantial portion of the time signal.

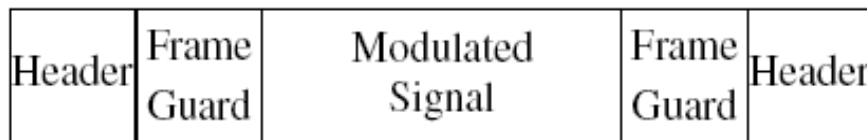


Figure 6. OFDM carriers allocated to IFFT bins

OFDM Modulator:

It is normal that the total number of transmitting data is not a multiple of the number of carriers. To convert the input data stream from serial to parallel, the modulator must pad a number of zeros to the end of the data stream in order for the data stream to fit into a 2-D matrix. Suppose a frame of data with 11,530 symbols is being transmitted by 400 carriers with a capacity of 30 symbols/carrier. 470 zeros are padded at the end in order for the data stream to form a 30-by-400 matrix, as shown in Figure 7.

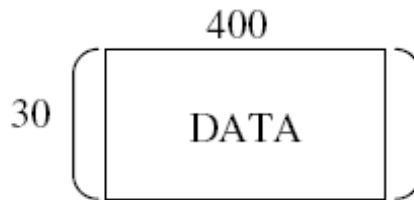


Figure 7. Data_tx_matrix

Differential Phase Shift Keying (DPSK) Modulation:

Before differential encoding can be operated on each carrier (column of the matrix), an extra row of reference data must be added on top of the matrix. Figure 8 shows a 31-by-400 resulted matrix. For each column, starting from the second row (the first actual data symbol), the value is changed to the remainder of the sum of its previous row and itself over the symbol size (power 2 of the PSK order).

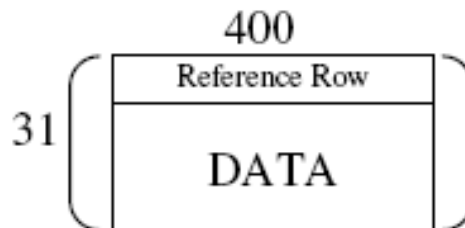


Figure 8. Differential Matrix

IFFT: Spectral Space to Time Signal

Figure 9 shows that the matrix is widened to IFFT size (for example: IFFT size = 1024) and becomes a 31-by-1024 IFFT matrix. Since each column of the DPSK matrix represents a carrier, their values are stored to the columns of the IFFT matrix at the locations where their corresponding carriers should reside. To obtain the transmitting time signal matrix, Inverse Fast Fourier Transform (IFFT) of this matrix is taken. Only the real part of the IFFT result is useful, so the imaginary part is discarded.

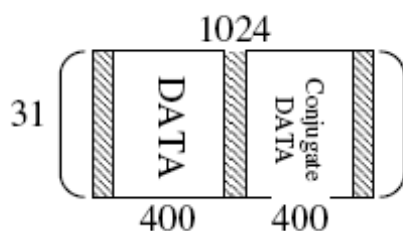


Figure 9. Pre-IFFT Matrix

Periodic Time Guard Insertion:

An exact copy of the last 25% portion of each symbol period (row of the matrix) is inserted to the beginning.

As shown in Figure 10, the matrix is further widened to a width of 1280. This is the periodic time guard that helps the receiver to synchronize when demodulating each symbol period of the received signal. The matrix now becomes a modulated matrix. By converting it to a serial form, a modulated time signal for one frame of data is generated.

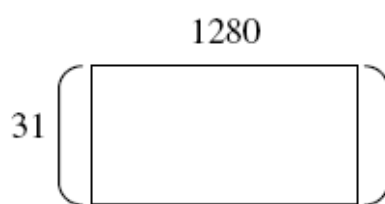


Figure 10. Modulated Matrixes

D. Communication Channel

A variable clipping in this MATLAB program is set by programmer. Peak power clipping is basically setting any data points with values over clipping below peak power to clipping below peak power. The peak-to- RMS ratios of the transmitted signal before and after the channel are shown for a comparison regarding this peak power clipping effect. An example is shown in Figure 11.

```
Summary of the OFDM transmission and channel modeling:
Peak to RMS power ratio at entrance of channel is: 14.893027 dB
Peak to RMS power ratio at exit of channel is: 11.502826 dB
#***** OFDM data transmitted in 5.277037 seconds *****#
```

$$\sigma \text{ of AWGN} = \sqrt{\frac{\text{variance of the modulated signal}}{\text{linear SNR}}}$$

Figure 11. OFDM Transmission Summary

Channel noise is modeled by adding a white Gaussian noise (AWGN) defined by:

E. OFDM Receiver

Frame Detector:

A trunk of received signal in a selective length is processed by the frame detector (ofdm_frame_detect.m) in order to determine the start of the signal frame. The selected portion of received signal is sampled to a shorter discrete signal with a sampling rate defined by the system.

A moving sum is taken over this sampled signal. The index of the minimum of the sampled signal is approximately the start of the frame guard while one symbol period further from this index is the approximate location for the start of the useful signal frame. The frame detector will then collect a moving sum of the input signal from about 10% of one symbol period earlier than the approximate start of the frame guard to about one third of symbol period further than the approximate start of the useful signal frame.

Demodulation Status Indicator:

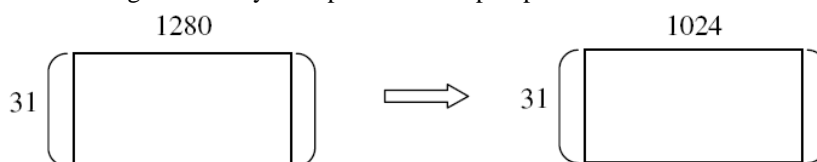
As mentioned, received OFDM signal is typically demodulated frame by frame. The OFDM receiver shows the progress of frames being demodulated. It is a neat idea to keep the number of displays for this progress within a reasonable range, so that the MATLAB command screen is not overwhelmed by these status messages. To achieve this, the first and last frames are designed to show for sure, the rest would have to meet a condition: $\text{rem}(k, \max(\text{floor}(\text{num_frame}/10), 1)) = 0$ where k is the variable to indicate the k -th frame being modulated, and num_frame is the total number of frames. It means that for a total number of frames being 20 or more, it only displays the n -th frame when n is an integer multiple of the round-down integer of a tenth of the total number of frames; and for a total number of frames being 19 or less, it shows every frame that is being modulated.

This would keep the total number of displays within the range from 11 to 19, provided that the total number of frames is more than 10; otherwise, it simply shows as many messages as the total number of frames.

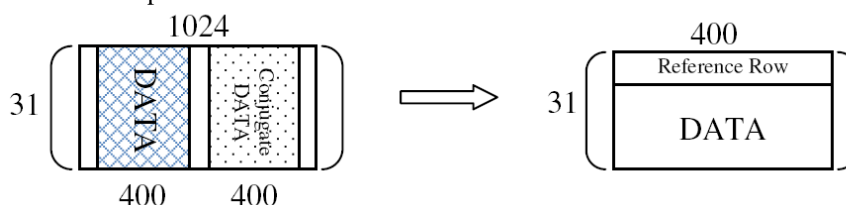
OFDM Demodulator:

Like any typical modulation/demodulation, OFDM demodulation is basically a reverse process of OFDM modulation. And like its modulator, the OFDM demodulator demodulates the received data frame by frame unless the transmitted data has length less than the designed total number of symbols per frame.

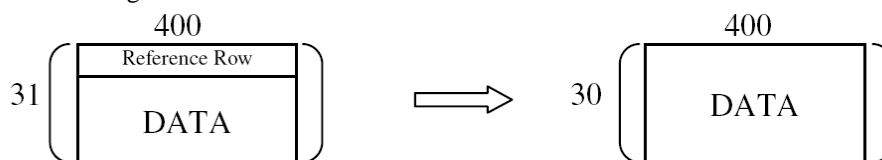
a) Periodic Time Guard Removal: The previous example used in section “OFDM Modulator” shall continue to be used for illustration. Figure 12 shows that after converting a frame of discrete time signal from serial to parallel, a length of 25% of a symbol period is discarded from all rows. Thus the remaining is then a number of discrete signals with the length of one symbol period lined up in parallel.



b) FFT Time Signal to Spectral Space: Fast Fourier Transform (FFT) of the received time signal is taken. This results the spectrum of the received signal. As shown in Figure 13, the columns in the locations of carriers are extracted to retrieve the complex matrix of the received data.



c) Differential Phase Shift Keying (DPSK) Demodulation: The phase of every element in the complex matrix is converted into 0-360 degrees range and translated to one of the values within the symbol size. The differential operation is performed in parallel on this new matrix to retrieve the demodulated data. This differential operation is basically calculating the difference between every two consecutive symbols in a column of the matrix. As shown in Figure 14.



The reference row is removed during this operation. Finally, a parallel to serial operation is performed and the demodulated data stream for this frame is obtained.

E. Error Calculations

Bit Error Rate (BER):

Demodulated data is compared to the original baseband data to find the total number of errors. Dividing the total number of errors by total number of demodulated symbols, the bit-error-rate (BER) is found.

Phase Error:

During the OFDM demodulation, before being translated into symbol values the received phase matrix is archived for calculating the average phase error, which is defined by the difference between the received phase and the translated phase for the corresponding symbol before transmission.

Percent Error of Pixels in the Received Image:

All afore mentioned error calculations are based on the OFDM symbols. What is more meaningful for the end-user of the OFDM communication system is the actual percent error of pixels in the received image. This is done by comparing the received image and original image pixel by pixel.

Program Display:

A summary showing the above error calculations is displayed at the end of the program. In an example shown in figure 15, an 800-by-600 image is transmitted by 400 carriers using an IFFT size of 1024, through a channel with 5 dB peak power clipping and 30 dB SNR white Gaussian noise.

```

***** Summary of Errors *****#
Data loss in this communication = 0.125000% (1200 out of 960000)
Total number of errors = 1174 (out of 958800)
Bit Error Rate (BER) = 0.122445%
Average Phase Error = 1.877366 (degree)
Percent error of pixels of the received image = 0.257708%
```

Figure 15. Error Calculations

IV. SIMULATION RESULTS

<i>Parameters</i>	<i>Values</i>
Source Image Size	800x600
IFFT Size	512
Number of Carrier	250
Modulation Method	QPSK
Peak Power Clipping	5dB
Signal to Noise Ratio	30dB

Table 01. User Input Values

Using above parameters we got BER of 0.028661% while the percent error in the output image pixels is 0.111227%. This is expected when the OFDM symbol size is not the same as word size of the source data i.e. modulation method is not 256-PSK. The reason is that a set of four QPSK symbols is mapped to one 8-bit word, and when one or more of the QPSK symbols in a set is decoded incorrectly, the whole 8-bit word is mistranslated, therefore, it counts as all 4 QPSK symbols are errors when considering the pixels percent error [7].

However, in BER calculation, the interest is in the accuracy of the Tx and Rx, thus it only counts the QPSK symbols that are decoded incorrectly. Average phase error of 2.059264 degree means that there's still a certain distance from the tolerance of 45 degree. With 0.111227% pixel percent error, the noise on the output image is easily observable, but the information content received is highly usable. This is due to the use of QPSK, in which received phases have 45 degree of tolerance. A sign of successful. By dropping the number of carriers and IFFT size to about half while all other parameters remain the same, the simulation runtime for both the transmitter and receiver don't seem to vary much. This is because the simulation program monitors the total number of symbols to form one frame of data, thus total number of frames did not vary much.

The runtime measured depends on the number of computer operations, which directly depends on the number of frames of data needed to be modulated and demodulated for a fixed number of symbols per frame [7].

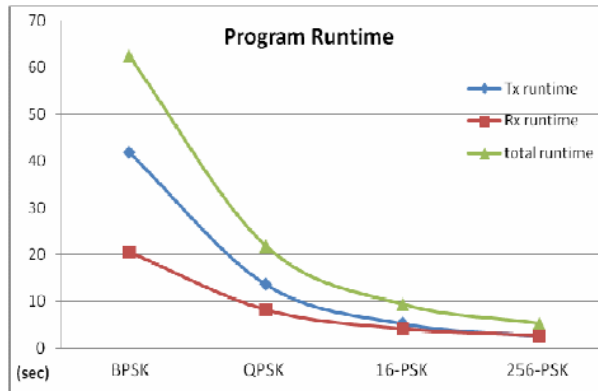


Figure 16. Program runtime

Conclusively, this runtime measurement does not reflect the variance of the efficiency based on varied numbers of carriers. However, it's meaningful to use this measurement in understanding the variance of efficiency based on varied orders of PSK. The runtimes tripled for a simulation with BPSK while other parameters remain the same

A plot shows that using 16-PSK and 256-PSK also verifies this theory. However, as shown in Figure BER increased massively by raising the PSK order, as a trade-off for decreasing runtime. SNR is inversely proportional to error rates. Figure 17 shows the relationship between the two for all four M-PSK methods. As expected, higher order PSK requires a larger SNR to minimize BER.

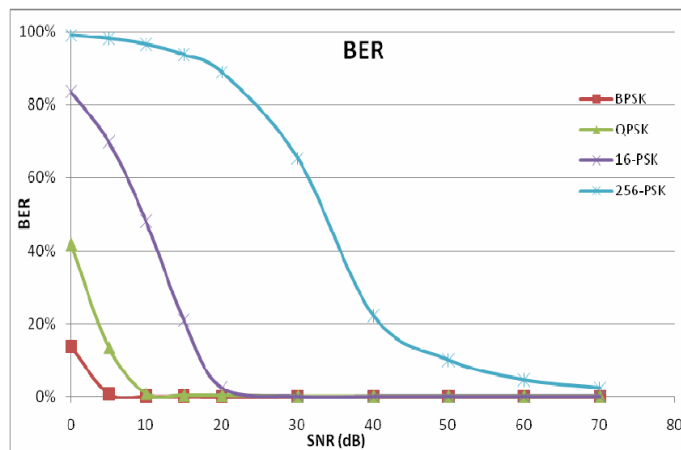


Figure 17. BER Vs SNR

Similarly, as shown in Figure 18, 256-PSK and 16-PSK require a relatively large SNR to transmit data with an acceptable percent error.

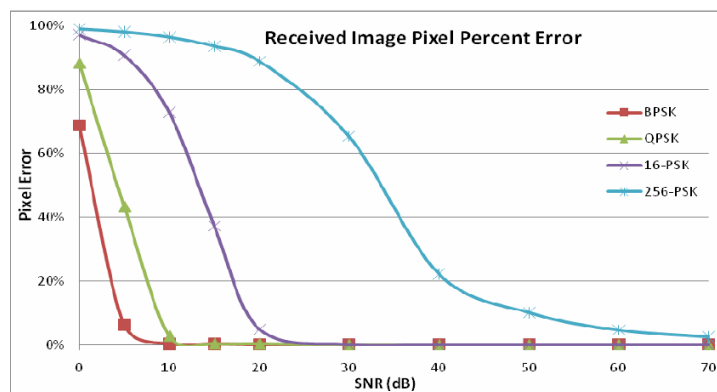


Figure 18. Pixel Error Vs SNR

Below shown the original image and received images for different orders of PSK with varied SNR.



Received Images using BPSK:



Figure 20. Received Image I Using BPSK

<i>Parameters</i>	<i>Values</i>
Source Image Size	800x600
IFFT Size	512
Number of Carrier	250
Modulation Method	BPSK
Peak Power Clipping	1dB
Signal to Noise Ratio	5dB

Table 02. User Input values for Image I

<i>Errors</i>	<i>Values</i>
Data loss in comm.	0.058594%
Total number of error	73369 (out of 3837750)
Bit Error Rate (BER)	1.911771%
Average Phase Error	27.571733 (degree)
Error in pixels	14.207708%

Table 03. Summa ry of Errors for Image I



Figure 21. Received Image II Using BPSK

Parameters	Values
Source Image Size	800x600
IFFT Size	512
Number of Carrier	250
Modulation Method	BPSK
Peak Power Clipping	1dB
Signal to Noise Ratio	30dB

Table 04. User Input values for Image II

Errors	Values
Data loss in comm.	0.058594%
Total number of error	0 (out of 3837750))
Bit Error Rate (BER)	0.000000%
Average Phase Error	1.407297 (degree)
Error in pixels	0.000000%

Table 05. Summary of Error for Image II

Received Images using QPSK:

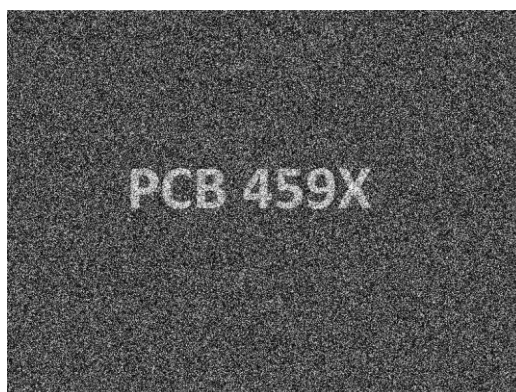


Figure 22. Received Image I Using QPSK

Parameters	Values
Source Image Size	800x600
IFFT Size	512
Number of Carrier	250
Modulation Method	QPSK
Peak Power Clipping	05dB
Signal to Noise Ratio	05dB

Table 06. User Input values for Image I

Errors	Values
Data loss in comm.	0.234375%
Total number of error	384902 (1915500)
Bit Error Rate (BER)	20.094075%
Average Phase Error	28.902475 (degree)
Error in pixels	59.086394%

Table 07. Summary of Error for Image I

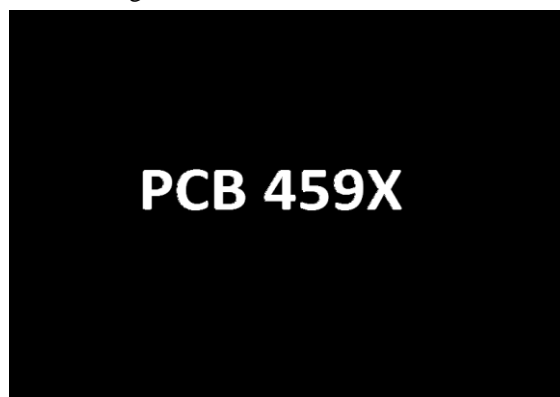


Figure 23. Received Image II Using QPSK

<i>Parameters</i>	<i>Values</i>
Source Image Size	800x600
IFFT Size	512
Number of Carrier	250
Modulation Method	QPSK
Peak Power Clipping	05dB
Signal to Noise Ratio	55dB

Table 08. User Input values for Image II

<i>Errors</i>	<i>Values</i>
Data loss in comm.	0.234375%
Total number of error	154 (out of 1915500)
Bit Error Rate (BER)	0.008040%
Average Phase Error	0.620729 (degree)
Error in pixels	0.031928%

Table 09. Summary of Error for Image II

Transmitter Plots (Plots of BPSK SNR: 30 dB):

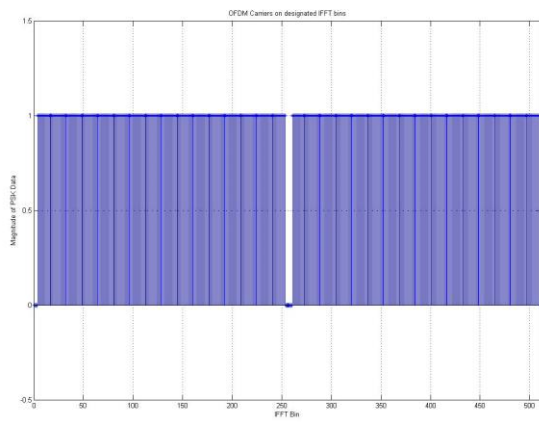


Figure 24. OFDM Carrier on Designated FFT Bins

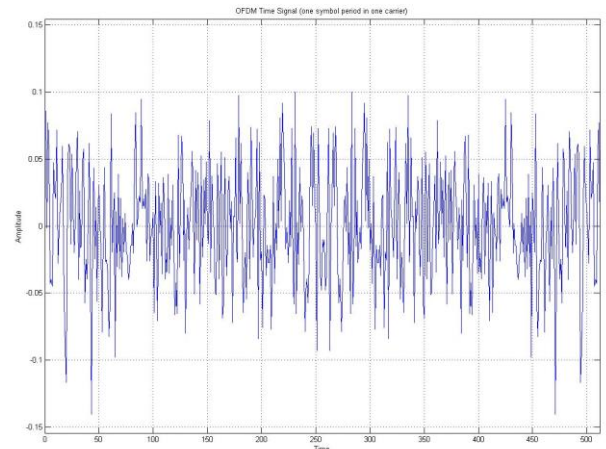


Figure 25. OFDM Time Signal

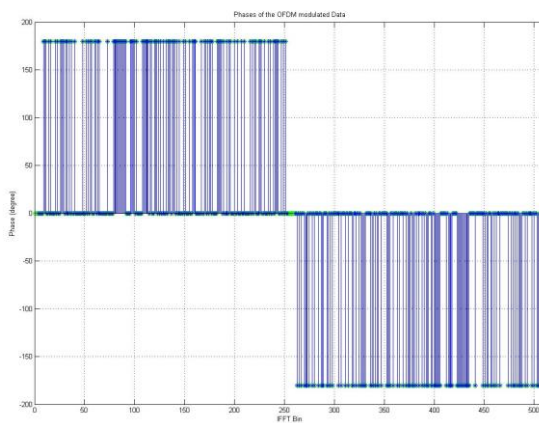


Figure 26. Phase of OFDM Modulated Data

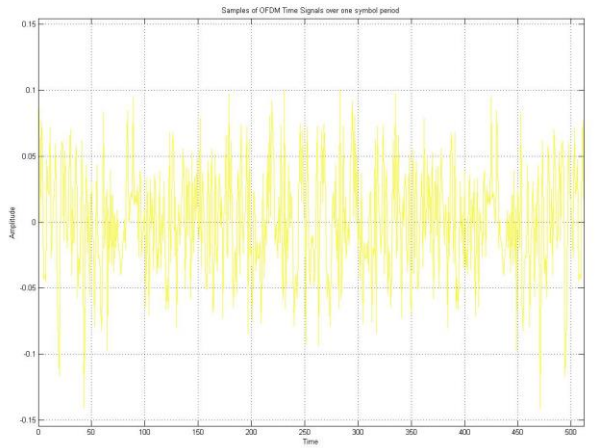


Figure 27. Sample of OFDM Time Signal

Receiver Plots (Plots of BPSK SNR: 30 dB)

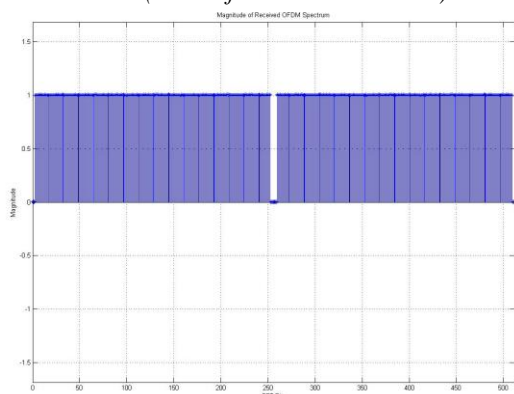


Figure 28. Magnitude of Received OFDM Spectrum



Figure 29. Phase of Received OFDM Spectrum

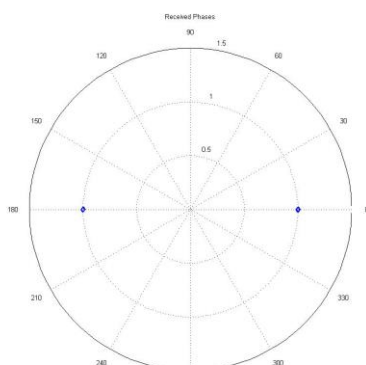


Figure 30. Received Phases

V. CONCLUSION

An OFDM trans-receiver is successfully simulated using MATLAB. All major components of an OFDM system are try to be covered. This has demonstrated the basic concept and feasibility of OFDM, which was thoroughly described and explained in this paper. It was noted that for some combinations of OFDM parameters, the simulation may fail for some trials but may succeed for repeated trails with the same parameters. It is because the random noise generated on every trial differs, and trouble may have been caused for the frame detector in the OFDM receiver due to certain random noise. Future work is required to debug this issue and make the frame detector free of error.

Other possible future works to enhance this simulation program include adding ability to accept input source data in a word size other than 8-bit, adding an option to use QAM (Quadrature amplitude modulation) instead of M-DPSK as the modulation method.

Acknowledgment

We submit our gratitude & sincere thanks to our supervisor Prof. Bhavesh Jaiswal and Prof. Pratik Patel, Department of Electronics and Communication Engineering, for their constant motivation and support during the course of our work. We would not be able to do justice to this work of ours, if we do not express our heartiest thanks to Prof. Sachin Sharma for providing a solid background for our studies and research thereafter. He has been great sources of inspiration to us and we thank him from the bottom of our heart.

REFERENCES

- [1] By J. Cyrus Sy, "Implementation of an OFDM Transceiver using an SDR Platform", Spectrum Signal Processing, 2006.
- [2] Abhishek Arun Dash, "OFDM System and PAPR reduction technique in OFDM", National Institute of Technology, Rourkela, 2008.
- [3] Satish Singh," Software implementation of OFDM for mobile radio channel", NIT Rouerkela, 2008.
- [4] Paul Guanming Lin, "OFDM SIMULATION in MATLAB", Faculty of California Polytechnic State University San Luis Obispo, June 2010.
- [5] Orlandos Grigoriadis, H. Srikanth Kamath, "OFDM SIM Ber Calculation Using Matlab Simulation For OFDM Transmission, IMECS 2008, 19-21 March, 2008, Hong Kong.
- [6] Alan C. Brooks, Stephen J. Hoelzer, Design and Implementation of Orthogonal Frequency Division Multiplexing (OFDM) Signaling, Department of Electrical and Computer Engineering.
- [7] T.Rappaport,"Wireless Communication Principles and practices"Prentice Hall.

Measurement Of Rn²²² Concentrations In The Air Of Peshraw & Darbandikhan Tunnels Located In Sulaimani Governorate Of Kurdistan Region-Iraq.

¹Kamal O. Abdullah, ²Ali H. Ahmed

¹ Physic Dep.-Faculty of Science and Science Education- University of Sulaimani-Kurdistan region-Iraq

² Physic Dep.-College of Science- University of Salahaddin- Erbil-Kurdistan region-Iraq

ABSTRACT: The purpose of this study was to measure the radon concentration in the air inside Darbandikhan and Peshraw tunnels located at Sulaimani governorate. The concentration of Rn²²² have been determined using CR-39 Solid-State Nuclear Track Detector Technique. It was found that the range of radon concentration inside Darbandikhan tunnel was (305.8 - 391.34) Bq/m³, and that of Peshraw tunnel was (2042.9 - 4277.89) Bq/m³. A concentration of several thousand Bq/m³ was observed at the inner most area of the Peshraw tunnel towards southern geographic which indicates that the radon concentration in the tunnel is basically governed by diffusion and mixing of radon gas with air.

Keywords: Radon-222 , SSNTD , activity , CR-39

I. INTRODUCTION

Radon is a naturally occurring noble gas (z=86) and all of its isotopes are radioactive. Because of its chemical inertness it does not bond to the surface of material, in marked contrast to its heavy metal daughters. From a health physics point of view, the main hazard is the alpha radiation dose to the lungs. This dose is mainly due to direct radiation from inhaled dust particles on which the radon daughter nuclide ions have become attached [1], therefore it's necessary to study this type of gas in the tunnels and in closed positions. Due to its long half life time (3.82d) relative to other isotopes, radon (Rn²²²) (a gas member in the uranium decay series) is considered to be the most significant isotope of radon problem in the environmental studies. the SSNTD (Solid State Nuclear Track Detector) technique, make a popular and well-established method of measurement in a large number of fields of radioactivity or nuclear interactions. The basis of this technique lies when heavy charged particle traverse a dielectric medium, they are able to leave long – lived trails of damage that may be observed either by transmission electron microscopy or under an ordinary optical microscope after etching the medium using NaOH for 6 hrs at 70 C^o temperature [2, 3].

The plastic SSNTD detectors are most widely used because they are more sensitive than crystal and glass. The type of CR-39 polymer (a poly allydiglycol) Carbonate can record all charged nucleons (protons) [2]. Cellulose nitrate and acetates can record alpha particles .The lexan ploy carbonate is one of the earliest plastic SSNTD to be used which can record the nuclei of charge (z>6). The shape and type of damage position on the film plastic detector depend on the mass, energy, the charge of the incident particle and on the type of solid state detector [2, 4]. The damage volumes of these positions depend upon the above factors adding on the type and concentration with temperature and time of chemical etching [3].

The interactions of radiation with these types of polymers occur due to degradation or molecular cross-linking with each other, these effects causing to change the polymer properties. Therefore, when radiation falls (incident) on these polymers, it causes excitation and ionization, as well as causing to cut the bond and producing damage traces on the polymer at the normal condition [5]. These traces have the capability to interacting with alkaline solution like (NaOH) comparing with the undamaged regions. Due to this interaction these regions have more energy than the others, then the chemical solution penetrate easily the radiate position causing bracing with high depth and diameter which can observe by optical microscope [3].

In Sulaimani governorate, till now there is no base line data concerning the radon concentration measurements in closed areas, especially for the Darbanikhan tunnel (located East-Southern of Sulaimani city, constructed before 50 years ago) and for the Peshraw tunnel (at Northern of Sulaimani city which was constructed before 4 years ago) where some ambiguities on their quality and health characteristics have been mentioned. Therefore, this work has been adopted to assess the radon levels inside both of the tunnels in comparison to the standard international values.

II. EXPERIMENTAL TECHNIQUE & CALCULATION

In this work, Solid-State Nuclear Track Detector techniques has been employed by using CR-39 detectors which were fixed inside the steel chambers in a form of 1X1.5 cm plastic detector pieces, (Fig. 1). The designed dosimeters have been suspended on the walls of tunnels at different positions along the tunnel. After 60 days of exposure the suspended dosimeters were collected.



Fig. (1): The designed dosimeter.

To calculate radon concentration using a dosimeter chamber, it's necessary to determine the diffusion constant (K) characteristic for the system using the relation [6]:

$$\rho = K C_a T \quad \dots\dots\dots(1)$$

Where P- Track density Tr\cm²

K- Diffusion constant

C_a- Rn concentration in air space inside the steel chamber (Bq\cm³)

T- Exposure time (60 days)

Then K can be calculated for the specified dimensions of the steel chamber [7]:

$$K = 1/4 (r)[2\cos \theta_t - r/R_\alpha] \quad \dots\dots\dots(2)$$

Where r - chamber radius for the diffusion volume (3.25 cm)

- θ_t - Threshold angle for the CR-39 detector (35°) ,[7]

- R _{α} - Range of α - particle in air from Rn

R _{α} can be calculated from this relation [8]:

$$R = (0.005 E_\alpha + 0.285) E_\alpha^{3/2} \quad \dots\dots\dots(3)$$

= 4.019cm (for alpha energy of 5.489 MeV)

Substituting these values in eq. (2), the diffusion constant is found to equal 0.058244 Tr.cm⁻².hr⁻¹/ Bq.m⁻³

For the present dosimeter

III. RESULTS AND DISCUSSIONS

Tables 1 & 2 presents the track density of α -particles on the CR-39 detectors within the dosimeters and the measured Rn-concentrations for both tunnels:

Table 1 (Darbandikhan tunnel)

Position (m) at side of Sulaimany	ρ (Tr/cm ²)	Ca (Bq/m ³)
-----	-----	-----
0	905.4	259.0824806
60	1153.8	330.1627635
120	1068.9	305.8684156
180	1134.9	324.7544811
240	1344.3	384.6748163
300	1316.7	376.7770071
360	1222.3	349.7642103
420	1120	320.4908088

480	1079.3	308.8444017
540	1320.4	377.8357714
600	1367.6	391.3421697
660	1251.3	358.0626331
720	1210	346.2445345
780	1173.6	335.8285832
840	1350.6	386.4775771

Table 2 (Peshraw tunnel)

(Peshraw Tunnel) at side of Sulaimany position (m) -----	P(Tr/cm ²) -----	Ca(Bq/m ³) -----
0	11334.1	3243.281139
100	9353.4	2676.498867
200	10516.6	3009.351464
300	14949.7	4277.894146
400	11805.7	3378.230662
500	10584.5	3028.781219
600	11719.2	3353.47847
700	14462.4	4138.452029
800	13450.9	3849.008768
900	12253.7	3506.426985
1000	14564.5	4167.6682
1100	10998.9	3147.362818
1200	7762.5	2221.258842
1300	8294.8	2373.577822
1400	8897.5	2546.041939
1500	8205.8	2348.110249
1600	9088.7	2600.754298
1700	9931.8	2842.009477
1800	8182.2	2341.35705
1900	8756	2505.551359
2000	7139.3	2042.928599
2100	7860	2249.158712
2200	5378	1538.928187

From Table 1, the radon concentration at the gates of Darbandikhan tunnel were 259.08 Bq/m³ and 386.48 Bq/m³, and along the tunnel length (800m) were ranges between (305.8 – 391.3) Bq/m³. From Table 2, the radon concentration at the gates of Peshraw tunnel were 3243.28 Bq/m³ and 1538.93 Bq/m³, and along the tunnel length (2200m) were ranges between (2042.93 – 4277.89) Bq/m³. In both tables, a higher radon concentration have been recorded at one of the tunnel gates (386.48 Bq/m³ for Darbandikhan and 3243.28 Bq/m³ for Peshraw tunnel). This may be referred to the regional wind currents that are lower in compare to the other side which exposes to higher air currents. The distribution of radon concentration within Darbandikhan and Peshraw tunnels are shown in Figures 1 and 2, respectively.

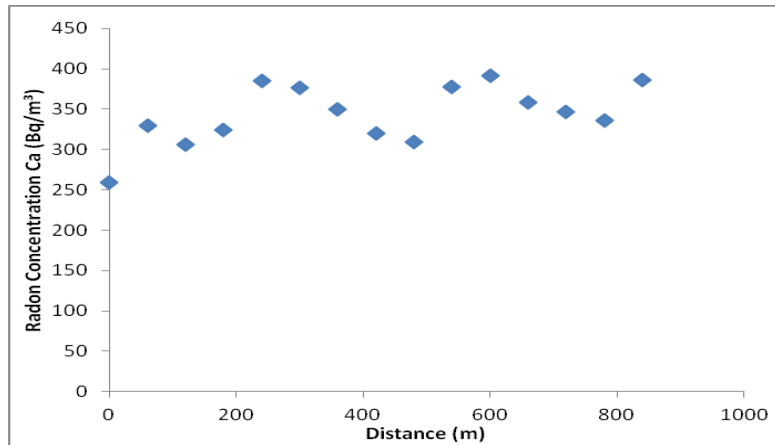


Figure (2): Variation of Radon Concentration with distances from gate of Darbandikhan tunnel.

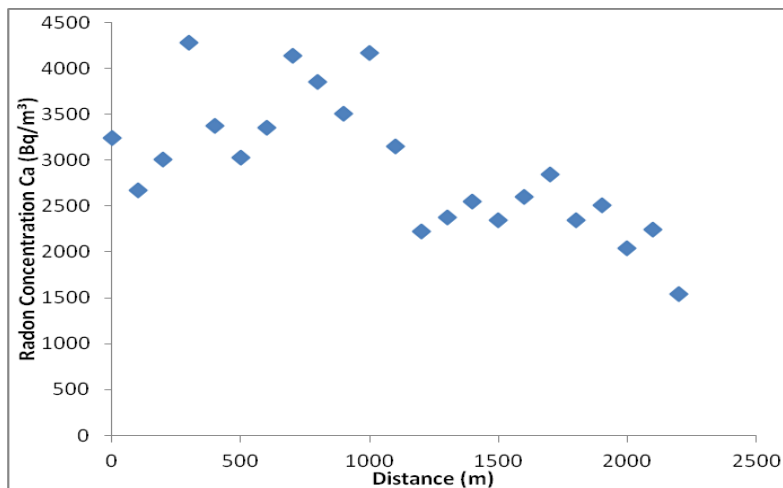


Figure (3): Variation of Radon Concentration with distances from gate of Peshraw tunnel.

In both figures, and in the same manner, two peaks have been appeared at approximately same distances from the tunnel ends. This phenomenon reveals that the radon concentration decreases with distance from inside to outside of the tunnel. At the center of the tunnel, the radon emanation from the rocks was directed toward the lower concentration regions at the ends, but the air directed inside of the tunnel from the gates retards this translation and causing accumulation at the indicated regions. Furthermore, these observations lead to the conclusion that the variation of the radon concentration in the tunnel air is mainly caused by a convection current due to stack effect induced by the temperature difference between the tunnel air and the outside air [9].

In general, the ventilation in both of the tunnels not exists. So the radon concentration levels were higher than those recorded for a tunnel in Korea 95.1 Bq/m³ [10], while they are still lower than those recorded for a tunnel in Japan 6500 Bq/m³ [9]. Nevertheless, it is necessary for the tunnels to have good ventilation for decreasing high radon concentrations and the other none desired gas concentrations.

From the results, it was clear that the radon concentration in Peshraw tunnel was higher than that of Darbandikhan tunnel which is attributed mainly to the length excess of Peshraw tunnel over that of Darbandikhan tunnel (about three times) that causes more trapping of radon gas to higher concentrations.

On the other hand, the operations of making tunnels involve drilling of the mountains with different geological formations and then covering the walls inside the tunnels with a large nugget of cement. In this work, the geology of the area is predominantly characterized by metamorphic rocks, these kinds of rocks usually rich in uranium minerals which is also be a radon source [11].

IV. CONCLUSION

In this work, the concentration of Rn was found very high in the Peshraw tunnel comparing to Darbandikhan tunnel due to the length difference. Both of the tunnels left without ventilation which causes higher radon concentration comparing to that of Korea but they are smaller than that of Japan due to geology and environmental formations.

REFERENCES

- [1] A. V. Nero and W. W. Nazaroff (1984), "Characterizing the source of radon indoors" Radiative Protection Dosimetry, Vol. 7, pp (23 – 29)
- [2] M.F.L Annunziata,"Hand book of Radioactivity Analysis " 2nd edition, Academic Press 2003.
- [3] Fliescher R.L. , price P.B. & Walker R.M. (1975)" Nuclear Tracks in Solids principles and Application" University of California Press.
- [4] Durrani S.A. & Bull R.K. Solid state nuclear track detection (1987) ,pergamaon press Oxford
- [5] Muhammed A. Aziz," Chemical Plasticity" book home for printing,University of Mousl, 1993.
- [6] Azam,A.,Naqvi A. H. and Srivastava D. S.,(1995)."Radium Concentration and Radon Exhalation Detectors".Nuclear Geophysics. Vol. 9, No. 6 , pp(653- 657).
- [7] Barillon R. ,Klein D.,Chambandet A. and D.C. " Comparision of effectiveness of three Radon Detectors (LR-115,CR-39 and Si. Diode pin) placed in Cylindrical Device- theory and experimental techniques ,Nuclear Track" Radiation measurement ,vol. 22,(1-4) , pp(281-282),1993.
- [8] Michael F. L' Annun Ziata "Radioactivity (Introduction and History) " 2007. Elsevier.
- [9] Muramatsu H., Tashiro Y., Hasegawa N. Misawa C., Minami M." Seasonal Variation of Rn²²² concentrations in the air of a tunnel located in Nagano city" , Environ Radioactive , Vol. 60 , No. 3 , pp (263 -274), 2002 .
- [10] Sangjun C. , Seonghin L. , Sanghuk Y., " Subway Workers Exposure to Radon in Korea" Womju Institute for Occupational and Environmental health, Korea , June 25-2012.
- [11] S. Verdelocco , D. Walker , P. Turkowsky, "Radon concentration in the Tunnels of a hydroelectric power station under construction in Italy" Radioactivity in the Environment, Vol. 7, pp (215 – 220), 2005.

Hydrological Modeling of Upper Indus Basin and Assessment of Deltaic Ecology

A. D. Khan¹, Shimaa Ghoraba², Jeff G. Arnold³, Mauro Di Luzio⁴

¹Director (GIS & Modeling), Pakistan Council of Research in Water Resources, Islamabad, Pakistan.

²Irrigation and Hydraulic Engineering Department, Faculty of Engineering, Tanta University, Egypt.

³Grassland Soil and Water Research Laboratory, United States Department of Agriculture, Temple Texas, USA

⁴Texas Agricultural Experiment Station, Blackland Research Center, Texas, USA

ABSTRACT : Managing water resources is mostly required at watershed scale where the complex hydrology processes and interactions linking land surface, climatic factors and human activities can be studied. Geographical Information System based watershed model; Soil and Water Assessment Tool (SWAT) is applied for study of hydrology of Upper Indus River Basin and assessment the impact of dry periods on environmental flow. The model is calibrated at two stations on Indus and Kabul Rivers. Climatic data of 22 weather stations falling in Pakistan, India, China and Afghanistan has been used for simulation period of 11 years (1994-2004). The model calibration for various water balance components yielded good agreement as indicated by coefficient of determination and Nash-Sutcliffe efficiency. The model output is for analysis of environmental flow in lower reaches and assessment of the Indus Delta ecohydrology. Results revealed that SWAT model can be used efficiently in semi-arid regions to support water management policies.

Keywords: Indus watershed modeling, hydrology, environmental flows, deltaic ecosystem, Indus Basin irrigation system, SWAT.

I. INTRODUCTION

Indus is a Tran- boundary river with its catchment falling in Afghanistan, Pakistan, China and India. It has the length of about 2748 Kms and its system is the prime source of water in water resource of Pakistan. Inflow to the Indus River system is derived from snow, glacier melt and rainfall upstream of the Indus Plain. The upper part of the Indus basin consists of glaciated mountains which receive snowfall in the winter season. The mountains with unbroken snow cover became the primary source of water for Indus [1]. Hydrologic impacts in the upper basin depend to a large extent upon climate change which has its effect on seasonal inflows and the peak discharges at the main rivers in the Indus River System.

The Indus basin has a total drainage area of 364,700 square miles, some 60 percent of which lies in Pakistan [2]. The Indus River and its tributaries rise in the sparsely populated glaciated mountains of western and central Asia. The Indus River itself contributes more than half the total flow and has a controlling storage at Tarbela Dam as the river emerges from the mountains [3]. The mountainous upper basin is influenced by continental climates of central Asia which have a westerlies pattern of circulation, late winter snowfalls, cold winters and short warm summer [4] This regional climatic pattern becomes highly complex within the high mountain ranges of Indus basin watershed.

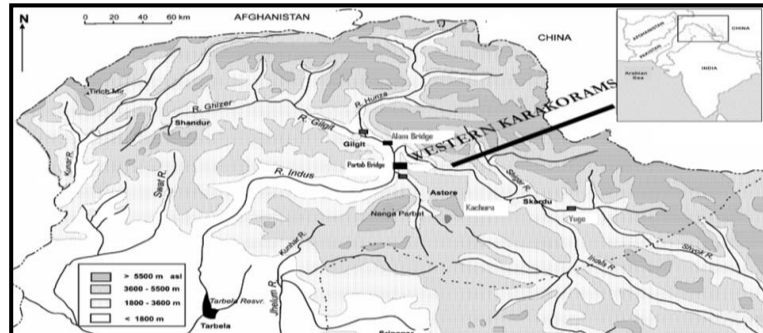
The water quality of Indus River and its tributaries is generally considered excellent for irrigation purposes. The total dissolved solids range from 60 mg/l in the upper reaches to 375 mg/l in the lower reaches of the Indus, which are at reasonable levels for irrigated agriculture and also as raw water for domestic use [5]. Sedimentation data collected by Water and Power Development Authority (WAPDA)[6] at 50 stations on River Indus revealed that the Indus and its tributaries carry about 0.135 Billion Cubic Meters (BCM) of sediment annually. Of this, nearly 60% remains in the system where it deposits in the reservoirs, canals, and irrigation fields. Annual silt clearance is undertaken in the canal systems to remove the deposited silt.

The main user of Indus River flows is Indus Basin Irrigation System (IBIS). The IBIS has been developed over the last 140 years [7]. This system comprises three western rivers, namely the Indus, the Jhelum and the Chenab, four reservoirs (Warsak, Tarbela, Mangla and Chashma), 23 diversion structures (barrages, headwork's and siphons), 12 inter-river link canals, and 45 canal commands. The length of the main irrigation

canals is 61,000 km in addition to the 1.6 million km of 100,000 watercourses. This system irrigates brings in about 195 BCM of water and irrigates about 18 million hectares of land in Indus Basin.

The objective of this study is to model the hydrology of Upper Indus Basin for development and management of water resources for irrigation and hydropower generation and study of ecohydrology in Indus Delta, Fig.(1). It also provides a baseline for study of climate changes and variability on various components of water balance, irrigated agriculture and environmental flow.

Figure 1: Location map of upper Indus River Basin



II. LITERATURE REVIEW

Watershed models simulate natural processes of the flow of water, sediment, chemicals, nutrients, and microbial organisms within watersheds, as well as quantify the impact of human activities on these processes. Simulation of these processes plays a fundamental role in addressing a range of water resources, environmental, and social problems [8]. Many models were developed for watershed hydrology but the availability of temporally and spatially data was the main constraint hindering the implementation of these models especially in developing countries [9]. Indus Basin is one of the World's well documented river basins. Modern age research and development activities are extending over one. These research activities included field and laboratory experimentation on irrigation and drainage, soil and water salinity, hydrology, water resources management and related agri- socio-economic disciplines. Modeling of water system started during late sixties and some of initial models were physical and prototype in nature. Short-term forecasting of river inflows was conducted by the Water & Power Development Authority (WAPDA) through lumped and semi-distributed models like the University of British Columbia Watershed Model (UBC) [10]. The output of this UBC model was taken as input to MODSIM for simulation of irrigation network in Indus Irrigation System [11]. The MODSIM simulations were made for hydrological studies and then impact assessment studies for the climate changes on water resources. Adaptation strategies were also proposed in this study. Another comprehensive model; applied in Indus Basin was; Indus Basin Model Revised (IBMR). This model addressed almost all important parameters; hydrology, cropping, economic, etc. All these models are lumped type hydrologic simulation models which are unable to represent the spatial variability of hydrologic processes and catchment parameters [12]. Therefore distributed models are now being applied in Indus Basin to assess the spatial variability of various watershed parameters. At 2013, a Distributed Hydrology Soil Vegetation Model (DHSVM) is applied in Sirn River (a tributary of Indus) by Winston [13] to predict the effects of land use change on the water resources.

For this case study, the soil and water assessment tool (SWAT) was chosen because it includes many useful components and functions for simulating the water balance components and the other watershed processes. SWAT is a distributed hydrological model which is developed by United State Department of Agriculture, Agricultural Research Services (USAD, ARS)[14]. The AVSWAT (Arc View- SWAT) provides an efficient preprocessor interface and postprocessor of SWAT model. AVSWAT is implemented within Arc View 3.x GIS and distributed as an extension of this software. A brief introduction to the SWAT model, AVSWAT and its illustrative application to the Upper North Bosque river watershed was discussed by Di Luzio[15]. SWAT model has an efficiency and reliability which confirmed in several areas around the world. It was tested and used in many regions of Africa by Shimelis [16], Asharge [17], and Fadil [18] and Asian Monsoon zone by Cindy [19].

III. MATERIAL AND METHODS

A GIS based watershed model; Soil and Water Assessment Tool (SWAT) is applied for study of hydrology of upper Indus River Basin (UIB). The methodologies used for this study include a description of

hydrological model and the special dataset which used in the simulation. The details are given in the following sections.

3.1. Description of the Study Area

The Indus River and its tributaries, the Jhelum, Chenab, and Sutlej rivers originate in the mountain headwaters of the Karakoram Himalaya, western Himalaya, and Hindu Kush Mountains which are located at the central Asia. The Upper Indus Basin (UIB) extends from the Tibetan Plateau to northeast Afghanistan, Fig.(1). It is considered to be the glacierized catchment basins of the Mountains. The main rivers are Indus River (3180km), and its Tributaries from the western Himalaya are the Jhelum, Chenab, Ravi, and Sutlez Rivers, from the Indian states of Jammu Kashmir and Himachal Pradesh, and the Kabul, Swat, and Chitral Rivers from the Hindu Kush Mountains. The ultimate source of the Indus is in Tibetan Plateau in China; it begins at the confluence of the Sengge and Gar rivers that drain the Nganglong Kangri and Gangdise Shan mountain ranges. The total surface area of the (UIB) is approximately 220,000 km² without Tibetan Plateau's rivers basin. Of this surface area, more than 60,000 km² is above 5000 m, the estimated mean altitude of the summer season freezing level.

The glaciers of the region flowing outward from this zone have been estimated to have a surface area of approximately 20,000 km², of which 7,000–8,000 km² is below the summer-season freezing level [13]. Winter precipitation is a principal sources of runoff from the UIB as snow that melts the following summer and glacier melt. Climatic variables are strongly influenced by altitude. Northern valley floors are arid with annual precipitation from 100 to 200 mm. Totals increase to 600 mm at 4400 m, and glaciological studies suggest accumulation rates of 1500 to 2000 mm at 5500 m [20]. Regression analysis of seasonal and annual temperatures of nine karakoram stations ranging in elevation from 1000 to 4700m give correlation coefficients greater than 0.98 and lapse rate ranging from 0.65 to 0.75° C/100 m [21]. Analysis of relationships between seasonal climate and runoff by Archer [22] suggested that the UIB could be divided into three distinct hydrological regimes in which rivers may differ significantly in their runoff response to changes in the driving variables of temperature and precipitation.

3.2. Description of SWAT Model

SWAT is a continuous time model that operates on daily time steps and uses a command structure for routing runoff and chemical through watershed. The model includes eight major components: hydrology, weather, erosion/sedimentation, soil temperature, and plant growth, nutrients, pesticide and land management. Integration of Geographic information system (GIS) and use of remote sensing data has further enhanced capability of hydrological model for solution of complex problems with large quantities of data associated with water systems and distributed nature of hydrological elements with much better resolution. (GIS) data for topography, soils and land-cover were used in the AVSWAT, an ArcView-GIS interface for the SWAT model [15]. Climate, precipitation, stream flow and water quality data were sourced and prepared according to SWAT input requirements. The topography of watershed was defined by a Digital Elevation Model (DEM). The DEM was used to calculate sub-basin parameters such as slope and to define the stream network. The soil data is required by the SWAT to define soil characteristics and attributes. The land-cover data provides vegetation information on ground and their ecological processes in lands and soils. The global view of SWAT model components including input, output and the spatial and GIS parts is given in Fig (2).

The hydrologic cycle is simulated by SWAT model based on the following water balance equation, which considers the unsaturated zone and shallow aquifer above the impermeable layer as a unit.

$$SW_t = SW_o + \sum_{i=1}^t (R_{day} - Q_{surf} - E_a - w_{seep} - Q_{gw})_i \quad (1)$$

where:

t is the time in days, SW_t is the final soil water content (mm), SW_o is the initial soil water content (mm), R_{day} is amount of precipitation on day i (mm), Q_{surf} is the amount of surface runoff on day i (mm), E_a is the amount of evapotranspiration on day i (mm), w_{seep} is the amount of water entering the vadose zone from the soil profile on day i (mm) and Q_{gw} is the amount of return flow on day i (mm).

The watershed are spatially distributed in nature because of it specially distributed vegetation and topography, soil and precipitation. The calibration of model needs stream flow data in temporal pattern. So in general two types of dataset are required; spatial data sets and temporal datasets. The used data and methodology applied is discussed in following section.

3.3. Spatial Dataset

The topography, landuse/landcover and soil characteristics are spatial datasets which defines the land system of any area. In hydrology, all these datasets contributes and controls the flow direction, runoff generation, infiltration, stream flow, sediment and nutrient transportation. First step in using SWAT model is to delineate the studied watershed and then divide it into multiple sub- basins based on Digital Elevation Model (DEM), Fig.(3). Thereafter, each sub-basin is sub-divided into homogeneous areas called hydrologic response units (HRUs) that GIS derives from the overlaying of slope, land use and soil layers. The aim is to set up and run the SWAT model on Upper Indus catchment with the existing multisource data to illustrate the possibility and the adaptability of the model to simulate the functioning of large-scale semi- arid watersheds. The main sets of data used are briefly explained below.

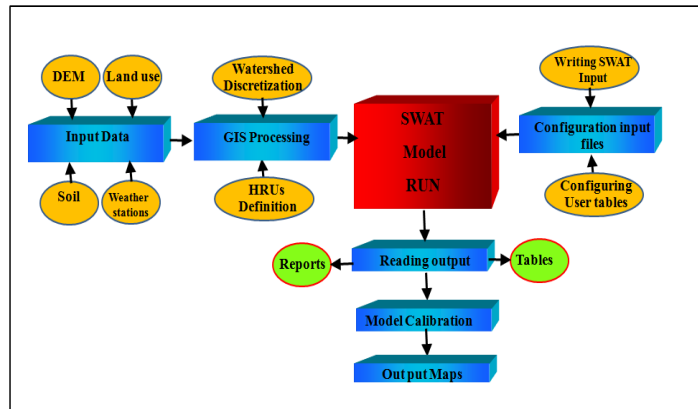


Figure 2: Components and input/output data of SWAT model

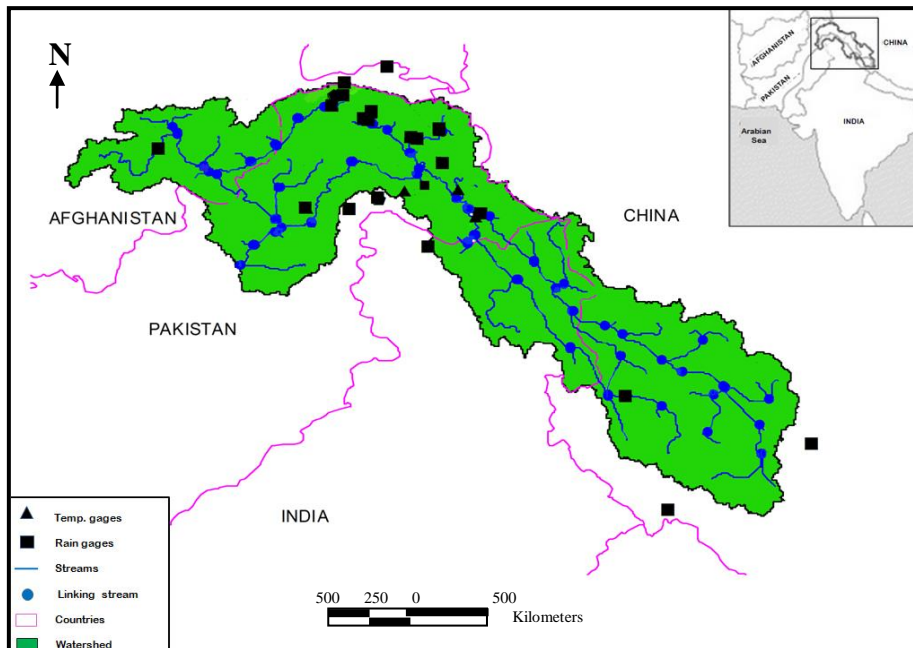


Figure3: Upper Indus Basin whole watershed and location of meteorological station (for key to Station positions and elevations, see Table II)

3.3.1. Catchment Delineation

Topography plays primary role in delineation of any catchment. The direction and pattern of flow is governed by the watershed divide drawn on the bases of elevations, stream network generation, slope and shape of the catchment. The delineation and definition of the topographic characteristics of the catchment has been derived form GTOPO30, Global Digital Elevation Model (DEM) with a horizontal grid spacing of 30 arc seconds (approximately 1 kilometer)[23]. From the present SWAT application, the average elevation of catchment is 2033 meters with the minimum value of 201 meters and maximum of 3864 meters from mean sea

level. Total catchment area is about 397986 Km² which extends from the Tibetan Plateau to northeast Afghanistan with hilly terrain and steep slopes. The whole Upper Indus Watershed is segmented in a total number of 101 sub-basins depending on topographic characteristics, Fig.(4).

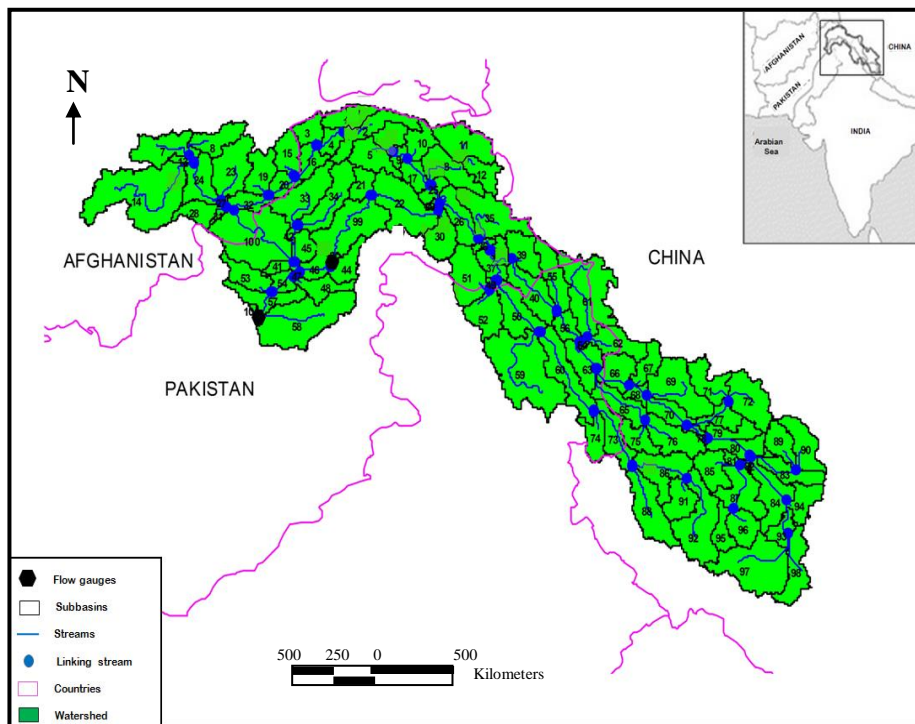


Figure 4: Delineation of sub-basin of Upper Indus Basin watershed

3.3.2. Land use

Land use can significantly affect the water cycle. As rainfalls, the canopy interception reduces the erosive energy of droplets and traps a portion of rainfall within canopy. The influence that land use exerted on these processes is a function of the density of plant cover and morphology of plant species. The land use data in project has been derived from the Global Environment Monitoring Unit site of the Institute for Environment and Sustainability at the European Commission's Joint Research Centre [24]. Land cover in catchment was distributed into 12 classes. The distribution of these classes resulted as: Residential-High Density: 0.14 %, Range-Brush;; 0.01%, Pasture; 4.26 %, Range-Grasses; 34.25%, Water; 0.34%, Oak; 1.54%, Southwestern US (Arid) Range ; 39.55 %, Pine; 6.96 %, Forest-Deciduous; 0.66 %, Forest-Evergreen; 1.1 3%, Agricultural Land-Close-grown; 0.48% and Agricultural Land-Row Crops; 10.68%. These land use types were reclassified using SWAT land use classes. The land use classes were converted from original land use classes to SWAT classes and defined using a look up table. Table I shows the land uses conversion from original land uses classes to SWAT classes.

3.3.3. Soil Data

Hydrological behavior of soil is characterized by its physical properties. To obtain this information, at a regional scale, 1:1 million soil vector maps was used where each cartographic unit was associated with one or two delineations corresponding to sub soil group of USDA[25]. Three soil delineated in the catchment; M-RM, GRV-CL, RM>GPZ have their corresponding USA series of Merino, Breswste and San Antrio series respectively. Soil parameters were determined by linking the soil map unit to the respective soil record and elaborated by using MUUF (Map Unit User File) method [26]. Derived Soil properties are given in Table II and briefly described as follows.

Table I: Land use - land cover classes used for AVSWAT in UIB watershed. The corresponding SWAT model crop growth or urban classes are also indicated

<i>Land use - Land cover class</i>	<i>SWAT classes</i>	<i>% Watershed Area</i>
Residential-High Density	URHD	0.14 %
Range-Brush	RNGB	0.01%
Pasture	PAST	4.26 %
Range-Grasses	RNGE	34.25%
Water	WATR	0.34%
Oak	OAK	1.54%
Southwestern US (Arid) Range	SWRN	39.55 %
, Pine	PINE	6.96 %
Forest-Deciduous	FRSD	0.66 %
Forest-Evergreen	FRSE	1.1 3%
Agricultural Land-Close-grown	AGRR	0.48%
Agricultural Land-Row Crops	AGRC	10.68%

The Merino series consists of very shallow and shallow, well drained soils formed in residuum and colluvium from monzonite and other granitic rocks, gneiss, tuff, and breccia. Merino soils are on undulating plateaus, ridgetops, and side slopes of intermontane basins and on mountainsides and mountain ridges. Slope ranges from 5 to 65 percent. The mean annual precipitation is about 22 inches, and the mean annual temperature is about 38 degrees F.

The Brewster series consists of very shallow or shallow, well drained, moderately permeable soils that formed in loamy materials weathered from igneous bedrock. These soils are on rolling to very steep hills and mountains. Slopes range from 5 to 60 percent.

The San Antonio series consists of deep, well drained, slowly permeable soils formed in ancient alluvial sediments. These soils are on nearly level to gently sloping uplands and stream terraces. Slopes range from 0 to 5 percent.

Table II: Derived Soil properties delineated in the catchment

<i>Soil Name</i>	<i>Merino</i>	<i>Brewster</i>	<i>San Antonio</i>
Soil Hydrologic Group:	A	A	A
Maximum rooting depth(mm):	2000	2000	200
Porosity fraction from which anions are excluded	0.50	0.50	0.5
Crack volume potential of soil:	000	0.00	0.00
Texture 1 :	Grv_SL	Grv-CL	CL
Depth (mm)	330mm	300mm	1520m
Bulk Density Moist (g/cc):	1.38	1.61	1.4
Ave. AW Incl. Rock Frag :	0.13	0.10	0.17
Ksat. (est.) (mm/hr)	883	672	0.9
Organic Carbon (weight %):	0.5	1.25	0.5
Clay (weight %):	16	27	39
Silt (weight %):	40	38	32
Sand (weight %):	44	35	29
Rock Fragments (vol. %):	27	47	4
Soil Albedo (Moist)	0.1	0.1	0.1
Erosion K	0.18	0.13	0.16
Salinity (EC, Form 5)	0 .00	0	0

3.3.4. Delineations of Hydrological Response Units

Land cover and soils in catchment system response to precipitation physically and governs the distribution of precipitation into; infiltration, evaporation and runoff after meeting the depression storage and abstraction. As combination of soil and land cover makes important responding units, therefore runoff generation process in SWAT is accomplished by subdividing the watershed into areas having unique land use and soil combination which are called; Hydrological Response Units (HRU's). Practically HRU's are derived by overlying the land use and soil type layer in each of the topographically derived sub-basin [27]. Total 101 topographically derived sub-basins are divided into 346 HRU's by keeping the threshold values 5 % for land use and 0 % for soils. This threshold is supposed to give full soil classes and maximum land use classes coverage in formation of the HRU's in watershed modeling.

3.4. Temporal Data

Rivers in the hydrological regimes may differ significantly in their runoff response to changes in the driving variables of temperature and precipitation. These varied responses to changes in the driving variables mean that caution must be exercised in the prediction of runoff response to climate change, especially in complex catchments with a mix of hydrological regimes. Therefore the long term meteorological datasets are required for the hydrological modeling.

3.4.1. Climate Data

The simulation is mainly for assessment of hydrological parameters; therefore temporal input to the model is hydrometeorology and stream flow. Snow and hydrology research division of Water and Power Development Authority (WAPDA) Pakistan has installed 17 recording type meteorological stations in Pakistani part of catchment in a well distributed manner. These stations record maximum and minimum temperature, relative humidity, solar radiation and snow melt equivalence of water on daily basis. This hydro- meteorological stations network covers only Pakistan part of the catchment. For coverage of catchment out of territorial boundary of Pakistan i.e. Afghanistan, China and India, World Meteorological Organization (WMO) network was used. Good quality data was available for three stations in China part of the catchment with full coverage. However the constraint of non availability of most recent data (1994 to 2004) has reduced the coverage in India and Afghanistan part as data of only one station for each of these countries was available in the catchment area. The location of weather station and data used in simulation is given in Table III.

Table III: List of stations used for meteorological datasets

3.4.2. Stream flow Data

S. NO	Station Name	Country	Location			Record Length (years)
			Long (deg.)	Lat. (deg.)	Elevation (meters)	
1	Bruzilp	Pakistan	75.09	35.90	4030	6/10/94 to 16/9/2004
2	Desoai	Pakistan	74.01	34.95	4356	12/1997 to 10/1/2004
3	Gilgit	Pakistan	72.43	36.33	1550	3/1/997 to 9/16/2004
4	Hushey	Pakistan	76.20	35.20	2995	9/13/1994 to 10/20/2004
5	Kelashp	Pakistan	73.17	36.28	3000	6/1/1994 to 10/22/2004
6	Khod	Pakistan	72.58	36.58	3455	6/1/1994 to 3/3/2004
7	Naltar	Pakistan	74.27	36.22	2810	6/6/1994 to 10/19/2004
8	Rama	Pakistan	74.82	35.37	3000	6/1/94 to 12/31/03
9	Rattu	Pakistan	74.82	36.50	2570	6/1/1994 to 2/31/2003
10	Saif-ul-Maluk	Pakistan	74.82	36.50	3200	10/16/1995 to 9 /15/2004
11	Shangla	Pakistan	72.60	34.38	2100	6/1/1994 to 9/26/2004
12	Shendup	Pakistan	72.53	36.83	3560	9/26/2004 to 9/26/2004
13	Shogran	Pakistan	73.47	34.60	2930	9/20/2000 to 9/28/2004
14	Uskorep	Pakistan	73.30	37.33	2977	7/13/1994 to 12/31/2003
15	Yasinp	Pakistan	73.30	36.45	3150	6/9/1994 to 10/1/2004
16	Zanipas	Pakistan	73.28	36.28	3000	7/3/1994 to 10/1/2004
17	Ziarat	Pakistan	74.43	36.22	3669	1/6/1994 to 1/10/2004
18	Kabul	Afghanistan	69.22	34.55	1791	1/6/1996 to 31/12/2004
19	Lumar	India	84.05	32.30	4420	1/1/2004 to 31/12/2004
20	Shiqua	China	80.08	32.50	4280	1/1/2004 to 31/12/2004
21	Sonap	China	75.32	34.32	2515	1/1/2004 to 31/12/2004
22	Tuko	China	81.43	30.55	4736	1/1/2004 to 31/12/2004

Stream flow data of Indus River System is gauged and well maintained at several stations along its course from its origin in mountains in north to its last takeout at Kotri in lower Indus Plain in south at Indus Delta region. The historic daily flow data was available for the period 1962- 2004 for calibration of flow simulations. Two gauging stations for stream flow data are used: Kakabagh Dam (Upstream) on Indus and Nowshera at Kabul River before it discharges into Indus at Attock and becomes the part of marvelous Indus Basin Irrigation System.

IV. MODEL SIMULATION

After completing all the model inputs pertaining to special and temporal datasets, the model is ready for simulation. The simulation is done for a period of 10 years from 1994 to 2004 which is the same period of availability of climate data. This simulation is saved as default one. The model is simulated many more times by changing the value of Curve Number (CN2), Soil Evaporation Compensation (ESCO), Lateral Flow Travel (ILAT_TTIME) and Groundwater Re-evaporation (GW_REEVAP) to get the best match between model output and observed data.

V. RESULTS AND DISCUSSIONS

The model calibration and the output maps are presented in this section. The details and discussions are given as following:

5.1. Model Calibration

The calibration step aims to determine the optimal values for the parameters specified by the user. Calibration of models at a watershed scale is a challenging task because of the possible uncertainties that may exist in the form of process simplification, processes not accounted for by the model, and processes in the watershed that are unknown to the modeler. The process of calibration was adopted to adjust parameters related to hydrology of the catchment. The stream flow data is processed for annual values to calibrate SWAT. The practice was carried out by referring stream flow data at two gauging stations. The river Kabul was calibrated at Nowshera in KPK province, before it joins the Indus near Attock. Discharge data for years 1994 to 2004 was used for comparison with the simulated flow. Indus has been also calibrated at the Kalabagh just before it enters into the Indus Plain. Kalabagh is a site proposed for construction of large dam for generation of hydropower and storage of water to meet increasing water demand of Worlds Largest Contiguous Indus Basin Irrigation System (IBIS). The comparison of simulated and measured flows are for the eleven years from 1994 to 2002. Fig. (5) and Fig. (6) show generally well respected for both calibration periods. The calibration of any surface water model in Indus is complicated because complexities and large size of watershed. The watershed contains high peaks, glaciated and snow melts as well as rained areas. Five model parameters are adjusted to bring simulated values close to the observed values model values close to the observed ones in the process of calibration. The Curve Number (CN2) is increased by 3 in all sub-watersheds; Soil Evaporation Compensation (ESCO) is increased by 0.1 and Lateral Flow Travel (ILAT_TTIME) is adjusted to 500. Similarly Groundwater Re-evaporation (GW_REEVAP) is adjusted as 0.3 and Hargreaves method selected for estimation of potential evapotranspiration for adjustment of mass balance components.

The result of flow calibration show a good correlation of observed and model simulated as shown in Figures (5&6) . At Nowshera station the average flow for the simulation period is 248 mm with the standard deviation of 78 whereas the average observed flow during the same period is about 292 mm with the standard deviation in series is 75. The correlation coefficients for simulated and observed flow are 67.5. For the second station at Kalabagh, the average flow for the simulation period is 290 mm with the standard deviation of 74 whereas the average observed flow during the same period is about 247 mm with the standard deviation in series is 74. The correlation coefficients for simulated and observed flow are 69, which can be termed as good.

To evaluate the performance of the model with calibrated parameters, the coefficient of Determination (R^2) and one of three statistic coefficients recommended by Moriasi [28] , Nash-Sutcliffe efficiency coefficient (NSE) were carried out. Coefficient of determination (R^2) is a good method to signify the consistently among observed and simulated data by following a best fit line. It ranges from zero with no linear relationship to 1.0 which is perfect linear relationship. Generally, values greater than 0.50 are considered acceptable and similarly the higher values represent the less error between the simulated and observed values [29], [30]. The value R^2 test of flow stands 0.54. It indicates that model results produced for the sedimentation are very good as well as the results for flow are good enough.

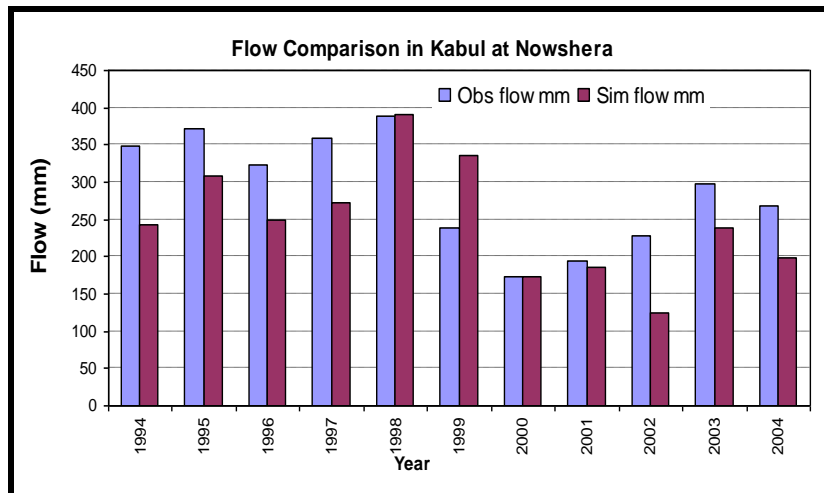


Figure 5: Comparison of annually observed and simulated stream flow at Nowshera

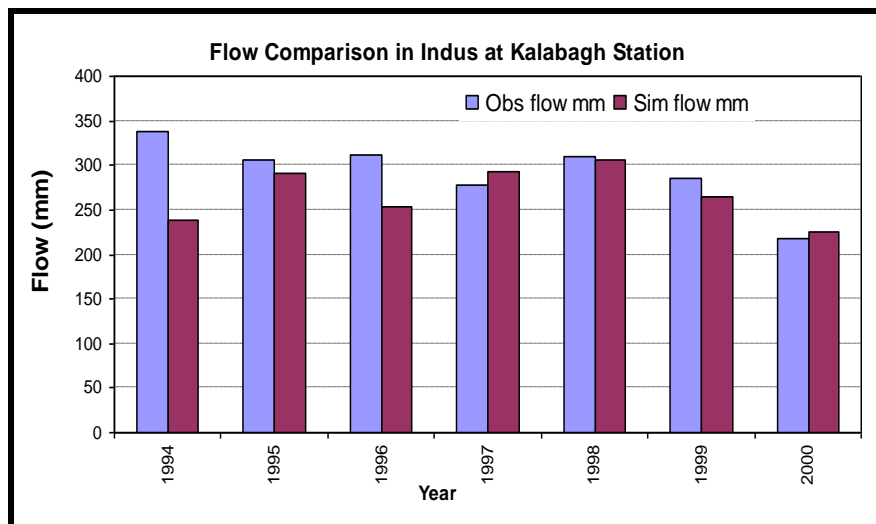


Figure 6: Comparison of annually observed and simulated stream flow at Kalabagh

The statistic operator Nash-Sutcliffe efficiency coefficient (NSE) [31] is a normalized statistic method use for the prediction of relative amount of the residual variance (“noise”) compared with measured data variance (“information”) as explained in the following equation:

$$NSE = 1 - \left[\frac{\sum_{i=1}^n (Y_i^{obs} - Y_i^{sim})^2}{\sum_{i=1}^n (Y_i^{obs} - Y_i^{mean})^2} \right] \quad (2)$$

Where Y_i^{obs} is the i th observation (streamflow), Y_i^{sim} is the i th simulated value, Y^{mean} is the mean of observed data and n is the total number of observations.

NSE ranges between $-\infty$ and 1.0 (1 inclusive), with $NSE=1$ being the optimal value. Values between 0.0 and 1.0 are generally viewed as acceptable levels of performance [28]. According to NSE method, the model result of 0.98 which is quite acceptable

5.2. Output Maps

SWAT model used the input data for soil, climate and land use to simulate the hydrology of Upper Indus River Basin and assessment of impact of drought and dry periods on environmental flow. A large watershed system in Pakistan, India, China and Afghanistan has been used for simulation. The simulation period is 11 years from 1994 to 2004. The model results are briefly summarized in the following output maps, Fig.(7)

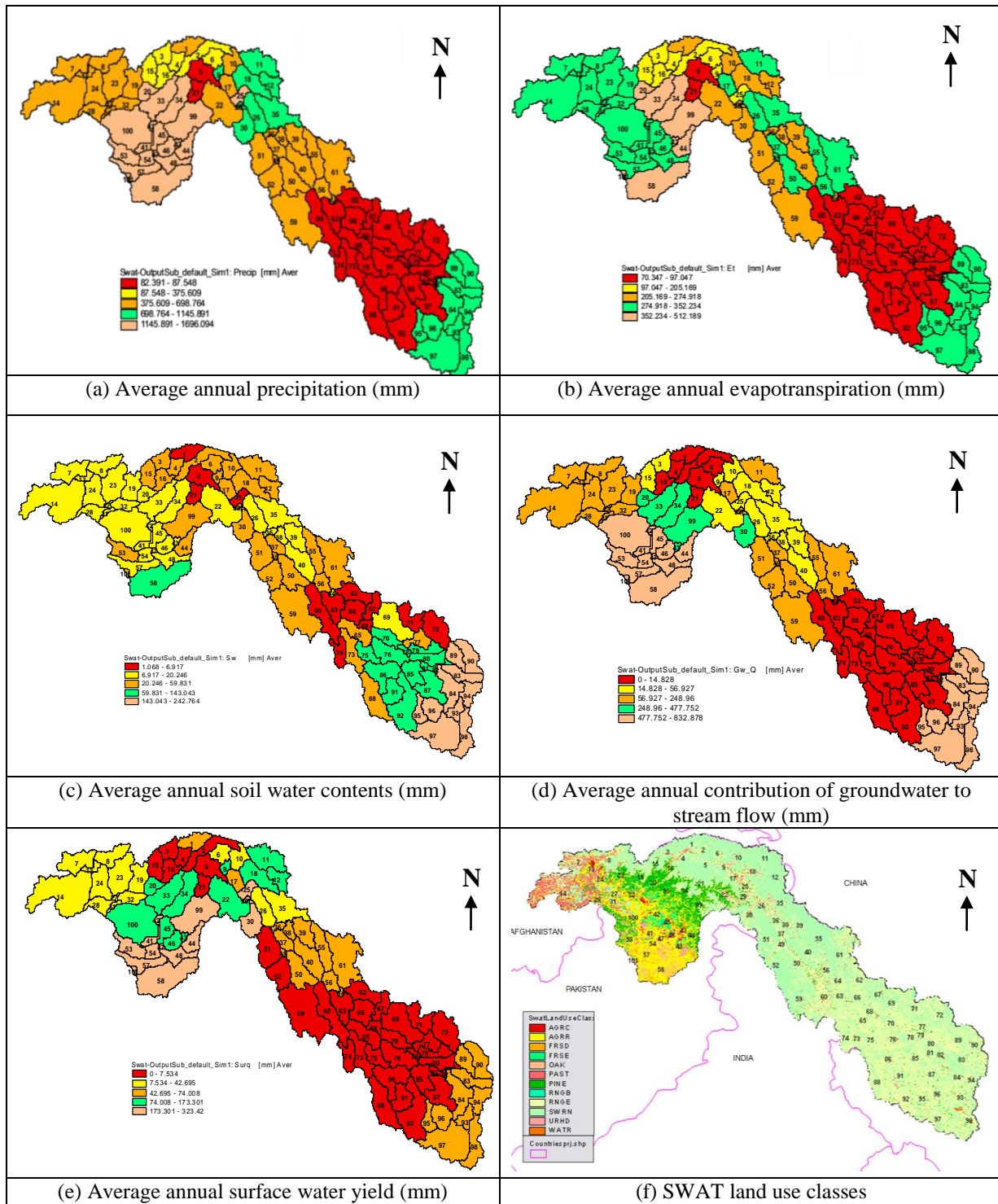


Figure 7: Distribution of Basic output hydrological components and land use of Upper Indus Basin watershed through 101 sub-basins for simulation period of 11 years (1994-2004).

The analysis of Figure 7 illustrates that: the precipitation varies very much spatially. The average annual precipitation of 652 mm with maximum of 1696 mm and minimum of 82 mm. the occurrence and magnitude of precipitation are influenced by the distribution of areas within each elevation band in the study area as shown in Fig.7(a). High mountain regions are characterized by altitudinal variations in the contribution of rainfall, snowmelt and glacier melt to runoff. Waters captured at high altitudes flow under gravity via the stream network or groundwater aquifers to the lowlands resulting in quite different hydrological regimes.

Changes in land use and vegetation affect not only runoff but also evapotranspiration. Increased evapotranspiration reduces the groundwater recharge and the contribution to river flow. However, great differences occur according to the plant species and the rate of production. Fig. 7(b) represents the amount and variation of evapotranspiration over the whole catchment, which ranges from 512mm to 70 mm with an average annual of 236 mm. The distribution of annual soil water content is presented by Fig. 7(c), the maximum value is 243 mm with the average annual of 51mm and minimum as low as 1mm.

Streams and other surface-water bodies may either gain water from ground water or lose (recharge) water to ground water. The contribution of ground water to total streamflow varies widely among streams. The effect of ground-water contribution to headwater streams on the volume of streamflow lower in a watershed is related partly to the volume of ground water contributed in the headwater area; that is, the larger flow is initially, the farther downstream that water will extend. Fig. 7(d) illustrates that the average annual contribution of groundwater in UIB to steam flow is about 202 mm with the maximum 832 mm and minimum of zero (for low precipitation), and total average annual surface water yield is 152 mm with the average maximum of 323 mm and minimum of even less than one mm as shown in Figures 7(d & e) respectively. These results of Upper Basin have practical consequences for flow forecasting on the River Indus and a significance for water resource use in the lower Indus.

VI. ECOHYDROLOGY

The river Indus intercepts mountains, feeds great Indus Basin Irrigation System (IBIS), transverses deserts and deltaic systems and finally drains into Arabian Sea. The last ecosystem intercepted by this mighty river is deltaic. The main use of Indus water is agriculture and provinces own right of its use. The survival of the Indus Delta is dependent on the silt-laden freshwater discharges from river which has been curtailed due to diversion of water for agriculture, power generation, and other uses in the upper reaches. The distributing of water among provinces is governed under water appointment accord signed in 1991 among provinces. It was agreed in accord that 12 Bm3 flow will be allocated for sustainability of freshwater dependent deltaic ecosystem. The freshwater flows into the delta during the recent years have been inconsistent and mostly below the minimum required quantity as shown in Fig.(8).

Figure 8 indicates that release of environmental flow to delta rather than the hydrological as the flow below Kotri Brage is highly variable for the same range of runoff in Upper Indus Watershed. The reduction in the inflow of freshwater has exposed complex deltaic ecosystem to several environmental and social stresses in the form of loss of habitat and biodiversity and a decline in the productive values of the ecosystem. The reasons for continuous reduction in discharges and consequent silt load are mainly due to construction of dams and diversion of water in canals. From 1992 onwards the reduction in water discharges below Kotri Barrage and natural drought periods are very conspicuous and so is the drastic reduction in silt load. This has not only degraded the development and health of mangroves but has facilitated the sea intrusion in the Indus delta.

Because of the volume and sustainability of stream flow is generated in head-waters areas, the model out put was used to analyze the environmental flow in lower delta. Figure 8 illustrates that the average precipitation is sufficient to generate runoff and groundwater recharge. The simulated runoff by the model have practical consequences for flow forecasting on the River Indus and its delta. The figure shows that there is enough water for downstream release so that freshwater release for sustainability of Deltaic ecosystem should taken at second

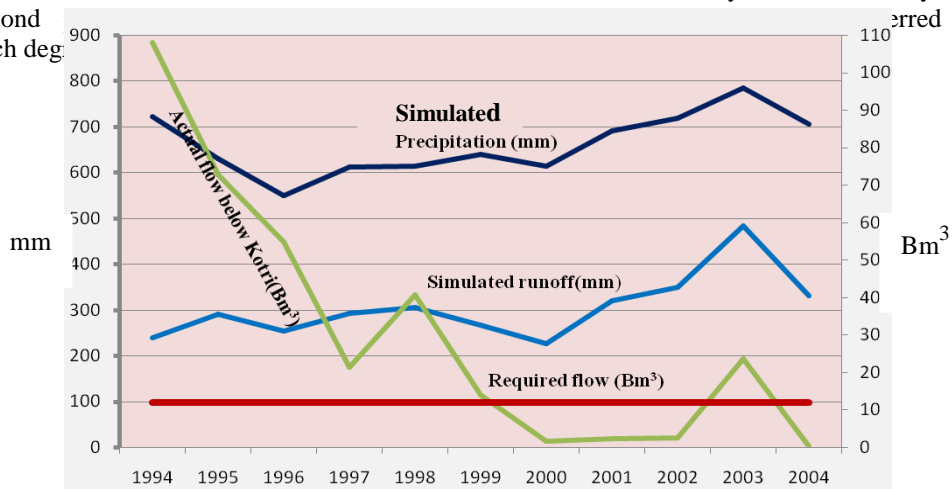


Figure 8: Availability of Water and Environmental Flow in Indus River

VII. CONCLUSIONS

The mountains region of UIB is a critical source of water for Pakistan and provide the main water source for the IBIS, one of the world's largest integrated irrigation networks. The River Indus is fed by a combination of melt water from seasonal and permanent snow fields and glaciers, and runoff from rainfall both during the winter and monsoon season. The hydrology of Upper Indus River Basin and the linkage between climatic variables and river flow is investigated by A GIS based watershed model Soil and Water Assessment Tool (SWAT). The impact of drought and dry periods on the ecohydrology of Indus Delta also assessed. Swat model was successfully calibrated in the UIB watershed. The evaluation of the model performance was carried out successfully with the recommended statistical coefficients. The comparison of observed and simulated flow stream at two gauging stations revealed a Nash-Sutcliffe coefficient superior to 0.98 and R^2 to 0.54 for calibration periods.

The analysis of output maps concluded that: the hydrological components of Upper Indus Basin watershed (precipitation, evapotranspiration, soil water content, surface water yield and contribution of groundwater to stream flow) differ between basins in the region and these affect the environmental flow of Indus River and the water resource use in the lower Indus. The variation of hydrological components within the basin due to the elevation range and the distribution of areas within each elevation band in the in the catchment, temperature variations, permanent snowfields and the glacierised proportion.

Freshwater release for sustainability of Deltaic ecosystem should taken at second priority whereas other uses like ; irrigation, power, drinking etc. are preferred during dry periods which degrades the deltaic ecosystem. Thereafter differing hydrological regimes over the mountains of northern Pakistan must be taken into account in the planning , design, management and operation of water resources of the River Indus and its delta.

This study had showed the utility of GIS to create combine and generate the necessary data to set up and run the hydrological models especially for those distributed and continuous. It also had demonstrated that the SWAT model works well in large mountainous watersheds and in semi-arid regions.

RECOMMEDATION

- 1- The calibrated model can be well used in UIB watershed to assess or predict other watershed components such as the impacts of land and climate changes on water quality and sediment yield.
- 2- The performances can be enhanced using some other global climate data and emissions scenarios to assess the potential impacts of climate change on the hydrology of whole Indus River basin as a macro scale model.
- 3- Solute transport model should be developed for Indus Delta to predict the saline water intrusions and for different scenarios of pumping of aquifer at different depths

REFERENCES

- [1] Ahmad N., *Water Resources of Pakistan* (Miraj-ud-Dn Press, Lahore, Pakistan, 1993).
- [2] MOWP, *Pakistan Water Sector Strategy: National Water Sector Profile* (Ministry of Water and Power, Vol. 5, October 2002).
- [3] Hayley J. Fowler and David R. Archer, " Hydro-climatological variability in the Upper Indus Basin and implications for water resources", Regional Hydrological Impacts of Climatic Change-Impact Assessment and Decision Making ,*Proceedings of symposium S6 held during the Seventh IAHS Scientific Assembly* at Foz do Iguacu, Brazil, April 2005, IAHS Publ. 295 (2005).
- [4] Rao, Y. P. , " The Climate of the Indian Subcontinent", *In Climate of Southern and Western Asia*, (Word Survey of Climatology New York: Elsevir., vol. 9 ,1981) 67-1123.
- [5] Hoekstra, M. Nurrudin, G.R. Shah, W.A. Shah, M.A. Domki and Q.M. Ali *Diagnostic Study of the Indus Delta Mangroves Ecosystem* (Sindh Forest & Wildlife Department, Karachi, 1997).
- [6] WAPDA (Water and Power Development Authority), *Terbala Dam Sedimentation Annual Report*, Pakistan, 2005.
- [7] Kahlown, M.A., Khan A. D. and Azam M., *World's Largest Contiguous Irrigation System: Developments, Successes, and Chellanges of Indus Irrigation System. In: Proceedings. The History of water*, Islamabad, Pakistan, 2000.
- [8] Vijay P. Singh and Donald K. Frevert, *Watershed Models*. (Taylor and Francis Group, LLC. New York, 2006).
- [9] V. P. Singh and D. A. Woolhiser, *Mathematical Modeling of Watershed Hydrology*, *Journal of Hydrologic Engineering*, ASCE, 7(4), 2002, 270-292.
- [10] Masood T. and Sana Ullah, *Draft Report on UBC Modeling of Jhelum* (Lahore, Pakistan,1991)
- [11] Munir A. B. and Najib A., "Climate Change Impact Assessment and Adaptation Strategies for Pakistan in Water Sector", Pakistan Science Foundation, (1997).
- [12] Ahmad M., A. Brooke, and G. P. Kutcher, *Guide to the Indus Basin Model Revised* (Washington, DC: World Bank, 1990).

- [13] Winston Yu, Yi-Chen Yang, Andre S., Donald A., Casey B., James W., Dario D. and Sherman R., *The Indus Basin of Pakistan: The Impacts of Climate Risks on Water and Agriculture* (The WORLD BANK, Washington, D.C. ,2013).
- [14] Arnold J. G., Sprinvasan R., Muttiah R. S. and Williams J. R., Large area Hydrologic Modeling and Assessment: Part 1 Model Development, *Journal of American Water Resources Association*, 34(1) ,1998, 73-89
- [15] Di Luzio M., Raghavan S. and Jeffrey G. Arnold, A GIS-Coupled Hydrological Model System for the Watershed Assessment of Agricultural Nonpoint and Point Source of Pollution, *Transaction in GIS*, 8(1), 2004, 113-136
- [16] Shimelis G. S., R. Srinivasan and B. Dargahi, Hydro-logical Modelling in the Lake Tana Basin, Ethiopia Using SWAT Model, *The Open Hydrology Journal*, 2(1) ,2008, 49-62.
- [17] Ashagre B. B., *SWAT to Identify Watershed Management Options: Anjeni Watershed, Blue Nile Basin, Ethiopia*, Master's Thesis, Cornell University, New York, 2009.
- [18] Fadil A., Rhinane H. , Kaoukaya A., Kharchaf Y. and Bachir O. A., Hydrologic Modeling of the Bouregreg Watershed (Morocco) Using GIS and SWAT Model, *Journal of Geographic Information System*, 3,October 2011, 279-289.
- [19] Cindy S. and Koichiro O., Dam Construction Impacts on Stream Flow and Nutrient Transport in Kase River Basin, *International journal of Civil and Environmental Engineering, IJCEE-IJENS*, 12 (3) , June (2012).
- [20] Wake C. P., Glaciochemical investigations as a tool to determine the spatial variation of snow accumulation in the Central Karakoram, Northern Pakistan, *Ann. Glaciol.* 13 ,1989, 279–284.
- [21] Archer D. R., *The climate and hydrology of northern Pakistan with respect to the assessment of flood risk to hydropower schemes* (GTZ/WAPDA, Lahore, Pakistan, 2001)
- [22] Archer D. R., Contrasting hydrological regimes in the upper Indus Basin, *Journal of Hydrology*, 274 , 2003, 198–210.
- [23] Verdin K.L., and Greenlee S. K., Development of Continental Scale Digital Elevation Models and Extraction of Hydrographic Features, *Third International Conference/Workshop on Integrating GIS and Environmental Modeling*, Santa Fe, New Mexico, January 21-26, 1996. National Center for Geographic Information and Analysis, Santa Barbara, California.
- [24] Agarwal, C., G. M. Green, J. M. Grove, T. P. Evans, and C. M. Schweik, A Review and Assessment of Land-Use Change Models: Dynamics of Space, Time, and Human Choice, General Technical Report NE-297, Newtown Square, Pennsylvania: U.S. Department of Agriculture, Forest Service, Northeastern Research Station, (2002).
- [25] Dyke Paull T., McMahon B., and Nichols M., Global Soils,2001. 1:1Million Digital Soil Map of the World. To be published by Trexas Experimenta l Stataion/Blackland research centre. Temple Texas. www.brc.tamous.edu
- [26] Bamour O, Kenyon P, Bettis. *MUUF, v2-14user: 's Manual* (Natural Resources Conservation Services, National Soil Survey Centre, Lincoln, NE, 1994).
- [27] User's Guide, ArcView Interface for SWAT 99-2, Balckland Research Centre, TAES, Temple Tx.,USA, ,1999.
- [28] Moriasi D. N, Arnold J.G., Van Liew, M.W., Bingner R. L., Harmel R. D. and Veith T.L., Model Evaluation Guidelines for Systematic Quantification of Accuracy in Watershed Simulations, *American Society of Agricultural and Biological Engineers*, 50(3) ,2007, 885–900.
- [29] Santhi C., Arnold J.G., Williams J.R., Dugas W.A., Srinivasan R. angHauck L.M., Validation of the SWAT Model on a Large River Basin with Point and Non-point Sources, *Journal of American Water Resources Association*, 37 (5) , 2001, 1169–1188.
- [30] Van Liew M.W., Veith T.L., Bosch D.D., Arnold J.G., Suitability of SWAT for the Conservation Effects Assessment Project: A Comparison on USDA-ARS Experimental Watersheds, *Journal of Hydrologic Engineering* 12 (2), 2007, 173–189.
- [31] Nash J. E. and Sutcliffe J. V., River Flow Forecasting through Conceptual Models, Discussion of Principles, *Journal of Hydrology*, 10(3) ,1970, 282-290.

A Comparison Of Smart Routings In Mobile Ad Hoc Networks(MANETs)

Gholamhasan Sajedy-Abkenar¹, Amirhossein Jozdani², Arash Dana³

¹(Scientific Association of Electrical & Electronic Engineering, Islamic Azad University Central Tehran Branch, Tehran, Iran,

²(Islamic Azad University, Pardis Branch,)

³(Islamic Azad University, Central Tehran Branch,)

ABSTRACT: The importance and the massive growth of many wireless networks, has consequently lead to creation of many different routing types, that each of them have tried to improve the network capabilities with different parameters. From this it can be deduced that, there is an essential need to develop an optimal routing network which as a complete routing should be more flexible than the existing ones. In the field of traditional routing, intelligent routing and the swarm intelligentsuch as ARA, several algorithms have been written that neither of them have been totally rejected nor used widely as the rule of thumb. In this paper it is tried to prove that by combination of several different routing algorithms, which have been presented so far, an intelligent routing network can be achieved that analyzes the properties in the different conditions and matches it with required routing types. Simulation results show that, the offered combined algorithm in general, has had a significant improvement in the various wireless network parameters, compared with each algorithm that are used separately.

Keywords: Ad Hoc Networks Routing Algorithms, Swarm Intelligent.

I. INTRODUCTION

Wireless Mobile Ad Hoc Networks that are called MANETs, have been considered more than one decade [1]. The most significant point about this kind of network is that, it has no infrastructure and can be used quite easily in critical situation with minimal cost. This network has moving nodes that can link to other nodes in two ways: direct and indirect. In the direct method, source node is located in the neighborhood of the destination node and the communication is done very easily, but in the indirect method as the origin node is not in the neighborhood of the destination node, middle nodes (as many as required) are used to carry the data in the communication [2].

Many routing algorithms have been presented, one of them is Ant Colony Optimization (ACO) algorithms [3] that is been used from 2002 until now in many different ways. Attention to other aspects of networking such as energy has produced many algorithms like EAAR [4]. It should be noted that improving all the parameters of a network for overall quality of service (QoS) lead to a better network completely but it is impossible due to network and environment conditions such as energy, mobility, traffic and many other parameters that are effective as well. Every algorithm under certain condition can improve only two or just a few parameters. In a paper [5] we have chosen few algorithms from several existing algorithms in ARA field but by considering and simulating different domains and routings under combined routing algorithms we have shown that the combined algorithms will produce a better result.

In this paper by combining and comparing several algorithms and applying them in various network conditions, a new algorithm is presented which is useful for networks that do not have a stable environmental situation. Simulation shows general improvements compared to the ones that are currently used separately. We initially examine types of routing tasks performed currently, then the combined routing algorithm is presented and briefly explained, and finally, simulation results and conclusion are presented.

II. KINDS OF ROUTING AND RELATED WORKS

In total there are 3 Routing categories, which are as follows: Proactive, Reactive and Hybrid.
1- proactive or (Table Driven): in this category, each node in the routing domain sends continuous messages to the other nodes in its neighborhood and the surrounding environment and stores the obtained information from

other nodes in the domain and maintains in a table of routes. However the used energy is quite high, this method has the advantage of being high-speed because the routes for the destination already are defined in the tables. Many algorithms in this category can be mentioned such as DSDV[6],WPR[7],GSR[8],FSR[9],STAR[10] and many other protocols.

2- Reactive routing (on demand): in this type of routing, only when there is a request at the source node to contact to the destination the routing beings and the transmission of the data begins just after the routing destination is been found. As it can be observed, this method is much slower than the proactive type because the destinations are not defined readily. There are also many routings in this category such as AODV[11],DSR[12],ROAM[13],TORA[14] and LMR[15] protocols.

3- Hybrid:as the name of this model suggests, it is a combination of two types of proactive and reactive routing. The tendency for this routing is obvious. In a Hybrid routing, proactive routing is used for near destination and proactive routing for farther destinations. ZRP[16], ZHLS[17], DDR[18] are some of the routings in this category.

III. THE PROPOSED ALGORITHMS AND USED ROUTINGS

In this part we briefly describe those routing algorithms that are going to be used in our intelligent combined algorithms. And finally we explain how they are combined. The routing that have been selected to be combine will cover a wide range of scenarios in a complex networks.

A)DSDV: that is an interactive (proactive) algorithm which is very convenient for small and compressed networks. The way that this algorithms works is as follow: as a proactive protocol, it works based on the shortest distance. DSDV has a table of all destination nodes, updates its tables frequently and contacts to all of its neighboring nodes. This frequent updates requires a massive bandwidth with a high energy consumption, however it does nothave a dead-end and never fail to find the required destination node.

B)OLSR:this algorithm acts on bases of Link-state (contrary to Distance-Vector), it creates a graph of the paths and the relationship between the nodes. On request it will choose the best route to the destination node from the saved information. The advantage of this method is that, the topology information is reviewed and updated at each count, and reduces the amount of control packets. Therefore OLSR is suitable for networks that are only active during specific periods of time and would not require to occupy bandwidth for a long time.

C) ARA & ARAMA:both of these algorithms are part of reactive algorithms and based on the move of ants in search of food. Therefore it can be said that these two algorithms find the route to the destination node by probability model. The simplified relationship in this algorithms is shown in equation 1, that $P_{i,j}$ is the probability of node j for choosing node i.

$$P_{i,j} = \begin{cases} \frac{\rho_{i,j}}{\sum_{k \in N_i} \rho_{i,k}} & .if \ j \in N_i \\ 0, & \forall j \notin N_i \end{cases} \quad (1)$$

One of the problems with this method is that the broadcast of the requested route in the network is not suitable for large networks with many nodes and does not consider the energy factor. So all types of ARA are not suitable for networks with lots of nodes and low-energy scattering.

D)EAAR:is another algorithm which is based on move ants algorithm with an obvious difference that specifically focuses on energy and the route has an appropriate longevity. In addition to this, there is a future for alternative routing in this algorithm which eliminate the need for any rerouting in the case when there is a missed route. The general formula for the probability of selecting the next node in this algorithm is shown in Equation 2.

$$P_{n,d} = \frac{(T_{n,d}^i)^\beta}{\sum (T_{j,d}^i)^\beta} \quad (2)$$

β is a scaling factor. Therefor it can be said that EAAR is suitable for networks with sparse and non-conventional energy with almost any number of a nodes.

E) ZRP: This routing algorithm works on the bases of regions or the Zone Code. The way it works is as follow: in any particular zone, there are routes from one node to all other nodes in that zone and it works in proactive or reactive way. But to find a node in a different area, the route is identified on the bases of the distance and selecting the central node for connection to destination node in other area, as shown in Figure 1 (an overview of routing domains).

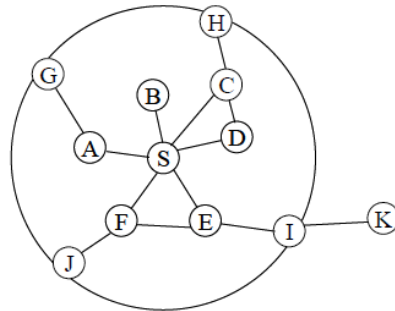


Figure 1: Classification of zone in ZRP

Therefore ZRP is suitable for networks that have less mobility and the nodes are scattered in specific areas that can be classified in zones.

F) DST[20]: in this Algorithms, graphs are formed in the shape of trees, within these graphs are nodes which can communicate with other trees. The advantage of this model is that because the routing between the trees may communicate (it has a specific time period) if the entry of new nodes into the network is large or nodes are taken out of the network, they all will be taken into the account. In this method only finding the destination is important and the paths taken is of no importance. So DST is appropriate for networks with wide spread nodes, where the rate of adding and removing nodes are high.

We have called our proposed algorithms ICRA (Intelligent Comparison Routing Algorithm). This comparison routing is a hybrid routing. All nodes before the call to any specific destination will collect data from their neighboring nodes on a continuous cycling base. Some important parameters are stored in the routing tables for each node, such as total number of neighboring nodes, the total free energy of them and network bandwidth which at the time of a request would be used to determine the type of algorithms in routing connection. For saving each of these parameters a set of standards has been defined. This has been illustrated in Table 1.

Table 1: Conditions of Selecting Algorithms

TypeAlgorithm	conditions
DSVD	The Number of neighboring nodes more than 50% of initial nodes
OLSR	Freebandwidthof1.5MB andno change inthe number ofneighboring nodes
ARA	Number of neighboring nodes is less than 50% of the initial nodes or the total energy is under 10,000 joules
ARAorEAAR	Excessive energy difference of neighboring nodes
ZPR	The Number of neighboring nodes about 30% of initial nodes and spatial stability of neighbors
DST	The number of nodes in each update period is more than 20% of previous state

In our simulation at the time of the request by programming and using some instructions, the right algorithm(s) would be chosen and applied to the routing process. If more than one algorithm can be used for a specific request, then our algorithm picks the algorithm that has minimum delay and also uses the least energy.

IV. SIMULATION AND RESULTS

Our simulations has carried out using Matlab2007b. Before considering details and results, there are couple of points which are so important and should be mentioned. On the one hand, the technology of sensor, battery and memory storage on a mobile phone or other devices have improved and on the other hand the importance of time is also much more critical. Therefore it can be assumed that nowadays, the priority is on less routing delay than on saving power consumption that has been considered in our method.

In our simulations it is tried to use parameters that are used in majority of networks and in the simulations, these can be seen in Table 2.

Table 2: Simulation assumptions

Parameter	Defaults
Dimension	$mumixaM2000 \times 2000m^2$
Initial number of nodes	Up to 100
Communication Range	350 Meters
Layer protocol MAC	IEEE 802.11
Mobility Model	Random Way Point
Path Loss Model	Free space
Initial Energy of Nodes	Upto 1000 Jules
Packet Length	64 & 128 Kb
Traffic Model	CBR
Channel Capacity	2 MB
Simulation Time	Each Time 1000 Second

There are several network performance parameters for assessing the performance of network. Energy consumption, packet delivery, delay, lost packet and number of missing nodes. Some of the most important of these parameter are considered in our algorithm. Simulation has been carried out many times using different algorithms. The number of delivered packets in 4 different duration of simulation has been noted and shown in the figure 2 for comparison.

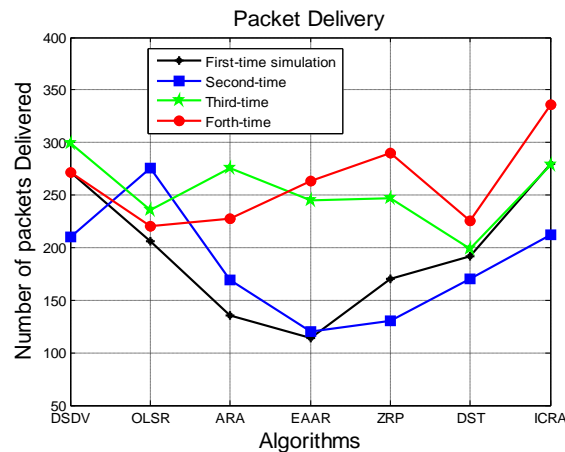


Figure 2: Number of delivered packets

The reason for running the simulation many times was because the conditions, the size and power of the network and the number nodes are random. As it can be seen in Figure 2, depending on the routing algorithm that is used, the number of delivered packages are different, but almost in all cases, this parameter of the proposed algorithm is better in comparison with the other algorithms which has predicted.

Next parameter which is considered, is the number of lost packets. The existing routing algorithms and multi-streaming EAAR is expected to have the least number of lost packets. Figure 3 shows the number of lost packets in the used algorithms.

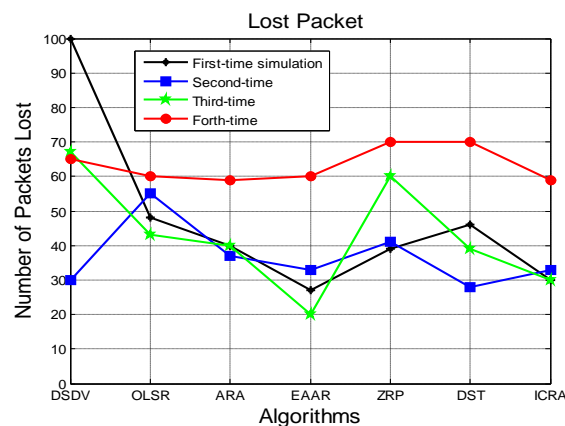


Figure 3: Number of Lost packets

As expected, in all cases EAAR algorithm has the lowest number of lost packets and in comparison to our algorithm is generally better than the other modes. Comparisons lost and delivered packets separately is not enough. For this problem the ratio of delivered packets to total packets in all simulations in Figure 4 has been illustrated that shows ICRA as a better algorithm.

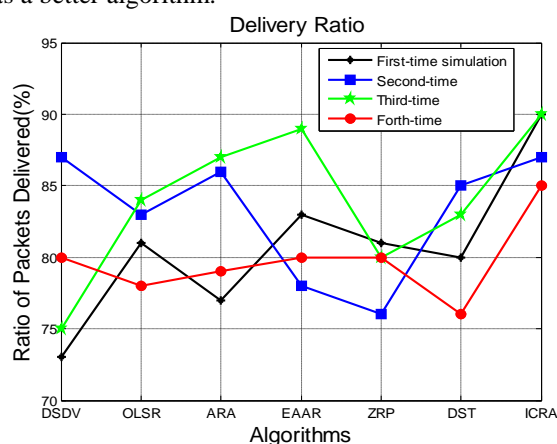


Figure 4: Ratio of Delivered Packetsto total packets

In Figure 4 we can see that our algorithm ICRA in more than 75% has better delivery ratio and according to this the reason of having inappropriatenumber of lost packets in Figure 2 is also explained. The next parameter is the energy consumption of the entire network. High energy consumption due to rational calculation and data analysis which is performed at each node, is predictable. Table 3 shows the Energy consumption in the entire network, and end to end delay in all of them.

Table 3: Energy and end-to-end delay

Averageend-to-end delay(sec)	Averageenergy consumptionof the entire network(kj)	Algorithm
0.9	37	DSDV
0.75	42	OLSR
1.2	40	ARA
1.1	42	EAAR
1	51	ZPR
1.2	59	DST
1	76	ICRA

As you can see in table 3, the proposed algorithm ICRA as was expected consumes more energy, but the calculations are reasonable and the delay is not relatively high. However, as mentioned earlier, it should be noted that nowadays, the energy consumption has a lower prioritythan the delay of the packets. Therefore the more energy that is used in the ICRA algorithm can be justified with more routing packets that have been sent by ICRA algorithm.

In Figure 5, the average total simulation time that each algorithm has spent can be observed.

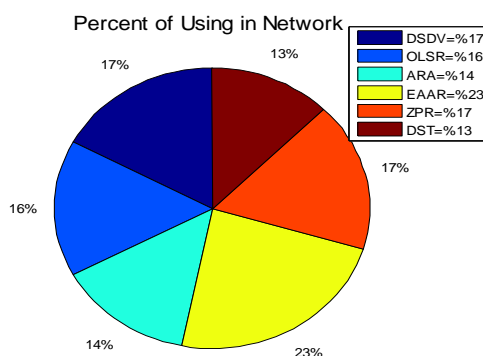


Figure 5: Percentage of total time of each algorithm during the simulation

Use of any routing algorithm during the total time of simulation is not predictable. However the basic parameters such as network size, nodes and the energy are selected randomly and it seems to be natural that each algorithm is used in different periods of time, but the differences between times are not high.

V. CONCLUSIONS

According to simulations that are performed and the recorded results we can conclude that however that the combination of routing algorithms does not affect the overall quality of the network, but is better to use these in a collection than using them separately. However increasing the number of routing algorithms that are used in these models is limited due to the limitation on high energy consumption, it would be much more effective and better presented for networks that have no energy constraints and are connected to a data center .

Future Works

For more comprehensive and thorough investigation, our aim is to extend our simulation via software NS2 and use new algorithms such as PSO. This model also provides an algorithm for wireless sensor networks that we are going to study and simulate it.

REFERENCES

- [1] Macker, J.P., Scott Corson, “ *M. Mobile ad-hoc networking and the IETF in Mob. Comput. Commun. Rev.* ” vol.2. ACM Press, New York, NY (1998) 9-15.
- [2] M. Roth, S. Wicker, Termit: “*ad-Hoc networking with stigmergy*,” Proceedings of IEEE Global Telecommunications Conference, vol. 5, San Francisco, USA , pp. 2937–2941, December 2003.
- [3] Guenes, M., Sorges, U., Bouazizi, I. “*ARA: the ant-colony based routing algorithm, for MANETs*,” Proc. of ICPPW’02, pp. 79–85, 2002 .
- [4] Guenes, M., Sorges, U., Bouazizi, I. “*ARA: the ant-colony based routing algorithm, for MANETs*,” Proc. of ICPPW’02, pp. 79–85, 2002 .
- [5] Gh.SajedyAbkenar, “*Intelligent Ant Based Routing Algorithm In Mobile Ad Hoc Networks*,” 5th International Conference On Advanced Networks And Telecommunication Systems, Bangalore, Karnataka, India 2011.
- [6] C.E. Perkins, T.J. Watson, *Highly dynamic destination sequenced distance vector routing (DSDV) for mobile computers*, in: ACM SIGCOMM_94 Conference on Communications Architectures, London, UK, 1994.
- [7] S. Murthy J.J. Garcia-Luna-Aceves, *A routing protocol for packet radio networks*, in: Proceedings of the First Annual ACM International Conference on Mobile Computing and Networking, Berkeley, CA, 1995, pp. 86–95.
- [8] T.-W. Chen, M. Gerla, *Global state routing: a new routing scheme for ad-hoc wireless networks*, in: Proceedings of the IEEE ICC, 1998.
- [9] M. Gerla, *Fisheye state routing protocol (FSR) for ad hoc networks*, Internet Draft, draft-ietf-manet-aodv-03.txt, work in progress, 2002.
- [10] J.J. Garcia-Luna-Aceves, C. Marcelo Spohn, *Source-tree routing in wireless networks*, in: Proceedings of the Seventh Annual International Conference on Network Protocols Toronto, Canada, October 1999, p. 273.
- [11] S. Das, C. Perkins, E. Royer, *Ad hoc on demand distance vector (AODV) routing*, Internet Draft, draft-ietf-manetaodv-11.txt, work in progress, 2002.
- [12] D. Johnson, D. Maltz, J. Jetcheva, *The dynamic source routing protocol for mobile ad hoc networks*, InternetDraft, draft-ietf-manet-dsr-07.txt, work in progress, 2002
- [13] J. Raju, J. Garcia-Luna-Aceves, *A new approach to ondemand loop-free multipath routing*, in: Proceedings of the 8th Annual IEEE International Conference on Computer Communications and Networks (ICCCN), Boston, MA, October 1999, pp. 522–527.
- [14] V.D. Park, M.S. Corson, *A highly adaptive distributed routing algorithm for mobile wireless networks*, in: Proceedings of INFOCOM, April 1997.
- [15] M.S. Corson, A. Ephremides, *A distributed routing algorithm for mobile wireless networks*, ACM/Baltzer Wireless Networks 1 (1) (1995) 61–81.
- [16] Z.J. Hass, R. Pearlman, *Zone routing protocol for ad-hoc networks*, Internet Draft, draft-ietf-manet-zrp-02.txt, work in progress, 1999.
- [17] M. Joa-Ng, I.-T. Lu, *A peer-to-peer zone-based two-level link state routing for mobile ad hoc networks*, IEEE Journal on Selected Areas in Communications 17 (8) (1999) 1415–1425.
- [18] N. Nikaiein, H. Laboid, C. Bonnet, *Distributed dynamic routing algorithm (ddr) for mobile ad hoc networks*, in: Proceedings of the MobiHOC 2000: First Annual Workshop on Mobile Ad Hoc Networking and Computing, 2000.
- [19] P. Jacquet, P. Muhlethaler, T. Clausen, A. Laouiti, A. Qayyum, L. Viennot, *Optimized link state routing protocol for ad hoc networks*, IEEE INMIC, Pakistan, 2001.
- [20] S. Radhakrishnan, N.S.V Rao, G. Racherla, C.N. Sekharan, S.G. Batsell, *DST—A routing protocol for ad hoc networks using distributed spanning trees*, in: IEEE Wireless Communications and Networking Conference, New Orleans, 1999.

Space Craft Power System Implementation using Neural Network

Savithra B.¹, Ajay M. P.²

¹(Masters in VLSI Design, Sri Shakthi Institute of Engineering and Technology, India)

²(Department of Electronics and Communication Engineering, Sri Shakthi Institute of Engineering and Technology, India)

ABSTRACT: The usage of renewable source of energy is increasing in recent days. This is widely used in the spacecrafts for the power system built there. The power system of a spacecraft can be simulated using artificial intelligence. Designing and implementing intelligent systems has become a crucial factor for the innovation and development of better products of space technologies. The artificial neural network is used in implementing non-linear problems. The weights for the neural networks are calculated using MATLAB-SIMULINK and the architecture of the design can be programmed in VHDL. The multilayer perceptron model is used for implementing the generator, controller and the battery. Back propagation algorithm is used in modeling this network since the error can be reduced significantly.

Keywords: Spacecraft, Artificial Neural Network, VHDL.

I. Introduction

A spacecraft is a vehicle, vessel or machine which is designed to fly in outer space. Spacecraft are used for a variety of purposes. Some applications in which spacecraft are used are communications, earth observation, meteorology, navigation, planetary exploration and transportation of humans and cargo. Spacecraft need an electrical power generation and distribution subsystem for powering the various spacecraft subsystems. The source for power available in the world nowadays are becoming very less. There are different technologies employed in power production. Photovoltaic are best known as a method for generating electric power by using solar cells to convert energy from the sun into a flow of electrons.

The Number of electronic applications using artificial neural network based solutions has increased considerably in the last few years. The main advantages of using ANN algorithms are simplifying the complicated algorithms, reducing heavy computation demands and improving fault tolerance.

The main objective is developing the photovoltaic simulator for the generating the power in the spacecraft. Several components are used in this simulation. An MLP(Multi-Layer Perceptron) is modeled for simulating each component of the system. After modeling an MLP the architecture of each component can be programmed using VHDL. The modeling of the MLP can be done with MATLAB-SIMULINK. The algorithm used in this modeling back-propagation which reduces the error significantly.

The paper is organized as follows: Section two gives the clear architecture of the system. Artificial Neural Network structure and the model is described briefly. Section four shows the implementation of the system. And section five gives the simulation results.

II. Architecture of the Power System

The block given in fig. 1 shows the complete architecture of the system. The components used in modeling this system are PV generator, Controller and a Battery. The PV generator is used to generate the current from the solar panel. This can be modeled with neural networks and the architecture of this generator can be programmed in VHDL. The battery is also modeled using MLP. The battery consists of accumulators. Each accumulator can deliver 2V.

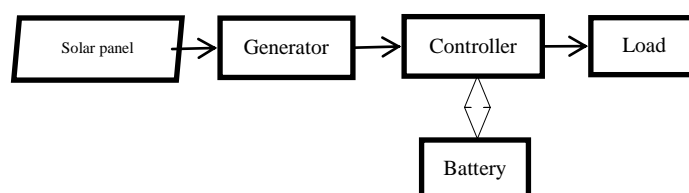


Figure 1 Block diagram of the power system

The controller modeling is also done with MLP. The controller is used to monitor the current generated by the generator module. The design of the controller[2] is shown in the fig. 2.

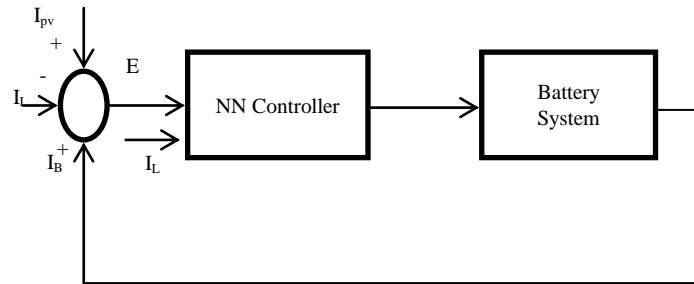


Figure 2 Block Diagram of the Controller

This controller is used in the power system of [1] instead of a regulator. Since the number of hidden layers and neurons in the controller is minimum the number of calculations can be reduced and the speed of the system will be improved.

III. Artificial Neural Networks

Artificial neural networks are information-processing systems that have the performance characteristics common to biological neurons. The neural network represents a network with a finite number of layers consisting of solitary elements that are similar to neurons with different types of connections between layers. The number of neurons in the layers is selected to be sufficient for the provision of the required problem solving quality. The number of layers is desired to be minimal in order to decrease the problem solving time. The structure of the neural network is shown in the fig. 3.

The weight updating is the major calculation in the neural networks. The neural network can be mathematically represented as given in the equation below.

$$y = f(y_j) \tag{1}$$

$$y_j = \sum_{i=1}^n x_i w_i + b \tag{2}$$

x_i is the input of the network. w_i is the weight co-efficient. b is the bias. y is the output of the neuron which is given by the $f(x)$. $f(x)$ is called the activation function. This activation function is a non-linear function that is widely used in feed-forward calculations of the algorithm.

$$f(y_j) = \frac{2}{(1+e^{-2y_j})-1} \tag{3}$$

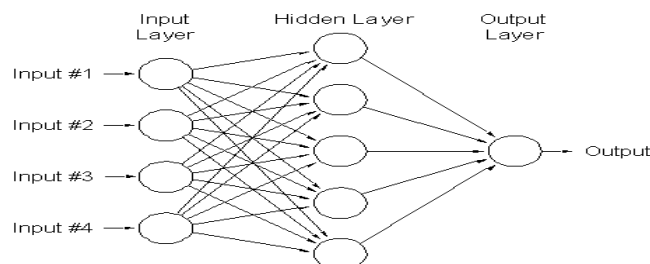


Figure 3 Neural Network Model

The main use of this neural network in the electronic applications is to reduce the error of the system. There are many algorithms designed for the implementation of the neural networks. The main algorithm that is widely used is the back-propagation algorithm which reduces the error significantly.

IV. Implementing the System

Generator: The PV generator can be designed with the artificial neural networks. The photovoltaic source from the solar panel is given to the generator. The input to the generator is solar radiation(H) and ambient temperature(T_a). The output of this will be voltage (V_{pv}) and current(I_{pv}).

Voltage and the current is the function of Temperature and radiation. It can be given by

$$V_{pv}, I_{pv} = f(T_a, H) \tag{4}$$

The neural network model for this contains an input layer, an output layer and two hidden layers. First hidden layer has seven neurons and second has nine neurons. The neural network model of the generator is given below with the inputs and outputs.

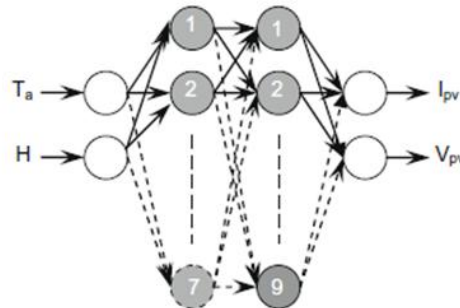


Figure 4 MLP Generator Model

Controller: the controller (Fig. 5 designing is the major part in the power system. Because it decides how the current generated from the solar panel should be utilized. The working of the controller will be disused briefly, before that the inputs for the controller is the error (E) and the load current (IL). The load current is the current value that is required by the system usage. That can be fixed manually.

The neural network model of controller is given below. This has a input layer, a output layer and a hidden layer with three neurons.

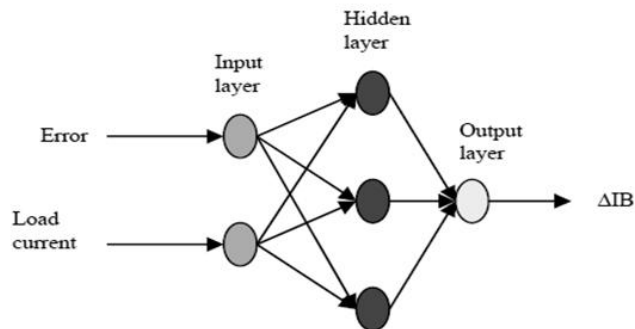


Figure 5 MLP Controller Model

The working of the controller is given in the fig. 6 as a flow chart.

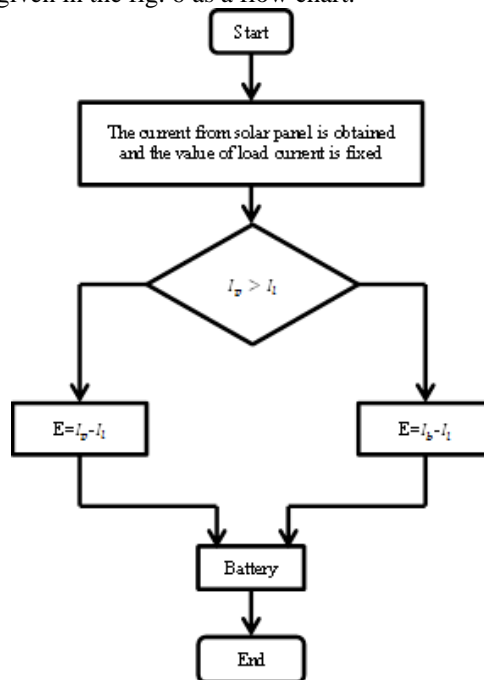


Figure 6 Flow chart of the working of controller

Battery: The battery is also designed with a multilayer neural network. The battery is used to store the excess current from the generator. The stored current can be further used in the eclipse time. The input data for the battery sub-system are the ambient temperature (T_a) the current coming from the regulator to battery (I_r). The output data is the battery voltage (V_b). The architecture of the battery consists of series of accumulators that can deliver 2V current.

The neural network design of the battery is given below in fig. 7.

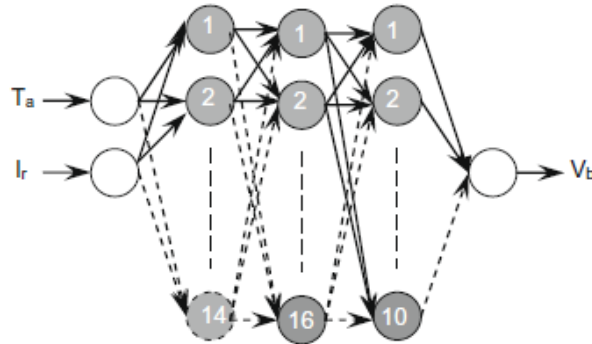


Fig. 7 MLP model of Battery

The design consists of an input layer, an output layer and three hidden layers. There are fourteen neurons in the first hidden layer, sixteen neurons in second hidden layer and ten neurons in second hidden layer.

I. RESULT

The ANN of each component is first modeled in the MATLAB-SIMULINK and the error of is calculated. The calculation of error is shown in the figure given below. This is the MATLAB command window with the calculations of error.

```

Command Window
0.0073

delk =
-0.0013

delw =
1.0e-04 *
0.7785
-0.4764
-0.0295
0.3071

delinj =
-0.0086
0.0079
0.0038
-0.0058

BPN for XOR function with bipolar input and output
Total epoch performed
1923

Error
0.0050

Final weight matrix and bias
fx >> |
    
```

Figure 8 Error and the weights calculated in MATLAB for ANN

So finally the weight matrix and the error can be calculated. Instead of calculating this each time the results can be saved in the .mat file which is the matrix file. That can be used further while programming the architecture of each component.

The architecture of each component is developed in MODELSIM. The simulation results are given below.

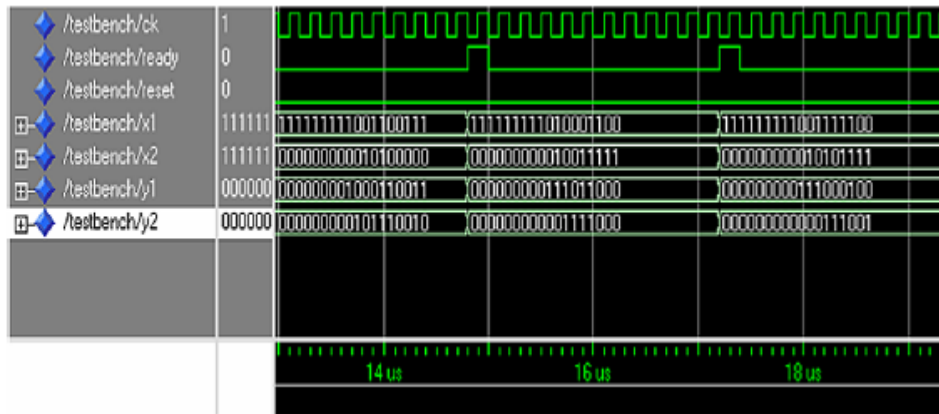


Figure 9 Simulation of MLP PV Generator in MODELSIM

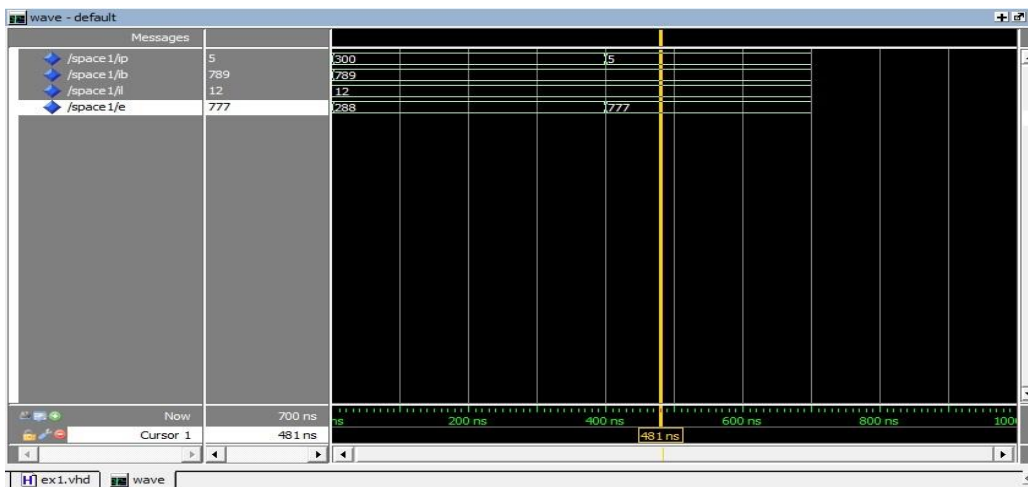


Fig. 10 Simulation of MLP Controller

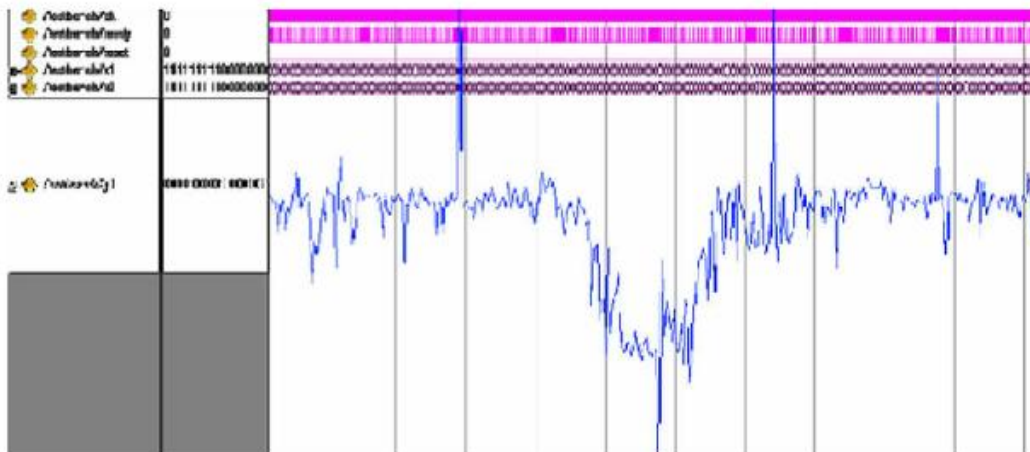


Fig. 11 Simulation of MLP PV Battery in MODELSIM

V. Conclusion

The simulation for a power system in spacecraft using neural networks is done. The advantage of using neural networks for this implementation is to improve the speed of the process and to solve the non-linear problems. A controller is first designed which decides how to utilize the current from the solar panel. The simulation of this architecture is done using ModelSim. The ANN's are simulated in MATLAB. The algorithm used for modeling the ANN is back propagation so the error can be minimum. The MATLAB is used for mathematical calculations and ModelSim for architecture development. The performance of this process can be

improved by reducing the number of hidden layers. Since the number of hidden layers increases the calculation increases which consumes more time. The utilization of solar power efficiently is the major part in this design. When the calculation speed increases the process of obtaining the current can also be improved. The suns movement varies in space often, so the power system speed must be improved.

References

- [1] Mellit, H. Mekki, A. Messai, H. Salhi, FPGA-based implementation of an intelligent simulator for stand-alone photovoltaic system, *Expert Systems with Applications* 37,2010
- [2] Hanaa T. El-Madany, Faten H. Fahmy, Ninet M. A. El-Rahman, and Hassen T. Dorrah., "Spacecraft Neural Network Control System Design using FPGA", World Academy of Science, Engineering and Technology, 2011.
- [3] Amos R. Omondi, and Jagath C. Rajapakse, "Power System Implementations of Neural Networks", Springer publisher, 2006.
- [4] H. Mekki, A. Mellit, H.Salhi, and B. Khaled, "Modeling and simulation of photovoltaic panel based on artificial neural networks and VHDL language", IEEE 2007.
- [5] Moufdi Hadjab, Smail Berrah and Hamza Abid, Neural network for modeling solar panel, *International Journal of Energy, Issue 1, Vol. 6, 2012.*
- [6] Hanaa T. El-Madany, Faten H. Fahmy, Ninet M. A. El-Rahman, and Hassen T. Dorrah., "Spacecraft Neural Network Control System Design using FPGA", World Academy of Science, Engineering and Technology, 2011.
- [7] Mehmet Tukek And Mustak Erhan Yalcin, "A New Architecture for Cellular Neural Network on Reconfigurable Hardware with an Advance Memory Allocation Method, in proc. of IEEE 2010 12th International Workshop on Cellular Nanoscale Networks and their Applications.

The Contribution of Solar Energy to Reduce Electricity Shortage in the Gaza Strip through Using Photovoltaic Panels as a Replacement to Roofing Tiles

Eng. Rafat Saikly¹, Dr. Aeman Aead², Prof. Dr. Samy Abu Naser³

¹Department of Engineering Profession, University College of Applied Sciences (UCAS),

²Department of Engineering, Faculty of Engineering & Information Technology, Al-Azhar University, Palestine

³Department of Information Technology, Faculty of Engineering & Information Technology, Al-Azhar University, Palestine

ABSTRACT: The Gaza Strip is suffering from a variety of problems due to the Israeli siege. Electricity shortage is one of the most profound problems causing regular power cuts with drastic effects on people's daily lives. The current electricity shortage reaches 48% of the required 400 MW demand. This study proposes a solution to this problem based on exploiting solar energy, which is highly available in the Gaza Strip, to overcome electricity shortage. Such solution would be suitable for an average household of five persons. From an economic perspective, there is a financial feasibility for replacing roofing tiles with photovoltaic panels. The savings of not using roofing tiles can be used to mount photovoltaic panels which in turn will have huge savings in cutting electricity bills. The overall aesthetic view of the house can also be improved.

Keywords: Electricity Shortage, Solar Energy, Energy consumption per Housing Unit, Photovoltaic Panels, Roofing Tile,

I. Introduction

In the uppermost position the variable floor becomes not only powerful security system for your pool, but also a part of the original courtyard that surrounds it. This is owed to the region of pool becoming entirely covered and inaccessible.

Renewable energy is the focus of attention of governments and researchers in the world due to many reasons, the most important one is the environmental damage resulting from the emission of harmful gases and global warming and the rising in temperature of the earth to have a negative impact on both humans and the environment.

For Palestine in general and Gaza in particular, the government and institutions must be thinking in the exploitation of these resources and the support of all related projects. Gaza Strip especially has two main sources available, they are the sun and the wind, that can be utilized in the production of electrical energy, which Gaza Strip is suffering from the shortages of it due to the siege imposed on it for a number of years. Because the production of large amounts of alternative energy, whether from the sun require large tracts of land and this is what is not available within the eligible populated regions, and there is an urgent need to supply the buildings with energy produced from renewable sources. All eyes of the world are directed toward benefiting from the rooftops either tiled or flat in energy production because of the many benefits it has, the most important of them the getting rid of the large electrical losses in the supply of housing units.

1.1 Research Objectives

The objectives of this research paper are to show that:

- alternative energy sources available in the Gaza Strip.
- how contribution of alternative energy can help in covering the deficit of energy in Gaza Strip
- how exploiting space rooftops in putting together alternative energy systems
- how the feasibility of replacing tiled roofs with Photovoltaic Panels

1.2 Total energy consumption in the Gaza Strip and the existing deficit

According to the statistics of the United Nations technical office for coordination of humanitarian affairs for the month of March 2012, as described in the figure 1, the total electric power fed to Gaza Strip is 217MW, while the energy consumption required for it is 359MW, a total deficit of 36.6% [1].

Adding to the crisis, the blockade imposed on the Gaza Strip since 2006, made it impossible to provide this much energy at the moment, so it imposes the deficit on the company of distributing electricity in the Gaza Strip and for years the company re-distribute the electrical loads available according to a specific timetable to all districts and provinces of Gaza Strip.

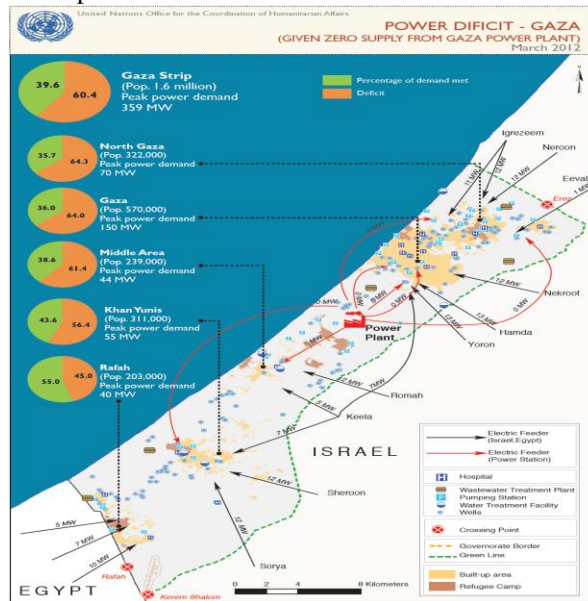


Figure 1: The distribution of available energy to the provinces in Gaza Strip. [2]

II. The Most Important Alternative Energy Sources Are Available In The Gaza Strip

Palestine in general and Gaza Strip in particular is not considered rich area of natural energy resources such as oil or natural gas only in very limited quantities barely cover the costs of extraction it, so moving attention to alternative energy or renewable sources, and there are many sources in Gaza Strip, including:

- **Solar energy**

Can be used in two ways:

- a. Photovoltaic: The generation of electricity through solar PV cells which are the cleanest types of energy and the most important.
- b. Solarthermie: The water heating by the sun is one of the oldest methods for the production of thermal energy and the most widespread in the world.

- **Wind energy**

This energy can be utilized in a positive way in the current era in electric power generation, based on wind speed.

- **Bio energy**

It can be produced from agricultural and animal waste.

2.1 How to take advantage of alternative energy sources to cover the deficit in the electric power in Gaza Strip

In recent years, high-raised buildings in the Gaza Strip had spread in line with the sharp increase in population; the consumption of electrical energy in these buildings is huge due to the high content of residential units, each consisting of an average of five members. What distinguishes these buildings in Gaza Strip that large tracts surfaces and most owners of these buildings prefer the tiled work surfaces in the last floor.

The following is a detailed study of the needs of residential units consisting of five members and the amount of consumption of energy and the necessary calculations for the solar photovoltage able to cover the needs of the housing unit.

2.2. Average daily requirement for the housing unit that consists of five members:

Based on the above, high-raised buildings in Gaza Strip consist of multiple residential units; each housing unit is composed of an average of five members [3].

The following table shows an example of a realistic amount of electric power consumed by such residential units per day, also illustrates the types of devices most commonly used in Gaza Strip, as well as the average number of working hours of each device and its consumption.

Table 1: Average daily consumption of energy for a housing unit that consists of five members

S.	Devices	Number of devices	Working hours	Consumption [W]	Total consumption [Wh]
1	Refrigerator	1	24	65	1560
2	PC	1	4	100	400
3	Fan	2	4	85	680
4	Television	1	5	120	600
5	Lighting PL	5	6	20	600
6	Water pump	1	1	1000	1000
7	Washer	1	2	1000	2000
8	Water Heater	1	2	1200	2400
9	Microwave	1	0.5	1000	500
Total daily consumption [Wh / day]					9740

The above table shows that the average daily consumption of a residential unit consisting of five members up to about 10KWh/day within 24 hours.

III. Utilization Of Solar Energy

To cover the consumption of a housing unit which is composed of five members, as shown in the table above is 10KW. In this research, a study of the possibility of making use of solar energy that can be provided in appropriate cost with local efforts in Gaza Strip.

The number of hours of solar radiation is linked directly to that of solar energy can be produced throughout the day or throughout the year. Figure 2 shows that the hours of solar radiation in Gaza Strip up to 8 hours per day [4] as an annual rate. This is the number of hours among the highest in the world, which confirms the feasibility of the use of solar photovoltaage in the production of alternative electrical energy in Gaza Strip.

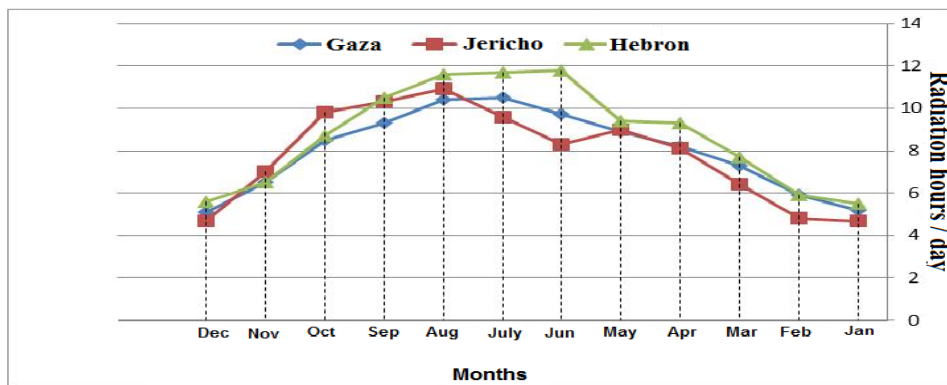


Figure 2: Average hours of solar radiation of Gaza city compared with Hebron and Jericho by months of the year 2007

From the above data, the average number of hours of solar radiation to Gaza City is clear that the rate is 8 hours per day throughout the year, after taking into account the peak hours of sunlight as the higher efficiency of solar cells and the gradual decrease in the efficiency with changing the angle of sunshine from hour to another, and the consequent weakness of the productive capacity of solar cells must take into account the angle of orientation of solar cells by sun preference in the four seasons of the year, while in the case of cells

moving on one axis is considered to change the orientation of cells depending on the movement of the sun is definitely better in terms of productivity about 30 % [6] .

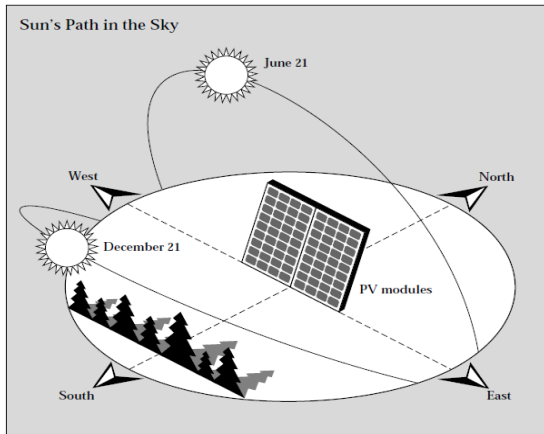


Figure 3. The sun's noontime height above the horizon changes seasonally. This is important to consider when sitting and positioning a PV array [7].

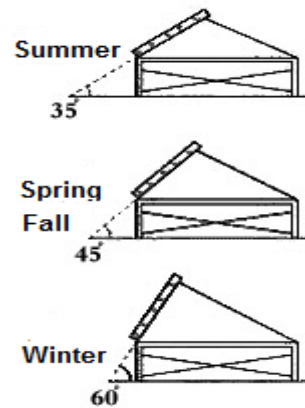


Figure 4. Angles installing solar cells to Gaza City by the four seasons of the year

According to figure 3 and figure 4 above and in order to avoid the high costs associated with movable cells, this study has focused only on fixed angle solar cells of 45o to make the most of solar radiation throughout the year, so to take advantage of daily solar radiation in Gaza. The real rate of the number of hours is about 6.5.

3.1 Installing solar cells on the roofs of building

As for the installation of solar cells on the roofs of buildings, there are two ways, either the traditional way, as shown in the figure 5a over tiled surfaces, or Figure 5b over high-rise buildings 45o angle in the direction of the south.



Figure 5b: Above the high-rise buildings



Figure 5a: Above tiled rooftops

3.2 Replacing tiled surfaces with solar panels

In this research a study of replacing tiled surfaces with solar panels was done in order to preserve the environment on one hand and the other hand to exploit the space available on the roofs of buildings in generating alternative energy from the sun. The aims of the researchers are to study the possibility of really utilizing these tiled surfaces, and to replace them with solar panels to be able to produce alternative energy to cover the deficit of these buildings.



Figure 4: Replacing tiled roofs with solar panels.

In terms of economic, aesthetic and construction, the replacement process is strong and weatherproof leaking water or heat of the sun into the building , except for the obvious exploitation of the surfaces in the production of electrical energy from sunlight.

3.3 The following are the advantages and disadvantages of replacing the tiled surfaces with solar panels

Advantages of surfaces consisting of solar panels compared to tile:

- Taking advantage of the surface area in the production of energy
- More beautiful than the tiled surfaces
- Does not require constant maintenance
- Considered more stable than the tiled, especially in the storm atmosphere
- More weatherproof than tiled

Disadvantages of surfaces consisting of solar panels compared to the tiled

- Increased losses in the production of energy in the case of high temperature under the solar panels
- Cost of tiled surfaces is less expensive than surfaces equipped with solar panels

In the event of replacing tiled surfaces with solar panels, there is a clear saving in term of the cost of the material associated with installing tiles, and a major benefit of solar photovoltage when generating electricity .

IV. Model Of Solar Photo voltage System Needed To Cover Housing Units Consisting Of Five Members

Due to the lack of available space above residential buildings, solar cells of the type (Mono crystalline) were selected because of their high efficiency of energy production with the least possible space compared to other solar cells [5,10]. Engineering calculations for a housing unit that consists of five members in Gaza City has been made on the basis of the following facts:

Table 2: Engineering data model for solar photovoltage system to cover the need of housing units consisting of five members of the electric power

The necessary data	Units
The daily energy consumption of the residential unit	10KW
The average daily number of hours of solar radiation	8 according to the source, 6.5 with high efficiency
Type of solar cells used	Mono crystalline, 270Wp
The dimensions of the cell length X width X thickness in centimeters	150X100X8 cm
Searing angle of solar panels	South with an of angle 45 ^o
Voltage needed to run electrical appliances	220V
Used batteries	12V/195Ah
Total electrical losses (by the efficiency of the system)	%20
The surface area of the building available	150m ²

The total daily energy = energy needed for residential unit + total loss of the electrical system
= 10KW + 20% * (10kW)
= 12KWh/day

Total daily Amp required per hour
= 12KWh / 12V
= 1000 Ah / day

The number of batteries needed to cover daily energy storage = total daily Amp necessary / Amp per hour battery.
= 1000 Ah / 195 Ah
= 5.12 batteries, taking into account the loss 6 batteries would be required.

Energy to be produced by the average daily hours of solar radiation = total power / average daily hours of solar radiation
 = 10KW / 6.5 hours
 = 1.55KWp

The number of solar panels required to cover the necessary energy = energy to be produced / energy of solar panels.

= 1.55KWp / 270Wp
 = 5.75 solar panels, taking into account the losses, 6 solar panels would be required.

The space required for a number of solar panels = number of solar panels * length of panel * width of the panel
 = 6 * 1.5m * 1m
 = 9 m²

The engineering calculations above show that the housing unit consisting of five members, which need about 10KW of energy per day requires 6 batteries, 6 solar panels, and a total area of approximately 9 m².

V. Economic Feasibility Of Replacing Tile Surfaces With Solar Panels

The following figure (see Figure 6) shows the continued decline in the price of solar panels over the past years [8], with an estimated price of 1 \$ / W, this means that the price of solar photovoltaic system for residential unit consisting of five members up to \$10,000.U.S.

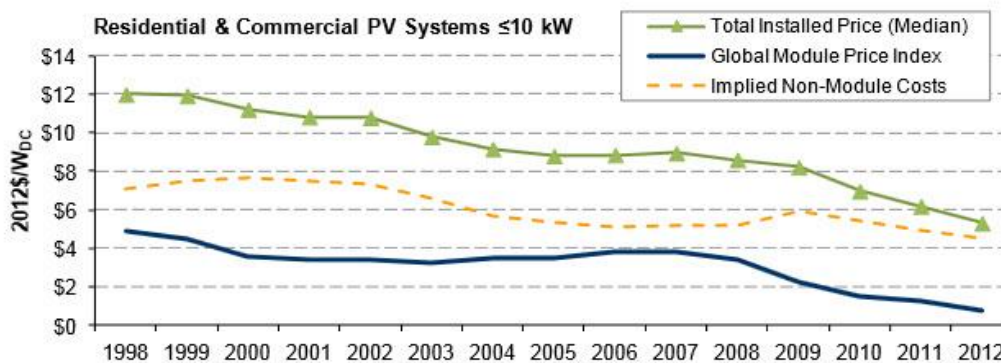


Figure 6: The cost of solar photovoltaic systems over the past years

It is known that the life span of the solar photovoltaic system is 25 years [9], that is, the total cost of the system must be fully distributed to the life span and in addition to the cost of regular maintenance.

5.1 Solar photovoltaic system without tiles (tiles replacement)

The total cost (25 year) = total cost of the solar photovoltaic system + the cost of regular maintenance
 = \$ 10,000 + 1000 dollars
 = \$ 11,000

5.2 TILED ROOFS WITHOUT SOLAR PHOTOVOLTAIC SYSTEM

The total cost (25 years) = consumption of the residential unit energy cost + 9m² of tiles
 = (10KW * 0.5 * NIS 365 Days * 25 years) + (9 m² * 48 shekels)
 = 45,625 shekels + 432 NIS
 = 46057 NIS
 = 13,159 US dollars

Total difference = 13,159 - 11,000 = 2,159 dollars

The above comparison shows that the replacement of tiled surfaces with solar photovoltaic system for a time frame of 25 years is better economically as a total amount of 2159 dollars, according to current prices for energy systems.

VI. Results And Recommendations

Due to the importance of the topic in general and to Palestine in particular, we recommend the followings:

- Invitation to exploit the roofs of high-rise buildings in the production of electrical energy from solar photo voltage system
- Support projects aimed at replacing the tiled roofs with solar panels.
- The state should contribute in alternative energy projects
- Exempt projects related to alternative energy from tax
- Buy surplus of the needs of citizens by linking it to the electricity network

VII. Conclusion

This study proposed a solution to the problem of electricity shortage in Gaza Strip due to the Israeli siege imposed on Gaza Strip. The solution is based on exploiting solar energy, which is highly available in the Gaza Strip, to overcome electricity shortage. Such solution would be suitable for an average household of five persons. From an economic perspective, there is a financial feasibility for replacing roofing tiles with photovoltaic panels. The savings of not using roofing tiles can be used to mount photovoltaic panels which in turn will have huge savings in cutting electricity bills. The overall aesthetic view of the house can also be improved.

REFERENCES

- [1] Gaza Electricity Distribution Company, the month of April of the year 2013, Gaza, Palestine.
- [2] The Humanitarian Impact Of Gaza's Electricity And Fuel Crisis, United Nations, March 2013
- [3] Central Bureau of Statistics, Expenditure and Consumption of Family Survey report, September 2011.
- [4] Central Bureau of Statistics, climatic conditions in the Palestinian territories, Annual Report 2007.
- [5] Solar energy, an invitation to exploit them before it is too late, Philadelphia cultural, Philadelphia University – Jordan, 2013.
- [6] Renewable energy, renewable energy technologies German success story , the German Energy Agency DENA, 2013.
- [7] Photovoltaics: Basic Design Principles and Components, March 1997.
- [8] <http://www.smartplanet.com/blog/bulletin/chart-of-the-day-sliding-us-solar-prices>, Date visited 20-11-2013.
- [9] Renewable Energy Solutions, Solar photovoltaic electricity system, 1. General Information, 2011.
- [10] <http://encyclobeamia.solarbotics.net/articles/photovoltaic.html> . Encyclobeamia.solarbotics.net. Date visited 22-11-2013.

A Review Paper On Effect Of Varying Welding Heat Inputs On Microstructure, Mechanical Properties And Corrosion Behaviors Of Ferritic Stainless Steel & Mild Steel

Mayank A. Gaodi¹, Prof. D. I. Sangotra²

¹(Department of Mechanical Engineering, YCCE Nagpur, RTMNU, Nagpur India)

²(Department of Mechanical Engineering, YCCE Nagpur, RTMNU, Nagpur India)

ABSTRACT: This paper focuses on analysis of varying welding heat inputs on material properties by different authors. The influence of welding process parameters such as welding current, travel speed and voltage on material properties has been identified. Ferritic Stainless Steel is a new grade of steel produced by Steel Authority Of India Limited. The use of FSS has been increased noticeably in building up of railway wagons, which were priorly built by Mild Steels. Ferritic Stainless Steel's amazing strength-to-weight ratio makes wagons lighter by 40 per cent yet, keeps them strong enough to take on 12 per cent more payload. As a result, trains travel faster, consume less fuel and increase efficiencies. This review tries to conclude the effects of variation in heat input on mechanical properties as well as microstructural properties of the welds.

Keywords: Bead on plate, FSS, heat inputs, SMAW

I. INTRODUCTION

Welding, the fusing of the surfaces of two workpieces to form one, is a precise, reliable, cost-effective, and "high-tech" method for joining materials. No other technique is as widely used by manufacturers to join metals and alloys efficiently and to add value to their products. Most of the familiar objects in modern society, from buildings and bridges, to vehicles, computers, and medical devices, could not be produced without the use of welding. Welding goes well beyond the bounds of its simple description. Welding today is applied to a wide variety of materials and products, using such advanced technologies as lasers and plasma arcs. The future of welding holds even greater promise as methods are devised for joining dissimilar and non-metallic materials, and for creating products of innovative shapes and designs.

1.1 Heat inputs:

Fundamental to the study of welding is the study of heat-flow. In welding, the application of a heat source is called energy input. It is defined as the quantity of energy introduced per unit length of weld from a traveling heat source. The energy input (heat input) is expressed in joules per meter or millimeter. This important measure is calculated as the ratio of total input power in Watts to its velocity:

$$H = fEI / V$$

Where:

f = heat transfer efficiency

E = volts

I = amperes

V = Travel velocity of heat source (mm/sec)

1.2 Shielded Metal Arc Welding:

Shielded metal arc welding (SMAW) is a manual arc welding process that uses a consumable electrode coated in flux to lay the weld. An electric current, in the form of either alternating current or direct current from a welding power supply, is used to form an electric arc between the electrode and the metals to be joined. As the weld is laid, the flux coating of the electrode disintegrates, giving off vapors that serve as a shielding gas and providing a layer of slag, both of which protect the weld area from atmospheric contamination. Because of the versatility of the process and the simplicity of its equipment and operation,

shielded metal arc welding is one of the world's most popular welding processes. It dominates other welding processes in the maintenance and repair industry.

1.3Bead on plate welding:

A bead weld or weld bead is the result of a welding pass that deposits filler material. Welding is a process that combines multiple pieces of metal by heating and softening them. With bead welding, a filler material is inserted in the space between the two materials. When the metal filler material cools, a strong bond is formed between the two surfaces.

1.4Ferritic Stainless Steel:

Ferritic stainless steel (FSS) with 12 wt% Cr developed to fill the gap between stainless steels and the rust prone carbon steels has been attracted as low cost utility stainless steels. They are now commonly used in the coal mining industry for bulk transport of coal and gold, for cane and beet sugar processing equipment, road and rail transport, power generation, petrochemical, pulp and paper industries etc. In fact, the use of these steels in the past few years has been increased markedly with their successful applications in passenger vehicles, coaches, buses, trucks, freight and passenger wagons.

1.5Mild Steel:

Mild steel is the least expensive of all steel and the most common steel used. Used in nearly every type of product created from steel, it is weldable, very hard and, although it easily rusts, very durable. Containing a maximum of 0.29% carbon, this type of steel is able to be magnetized and used in almost any project that requires a vast amount of metal. Its structural strength prevents it from being used to create load-bearing girders and structural beams.

II. LITERATURE REVIEW

M V Venkatesan, N Murugan, B M Prasad, A Manickavasagam [1] discussed the influence of flux cored arc welding (FCAW) process parameters such as welding current, travel speed, voltage and CO₂ shielding gas flow rate on bowing distortion of 409M ferritic stainless steel sheets of 2 mm in thickness. The bowing distortions of the welded plates were measured using a simple device called profile tracer. An experimental regression equation was developed to predict the bowing distortion and with this equation, it is easy to select optimized process parameters to achieve minimum bowing distortion. It is revealed that the FCAW process parameters have significant influence on bead profile and the bowing distortion.

E. Taban, E. Deleu, A. Dhooge, E. Kaluc [2] presented microstructural and toughness properties and mechanical properties of gas metal arc welded 6 mm thick modified X2CrNi12 stainless steel with two different heat inputs. According to results, grain size has dominant effect on impact toughness. Grain coarsening has no adverse influence either on tensile properties or on bend properties but the heat affected zone impact toughness for sub-zero temperatures generally decreases and this depends on the amount of grain coarsened microstructures and eventual precipitates present.

P. Kanjilal, T.K. Pal, S.K. Majumdar [3] developed a rotatable designs based on statistical experiments for mixtures to predict the combined effect of flux mixture and welding parameters on submerged arc weld metal chemical composition and mechanical properties. Bead-on-plate weld deposits on low carbon steel plates were made at different flux composition and welding parameter combinations. The results show that flux mixture related variables based on individual flux ingredients and welding parameters have individual as well as interaction effects on responses, viz. weld metal chemical composition and mechanical properties.

P.K. Palani, N. Murugan [4] investigated the effect of cladding parameters such as welding current, welding speed, and nozzle-to-plate distance on the weld bead geometry. The experiments were conducted for 317L flux cored stainless steel wire of size 1.2 mm diameter with IS:2062 structural steel as a base plate. Sensitivity analysis was performed to identify the process parameters exerting the most influence on the bead geometry and to know the parameters that must be most carefully controlled. Studies reveal that a change in process parameters affects the bead width, dilution, area of penetration, and coefficient of internal shape more strongly than it affects the penetration, reinforcement, and coefficient of external shape.

V.M. Sánchez-Cabrera, C. Rubio-González [5] performed welding with two alternative ways, preheating the welded parts and using similar filler material or using an austenitic stainless steel filler metal without preheating. This research work consists in identifying and comparing, for these two alternatives, the effect on microstructure, fracture toughness and fatigue crack growth rate of the welded joint. On the first alternative, using a GMAW welding process and similar filler metal, the variable is preheating temperature, with the purpose of minimizing internal residual stresses and the level of diffusible hydrogen. On the second

alternative, also using a GMAW welding process and austenitic stainless steel filler metal (greater hydrogen solubility), the variable is hydrogen concentration in the argon shielding gas with the purpose of diffusing hydrogen to the heat affected zone. The results indicate how the thermal cycle, different hydrogen levels and hydrogen trapping sites affect the mechanical properties.

A K Lakshminarayanan , V Balasubramanian [6] investigated The microstructure analysis and mechanical properties evaluation of laser beam welded AISI 409M ferritic stainless steel joints. Single pass autogeneous welds free of volumetric defects were produced at a welding speed of 3000 mm/min. The joints were subjected to optical microscope, scanning electron fractography , microhardness , transverse and longitudinal tensile, bend and charpy impact toughness testing. The coarse ferrite grains in the base metal were changed into dendritic grains as a result of rapid solidification of laser beam welds. Tensile testing indicates overmatching of the weld metal is relative to the base metal. The joints also exhibited acceptable impact toughness and bend strength properties.

M. Mukherjee and T.K. Pal [7] described The effect of heat input on martensite formation and impact properties of gas metal arc welded modified ferritic stainless steel (409M) sheets (as received) with thickness of 4 mm. The welded joints were prepared under three heat input conditions, i.e: 0.4, 0.5 and 0.6 kJ/mm using two different austenitic filler wires (308L and 316L) and shielding gas composition of Ar + 5% CO₂. The welded joints were evaluated by microstructure and charpy impact toughness. The dependence of weld metal microstructure on heat input and filler wires were determined by dilution calculation, Cr/Ni ratio, stacking fault energy (SFE), optical microscopy (OM) and transmission electron microscopy (TEM). It was observed that the microstructure as well as impact property of weld metal was significantly affected by the heat input and filler wire. Weld metals prepared by high heat input exhibited higher amount of martensite laths and toughness compared with those prepared by medium and low heat inputs, which was true for both the filler wires. Furthermore, 308L weld metals in general provided higher amount of martensite laths and toughness than 316L weld metals.

Jerzy Nowacki, Paweł Rybicki [8] determined The influence of the heat input submerged arc welding (SAW) of duplex steel UNS S31803 on kind and quantity of welded butt joints defects. Analysis of welding heat input influence on mechanical properties of test joints using heat input from 2.5 to 4.0 kJ/mm. For analysis of welding heat input influence on creation of welding imperfections, there were executed welding of sheet of thickness 10–32mm using two ranges of the welding heat input: up to 2.5 and up to 3 kJ/mm. It was shown that submerged arc welding of duplex steel with the heat input from 2.5 up to 4.0 kJ/mm has no negative influence on mechanical properties of the joints. Experiment showed, that welding with heat input up to 3.0 kJ/mm reduces welding defects of joints, e.g. slags, lack of a joint penetration for plates of thickness of 10–23 mm, as well as sticks, cracks, and the thoroughly decrease of other defects existence. Usage of larger welding heat input provides the best joints quality.

M Yousefieh, M Shamanian, A Saatchi [9] studied the effect of heat input variations on the microstructure and corrosion resistance of a DSS UNS S32760 in artificial sea water media. The corrosion resistance in 3.5% of NaCl solution was evaluated by potentiostatic polarization tests at room temperature. It is found that the presence of sigma phase and Cr₂N decreases the corrosion potential. The specimen with heat input of approximately 0.95 kJ/mm have the best corrosion characteristics, which is the result for the lack of deleterious phases such as sigma and Cr₂N and balanced ferrite-austenite proportion.

Huaipei Zheng, Xiaoning, Laizhu Jiang, Baosen Wang, Zhenyu Liu, Guodong Wang [10] investigated the corresponding microstructures in HTHAZ with different chemical compositions and heat inputs through thermal simulation tests. There are several primary conclusions: (1) When ferrite factor (FF) is above 9.0, the microstructure in HTHAZ is fully ferrite or a small amount of martensite net likely distributing along delta ferrite grain boundaries. On the other hand, if FF is below 9.0, the martensite content increases with the decreasing of FF. (2) Heat input influences the microstructure of high FF steel in HTHAZ. The martensite content and its distribution of low FF steel are not sensitive to heat inputs, but the grain size grows up with the increase of heat inputs. (3) The coarse Ti-rich particles in low FF steels containing Ti can promote intragranular austenite formation inside delta ferrite resulting in packet morphology of martensite.

M.O.H. Amuda [11] investigated the effects by producing the welds on a 1.5mm thick plate of 16 wt% Cr FSS conforming to AISI 430 commercial grade, using TIG torch in argon environment at a heat flux between 1008W to 1584W and speed between 2.5mm/s and 3.5mm/s. The width of the sensitization zone increases with increasing the heat input. The depth of the sensitization zone in the thickness direction is insignificant and it is generally within one half of a millimetre. The use of heat input greater than 432J/mm increases the development of sensitized regions. This level of heat input corresponds to heat fluxes in the range 1008-1296W and welding speed between 3mm/s and 3.5mm/s. Under this condition the average cooling time is about 10s. Most grain attack is restricted to the ferrite-ferrite grain boundaries. The ferrite martensite boundaries do not show visible attack. This indicates that welding condition that promotes the formation of martensite in the HAZ is ideal for the presentation of sensitization.

J. Pekkarinen [12] focused to determine empirically, which microstructural changes occur in ferritic and duplex stainless steel when heat input is controlled by welding parameters. They concluded that microstructure of ferritic stainless steel grade 1.4003 is fully martensitic in all welding parameters combination used. Hardness of martensite structure is dependent on heat input, increasing heat input decreasing the hardness. In duplex stainless steels microstructure is very much dependent on cooling rate. Ferrite content is decreasing with increasing heat input and the microstructure is however dependant also on composition and therefore the suitable welding parameters must be adjusted for each steel grade separately.

Bipin Kumar Srivastav, S.P. Tewari [13] studied the effect of arc welding parameters on quality of welds and concluded that several process control parameters in SAW influence bead geometry, microstructure as well as weld chemistry. Their combined effect is reflected on the mechanical properties of the weld in terms of the weld quality as well as joint performance. The selection of the suitable process parameters are the primary means by which acceptable heat affected zone properties, optimized bead geometry and minimum residual stresses are created. The mechanical properties of the weld are influenced by the composition of the base metal and to a large extent by the weld bead geometry and shape relationship as well. It observed that with increase in electrode stick out, hardness of the weldment increases, yield strength and impact value decreases, ultimate tensile strength of the joint initially decreases but thereafter increases provided welding current and voltage arc kept at a constant level. The function of the flux ingredients such as CaO, MgO, CaF₂ and Al₂O₃ in submerged arc welding studied and concluded that among the flux ingredients, MgO appears to be important on its own in influencing the mechanical properties.

Eslam Ranjibamode [14] studied the microstructural characteristics of tungsten inert gas (TIG) welded AISI 409 ferritic stainless steel and effect of the welding parameters on grain size local mis-orientation and low angle grain boundaries was investigated. It concluded that the welding plastic strain is an increasing factor for local misorientation and low angle grain boundaries. It shows that the final state of strain is the result of the competition between welding plastic strains and stress relieving from recrystallization.

M.O.H Amuda and S. Mridha [15] reports the microstructural features of FSS welds produced under different heat input rates along with the governing parameters of welding like travel speed, welding current and material properties and investigated that irrespective of the welding condition, the primary solidification structure changed from a predominantly ferritic structure to a matrix interspersed with increasing fraction of inter dendritic martensite in the weld metal grain boundary martensite in the heat affected zone. This implies that below the critical welding current value, the mechanical properties of ferritic steel weld might be influenced by both welding current and speed.

III. CONCLUSION

1. Excessive welding speed can exacerbate sensitization during low heat input welding.
2. Welding conditions that promotes the formation of martensite in the HAZ can be ideal for the prevention of sensitization.
3. Variation in heat input resulted in significant changes in the mechanical properties of the weld.

IV. ACKNOWLEDGEMENTS

I wish to express my gratitude to Prof. D. I. Sangotra for valuable discussions and guidelines concerning the manuscript.

REFERENCES

- [1] M V Venkatesan, N Murugan, B M Prasad, A Manickavasagam, "Influence of FCA Welding Process Parameters on Distortion of 409M Stainless Steel for Rail Coach Building", *JOURNAL OF IRON AND STEEL RESEARCH, INTERNATIONAL*. 2013, 20(1): 71-78
- [2] E. Taban, E. Deleu, A. Dhooge, E. Kaluc, "Gas metal arc welding of modified X2CrNi12 ferritic stainless steel" *Kovove Mater.* 45 2007 67-74
- [3] P. Kanjilal, T.K. Pal, S.K. Majumdar, "Combined effect of flux and welding parameters on chemical composition and mechanical properties of submerged arc weld metal", *Journal of Materials Processing Technology* 171 (2006) 223-231.
- [4] P.K. Palani, N. Murugan, "Sensitivity Analysis for Process Parameters in Cladding of Stainless Steel by Flux Cored Arc Welding", *Journal of Manufacturing Processes* Vol. 8/No. 2,2006
- [5] V.M. Sánchez-Cabrera, C. Rubio-González, "Effect of preheating temperature and filler metal type on the microstructure, fracture toughness and fatigue crack growth of stainless steel welded joints", *Materials Science and Engineering A* 452-453 (2007) 235-243
- [6] A K Lakshminarayanan, V Balasubramanian, "Evaluation of Microstructure and Mechanical Properties of Laser Beam Welded AISI 409M Grade Ferritic Stainless Steel", *JOURNAL OF IRON AND STEEL RESEARCH, INTERNATIONAL*. 2012, 19(1): 72-78

- [7] M. Mukherjee and T.K. Pal, " Influence of Heat Input on Martensite Formation and Impact Property of Ferritic-Austenitic Dissimilar Weld Metals", J. Mater. Sci. Technol., 2012, 28(4), 343{352.
- [8] Jerzy Nowacki, Paweł Rybicki, " The influence of welding heat input on submerged arc welded duplex steel joints imperfections", Journal of Materials Processing Technology 164–165 (2005) 1082–1088
- [9] M Yousefieh, M Shamanian, A Saatchi, "Influence of Heat Input in Pulsed Current GTXW Process on Microstructure and Corrosion Resistance of Duplex Stainless Steel Welds", JOURNAL OF IRON AND STEEL RESEARCH, INTERNATIONAL., 2011, 18(9): 65-69, 78
- [10] Huabei Zheng, Xiaoning, Laizhu Jiang, Baosen Wang, Zhenyu Liu, Guodong Wang, " Study on microstructure of low carbon 12% chromium stainless steel in high temperature heat-affected zone", Materials and Design 31 (2010) 4836–484
- [11] M.O.H. Amuda, "Analysis of Sensitization Profile in Medium Chromium Ferritic Stainless Steel (FSS) Welds", International Journal of Integrated Engineering, Vol. 3 No. 1 (2011) p. 17-22
- [12] J. Pekkarinen, V. Kujanpää, 2010. The effects of laser welding parameters on the microstructure of ferritic and duplex stainless steels weld. Elsevier B.V. p.517-523.
- [13] Bipin Kumar Srivastava; S.P. Tewari, Jyoti Prakash. 2010. A review on effect of arc welding parameters on mechanical behaviour of ferrous metals/alloys. International Journal of Engineering science and Technology; Vol.2 (5), p1425-1432
- [14] Eslam Ranjbar Nodeh, 2010. Investigation of the Effect of Welding Parameters on HAZ of AISI409 Using EBSD. Journal of Material Science Vol.2, No. 1, 46-53
- [15] M.O.H. Amuda and S. Mridha. 2009. Microstructural features of AISI 430 ferritic stainless steel (fss) weld produced under varying process parameters. International Journal of Mechanical and Materials Engineering. p.160-166.

A Robust Watermarking Technique Based On Dwt on Digital Images

B. Mohan Swaroop, Assistant Professor,
Potti Sriramulu Chalavadi Mallikharjunarao College of Engg & Tech

ABSTRACT: In this paper a robust watermark scheme for copyright protection is proposed. By modifying the original image in transform domain and embedding a watermark in the difference values between the original image and its reference image, the proposed scheme overcomes the weak robustness problem of embedding a watermark in the spatial domain. Besides the watermark extraction does not require the original image so it is more practical in real application. The experimental results show that the proposed scheme provides not only good image quality, but also robust against various attacks such as compression and noise addition.

Many image transforms have been considered and the most prominent among them is the discrete cosine transform (DCT) which has also been favored in the early image and coding standards. Hence, there is a large number of watermarking algorithms that use either a block based or global DCT. But the disadvantage in DCT is that it has only frequency resolution and no time resolution.

A new multi resolution watermarking method for digital images has been introduced. Wavelets are mathematical functions that cut the data into different frequency components and then study each component with a resolution matched to its scale. The method is based on the discrete wavelet transform (DWT). Pseudo-random codes are added to the large coefficients at the high and middle frequency bands of the DWT of an image. It is more robust to proposed methods to some common image distortions, such as image compression, image rescaling/stretching.

Keywords: Digital Watermarking, Discrete wavelet transform, Information security, Encryption, Steganography.

I. INTRODUCTION

A great deal of information is now being created, stored, and distributed in digital form. Newspapers, and magazines, for example, have gone online to provide real-time coverage of stories with high-quality audio, still images, and even video sequences. The growth in use of public networks such as the Internet has further fueled the online presence of publishers by providing a quick and inexpensive way to distribute their work. The explosive growth of digital media is not limited to news organizations, however. Commercial music may be purchased and downloaded off of the Internet, stock photography vendors digitize and sell photographs in electronic form, and Digital Versatile Disc (DVD) systems provide movies with clear images and CD quality sound.

Unfortunately, media stored in digital form are vulnerable in a number of ways. First of all, digital media may be simply copied and redistributed, either legally or illegally, at low cost and with no loss of information. In addition, today's fast computers allow digital media to be easily manipulated, so it is possible to incorporate portions of a digital signal into one's own work without regard for copyright restrictions placed upon the work. Encryption is an obvious way to make the distribution of digital media more secure, but often there is no way to protect information once it has been decrypted into its original form. The ability for pirates to easily copy works is one of the last hurdles that keep publishers from completely adopting online distribution systems.

Digital watermarking is seen as a partial solution to the problem of securing copyright ownership. Essentially, watermarking is defined as the process of embedding sideband data directly into the samples of a digital audio, image, or video signal. Sideband data is typically "extra" information that must be transmitted along with a digital signal, such as block headers or time synchronization markers. It is important to realize that a watermark is not transmitted in addition to a digital signal, but rather as an integral part of the signal samples. The value of watermarking comes from the fact that regular sideband data may be lost or modified when the digital signal is converted between formats, but the samples of the digital signal are (typically) unchanged.

The earliest forms of information hiding can actually be considered to be highly crude forms of private-key cryptography; the “key” in this case being the knowledge of the method being employed (security through obscurity). Steganography books are filled with examples of such methods used throughout history. Greek messengers had messages tattooed into their shaved head, concealing the message when their hair finally grew back. Wax tablets were scraped down to bare wood were a message was scratched. Once the tablets were re-waxed, the hidden message was secure. Over time these primitive cryptographic techniques improved, increasing speed, capacity and security of the transmitted message.

II. WATERMARKING

Although steganography and watermarking both describe techniques used for covert communication, steganography typically relates only to covert point to point communication between two parties. Steganographic methods are not robust against attacks or modification of data that might occur during transmission, storage or format conversion.

Watermarking, as opposed to steganography, has an additional requirement of robustness against possible attacks. An ideal steganographic system would embed a large amount of information perfectly securely, with no visible degradation to the cover object. An ideal watermarking system, however, would embed an amount of information that could not be removed or altered without making the cover object entirely unusable.

As a side effect of these different requirements, a watermarking system will often trade capacity and perhaps even some security for additional robustness. The working principle of the watermarking techniques is similar to the steganography methods. A watermarking system is made up of a watermark embedding system and a watermark recovery system. The system also has a *key* which could be either a public or a secret key. The *key* is used to enforce security, which is prevention of unauthorized parties from manipulating or recovering the watermark. The embedding and recovery processes of watermarking are shown in below figures.

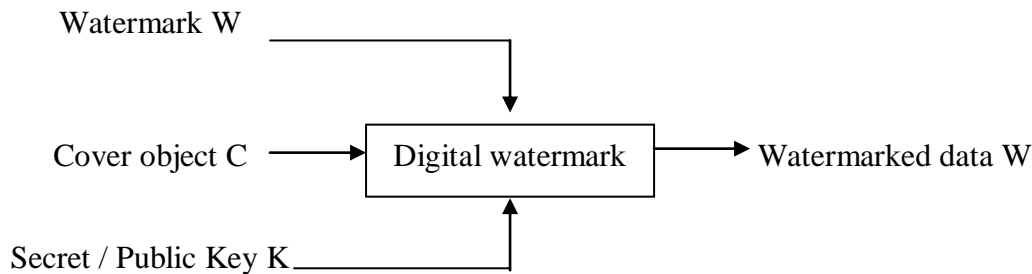


Fig-1.1 Digital watermarking – Embedding/Encryption

For the embedding process the inputs are the watermark, cover object and the secret or the public key. The watermark used can be text, numbers or an image. The resulting final data received is the watermarked data *W*.

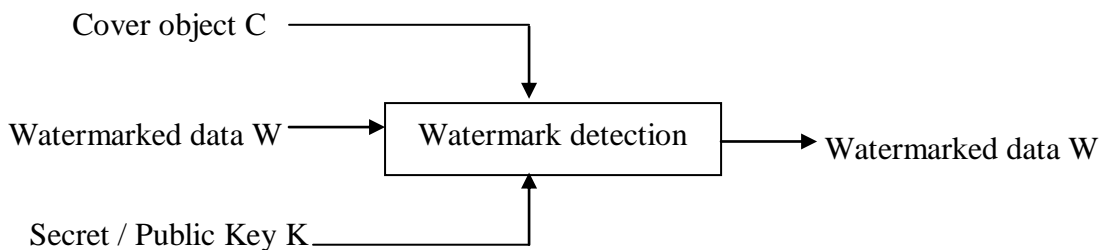


Fig-1.2 Digital watermarking – Decoding

The inputs during the decoding process are the watermark or the original data, the watermarked data and the secret or the public key. The output is the recovered watermark *W*.

III. THE PROPOSED SCHEME

The proposed scheme utilizes the concept of Joo et al.’s scheme to embed a watermark into an image.

Motivation for the proposed scheme

In 2002, Joo et al. proposed a robust watermark scheme by embedding a watermark into wavelet low frequency sub-band. It is briefly introduced as follows. First, an image with size of 512 by 512 pixels is transformed into wavelet coefficients by three-level wavelet transform and extract the sub-band LL_3 . The

extracted sub-band LL_3 is further decomposed into four sub-bands and then three high frequency sub-bands (LH_4, HL_4, HH_4) are set to zero.

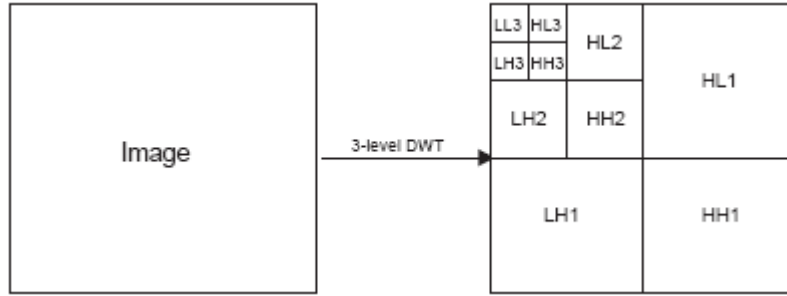


Fig. 1.3 Three-level wavelet decomposition of an image

After performing inverse wavelet transform, its reference sub-band LL_3' is obtained. The information idx of embedding location in the watermark embedding process is obtained by sorting $LL_3 - LL_3'$. Finally, the watermark information is embedded into the sub band LL_3 by $LL_3 = LL_3' \pm k \times w(idx(i))$, where k is a factor for controlling embedding intensity and w is a pseudo-random binary sequence with the length of 1000 bits generated by using a seed, w belongs to $\{1, -1\}$. Besides, due to the fact that change to LL_3 values also cause some change to its reference LL_3' values, hence, the embedding process is repeated. As the embedding process is repeated, the image quality is decreased but its reliability is increased.

In watermarking extraction process, the original image is required for obtaining the watermark embedding location. According to the embedding location, the watermark can be extracted by comparing the two sub-bands LL_3 and LL_3' . Finally, the extracted watermark is compared with the original watermark by similarity measure formula. We know that, for an image, most of energy is concentrated on low-frequency and human eyes are sensitive to the change of low-frequency. Although the above scheme provides the characteristics of robustness and imperceptibility, but the embedding process is quite time-consuming. Besides, the original image is required in the watermark extraction process, which is impractical in real application.

The watermark embedding

The original image X is a gray-level image with M by N pixels. The watermark W is a pseudo random bit-sequence generated by using a seed. They are defined as follows:

$$X = \{x(i, j) | 0 \leq i \leq M-1, 0 \leq j \leq N-1, 0 \leq x(i, j) \leq 255\} \text{ and}$$

$$W = \{w(k) | 1 \leq k \leq n, w(k) \in \{1, -1\}\}$$

First, the original image is modified in transform domain. Then, a watermark is embedded into the original image according to the difference values between the original image and its reference image.

Input: An original image X and watermark W .

Output: A watermarked image X_w and a sequence idx of embedding location.

1. **Step 1:** Transform the original image into wavelet coefficients by one-level wavelet transform.
2. **Step 2:** Set three high-frequency sub-bands LH_1, HL_1 and HH_1 to zero.
3. **Step 3:** Perform inverse wavelet transform and obtain its reference image.
4. **Step 4:** Compute the differences between the original image X and its reference image X' . Then obtain location $idx(i, j)$ such that $s < |x(i, j) - x'(i, j)| < t$, where s and $t \in Z^+$.
5. **Step 5:** According to the result of Step 4, randomly select some locations to embedding. The watermark is embedded as follows.

Note that the embedding process does not require repeat. Furthermore, the sequence idx of embedding locations should keep as the secret key for subsequent watermark extraction. The watermark embedding block diagram is shown as Fig. 1.4.

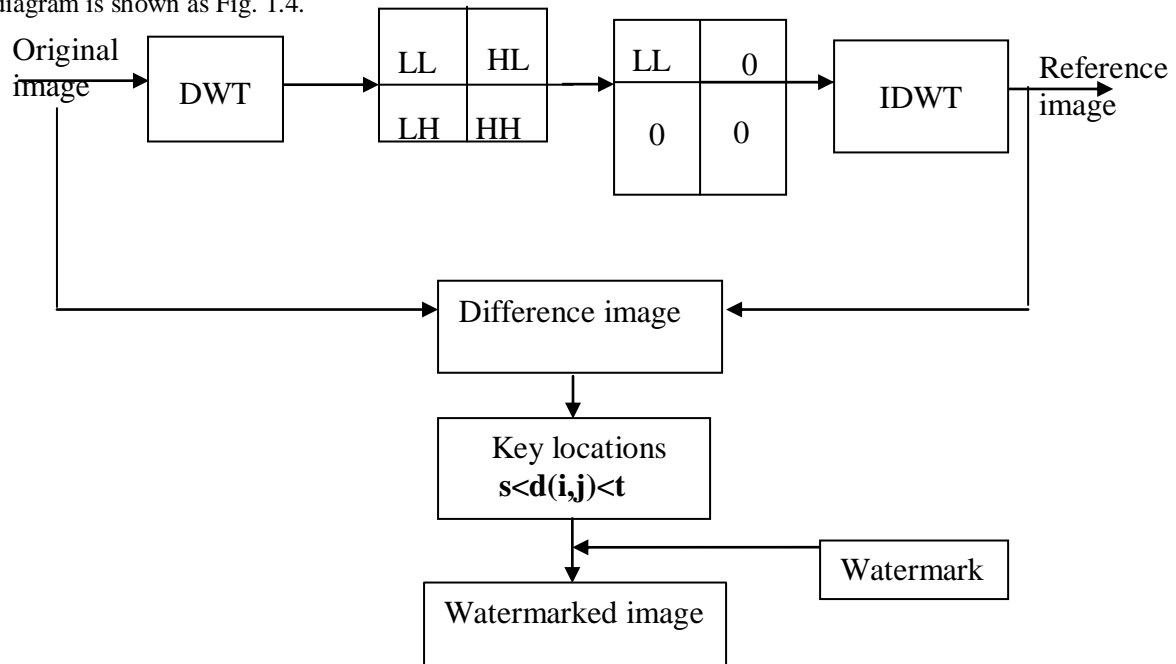


Fig 1.4 The block diagram of watermark embedding process

MATLAB code for watermark embedding

```
function aw=embedd(w,a,a1,idx,s,t)
[m,n]=size(a);
[p,q]=size(idx);
alpha=round((s+t)/2);
for z=1:1:length(w)
    i=idx(z,1);
    j=idx(z,2);
    if w(1,z)==1
        a(i,j)=a1(i,j)+ alpha;
    else
        a(i,j)=a1(i,j)- alpha;
    end
end
aw=a;
end
```

MATLAB code for watermark extraction

```
function w=extract(a,a1,idx,n)
for z=1:1:n
    i=idx(z,1);
    j=idx(z,2);
    if a(i,j)>=a1(i,j)
        w(1,z)=1;
    end
    if a(i,j)< a1(i,j)
        w(1,z)=0;
    end
end
end
```

IV. OUTPUT IMAGES

In the following experiments, two gray-level images with size of 256 by 256, Lena is as the test image. The watermark is a pseudo random bit-sequence with length of 1000 bits generated by using the seed number 250. We choose $\alpha = 7$ to balance the trade off between the robustness and imperceptibility.

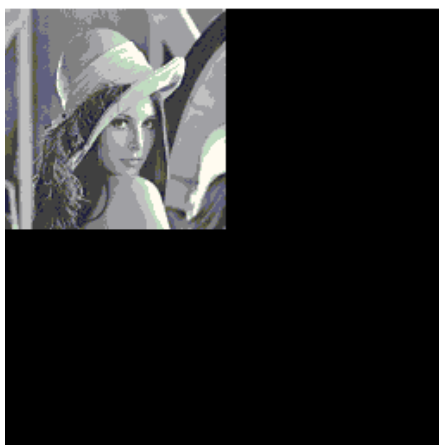


Fig 1.7 Modified DWT Image



Fig 1.8 IDWT Image



Fig 1.9 Difference Image

V. CONCLUSION

Although the above scheme provides the characteristic of robustness and imperceptibility, but the embedding process is quite time-consuming. Besides, the original image is required in the watermark extraction process which is impractical in real application. The concept of Joo et al.'s scheme and propose a robust watermark scheme using self-reference image. By transforming the original image in wavelet domain and embedding a watermark in the difference values between the original image and its reference image, the proposed scheme overcomes the weak robustness problem of embedding a watermark in the spatial domain. Besides, the watermark embedding does not require repeat in the watermark embedding process and we can use a secure encryption algorithm, such as RSA, to increase security of the proposed scheme. The watermark extraction also does not require the original image so the application is more practical in real application for ownership verification. The experimental results show that the proposed technique provides good image quality

and robust to various attacks. In summary, the proposed method has the following contributions. Firstly, the watermark extraction process does not require the original image. Thus, it may be applied easily to Internet. Secondly, the proposed scheme overcomes the weak robustness problem of embedding a watermark in the spatial domain. Thirdly, the embedded watermark can survive under various attacks.

REFERENCES

- [1] D.-C. Lou, J.-L. Liu, A robust watermarking scheme based on the just-noticeable-distortion, *Journal of Chung Cheng Institute of Technology* 31 (2) (2003) 11 – 22.
- [2] I.J. Cox, J. Kilian, F.T. Leighton, T. Shamoan, Secure spread spectrum watermarking for multimedia, *IEEE Transactions on Image Processing* 6 (12) (1997) 1673– 1687.
- [3] S. Joo, Y. Suh, J. Shin, H. Kikuchi, S.-J. Cho, A new robust watermark embedding into wavelet DC components, *ETRI Journal* 24 (5) (2002) 401–404.
- [4] C.-T. Hsu, J.-L. Wu, Multi resolution watermarking for Digital image, *IEEE Transactions on Circuits and Systems, 2, Analog and Digital Signal Processing* 45 (8) (1998) 1097– 1101.
- [5] C.-S. Lu, S.-K. Huang, C.-J. Sze, M. Liao, Cocktail watermarking for digital image protection, *IEEE Transactions on Multimedia* 2 (4) (2000) 209–224.
- [6] W. Zeng, B. Liu, A statistical watermark detection technique without using original images for resolving rightful ownerships of digital images, *IEEE Transactions on Image Processing* 8 (11) (1999) 1534–1548.
- [7] S. Stankovic, I. Djurovic, I. Pitas, Watermarking in the space/spatial-frequency domain using two-dimensional Radon–Wigner distribution, *IEEE Transactions on Image Processing* 10 (4) (2001) 650– 658.
- [8] M.-S. Hsieh, D.-C. Tseng, Y.-H. Huang, Hiding digital watermarks using multi resolution wavelet transform, *IEEE Transactions on Industrial Electronics* 48 (5) (2001) 875–882
- [9] S.-C. Chu, J.F. Roddick, Z.-M. Lu, J.-S. Pan, A digital image watermarking method based on labeled bisecting clustering algorithm, *IEICE Transactions on Fundamentals* E87-A (1) (2004) 282–285.
- [10] Peter H.W. Wong, Oscar C. Au, Y.M. Yeung, A novel blind multiple watermarking technique for images, *IEEE Transactions on Circuits and Systems for Video Technology* 13 (8) (2003) 813– 830.

Analysis and Design of Transmission Tower

Gopi Sudam Punse

ABSTRACT: In this thesis Analysis and Design of narrow based Transmission Tower (using Multi Voltage Multi Circuit) is carried out keeping in view to supply optimum utilization of electric supply with available ROW and increasing population in the locality, in India.

Transmission Line Towers constitute about 28 to 42 percent of the total cost of the Transmission Lines. The increasing demand for electrical energy can be met more economical by developing different light weight configurations of transmission line towers.

In this project, an attempt has been made to make the transmission line more cost effective keeping in view to provide optimum electric supply for the required area by considering unique transmission line tower structure. The objective of this research is met by choosing a 220KV and 110KV Multi Voltage Multi Circuit with narrow based Self Supporting Lattice Towers with a view to optimize the existing geometry. Using STAAD PRO v8i analysis and design of tower has been carried out as a three dimensional structure. Then, the tower members are designed.

I. INTRODUCTION

1.1 Transmission Line Tower

India has a large population residing all over the country and the electricity supply need of this population creates requirement of a large transmission and distribution system. Also, the disposition of the primary resources for electrical power generation viz., coal, hydro potential is quite uneven, thus again adding to the transmission requirements. Transmission line is an integrated system consisting of conductor subsystem, ground wire subsystem and one subsystem for each category of support structure. Mechanical supports of transmission line represent a significant portion of the cost of the line and they play an important role in the reliable power transmission. They are designed and constructed in wide variety of shapes, types, sizes, configurations and materials. The supporting structure types used in transmission lines generally fall into one of the three categories: lattice, pole and guyed.

The supports of EHV transmission lines are normally steel lattice towers. The cost of towers constitutes about quarter to half of the cost of transmission line and hence optimum tower design will bring in substantial savings. The selection of an optimum outline together with right type of bracing system contributes to a large extent in developing an economical design of transmission line tower. The height of tower is fixed by the user and the structural designer has the task of designing the general configuration and member and joint details.

The goal of every designer is to design the best (optimum) systems. But, because of the practical restrictions this has been achieved through intuition, experience and repeated trials, a process that has worked well. Power Grid Corporations of India Limited has prescribed the following steps to.

Optimized the Design of Power Transmission Lines:-

- Selection of clearances.
- Insulator and insulator string design.
- Bundle conductor studies.
- Tower configuration analysis.
- Tower weight estimation.
- Line cost analysis and span optimization.
- Economic evaluation of line.



Figure 1.1 Transmission line tower

1.2 LITERATURE REVIEW

Research paper

1.2.1 Y. M. Ghugal , U. S. Salunkhe [1] “Analysis and Design of Three and Four Legged 400KV Steel Transmission Line Towers: Comparative Study” H.O.D. Applied Mechanics Department, Govt. College of Engineering, Aurangabad Maharashtra (India), Post Graduate Student of M.E. (Structural Engineering), Applied Mechanics Department, Govt. College of Engineering, Aurangabad.

International Journal of Earth Sciences and Engineering 691

ISSN 0974-5904, Volume 04, No 06 SPL, October 2011, pp 691-694

Abstract:

The four legged lattice towers are most commonly used as transmission line towers. Three legged towers only used as telecommunication, microwaves, radio and guyed towers but not used in power sectors as transmission line towers. In this study an attempt is made that the three legged towers are designed as 400 KV double circuit transmission line tower. The present work describes the analysis and design of two self-supporting 400 KV steel transmission line towers viz three legged and four legged models using common parameters such as constant height, bracing system, with an angle sections system are carried out. In this study constant loading parameters including wind forces as per IS: 802 (1995) are taken into account. After analysis, the comparative study is presented with respect to slenderness effect, critical sections, forces and deflections of both three legged and four legged towers. A saving in steel weight up to 21.2% resulted when a three legged tower is compared with a four legged type.

1.2.2 V. Lakshmi1, A. Rajagopala Rao [2] “EFFECT OF MEDIUM WIND INTENSITY ON 21M 132kV TRANSMISSION TOWER” Assistant Professor, Civil Engineering, JNT University Kakinada, Andhra Pradesh, India, Professor of Civil Engineering (Retd) JNT University Kakinada, Andhra Pradesh, India,

ISSN: 2250-3676 Volume-2, Issue-4, 820 – 824

Abstract:

In this paper the performance of 21M high 132kV tower with medium wind intensity is observed. The Recommendations of IS 875-1987, Basic wind speeds, Influence of height above ground and terrain, Design wind speed, Design wind pressure, Design wind force is explained in detailed. An analysis is carried out for the tower and the performance of the tower and the member forces in all the vertical, horizontal and diagonal members are evaluated. The critical elements among each of three groups are identified. In subsequent chapters the performance of tower under abnormal conditions such as localized failures are evaluated. The details of load calculation, modeling and analysis are discussed. The wind intensity converted into point loads and loads are applied at panel joints.

1.2.3 M.Selvaraj, S.M.Kulkarni, R.Ramesh Babu [3] “Behavioural Analysis of built up transmission line tower from FRP pultruded sections” Central Power Research Institute, Bangalore, India , National Institute of Technology Karnataka, Mangalore, India

ISSN 2250-2459, Volume 2, Issue 9, September 2012

Abstract:

The power transmission line towers will have to be built with new design concepts using new materials, reduction of construction costs and optimizing power of delivery with restricted right of way. This paper discusses experimental studies carried out on a X-braced panel of transmission line tower made from FRP pultruded sections. Mathematical model of individual members and members in the X-braced panel are generated using FEM software to study the analytical correlation with the experiments. The member stresses are monitored using strain gauges during full scale testing. Conclusions are drawn based on these studies.

1.2.4 S.Christian Johnson 1 G.S.Thirugnanam [4]

Research Scholar, Head & Professor in civil Engg. IRTT “Experimental study on corrosion of transmission line tower foundation and its rehabilitation” International Journal of Civil and Structural Engineering
ISSN 0976 – 4399 Volume 1, No 1, 2010

Abstract:

In transmission line towers, the tower legs are usually set in concrete which generally provides good protection to the steel. However defects and cracks in the concrete can allow water and salts to penetrate with subsequent corrosion and weakening of the leg. When ferrous materials oxidized to ferrous oxide (corrosion) its volume is obviously more than original ferrous material hence the chimney concrete will undergo strain resulting in formation of cracks. The cracks open, draining the water in to chimney concrete enhancing the corrosion process resulting finally in spalling of chimney concrete. This form of corrosion of stub angle just above the muffing or within the muffing is very common in saline areas. If this is not attended at proper time, the tower may collapse under abnormal climatic conditions. Maintenance and refurbishment of in-service electric power transmission lines require accurate knowledge of components condition in order to develop cost effective programs to extend their useful life. Degradation of foundation concrete can be best assessed by excavation. This is the most rigorous method since it allows determination of the extent and type of corrosion attack, including possible involvement of microbial induced corrosion. In this paper, Physical, Chemical and electro chemical parameters, studied on transmission line tower stubs excavated from inland and coastal areas have been presented. A methodology for rehabilitation of transmission tower stubs has been discussed.

1.2.5 F.Albermani and M. Mahendran [5] “Upgrading Of Transmission Towers Using Of Diaphragm Bracing System” Dept. of Civil Engineering, University of Queensland, Brisbane, Australia School of Civil Engineering, Queensland University of Technology, Brisbane, Australia Dept. of Building and Construction, City University of Hong Kong, Hong Kong .

Abstract:

Many older transmission towers are designed based on tension-only bracing systems with slender diagonal members. However, the increased demand in power supply and changing global weather patterns mean that these towers require upgrading to carry the resultant heavier loading. The failure of a single tower can rapidly propagate along the line and result in severe damage that costs many millions of dollars. Hence, this research project is aimed at developing efficient upgrading schemes using diaphragm bracings. Tower strength improvement was investigated by adding a series of diaphragm bracing types at mid-height of the slender diagonal members. Analytical studies showed that considerable strength improvements could be achieved using diaphragm bracings. They also showed the effects of different types of bracings, including those of joining the internal nodes of diaphragm members and the location of diaphragms. Experimental studies were undertaken using a tower sub-structure assembly that was strengthened with a variety of diaphragm bracings under two types of loading. The results confirmed the analytical predictions and allow recommendations on the most efficient diaphragm bracing types. This type of upgrading scheme using the most efficient diaphragm bracing type was successfully implemented on an existing 105 m height TV tower. This paper presents the details of both the analytical and experimental studies and their results.

1.2.6 N.PrasadRao, G.M.Samuel Knight, S.J.Mohan, N. Lakshmanan [6] “Studies on failure of transmission line towers in testing” College of Engineering Guindy ,Anna University, Chennai 600 025 India, Structural Engineering Research Center, Chennai 600 113,India

Abstract:

The towers are vital components of the transmission lines and hence, accurate prediction of their failure is very important for the reliability and safety of the transmission system. When failure occurs, direct and indirect losses are high, leaving aside other costs associated with power disruption and litigation. Different

types of premature failures observed during full scale testing of transmission line towers at Tower Testing and Research Station, Structural Engineering Research Centre, Chennai are presented. Failures that have been observed during testing are studied and the reasons discussed in detail. The effect of non-triangulated hip bracing pattern and isolated hip bracings connected to elevation redundant in 'K' and 'X' braced panels on tower behaviour are studied. The tower members are modelled as beam column and plate elements. Different types of failures are modelled using finite element software and the analytical and the test results are compared with various codal provisions. The general purpose finite element analysis program NE-NASTRAN is used to model the elasto-plastic behaviour of towers. Importance of redundant member design and connection details in overall performance of the tower is discussed.

1.2.7 G.Visweswara Rao[7] "OPTIMUM DESIGNS FOR TRANSMISSION LINE TOWERS" Senior research Analyst, Engineering Mechanics Research India, 907 Barton Centre Bangalore-560 001, India Computer & Structures vol.57.No.1.pp.81-92, 1995

Abstract:

A method for the development of optimized tower designs for extra high-voltage transmission lines is presented in the paper. The optimization is with reference to both tower weight and geometry. It is achieved by the control of a chosen set of key design parameters. Fuzziness in the definition of these control variables is also included in the design process. A derivative free method of nonlinear optimization is incorporated in the program, specially developed for the configuration, analysis and design of transmission line towers. A few interesting result of both crisp and fuzzy optimization, relevant to the design of a typical double circuit transmission line tower under multiple loading condition, are presented.

II. ANALYSIS OF TRANSMISSION LINE TOWER

2.1 Details of Electric Tension Tower 220kv over 110kv

Wind Pressure Details:-

Basic wind speed $V_b = 44$ m/s

Wind zone – 3

Reliability level – 2

Terrain category – 2

Reference wind speed = $VR = V_b/K_o$
 $= 44/1.375 = 32$ m/s

Design wind speed

$V_d = VR * K1 * K2$

$K1 = 1.11$

$K2 = 1$

$V_d = 32 * 1.11 * 1 = 35.52$ m/s

Design wind pressure $P_d = 0.6 * V_d^2$
 $= 0.6 * 35.52^2$
 $= 757$ N/m²
 $= 77.17$ Kg/m²

Max. Temperature of conductor = 75⁰C

Max. Temperature of earth wire = 53⁰C

Everyday temperature = 32⁰C

Min. temperature = 0⁰C

For 220KV : Conductor wire

Total wind load on conductor = $C_{dc} * G_c * A_e * P_d * \text{space factor}$

$C_{dc} = 1$

$G_c = 2.32$

$A_e = 3.16 * 10^{-2} * 1$ m²/m

$= 3.16 * 10^{-2}$ m²/m

Space factor = 0.6

For 100% wind, $P_d = 1 * 2.32 * 3.18 * 10^{-2} * 77.17 * 0.6$
 $= 3.416$

For 36% wind, $P_d = 0.36 * 1 * 2.32 * 3.18 * 10^{-2} * 77.17 * 0.6$
 $= 1.25$

For 75% wind, $P_d = 0.75 * 1 * 2.32 * 3.18 * 10^{-2} * 77.17 * 0.6$

$$= 2.562$$

$$W = 2.004$$

$$\sqrt{Pd^2 + w^2}$$

$$Q1 = \frac{w}{T}$$

BY parabola equation

$$T^2(T - K + A_{\text{aet}}) = W^2 L^2 EA / 24Q^2$$

$$T = \text{UTS}/\text{FOS} = 16438/4 = 4109.5$$

Initial cond. – at 32°C & 0% wind

$$4109.5^2 (4109.5 - K + 1.93 \times 10^{-5} \times 5.97 \times 10^{-4} \times 7 \times 10^9 \times 32) = 2.004^2 \times 320^2 \times 7 \times 10^9 \times 5.97 \times 10^{-4} / 24 \times 1^2$$

$$K = 2450.326$$

Put K = 2450.326 in above equation, find out tension and sag in conductor as given in below mentioned table.

$$\text{Sag} = W \cdot L^2 / 8T$$

Ground wire

Total wind load on conductor = Cdc * Gc * Ae * Pd * space factor

$$C_{dc} = 1.2$$

$$G_c = 2.39$$

$$A_e = 9.45 \times 10^{-3} \times 1 \text{ m}^2/\text{m}$$

$$= 9.45 \times 10^{-3} \text{ m}^2/\text{m}$$

Space factor = 0.6333

$$\text{For 100\% wind, } Pd = 1.2 \times 2.39 \times 9.45 \times 10^{-3} \times 77.17 \times 0.6 = 1.255$$

$$\text{For 36\% wind, } Pd = 0.36 \times 1.2 \times 2.39 \times 9.45 \times 10^{-3} \times 77.17 \times 0.6 = 0.452$$

$$\text{For 75\% wind, } Pd = 0.75 \times 1.2 \times 2.39 \times 9.45 \times 10^{-3} \times 77.17 \times 0.6 = 0.941$$

$$W = 0.429$$

$$\sqrt{Pd^2 + w^2}$$

$$Q1 = \frac{w}{T} \dots\dots\dots \text{as per IS 5613}$$

By parabola equation

$$T^2(T - K + A_{\text{aet}}) = W^2 L^2 EA / 24Q^2$$

$$T = \text{UTS}/\text{FOS} = 5913/4 = 1478.25$$

Initial cond. – at 32°C & 0% wind

$$1478.25^2 (1478.25 - K + 1.15 \times 10^{-5} \times 5.46 \times 10^{-5} \times 1.93 \times 10^{10} \times 32) = 0.429^2 \times 320^2 \times 1.93 \times 10^{10} \times 5.46 \times 10^{-5} / 24 \times 1^2$$

$$K = 1487.374$$

Sag in ground wire at 0@ C & 0% wind = 90% of sag in conductor 0@ C & 0% wind

$$= 0.9 \times 4.981 = 4.48$$

Put K = 1487.374 in above equation, find out tension and sag in conductor.

$$\text{Sag} = W \cdot L^2 / 8T$$

For 110KV : Conductor wire

Total wind load on conductor = Cdc * Gc * Ae * Pd * space factor

$$C_{dc} = 1$$

$$G_c = 2.12$$

$$A_e = 2.1 \times 10^{-2} \times 1 \text{ m}^2/\text{m}$$

$$= 2.1 \times 10^{-2} \text{ m}^2/\text{m}$$

Space factor = 0.6

$$\text{For 100\% wind, } Pd = 1 \times 2.12 \times 2.1 \times 10^{-2} \times 77.17 \times 0.6 = 2.061$$

$$\text{For 36\% wind, } Pd = 0.36 \times 1 \times 2.12 \times 2.1 \times 10^{-2} \times 77.17 \times 0.6 = 0.742$$

$$\text{For 75\% wind, } Pd = 0.75 \times 1 \times 2.12 \times 2.1 \times 10^{-2} \times 77.17 \times 0.6 = 1.546$$

$$W = 0.974$$

$$\sqrt{Pd^2 + w^2}$$

$$Q1 = \frac{w}{T}$$

BY parabola equation

$$T^2(T - K + A_{\text{aet}}) = W^2 L^2 EA / 24Q^2$$

$$T = \text{UTS}/\text{FOS} = 9144/4 = 2286$$

Initial cond. – at 32°C & 0% wind

$$2286^2 (2286 - K + 1.78 \times 10^{-5} \times 2.62 \times 10^{-4} \times 8.16 \times 10^9 \times 32) = 0.942^2 \times 320^2 \times 8.16 \times 10^9 \times 2.62 \times 10^{-4} / 24 \times 1^2$$

K = 1848

Put K = 1848 in above equation, find out tension and sag in conductor.

$$\text{Sag} = W \cdot L^2 / 8T$$

2.2 GEOMETRY OF TOWER

1. Vertical spacing between conductors of 220KV = 5.5 m
2. Vertical spacing between top conductor and ground wire = 7.45 m
3. Vertical spacing between conductors of 110KV = 4.5m
4. Clearance between BC and TC1(including insulator string = 2.34m) = 7m
5. Ground clearance = 7.015m
6. Extra height at ground level = 3.665m
7. Max. sag = 7m
8. Height of Insulator string = 1.82 m

Total height of tower = 1+2+3+4+5+6+7+8+9 = **53.95 m**

Cross arm length 220KV = 4.6m

Cross arm length 110KV = 3.8m

Base width $1/8 \times 53.95 = 6.774$ say 6m

Width at waist level = $1/2 \times 6 = 3\text{m}$standard practice in use

Inclination at base = 2.419^0

Please see the Excel sheet attached

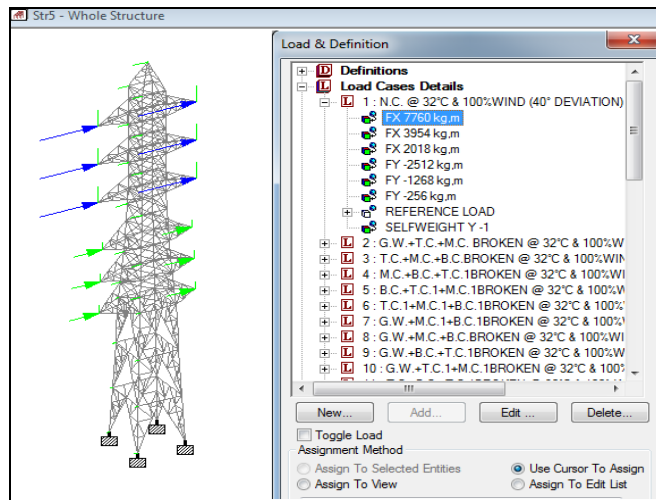


Figure 4.1

LOAD CASE 1:- Loads acting on transmission tower under normal (intact wire) Condition.

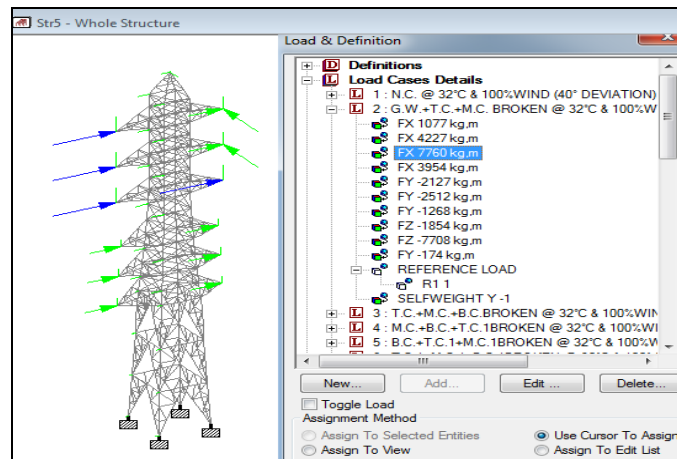


Figure 4.2

LOAD CASE 2:- Loads acting on transmission tower under broken wire condition.

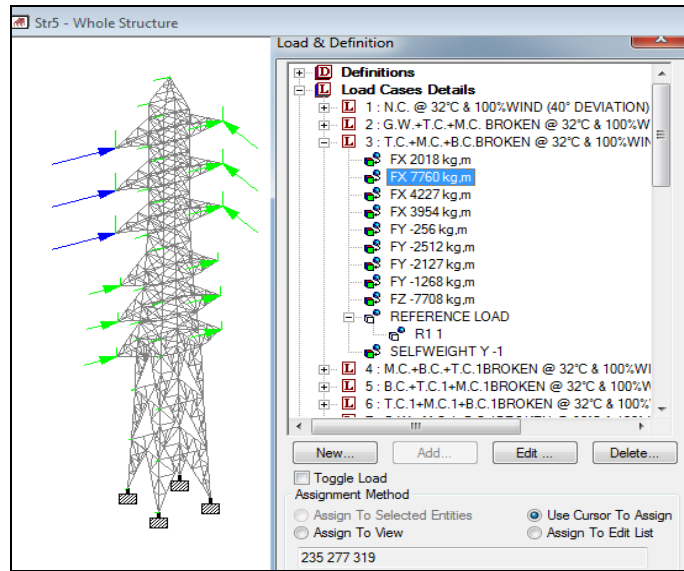


Figure 4.3

LOAD CASE 3:- Loads acting on transmission tower under broken wire condition

2.3 RESULT :-

Different Values of stresses obtained from STAAD - Pro V8i are as,

LEG MEMBER		
Beam	L/C	Axial N/mm2
57	1	-753.11
58	1	-636.08
59	1	-497.34
75	1	-753.12
76	1	-753.12
77	1	-636.09
78	1	-636.09
79	1	-497.34
80	1	-497.34
195	1	790.005
196	1	672.947
197	1	534.176
213	1	790.003
214	1	790.001
215	1	672.945
216	1	672.943
217	1	534.174
218	1	534.175
333	1	743.78
334	1	634.02

BRACINGS		
Beam	L/C	Axial N/mm2
6	1	74.992
10	1	80.152
14	1	87.46
33	1	0.157
37	1	0.172
63	1	-174
64	1	-199.8
65	1	-233.7
69	1	-0.371
70	1	-0.44
71	1	-0.532
87	1	-174
88	1	-174
89	1	-199.8
90	1	-199.8
91	1	-233.7
92	1	-233.7
99	1	-0.372
100	1	-0.371
101	1	-0.439

OTHER DIAGONALS		
Beam	L/C	Axial N/mm2
123	1	-0.004
124	1	0.002
125	1	-0.007
126	1	0.001
127	1	0.004
128	1	-0.004
129	1	0.002
130	1	-0.011
131	1	0.002
132	1	0.004
133	1	-0.001
134	1	0
135	1	-0.008
136	1	0.003
137	1	0.003
153	1	-0.002
154	1	0.001
155	1	0.001
156	1	-0.004
157	1	0.001

335	1	504.169		102	1	-0.439		158	1	0.001
351	1	743.779		103	1	-0.53		159	1	-0.001
352	1	743.776		104	1	-0.53		160	1	-0.003
353	1	634.018		111	1	74.992		161	1	0.002
354	1	634.016		112	1	80.152		162	1	-0.001
355	1	504.167		113	1	87.46		163	1	0
356	1	504.168		117	1	0.157		164	1	-0.001
471	1	-706.89		118	1	0.172		165	1	-0.005
472	1	-597.15		183	1	-0.156		166	1	0.003
473	1	-467.32		184	1	-0.171		167	1	-0.001
489	1	-706.89		185	1	-44.57		261	1	-0.002
490	1	-706.9		189	1	-70.73		262	1	0.001
491	1	-597.15		190	1	-75.45		263	1	-0.001
492	1	-597.16		191	1	-80.22		264	1	0
493	1	-467.33		201	1	0.373		265	1	0.001
494	1	-467.34		202	1	0.442		266	1	-0.004
597	1	-149.32		203	1	0.533		267	1	0.003
598	1	-151.59		207	1	173.96		268	1	-0.002
599	1	179.969		208	1	199.8		269	1	-0.001
600	1	178.235		209	1	233.7		270	1	0.001
605	1	-115.43		225	1	0.373		271	1	-0.003
606	1	-79.894		226	1	0.373		272	1	0.002
607	1	-120.41		227	1	0.44		273	1	0.003
608	1	-81.925		228	1	0.441		274	1	-0.003
609	1	140.432		229	1	0.531		275	1	0.001
610	1	97.978		230	1	0.532		291	1	-0.005
611	1	133.504		237	1	173.96		292	1	0.001
612	1	98.873		238	1	173.96		293	1	0.004
681	1	-52.997		239	1	199.79		294	1	-0.001
682	1	-52.623		240	1	199.79		295	1	0
683	1	71.268		241	1	233.69		296	1	-0.013
684	1	70.752		242	1	233.7		297	1	0.001
689	1	-35.244		249	1	-0.156		298	1	0.004
690	1	-17.945		250	1	-0.171		299	1	-0.001
691	1	-38.693		251	1	-44.57		300	1	0.002
692	1	-17.607		255	1	-70.73		301	1	-0.005
693	1	49.069		256	1	-75.45		302	1	0.001
694	1	25.484		257	1	-80.22		303	1	0.006
695	1	43.915		321	1	-66.62		304	1	-0.003
696	1	27.322		322	1	-70.94		305	1	0.002
761	1	-9.418		323	1	-75.2		399	1	-0.009
762	1	-10.799		327	1	0.156		400	1	0.001
763	1	9.138		328	1	0.172		401	1	-0.001

764	1	17.29		329	1	-44.19		402	1	0
829	1	503.282		339	1	164.16		403	1	0.004
830	1	-469.84		340	1	188.19		404	1	-0.005
831	1	-441.06		341	1	219.71		405	1	0.001
832	1	474.501		345	1	-0.372		406	1	0.003
833	1	479.849		346	1	-0.439		407	1	-0.001
834	1	-432.89		347	1	-0.529		408	1	0.004
835	1	-406.82		363	1	164.16		409	1	-0.005
836	1	453.777		364	1	164.15		410	1	0.001
873	1	-364.02		365	1	188.19		411	1	0.005
874	1	421.143		366	1	188.19		412	1	-0.003
875	1	444.156		367	1	219.7		413	1	0.003
876	1	-387.04		368	1	219.71		429	1	-0.002
885	1	-351.47		375	1	-0.372		430	1	0.001
886	1	397.237		376	1	-0.371		431	1	0.001
887	1	377.707		377	1	-0.441		432	1	-0.001
888	1	-331.94		378	1	-0.44		433	1	0
1022	1	-193.48		379	1	-0.531		434	1	-0.004
1023	1	231.775		380	1	-0.53		435	1	0.003
1024	1	234.981		387	1	-66.62		436	1	-0.002
1025	1	-196.68		388	1	-70.94		437	1	-0.001
1030	1	-240.57		389	1	-75.2		438	1	-0.001
1031	1	-291.69		393	1	0.156		439	1	-0.003
1032	1	287.108		394	1	0.172		440	1	0.002
1033	1	332.089		395	1	-44.19		441	1	0.003
1034	1	296.506		459	1	-0.155		442	1	-0.003
1035	1	347.075		460	1	-0.171		443	1	-0.001
1036	1	-249.97		465	1	70.887		537	1	-0.002
1037	1	-306.68		466	1	75.633		538	1	0.001
1304	1	5.326		467	1	82.441		539	1	-0.004
1305	1	-2.028		477	1	0.373		540	1	0.001
1306	1	6.126		478	1	0.441		541	1	0.001
1307	1	1.319		479	1	0.53		542	1	-0.001
1308	1	-10.738		483	1	-164.2		543	1	0
1309	1	-5.346		484	1	-188.2		544	1	-0.006
1310	1	11.164		485	1	-219.7		545	1	0.002
1311	1	5.767		501	1	0.372		546	1	0.001
1328	1	-5.347		502	1	0.373		547	1	0
1345	1	-6.13		503	1	0.441		548	1	-0.001
1346	1	6.602		504	1	0.441		549	1	-0.005
1347	1	6.603		505	1	0.532		550	1	0.003
1348	1	-6.136		506	1	0.532		551	1	0.001
1349	1	-6.132		513	1	-164.2		567	1	-0.004

1350	1	-6.133		514	1	-164.2		568	1	0.002
1351	1	6.603		515	1	-188.2		569	1	0.004
1352	1	6.605		516	1	-188.2		570	1	-0.007
1353	1	6.605		517	1	-219.7		571	1	0.001
1354	1	6.607		518	1	-219.7		572	1	-0.001
1355	1	-6.134		525	1	-0.155		573	1	-0.001
1356	1	-6.133		526	1	-0.171		574	1	-0.005

III. DESIGN PARAMETERS

Based on the wind speed map the entire country has been divided into six wind zones with max. wind speed of 55 m/sec. and min. wind speed of 33 m/sec. Basic wind speeds for the six wind zones are

Wind Zone		Basic Wind Speed (m/sec)	
1	33		
2	39		
3	44		
4	47		
5			50
	6	55	

In case the line traverses across the border of wind zones, the higher wind speed may be considered.

3.1 Reference Wind Speed VR

It is extreme value of wind speed over an average period of 10 minute duration and is to be calculated from basic wind speed 'vb' by the following relationship

$$VR = Vb/K$$

Where K_o is a factor to convert 3-second peak gust speed into average speed of wind during 10 minutes period at a level of 10 meters above ground. K_o is to be taken as 1.375.

3.2 Design Wind Speed Vd

Reference wind speed obtained shall be modified to include the following effects to get the design wind speed:

- (i) Risk Coefficient K₁
- (ii) Terrain Roughness coefficient K₂

It is expressed as follows:-

$$V = V_R \times K_1 \times K_2$$

3.3 Risk Coefficient K₁

Below Table gives the values of Risk Coefficient K₁ for different wind zones for three Reliability Levels.

Risk Coefficient K₁ for Different Reliability Levels and Wind Zones

Table No. 5.1

Reliability Level	1	Coefficient K ₁	wind 2 zones:	4	5	6
1(50 yr return period)	1.00	1.00	3	1.00	1.00	1.00
2(150 yr return period)	1.08	1.10		1.12	1.13	1.14
3 (300 yr return period)	1.17	1.22		1.27	1.28	1.30

3.4 Terrain Roughness Coefficient K₂

Below, gives the values of coefficient K₂ of the three categories of terrain roughness corresponding to an average 10-minute wind speed.

Terrain Roughness Coefficients K₂

Terrain Category	1	2	3
Coefficient K ₂	1.08	1.00	0.85

3.5 Terrain Categories

- (a) Category 1 - Coastal areas, deserts and large stretches of water.
- (b) Category 2 - Normal cross-country lines with very few obstacles.
- (c) Category 3 - Urban built-up areas or forest areas.

3.6 Design Wind Pressure Pd

The design wind pressure on towers, conductors and insulators shall be obtained by the following relationship:-

$$Pd = 0.6Vd^2$$

where Pd = design wind pressure in N/m² and Vd = Design wind speed in m/s.

Design wind pressure Pd for all the three Reliability levels and pertaining to six wind zones and the three terrain categories have been worked out and given in Table below :

**Design Wind Pressure Pd, in N/m²
(Corresponding to wind velocity at 10 m height)**

Table No. 3.2

Reliability Level	Terrain Category	Wind pressure Pd for wind zones					
		1 6	2	3	4	5	6
1	1	403	563	717	818	925	1120
	2	346	483	614	701	793	960
	3	250	349	444	506	573	694
2	1	470	681	883	1030	1180	1460
	2	403	584	757	879	1010	1250
	3	291	422	547	635	732	901
3	1	552	838	1120	1320	1520	1890
	2	473	718	960	1130	1300	1620
	3	342	519	694	817	939	1170

3.7 Wind Loads

(A) Wind Load on Tower

In order to determine the wind load on tower, the tower is divided into different panels having a height 'h'. These panels should normally be taken between the intersections of the legs and bracings. For a lattice tower, the wind load Fwt in Newtons, for wind normal to a face of tower, on a panel height 'h' applied at the centre of gravity of the panel is :-

$$Fwt = Pd \times C_{dt} \times Ae \times G_T$$

Pd = Design wind pressure in N/m²

C_{dt} = Drag Coefficient pertaining to wind blowing against any face of the tower. Values of C_{dt} for the different solidity ratios are given in Table

Ae = Total net surface area of the legs and bracings of the panel projected normally on face in m². (The projections of the bracing elements of the adjacent faces and of the plan-and-hip bracing bars may be neglected while determining the projected surface of a face).

G_T = Gust Response Factor, perpendicular to the ground roughness and depends on the height above ground. Values of GT for the three terrain categories are given in Table below,

Drag Coefficient C_{dt} for Towers

Table No. 3.3

Solidity Ratio	Drag Coefficient, C _{dt}
Upto 0.05	3.6
0.1	3.4
0.2	2.9
0.3	2.5

0.4 2.2
 0.5 and above 2.0

Solidity ratio is equal to the effective area (projected area of all the individual elements) of a frame normal to the wind direction divided by the area enclosed by the boundary of the frame normal to the wind direction.

Gust Response Factor for Towers (GT) and for Insulators (GI)

Table No. 3.4

Height above 2	Values of GT and GI for terrain Category 3			Ground m 1
	Upto 10	1.70	1.92	
20	1.85	2.20	2.82	
30	1.96	2.30	2.98	
40	2.07	2.40	3.12	
50	2.13	2.48	3.24	
60	2.20	2.55	3.34	
70	2.26	2.62	3.46	
80	2.31	2.69	3.58	

(B) Wind Load on Conductor and Groundwire

The load due to wind on each conductor and groundwire, F_{wc} in Newtons applied at supporting point normal to the line shall be determined by the following expression :

$$F_{wc} = Pd \cdot L \cdot d \cdot G_c \cdot C_{dc}$$

where:

P_d = Design wind pressure in N/m^2 ;

L = Wind span, being sum of half the span on either side of supporting point, in metres. d = Diameter of conductor/groundwire, in metres.

G_c = Gust Response Factor which takes into account the turbulence of the wind and the dynamic response of the Conductor. Values of G_c are already discussed for the three terrain categories and the average height of the conductor above the ground.

C_{dc} = Drag coefficient which is 1.0 for conductor and 1.2 for Groundwire.

(C) Wind Load on Insulator Strings

Wind load on insulator strings ' F_{wi} ' shall be determined from the attachment point to the centre line of the conductor in case of suspension tower and upto the end of clamp in case of tension tower, in the direction of the wind as follows :

$$F_{wi} = 1.2 \cdot Pd \cdot A_i \cdot G_i$$

Where

P_d = Design Wind pressure in N/m^2

A_i = 50 Per cent of the area of Insulator string projected on a plane parallel to the longitudinal axis of the string (1/2 x diameter x length).

G_i = Gust Response Factor, depending on the ground roughness and height of insulator attachment above ground. Values of G_i for the three terrain categories.

3.8 Temperature

To evolve design of tower, three temperatures i.e. Max. temperature, min. temperature and everyday temperature are very important. Tower height as well as sag and tension calculations of conductor and earthwire vary with the change in the above three temperatures.

The temperature range varies for different parts of India under different seasonal conditions. The absolute max. and min. temperatures which may be expected in different localities in country are indicated on the maps of India respectively. The temperatures indicated in these maps are the air temperatures in shade. The max. conductor temperatures may be obtained after allowing increase in temperature due to solar radiation and heating

effect due to current etc. over the absolute max. temperature given below. After giving due thought to several aspects such as flow of excess power in emergency during summer time etc. the following three designs temperatures have been fixed :-

- (a) Max. temperature of ACSR conductor = 75 deg C
- (b) Max. temperature of AAAC conductor = 85 deg C
- (c) Max. temperature of earthwire = 53 deg C
- (d) Min. temperature (ice-free zone) = - 5 deg C to + 10 deg C
(depends on location of the trans, line however 0°C widely used in the country)
- (e) Everyday Temperature 32°C (for most parts of the country).

For region with colder climates (-5 deg C or below) the respective Utility will decide the everyday temperature.

3.9 Lightning Consideration for Tower Design

As the overhead transmission lines pass through open country, these are subjected to the effects of lightning. The faults initiated by lightning can be of the following three types:-

- (i) Back flash over: When lightning strikes on a tower or on the earthwire near the tower which raises the tower potential to a level resulting in a discharge across the insulator string.
- (ii) Midspan flash over: When lightning strikes on earth wire raising local potential of the earth wire such that a breakdown in the air gap between earthwire and phase conductor results.
- (iii) Shielding failure: When lightning strikes on the phase conductor directly resulting in a flashover across the insulator string.

3.10 Seismic Consideration

The transmission line tower is a pin-jointed light structure comparatively flexible and free to vibrate and max. wind pressure is the chief criterion for the design. Concurrence of earthquake and max. wind condition is unlikely to take place and further seismic stresses are considerably diminished by the flexibility and freedom for vibration of the structure. This assumption is also in line with the recommendation given in cl. no. 3.2 (b) of IS: 1893-1984. Seismic considerations, therefore, for tower design are ignored and have not been discussed in this paper.

3.11 New Concepts in Transmission Line Design

The new concepts in transmission line design philosophy include the following major changes in the design method :-

- (i) Design based on limit load concept;
- (ii) Use of probabilistic method of design;
- (iii) Use of Reliability levels in transmission lines design;
- (iv) Use of Co-ordination in strength of line components;
- (v) Use of six basic wind speeds converted to 10-minutes average speeds corresponding to 10-meter height over mean retarding surface as the basis for wind loads on transmission lines instead of three wind zones corresponding to 30 metre height over mean retarding surface in use earlier;
- (vi) Consideration of the effects of terrain category and topography of transmission line corridors in the design wind speeds.

IV. DESIGN OF TRANSMISSION LINE TOWER

4.1 Design of leg member

NC 32°C & 100% wind

$$GW \quad (2018+745) * 53.95 = 149064$$

$$TC \quad (2*7760+2777)*46.5 = 850811$$

$$MC \quad (2*7760+3030)*41 = 760550$$

$$BC \quad (2*7760+2972)*35.5 = 656466$$

$$TC1 \quad (3954*2+3308)*28.5 = 319656$$

$$MC1 \quad (2*3954+2662)*24 = 253680$$

$$BC1 \quad (2*3954+2739)*19.5 = 207617$$

$$M \quad = \quad 3198 \times 10^3 \text{ Kg-m}$$

$$\text{Max. Stress} = M/2w \cos \phi = 3198 \times 10^3 / 2 * 5.4 * 0.9982$$

$$= 296 \times 10^3$$

$$\text{Vertical load max} = \frac{256 + 2512 * 6 + 1268 * 6}{4}$$

$$= 5734$$

$$\text{Vertical load min} = \frac{119 + 1871 \cdot 6 + 956 \cdot 6}{4}$$

$$= 4270$$

Self wt of tower = $10000/4 = 2500$ approx.

$$\text{Compression} = 305 \times 10^3$$

$$\text{Tension} = 290 \times 10^3$$

Use ISA 100X100X8 Double angle back to back section

$$L = 2340/0.999 = 2342.342$$

$$l/r = 234.23/3.07 = 76.296$$

yield stress of mild steel = 2550 Kg/cm^2

from curve no. 1 $F_c = 2503$

$$\text{ultimate compressive stress} = 2503 \cdot 30.78 = 77204 < 305 \times 10^3$$

Use ISA 200X200X25 Double angle back to back section

$$l/r = 38.5 = 39$$

$$\text{ultimate compressive stress} = 2427 \cdot 183.30 = 445 \times 10^3 > 305 \times 10^3$$

S.M. = 1.46

$$K = \frac{5A_1}{5A_1 + A_2}$$

$$= \frac{5 \cdot 200 \cdot 25}{5 \cdot 200 \cdot 25 + 200 \cdot 25}$$

$$= 0.833$$

$$\text{Net area for tension} = (200 \cdot 25 + 0.833 \cdot 200 \cdot 25) \cdot 2$$

$$= 183.30$$

$$\text{ultimate tensile stress} = 2550 \cdot 183.30 = 467 \times 10^3 > 305 \times 10^3$$

S.M. = 1.233

Use 20mm dia bolts 6Nos.

Ultimate shearing strength (single shear) = 59586 kg

Ultimate bearing strength (single shear) = 98018 kg

Ultimate shearing strength (double shear) = 119X10 kg

4.2 Design of bracings

ΣF_b for transverse face bracing

$$\text{GW} \quad (2018 + 745) \cdot 0.2 = 2763$$

$$\text{TC} \quad (2 \cdot 7760 + 2777) \cdot 3 = 54891$$

$$\text{MC} \quad (2 \cdot 7760 + 3030) \cdot 3 = 55650$$

$$\text{BC} \quad (2 \cdot 7760 + 2972) \cdot 3 = 55476$$

$$\text{TC1} \quad (3954 \cdot 2 + 3308) \cdot 3.59 = 40265$$

$$\text{MC1} \quad (2 \cdot 3954 + 2662) \cdot 3.97 = 41963$$

$$\text{BC1} \quad (2 \cdot 3954 + 2739) \cdot 4.52 = 47912$$

$$\Sigma F_b = 355 \times 10^3$$

$$\text{Stress} = \Sigma F_b / 4w \cos \phi = 355 \times 10^3 / 4 \cdot 5.4 \cdot 0.9982$$

$$= 16 \times 10^3 \text{ (C\&T)}$$

$$L = 2320$$

Use ISA 90 X 90 X 12 Double angle back to back section

$$l/r = 232/2.270 = 85.6$$

$$\text{ultimate compressive stress} = 1726 \cdot 28.74 = 48 \times 10^3 > 16 \times 10^3$$

S.M. = 3

$$K = \frac{5A_1}{5A_1 + A_2}$$

$$= \frac{5 \cdot 90 \cdot 12}{5 \cdot 90 \cdot 12 + 90 \cdot 12}$$

$$= 0.833$$

$$\text{Net area for tension} = (90 \cdot 12 + 0.833 \cdot 90 \cdot 12) \cdot 2$$

$$= 40 \text{ cm}^2$$

$$\text{ultimate tensile stress} = 2550 \cdot 40 = 102 \times 10^3 > 16 \times 10^3$$

S.M. = 6.37

Use 20mm dia bolts 4Nos.

Ultimate shearing strength (single shear) = 39724
 Ultimate bearing strength (single shear) = 65345
 Ultimate shearing strength (double shear) = 79333

4.3 Design of other diagonals

Stress = 16×10^3 (C&T)

L = 2390

Use ISA 65X65X8 single angle section

$l/r = 239/1.25 = 191.2$

Ultimate compressive stress = $1387 \times 9.76 = 13.53 \times 10^3 < 16 \times 10^3$

Use ISA 100 X 100 X 8 single angle section

$l/r = 239/3.07 = 77.85$

$$K = \frac{3A_1}{3A_1 + A_2}$$

$$= \frac{3 \times 100 \times 8}{3 \times 100 \times 8 + 100 \times 8}$$

$$= 0.75$$

Net area for tension = $(100 \times 8 + 0.75 \times 100 \times 8)$
 = 14

ultimate tensile stress = $2550 \times 14 = 35.7 \times 10^3 > 16 \times 10^3$

S.M. = 2.18

Use 20mm dia bolts 6Nos.

Ultimate shearing strength (single shear) = 39724

Ultimate bearing strength (single shear) = 65345

Ultimate shearing strength (double shear) = 79333

4.4 Design of cross arm

a) Upper member:-

Length = $\sqrt{(1.375^2 + 4.84^2)} = 5.032$

$$St = \frac{1406 \times 5.032}{2 \times 4.84}$$

$$= \pm 731$$

$$Sv = \frac{3214 \times 5.032}{2 \times 1.375}$$

$$= 5881$$

$$Sl = \frac{4109 \times 5.032}{2 \times 3}$$

$$= \pm 3446$$

Compression = 10056

Tension = 4177

$L = 5.032/3 = 1.677$

$l/r = 167.7 / 3.07 = 54.625$

ultimate compressive stress = $1970 \times 28.74 = 55 \times 10^3 > 10 \times 10^3$

S.M. = 3.43

$$K = \frac{5A_1}{5A_1 + A_2}$$

$$= \frac{5 \times 100 \times 8}{5 \times 100 \times 8 + 100 \times 8}$$

$$= 0.833$$

Net area for tension = $(100 \times 8 + 0.833 \times 100 \times 8) \times 2$
 = 29.32

Ultimate tensile stress = $2550 \times 29.32 = 75 \times 10^3 > 4.1 \times 10^3$

b) Lower member :-

Length = $\sqrt{(1.375^2 + 4.84^2 + 3^2)} = 5.858$

$$Sv = \frac{3984 \times 5.858}{2 \times 1.375}$$

$$= 8487$$

$l/r = 585.8 / 3.07 = 191$

Ultimate tensile stress = $2550 \times 30.7 = 78 \times 10^3 > 4.1 \times 10^3$

Use 20mm dia bolts 6Nos.

Ultimate shearing strength (single shear) = 39724

Ultimate bearing strength (single shear) = 65345

Ultimate shearing strength (double shear) = 79333

CONCLUSION:

Use ISA 200X200X 25 Double angle back to back section for leg member

Use ISA 90X90X 12 Double angle back to back section for bracings and cross arm

Use ISA 100x100X 8 Single angle section for other diagonals.

4.5 RESULT :-

Compression and Tensile force acting on the tower and obtained from STAAD Pro-V8i are as,

Table No. 6.1

LEG MEMBER				BRACINGS				OTHER DIAGONALS			
Beam	L/C	Compression kg	Tension Kg	Beam	L/C	Compression kg	Tension Kg	Beam	L/C	Compression kg	Tension Kg
57	1	2.34E+05	2.34E+05	6	1	14841.721	-14841.721	123	1	-0.829	0.453
58	1	1.98E+05	3.12E+05	10	1	15860.281	-19851.965	124	1	0.418	0.437
59	1	1.55E+05	3.59E+05	14	1	16901.445	-22902.618	125	1	-1.113	0.428
75	1	2.34E+05	3.24E+05	33	1	-54.179	-21272.222	126	1	0.136	0.435
76	1	2.34E+05	2.90E+05	37	1	-59.751	-19508.161	127	1	0.705	0.441
77	1	1.98E+05	2.55E+05	63	1	-34421.587	-17593.517	128	1	-0.798	0.448
78	1	1.98E+05	2.39E+05	64	1	-39525.147	-16374.135	129	1	0.36	0.452
79	1	1.55E+05	3.07E+05	65	1	-46225.431	-20052.837	130	1	-1.545	0.438
80	1	1.55E+05	2.75E+05	69	1	130.627	-18332.961	131	1	0.235	0.444
195	1	2.46E+05	2.43E+05	70	1	154.341	-16457.506	132	1	0.673	0.451
196	1	2.10E+05	3.26E+05	71	1	185.709	-21182.74	133	1	-0.47	0.434
197	1	1.67E+05	2.94E+05	87	1	-34421.643	-19307.288	134	1	0.092	0.441
213	1	2.46E+05	2.90E+05	88	1	-34421.805	-19223.915	135	1	-0.961	0.441
214	1	2.46E+05	2.92E+05	89	1	-39524.799	-19396.77	136	1	0.37	0.441
215	1	2.10E+05	2.87E+05	90	1	-39525.847	-19313.396	137	1	0.642	0.442
216	1	2.10E+05	2.85E+05	91	1	-46222.823	-19424.788	153	1	-0.506	0.442
217	1	1.67E+05	1.44E+05	92	1	-46224.895	-8827.504	154	1	0.313	0.471
218	1	1.67E+05	2.10E+05	99	1	130.386	-13042.086	155	1	0.188	0.458
333	1	2.36E+05	2.50E+05	100	1	130.659	-15611.98	156	1	-0.847	0.45
334	1	2.01E+05	2.21E+05	101	1	154.67	-14324.424	157	1	0.136	0.455
335	1	1.59E+05	1.92E+05	102	1	154.66	-12927.625	158	1	-0.172	0.461
351	1	2.36E+05	1.64E+05	103	1	186.274	-11407.839	159	1	-0.015	0.466
352	1	2.36E+05	1.49E+05	104	1	186.303	-10304.371	160	1	-0.511	0.469
353	1	2.01E+05	2.06E+05	111	1	14841.632	-13220.955	161	1	0.235	0.458
354	1	2.01E+05	1.80E+05	112	1	15860.208	-11840.116	162	1	-0.188	0.463
355	1	1.59E+05	1.53E+05	113	1	16901.384	-10357.731	163	1	-0.213	0.469
356	1	1.59E+05	2.23E+05	117	1	-54.179	-14243.94	164	1	0.021	0.455

471	1	-	2.24E+05	1.96E+05	118	1	-59.751	-12748.756	165	1	-0.747	0.46
472	1	-	1.89E+05	1.92E+05	183	1	54.877	-12695.395	166	1	0.37	0.461
473	1	-	1.48E+05	1.94E+05	184	1	60.565	-12829.239	167	1	-0.188	0.46
489	1	-	2.24E+05	1.90E+05	185	1	-5686.867	-12775.879	261	1	-0.398	0.461
490	1	-	2.24E+05	1.88E+05	189	1	-13992.334	-12874.265	262	1	0.207	0.462
491	1	-	1.89E+05	5.23E+02	190	1	-14923.574	12.473	263	1	-0.253	0.499
492	1	-	1.89E+05	4.83E+03	191	1	-16265.538	896.249	264	1	0.05	0.499
493	1	-	1.48E+05	3.44E+04	201	1	-130.396	42.547	265	1	0.188	0.493
494	1	-	1.48E+05	4.05E+04	202	1	-154.044	589.199	266	1	-0.749	0.492
597	1	-	4.55E+04	6.72E+04	203	1	-185.83	-325.072	267	1	0.522	0.487
598	1	-	5.07E+04	7.05E+04	207	1	34422.623	244.492	268	1	-0.588	0.487
599	1	58371.33 4	9.44E+04	208	1	39527.652	-744.483	269	1	-0.056	0.482	
600	1	-	5.38E+04	9.91E+04	209	1	46225.82	-703.693	270	1	0.188	0.481
605	1	-	3.50E+04	1.08E+05	225	1	-130.33	-1189.658	271	1	-0.544	0.48
606	1	-	2.38E+04	1.10E+05	226	1	-130.151	-1012.746	272	1	0.309	0.479
607	1	-	3.94E+04	1.17E+05	227	1	-154.52	-1505.023	273	1	0.12	0.478
608	1	-	2.75E+04	1.18E+05	228	1	-154.033	-1341.662	274	1	-0.204	0.478
609	1	45677.37 1	1.24E+05	229	1	-186.139	-1838.798	275	1	0.188	0.476	
610	1	32185.73	1.98E+05	230	1	-185.827	-15860.281	291	1	-0.924	-0.418	
611	1	-	4.05E+04	2.64E+05	237	1	34422.082	-21371.774	292	1	0.295	-0.441
612	1	-	2.96E+04	3.02E+05	238	1	34422.309	-24727.628	293	1	0.705	-0.455
681	1	-	1.56E+04	2.71E+05	239	1	39526.762	-22934.119	294	1	-0.474	-0.449
682	1	-	1.79E+04	2.40E+05	240	1	39526.351	-20993.571	295	1	0.05	-0.442
683	1	-	2.35E+04	2.12E+05	241	1	46223.461	-18887.38	296	1	-1.944	-0.435
684	1	21053.53 5	1.98E+05	242	1	46225.393	-17546.002	297	1	0.319	-0.429	
689	1	-	1.06E+04	2.57E+05	249	1	54.877	-21592.743	298	1	-0.028	-0.443
690	1	-	5.04E+03	2.29E+05	250	1	60.565	-19700.799	299	1	-0.056	-0.436
691	1	-	1.28E+04	2.02E+05	251	1	-5686.867	-17637.717	300	1	0.297	-0.429
692	1	-	6.14E+03	2.74E+05	255	1	-13992.246	-22835.685	301	1	-0.825	-0.448
693	1	-	1.60E+04	2.47E+05	256	1	-14923.499	-20772.602	302	1	0.239	-0.44
694	1	8548.971	2.43E+05	257	1	-16265.479	-20680.889	303	1	0.334	-0.44	
695	1	13216.78 3	2.44E+05	321	1	-13345.315	-20871.037	304	1	-0.204	-0.441	
696	1	-	8.01E+03	2.40E+05	322	1	-14213.476	-20779.323	305	1	0.266	-0.441
761	1	-	2.58E+03	2.36E+05	323	1	-15488.474	-20901.858	399	1	-1.554	-0.443
762	1	-	3.51E+03	1.22E+05	327	1	-54.355	-9542.891	400	1	0.298	-0.393
763	1	-	3.60E+03	1.78E+05	328	1	-59.594	-14179.118	401	1	-0.488	-0.412
764	1	-	5.11E+03	2.11E+05	329	1	-5820.379	-17006.116	402	1	0.052	-0.423

829	1	1.59E+05	1.84E+05	339	1	32880.296	-15589.747	403	1	0.705	-0.419
830	1	1.49E+05	1.59E+05	340	1	37701.356	-14053.207	404	1	-0.899	-0.414
831	1	1.41E+05	1.35E+05	341	1	44024.688	-12381.374	405	1	0.32	-0.408
832	1	1.51E+05	1.23E+05	345	1	130.405	-11167.509	406	1	-0.063	-0.403
833	1	1.54E+05	1.73E+05	346	1	154.517	-14375.882	407	1	-0.05	-0.414
834	1	1.33E+05	1.49E+05	347	1	186.313	-12856.898	408	1	0.673	-0.408
835	1	1.24E+05	1.27E+05	363	1	32879.77	-11226.208	409	1	-0.817	-0.402
836	1	1.45E+05	1.87E+05	364	1	32879.033	-15501.213	410	1	0.235	-0.418
873	1	1.08E+05	1.65E+05	365	1	37700.494	-13856.443	411	1	0.304	-0.412
874	1	1.37E+05	1.61E+05	366	1	37701.614	-13797.744	412	1	-0.192	-0.412
875	1	1.45E+05	1.62E+05	367	1	44022.448	-13944.979	413	1	0.642	-0.413
876	1	1.17E+05	1.58E+05	368	1	44024.287	-13886.278	429	1	-0.396	-0.413
885	1	1.08E+05	1.55E+05	375	1	130.473	-13994.508	430	1	0.205	-0.414
886	1	1.30E+05	5.76E+02	376	1	130.652	13.566	431	1	0.188	-0.355
887	1	1.20E+05	4.95E+03	377	1	154.046	985.761	432	1	-0.254	-0.348
888	1	9.90E+04	3.20E+04	378	1	154.534	46.651	433	1	0.052	-0.349
102 2	1	5.55E+04	3.74E+04	379	1	186.008	647.994	434	1	-0.739	-0.344
102 3	1	7.33E+04	6.12E+04	380	1	186.328	-357.743	435	1	0.513	-0.346
102 4	1	7.89E+04	6.39E+04	387	1	-13345.404	268.804	436	1	-0.593	-0.341
102 5	1	61205.53 4	8.43E+04	388	1	-14213.549	-819.112	437	1	-0.05	-0.344
103 0	1	68855.22 3	8.75E+04	389	1	-15488.535	-774.241	438	1	-0.188	-0.343
103 1	1	8.72E+04	9.44E+04	393	1	-54.355	-1308.823	439	1	-0.536	-0.345
103 2	1	9.26E+04	9.54E+04	394	1	-59.594	-1114.211	440	1	0.302	-0.343
103 3	1	1.05E+05	1.01E+05	395	1	-5820.379	-1655.738	441	1	0.103	-0.345
103 4	1	9.97E+04	1.00E+05	459	1	55.06	-1476.032	442	1	-0.192	-0.344
103 5	1	1.13E+05	1.04E+05	460	1	60.507	-2022.903	443	1	-0.188	-0.347
103 6	1	75980.94 5	1.55E+05	465	1	14195.828	-16901.445	537	1	-0.508	0.737
103 7	1	9.57E+04	2.07E+05	466	1	15149.086	-24335.337	538	1	0.316	0.847
130 4	1	1.54E+03	2.35E+05	467	1	16099.075	-28262.859	539	1	-0.847	0.914
130 5	1	8.58E+01	2.07E+05	477	1	-130.19	-25499.538	540	1	0.134	0.876
130 6	1	1.60E+03	1.82E+05	478	1	-154.237	-22723.928	541	1	0.188	0.836
130 7	1	7.79E+02	1.60E+05	479	1	-186.385	-19676.647	542	1	-0.366	0.793
130 8	1	-3364.292	1.50E+05	483	1	-32878.314	-18270.415	543	1	0.166	0.767
130 9	1	-1671.922	1.98E+05	484	1	-37700.855	-24093.307	544	1	-0.98	0.85
131 0	1	3.51E+03	1.74E+05	485	1	-44023.549	-21464.388	545	1	0.229	0.811
131	1	1.82E+03	1.54E+05	501	1	-130.432	-18796.407	546	1	0.188	0.769

1											
132		-									
8	1	1.67E+03	2.12E+05	502	1	-130.158	-25633.943	547	1	-0.22	0.875
134		-									
5	1	1.92E+03	1.91E+05	503	1	-154.311	-22965.958	548	1	0.028	0.833
134		-									
6	1	2.07E+03	1.88E+05	504	1	-154.159	-22439.97	549	1	-0.729	0.831
134		-									
7	1	2072.773	1.87E+05	505	1	-185.824	-22831.554	550	1	0.357	0.834
134		-									
8	1	1.93E+03	1.83E+05	506	1	-185.802	-22305.566	551	1	0.188	0.832
134		-									
9	1	1.92E+03	1.78E+05	513	1	-32878.379	-22197.94	567	1	-0.831	0.833
135		-									
0	1	1.92E+03	9.52E+04	514	1	-32878.535	-10465.731	568	1	0.416	0.611
135		-									
1	1	2074.123	1.40E+05	515	1	-37699.825	-16702.273	569	1	0.705	0.704
135		-									
2	1	2076.314	1.64E+05	516	1	-37701.11	-20004.543	570	1	-1.099	0.76
135		-									
3	1	2074.688	1.40E+05	517	1	-44022.345	-17794.725	571	1	0.134	0.73
135		-									
4	1	2076.878	1.19E+05	518	1	-44023.786	-15575.305	572	1	-0.468	0.698
135		-									
5	1	1.92E+03	9.98E+04	525	1	55.06	-13011.355	573	1	0.049	0.663
135		-									
6	1	1.92E+03	9.16E+04	526	1	60.507	-11735.359	574	1	-0.659	0.639

4.6 Foundation Details :-

FOUNDATION LOADINGS Kg

Compression = $2.77 * 10^5$

Tension = $2.77 * 10^5$

Transverse = 23860.5

Longitudinal = 10594.9

STRUCTURE DETAIL

Width (Trans.) X Width (Long.)

6M X 6M

Slope (Trans.) X Slope (Long.)

2.419509 ° X 2.419509 °

True Length Factor

Transverse 1.00089

Longitudinal 1.00089

FOUNDATION PROFILE

Depth of Foundation = 2M

Transverse Width = 1.8 M

Longitudinal Width = 1.8M

Height of concrete block = 1.5M

Depth of Anchor/Grout bar = 1.2M

Height of chimney = 0.5M

Chimney Width = 0.75M

Muffing Height = 0.35M

SOIL DETAIL

Type of Soil ----- HARD ROCK

Weight of Rock = 1600 Kg/cu.m

U.B.C = 125000 Kg/Sq.m

Frictional resistance between rock and concrete = 4 kg/Sq.cm

Frictional resistance between rock and grout (As per CBIP manual pg. no. 267) = 2 kg/Sq.cm.

Weight of concrete = 2300 Kg/Sq.m

Fe = 415 N/mm²

Fck = 2 N/mm²

FOUNDATION DESIGN CALCULATION

Volume of concrete in M³

Muffing = 0.197 M³
 Chimney = 0.281 M³
 Concrete block = 4.860 M³
Total = 5.338 M³

Over load due to Concrete in Kg

Muffing = 452.81
 Chimney = 196.88
 Concrete block = 3402.00
 Total = 4051.69 Kg
 Total thrust on foundation = 277000 + 4051.69
 = 281051.69 Kg

CHECK OF FOUNDATION IN BEARING

Ultimate strength of rock in bearing = 1.8² x 125000
 = 405000 Kg
 = 405000 > 281051
 F.O.S = 1.44

CHECK OF FOUNDATION IN UPLIFT

Concrete block
 Net uplift = 277000 - 4051.69
 = 272948 Kg
 Ultimate frictional strength between rock and concrete = 180 X 150 X 4 X 4
 = 432000 Kg
 Uplift resisted by 4 NOS. 20 ϕ
 = (No. of bar X pi(π) X Dia. of bar X Depth of anchor bar X Bond between rock & Grout)
 = 4 X 3.14 X 2 X 120 X 2
 = 6028.80 (I)
 = Bond between rock anchor steel and grout
 = π X 2 X 120 X 12 X 4
 = 36191.14 > 6028.80 (II)
 Total resistance against uplift = 432000 + 6028.80 (Min. of ((I) & (II))
 = 438028.80 > 272948
 FOS = 1.623

ANCHOR (TOR) BARS ASSUMED

CHECK AGAINST UPROOTING OF STUB

SECTION OF STUB JL 200X200X16

Cover = 10 Cm

Design Uplift = 277000 Kg

Cleats Provided = 6 NOS OF 110X110X10

Bolts = 24 Nos of 20 mm dia.

Ultimate resistance of Stub in Bond =

$$U_s = [D \times \{X \times 2.0 + (X - T_s) \times 2.0\} - N_p \times \{X + (X - T_s)\} \times k] \times S$$

Where , X = Flange width of Stub = 20 cm

D = Depth of Stub in slab (Concrete Block) = 140 cm

S = Ultimate permissible bond stress between stub and concrete = 12 kg/cm².....

Page No.267 (CBIP manual)

Ts = Thickness of stub section = 1.6 cm

Np = No of cleat pair (Pair consists of outer & inner cleats) = 6 Nos.

k = Flange width of cleat section = 11 cm

$$U_s = (140 \times (20 \times 2.0 + (20 - 1.6) \times 2.0) - 6 \times (20 + (20 - 1.6)) \times 11) \times 12$$

$$= 98611 \text{ kgs}$$

Load resisted by cleat in bearing :-

Least resistance offered by cleats in bearing / bolt :-
 $x (k-Ct)$

$$Uc = b \times (Lo+Li) \times Np$$

Where,

b = Ultimate bearing pressure in concrete = 91.75 cm

Lo = Length of outer cleat = 40 cm

Li = Length of inner cleat = 25 cm

Ct = Thickness of cleat section = 1.0 cm

$$Uc = 91.75 \times (40 + 25) \times 6 \times (11 - 1)$$

$$= 357825 \text{ kg} \dots \dots \dots (I)$$

Resistance against uplift :-

$$= 98611.2 + 357825$$

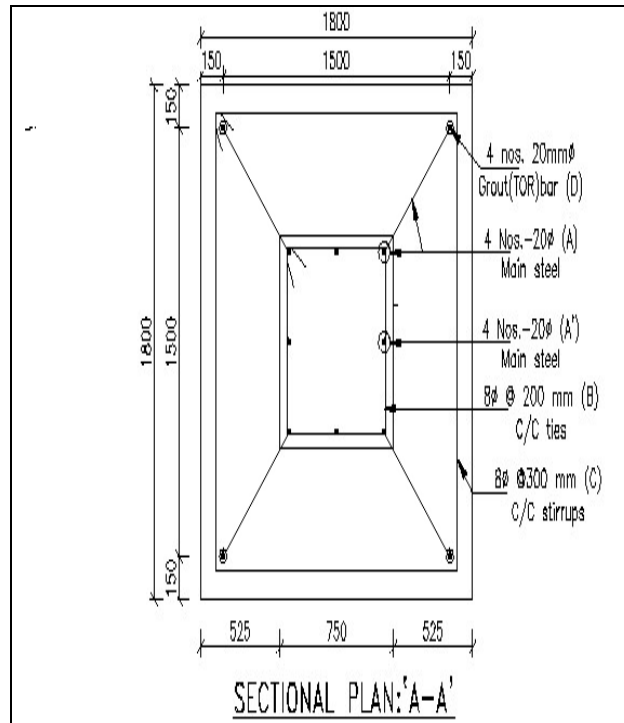
$$456436 > 277000$$

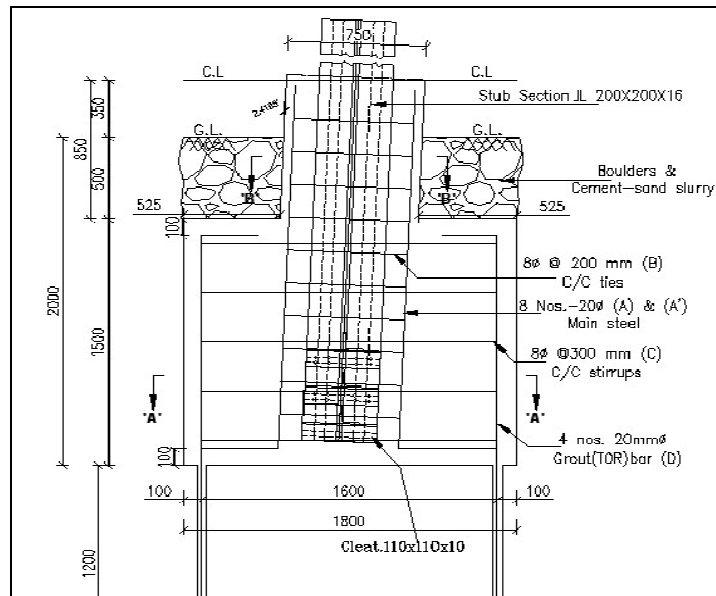
$$FOS = 1.648$$

NOTE:

- 1 Nominal Reinforcement provide.
- 2 Stub to be cut, holes to be drilled and cold zinc rich paint/galvanising to be applied at site.
- 3 Grout holes to be 20 mm bigger than dia of grout bar.
- 4 Cement sand mix 1:1 Ratio to be used for grouting through grouting pump.
- 5 Entire concrete block (slab) should be embedded in hard rock irrespective of level of hard rock encountered.

4.6.1 Details of foundation drawing is given





V. CONCLUSION

Narrow based steel lattice transmission tower structure plays a vital role in its performance especially while considering eccentric loading conditions for high altitude as compared to other normal tower. Narrow based steel lattice transmission tower considered in this paper can safely withstand the design wind load and actually load acting on tower. The bottom tier members have more role in performance of the tower in taking axial forces and the members supporting the cables are likely to have localized role. The vertical members are more prominent in taking the loads of the tower than the horizontal and diagonal members, the members supporting the cables at higher elevations are likely to have larger influence on the behavior of the tower structure. The effect of twisting moment of the intact structure is not significant. The Geometry parameters of the tower can efficiently be treated as design Variables and considerable weight reduction can often be achieved as a result of geometry changes. The tower with angle section and X-bracing has the greater reduction in weight after optimization. Tube section is not economic to use in this type of transmission tower. Total weight of tower considering weight of nut bolts, anchor bolts, hardware etc works out to 30 to 35 Tonne.

Scope of Present Work:-

- Continuous demand due to increasing population in all sectors viz. residential, commercial and industrial leads to requirement of efficient, consistent and adequate amount of electric power supply which can only fulfilled by using the Conventional Guyed Transmission Towers.
- It can be substituted between the transmission line of wide based tower where narrow width is required for certain specified distance.
- Effective static loading on transmission line structure, conductor and ground wire can be replaced with the actual dynamic loading and the results can be compared.
- Attempt in changing the shape of cross arm can lead to wonderful results.
- Rapid urbanization and increasing demand for electric, availability of land leads to involve use of tubular shape pole structure.
- Iso restricted area (due to non-availability of land), more supply of electric energy with available resources and for continuous supply without any interruption in the transmission line, will demand the use of high altitude narrow based steel lattice transmission tower

REFERENCES

Journal

- [1] Y. M. Ghugal, U. S. Salunkhe "Analysis and Design of Three and Four Legged 400KV Steel Transmission Line Towers: Comparative Study" International Journal of Earth Sciences and Engineering 691 ISSN 0974-5904, Volume 04, No 06 SPL, October 2011, pp 691-694
- [2] V. Lakshmi1, A. Rajagopala Rao "Effect Of Medium Wind Intensity On 21M 132kV Transmission Tower" ISSN: 2250-3676 Volume-2, Issue-4, 820 – 824

- [3] M.Selvaraj, S.M.Kulkarni, R.Ramesh Babu “Behavioral Analysis of built up transmission line tower from FRP pultruded sections” ISSN 2250-2459, Volume 2, Issue 9, september 2012
- [4] S.Christian Johnson 1 G.S.Thirugnanam “Experimental study on corrosion of transmission line tower foundation and its rehabilitation” International Journal Of Civil And Structural Engineering ISSN 0976 – 4399 Volume 1, No 1, 2010
- [5] F. Albermani, M. Mahendran and S. Kitipornchai “Upgrading of Transmission Towers Using a Diaphragm Bracing System” International Journal Of Civil And Structural Engineering Volume2, No2, 2008
- [6] N.PrasadRao, G.M.SamuelKnight, S.J.Mohan, N. Lakshmanan “Studies on failure of transmission line towers in testing”
- [7] G.Visweswara Rao “ Optimum Designs For Transmission Line Towers” Computer & Structures vol.57.No.1.pp.81-92, 1995
- [8] Indian Standards,”Use of structural steel in overhead transmission line tower”,IS 802(part 1):1967, Bureau of Indian Standards , New Delhi.
- [9] Indian Standards,”General construction in steel”IS 800:2007, Bureau of Indian Standards , New Delhi
- [10] Indian Standards,”Aluminium conductors for overhead transmission purposes”IS 398(part II):1976, Bureau of Indian Standards , New Delhi.
- [11] Indian Standards,”Galvanised stay strand (second revision)”IS 2141:1779, Bureau of Indian Standards New Delhi.

Study of Failure Modes of Rolling Bearings: A Review

Mr. Nikhil D. Moundekar¹, Prof. B.D. Deshmukh²

^{1,2}(Department of Mechanical Engineering, Y.C.C.E., Nagpur University, India)

ABSTRACT: In an industry, the failure of bearing is one of the main causes responsible for machining breakdowns. Rolling bearings consist of bearing rings, rolling elements and cages for the support of rolling elements. Bearing life refers to the total number of revolutions (or time period) a bearing performs satisfactorily under stated conditions before failure. The typical failure modes are crack, improper lubrication and greasing, and improper loading of bearing on to the shaft. The work presented here involves various modes of failures and diagnoses of damaged rolling bearings.

Keywords: Failure, Lubrication, Pitting, Rolling Bearing Temperature, Wearing.

I. INTRODUCTION

This paper comprises of study of various modes of failure of rolling bearings along with their diagnosis. The bearing failure is one of the main reasons why the production is low in an industry. Rolling element bearings are widely used in an industry. Many problems associated with machineries are attributed due to the bearing failures. In order to reduce down time and to maintain product quality in a highly automated factory, it is essential to detect bearing status. Bearing damage is generally accompanied by a gradual deterioration in the operating behavior. Typical causes are material flaking of the contact surfaces in cases of fatigue damage. In order to prevent major damage it is generally sufficient for the operating personnel to detect uneven running or unusual noise in the bearing system.

Investigation of rolling bearing damages has been discussed below. It will help to understand about various behaviors of bearing.

II. INVESTIGATION OF ROLLING BEARING DAMAGE

Bearing damage can be analyzed by studying:

- The operating behavior of bearing arrangement and machine
- The condition of the dismantled bearing.

Symptoms	Source of Trouble	Examples
Uneven running	<ul style="list-style-type: none"> • Damaged rings or rolling elements • Contamination • Excessive clearance 	<p><u>Motor vehicles:</u> increased wheel wobble and vibration of steering system</p> <p><u>Fans:</u> increasing vibration</p> <p><u>Sawmills:</u> increasing knocking in connecting rods.</p>
Reduced working accuracy	<ul style="list-style-type: none"> • Wear due to contaminants or insufficient lubrication • Damaged rings or rolling elements • Changed adjustments (clearance or preload) 	<p><u>Lathe:</u> Gradual development of chatter marks on work piece</p> <p><u>Grinders:</u> Waviness of ground surface</p> <p><u>Cold rolling mill:</u> periodic surface defects on rolled material such as stretcher strains, ghost lines, etc.</p>
Uncommon running noise: Whining or high pitched noise	Insufficient operating clearance	Electric motors, gears; with gearboxes, the bearing noise is hard to identify since it is generally drowned in the running noise of the gears.
Low pitched rumbling or irregular noise	<ul style="list-style-type: none"> • Excessive operating clearance • Damaged running surfaces 	

	<ul style="list-style-type: none"> • Contamination • Inadequate lubricant 	
Gradual change in running noise	<ul style="list-style-type: none"> • Changes in operating clearance caused by temperature • Damaged raceway (from contamination or fatigue) 	

III. UNUSUAL OPERATING BEHAVIOR

The surest way to detect sudden bearing damage is to monitor the bearing temperature. Sudden damage is for example a consequence of lubrication breakdown.

3.1 Normal temperature behavior:

After commencement of bearing operation, the temperature which is generally measured at the outer ring gradually approaches a constant value (steady state temperature).

3.2 Disturbed behavior:

Temperature surge (interrupted lubricant supply, severe bearing damage, impeded running and danger of overheating). Increase of steady state temperature (deterioration of lubrication).

IV. EXAMINATION OF DISMOUNTED ROLLING BEARINGS

4.1 Determination of operating data:

- 4.1.1 application
- 4.1.2 bearing arrangement
- 4.1.3 speed
- 4.1.4 load
- 4.1.5 surrounding parts
- 4.1.6 environmental conditions
- 4.1.7 lubrication
- 4.1.8 sealing

4.2 Examination of the bearing environment

- 4.2.1 cleanliness inside and outside of seals
- 4.2.2 forces required to remove the securing components

4.3 Taking of lubricant samples

- 4.3.1 grease lubrication
- 4.3.2 oil lubrication

4.4 Marking of the bearings

- 4.4.1 mark position of rings relative to shaft and housing
- 4.4.2 mark or tie together parts of separable bearings
- 4.4.3 indicate on tags, mounting location of bearing

4.5 Examination of the seats

- 4.5.1 dismantling forces
- 4.5.2 dimensional tolerances of shaft and housing
- 4.5.3 form tolerances of seats (oval deformation)
- 4.5.4 roughness of seats (reduction of interference)
- 4.5.5 fretting corrosion

4.6 Assessment of the complete bearing:

Inspect:

- 4.6.1 general condition i.e. mounting marks, fretting corrosion, ring fractures, dimensional accuracy
- 4.6.2 condition of seals and dust shields
- 4.6.3 condition of cage
- 4.6.4 manual rotation
- 4.6.5 measuring of bearing clearance

4.7 Inspection of bearing components.

V. TYPICAL ROLLING BEARING DAMAGE

Rolling bearing damage may result in a complete failure of the rolling bearing at least, however, in a reduction in operating efficiency of the bearing arrangement. Bearing damage does not always originate from the bearing alone. Damage due to bearing defects in material or workmanship is exceptional.

Typical reasons for rolling bearing damage:

- 1. Inexpert mounting:**
 - a. Incorrect mounting method, wrong tools
 - b. Contamination
 - c. too tight fit
 - d. too loose fit
 - e. misalignment
- 2. Abnormal conditions during operation:**
 - a. overloads, absence of load
 - b. vibrations
 - c. excessive speeds
- 3. Unfavorable environmental influences:**
 - a. external heat
 - b. dust, dirt
 - c. passage of electric current
 - d. humidity
 - e. aggressive media
- 4. Inadequate lubrication:**
 - a. unsuitable lubricant
 - b. lack of lubricant
 - c. over lubrication

5.1 Rolling Element Indentations, Score Marks

5.1.1 Rolling element indentations:

Symptoms:

Indentations at rolling element pitch in the raceways of non-separable bearings.

Cause:

Mounting forces were applied through the rolling elements (wrong mounting sequence, inadequate tools).

Remedy:

Mount the tight fitted ring first. In the case of tight fits for both rings mount them simultaneously with the aid of a suitable disc.

5.1.2 Score marks:

Symptoms:

Score marks at rolling element pitch parallel to the axis in raceways of separable bearings.

Cause:

The ring was forced out-of-square into the rolling element set.

Remedy:

Prevent misalignment during mounting of separable bearings. Assemble parts at the save time turning them relative to each other. Use mounting sleeve, if necessary.

5.2 Foreign Particle Indentations:

Symptoms:

- i. shallow indentations with very low raised edges caused by soft particles
- ii. Deep indentations with higher raised edges caused by hard particles; significant danger of premature fatigue
- iii. Many small indentations with high raised edges caused by brittle particles.

Causes:

- i. Dirty mounting conditions
- ii. Penetration of contaminants (defective sealing)
- iii. Contaminated lubricant

Remedy:

- i. Cleanliness during mounting and maintenance of the rolling bearings
- ii. Use of suitable seals, replacement of defective seals
- iii. Periodic exchange of lubricant (washing-out of the bearings).

5.3 Corrosion Damage:

5.3.1 Corrosion due to Humidity (Rust):

Symptoms:

Brownish discoloration of the complete bearing surface, consequential wear and premature fatigue, originating from the rust pits.

Causes:

- i. Unsuitable storage (more than 60% relative air humidity in the warehouse)
- ii. Extreme temperature vibrations (condensation moisture)
- iii. Seal failure (accelerated by the abrasive action of dirt)
- iv. Unsuitable lubricant

Remedy:

- i. Storage conditions to comply with the specifications of the rolling bearing manufacturer
- ii. Improvement of the seal
- iii. Lubricant with corrosion inhibitors

5.3.2 Corrosion due to Aggressive Media:

Symptoms:

Generally black etching pits

Causes:

- i. Unsuitable storage (aggressive chemicals stored in the same room)
- ii. Seal failure
- iii. Unsuitable lubricant

Remedy:

- i. Storage conditions to comply with the specification of rolling bearing manufacturer
- ii. Lubricant with corrosion inhibitors.

5.4 Vibrating with Bearing Stationary:

Symptoms:

Marks in the raceway surface at rolling element pitch. Compared with the marks caused by the incorrect mounting they have no raised edges.

Cause:

Vibrations (minute movements) of stationary machines in the areas of the components in rolling contact causing wear.

Remedy:

Operate endangered machines continuously at low speeds; use safety devices during transport which unload or preload the bearings.

5.5 Fretting Corrosion:

Symptoms:

Wear at the fitting surface (bore, outside diameter), possible consequences might be (a). Fatigue fracture of rotating components (generally shafts). (b). Impended floating bearing function of the stationary components (generally housings).

Causes:

- i. Relative movements between components with too loose a fit
- ii. Shaft bending, housing deformation.

Remedy:

- i. Tight fits
- ii. Rigid shaft (housing)
- iii. Bearing seat coating.

5.6 Craters and Fluting due to Passage of Electric Current:

5.6.1 Craters:

Symptoms:

Craters in the raceway due to local melting at the contact area of the parts in rolling contact, sometimes several craters are generated in a row.

Cause:

Arcing, e.g. during welding or in case of earth failure.

Remedy:

During electro welding, do not direct current through the bearing (earthing).

5.6.2 Fluting:

Symptoms:

Brownish marks over the entire raceway circumference parallel to the axis

Cause:

Prolonged passage of alternating or direct current, even low currents cause marking.

Remedy:

Prevent current flow through the bearing (earthing, isolation).

5.7 Cage Damage:

5.7.1 Cage Damage due to Vibrations:

Symptoms:

- i. Loosening of the rivets, rivet fracture.
- ii. Fracture of the cage pockets

Cause:

Vibrations or impacts in addition to the normal cage loads, e.g. in vibration machinery or vehicles

Remedy:

During electro welding, do not direct current through the bearing (earthing).

5.7.2 Damage due to Misalignment:

Symptoms:

Heavy wear at the crosspieces between the cage pockets, deformation or fracture may occur.

Causes:

Inclination of the rings relative to each other, e.g. in the case of ball bearings under combined load resulting in different circumferential speeds of the rolling elements. High cage load in the circumferential direction, especially in case of insufficient lubrication.

Remedy:

Prevent misalignment by employing self-aligning bearings, or use bearings with polyamide cages.

5.8 Wear Damage:

Symptoms:

Roughening of the contact areas between rolling elements and raceways, abrasion of metal, increased bearing clearance or reduced preload.

Causes:

Insufficient load carrying lubricant film (inadequate, aged or contaminated lubricant); wear is promoted by foreign particles and abrasion.

Remedy:

Sufficient load carrying lubricant film (higher viscosity, EP additives), shorter lubricating intervals, improved sealing.

5.9 Seizure under High Load:

Symptoms:

Localized welding of the components in rolling contact (metal particles are torn away and applied to the opposite surface); bearings with a high proportion of sliding contact friction (tapered roller bearings, spherical roller thrust bearings) are particularly susceptible.

Causes:

- i. Starved lubrication under high load and speed (operating viscosity too low)
- ii. Starved lubrication under high load and low speed due to insufficient hydrodynamic lubricating film between roller face and lip
- iii. Too high preload of the bearing arrangement
- iv. Detrimental preload due to heat expansion
- v. Skewing of rollers, e.g. in case of raceway wears.

Remedy:

- i. Improvement of the lubrication (lubricant, EP additives, lubricant quantity, lubricant supply)
- ii. Reduction of the preload or increase of the axial clearance.

5.10 Skidding Damage:

Symptoms:

Roughening of raceways and rolling elements, wear resulting from seizure.

Causes:

Rolling element sliding on the raceway in the case of low bearing loads and in the case of starved lubrication.

Remedy:

- i. Preloading of the bearings, e.g. with springs
- ii. Sufficiently high load during test run
- iii. Improvement of the lubrication.

5.11 Fatigue Damage:

5.11.1 Classical Fatigue:

Symptoms:

Subsurface cracks of raceway and rolling elements, material flaking (relatively deep pitting), undamaged areas of the raceway indicate good lubrication in the early stage of the damage.

Cause:

Fatigue life of a dynamically stressed bearing being reached.

Remedy:

Bearing must be replaced.

5.11.2 Fatigue due to Insufficient Lubrication:

Symptoms:

Large-area, superficial pitting, originating from the surface. Undamaged areas of the raceway are grey.

Cause:

Insufficient lubrication, resulting in an increase in friction and material stressing at the raceway surface.

Remedy:

Provision of load carrying lubricant film (EP additives, if necessary), increase in lubricant quantity.

5.11.3 Fatigue due to the Surface Distress:

Symptoms:

Material flaking, widening in the direction of cycling.

Cause:

Damage to the raceway, hard particle indentations is particularly hazardous.

Remedy:

- i. Cleanliness and care during mounting
- ii. Improvement in the sealing
- iii. Clean lubricant.

5.11.4 Fatigue to Local Overhead:

Symptoms:

Contact ellipse "cut off" by the raceway boundary of a ball bearing. Fatigue damage at the edges of rolling element and track of roller bearings.

Cause:

- i. Mainly moment load
- ii. Misalignment of the bearing rings in misaligned housing bores or at out-of-square abutment surfaces
- iii. Shaft deflection.

5.11.5 Fatigue due to Wear:

Symptoms:

Localized flaking, e.g. of rolling elements.

Cause:

Alteration in the geometry of components in rolling contact due to wear: e.g. in the case of contaminated lubricant or ingress of foreign particles through defective seals; consequence: local overhead.

Remedy:

- i. Frequent change of lubricant
- ii. Filtering of contaminated oil
- iii. Improved sealing
- iv. Early replacement of worn seals.

5.12 Damage due to Overheating:

The cause of damage is difficult to determine from the damage pattern of an overheated bearing.

Symptoms:

Temperature surge leading to catastrophic failure due to bearing seizure.

Causes:

In addition to impeded running due to cage fracture there are the following causes:

- i. Insufficient clearance under operating conditions, especially of high speed bearings
- ii. Over lubrication
- iii. Starved lubrication (inadequate viscosity, interrupted supply).

Remedy:

- i. Increase bearing clearance or reduce preload until steady state temperature is reached
- ii. Avoid lubricant retention within the bearing (provide outlets)
- iii. Use adequate lubricant, check lubricating unit.

VI. CONCLUSION

The main aim of this review paper is to have a proper understanding of different bearing failures, their symptoms, causes and remedies over them. The first indication of rolling bearing damage is an unusual operating behavior of the bearing system. The above discussion of damaged bearings reveals a wide and varied range of phenomena. The inspection of bearing itself is frequently insufficient to pinpoint the cause of damage, it is also necessary to consider the surrounding components, the lubrication and sealing as well as the operating and environmental conditions.

Acknowledgements

We wish to express our gratitude to Mr. Samin Raza Zaidi, INDUS Paper Boards Pvt. Ltd., Nagpur for valuable discussions and guidelines concerning the manuscript.

REFERENCES

Journal Papers:

- [1] K. Gurumoorthy and Arindam Ghosh, "Failure Investigation of a Taper Roller Bearing: A Case Study", *Engineering Failure Analysis*, 30 April, 2013, Elsevier.
- [2] D. Scott, "Bearing Failures Diagnosis and Investigation", *Wear*, 25(1973) 199-213, Elsevier.
- [3] Iain Le May, "Case Studies of Three Fatigue Failure Evaluations in Aircraft", *Fatigue 2010, Procedia Engineering 2 (2010) 59-64*.
- [4] Viktor Gerdun, Tomaz Sedmak, Viktor Sinkovec, Igor Kovse and Bojan Sene, "Failure of Bearings and Axels in Railway Freight Wagons", *Engineering Failure Analysis (14)2007 884-894, Elsevier*.
- [5] K. Gurumoorthy, Bradley D. Faye and Arindam Ghosh, "Handling Abuse Causes Premature Bearing Failures", *Engineering Failure Analysis*, 13 June, 2013, Elsevier.
- [6] T. Williams, X. Ribadeneira, S. Billington and T. Kurfess, "Rolling Element Bearing Diagnostics in Run-To-Failure Lifetime Testing", *Mechanical Systems and Signal Processing (2001) 15(5), 979-993*.

Data Leakage Detection using Distribution Method

Anis Sultana Syed, Mini

Dept of CS, Nimra College of Engineering and Tech...

ABSTRACT: Modern business activities rely on extensive email exchange. Email leakages have become widespread, and the severe damage caused by such leakages constitutes a disturbing problem for organizations. We study the following problem: A data distributor has given sensitive data to a set of supposedly trusted agents (third parties). If the data distributed to third parties is found in a public/private domain then finding the guilty party is a nontrivial task to distributor. Traditionally, this leakage of data is handled by water marking technique which requires modification of data. If the watermarked copy is found at some unauthorized site then distributor can claim his ownership. To overcome the disadvantages of using watermark [2], data allocation strategies are used to improve the probability of identifying guilty third parties. The distributor must assess the likelihood that the leaked came from one or more agents, as opposed to having been independently gathered by other means. In this project, we implement and analyze a guilt model that detects the agents using allocation strategies without modifying the original data. The guilty agent is one who leaks a portion of distributed data. We propose data allocation strategies that improve the probability of identifying leakages. In some cases we can also inject "realistic but fake" data record to further improve our chances of detecting leakage and identifying the guilty party. The algorithms implemented using fake objects will improve the distributor chance of detecting guilty agents. It is observed that by minimizing the sum objective the chance of detecting guilty agents will increase. We also developed a framework for generating fake objects.

Keywords: Sensitive Data, Fake Objects, Data Allocation Strategies

I. INTRODUCTION

Demanding market conditions encourage many companies to outsource certain business processes (e.g. marketing, human resources) and associated activities to a third party. This model is referred as Business Process Outsourcing (BPO) and it allows companies to focus on their core competency by subcontracting other activities to specialists, resulting in reduced operational costs and increased productivity. Security and business assurance are essential for BPO. In most cases, the service providers need access to a company's intellectual property and other confidential information to carry out their services. For example a human resources BPO vendor may need access to employee databases with sensitive information (e.g. social security numbers), a patenting law firm to some research results, a marketing service vendor to the contact information for customers or a payment service provider may need access to the credit card numbers or bank account numbers of customers.

The main security problem in BPO is that the service provider may not be fully trusted or may not be securely administered. Business agreements for BPO try to regulate how the data will be handled by service providers, but it is almost impossible to truly enforce or verify such policies across different administrative domains. Due to their digital nature, relational databases are easy to duplicate and in many cases a service provider may have financial incentives to redistribute commercially valuable data or may simply fail to handle it properly. Hence, we need powerful techniques that can detect and deter such dishonest.

We study nonobtrusive techniques for detecting leakage of a set of objects or records. Specifically, we study the following scenario: After giving a set of objects to agents, the distributor discovers some of those same objects in an unauthorized place. (For example, the data may be found on a web site, or may be obtained through a legal discovery process.) At this point the distributor can assess the likelihood that the leaked data came from one or more agents, as opposed to having been independently gathered by other means. We develop a model for assessing the "guilt" of agents. We also present algorithms for distributing objects to agents, in a way that improves our chances of identifying a leaker. Finally, we also consider the option of adding "fake" objects to the distributed set.

II. PROBLEM DEFINITION

Suppose a distributor owns a set $T = \{t_1, t_m\}$ of valuable data objects. The distributor wants to share some of the objects with a set of agents U_1, U_2, \dots, U_n but does not wish the objects be leaked to other third parties. An agent U_i receives a subset of objects R_i which belongs to T , determined either by a sample request or an explicit request,

Sample Request $R_i = \text{SAMPLE}(T, m_i)$: Any subset of m_i records from T can be given to U_i . Explicit Request $R_i = \text{EXPLICIT}(T, \text{cond}_i)$: Agent U_i receives all the T objects that satisfy cond_i .

The objects in T could be of any type and size, e.g., they could be tuples in a relation, or relations in a database. After giving objects to agents, the distributor discovers that a set S of T has leaked. This means that some third party called the target has been caught in possession of S . For example, this target may be displaying S on its web site, or perhaps as part of a legal discovery process, the target turned over S to the distributor. Since the agents U_1, U_2, \dots, U_n , have some of the data, it is reasonable to suspect them leaking the data. However, the agents can argue that they are innocent, and that the S data was obtained by the target through other means.

2.1 Agent Guilt Model

Suppose an agent U_i is guilty if it contributes one or more objects to the target. The event that agent U_i is guilty for a given leaked set S is denoted by G_i / S . The next step is to estimate $\Pr\{G_i / S\}$, i.e., the probability that agent G_i is guilty given evidence S .

To compute the $\Pr\{G_i / S\}$, estimate the probability that values in S can be “guessed” by the target. For instance, say some of the objects in t are emails of individuals. Conduct an experiment and ask a person to find the email of say 100 individuals, the person may only discover say 20, leading to an estimate of 0.2. Call this estimate as P_t , the probability that object t can be guessed by the target.

The two assumptions regarding the relationship among the various leakage events.

Assumption 1: For all $t, t' \in S$ such that $t \neq t'$ the provenance of t is independent of the provenance of t' . The term provenance in this assumption statement refers to the source of a value t that appears in the leaked set. The source can be any of the agents who have t in their sets or the target itself.

Assumption 2: An object $t \in S$ can only be obtained by the target in one of two ways. A single agent U_i leaked t from its own R_i set, or

The target guessed (or obtained through other means) t without the help of any of the n agents.

To find the probability that an agent U_i is guilty given a set S , consider the target guessed t_1 with probability p and that agent leaks t_1 to S with the probability $1-p$. First compute the probability that he leaks a single object t to S . To compute this, define the set of agents $V_t = \{U_i / t \in R_i\}$ that have t in their data sets. Then using Assumption 2 and known probability p , we have

$$\Pr\{\text{some agent leaked } t \text{ to } S\} = 1 - p \tag{1.1}$$

Assuming that all agents that belong to V_t can leak t to S with equal probability and using Assumption 2 obtain,

$$\Pr\{t \text{ leaked to } S\} = \frac{1 - p}{|V_t|} \quad \dots 1.2$$

$$0, \quad |V_t| \neq 0$$

Given that agent U_i is guilty if he leaks at least one value to S , with Assumption 1 and Equation 1.2 compute the probability $\Pr\{G_i / S\}$, agent U_i is guilty,

$$\Pr\{G_i / S\} = \prod_{t \in S \cap R_i} \left(1 - \frac{1-p}{|V_t|} \right) \tag{1.3}$$

2.2 Data Allocation Problem

The distributor “intelligently” gives data to agents in order to improve the chances of detecting a guilty agent. There are four instances of this problem, depending on the type of data requests made by agents and whether “fake objects” [4] are allowed. Agent makes two types of requests, called sample and explicit. Based on the requests the fake objects are added to data list. Fake objects are objects generated by the distributor that are not in set T . The objects are designed to look like real objects, and are distributed to agents together with the T objects, in order to increase the chances of detecting agents that leak data.

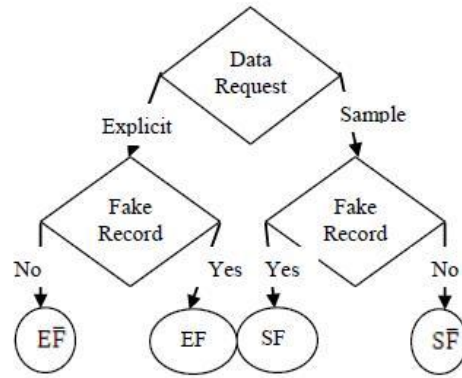


Fig 1: Leakage Problem Instances

The Fig. 1 represents four problem instances with the names EF , $E\%$, SF and $S\bar{F}$, where E stands for explicit requests, S for sample requests, F for the use of fake objects, and $\%$ for the case where fake objects are not allowed.

The distributor may be able to add fake objects to the distributed data in order to improve his effectiveness in detecting guilty agents. Since, fake objects may impact the correctness of what agents do, so they may not always be allowable. Use of fake objects is inspired by the use of “trace” records in mailing lists. The distributor creates and adds fake objects to the data that he distributes to agents. In many cases, the distributor may be limited in how many fake objects he can create.

In EF problems, objective values are initialized by agent’s data requests. Say, for example, that $T = \{t_1, t_2\}$ and there are two agents with explicit data requests such that $R_1 = \{t_1, t_2\}$ and $R_2 = \{t_1\}$. The distributor cannot remove or alter the R_1 or R_2 data to decrease the overlap $R_1 \cap R_2$. However, say the distributor can create one fake object ($B = 1$) and both agents can receive one fake object ($b_1 = b_2 = 1$). If the distributor is able to create more fake objects, he could further improve the objective.

2.3 Optimization Problem

The distributor’s data allocation to agents has one constraint and one objective. The distributor’s constraint is to satisfy agents’ requests, by providing them with the number of objects they request or with all available objects that satisfy their conditions. His objective is to be able to detect an agent who leaks any portion of his data.

We consider the constraint as strict. The distributor may not deny serving an agent request and may not provide agents with different perturbed versions of the same objects. The fake object distribution as the only possible constraint relaxation

The objective is to maximize the chances of detecting a guilty agent that leaks all his data objects.

The $\Pr \{G_j/S = R_i\}$ or simply $\Pr \{G_j/R_i\}$ is the probability that U_j agent is guilty if the distributor discovers a leaked table S that contains all R_i objects. The difference functions

$\Delta(_, _)*$ is defined as:

$$\Delta(_, _)* = \Pr \{G_i/R_i\} - \Pr \{G_j/R_i\} \tag{1.4}$$

1) *Problem definition:* Let the distributor have data requests from n agents. The distributor wants to give tables R_1, \dots, R_n to agents U_1, \dots, U_n respectively, so that

Distribution satisfies agents’ requests; and

Maximizes the guilt probability differences (i, j) for all $i, j = 1 \dots n$ and $i \neq j$.

Assuming that the R_i sets satisfy the agents’ requests, we can express the problem as a multi-criterion 2) *Optimization problem:*

$$\text{Maximize } (\dots, (i, j), \dots) \quad i \neq j \tag{1.5}$$

(over R_1, \dots, R_n)

The approximation [3] of objective of the above equation does not depend on agent’s probabilities and therefore minimize the relative overlap among the agents as

$$\text{Minimize } (\dots, \dots) \quad i \neq j \tag{1.6}$$

(over R_1, \dots, R_n)

This approximation is valid if minimizing the relative overlap, $\frac{|R_i \cap R_j|}{|R_i|}$, maximizes (i, j) .

2.4 Objective Approximation

In case of sample request, all requests are of fixed size. Therefore, maximizing the chance of detecting a guilty agent that leaks all his data by minimizing, $\frac{|R_i \cap R_j|}{|R_i|}$ is equivalent to minimizing $(|R_i \cap R_j|)$. The minimum

value of $(|R_i \cap R_j|)$ maximizes $\Pi(|R_i \cap R_j|)$ and (i, j) , since $\Pi(|R_i|)$ is fixed.

∩

If agents have explicit data requests, then overlaps $|R_i \cap R_j|$ are defined by their own requests and $|R_i \cap R_j|$ are fixed. Therefore, minimizing $|R_i \cap R_j|$ is equivalent to maximizing $|R_i|$ (with the addition of

fake objects). The maximum value of $|R_i|$ minimizes $\Pi(|R_i|)$ and maximizes (i, j) , since $\Pi(|R_i \cap R_j|)$ is fixed.

Our paper focuses on identifying the leaker. So we propose to trace the ip address of the leaker. The file is sent to the agents in the form of email attachments which need a secret key to download it. This secret key is generated using a random function and send to the agent either on the mobile number used at registration or to the other global email service account such as gmail.

Whenever the secret key mismatch takes place the fake file gets downloaded. To further enhance our objective approximation ip address tracking [5][6][7] is done of the system where fake object is downloaded. Various commands are available for getting ip address information. Ping, tracert, nslookup, etc anyone may be used to get it. The ip address is traced with the time so as to overcome problem of dynamic ip addressing. But as we are doing this for an organisation there is no problem of dynamic ip. Or else if looking for the ip address universally it is unique for that period of time therefore it can be traced to unique system of the leaker.

III. ALLOCATION STRATEGIES

In this section the allocation strategies [1] solve exactly or approximately the scalar versions of Equation 1.7 for the different instances presented in Fig. 1. In Section A deals with problems with explicit data requests and in Section B with problems with sample data requests.

3.1 Explicit Data Request

In case of explicit data request with fake not allowed, the distributor is not allowed to add fake objects to the distributed data. So Data allocation is fully defined by the agent's data request.

In case of explicit data request with fake allowed, the distributor cannot remove or alter the requests R from the agent. However distributor can add the fake object. In algorithm for data allocation for explicit request, the input to this is a set of request R_1, R_2, \dots, R_n from n agents and different conditions for requests. The e-optimal algorithm finds the agents that are eligible to receiving fake objects. Then create one fake object in iteration and allocate it to the agent selected. The e-optimal algorithm minimizes every term of the objective summation by adding maximum number b_i of fake objects to every set R_i yielding optimal solution.

Step 1: Calculate total fake records as sum of fake records allowed. Step 2: While total fake objects > 0

Step 3: Select agent that will yield the greatest improvement in the sum objective

$$\text{argmax } \left(\frac{1}{|R_i|} - \frac{1}{|R_i|+1} \right) \sum_j R_i \cap R_j$$

i.e. i =

Step 4: Create fake record

Step 5: Add this fake record to the agent and also to fake record set. Step 6: Decrement fake record from total fake record set.

Algorithm makes a greedy choice by selecting the agent that will yield the greatest improvement in the sum-objective.

3.2 Sample Data Request

With sample data requests, each agent U_i may receive any T from a subset out of $\binom{T}{m}$ different ones.

Hence, there are $\prod_{i=1}^n \binom{T}{m}$ different allocations. In every allocation, the distributor can permute T objects and keep the same chances of guilty agent detection. The reason is that the guilt probability depends only on which agents have received the leaked objects and not on the identity of the leaked

objects. Therefore, from the distributor's perspective there $\prod_{i=1}^n \binom{T}{m} / |T|$ are different allocations. An object allocation that satisfies requests and ignores the distributor's objective is to give each agent a unique subset of T of size m. The s-max algorithm allocates to an agent the data record that yields the minimum increase of the maximum relative overlap among any pair of agents. The s-max algorithm is as follows.

Step 1: Initialize $\text{Min_overlap} \leftarrow 1$, the minimum out of the maximum relative overlaps that the allocations of different objects to U

i

Step 2: for $k \in \{k \mid t_k \in R_i\}$ do

Initialize $\text{max_rel_ov} \leftarrow 0$, the maximum relative overlap between R_i and any set R_j that the allocation of t to U

Step 3: for all $k_j = 1, \dots, n : j = i$ and $t_k \in R_j$ do Calculate absolute overlap as

$\text{abs_ov} \leftarrow |R_i \cap R_j| + 1$ Calculate relative overlap as $\text{rel_ov} \leftarrow \text{abs_ov} / \min(m_i, m_j)$

Step 4: Find maximum relative as $\text{max_rel_ov} \leftarrow \text{MAX}(\text{max_rel_ov}, \text{rel_ov})$ If $\text{max_rel_ov} \leq \text{min_overlap}$ then $\text{min_overlap} \leftarrow \text{max_rel_ov}$

$\text{ret_k} \leftarrow k$ Return ret_k

It can be shown that algorithm s-max is optimal for the sum-objective and the max-objective in problems where $M \leq |T|$ and $n < |T|$. It is also optimal for the max-objective if $|T| \leq M \leq 2|T|$ or all agents request data of the same size.

It is observed that the relative performance of algorithm and main conclusion do not change. If p approaches to 0, it becomes easier to find guilty agents and algorithm performance converges. On the other hand, if p approaches 1, the relative differences among algorithms grow since more evidence is needed to find an agent guilty.

The algorithm presented implements a variety of data distribution strategies that can improve the distributor's chances of identifying a leaker. It is shown that distributing objects judiciously can make a significant difference in identifying guilty agents, especially in cases where there is large overlap in the data that agents must receive.

IV. RELATED WORK

The presented guilt detection approach is related to the data provenance problem [8]: tracing the lineage of S objects implies essentially the detection of the guilty agents. Suggested solutions are domain specific, such as lineage tracing for data warehouses [9], and assume some prior knowledge on the way a data view is created out of data sources. Our problem formulation with objects and sets is more general and simplifies lineage tracing, since we do not consider any data transformation from R_i sets to S .

As far as the allocation strategies are concerned, our work is mostly relevant to watermarking that is used as a means of establishing original ownership of distributed objects. Watermarks were initially used in images, video and audio data [2] whose digital representation includes considerable redundancy. Our approach and watermarking are similar in the sense of providing agents with some kind of receiver-identifying information. However, by its very nature, a watermark modifies the item being watermarked. If the object to be watermarked cannot be modified then a watermark cannot be inserted.

In such cases methods that attach watermarks to the distributed data are not applicable. Finally, there are also lots of other works on mechanisms that allow only authorized users to access sensitive data. Such approaches prevent in some sense data leakage by sharing information only with trusted parties. However, these policies are restrictive and may make it impossible to satisfy agents' requests.

V. CONCLUSION

In doing a business there would be no need to hand over sensitive data to agents that may unknowingly or maliciously leak it. And even if we had to hand over sensitive data, in a perfect world we could watermark each object so that we could trace its origins with absolute certainty. However, in many cases we must indeed work with agents that may not be 100% trusted, and we may not be certain if a leaked object came from an agent or from some other source. In spite of these difficulties, we have shown it is possible to assess the likelihood that an agent is responsible for a leak, based on the overlap of his data with the leaked data and the data of other agents, and based on the probability that objects can be "guessed" by other means.

Our model is relatively simple, but we believe it captures the essential trade-offs. The algorithms we have presented implement a variety of data distribution strategies that can improve the distributor's chances of identifying a leaker. We have shown that distributing objects judiciously can make a significant difference in identifying guilty agents, especially in cases where there is large overlap in the data that agents must receive.

Our future work includes the investigation of agent guilt models that capture leakage scenarios that are not studied in this paper. For example, what is the appropriate model for cases where agents can collude and identify fake tuples? A preliminary discussion of such a model is available in. Another open problem is the

extension of our allocation strategies so that they can handle agent requests in an online fashion (the presented strategies assume that there is a fixed set of agents with requests known in advance).

REFERENCES

- [1]. Rudragouda G Patil, "Development of Data leakage Detection Using Data Allocation Strategies International Journal of Computer Applications in Engineering Sciences [VOL I, ISSUE II, JUNE 2011, [ISSN: 2231-4946].
- [2]. S. Czerwinski, R. Fromm, and T. Hodes. Digital music distribution and audio watermarking.
- [3]. L. Sweeney. Achieving k-anonymity privacy protection using generalization and suppression, 2002.
- [4]. S. U. Nabar, B. Marthi, K. Kenthapadi, N. Mishra, and R. Motwani. Towards robustness in query auditing. In VLDB '06.
- [5]. Stevens Le Blond, Chao Zhang Arnaud Legout, Keith Ross, Walid Dabbous, Exploiting P2P Communications to Invade Users' Privacy
- [6]. How to Trace an IP Address <http://www.wikihow.com/Trace-an-IP-Address>
- [7]. P. Buneman, S. Khanna, and W. C. Tan. Why and where: A characterization of data provenance. In J. V. den Bussche and V. Vianu, editors, Database Theory - ICDT 2001, 8th International Conference, London, UK, January 4-6, 2001, Proceedings, volume 1973 of Lecture Notes in Computer Science, pages 316-330. Springer, 2001

A Neighbor Coverage-Based Probabilistic Rebroadcast for Reducing Routing Overhead In Mobile Ad Hoc Networks

S. Divya¹, Dr. M. Rajaram², Dr. Selvakumar³

¹PG Scholar, Department of CSE Sri Ramakrishna Engineering College

²Professor Anna University Chennai

³Professor, Department Of SE (PG) Sri Ramakrishna Engineering College

ABSTRACT: Mobile ad hoc networks consist of a collection of mobile nodes without having a fixed infrastructure. Due to the infrastructure less network, there exist frequent link breakages which lead to frequent path failures and route discoveries. A mobile node blindly rebroadcasts the first received route request packets unless it has a route to the destination, and thus it causes the broadcast storm problem. So, rebroadcast is very costly and consumes too much network resource. In the existing System, different mechanisms are proposed for improving the routing performance. In the gossip-based routing overhead is reduced. However, when the network density is high, the gossip-based approach is limited. In the Dynamic Probabilistic Route Discovery scheme, each node determines the forwarding probability according to the number of its neighbors and the set of neighbors which are covered by the previous broadcast. So, coverage-based probabilistic rebroadcast protocol for reducing routing overhead in MANET propose a novel Ra rebroadcast delay to determine the rebroadcast order, and then it obtain the more accurate additional coverage ratio by sensing neighbor coverage knowledge. The advantages of the neighbor coverage knowledge and the probabilistic mechanism, which can significantly decrease the number of retransmissions so as to reduce the routing overhead, and can also improve the routing performance. To improve the quality of routing particularly in mobile ad hoc networks, improved routing protocol have been proposed such as Optimized Link State Routing Protocol (OLSR).

I. INTRODUCTION

Introduction about MANET

MANET stands for "Mobile Ad Hoc Network." A MANET is a type of adhoc network that can change locations and configure itself on the fly. Because MANETS are mobile, they use wireless connections to connect to various networks. This can be a standard Wi-Fi connection, or another medium, such as a cellular or satellite transmission.

Some MANETs are restricted to a local area of wireless devices, while others may be connected to the Internet. For example, A VANET (Vehicular Ad Hoc Network), is a type of MANET that allows vehicles to communicate with roadside equipment. While the vehicles may not have a direct Internet connection, the wireless roadside equipment may be connected to the Internet, allowing data from the vehicles to be sent over the Internet. The vehicle data may be used to measure traffic conditions or keep track of trucking fleets. Because of the dynamic nature of MANETs, they are typically not very secure, so it is important to be cautious what data is sent over a MANET.

A mobile ad hoc network (MANET) is self-configuring Infrastructureless network of mobile devices connected by wireless. Ad hoc is Latin and means "for this purpose". Each device in a MANET is free to move independently in any direction, and will therefore change its links to other devices frequently. Each must forward traffic unrelated to its own use, and therefore be a router. The primary challenge in building a MANET is equipping each device to continuously maintain the information required to properly route traffic. Such networks may operate by themselves or may be connected to the larger Internet. MANETs are a kind of Wireless ad hoc network that usually has a routable networking environment on top of a Link Layer ad hoc network.

The growth of 802.11/Wi-Fi wireless networking have made MANETs a popular research topic since the mid-1990s. Many academic papers evaluate protocols and their abilities, assuming varying degrees of mobility within a bounded space, usually with all nodes within a few hops of each other. Different protocols are then evaluated based on measures such as the packet drop rate, the overhead introduced by the routing protocol, end-to-end packet delays, network throughput etc. OLSR reduces control packets by selecting only partial

neighbor nodes for packet forwarding. OLSR is an optimization of a pure link state protocol in mobile ad hoc network, First it reduces a size of control packets. Second it minimize the flooding of the control traffic by using selecting node called multipoint relay. This technique reduces number of retransmission in flooding.

II. PROPOSED SYSTEM

In the proposed system, we introduce an innovative approach called neighbor coverage-based probabilistic rebroadcast protocol. Therefore,

- ✓ In order to effectively exploit the neighbor coverage knowledge, we need a novel rebroadcast delay to determine the rebroadcast order, and then we can obtain a more accurate additional coverage ratio.
- ✓ 2) In order to keep the network connectivity and reduce the redundant retransmissions, we need a metric named connectivity factor to determine how many neighbors should receive the RREQ packet.

After that, by combining the additional coverage ratio and the connectivity factor, we introduce a rebroadcast probability, which can be used to reduce the number of rebroadcasts of the RREQ packet, to improve the routing performance.

The main contributions of this paper

- Propose a novel scheme to calculate the rebroadcast delay. The rebroadcast delay is to determine the forwarding order. The node which has more common neighbors with the previous node has the lower delay. If this node rebroadcasts a packet, then more common neighbors will know this fact. Therefore, this rebroadcast delay enables the information that the nodes have transmitted the packet spread to more neighbors, which is the key to success for the proposed scheme.
- Propose a novel scheme to calculate the rebroadcast probability. The scheme considers the information about the uncovered neighbors (UCN), connectivity metric and local node density to calculate the rebroadcast probability.

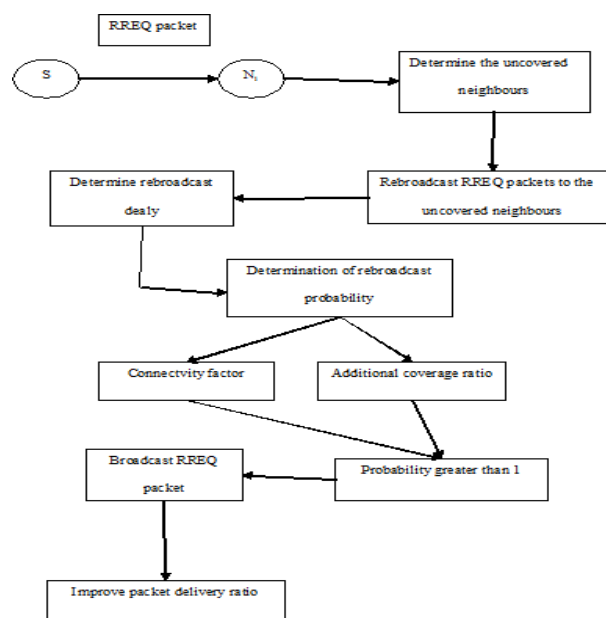
The rebroadcast probability is composed of two parts:

- ❖ additional coverage ratio, which is the ratio of the number of nodes that should be covered by a single broadcast to the total number of neighbors;
- ❖ Connectivity factor, which reflects the relationship of network connectivity and the number of neighbors of a given node.

Advantages of Proposed System

- Increase the packet delivery ratio
- Decrease the average end-to-end delay
- Decrease the number of retransmissions
- Improve the routing performance

III. ARCHITECTURE DIAGRAM



In this architecture source node sends RREQ packet to its N_i , it determine the uncovered neighbors and rebroadcast the RREQ packet to the uncovered neighbors. In order to effectively exploit the neighbor coverage knowledge, it need a novel rebroadcast delay to determine the rebroadcast order, and then it obtain a more accurate additional coverage ratio; In order to keep the network connectivity and reduce the redundant retransmissions, it need a metric named connectivity factor to determine how many neighbors should receive the RREQ packet. After that, by combining the additional coverage ratio and the connectivity factor, we introduce a rebroadcast probability, which can be used to reduce the number of rebroadcasts of the RREQ packet, to improve the routing performance.

3.1 Network module

An undirected graph $G(V, E)$ where the set of vertices V represent the mobile nodes in the network and E represents set of edges in the graph which represents the physical or logical links between the mobile nodes. Sensor nodes are placed at a same level. Two nodes that can communicate directly with each other are connected by an edge in the graph. Let N denote a network of m mobile nodes, N_1, N_2, \dots, N_m and let D denote a collection of n data items $d_1; d_2; \dots; d_n$ distributed in the network. For each pair of mobile nodes N_i and N_j , let t_{ij} denote the delay of transmitting a data item of unit-size between these two nodes.

3.2 Identification of Uncovered Neighbors Set

When node n_i receives an RREQ packet from its previous node s , it can use the neighbor list in the RREQ packet to estimate how many its neighbors have not been covered by the RREQ packet from s . If node n_i has more neighbors uncovered by the RREQ packet from s , which means that if node n_i rebroadcasts the RREQ packet, the RREQ packet can reach more additional neighbor nodes. To quantify this, we define the UnCovered Neighbors set $U(n_i)$ of node n_i as follows:

$$U(n_i) = N(n_i) - [N(n_i) \cap N(s)] - \{s\}$$

where $N(s)$ and $N(n_i)$ are the neighbors sets of node s and n_i , respectively. s is the node which sends an RREQ packet to node n_i . From this we obtain the initial UCN set.

3.3 Determination of Rebroadcast Delay

Due to broadcast characteristics of an RREQ packet, node n_i can receive the duplicate RREQ packets from its neighbors. Node n_i could further adjust the $U(n_i)$ with the neighbor knowledge. In order to sufficiently exploit the neighbor knowledge and avoid channel collisions, each node should set a rebroadcast delay. The rebroadcast delay $T_d(n_i)$ of node n_i is defined as follows:

$$T_p(n_i) = 1 - \frac{|N(s) \cap N(n_i)|}{|N(s)|}$$

$$T_d(n_i) = \text{Max Delay} \times T_p(n_i)$$

Where $T_p(n_i)$ is the delay ratio of node n_i , and MaxDelay is a small constant delay. $| \cdot |$ is the number of elements in a set. Stann et al. [9] proposed a Robust Broadcast Propagation (RBP) protocol to provide near-perfect reliability for flooding in wireless networks, and this protocol also has a good efficiency. The above rebroadcast delay is defined with the following reasons: First, the delay time is used to determine the node transmission order. To sufficiently exploit the neighbor coverage knowledge, it should be disseminated as quickly as possible. When node s sends an RREQ packet, all its neighbors $n_i, i = 1, 2, \dots, |N(s)|$ receive and process the RREQ packet. We assume that node n_k has the largest number of common neighbors with node s , according to (2), node n_k has the lowest delay.

3.4 Determination of Rebroadcast Probability

The node which has a larger rebroadcast delay may listen to RREQ packets from the nodes which have lower one. For example, if node n_i receives a duplicate RREQ packet from its neighbor n_j , it knows that how many its neighbors have been covered by the RREQ packet from n_j . Thus, node n_i could further adjust its UCN set according to the neighbor list in the RREQ packet from n_j . Then, the $U(n_i)$ can be adjusted as follows:

$$U(n_i) = [U(n_i) \cap N(n_j)].$$

After adjusting $U(n_i)$ the, the RREQ packet received from n_j is discarded. When the timer of the rebroadcast delay of node n_i expires, the node obtains the final UCN set. The nodes belonging to the final UCN set are the nodes that need to receive and process the RREQ packet. Note that, if a node does not sense any duplicate RREQ packets from its neighborhood, its UCN set is not changed, which is the initial UCN set. Now, we study how to use the final UCN set to set the rebroadcast probability.

3.4.1 Additional Coverage ratio

We define the additional coverage ratio ($R_a(n_i)$) of node n_i as

$$R_a(n_i) = \frac{|U(n_i)|}{|N(n_i)|}$$

This metric indicates the ratio of the number of nodes that are additionally covered by this rebroadcast to the total number of neighbors of node n_i . The nodes that are additionally covered need to receive and process the RREQ packet. As R_a becomes bigger, more nodes will be covered by this rebroadcast, and more nodes need to receive and process the RREQ packet, and, thus, the rebroadcast probability should be set to be higher.

3.4.2 Connectivity factor

We define the minimum $F_c(n_i)$ as a connectivity factor, which is

$$F_c(n_i) = \frac{N_c}{|N(n_i)|}$$

Where $N_c = 5.1774 \log n$, and n is the number of nodes in the network. when $|N(n_i)|$ is greater than N_c , $F_c(n_i)$ is less than 1. That means node is in the dense area of the network, then only part of neighbors of node n_i forwarded the RREQ packet could keep the network connectivity. And when $|N(n_i)|$ is less than N_c , $F_c(N_i)$ is greater than 1. That means node n_i is in the sparse area of the network, then node n_i should forward the RREQ packet in order to approach network connectivity.

Combining the additional coverage ratio and connectivity factor, we obtain the rebroadcast probability $pre(n_i)$ of node n_i .

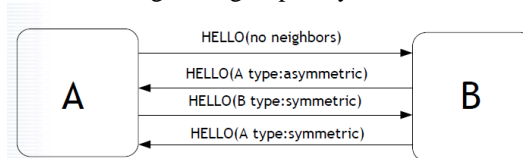
$$pre(n_i) = F_c(n_i) \cdot R_a(n_i).$$

Where, if the $pre(n_i)$ is greater than 1, we set the $pre(n_i)$ to 1.

Although the parameter R_a reflects how many next-hop nodes should receive and process the RREQ packet, it does not consider the relationship of the local node density and the overall network connectivity. The parameter F_c is inversely proportional to the local node density. That means if the local node density is low, the parameter F_c increases the rebroadcast probability, and then increases the reliability of the NCPR in the sparse area.

3.5 Neighbor Sensing:

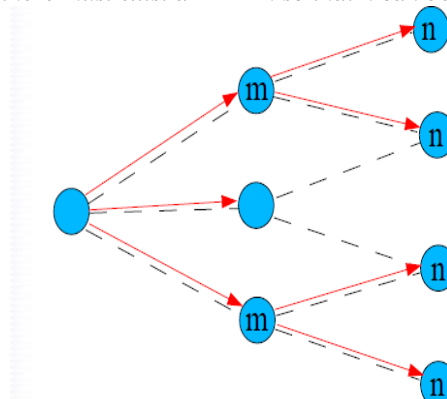
Neighbors and links are detected by HELLO messages. All nodes transmit HELLO messages on a given interval. These contain all heard-of neighbors grouped by status.

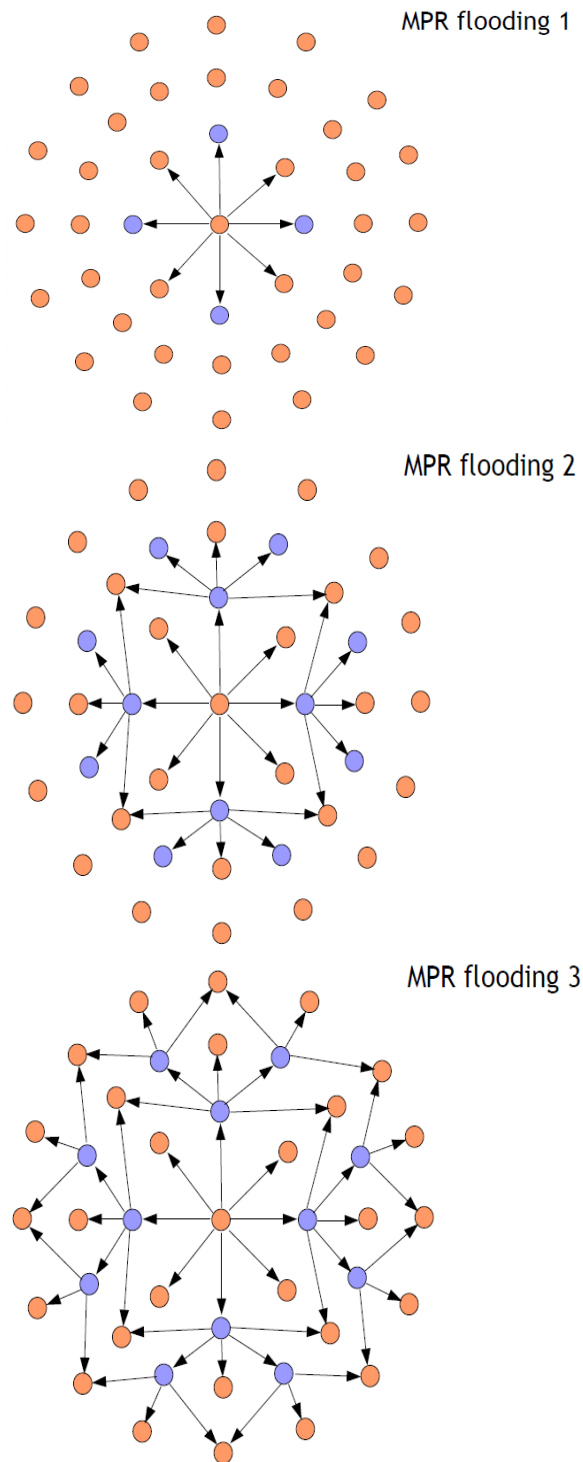


3.6 Multi point relay selection

Each node select its own multi point relays. Reduce the number of duplicate retransmissions while forwarding a broadcast packet. Restricts the set of nodes retransmitting a packet from all nodes(regular flooding) to a subset of all nodes. The size of this subset depends on the topology of the network. All nodes selects and maintains their own MPRs.

Rule: "For all 2 hop neighbors n there must exist a MPR m so that n can be contacted via m ."

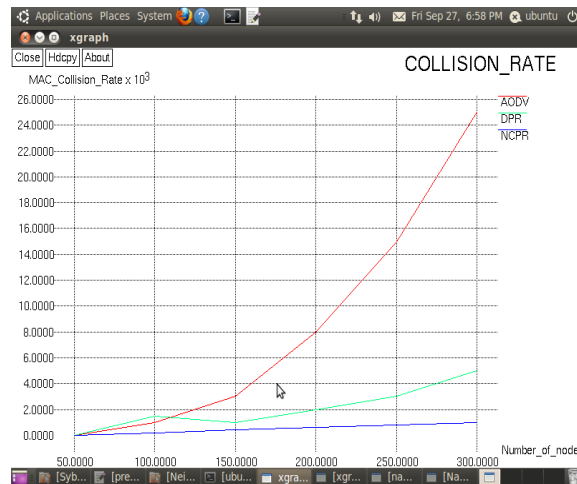




IV. PERFORMANCE EVALUATION

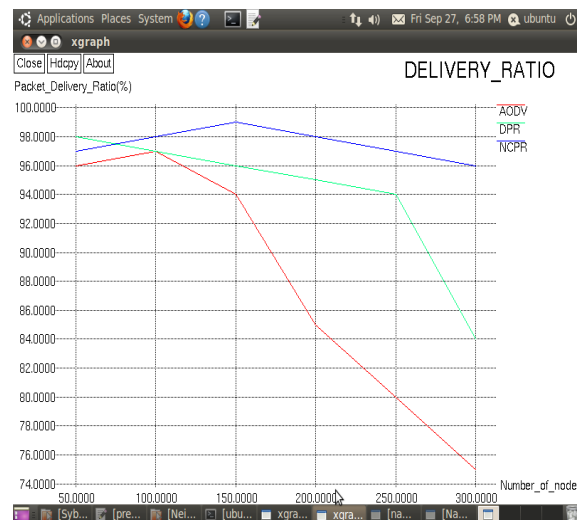
Finally in this module the performance of the existing and the proposed approaches were illustrated and evaluated. Finally, existing algorithms like Ad hoc On-demand Distance Vector Routing (AODV) and Dynamic Source Routing (DSR) and Proposed Neighbor coverage-based probabilistic rebroadcast (NCPR) protocol are compared. Based on the comparison and the result from experiment show the Neighbor coverage-based probabilistic rebroadcast (NCPR) protocol proposed approach works better than the other existing systems in terms of collision rate and packet delivery ratio.

4.1 Collision rate



The Collision rate is shown in this graph. In the X-axis number of nodes are taken. Y-axis Collision rate is taken. This graph clearly shows that the number of nodes are increases the collision rate is increases in existing methods. But in the proposed coverage based probabilistic rebroadcast protocol, the collision rate is decreases.

4.2 Delivery ratio



The Packet delivery ratio is shown in this graph. In the X-axis number of nodes is taken. Y-axis packet delivery ratio is taken. This graph clearly shows that the number of nodes is increases the packet delivery ratio is decreases in existing methods. But in the proposed coverage based probabilistic rebroadcast protocol, the packet delivery ratio is increases.

V. CONCLUSION AND FUTURE WORK

A neighbor coverage-based probabilistic rebroadcast protocol is used to reduce the routing overhead in the mobile ad hoc networks. Because of the random movement of the nodes in the mobile ad hoc networks, there is a frequent link breakage which leads to path failure and route discoveries. So, we use neighbor coverage knowledge, we propose a novel rebroadcast delay to determine the rebroadcast order and rebroadcast probability. To determine the rebroadcast probability we calculate additional coverage ratio and connectivity factor. So, we effectively decrease the number of retransmissions so as to reduce the routing overhead, and can also improve the routing performance.

For future work, we monitoring the links lifetime of the mobile nodes in the wireless network, in the past and in the present, to predict its behavior, in the future without considering directly parameters depending by underlying mobility model such as node speed or direction.

REFERENCES

- [1] C. Perkins, E. Belding-Royer, and S. Das, Ad Hoc On-Demand Distance Vector (AODV) Routing, IETF RFC 3561, 2003.
- [2] D. Johnson, Y. Hu, and D. Maltz, The Dynamic Source Routing Protocol for Mobile Ad Hoc Networks (DSR) for IPv4, IETF RFC 4728, vol. 15, pp. 153-181, 2007.
- [3] X. Wu, H.R. Sadjadpour, and J.J. Garcia-Luna-Aceves, "Routing Overhead as a Function of Node Mobility: Modeling Framework and Implications on Proactive Routing," Proc. IEEE Int'l Conf. Mobile Ad Hoc and Sensor Systems (MASS '07), pp. 1-9, 2007.
- [4] S.Y. Ni, Y.C. Tseng, Y.S. Chen, and J.P. Sheu, "The Broadcast Storm Problem in a Mobile Ad Hoc Network," Proc. ACM/IEEE MobiCom, pp. 151-162, 1999.
- [5] A. Mohammed, M. Ould-Khaoua, L.M. Mackenzie, C. Perkins, and J.D. Abdulai, "Probabilistic Counter-Based Route Discovery for Mobile Ad Hoc Networks," Proc. Int'l Conf. Wireless Comm. and Mobile Computing: Connecting the World Wirelessly (IWCMC '09), pp. 1335-1339, 2009.
- [6] B. Williams and T. Camp, "Comparison of Broadcasting Techniques for Mobile Ad Hoc Networks," Proc. ACM MobiHoc, pp. 194-205, 2002.
- [7] J. Kim, Q. Zhang, and D.P. Agrawal, "Probabilistic Broadcasting Based on Coverage Area and Neighbor Confirmation in Mobile Ad Hoc Networks," Proc. IEEE GlobeCom, 2004.
- [8] Z. Haas, J.Y. Halpern, and L. Li, "Gossip-Based Ad Hoc Routing," Proc. IEEE INFOCOM, vol. 21, pp. 1707-1716, 2002.
- [9] W. Peng and X. Lu, "On the Reduction of Broadcast Redundancy in Mobile Ad Hoc Networks," Proc. ACM MobiHoc, pp. 129-130, 2000.
- [10] A. Keshavarz-Haddady, V. Ribeiro, and R. Riedi, "DRB and DCCB: Efficient and Robust Dynamic Broadcast for Ad Hoc and Sensor Networks," Proc. IEEE Comm. Soc. Conf. Sensor, Mesh, and Ad Hoc Comm. and Networks (SECON '07), pp. 253-262, 2007.

Design of High Speed Low Power Multiplier Using Nikhilam Sutra with Help of Reversible Logic

Manjeet Singh Sankhwar, Rajesh Khatri

Department of Electronics & Instrumentation SGSITS Indore, India

ABSTRACT: Multipliers are vital components of any processor or computing machine. More often than not, performance of microcontrollers and Digital signal processors are evaluated on the basis of number of multiplications performed in unit time. Hence better multiplier architectures are bound to increase the efficiency of the system. Vedic multiplier is one such promising solution. Its simple architecture coupled with increased speed forms an unparalleled combination for serving any complex multiplication computations. Tagged with these highlights, implementing this with reversible logic further reduces power dissipation. Power dissipation is another important constraint in an embedded system which cannot be neglected. In this paper we bring out a Vedic multiplier known as "Nikhilam Sutra multiplier". The —Nikhilam Navatascaram Dasatah literally means —All from Nine and the last from Ten. The sutra basically means start from the left most digit and begin subtracting $_9$ ' from each of the digits; but subtract $_10$ ' from the last digit. This will be implemented using reversible logic, which is the first of its kind. This multiplier may find applications in Fast Fourier Transforms (FFTs), and other applications of DSP like imaging, software defined radios, wireless communications.

Index Terms: Reversible Logic, Nikhilam Sutra, vedic multiplier, Quantum cost, Total reversible logic implementation cost.

I. INTRODUCTION

Vedic mathematics is the ancient Indian system of mathematics which mainly deals with Vedic mathematical formulae and their application to various branches of mathematics. Vedic mathematics was reconstructed from the ancient Indian scriptures (Vedas) by Sri Bharati Krishna Tirtha after his research on Vedas. He constructed 16 sutras and 16 upa sutras after extensive research in Atharva Veda. The most famous among these 16 are Nikhilam Sutram, Urdhva Tiryakbhayam, and Anurupye. It has been found that Nikhilam is the most efficient among these. The beauty of Vedic mathematics lies in the fact that it reduces otherwise cumbersome looking calculations in conventional mathematics to very simple ones. This is so because the Vedic formulae are claimed to be based on the natural principles on which the human mind works. Hence multiplications in DSP blocks can be performed at faster rate. This is a very interesting field and presents some effective algorithms which can be applied to various branches of engineering. Digital signal processing (DSP) is the technology that is omnipresent in almost every engineering discipline. Faster additions and multiplications are the order of the day. Multiplication is the most basic and frequently used operations in a CPU. Multiplication is an operation of scaling one number by another. Multiplication operations also form the basis for other complex operations such as convolution, Discrete Fourier Transform, Fast Fourier Transforms, etc. With ever increasing need for faster clock frequency it becomes imperative to have faster arithmetic unit. Hence Vedic mathematics can be aptly employed here to perform multiplication.

Reversible logic is one of the promising fields for future low power design technologies. Since one of the requirements of all DSP processors and other hand held devices is to minimize power dissipation multipliers with high speed and lower dissipations are critical. This paper proposes an implementation of Reversible Nikhilam Multiplier which consists of two cardinal features. One is the fast multiplication feature derived from Vedic algorithm Nikhilam sutra and another is the reduced heat dissipation by the virtue of implementing the circuit using reversible logic gates. The paper is partitioned into Six sections. Section (ii) gives literature survey, Section (iii) deals with reversible logic. Section (IV) explains the Nikhilam sutra algorithm. Section (V) elaborates on the design aspects of Reversible Nikhilam vedic sutra Multiplier. Section (vi) Evaluation Conclusions and references follow.

II. LITERATURE SURVEY

Energy loss is an important consideration in digital circuit design. A part of this problem arises from the technological non ideality of switches and materials. The other part of the problem arises from Landauer's principle for which there is no solution. **Landauer's Principle states that logical computations that are not reversible necessarily generate $k \cdot T \cdot \ln(2)$ joules of heat energy, where k is the Boltzmann's Constant $k=1.38 \times 10^{-23}$ J/K, T is the absolute temperature** at which the computation is performed. Although this amount of heat appears to be small, Moore's Law predicts exponential growth of heat generated due to information lost, which will be a noticeable amount of heat loss in next decade. **Also by second law of thermodynamics any process that is reversible will not change its entropy.** On thermo dynamical grounds, the erasure of one bit of information from the mechanical degrees of a system must be accompanied by the thermalization of an amount of $k \cdot T \cdot \ln(2)$ joules of energy. The information entropy H can be calculated for any probability distribution. Similarly the thermodynamic entropy S refers to thermodynamic probabilities specifically. Thus gain in entropy always means loss of information, and nothing more. Design that does not result in information loss is called reversible. It naturally takes care of heat generated due to information loss. Bennett showed that zero energy dissipation would be possible only if the network consists of reversible logic gates, Thus reversibility will become an essential property in future circuit design technologies.

III. REVERSIBLE LOGIC

Reversible logic is a promising computing design paradigm which presents a method for constructing computers that produce no heat dissipation. Reversible computing emerged as a result of the application of quantum mechanics principles towards the development of a universal computing machine. Specifically, the fundamentals of reversible computing are based on the relationship between entropy, heat transfer between molecules in a system, the probability of a quantum particle occupying a particular state at any given time, and the quantum electrodynamics between electrons when they are in close proximity. The basic principle of reversible computing is that a bi-jective device with an identical number of input and output lines will produce a computing environment where the electrodynamics of the system allow for prediction of all future states based on known past states, and the system reaches every possible state, resulting in no heat dissipation. A reversible logic gate is an N -input N -output logic device that provides one to one mapping between the input and the output. It not only helps us to determine the outputs from the inputs but also helps us to uniquely recover the inputs from the outputs. Garbage outputs are those which do not contribute to the reversible logic realization of the design. Quantum cost refers to the cost of the circuit in terms of the cost of a primitive gate. Gate count is the number of reversible gates used to realize the function. Gate level refers to the number of levels which are required to realize the given logic functions.

The following are the important design constraints for reversible logic circuits.

1. Reversible logic gates do not allow fan-outs.
2. Reversible logic circuits should have minimum quantum cost.
3. The design can be optimized so as to produce minimum number of garbage outputs.
4. The reversible logic circuits must use minimum number of constant inputs.
5. The reversible logic circuits must use a minimum logic depth or gate levels.

The basic reversible logic gates encountered during the design are listed below:

1. Feynman Gate :

It is a 2×2 gate and its logic circuit is as shown in the figure. It is also known as Controlled Not (CNOT) Gate. It has quantum cost 1 and is generally used for Fan Out purposes.

2. Peres Gate :

It is a 3×3 gate and its logic circuit is as shown in the figure. It has quantum cost 4. It is used to realize various Boolean functions such as AND, XOR.

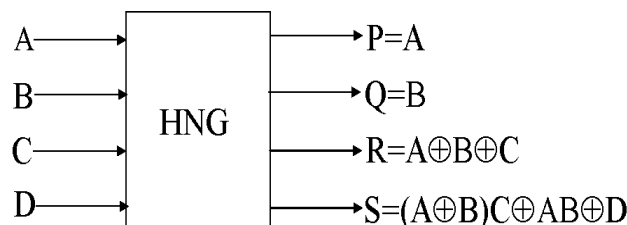
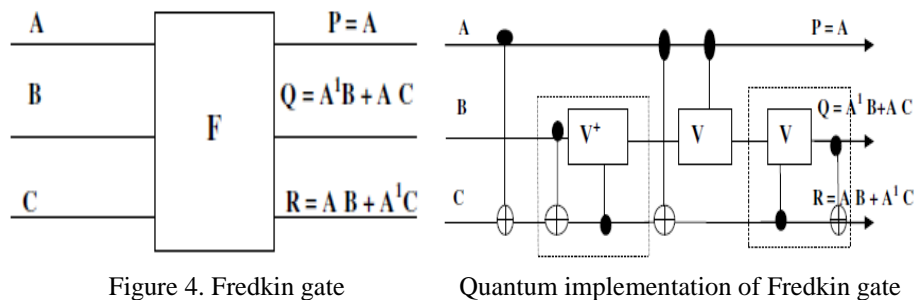
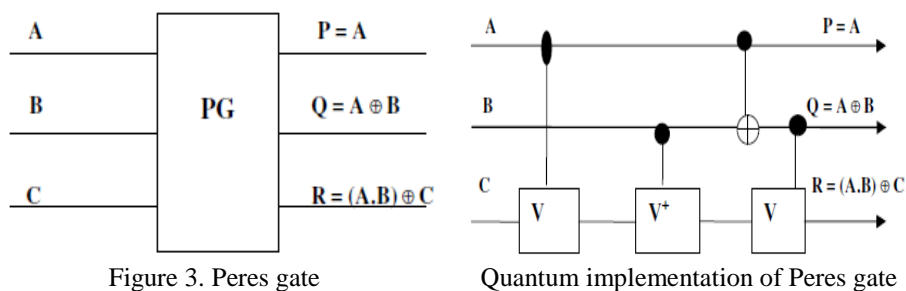
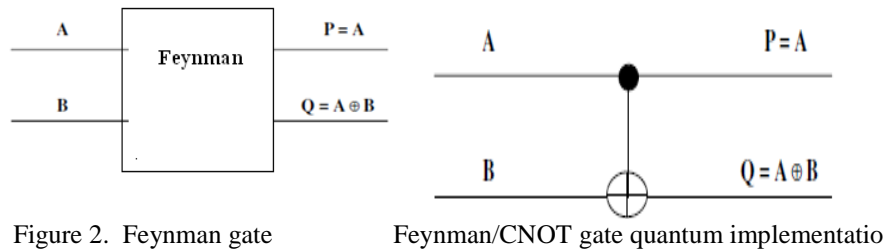
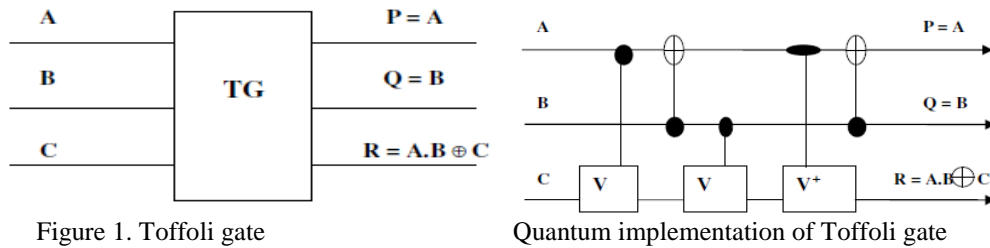
3. Fred kin Gate :

It is a 3×3 gate and its logic circuit is as shown in the figure. It has quantum cost 5. It can be used to implement a Multiplexer.

4. HNG Gate :

It is a 4×4 gate and its logic circuit is as shown in the figure. It has quantum cost 6. It is used for designing ripple carry adders. It can produce both sum and carry in a single gate thus minimizing the garbage and gate counts.

5. **Toffoli Gate** : The 3*3 Reversible gate with 3 inputs and 3 outputs. It has Quantum cost 5



IV. NIKHILAM SUTRA MULTIPLICATION ALGORITHM

The —Nikhilam Navatascaram Dasatah literally means —All from Nine and the last from Ten. The sutra basically means start from the left most digit and begin subtracting ‘9’ from each of the digits; but subtract ‘10’ from the last digit. The following example illustrates the way in which this Sutra could reduce the number of iterations to reduce the whole Multiplication.

To multiply 92 and 89. Apply Nikhilam Sutra – —All from nine and last from ten on both the numbers —

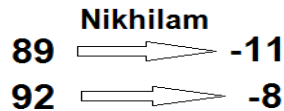


Figure 1

The arrows in Figure 2 indicate the operation of the Nikhilam Sutra being performed, viz. the subtraction of 10 from the last digit and 9's from all the other digits starting with the leftmost digit.

□ Now we write this down side-by-side,

$$\begin{array}{r} 92 \quad -08 \\ 89 \quad -11 \\ \hline \end{array}$$

□ Multiply (-08) and (-11) to get -88 .

$$\begin{array}{r} 92 \quad -08 \\ 89 \quad -11 \quad \times \\ \hline \quad \quad 88 \end{array}$$

□ Now we cross-add. This is done by both —adding 92 and -11 to get 81 or —adding 89 and -08 to get 81.



□ Note that in both operations you get the same answer that is -81 which is written below to get the solution.

$$\begin{array}{r} 92 \quad -08 \\ \times 89 \quad -11 \\ \hline 81 \quad 88 \end{array}$$

This technique works very well if the numbers to be multiplied are near a base. Upon little alteration, this also works very well for any pair of numbers.

Case (i): Both the numbers are lower than the base.

EXP.1 986*989. Base is 1000

986	14
989	11
986-11	14*11
989-14	
975	154

So $986*989=975154$

Case (ii): Both the numbers are higher than the base.

EXP.2 104*102. Base is 100

104	04
102	02
104+2	04*02

102+4

106 08

So 104*102=10608

Case (iii): One number is more and other is less than the base.

EXP.3 998*1025.Base is 1000

998	002
1025	025
998-25	2*25
1025+2	
1023	50 (since the complement of 50 is 950 for the base 1000)

We get 1023 950 But we have to subtract 1 from 1023

So 998*1025= 1022950

After this illustration, we now discuss the operational principle of Nikhilam Sutra by taking the case of multiplication of two

n-bit numbers x and y having complements $x = 10n - x$ and $y = 10n - y$ respectively.

The required product p is defined as: $p = xy \dots (1)$

which can be reframed by adding and subtracting $102n + 10n(x + y)$ to the right hand side as:

$$p = xy + 102n - 102n + 10n x + y - (x + y) \dots (2)$$

The above terms can be clubbed as follows:

$$p = 10n x + y - 102n + 102n - 10n x + y + xy = 10n x + y - 10n + 10n - x 10n - y = 10n x - y + x y = 10n y - x + \{x y\} \dots (3)$$

From (3), the expressions of LHS and RHS can be deduced, which come out to be:

$$LHS = x - y = \{y - \} \dots (4)$$

$$RHS = \{ \} \dots (5)$$

Hence the multiplication of two n-bit numbers is reduced to the multiplication of their complements. To take full advantage of this reduction, it should be ensured that the numbers obtained after taking the complements are lesser than the original numbers.

This condition is satisfied if both the original numbers are greater than $10n/2$, i.e., $x > 10n/2$ and $y > 10n/2$.

This is the reason why it is said that the Nikhilam Sutra is efficacious in the multiplication of large numbers than the smaller ones.

V. DETAILED DESIGN (PROPOSED ARCHITECTURE)

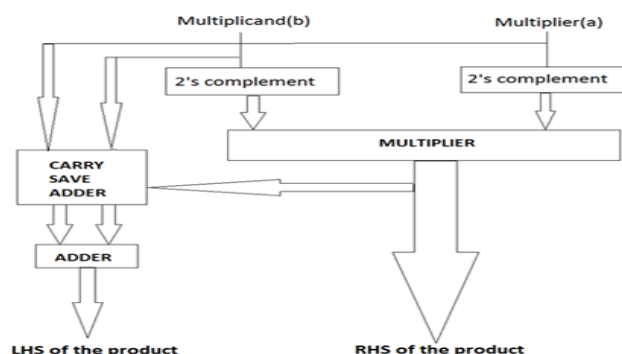


Figure 2

5.1. Top Module:

The block diagram for proposed multiplier is shown in the figure2. As we are using binary numbers in digital signal processing applications we have implemented for binary system. The multiplication can be done using the complemeter, CSA adder and adder. The RHS of the product can be obtained by the multiplication of complimented outputs of multiplier and multiplicand and the LHS of the product can be obtained by addition using a CSA. This can be used for the multiplication of any number of bits. In this paper, we have presented a 4x4 architecture applying the Nikhilam Algorithm. In the figure 2, the two inputs a and b represents the 4 bit multiplier and 4 bit multiplicand respectively.

5.2. Internal blocks:

5.2.1 2's complemeter:

The multiplicand and the multiplier are given as inputs to the two 2's complemeter blocks. The logic implementation of the 4 bit 2's complemeter is presented in figure3

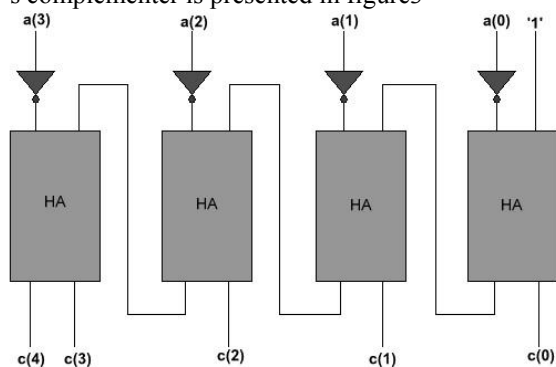


Figure3

In figure3, the —HA represents a Half Adder block.

5.2.2 Multiplier:

Now, the complemented output of multiplier (-a) and the complemented multiplicand (-b) are then produced. These complemented outputs of multiplier and multiplicand are given as inputs to the multiplier block. The 4x4 multiplier architecture that we employed is based on calling a 2x2 multiplier so as to ease the multiplication procedure. This implementation is represented by the following figure 4. Here, a and b are the 2-bit (or the 4-bit) multiplier and multiplicand respectively which are being multiplied to produce the final 4-bit(or the 8-bit) product vector. The half of the LSB bits of multiplication output is taken as RHS product of the total multiplication.

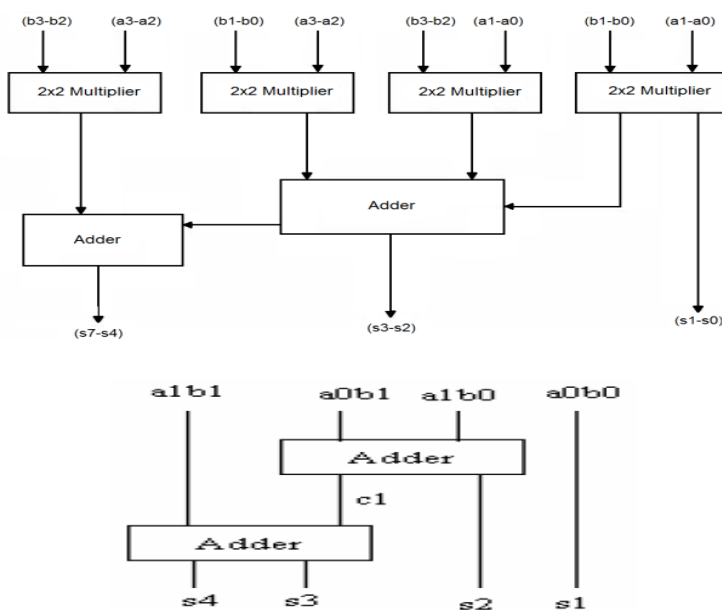


Figure 4

5.2.3 CSA:

The carry-save unit consists of n full adders, as shown in Figure 5 each of which computes a single sum and carry bit based solely on the corresponding bits of the three input numbers.

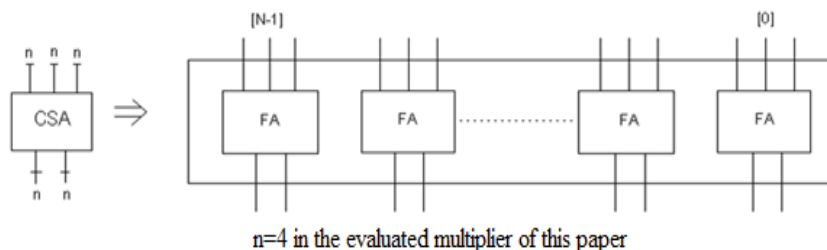


Figure 5

With three n - bit numbers a_i , b_i , and c_i given to it, it produces a partial sum ψ_i and a shift-carry σ_i according to the below equations:-

$$\psi_i = a_i \oplus b_i \oplus c_i$$

$$\sigma_i = (a_i \oplus b_i) \vee (a_i \oplus c_i) \vee (b_i \oplus c_i)$$

These ψ_i and σ_i are then added using a conventional adder, to produce the sum of the three inputs. The multiplier, multiplicand and the half of MSB bits are given as inputs to the CSA. The two outputs i.e., sum vector and carry vector obtained from the CSA adder are given to the inputs for the adder block. The output we obtain is labeled the LHS of the required multiplication product. As we are using CSA, the delay will be reduced and the number of components gets reduced for addition mechanism. This is the main advantage of the multiplier based on Nikhilam over the multiplier based on conventional algorithms proposed in the a fore mentioned algorithms in [1].

VI. EVALUATION

The design of the reversible 2,4,8,16 bit multiplier is logically verified using XILINX 8.1i and MODELSIM SE 6.5. Synthesis and Implementation is done using Xilinx Spartan-3E Fpga Board of device family xc3s500e-4fg320. The simulation results are as shown in figures .

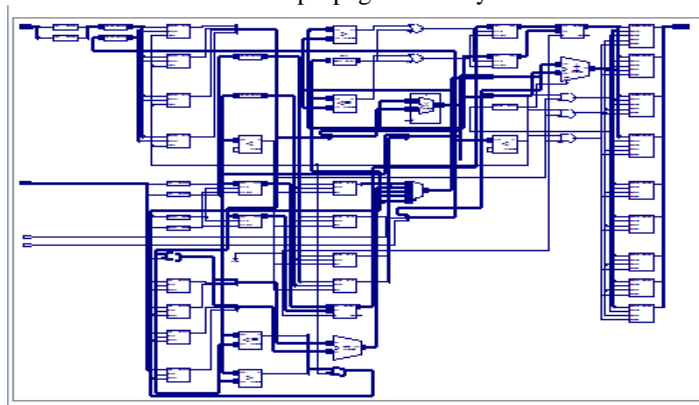
Here we introduce a new function called the "Total Reversible Logic Implementation Cost (TRLIC)" which is defined as the sum of all the cost metrics of a given reversible circuit. The TRLIC can be deemed as a parameter which reflects the overall performance of a reversible logic circuit. $TRLIC = \sum(NG, CI, QC, GO)$

Where NG is the number of gates in the reversible circuit. CI is the number of constant inputs, QC is the quantum cost of the circuit. GO is the number of garbage outputs. The following are the important design constraints for any reversible logic circuits.

1. Reversible logic circuits should have minimum quantum cost.
2. The design can be optimized so as to produce minimum number of garbage outputs.
3. The reversible logic circuits must use minimum number of constant inputs.
4. The reversible logic circuits must use a minimum number of reversible gates.

6.1. Simulation Methodology

Xilinx 8.1i has been used to simulate the wave forms. The simulator carefully modeled the interconnections, the associated blocks and the propagation delays.

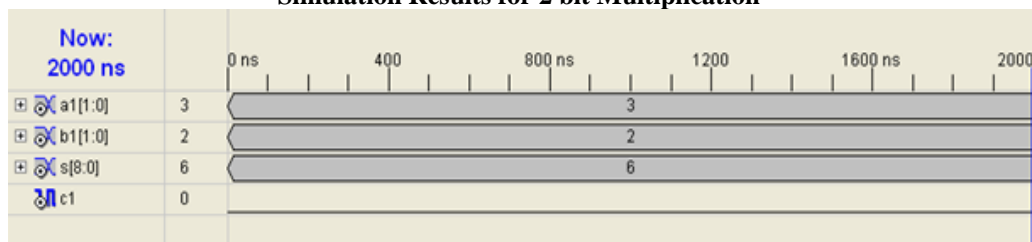


RTL Schematic

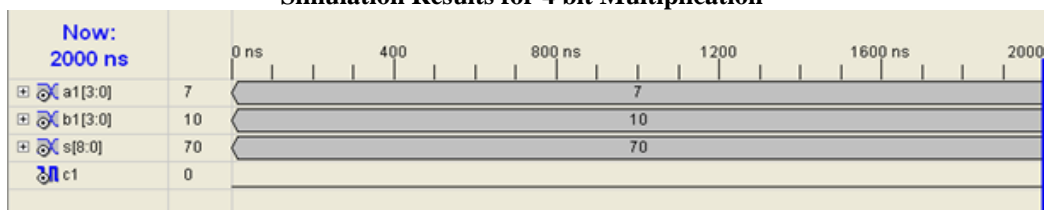
6.2.Results

In this section we show results for the Vedic multiplier based on Nikhilam Sutra . Multiplier based on Nikhilam Algorithm utilizes smaller area and produces littler delay than the conventional multiplier.

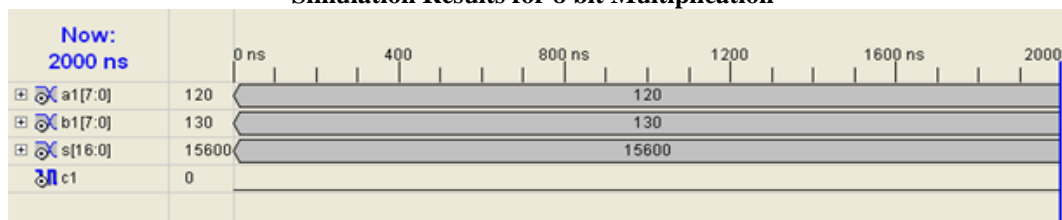
Simulation Results for 2 bit Multiplication



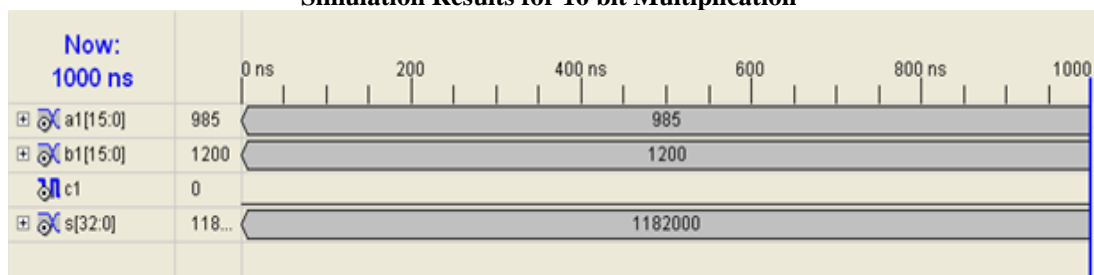
Simulation Results for 4 bit Multiplication



Simulation Results for 8 bit Multiplication



Simulation Results for 16 bit Multiplication



CONCLUSION

The proposed Vedic multiplier architecture exhibits speed improvements. The Vedic multiplier employing Nikhilam Sutra found to be better than conventional multiplier in terms of speed when magnitude of both operands are more than half of their maximum values . This approach may be well suited for multiplication of numbers with more than 16 bit size.

REFERENCES

- [1] Charles. Roth Jr. "Digital Systems Design using VHDL,," Thomson Brooks/Cole, 7th reprint, 2005.
- [2] Jagadguru Swami Sri Bharati Krishna Tirthaji Maharaja, Vedic Mathematics: Sixteen Simple Mathematical Formulae from the Veda, Delhi (1965).
- [3] H. Thapliyal , M. B. Shrinivas and H. Arbania, "Design and Analysis of a VLSI Based High Performance Low Power Parallel Square Architecture", Int. Conf. Algo. Math. Comp. Sc., LasVegas, June 2005, pp. 72-76.
- [4] P. D. Chidgup kar and M. T. Karad, "The Imp limentation of Vedic Algorithms in Digital Signal Processing", Global J. of Engg. Edu, vol.8, no.2, 2004.
- [5] Shamim Akhter,"VHDL Implementation Of Fast NXN Multiplier Based On Vedic Mathematics", Jay p ee Institute of Information Technology University, Noida, 201307 UP, INDIA, 2007 IEEE.

- [6] Rakshith Saligram and Rakshith T.R. "Design of Reversible Multipliers for linear filtering Applications in DSP" International Journal of VLSI Design and Communication systems, Dec-12
- [7] R. Landauer, "Irreversibility and Heat Generation in the Computational Process", IBM Journal of Research and Development, 5, pp.183-191, 1961.
- [8] C.H. Bennett, "Logical reversibility of Computation", IBM J. Research and Development, pp.525-532, November 1973.
- [9] R. Feynman, "Quantum Mechanical Computers," Optics News, Vol.11, pp. 11-20, 1985.
- [10] H. Thapliyal and M.B. Srinivas, "Novel Reversible Multiplier Architecture Using Reversible TSG Gate", Proc.IEEE International Conference on Computer Systems and Applications, pp. 100-103, March 2006.
- [11] Shams, M., M. Haghparast and K. Navi, Novel reversible multiplier circuit in nanotechnology. World Appl. Sci. J., 3(5): 806-810.
- [12] Somayeh Babazadeh and Majid Haghparast, "Design of a Nanometric Fault Tolerant Reversible Multiplier Circuit" Journal of Basic and Applied Scientific Research, 2012.
- [13] Thapliyal, H., M.B. Srinivas and H.R. Arabnia, 2005, A Reversible Version of 4x4 Bit Array Multiplier with Minimum Gates and Garbage Outputs, Int. Conf. Embedded System, Applications (ESA'05), Las Vegas, USA, pp: 106-114.
- [14] M. Haghparast et al. , "Design of a Novel Reversible Multiplier Circuit using HNG Gate in Nanotechnology," in World Applied Science Journal, Vol. 3, No. 6, pp. 974-978, 2008.
- [15] M. S. Islam et al. , "Realization of Reversible Multiplier Circuit," in Information Tech. 1, Vol. 8, No. 2, pp. 117-121, 2005.
- [16] K. Navi, M. Haghparast, S. JafaraliJassbi, O.Hashempour, Design of a novel reversible multiplier circuit using HNG gate, World Sci. 1 3 (6).
- [17] M. Shams et al., "Novel Reversible Multiplier Circuits in Nanotechnology," in World Applied Science Journal, Vol. 3, No. 5, pp. 806- 810, 2008.
- [18] M S Islam, M M Rahman, Z Begum and M Z Hafiz, 2009. Low Cost Quantum Realization of Reversible Multiplier Circuit. Information Technology Journal, vol. 8(2), pp. 208-213.
- [19] E. Fredkin and T. Toffoli, "Conservative Logic", Int'l J Theoretical Physics Vol 121, pp.219-253, 1982.
- [20] A. Peres, Reversible logic and quantum computers, Phys. Rev. A 32 (1985) 3266-3276.
- [21] Rakshith Saligram and Rakshith T.R. "Novel Code Converter Employing Reversible Logic", International Journal of Computer Applications (IJCA), August 2012.
- [22] G Ganesh Kumar and V Charishma, Design of high speed vedic multiplier using vedic mathematics techniques, Int'l J. of Scientific and Research Publications, Vol. 2 Issue 3 March 2012
- [23] Vedic Mathematics: <http://www.hinduism.co.za/vedic.html>
- [24] 24.Rakshith Saligram and Rakshith T.R. " Design of high speed low power multiplier using Reversible logic : a vedic Mathematical Approach (ICCPCT), 2013.

About The Authors

	<p>Manjeet Singh Sankhwar has 3 years of Teaching experience and presently pursuing Mtech in Micro Electronics & VLSI Design in SGSITS Indore, India in 2014 .He received his Bachelor of Engineering in Electronics and Communication from UIT-RGPV Bhopal, India in 2008 . His main research interests include Low Power VLSI design , Digital design.</p>
	<p>Mr. Rajesh Khatri has 20 years of Teaching experience and presently working as Associate Professor in Department of Electronics & Instrumentation Engineering at SGSITS Indore. He received his Bachelor of Engineering in Electronics and Communication from SGGGS Institute of Technology Nanded , India in 1990 . He received his Master of Engineering in Instrumentation from SGGGS Institute of Technology Nanded ,India in 1995 .</p>

Hopf-Bifurcation Ina Two Dimensional Nonlinear Differential Equation

¹Hemanta Kumar Sarmah, ²Tapan Kumar Baishya, ³Mridul Chandra Das

^{1,3}Department of Mathematics, Gauhati University, Assam

²Department of Mathematics, Debraj Roy College, Golaghat, Assam

ABSTRACT: In this paper we have investigated the stability nature of Hopf bifurcation in a two dimensional nonlinear differential equation. Interestingly, our considered model exhibits both supercritical and subcritical Hopf bifurcation for certain parameter values which marks the stability and instability of limit cycles created or destroyed in Hopf bifurcations respectively. We have used the Center manifold theorem and the technique of Normal forms in our investigation.

Keywords: Hopf bifurcation, supercritical Hopf bifurcation, subcritical Hopf bifurcation, Centre manifold, normal form.

I. INTRODUCTION

From historical point of view, search on the existence of periodic solution plays a fundamental role in the development of qualitative study of dynamical systems. There are many methods for locating the periodic solutions, for example the Poincare return map, Melnikov integral, bifurcation theory etc. In this paper we have used Center manifold theorem, Normal forms and Hopf bifurcation theorem to study the behaviour of the limit cycle.

The term Hopf bifurcation (also sometimes called Poincare Andronov-Hopf bifurcation) refers to the local birth or death of a periodic solution (self-excited oscillation) from an equilibrium as a parameter crosses a critical value. In a differential equation a Hopf bifurcation typically occurs when a complex conjugate pair of eigenvalues of the linearized flow at a fixed point becomes purely imaginary. The uniqueness of such bifurcations lies in two aspects: unlike other common types of bifurcations (viz., pitchfork, saddle-node or transcritical) Hopf bifurcation cannot occur in one dimension. The minimum dimensionality has to be two. The other aspect is that Hopf bifurcation deals with birth or death of a limit cycle as and when it emanates from or shrinks onto a fixed point, the focus. Recently, Hopf bifurcation of some famous chaotic systems has been investigated and it is becoming one of the most active topics in the field of chaotic systems.

Hopf bifurcation has played a pivotal role in the development of the theory of dynamical systems in different dimensions. Following Hopf's original work [1942], Hopf and generalized Hopf bifurcations have been extensively studied by many researchers [3,10,15,19,20,21,24,29,32,33,37].

As is well known, Hopf bifurcation gives rise to limit cycles, which are typical oscillatory behaviors of many nonlinear systems in physical, social, economic, biological, and chemical fields. These oscillatory behaviors can be beneficial in practical applications, such as in mixing, monitoring, and fault diagnosis in electromechanical systems [11,15,25]. Also, the properties of limit cycles are very useful in modern control engineering, such as auto tuning of PID controller [39] and process identification [36]. Early efforts in Hopf bifurcation control [38] focused on delaying the onset of this bifurcation [1] or stabilizing an existing bifurcation [40].

II. CENTRE MANIFOLD THEOREM AND ITS ROLE IN HOPF BIFURCATION

The center manifold theorem in finite dimensions can be traced to the work of Pliss [28], Sositaisvili [31] and Kelley [22]. Additional valuable references are Guckenheimer and Holmes [15], Hassard, Kazarinoff, and Wan [16], Marsden and McCracken [24], Carr [7], Henry [18], Sijbrand [30], Wiggins [37] and Perko [27].

The center manifold theorem is a model reduction technique for determining the local asymptotic stability of an equilibrium of a dynamical system when its linear part is not hyperbolic. The overall system is asymptotically stable if and only if the Center manifold dynamics is asymptotically stable. This allows for a substantial reduction in the dimension of the system whose asymptotic stability must be checked. In fact, the center manifold theorem is used to reduce the system from N dimensions to 2 dimensions [17]. Moreover, the

Centermanifold and its dynamics need not be computed exactly; frequently, a low degree approximation is sufficient to determine its stability [4].

We consider a nonlinear system

$$\dot{x} = f(x), x \in R^n \quad (1)$$

Suppose that the system (1) has an equilibrium point x_0 at the parameter value $\mu = \mu_0$ such that $f(x_0) = 0$. In order to study the behaviour of the system near x_0 we first linearise the system (1) at x_0 . The linearised system is

$$\dot{x} = Ax, x_0 \in R^n \quad (2)$$

Where $A = Df(x_0)$ is the Jacobian matrix of f of order $n \times n$. The system has invariant subspaces E^s , E^u , E^c , corresponding to the span of the generalised eigenvectors, which in turn correspond to eigenvalues having negative real part, positive real part and zero real part respectively. The subspaces are so named because orbits starting in E^s decay to zero as t tends to ∞ , orbits starting in E^u become unbounded as t tends to ∞ and orbits starting in E^c neither grow nor decay exponentially as t tends to ∞ . Theoretically, it is already established that if we suppose $E^u = \emptyset$, then any orbit will rapidly decay to E^c . Thus, if we are interested in long term behaviour (i.e. stability) we need only to investigate the system restricted to E^c .

The Hartman-Grobman Theorem [21] says that in a neighbourhood of a hyperbolic critical point x_0 , the nonlinear system (1) is topologically conjugate to the linear system (2), in a neighbourhood of the origin. The Hartman-Grobman theorem therefore completely solves the problem of determining the stability and qualitative behaviour in a neighbourhood of a hyperbolic critical point.

In case of non-hyperbolic critical point, the Hartman-Grobman Theorem is not applicable and its role is played by the center manifold theorem. The center manifold theorem shows that the qualitative behaviour in a neighbourhood of a non-hyperbolic critical point x_0 of the nonlinear system (1) with $x \in R^n$ is determined by its behaviour on the center manifold near x_0 . Since the center manifold is generally of smaller dimension than the system (1), this simplifies the problem of determining the stability and qualitative behaviour of the flow near a non-hyperbolic critical point of (1).

III. CENTER MANIFOLD THEOREM FOR FLOWS

The statement of the Center Manifold Theorem for Flows is as follows :

Let f be a C^r vector field on R^n vanishing at the origin ($f(0) = 0$) and let $A = Df(0)$. Divide the spectrum of A into three parts, $\sigma_s, \sigma_c, \sigma_u$ with

$$\operatorname{Re} \lambda \begin{cases} < 0 & \text{if } \lambda \in \sigma_s \\ = 0 & \text{if } \lambda \in \sigma_c \\ > 0 & \text{if } \lambda \in \sigma_u \end{cases}$$

Let the (generalised) eigenspaces of σ_s, σ_c and σ_u be E^s, E^c and E^u , respectively. Then there exist C^r stable and unstable invariant manifolds W^s and W^u tangent to E^s and E^u at 0 and a C^{r-1} center manifold W^c tangent to E^c at 0. The manifolds W^s, W^u, W^c are all invariant for the flow of f . The stable and unstable manifolds are unique, but W^c need not be [7,15].

The system (1) can be written in diagonal form

$$\begin{aligned} \dot{x} &= A^c x + f_1(x, y, z) \\ \dot{y} &= A^s y + f_2(x, y, z) \\ \dot{z} &= A^u z + f_3(x, y, z) \end{aligned} \quad (3)$$

$$\text{with} \quad \begin{aligned} f_1(0,0,0) &= 0, & Df_1(0,0,0) &= 0 \\ f_2(0,0,0) &= 0, & Df_2(0,0,0) &= 0 \\ f_3(0,0,0) &= 0, & Df_3(0,0,0) &= 0 \end{aligned}$$

Where f_1, f_2, f_3 are some C^r , ($r \geq 2$) in some neighbourhood of the origin, A^c, A^s and A^u on the blocks are in the canonical form whose diagonals contain the eigenvalues with $\operatorname{Re} \lambda = 0$, $\operatorname{Re} \lambda < 0$ and $\operatorname{Re} \lambda > 0$, respectively, $(x, y, z) \in R^c \times R^s \times R^u$, $c = \dim E^c$ since the system (3) has c eigenvalues with zero real part, $s = \dim E^s$ and $u = \dim E^u$, f_1, f_2 and f_3 vanish along with their first partial derivatives at the origin.

If we assume that the unstable manifold is empty, then (3) becomes

$$\begin{aligned} \dot{x} &= A^c x + f_1(x, y) \\ \dot{y} &= A^s y + f_2(x, y) \end{aligned} \quad (4)$$

$$\text{where} \quad \begin{aligned} f_1(0,0) &= 0, & Df_1(0,0) &= 0, \\ f_2(0,0) &= 0, & Df_2(0,0) &= 0, \end{aligned}$$

A^c is a $c \times c$ matrix having eigenvalues with zero real parts, A^s is an $s \times s$ matrix having eigenvalues with negative real parts, and f_1 and f_2 are C^r functions ($r \geq 2$.)

The following theorems established by Carr [7] in fact forms the basis of our discussion on the role of Centre manifold theorem in Hopf bifurcation and so we have stated them below :

Theorem3.1:

There exists a C^r center manifold,

$$W^c = \{(x, y) | y = h(x), |x| < \delta, h(0) = 0, Dh(0) = 0\},$$

for δ sufficiently small, for (4) such that the dynamics of (4) restricted to the center manifold is given by the c -dimensional vector field

$$\dot{u} = A^c u + f_1(u, h(u)) \quad (5)$$

Theorem3.2:

(i) Suppose the zero solution of (5) is stable (asymptotically stable)(unstable) then the zero solution of (4) is also stable (asymptotically stable) (unstable).

(ii) Suppose the zero solution of (5) is stable. Then if $(x(t), y(t))$ is a solution of (4) with $(x(0), y(0))$ sufficiently small, there is a solution $u(t)$ of (5) such that as $t \rightarrow \infty$

$$\begin{aligned} x(t) &= u(t) + O(e^{-\gamma t}) \\ y(t) &= h(u(t)) + O(e^{-\gamma t}) \end{aligned}$$

where $\gamma > 0$ is a constant.

From the theorem 2.2 it is clear that the dynamics of (5) near $u = 0$ determine the dynamics of (4) near $(x, y) = (0, 0)$.

To calculate $h(x)$ substitute $y = h(x)$ in the second component of (3) and using the chain rule, we obtain

$$N(h(x)) = Dh(x)[A^c x + f_1(x, h(x))] - Ch(x) - g(x, h(x)) = 0 \quad (6)$$

with boundary conditions $h(0) = Dh(0) = 0$. This differential equation for h cannot be sloved exactly in most cases, but its solution can be approximated arbitrarily closely as a Taylor series at $x = 0$.

Theorem 3.3 :

If a function $\phi(x)$, with $\phi(0) = D\phi(0) = 0$, can be found such that $N(\phi(x)) = O(|x|^p)$ for some $p > 1$ as $|x| \rightarrow 0$ then it follows that

$$h(x) = \phi(x) + O(|x|^p) \text{ as } |x| \rightarrow 0$$

This theorem allows us to compute the center manifold to any desired degree of accuracy by solving (6) to the same degree of accuracy.

In the discussion above we have assumed the unstable manifold is empty at the bifurcation point. If we include the unstable manifold then we must deal with the system (3). In this case $(x, y, z) = (0, 0, 0)$ is unstable due to the existence of a u -dimensional unstable manifold. However, much of the center manifold theory still applies, in particular Theorem 2.1 concerning existence, with the center manifold being locally represented by

$$W^c(0) = \{(x, y, z) \in R^c \times R^s \times R^u | y = h_1(x), z = h_2(x), h_i(0) = 0, Dh_i(0) = 0, i = 1, 2\}$$

for x sufficiently small. The vector field restricted to the center manifold is given by

$$\dot{u} = Au + f(x, h_1(u), h_2(u))$$

IV. HOPF BIFURCATION AND NORMAL FORM

One of the basic tools in the study of dynamical behavior of a system governed by nonlinear differential equations near a bifurcation point is the theory of normal forms. Normal form theory has been widely used in the study of nonlinear vector fields in order to simplify the analysis of the original system [5, 8,9, 14,15,23, 26,47].

Several efficient methodologies for computing normal forms have been developed in the past decade [2,12, 13, 34,41, 42,43, 44,45,46].

The method of normal forms can be traced back to the Ph.D thesis of Poincare. The books by Van der Meer [35] and Bryuno [6] give valuable historical background.

The basic idea of normal form theory is to employ successive, near identity nonlinear transformations to eliminate the so called non-resonant nonlinear terms, and retaining the terms which can not be eliminated (called resonant terms) to form the normal form and which is sufficient for the study of qualitative behavior of the original system.

The Local Center Manifold Theorem in the previous section showed us that, in a neighborhood of a nonhyperbolic critical point, determining the qualitative behavior of (1) could be reduced to the problem of determining the qualitative behavior of the nonlinear system

$$\dot{x} = A^c x + F(x) \quad (7)$$

on the center manifold. Since the dimension of the center manifold is typically less than n , this simplifies the problem of determining the qualitative behavior of the system (1) near a nonhyperbolic critical point. However, analyzing this system still may be a difficult task. The normal form theory allows us to simplify the nonlinear part, $F(x)$, of (7) in order to make this task as easy as possible. This is accomplished by making a nonlinear, analytic transformation (called near identity transformation) of coordinates of the form

$$x = y + h(y), \text{ where } h(y) = O(|y|^2) \text{ as } |y| \rightarrow 0. \quad (8)$$

Suppose that $Df_\mu(x_0)$ has two purely imaginary eigenvalues with the remaining $n - 2$ eigenvalues having nonzero real parts. We know that since the fixed point is not hyperbolic, the orbit structure of the linearised vector field near $(x, \mu) = (x_0, \mu_0)$ may reveal little (and, possibly, even incorrect) information concerning the nature of the orbit structure of the nonlinear vector field (1) near $(x, \mu) = (x_0, \mu_0)$. But by the center manifold theorem, we know that the orbit structure near $(x, \mu) = (x_0, \mu_0)$ is determined by the vector field (1) restricted to the center manifold.

On the center manifold the vector field (1) has the following form

$$\begin{pmatrix} \dot{x} \\ \dot{y} \end{pmatrix} = \begin{pmatrix} \operatorname{Re}\lambda(\mu) & -\operatorname{Im}\lambda(\mu) \\ \operatorname{Im}\lambda(\mu) & \operatorname{Re}\lambda(\mu) \end{pmatrix} \begin{pmatrix} x \\ y \end{pmatrix} + \begin{pmatrix} f^1(x, y, z) \\ f^2(x, y, z) \end{pmatrix} \quad (x, y, \mu) \in \mathbb{R}^1 \times \mathbb{R}^1 \times \mathbb{R}^1 \quad (9)$$

Where f^1 and f^2 are nonlinear in x and y and $\lambda(\mu)$, $\bar{\lambda}(\mu)$ are the eigenvalues of the vector field linearized about the fixed point at the origin.

Now, if we denote the eigenvalue

$$\lambda(\mu) = \alpha(\mu) + i\omega(\mu), \quad (10)$$

Then for our assumption of non hyperbolic nature we have

$$\alpha(0) = 0, \quad \omega(0) \neq 0 \quad (11)$$

Now we transform the equation (9) to the normal form. The normal form is found to be

$$\begin{aligned} \dot{x} &= \alpha(\mu)x - \omega(\mu)y + (a(\mu)x - b(\mu)y)(x^2 + y^2) + O(|x|^5, |y|^5) \\ \dot{y} &= \omega(\mu)x + \alpha(\mu)y + (b(\mu)x + a(\mu)y)(x^2 + y^2) + O(|x|^5, |y|^5) \end{aligned} \quad (12)$$

In polar coordinates the equation (12) can be written as

$$\begin{aligned} \dot{r} &= \alpha(\mu)r + a(\mu)r^3 + O(r^5), \\ \dot{\theta} &= \omega(\mu) + b(\mu)r^2 + O(r^4) \end{aligned} \quad (13)$$

Since we are interested in the dynamics near $\mu = 0$, therefore expanding in Taylor's series the coefficients in (13) about $\mu = 0$, the equation (13) becomes

$$\begin{aligned} \dot{r} &= \alpha'(0)\mu r + a(0)r^3 + O(\mu^2 r, \mu r^3, r^5), \\ \dot{\theta} &= \omega(0) + \omega'(0)\mu + b(0)r^2 + O(\mu^2, \mu r^2, r^4) \end{aligned} \quad (14)$$

where “'” denotes differentiation with respect to μ and we have used the fact that $\alpha(0) = 0$.

Our goal is to understand the dynamics of (14) for small r and μ . This is accomplished in two steps. In the first step, we neglect the higher order terms of (14) to get a “truncated” normal form and in the second step we study the dynamics exhibited by the truncated normal form as it is well known that the dynamics exhibited by the truncated normal form are qualitatively unchanged when one considers the influence of the previously neglected higher order terms [37].

Now, neglecting the higher order terms in (14) gives

$$\begin{aligned} \dot{r} &= d\mu r + ar^3, \\ \dot{\theta} &= \omega + c\mu + br^2 \end{aligned} \quad (15)$$

where for ease of notation, we have

$$\alpha'(0) \equiv d, \quad a(0) \equiv a, \quad \omega(0) \equiv \omega, \quad \omega'(0) \equiv c, \quad b(0) \equiv b$$

For $-\infty < \frac{\mu d}{a} < 0$ and μ sufficiently small, the solution of (15) is given by

$$(r(t), \theta(t)) = \left(\sqrt{-\frac{\mu d}{a}}, \left[\omega + \left(c - \frac{bd}{a} \right) \mu \right] t + \theta_0 \right)$$

which is a periodic orbit for (15) and the periodic orbit is asymptotically stable for $a < 0$ and unstable for $a > 0$ [15, 37].

In practice, a is straight forward to calculate. It can be calculated simply by keeping track of the coefficients carefully in the normal form transformation in terms of the original vector field. The expression of a for a two dimensional system of the form

$$\begin{pmatrix} \dot{x} \\ \dot{y} \end{pmatrix} = \begin{pmatrix} 0 & -\omega \\ \omega & 0 \end{pmatrix} \begin{pmatrix} x \\ y \end{pmatrix} + \begin{pmatrix} f(x, y) \\ g(x, y) \end{pmatrix}$$

with $f(0) = 0 = g(0) = 0$, is found to be [15, 16, 24]

$$a = \frac{1}{16} (f_{xxx} + f_{xyy} + g_{xxy} + g_{yyy}) + \frac{1}{16\omega} (f_{xy}(f_{xx} + f_{yy}) - g_{xy}(g_{xx} + g_{yy}) - f_{xx}g_{xx} + f_{yy}g_{yy})$$

In fact, all the above discussions gets converged in the famous Hopf Bifurcation Theorem which states as follows :

Let the eigenvalues of the linearized system of $\dot{x} = f_\mu(x)$, $x \in \mathbb{R}^n$, $\mu \in \mathbb{R}$ about the equilibrium point be given by $\lambda(\mu)$, $\bar{\lambda}(\mu) = \alpha(\mu) \pm i\beta(\mu)$. Suppose further that for a certain value of μ say $\mu = \mu_0$, the following conditions are satisfied:

$$1. \quad \alpha(0) = 0, \beta(0) = \omega \neq 0$$

$$2. \quad \left. \frac{d\alpha(\mu)}{d\mu} \right|_{\mu=\mu_0} = d \neq 0$$

(transversality condition: the eigenvalues cross the imaginary axis with nonzero speed)

$$3. \quad a \neq 0, \text{ where}$$

$$a = \frac{1}{16} (f_{xxx} + f_{xyy} + g_{xxy} + g_{yyy}) + \frac{1}{16\omega} (f_{xy}(f_{xx} + f_{yy}) - g_{xy}(g_{xx} + g_{yy}) - f_{xx}g_{xx} + f_{yy}g_{yy})$$

where f_{xy} denotes $\left. \frac{\partial^2 f_\mu}{\partial x \partial y} \right|_{\mu=\mu_0} (x_0, y_0)$, etc.

(genericity condition)

then there is a unique three-dimensional center manifold passing through (x_0, μ_0) in $R^n \times R$ and a smooth system of coordinates (preserving the planes $\mu = \text{const.}$) for which the Taylor expansion of degree 3 on the center manifold is given by (12). If $a \neq 0$, there is a surface of periodic solutions in the center manifold which has quadratic tangency with the eigenspace of $\lambda(\mu_0), \bar{\lambda}(\mu_0)$ agreeing to second order with the paraboloid $\mu = -(a/d)(x^2 + y^2)$. If $a < 0$, then these periodic solutions are stable limit cycles, while if $a > 0$, the periodic solutions are repelling (unstable limit cycles).

V. DISCUSSION ON THE BASIS OF OUR CONSIDERED MODEL

We discuss the following model taken from [15].

$$\begin{aligned} \dot{x} &= y \\ \dot{y} &= \mu_1 + \mu_2 y + \mu_3 x^2 + \mu_4 xy \end{aligned} \quad (16)$$

In our analysis, we fix μ_3 and μ_4 for simplicity. It is seen that, with suitable rescaling and letting $(x, y) \rightarrow (-x, -y)$, for any $\mu_3, \mu_4 \neq 0$ the possible cases can be reduced to two: $\mu_3 = 1$ and $\mu_4 = \pm 1$.

Case 1: $\mu_3 = 1, \mu_4 = -1$ (Super-critical Hopf bifurcation)

In this case the system (2) becomes

$$\begin{aligned} \dot{x} &= y \\ \dot{y} &= \mu_1 + \mu_2 y + x^2 - xy \end{aligned} \quad (17)$$

The fixed points of (17) are given by

$$(x, y) = (\pm\sqrt{-\mu_1}, 0)$$

which exists for $\mu_1 \leq 0$. We denote both the fixed points as $P_1 = (x_+, 0) = (+\sqrt{-\mu_1}, 0)$ and $P_2 = (x_-, 0) = (-\sqrt{-\mu_1}, 0)$, where $x_\pm = \pm\sqrt{-\mu_1}$.

The Jacobian matrix J for the linearized system is

$$J = \begin{pmatrix} 0 & 1 \\ 2x - y & \mu_2 - x \end{pmatrix}$$

The Jacobian matrix J at the fixed point $P_1 = (\sqrt{-\mu_1}, 0)$ is

$$J = \begin{pmatrix} 0 & 1 \\ 2\sqrt{-\mu_1} & \mu_2 - \sqrt{-\mu_1} \end{pmatrix}$$

The eigenvalues are given by

$$\lambda = \frac{\mu_2 - \sqrt{-\mu_1} \pm \sqrt{(\mu_2 - \sqrt{-\mu_1})^2 + 8\sqrt{-\mu_1}}}{2}$$

$$\text{Let } \lambda_1 = \frac{\mu_2 - \sqrt{-\mu_1} + \sqrt{(\mu_2 - \sqrt{-\mu_1})^2 + 8\sqrt{-\mu_1}}}{2} \quad \& \quad \lambda_2 = \frac{\mu_2 - \sqrt{-\mu_1} - \sqrt{(\mu_2 - \sqrt{-\mu_1})^2 + 8\sqrt{-\mu_1}}}{2}$$

We observe that $\lambda_1 > 0$ and $\lambda_2 < 0$ for $\mu_1 < 0$ and for all μ_2 .

Thus the fixed point $P_1 = (\sqrt{-\mu_1}, 0)$ is a saddle point.

The Jacobian matrix J at the fixed point $P_2 = (-\sqrt{-\mu_1}, 0)$ is

$$J = \begin{pmatrix} 0 & 1 \\ -2\sqrt{-\mu_1} & \mu_2 + \sqrt{-\mu_1} \end{pmatrix}$$

The eigenvalues are given by $\lambda = \frac{\mu_2 + \sqrt{-\mu_1} \pm \sqrt{(\mu_2 + \sqrt{-\mu_1})^2 - 8\sqrt{-\mu_1}}}{2}$

$$\text{Let } \lambda_1 = \frac{\mu_2 + \sqrt{-\mu_1} + \sqrt{(\mu_2 + \sqrt{-\mu_1})^2 - 8\sqrt{-\mu_1}}}{2} \quad \& \quad \lambda_2 = \frac{\mu_2 + \sqrt{-\mu_1} - \sqrt{(\mu_2 + \sqrt{-\mu_1})^2 - 8\sqrt{-\mu_1}}}{2}$$

The fixed point P_2 is stable for $\mu_2 + \sqrt{-\mu_1} < 0$ i.e. $\mu_2 < -\sqrt{-\mu_1}$ and unstable for $\mu_2 > \sqrt{-\mu_1}$.

Next, we verify the conditions for Hopf bifurcations at $\mu_2 = -\sqrt{-\mu_1}$.

(1). For $\mu_2 = -\sqrt{-\mu_1}$, $\mu_1 < 0$, the eigenvalues on $(x_-, 0)$ are given by

$$\lambda_{1,2} = \pm i\sqrt{2\sqrt{-\mu_1}} (= \pm i\sqrt{-2x_-})$$

(2). Also we have $\left. \frac{d}{db} (Re\lambda(\mu_2)) \right|_{\mu_2=\mu_{20}} = 1 \neq 0$

(3). Stability of the Hopf bifurcation:

To study the stability of the Hopf bifurcation, we change coordinates twice, first to bring the point $(-\sqrt{-\mu_1}, 0)$ to the origin and then to put the vector field into standard form.

Letting $\bar{x} = x - x_-$ and $\bar{y} = y$, we obtain

$$\begin{pmatrix} \dot{\bar{x}} \\ \dot{\bar{y}} \end{pmatrix} = \begin{pmatrix} 0 & 1 \\ 2x_- & 0 \end{pmatrix} \begin{pmatrix} \bar{x} \\ \bar{y} \end{pmatrix} + \begin{pmatrix} 0 \\ \bar{x}^2 - \bar{x}\bar{y} \end{pmatrix} \tag{18}$$

The coefficient matrix of the linear part is $A = \begin{pmatrix} 0 & 1 \\ -2\sqrt{-a} & 0 \end{pmatrix} = \begin{pmatrix} 0 & 1 \\ 2x_- & 0 \end{pmatrix}$

The eigenvalues are $\lambda = \pm i\sqrt{-2x_-} (= \pm i\omega)$ where $\omega = \sqrt{-2x_-}$

Therefore the eigenvectors corresponding to the eigenvalue λ are $\begin{pmatrix} 1 \\ \pm i\sqrt{-2x_-} \end{pmatrix}$

Then, using the linear transformation

$$\begin{pmatrix} \bar{x} \\ \bar{y} \end{pmatrix} = T \begin{pmatrix} u \\ v \end{pmatrix}$$

where $T = \begin{pmatrix} 0 & 1 \\ \sqrt{-2x_-} & 0 \end{pmatrix}$ is the matrix of real and imaginary parts of the eigenvectors of the eigenvalues $\lambda = \pm i\sqrt{-2x_-}$, we obtain the system with linear part in standard form as:

$$\begin{pmatrix} \dot{u} \\ \dot{v} \end{pmatrix} = \begin{pmatrix} 0 & -\sqrt{-2x_-} \\ \sqrt{-2x_-} & 0 \end{pmatrix} \begin{pmatrix} u \\ v \end{pmatrix} + \begin{pmatrix} f(u, v) \\ g(u, v) \end{pmatrix}$$

where the nonlinear terms are

$$f(u, v) = \frac{1}{\sqrt{-2x_-}}v^2 - uv, \quad g(u, v) = 0$$

and we have the following:

$$\begin{aligned} f_u = -v, f_{uu} = 0, f_{uuu} = 0, & \quad f_{uv} = -1, f_{uvv} = 0, f_v = \frac{1}{\sqrt{-2x_-}}2v - u, f_{vv} = \frac{2}{\sqrt{-2x_-}}, \\ g_u = 0, g_{uu} = 0, g_{uuv} = 0, & \quad g_v = 0, g_{vv} = 0, g_{vvv} = 0, g_{uv} = 0 \end{aligned}$$

Substituting these in the relation

$$a = \frac{1}{16}[f_{uuu} + f_{uvv} + g_{uuv} + g_{vvv}] + \frac{1}{16\omega}[f_{uv}(f_{uu} + f_{vv}) - g_{uv}(g_{uu} + g_{vv}) - f_{uu}g_{uu} + f_{vv}g_{vv}]$$

We get $a = \frac{1}{16x_-}$ that is $a = -\frac{1}{16\sqrt{-\mu_1}} < 0$ for $\mu_1 < 0$ [as f_{xy} denotes $\frac{\partial^2 f}{\partial x \partial y}(0,0)$]

The bifurcation is therefore supercritical and we have a family of stable periodic orbits. Thus, we can conclude that the system undergoes supercritical Hopf bifurcation for parameter values given by $\mu_2 = -\sqrt{-\mu_1}$. Below, we have given support to our above mentioned theoretical result through numerical simulation. In the first column of Figure 1, figures $a(I)$, $a(II)$ and $a(III)$ shows the phase orbit and the vector field and the figures $b(I)$, $b(II)$ and $b(III)$ shows the corresponding time series plot for our considered model for different parameter values and initial points. In $a(I)$ and $b(I)$, the parameter values are taken to be $\mu_1 = -1, \mu_2 = -1.1$ which is just before the occurrence of supercritical Hopf bifurcation at $\mu_1 = -1, \mu_2 = -1$ (according to our theoretical result). Here, we have considered the initial point as $x_0 = 0.4, y_0 = -0.01$. The figure $a(I)$ shows that the origin is stable and the orbit spirals to it. The same conclusion is supported by the time series plot shown in figure $b(I)$. For the next figures in $a(II)$ and $b(II)$, we have considered the parameter values $\mu_1 = -1, \mu_2 = -0.9$ which is just after the occurrence of supercritical Hopf bifurcation. We considered the initial point as $x_0 = -0.66, y_0 = -0.06$, which is inside the limit cycle produced during the Hopf bifurcation. The figure $a(II)$ shows that the origin is unstable and the orbit spiral away from it onto the smooth invariant closed curve encircling it (the limit cycle). The same conclusion is supported by the time series plot shown in $b(II)$. In figure $a(III)$ and $b(III)$ we have kept the parameter values same with the earlier case but changed the initial point as a point outside the limit cycle. Here we have considered $\mu_1 = -1, \mu_2 = -0.9$ with initial point $x_0 = 0.6, y_0 = 0$. Figure $a(III)$ and $b(III)$ shows that the orbit spiral towards the invariant circle. So, our numerical simulation clearly supports our conclusion that that the system undergoes supercritical Hopf bifurcation for parameter values given by $\mu_2 = -\sqrt{-\mu_1}$.

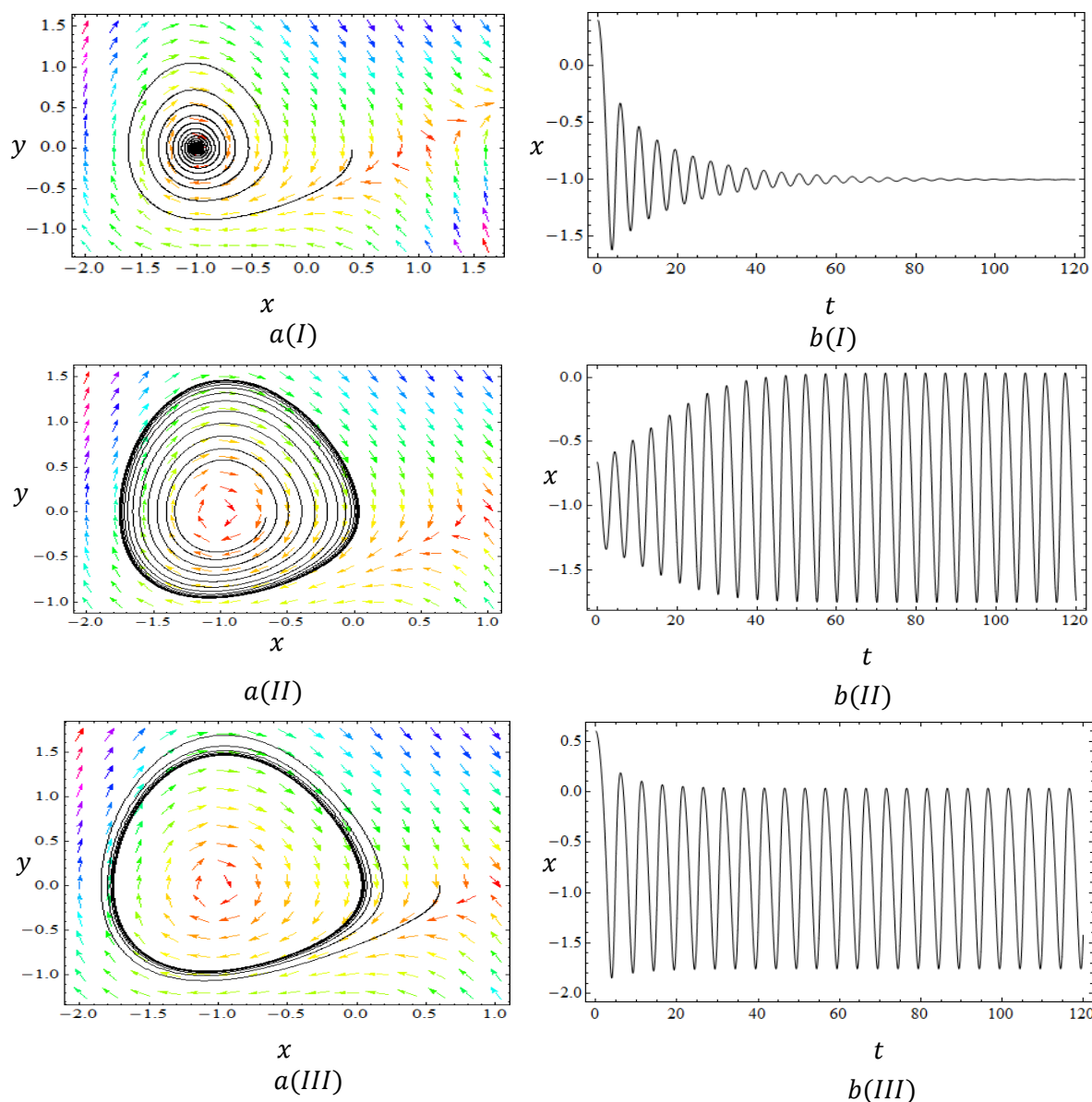


Fig1.The Phase orbit and time series of Eq. (16).a(I) and b(I) before the Hopf bifurcation at the parameter value $\mu_1 = -1, \mu_2 = -1.1$ with initial point $x_0 = 0.4, y_0 = -0.01$, the origin is stable and the orbit spirals to it.a(II) and b(II)after the Hopf bifurcation at the parameter value $\mu_1 = -1, \mu_2 = -0.9$ with initial point $x_0 = -0.66, y_0 = -0.06$, which is inside the limit cycle, the origin is unstable and the orbit spiral away from it and onto a smooth invariant closed curve encircling it.a(III) and b(III)after the Hopf bifurcation at the parameter value $\mu_1 = -1, \mu_2 = -0.9$ with initial point $x_0 = 0.6, y_0 = 0$ which is outside the invariant circle(limit cycle), the orbit spiral towards the invariant circle.

Case 2. $\mu_1 = 1, \mu_2 = 1$ (Subcritical Hopf bifurcation)

In this case the system (16) becomes

$$\begin{aligned} \dot{x} &= y \\ \dot{y} &= \mu_1 + \mu_2 y + x^2 + xy \end{aligned} \tag{19}$$

The fixed points of (19) are given by

$$(x, y) = (\pm\sqrt{-\mu_1}, 0)$$

which exists for $\mu_1 \leq 0$. We denote both the fixed as $P_1 = (x_+, 0) = (+\sqrt{-\mu_1}, 0)$ and $P_2 = (x_-, 0) = (-\sqrt{-\mu_1}, 0)$, where $x_{\pm} = \pm\sqrt{-\mu_1}$.

The Jacobian matrix J for the linearized system is

$$J = \begin{pmatrix} 0 & 1 \\ 2x + y & \sqrt{\mu_2 + x} \end{pmatrix}$$

The Jacobian matrix J at the fixed point $P_1 = (\sqrt{-\mu_1}, 0)$ is $J = \begin{pmatrix} 0 & 1 \\ 2\sqrt{-\mu_1} & \mu_2 + \sqrt{-\mu_1} \end{pmatrix}$

$$\lambda = \frac{\mu_2 + \sqrt{-\mu_1} \pm \sqrt{(\mu_2 + \sqrt{-\mu_1})^2 + 8\sqrt{-\mu_1}}}{2}$$

Let $\lambda_1 = \frac{\mu_2 + \sqrt{-\mu_1} + \sqrt{(\mu_2 + \sqrt{-\mu_1})^2 + 8\sqrt{-\mu_1}}}{2}$ & $\lambda_2 = \frac{\mu_2 + \sqrt{-\mu_1} - \sqrt{(\mu_2 + \sqrt{-\mu_1})^2 + 8\sqrt{-\mu_1}}}{2}$

We observe that $\lambda_1 > 0$ and $\lambda_2 < 0$ for $\mu_1 < 0$ and for all μ_2 .

Thus the fixed point $P_1 = (\sqrt{-\mu_1}, 0)$ is a saddle point.

The Jacobian matrix J at the fixed point $P_2 = (-\sqrt{-\mu_1}, 0)$ is $J = \begin{pmatrix} 0 & 1 \\ -2\sqrt{-\mu_1} & \mu_2 - \sqrt{-\mu_1} \end{pmatrix}$

The eigenvalues are given by $\lambda = \frac{\mu_2 - \sqrt{-\mu_1} \pm \sqrt{(\mu_2 - \sqrt{-\mu_1})^2 - 8\sqrt{-\mu_1}}}{2}$

Let $\lambda_1 = \frac{\mu_2 - \sqrt{-\mu_1} + \sqrt{(\mu_2 - \sqrt{-\mu_1})^2 - 8\sqrt{-\mu_1}}}{2}$ & $\lambda_2 = \frac{\mu_2 - \sqrt{-\mu_1} - \sqrt{(\mu_2 - \sqrt{-\mu_1})^2 - 8\sqrt{-\mu_1}}}{2}$

The fixed point P_2 is stable for $\mu_2 - \sqrt{-\mu_1} < 0$ i.e. $\mu_2 < \sqrt{-\mu_1}$ and unstable for $\mu_2 > \sqrt{-\mu_1}$.

Next, we verify the conditions for Hopf bifurcations at $\mu_2 = \sqrt{-\mu_1}$

(1). For $\mu_2 = \sqrt{-\mu_1}$, $\mu_1 < 0$, the eigenvalues on $(x_-, 0)$ are given by

$$\lambda_{1,2} = \pm i\sqrt{2\sqrt{-\mu_1}} (= \pm i\sqrt{-2x_-})$$

(2). Also we have observed that $\left. \frac{d}{d\mu_2} (Re \lambda(\mu_2)) \right|_{\mu_2 = \mu_{20}} = 1 \neq 0$

(3). Stability of the Hopf bifurcation:

To study the stability of the Hopf bifurcation, we change coordinates twice, first to bring the point $(-\sqrt{-\mu_1}, 0)$ to the origin and then to put the vector field into standard form.

Letting $\bar{x} = x - (-\sqrt{-\mu_1})$ and $\bar{y} = y$, we obtain

$$\begin{pmatrix} \dot{\bar{x}} \\ \dot{\bar{y}} \end{pmatrix} = \begin{pmatrix} 0 & 1 \\ -2\sqrt{-\mu_1} & 0 \end{pmatrix} \begin{pmatrix} \bar{x} \\ \bar{y} \end{pmatrix} + \begin{pmatrix} 0 \\ \bar{x}^2 + \bar{x}\bar{y} \end{pmatrix}$$

The coefficient matrix of the linear part is $A = \begin{pmatrix} 0 & 1 \\ -2\sqrt{-\mu_1} & 0 \end{pmatrix} = \begin{pmatrix} 0 & 1 \\ 2x_- & 0 \end{pmatrix}$

The eigenvalues are $\lambda = \pm i\sqrt{2\sqrt{-\mu_1}} = \pm i\sqrt{-2x_-} (= \pm i\omega)$ where $\omega = \sqrt{-2x_-}$

Therefore the eigenvectors corresponding to the eigenvalue λ are $\begin{pmatrix} 1 \\ \pm i\sqrt{-2x_-} \end{pmatrix}$

Then, using the linear transformation

$$\begin{pmatrix} \bar{x} \\ \bar{y} \end{pmatrix} = T \begin{pmatrix} u \\ v \end{pmatrix}$$

where $T = \begin{pmatrix} 0 & 1 \\ \sqrt{-2x_-} & 0 \end{pmatrix}$ is the matrix of real and imaginary parts of the eigenvectors of the eigenvalues $= \pm i\sqrt{-2x_-}$, we obtain the system with linear part in standard form:

$$\begin{pmatrix} \dot{u} \\ \dot{v} \end{pmatrix} = \begin{pmatrix} 0 & -\sqrt{-2x_-} \\ \sqrt{-2x_-} & 0 \end{pmatrix} \begin{pmatrix} u \\ v \end{pmatrix} + \begin{pmatrix} f(u, v) \\ g(u, v) \end{pmatrix}$$

where the nonlinear terms are

$$f(u, v) = uv + \frac{1}{\sqrt{-2x_-}} v^2$$

$$g(u, v) = 0$$

and we have the following:

$$f_u = v, f_{uu} = 0, f_{uuu} = 0, f_{uv} = 1, f_{uvv} = 0, f_v = u + \frac{1}{\sqrt{-2x_-}} 2v = 0, f_{vv} = \frac{2}{\sqrt{-2x_-}}$$

$$g_u = 0, g_{uu} = 0, g_{uuv} = 0, g_v = 0, g_{vv} = 0, g_{vvv} = 0, g_{uv} = 0$$

Substituting these in the relation

$$a = \frac{1}{16} [f_{uuu} + f_{uvv} + g_{uuv} + g_{vvv}] + \frac{1}{16\omega} [f_{uv}(f_{uu} + f_{vv}) - g_{uv}(g_{uu} + g_{vv}) - f_{uu}g_{uv} + f_{vv}g_{vv}]$$

We get $a = -\frac{1}{16x_-}$ that is $a = \frac{1}{16\sqrt{-\mu_1}} > 0$ for $\mu_1 < 0$ [as f_{xy} denotes $\frac{\partial^2 f}{\partial x \partial y}(0,0)$]

The bifurcation is therefore subcritical and we have a family of unstable periodic orbits. Thus, we can conclude that the system undergoes subcritical Hopf bifurcation for parameter values given by $\mu_2 = \sqrt{-\mu_1}$.

Below, we have given support to our above mentioned theoretical result through numerical simulation. In the first column of Figure 2, figures $a(I)$, $a(II)$ and $a(III)$ shows the phase orbit and the vector field and the figures $b(I)$, $b(II)$ and $b(III)$ shows the corresponding time series plot for our considered model for different parameter values and initial points. In $a(I)$ and $b(I)$, the parameter values are taken to be $\mu_1 = -1, \mu_2 = 0.9$ which is just before the occurrence of subcritical Hopf bifurcation at $\mu_1 = -1, \mu_2 = 1$ (according to our theoretical result)

with initial point $x_0 = -1.7, y_0 = 0$ which is inside the limit cycle. The figure $a(I)$ shows that the origin is stable and the orbit spirals to it. The same conclusion is supported by the time series plot shown in figure $b(I)$. For the next figures in $a(II)$ and $b(II)$, we have considered the parameter values $\mu_1 = -1, \mu_2 = -0.9$ which is before the occurrence of subcritical Hopf bifurcation. We considered the initial point as $x_0 = -1.8, y_0 = 0$, which is outside the limit cycle produced during the Hopf bifurcation. The figure $a(II)$ shows that the origin is stable and the limit cycle is unstable. The orbit spiral away from the limit cycle. The same conclusion is supported by the time series plot shown in $b(II)$. In figure $a(III)$ and $b(III)$ we have considered parameter values $\mu_1 = -1, \mu_2 = 1.1$ which is just after the subcritical Hopf bifurcation. The initial point was taken as $x_0 = -0.9, y_0 = 0$. Figure $a(III)$ and $b(III)$ shows that the origin is unstable, the orbits spiral away from it and no limit cycle exists in the neighbourhood. So, our numerical simulation clearly supports our conclusion that that the system undergoes subcritical Hopf bifurcation for parameter values given by $\mu_2 = \sqrt{-\mu_1}$.

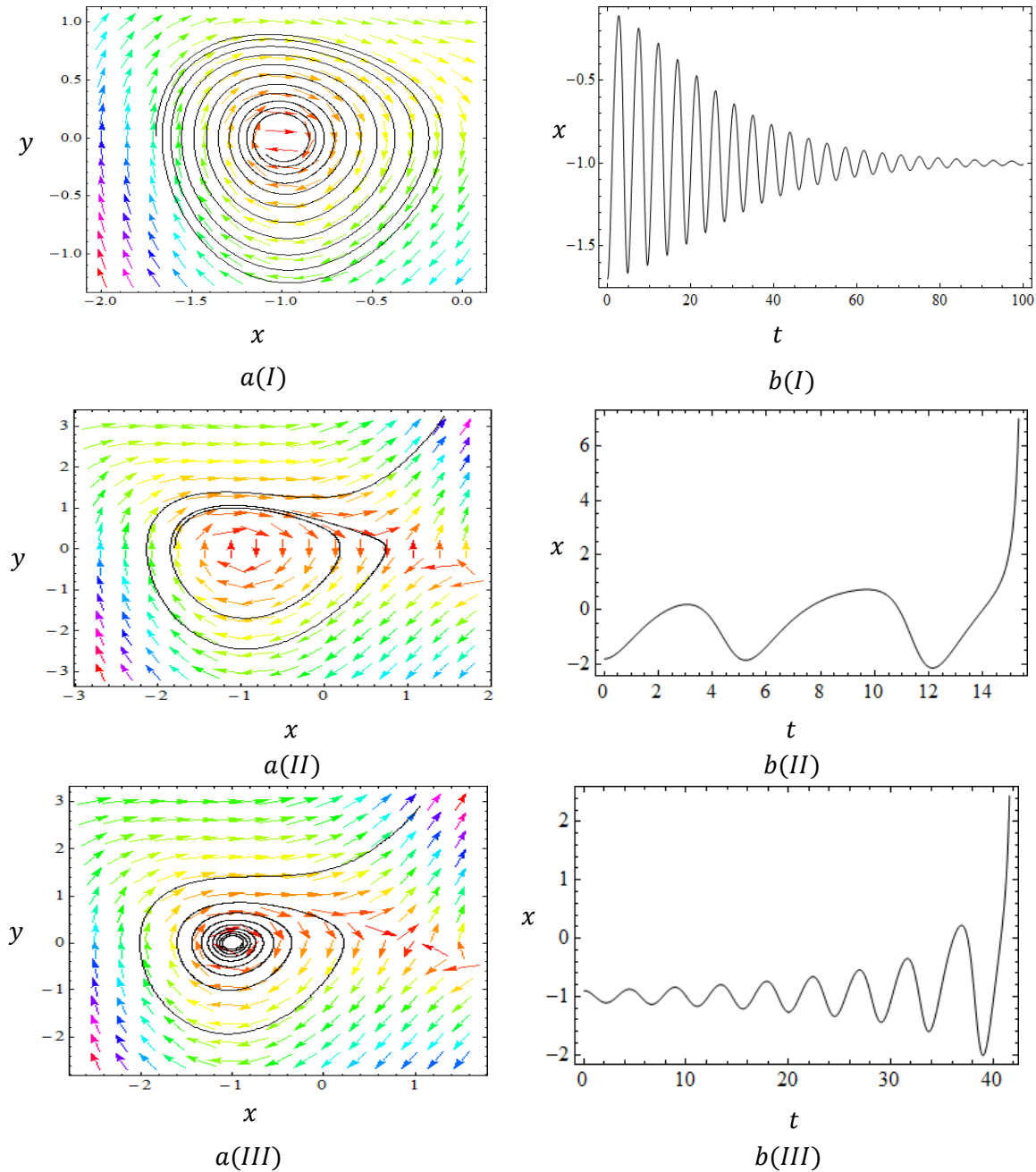


Fig2. The Phase orbit and time series of Eq. (4). $a(I)$ and $b(I)$ before the Hopf bifurcation at the parameter value $\mu_1 = -1, \mu_2 = 0.9$ with initial point $x_0 = -1.7, y_0 = 0$, which is inside the limit cycle, the origin is stable and the limit cycle is unstable, the orbit spirals to the origin. $a(II)$ and $b(II)$ before the Hopf bifurcation

at the parameter value $\mu_1 = -1, \mu_2 = -0.9$ with initial point $x_0 = -1.8, y_0 = 0$, which is outside the limit cycle, the origin is stable and limit cycle is unstable and the orbit spiral away from it. (a(III) and b(III)) after the Hopf bifurcation at the parameter value $\mu_1 = -1, \mu_2 = 1.1$ with initial point $x_0 = -0.9, y_0 = 0$, the origin is unstable, the orbits spiral away from it and there is no limit cycle exists.

VI CONCLUSION

We have presented Hopf bifurcation of a nonlinear system, which admits both supercritical and subcritical cases depending upon different parameter values. The results were derived theoretically with the help of center manifold theory and normal form method. Numerical simulations were presented in support of the conclusions drawn theoretically.

REFERENCES

- [1] Abed, E. H. and Fu, J.-H. "Local feedback stabilization and bifurcation control. I. Hopf bifurcation," *Systems & Control Letters*, vol. 7, no. 1, pp. 11–17, 1986.
- [2] AAlgaba, A., Freire, E. & Gamero, E. [1998] "Hypernormal form for the Hopf-zero bifurcation," *Int. J. Bifurcation and Chaos* 8, 1857–1887.
- [3] Balachandran, B. and Nayfeh, A.H.: *Nonlinear Dynamics*, 3, 19 (1992)
- [4] Boumediene Hamzi, Wei Kang, and Arthur J. Krener: *The Controlled Center Dynamics. Multiscale Model. Simul.*, 3(4), 838–852. (15 pages)
- [5] Broer, H.W.; Chow, S.N., Kim, Y.I. and Vegter, G: The Hamiltonian double-zero eigenvalues, *Fields Institute communications*, 4 (1995) 1-20]
- [6] Bryuno, A.D. [1989]. *Local Methods in Nonlinear Differential Equations. Part I. The Local Method of Nonlinear Analysis of Differential Equations. Part II. The Sets of Analyticity of a Normalizing Transformation.* Springer-Verlag: New York, Heidelberg, Berlin.
- [7] Carr, J. [1981]. *Applications of Center Manifold Theory.* Springer-Verlag: New York, Heidelberg, Berlin.
- [8] Chow, S.-N., Li, C.-Z. & Wang, D. [1994] *Normal Forms and Bifurcations of Planar Vector Fields* (Cambridge University Press, Cambridge).
- [9] Chua L.O. and KoKubu, H. : Normal forms for nonlinear vector fields-Part I: Theory and algorithm, *IEEE Trans. Circuits and systems* 35 (1988) 863-880
- [10] Das D., Banerjee, D. and Bhattacharjee, J. K.: Super-critical and Sub-Critical Hopf bifurcations in two and three dimensions. *arXiv:1309.5470v1*
- [11] Dercole, F. and Maggi, S.: "Detection and continuation of a border collision bifurcation in a forest fire model," *Applied Mathematics and Computation*, vol. 168, no. 1, pp. 623–635, 2005
- [12] Gazor, M. & Yu, P. [2012] "Spectral sequences and parametric normal forms," *J. Diff. Eqs.* 252, 1003–1031.
- [13] Gin'e, J. & Santallusia, X. [2001] "On the Poincar'e–Lyapunov constants and the Poincar'e series," *Appl. Math. (Warsaw)* 28, 17–30.
- [14] Golubisky, M.S. and Schaeffer D.G.: *Singularities and Groups in Bifurcation Theory*, Springer-Verlag, New York, 1985.
- [15] Guckenheimer J, Holmes P.: *Nonlinear oscillations, dynamical systems, and bifurcations of vector fields.* New York: Springer-Verlag; 1983.
- [16] Hassard, B.D. ; Kazarinoff, N.D. and Wan, Y.H.: *Theory and Applications of Hopf Bifurcations*, London Mathematical Society, Lecture Note Series, 41, Cambridge University Press, 1981.
- [17] Hassard, B. and Wan, Y.H.: *Bifurcation Formulae Derived from Center Manifold Theory.* *Journal of mathematical analysis and applications* 63, 297-312 (1978)
- [18] Henry, D. [1981]. *Geometric Theory of Semilinear Parabolic Equations.* Springer Lecture Notes in Mathematics, vol. 840. Springer-Verlag: New York, Heidelberg, Berlin.
- [19] Holmes, P. J. & Marsden, J. E. [1977]-Bifurcations to divergence and flutter in flow-induced oscillations: A finite-dimensional analysis," *J. Sound Vib.* 53, 471-503.
- [20] Huseyin, K.: *Multiple-Parameter Stability Theory and Its Applications* (Oxford University Press, Oxford, 1986).
- [21] Jordan, D. W. and Smith, P. : *Nonlinear Ordinary Differential Equations* (Oxford University Press, Oxford, 1987).
- [22] Kelley, A.: *The stable, center-stable, center, center-unstable, unstable manifolds.* An appendix in *Transversal Mappings and Flows*, R. Abraham and J. Robbin. Benjamin: New York, 1967.
- [23] Kunzostov, Y.A.: *Elements of Applied, Bifurcation Theory*, Second Edition, Springer-Verlag new-York Berlin Heidelberg, 2000.
- [24] Marsden, J.E. & McCracken, M.: *The Hopf bifurcation and its applications* (Springer-Verlag, New-York, 1976).
- [25] Ma, Y.; Agarwal, M. and Banerjee, S. "Border collision bifurcations in a soft impact system," *Physics Letters A*, vol. 354, no. 4, pp. 281–287, 2006.
- [26] Nayfeh, A.H. 'Methods of Normal Forms', John Wiley and Sons, New York, 1993.
- [27] Perko, L. : *Differential equations and Dynamical systems.* Springer, 2000.
- [28] Pliss, V.A. [1964]. The reduction principle in the theory of stability of motion. *Soviet Math.* 5, 247-250.
- [29] Ruelle, D.; Takens, F. : On the nature of turbulence; *Commun. math. Phys.* 20, 167-192, 1971
- [30] Sijbrand, J.: Properties of center manifolds. *Trans. Am. Math. Soc.* 289, 431-469, 1985
- [31] Sotitsaivili, A.N. : Bifurcations of topological type of a vector field near a singular point. *Trudy Sero. Petrovsk.* (1975) ,279-309.

- [32] Strogatz, S.H., : Nonlinear Dynamics and Chaos, Perseus Book Publishing, LLC, Cambridge,MA (1994).
- [33] Takens, F. :Unfoldings of certain singularities of vector fields: Generalized Hopf bifurcations," J. Di. Eqns. 14, 476-493, 1973.
- [34] Tian Y. and Yu P.: An explicit recursive formula for computing the normal form and cener manifold of general n-dimensional differential systems associated with Hopf bifurcation. Int. Journal of Bifurcation and Chaos, vol 23, No. 6 ,2013, 1-18
- [35] van der Meer, J.C.: The Hamiltonian Hopf Bifurcation. Springer Lecture Notes in Mathematics, vol. 1160. Springer-Verlag: New York, Heidelberg, Berlin.1985.
- [36] Wang, Q. G.; Lee, T. H. and C. Lin, Relay Feedback: Analysis, Identification and Control, Springer, London,UK, 2003.
- [37] Wiggins, S.: Introduction to applied nonlinear dynamical systemsand chaos. New York: Springer-Verlag; 1990.
- [38] Wu, R. and Li, X: Hopf Bifurcation Analysis and Anticontrol of Hopf Circles of the Rössler-Like System. Hindawi Publishing Corporation Abstract and Applied Analysis Volume 2012, Article ID 341870, 16 pages doi:10.1155/2012/341870
- [39] Yu, C. C. : Autotuning of PID Controllers: A Relay Feedback Approach, Springer, Berlin, Germany, 1999
- [40] Yuen, P. K. and Bau, H. H.:“Rendering a subcritical Hopf bifurcation supercritical,” Journal of FluidMechanics, vol. 317, pp. 91–109, 1996.
- [41] Yu, P. : Computation of Normal form via a perturbation technique. Journal of sound and Vibration 211(1), (1998), 19-38
- [42] Yu, P. [2003] “A simple and efficient method for computing center manifold and normal forms associated with semisimple cases,” Dyn. Contin. Discr. Impul. Syst. Series B: Appl. Algorith. 10, 273–286
- [43] Yu, P.: simplest normal forms of Hopf and Generalized Hopf bifurcations . International Journal of Bifurcation and Chaos, Vol. 9, No. 10 (1999) 1917-1939
- [44] Yu,P. ; Yuan, Y: A matching pursuit technique for computing thesimplest normal forms of vector fields. Journal of Symbolic Computation 35 (2003) 591–615
- [45] Yu, P. & Yuan, Y. [2003] “An efficient method for computing, the simplest normal forms of vector fields,” Int. J. Bifurcation and Chaos 13, 19–46.
- [46] Yu, P. & Leung, A. Y. T. [2003a] “The simplest normalform of Hopf bifurcation,” Nonlinearity 16, 277–300.
- [47] Yu, P. and Yuan, P. "The simplest normal form for the singularity of a pure imaginary pair and a zero eigenvalue," Dynamics of Continuous, Discrete and Impulsive Systems Series B: Applications & Algorithms,8b(2), 219-249, 2001.

Assessment of the Accuracy of Processing GPS Static Baselines Up To 40 Km Using Single and Dual Frequency GPS Receivers.

Khaled Mohamed Abdel Mageed

Assoc. Prof., Dept. of Civil Eng., Higher Technological Institute, Egypt

ABSTRACT: GPS applications can be grouped into static applications and kinematic applications. Static applications of GPS can be used in geodetic surveying, Aerial photogrammetric surveying, land surveying, orthometric height determination, topographic mapping, monitoring structural deformations, and engineering surveys; while kinematic applications of GPS, can be used in attitude determination of a moving body. On the other hand, GPS receivers can be categorized into two types: single frequency receivers which access the L1 frequency only, while dual frequency receivers which access both L1 and L2 frequencies. Single frequency receivers are affected more by ionospheric errors than dual frequency receivers, but they are less expensive, making them adaptable for certain surveying applications.

This paper investigates the accuracy of the discrepancies in Cartesian coordinates X, Y, and Z and the horizontal and spatial position P, in case of using single frequency and dual frequency GPS receivers for solving GPS baselines up to 40 km by static GPS technique. The results supported with statistical analysis showed that the horizontal positional discrepancy P2d between the single and dual frequency data has a mean value of 11.5mm with 3.5mm standard deviation, while the spatial positional discrepancy P3d has a mean value of 14.2mm with standard deviation 4.2mm. These findings are satisfying the standard and specification of establishing the first-order geodetic networks, as per the Federal Geodetic Control Committee FGCC. This means that the GPS single frequency receivers, which are less expensive than the dual frequency receivers, can be used in establishing GPS first-order control networks, up to 40 km baseline's lengths.

Keywords: GPS: Single frequency data: Dual frequency data.

I. INTRODUCTION

GPS has several applications in the field of geodesy, surveying, and mapping. GPS can be considered as one of the most distinct positioning systems for modern geodetic applications. Its benefits can be clearly shown in its practical applications as applied in surveying tasks. Generally, GPS applications can be grouped into static applications and kinematic applications. Static applications are concerned with positioning of stationary points, while kinematic applications are concerned with the positioning of moving objects. Static applications of GPS can be used in geodetic surveying, Aerial photogrammetric surveying, land surveying, orthometric height determination, topographic mapping, monitoring structural deformations, and engineering surveys. On the other hand, kinematic applications of GPS, can be used in attitude determination of a moving body, where the attitude is defined as the orientation of a specific coordinate system in a land vehicle, a ship, or an aircraft, with respect to a global or local coordinate system [1].

GPS measurements are subjected to some errors, which are affecting the accuracy of the final results. There are two basic types of errors, which are the systematic errors or biases, and the random errors. Generally, the biases affecting the GPS measurements fall into three categories, which are: satellite biases, station biases, and signal propagation biases. Satellite biases consist of biases in satellite ephemeris and satellite clock. Ground station biases usually consist of receiver clock bias, receiver noise and antenna phase center variation. The signal propagation biases appear due to tropospheric refraction, ionospheric refraction, and multipath. Biases in GPS are greatly eliminated either by modeling or by using special observing techniques, based on the concept of differenced modes. In addition to the mentioned three groups of GPS biases, the accuracy of the computed GPS position is also affected by the geometric locations of the GPS satellites as can be detected by the receiver. The more spread out the satellites are in the sky, the better the obtained accuracy of the GPS derived 3-d coordinates [2].

GPS receivers can be categorized into two types: single frequency receivers which access the L1 frequency only, while dual frequency receivers which access both L1 and L2 frequencies. The single frequency receivers output the raw C/A code pseudoranges, the L1 carrier phase measurements, and the navigation message, and gives accuracy about 1cm+2ppm. The dual frequency receivers is the most sophisticated and most expensive receiver type. This type of receiver is capable of measuring all the GPS observables, which are: L1, L2 carriers, C/A code, and P-code, and gives accuracy 5mm+1ppm [3]. Single frequency receivers are affected more by ionospheric errors than dual frequency receivers, but they are less expensive, making them adaptable for certain surveying applications. On the other hand, Dual frequency, multiple channel receivers can compensate better for ionospheric errors and these receivers are ideal for geodetic applications.

This paper investigates the accuracy of the discrepancies in Cartesian coordinates X, Y, and Z and the horizontal and spatial position P, in case of using single frequency and dual frequency GPS receivers for solving GPS baselines up to 40 km by static GPS technique. The GPS observables including code and phase measurements will be reviewed. The static GPS technique along with its field procedure and desired accuracy will be introduced. The methodology of investigation and the description of the field test will be presented. Finally, the analysis of the obtained results supported with the statistical analysis will be shown, from which the important conclusions and recommendations will be drawn.

II. REVIEW OF GPS OBSERVABLES

GPS observables are ranges which are deduced from measured time or phase differences based on a comparison between received signals and generated signals. Unlike the terrestrial distance measurements, GPS uses the so-called one-way concept, where, two clocks are used, namely one in the satellite, and the other in the receiver. Thus, the ranges are affected by satellite and receiver clocks errors and, consequently, they are denoted as pseudoranges. There are two types of GPS observables, namely the code pseudoranges and carrier phase observables. In general, the pseudorange observations are used for coarse navigation, whereas the carrier phase observations are used in high-precision surveying applications. That is due to the fact that the accuracy of the carrier phase observations is higher than the accuracy of code observations, [4].

Beside the two GPS observables, the GPS satellite transmits a navigation message. The navigation message is a data stream added to both L1 and L2 carriers as binary biphasic modulation at a low rate of 50 Kbps. It consists of 25 frames of 1500 bits each, or 37500 bits in total. This means that, the transmission of the complete navigation message takes 750 seconds. The navigation message contains, along with other information, the coordinates of the GPS satellites as a function of time, the satellite health status, the satellite clock correction, the satellite almanac, and atmospheric data. Each satellite transmits its own navigation message with information on the other satellites, such as the approximate location and health status [5].

2.1 Code Pseudorange Observables

The code pseudorange is a measure of the distance between the satellite and the receiver. The P-code, C/A-code can be used to determine the code pseudorange. These ranges can be determined by multiplying the speed of light by the time shift required to match the code generated in the receiver with the code received from the satellite (figure 1). Analogously, the delays of the clocks with respect to GPS system time frame will lead to timing error. The tropospheric and ionospheric delays affect the measured code pseudorange [6]. The general form of code pseudorange observation equation is:

$$P = \rho + c(dt - dT) + d_{ion} + d_{trop} + d_{orb} + \epsilon_p \quad (1)$$

Where: P is the observed pseudorange, ρ is the unknown geometric satellite to receiver range, c is speed of light which is approximately equal to 300,000 km/s, dt and dT are satellite and receiver clock errors respectively, d_{ion} , d_{trop} , are the error due to ionospheric, tropospheric refraction respectively, d_{orb} is the orbital error and ϵ_p is the code measurement noise.

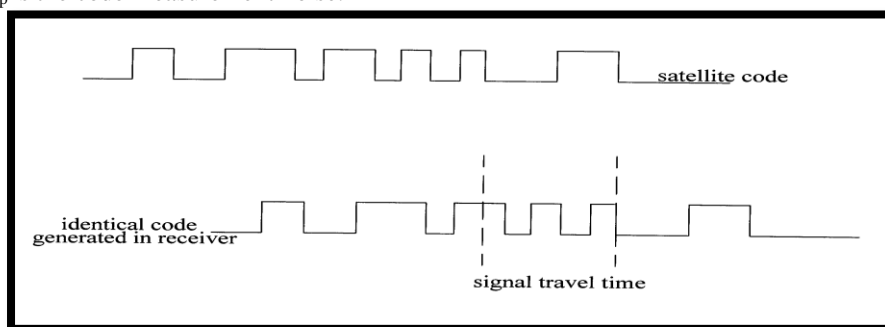


Fig. 1: GPS Pseudorange Observables

The precision of a pseudorange derived from code measurement has been about 1% of the chip length. Consequently, a precision of about 3m, 0.3m is achieved with C/A-code and P-code pseudoranges respectively. However, recent development indicates that a precision of about 0.1% of the chip length may be obtained [7].

Many applications are based on the pseudorange observations, mostly related to the fields of navigation, where the instantaneous positions are required. Note in equation (1) that, the bias term d_{ion} can be determined, with high percentage, in case of using dual frequency receivers, since the ionospheric effect is frequency dependant, and its estimation parameters are usually transmitted within the satellite message [8]. Concerning the tropospheric effect term d_{trop} , it can be evaluated to more than 95%, using an adopted model, which is a function of measured meteorological quantities, such as humidity, pressure, and temperature, of the atmosphere surrounding the receiver position. Concerning the orbital bias term d_{orb} , it can be estimated from satellite orbital dynamics continuous analysis, at the master control station, and included in the satellite-transmitted message also. The satellite and receiver clocks biases term $(dt-dT)$, is usually treated as one unknown parameter. Hence, equation (1) of observed pseudorange will be left out with only four unknowns parameters, which are the 3-d geocentric cartesian coordinates (X, Y, Z) of the receiver antenna position, in addition to the clock bias term. Of course, in order to solve such an equation, for the four unknown parameters, one needs to have four of these observation equations. This is why the GPS system is designed, such that at least four GPS satellites can be observed simultaneously at the same time from the ground receiver. However, for more reliability of the derived receiver 3-d coordinates, collected observations from several satellites, over a certain period called session, must be performed, in order to apply the least squares estimation process, with a high degree of freedom [9].

2.2 Carrier Phase Observables

The range between the receiver and satellite can be obtained through the carrier phase. The range would simply be the sum of the total number of full carrier cycles plus fractional cycle at the receiver and the satellite, multiplied by the carrier wave length (figure 2). The ranges determined with the carriers are more accurate than those obtained by the codes [10]. This is due to the fact that, the wavelength of the carrier signal (19cm in case of L1) is smaller than the codes. However, there is a problem that the carriers are just pure sinusoidal waves, which means that all cycles look the same. Therefore, the GPS receiver has no means to differentiate one cycle from the other. In other words, the receiver cannot determine the total number of the complete cycles between the satellite and receiver when switched on. The receiver can only measure a fraction of a cycle accurately, while the initial number of complete cycles remains unknown, or ambiguous [11]. This initial cycle ambiguity remains unchanged over time as long as no signal loss or cycle slip occurs.

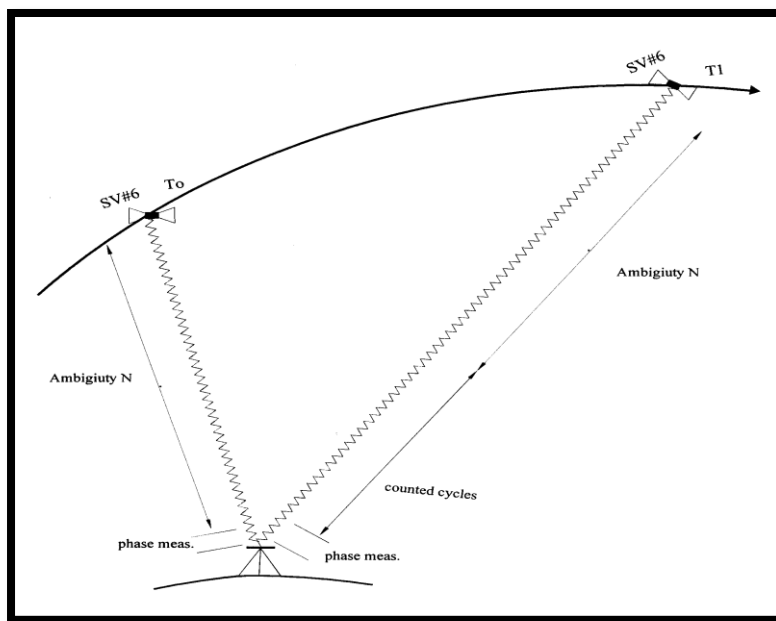


Fig. 2: GPS Carrier Phase Observables

The observation equation of the phase pseudorange is:

$$\Phi = \rho + c(dt - dT) + \lambda N - d_{ion} + d_{trop} + d_{orb} + \varepsilon_{\phi} \quad (2)$$

Where, the measured phase is indicated in meters by Φ , λ is the carrier wavelength, N is the phase ambiguity, and ε_{ϕ} is the combined receiver and multipath noise, and the other remaining symbols are the same as defined

in equation (2). The same analysis of the bias terms and unknown parameters, as given in the previous subsection, holds true here also for the case of carrier phase observation equation. The only difference here is the ambiguity term N , which can be solved for, using a certain adopted technique, which will be discussed later. This means, again, that at least four satellites should be in view at the time, which can be simultaneously tracked from the same ground receiver. On the other hand, for both cases of code pseudorange and carrier phase pseudorange, most of the bias terms can be eliminated, or minimized by following a certain technique for collecting GPS measurements, such as single, double, and triple differences; and/or using mathematical model; and/or using linear combination [12].

Accuracy of the carrier phase measurements can reach the centimetre level or even less. Accordingly, all GPS precise geodetic applications are mainly based on this type of observables. Such applications include monitoring of local and regional crustal deformations, and the establishment of geodetic control networks. Both types of GPS observables are different in their nature. The pseudorange is an instantaneous observation, which is in principle independent of post measurements, whereas the carrier phase measurement is continuous and dependent on the tracking history. In fact, the two types of GPS observables can be combined in the so-called phase-smoothed pseudorange, [13]. In this concept, the change of phase over time is added to the initial pseudorange to get an estimate of the current pseudorange observation. The noise of the resulting new observable will be lower than the noise of the original pseudorange. In addition, this approach has the advantage of the significant reduction of multipath effect, which affects the carrier phase observations much less than the pseudoranges.

III. GPS STATIC TECHNIQUE

The selection of the observation technique in a GPS survey depends upon the particular requirements of the project, and the desired accuracy especially is playing a dominant role. The GPS observation techniques include: single point positioning SPP; differential positioning DGPS; and relative positioning. Relative positioning includes: static, rapid static, stop and go, kinematic, real time kinematic RTK. GPS single point positioning employs one GPS receiver, while DGPS and relative GPS positioning employ two or more GPS receivers, simultaneously tracking the same satellites. Surveying works with GPS have conventionally been carried out in the relative and differential positioning techniques. This is mainly due to the higher positioning accuracy obtained from the relative and differential techniques, compared to that of the GPS point positioning. A major disadvantage of GPS relative and differential techniques, however, is the dependency on the measurements or corrections from the reference receiver [14].

GPS Static relative positioning is the common method for control networks, due to its high accuracy. Static relative positioning by carrier phase at present, is the most frequently used method by surveyors, as it is more accurate as compared to the code pseudorange measurements. The principle of static relative positioning, is based on determining the vector between two stationary receivers, this vector is often called baseline. According to this terminology, the process is called single or multipoint baseline determination. In static surveying 1 ppm to 0.1 ppm accuracies are achieved, which is equivalent to few centimetres and millimetres accuracy, for short baselines of some kilometres [3].

The field procedure of relative static survey, is performed by placing a receiver on a known point, and placing the second receiver on the unknown point, and collecting simultaneously data from at least four satellites. The observing time required to fix the position, is called a session. This time is varying according to baseline length, satellite configuration, selective availability, atmospheric conditions, and the required accuracy. Normally, one-hour observation period is required to each baseline. However, to increase the accuracy, the receiver may be kept observing for longer period especially, in case of long length baselines. Figure (3) shows the basic idea of GPS static technique. Typically, the range of accuracy for static survey, is normally 0.3–1.0 cm + 1–2 ppm. [2].

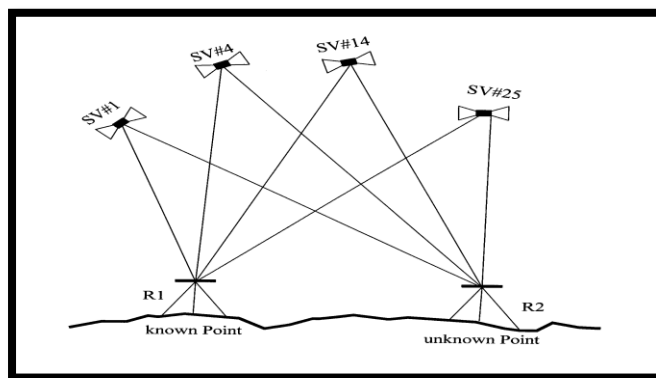


Fig. 3: Concept of GPS Static Technique

After completing the field work, the collected data is downloaded from the receivers to the PC for processing. Different processing options may be selected depending on the baseline length, and other factors. For example, if the baseline is relatively short, say, 15-20km, resolving the ambiguity would be a key issue to ensure high precision accuracy. On the other hand, if the baseline is relatively long, the user may select the ionosphere free linear combination to remove the effect of the ionosphere. For very long baselines, over 1000km, it is recommended to process the data using scientific software such as BERNES software, developed by the University of Bern, rather than using commercial software [3]. The static surveying is usually applied in high accuracy surveying projects, such as establishing new geodetic networks, densification of existing first order control networks or lower order network, crustal movements, and structural deformation.

IV. METHODOLOGY OF INVESTIGATION

The objective of this paper is to statically analyze the difference in 3-d coordinates, as well as the horizontal and spatial positions, resulted from processing GPS baselines up to 40 km collected by static GPS technique, using single frequency data L1, and dual frequency data L1 and L2. A number of 15 GPS static baselines with approximate distances from 1.5 km to 42.5 km, were processed two times: the first one using single frequency L1 data, and the second one using the dual frequency data L1 and L2.

The field test was conducted at Taif city, Saudi Arabia on April 2012. A dual frequency GPS receiver of Topcon GR3 was setup at a reference control point [15]. A second dual frequency receiver of the same type of Topcon GR3 was set up sequentially on 15 new control points of approximate distances from 1.5 km to 42.5 km, from the base station. The observational operating parameters were the same for the two receivers, which are: static mode, elevation angle 15°, and 10 seconds rate of observations. The observational durations of the baselines were as shown in table 1.

Table 1: duration of GPS static observation data

Baselines Range (km)	Duration (minutes)
1 to 5	30
5 to 10	45
10 to 15	60
15 to 20	90
20 to 25	120
25 to 30	150
30 to 35	180
35 to 42	210

The raw data of the GPS campaign were downloaded and transferred to Rinex format using Topcon Link software [16]. The processing of the Rinex data was conducted using Leica Geo Office software [17]. The data were processed two times: the first run was using L1 data, while the second run was using L1 and L2 data. The 3-d cartesian coordinates for every baseline in each run were archived for the statistical analysis.

V. ANALYSIS OF RESULTS

The analysis of the results will be based on comparing the discrepancies in X, Y, and Z coordinates between processing 15 GPS baselines using dual frequency data L1 and L2, against processing the same baselines with single frequency data L1 only. The cartesian discrepancies are:

$$\begin{aligned} \Delta X_{dul-sin} &= X_{dul} - X_{sin} \\ \Delta Y_{dul-sin} &= Y_{dul} - Y_{sin} \\ \Delta Z_{dul-sin} &= Z_{dul} - Z_{sin} \end{aligned} \tag{3}$$

Where: $\Delta X_{dul-sin}$, $\Delta Y_{dul-sin}$, and $\Delta Z_{dul-sin}$: the X, Y, and Z discrepancies between using dual and single frequency data.

X_{dul} , Y_{dul} , and Z_{dul} : the X, Y, and Z coordinates resulted from using dual frequency data L1 and L2.

X_{sin} , Y_{sin} , and Z_{sin} : the X, Y, and Z coordinates resulted from using single frequency data L1.

The 2-d and 3-d positional discrepancy between the two solutions ΔP_{2d} , ΔP_{3d} , as well as the standard deviation $\sigma_{\Delta P_{2d}}$, $\sigma_{\Delta P_{3d}}$ can be calculated from [18]:

$$\Delta P_{2d} = \sqrt{(\Delta X_{dul-sin})^2 + (\Delta Y_{dul-sin})^2} \quad \Delta P_{3d} = \sqrt{(\Delta X_{dul-sin})^2 + (\Delta Y_{dul-sin})^2 + (\Delta Z_{dul-sin})^2} \tag{4}$$

$$\sigma_{\Delta P_{2d}}^2 = \sigma_{\Delta X_{dul-sin}}^2 + \sigma_{\Delta Y_{dul-sin}}^2 \quad \sigma_{\Delta P_{3d}}^2 = \sigma_{\Delta X_{dul-sin}}^2 + \sigma_{\Delta Y_{dul-sin}}^2 + \sigma_{\Delta Z_{dul-sin}}^2 \tag{5}$$

The discrepancies in X, Y, Z and 2-d and 3-d position P, between processing the GPS data using dual and single frequency data are shown in Table (2).

Table 2: The discrepancies in X, Y, Z, and position P

Baseline Id	Baseline Length (km)	ΔX (mm)	ΔY (mm)	ΔZ (mm)	ΔP_{2d} (mm)	ΔP_{3d} (mm)
1	1.6	-0.9	1.4	0.8	1.7	1.8
2	3.0	4.5	8.2	5.8	9.4	11.0
3	4.8	3.8	0.8	-15.9	3.9	16.4
4	7.3	-0.5	-3.3	-5.0	3.3	6.0
5	9.4	4.0	-1.2	-4.8	4.2	6.4
6	11.0	10.3	3.6	-4.5	10.9	11.8
7	13.7	16.0	15.3	12.6	22.1	25.5
8	15.4	-12.1	-6.4	-2.1	13.7	13.8
9	18.7	16.2	-13.8	11.9	21.3	24.4
10	22.2	-5.2	1.0	1.4	5.3	5.5
11	25.7	-15.6	4.7	1.2	16.3	16.3
12	28.2	-10.0	-14.5	-14.0	17.6	22.5
13	33.4	15.3	-0.4	-17.6	15.3	23.3
14	37.3	6.3	-19.2	-7.2	20.2	21.5
15	42.5	2.0	-7.1	-1.1	7.4	7.5

Figure (4) shows the X, Y, and Z coordinate discrepancies for the 15 baselines derived from dual and single frequency data. In addition, Figure (5) shows the 2-d and 3-d positional discrepancies P for the same baselines.

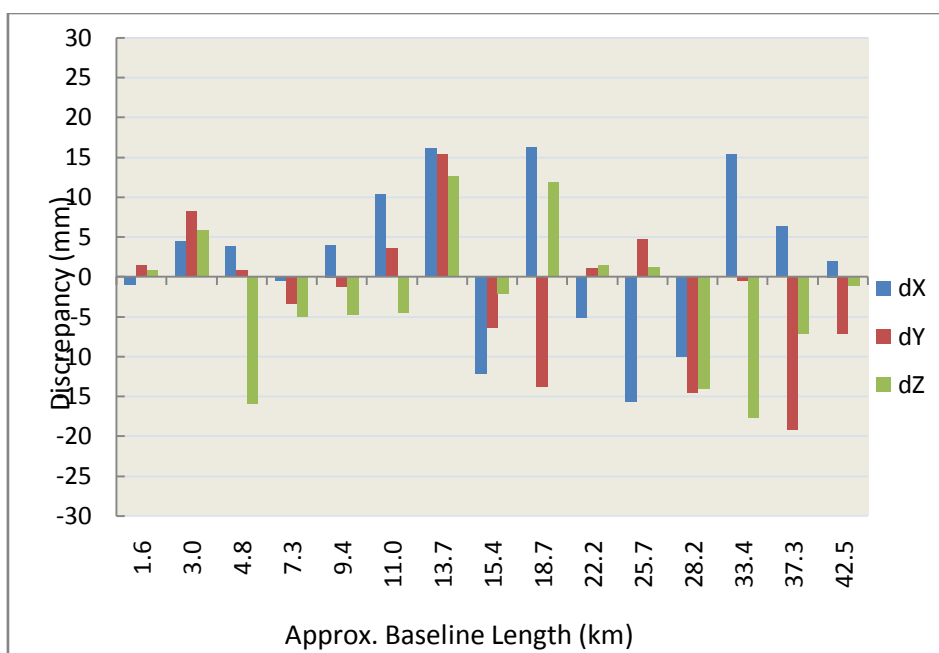


Figure 4: Variation of the X, Y, and Z coordinate discrepancies

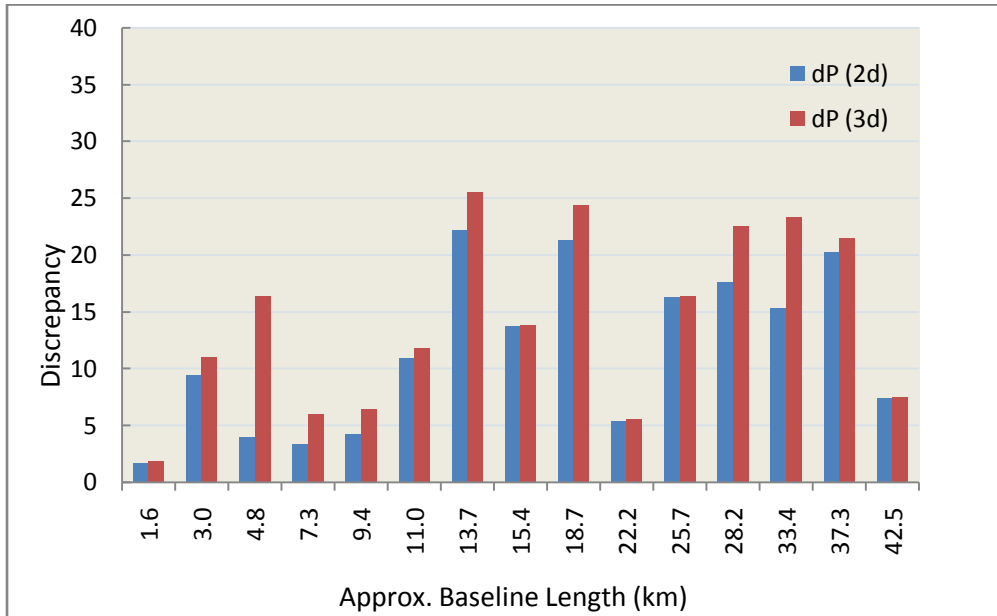


Figure 5: Variation of the Positional discrepancies

The previous figures are supported by descriptive statistics to measure the quality of the obtained results. Table (3) shows these descriptive statistics. For instance, the X-coordinate discrepancies have mean value 2.3mm and SD 10mm for single determination. The Y-coordinate discrepancies have mean value of -2.1mm and 9.1mm SD for single determination. The Z-coordinate discrepancies have -2.6mm mean value and 9mm SD for single determination. Finally, the 2-d and 3-d positional discrepancies have 11.5mm, 14.2mm mean value respectively; with SD 13.5mm, and 16.2mm respectively.

Table 3: Descriptive statistics of the discrepancies (mm)

Disc.	Max.	Min.	Range	Mean	S.D _{single}	S.D _{mean}
ΔX	16.2	-15.6	31.8	2.3	10.0	2.6
ΔY	15.3	-19.2	34.5	-2.1	9.1	2.3
ΔZ	12.6	-17.6	30.2	-2.6	9.0	2.3
ΔP _{2d}	22.1	1.7	20.5	11.5	13.5	3.5
ΔP _{3d}	25.5	1.8	23.6	14.2	16.2	4.2

In order to check any systematic errors in the sample of the resulted discrepancies, the sample mean should be examined according to its deviation from the mean of the population which equal to zero [18]. This random sample is assumed to be normally distributed and had taken from a population of unknown true mean μ equal to zero. The following confidence interval can be used:

$$\mu - T .SD_{mean} < m < \mu + T .SD_{mean} \tag{6}$$

Where μ is the population mean ($\mu = 0$), SD_{mean} is the sample standard deviation, T is the Student t-distribution corresponding to sample size n and degree of freedom df equal to n-1, assuming that the confidence level is 95%. Table 4 shows the results of this test which indicates that no significant systematic errors are existing in the discrepancies between the two solutions.

Table 4: Testing of deviation of the sample mean

Disc.	Df	T	SD _{mean}	Lower limit	Mean	Upper limit	Test result
ΔX	14	2.14	2.6 mm	-5.6 mm	2.3 mm	5.6 mm	pass
ΔY			2.3 mm	-4.9 mm	-2.1 mm	4.9 mm	pass
ΔZ			2.3 mm	-4.9 mm	-2.6 mm	4.9 mm	pass

VI. CONCLUSIONS

This paper analyzes the difference in Cartesian coordinates X, Y, and Z between processing GPS baselines which are collected with static technique, in case of using single frequency data L1, and in case of using dual frequency data L1 and L2. A field test consists of 15 GPS static baselines, was made for the purpose of the analysis. The baseline lengths were ranged from 1.5 km to 42.5 km.

The results supported with statistical analysis showed that the differences in the cartesian coordinates between processing GPS static baselines using single and dual frequency data have mean values of 2.3mm, 2.1mm, and 2.6mm in X, Y, and Z coordinates respectively. The standard deviations of these means are: 2.6mm, 2.3mm, and 2.3mm for the 3-d cartesian components respectively. The horizontal positional discrepancy P_{2d} between the single and dual frequency data has a mean value of 11.5mm with 3.5mm standard deviation, while the spatial positional discrepancy P_{3d} has a mean value of 14.2mm with standard deviation 4.2mm. The relative accuracy of the horizontal positioning using GPS single frequency data is about 1:370,000, which satisfying the standard and specification of establishing the first-order geodetic networks which is 1:120,000, as per the Federal Geodetic Control Committee FGCC.

The previous results showed that there are no significant differences in the resulted cartesian coordinates in case of processing GPS baselines collected with static technique, using single frequency data L1, or using dual frequency data L1 and L2. This means that the GPS single frequency receivers, which are less expensive than the dual frequency receivers, can be used in establishing GPS first-order control networks, up to 40 km baseline's lengths.

REFERENCES

- [1] Abdel Mageed, Kh. M, Accuracy Comparison and Time Saving between GPS Stop & Go, Kinematic, and Kinematic On The Fly Techniques, *Ain Shams Journal of Civil Engineering*, vol. 1, 2009.
- [2] Hofmann-Wellenhof, B., H. Lichtenegger and J. Collins, *Global Positioning System - Theory and Practice. 5th Revised Edition* (Springer-Verlag, New York, 2001).
- [3] El-Rabbany, A, *Introduction to the Global Positioning System GPS* (Artech House Mobile Communications Series, Boston, London, 2002).
- [4] Leick A, *GPS Satellite Surveying* (A Wiley Inter-Science Publications, John Wiley & Sons, New York, 1995).
- [5] Langley, R. B. The GPS Observables. *GPS World*, 4 (2), 1993.
- [6] Guochang, Xu, *GPS Theory, Algorithms, and Applications Second Edition* (Springer Publishing, New York, 2007).
- [7] Rizos, C, *Principles and Practice of GPS Surveying* (Monograph 17, School of Geomatics Engineering, the University of New south Wales, 1997).
- [8] Abdel Mageed, Kh. M., Accuracy Assessment for Processing GPS Short Baselines using Ionosphere-free Linear Combination, . *Australian Journal of Basic and Applied Sciences*.Sep. 2011.
- [9] Anderson, J. M. and E. M. Mikhail, *Surveying: Theory and Practice 7th Edition* (McGraw-Hill, New York, USA, 1998).
- [10] Kaplan, E., *Understanding GPS: Principles and Applications* (Norwood, MA: Artech House, 1996).
- [11] Seeber G., *Satellite Geodesy: Foundations, Methods and Applications* (Walter de Gruyter, Berlin, 1993).
- [12] Gurtner W., G. Beutler, and M. Rothacher: Combination of GPS observations made with different receiver types. *5th International Geodetic Symposium on Satellite Positioning*, Las Cruces, New Mexico, 1989.
- [13] Kleusberg A. and R. B. Langley, The limitations of GPS, *GPS World*, 1 (2), 1990.
- [14] Gerdan, G.P., Rural Cadastral Surveying with the Global Positioning System, *The Australian Surveyor*, 36 (3) 1991.
- [15] Topcon Company, *GR-3 Operator's Manual*, 2007.
- [16] Topcon Company, *Topcon Link Reference Manual*, 2009.
- [17] Leica Company, *Leica Geo Office Online Help*, 2010.
- [18] Comery, A., P. Bott and H. Lee, *Elementary Statistics: A Problem-Solving Approach, Second Edition*, (Brown Publishers, California, USA, 1989).

Heat Source Effects in Heat and Mass Transfer Of Nano Fluid Flow past a Sheet

G. V. P. N. Srikanth¹, B. Suresh Babu², Dr. G. Srinivas¹

¹Department of Mathematics, Guru Nanak Institute of Technology, Hyderabad, India

²Department of Mathematics, Sreyas Institute of Engineering & Technology, Hyderabad, India

ABSTRACT: The Heat source/sink and suction/injection effects are studied during the Heat and Mass transfer through copper, water nano-fluid along an inclined permeable oscillating flat sheet. The governing equations are solved and the influence of various parameters is analyzed. The Rate of heat transfer for volume fraction against heat source is also analyzed.

Keywords: Nano - fluid, MHD, Inclined plate, Method of line.

List of symbols:

- B_0 Constant applied magnetic field (Wb m^{-2})
 C_p Specific heat at constant pressure ($\text{J kg}^{-1} \text{K}^{-1}$)
 g Gravity acceleration (m s^{-2})
 J Current density
 M Dimensionless magnetic field parameter
 n Dimensionless frequency
 Nu Local Nusselt number
 Pr Prandtl number
 Q Dimensional heat source (kJ s^{-1})
 Q_H Dimensionless heat source parameter (kJ s^{-1})
 s Dimensionless suction parameter
 t Dimensionless time (s)
 T Local temperature of the nano-fluid (K)
 T_w Wall temperature (K)
 T_∞ Temperature of the ambient nano-fluid (K)
 u, w Dimensionless velocity components (m s^{-1})
 U_0 Characteristic velocity (m s^{-1})
 w_0 Mass flux velocity
 k Thermal conductivity
 D_f Diffusivity of water
 D_s Diffusivity of copper

Greek symbols:

- α Thermal diffusivity ($\text{m}^2 \text{s}^{-1}$)
 β_T Thermal expansion coefficient (K^{-1})
 β_c Molecular expansion coefficient
 ε Dimensionless small quantity ($\ll 1$)
 ϕ Solid volume fraction of the nano-particles
 μ Dynamic viscosity (Pa s)

ψ	Kinematic viscosity ($\text{m}^2 \text{s}^{-1}$)
θ	Dimensionless temperature
σ	Electrical conductivity ($\text{m}^2 \text{s}^{-1}$)
σ_1	Stefan-Boltzmann constant
δ	Mean absorption Coefficient
γ	Inclination angle of the plate
ρ	Density
C	Dimensionless diffusion

Superscript

– Dimensional quantities

Subscripts

f Fluid
s Solid
nf Nano-fluid

I. INTRODUCTION

Research in the field of Heat and Mass transfer challenging the cooling of many systems used in day to day life of mankind. The heat and mass transfer enhances enormously when nano-particles are suspended in liquids like water, ethylene glycol etc. This has substantiated by Das, Choi and Patel (2006) in their review paper. In this scenario cooling systems demand the very low heat and mass transfer rate through nano – fluids and heat mass energy systems like automobiles demanding the high heat and mass transfer rate through nano – fluids.

Kuznetsov and Nield (2010) studied the classical problem of free convection boundary layer flow of a viscous and incompressible fluid (Newtonian fluid) past a vertical flat plate to the case of nano-fluids. In these papers the authors have used the nano-fluid model proposed by Buongiorno (2006). Although this author discovered that seven slip mechanisms take place in the convective transport in nano-fluids, it is only the Brownian diffusion and the thermophoresis that are the most important when the turbulent flow effects are absent. More recently, Khan and Aziz (2011) studied Natural convection flow of a nano-fluid over a vertical plate with uniform surface heat flux. M. A. A. Hamad and I. Pop (2011) presented in their recent paper that the solid volume and heat source enhances the heat and mass transfer rate. This brief survey clearly indicates that a definitive conclusion regarding the role of nano-particles in enhancing natural convective transport is yet to be reached. Recently Anwar et.al (2012) studied the conjugate effects of heat and mass transfer of nano-fluids over a non-linear stretching sheet.

In this paper we aim to investigate the MHD Cu – water nano-fluid flow and the heat and mass transfer past a vertical infinite permeable inclined oscillating flat plate under heat and mass source and suction.

II. MATHEMATICAL FORMULATION

Consider the unsteady three dimensional free convection flow of a nano-fluid past a vertical permeable semi-infinite plate in the presence of an applied magnetic field with constant heat source. We consider a Cartesian coordinate system $(\bar{x}, \bar{y}, \bar{z})$. The flow is assumed to be in the \bar{x} direction, which is taken along the plate, and \bar{z} - axis is normal to the plate. We assume that the plate has an oscillatory movement on time \bar{t} and frequency \bar{n} with the velocity $u(0,t)$, which is given $u(0,t) = U_0(1 + \varepsilon \cos(nt))$, where ε is a small constant parameter ($\varepsilon \ll 1$) and U_0 is the characteristic velocity. We consider that initially ($t < 0$) the fluid as well as the plate is at rest. A uniform external magnetic field B_0 is taken to be acting along the \bar{z} -axis. We consider the case of a short circuit problem in which the applied electric field $E = 0$, and also assume that the induced magnetic field is small compared to the external magnetic field B_0 . The surface temperature is assumed to have the constant value T_w while the ambient temperature has the constant value T_∞ , where $T_w > T_\infty$. The conservation equation of current density $\nabla \cdot J = 0$ gives $J_z = \text{constant}$. Since the plate is electrically non-conducting, this constant is zero. It is assumed that the plate is infinite in extent and hence all physical quantities do not depend on \bar{x} and \bar{y} but depend only on \bar{z} and \bar{t} ,

$$\text{i.e.} \quad \frac{\partial u}{\partial x} + \frac{\partial v}{\partial y} = 0$$

It is further assumed that the regular fluid and the suspended nano-particles are in thermal equilibrium and no slip occurs between them. Under Bossinesq and boundary layer approximations, the boundary layer equations governing the flow and temperature are,

$$\frac{\partial w}{\partial z} = 0 \dots\dots\dots(1)$$

$$\frac{\partial u}{\partial t} + w \frac{\partial u}{\partial z} = \frac{1}{\rho_{nf}} \left[\mu_{nf} \frac{\partial^2 u}{\partial z^2} + (\rho \beta_T)_{nf} g (T - T_\infty) \cos \gamma + (\rho \beta_c)_{nf} g (c - c_\infty) \cos \gamma - \sigma B_0^2 u \right] \dots\dots\dots(2)$$

$$\frac{\partial T}{\partial t} + w \frac{\partial T}{\partial z} = \alpha_{nf} \frac{\partial^2 T}{\partial z^2} - \frac{Q}{(\rho c_p)_{nf}} (T - T_\infty) \dots\dots\dots(3)$$

$$\frac{\partial c}{\partial t} + w \frac{\partial c}{\partial z} = D_{nf} \frac{\partial^2 c}{\partial z^2} \dots\dots\dots(4)$$

The appropriate initial and boundary conditions for the problem are given by

$$\left. \begin{aligned} u(z,t) = 0, T = T_\infty, c = c_\infty \quad \text{for } t < 0 \quad \forall z \\ u(0,t) = U_0 \left[1 + \frac{\varepsilon}{2} (e^{i n t} + e^{-i n t}) \right], T(0,t) = T_w, c(0,t) = c_w \\ u(\infty,t) \rightarrow 0, T(\infty,t) \rightarrow T_\infty, c(\infty,t) \rightarrow c_\infty, \varepsilon \ll 1 \end{aligned} \right\} t \geq 0 \dots\dots\dots(5)$$

Thermo-Physical properties are related as follows:

$$\begin{aligned} \rho_{nf} &= (1-\phi) \rho_f + \phi \rho_s, \quad \mu_{nf} = \frac{\mu_f}{(1-\phi)^{2.5}}, \quad \alpha_{nf} = \frac{k_{nf}}{(\rho c_p)_{nf}} \\ (\rho c_p)_{nf} &= (1-\phi) (\rho c_p)_f + \phi (\rho c_p)_s \\ (\rho \beta)_{nf} &= (1-\phi) (\rho \beta)_f + \phi (\rho \beta)_s, \\ k_{nf} &= k_f \left[\frac{k_s + 2k_f - 2\phi(k_f - k_s)}{k_s + 2k_f + \phi(k_f - k_s)} \right] \dots\dots\dots(6) \end{aligned}$$

The thermo-physical properties (values) of the materials used are as follows.

Table I

Physical Properties	Water	Copper(Cu)
C_p (J / kg K)	4,179	385
ρ (kg / m ³)	997.1	8,933
κ (W / m K)	0.613	400
$\beta_T \times 10^{-5}$ (1/K)	21	1.67
$\beta_c \times 10^6$ (m ² /h)	298.2	3.05

We consider the solution of Esq. (1) as $w = -w_0 \dots\dots\dots(7)$

Where the constant w_0 represents the normal velocity at the plate which is positive for suction ($w_0 > 0$) and negative for blowing or injection ($w_0 < 0$). Thus, we introduce the following dimensionless variables:

$$z = \left(\frac{\psi_f}{U_0}\right)Z, \quad t = \left(\frac{\psi_f}{U_0^2}\right)t^*, \quad n = \left(\frac{U_0^2}{\psi_f}\right)\eta, \quad u = UU_0, \quad \theta = \frac{T-T_\infty}{T_w-T_\infty}, \quad c = \frac{c-c_\infty}{c_w-c_\infty} \quad \dots\dots\dots (8)$$

Using equations 5,6,7,8 the Esq. 2,3&4 can be written in the following dimensionless form:

$$\left[1-\phi + \phi \left(\frac{\rho_s}{\rho_f}\right)\right] \left(\frac{\partial U}{\partial \tau} - S \frac{\partial U}{\partial Z}\right) = \frac{1}{(1-\phi)^{2.5}} \frac{\partial^2 U}{\partial Z^2} + \left[1-\phi + \phi \frac{(\rho \beta_T)_s}{(\rho \beta_T)_f}\right] \theta \cos \gamma + \left[1-\phi + \phi \frac{(\rho \beta_c)_s}{(\rho \beta_c)_f}\right] c \cos \gamma - MU \quad \dots\dots\dots (9)$$

$$\left[1-\phi + \phi \frac{(\rho c_p)_s}{(\rho c_p)_f}\right] \left(\frac{\partial \theta}{\partial \tau} - S \frac{\partial \theta}{\partial Z}\right) = \frac{1}{p_r} \left[\frac{k_{nf}}{k_f} \frac{\partial^2 \theta}{\partial Z^2}\right] - \frac{1}{p_r} Q_H \theta \quad \dots\dots\dots (10)$$

$$\left[1-\phi + \phi \frac{(\rho c_p)_s}{(\rho c_p)_f}\right] \left(\frac{\partial c}{\partial \tau} - S \frac{\partial c}{\partial Z}\right) = \frac{1}{Sc} \left[\frac{\partial^2 c}{\partial Z^2}\right] \quad \dots\dots\dots (11)$$

Where the corresponding boundary conditions (5) can be written in the dimensionless form as:

$$\left. \begin{aligned} U(z,t) = 0, \quad \theta(z,t) = 0, \quad c(z,t) = 0 \quad \text{for } t < 0 \quad \forall z \\ U(0,t) = U_0 \left[1 + \frac{\varepsilon}{2}(e^{int} + e^{-int})\right], \quad \theta(0,t) = 1, \quad c(0,t) = 1 \\ U(\infty,t) \rightarrow 0, \quad \theta(\infty,t) \rightarrow 0, \quad c(\infty,t) \rightarrow 0 \end{aligned} \right\} \forall t \geq 0 \quad \dots\dots\dots (12)$$

Here p_r is the Prandtl number, S is the suction ($S>0$) or injection ($S<0$) parameter, M is the magnetic parameter, $Q_H (> 0)$ is the heat source parameter or $Q_H (< 0)$ is the heat sink parameter, Sc is the Schmidt number, which are defined as:

$$p_r = \frac{\psi_f}{\alpha_f}, \quad S = \frac{w_0}{U_0}, \quad M = \frac{\sigma B_0^2 \psi_f}{\rho_f U_0^2}, \quad Q_H = \frac{Q \psi_f^2}{k_f U_0^2}, \quad Sc = \frac{\psi_f}{d_f}$$

Where the velocity characteristic U_0 is defined as

$$U_0 = \left[g \beta_f (T_w - T_\infty) \psi_f\right]^{1/3} \quad \dots\dots\dots (13)$$

The local Nusselt number Nu in dimensionless form:

$$Nu = - \frac{k_{nf}}{k_f} \theta'(0) \quad \dots\dots\dots (14)$$

III RESULTS AND DISCUSSIONS

The governing equations are solved by using Method of lines with the help of Mathematica package. The variations of velocity U and temperature θ are graphically exhibited and the Heat Transfer rate (Nu) is exhibited in Table – II for various values of ϕ , S , M , α , Q_H by keeping $Pr = 6.2$, $nt = \pi/2$ and $\varepsilon = 0.02$. The effect of various parameters is as follows.

The increase of solid volume fraction reduces the velocity Fig.1 and enhances the temperature Fig.6. The thickness of momentum and the thermal boundary layers decreases with increase in ϕ . From Fig.2&7 the momentum and thermal boundary layers decreases for injection or suction. From Fig. 3 & 8 the momentum and thermal boundary layers decreasing for heat sink or source Q_H . The variations of velocity and temperature with magnetic parameter M are depicted in Figs. 4 & 9. The effects of inclination angle α on velocity and temperature

are exhibited in Figs. 5 & 10. The increase in inclination reduces the velocity and enhances the temperature. From Fig.11 it is observe that the increase in diffusivity or the decrease in viscosity increases the velocity. The same is observed in diffusion with variation of Sc Fig.12.

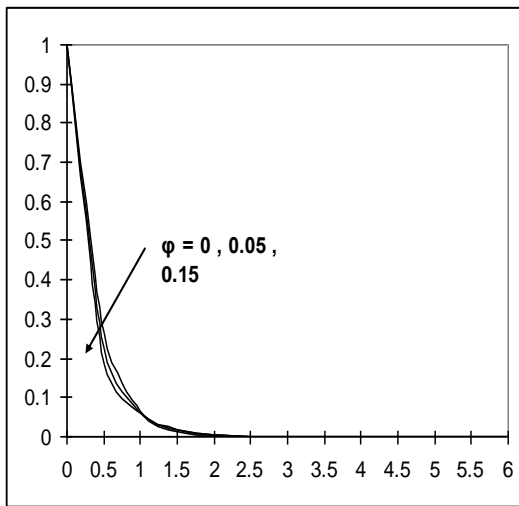


Fig.1 Variation of U with ϕ

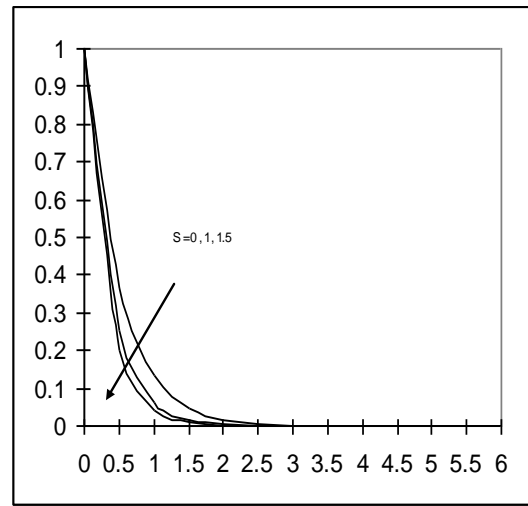


Fig.2 Variation of U with S

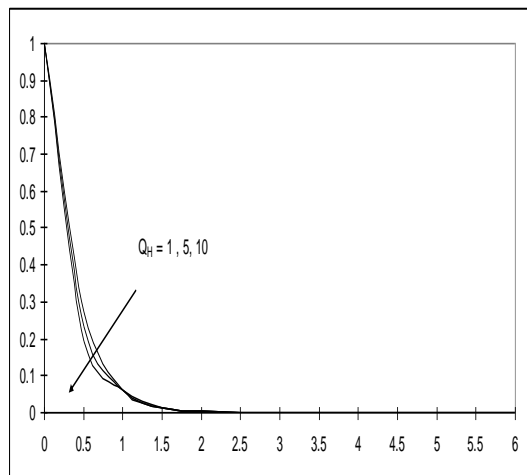


Fig.3 Variation of U with Q_H

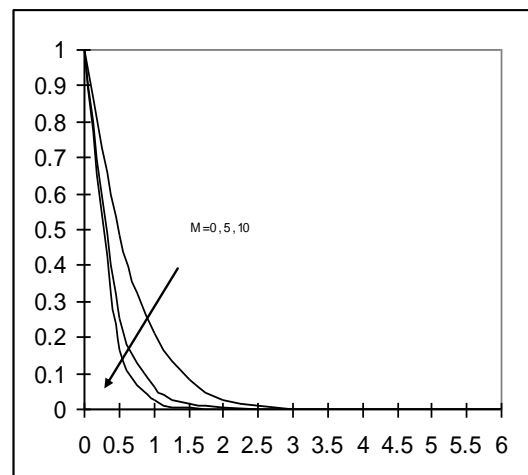


Fig.4 Variation of U with M

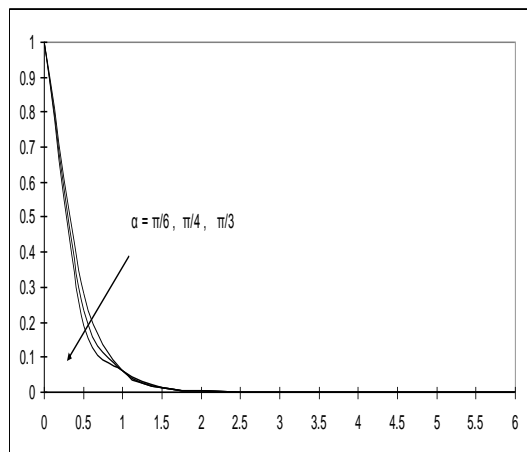


Fig.5 Variation of U with α

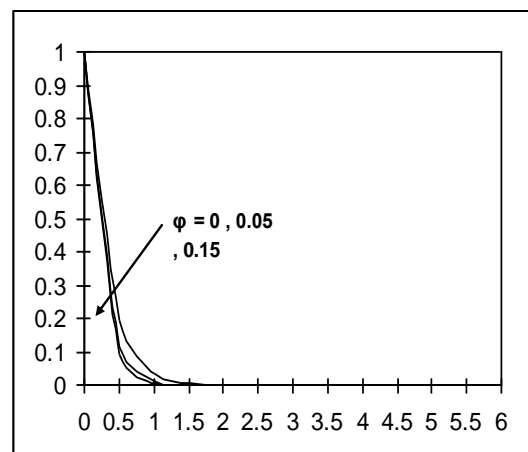


Fig.6 Variation of θ with ϕ

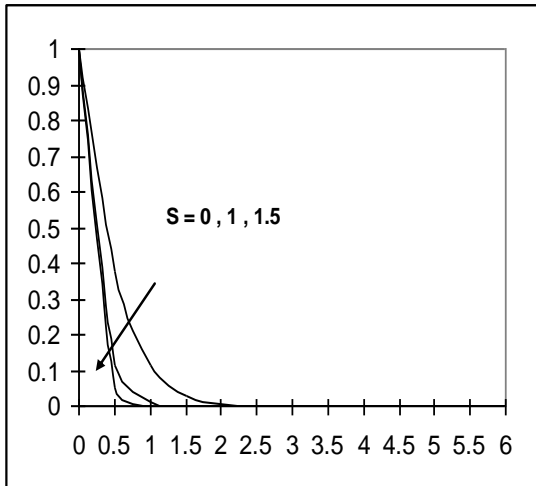


Fig.7 Variation of θ with S

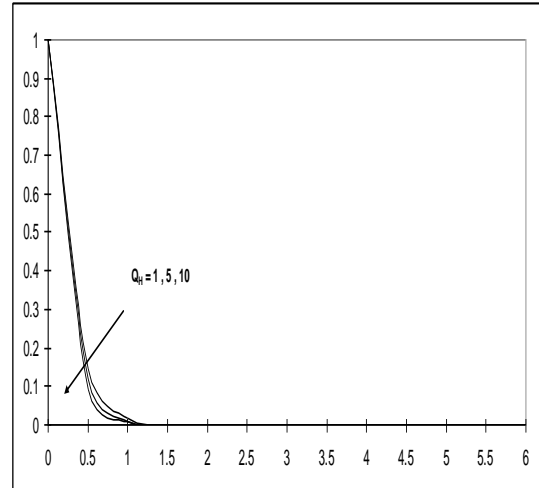


Fig.8 Variation of θ with Q_H

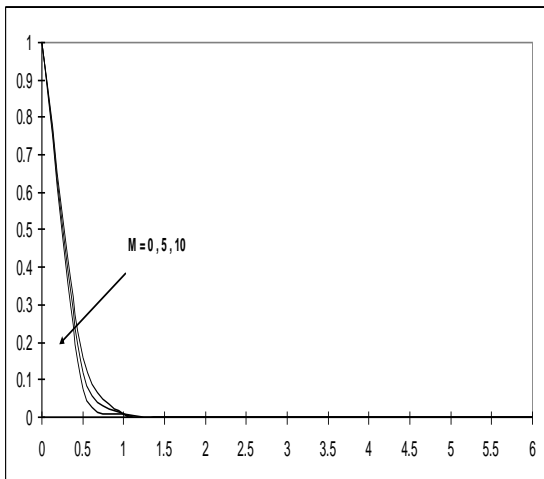


Fig.9 Variation of θ with M

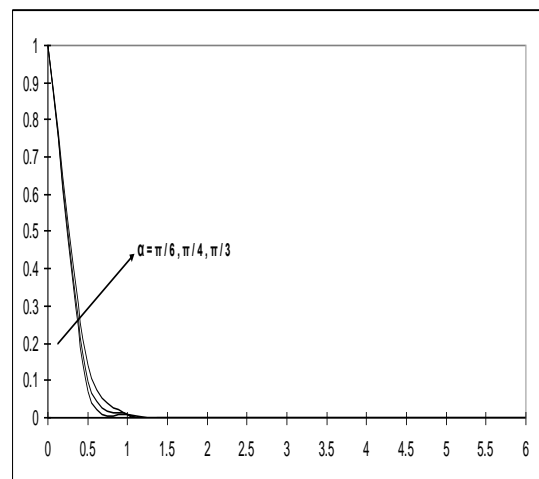


Fig.10 Variation of θ with α

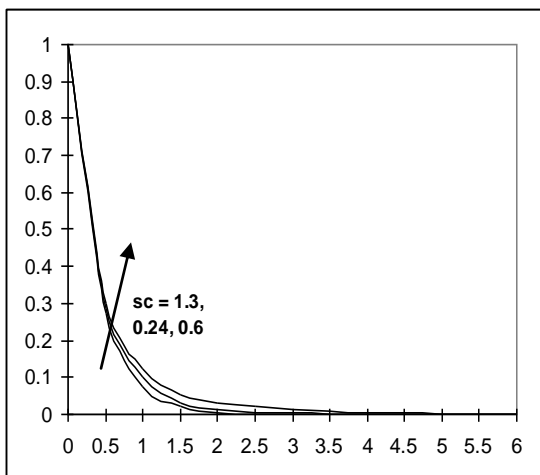


Fig.11 Variation of U with Sc

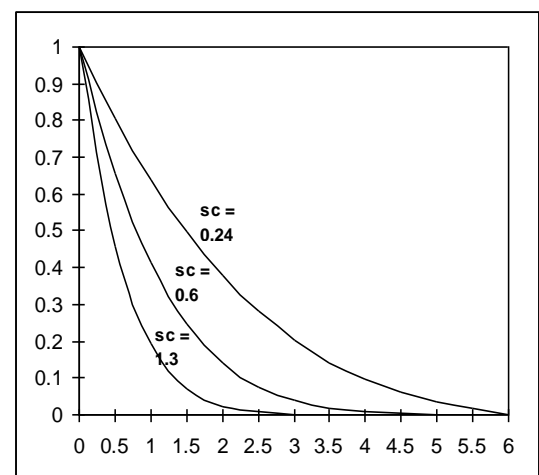


Fig.12 Variation of C with Sc

Nusselt Number:

Table II

$$S = 1; M = 5; \alpha = \frac{\pi}{3}; Sc = 0.6$$

ϕ	$Q_H = 5$	$Q_H = 10$
0	4.5034	4.8933
0.05	4.9525	5.4462
0.15	5.8815	6.6397
0.2	6.3913	7.3178

REFERENCES

[1]. M.I Anwar, I.Khan , S.Sharidan and M.Z.Salleh , conjugate effects of heat and mass transfer of Nano Fluids over a non- linear stretching sheet (2012)IJPS vol 7(26), pp 4081-4092.
[2]. Buongiorno J (2006) Convective transport in nano-fluids. ASME J Heat Transfer [128:240–250].
[3]. M. A. A. Hamad, I. Pop, Unsteady MHD free convection flow past a vertical permeable flat plate In a rotating Frame of reference with constant heat source in a nano-fluid, Heat Mass Transfer (2011)[47:1517–1524].
[4]. Khan, W.A., A. Aziz (2011).Natural convection flow of a nano-fluid over a vertical plate with Uniform surface heat flux, International Journal of Thermal Sciences, [50: 1207-1214].
[5]. Kuznetsov AV, Nield DA (2010) Natural convective boundary layer flow of a nano-fluid past a vertical plate Int J Therm Sci[288:243–247].
[6]. Sarit Kumar Das, Stephen U.S. CHOI , Hrishikesh E. Patel, Heat Transfer in Nano-fluids – A Review
[7]. Heat Transfer Engineering, [27(10):3–19, 2006].

Towards Secure and Dependable Storage Services in Cloud Computing

Aarthi T.¹, Mrs. Rathi G.², Prabakaran R. S.³

PG Scholar (CSE)¹, Assistant professor UG(CSE)², PG Scholar(CSE)³
Sri Ramakrishna Engineering College Coimbatore

ABSTRACT: Cloud Computing has emerged as one of the most influential paradigms in the IT industry for last few years. In such computing the data confidentiality, flexibility and access control are the main parameters to be considered in the research area. The proposed system investigate the problem of data security in cloud data storage. To achieve the availability and quality of cloud data storage service for users, the proposed system designs an distributed scheme with explicit dynamic data support, that includes block update, delete, and append. It also rely on erasure-correcting code in the file distribution preparation to provide redundancy parity vectors and guarantee the data dependability. The homomorphic token with distributed verification of erasure coded data, which achieves the integration of storage. The system ensures the security and dependability for cloud data storage under the aforementioned adversary model. Analysis shows that this scheme is highly efficient and resilient against byzantine failure, severals data modification attack and colliding attacks.

Keywords: user, cloud server, third party auditor, public auditing

I. INTRODUCTION TO CLOUD COMPUTING

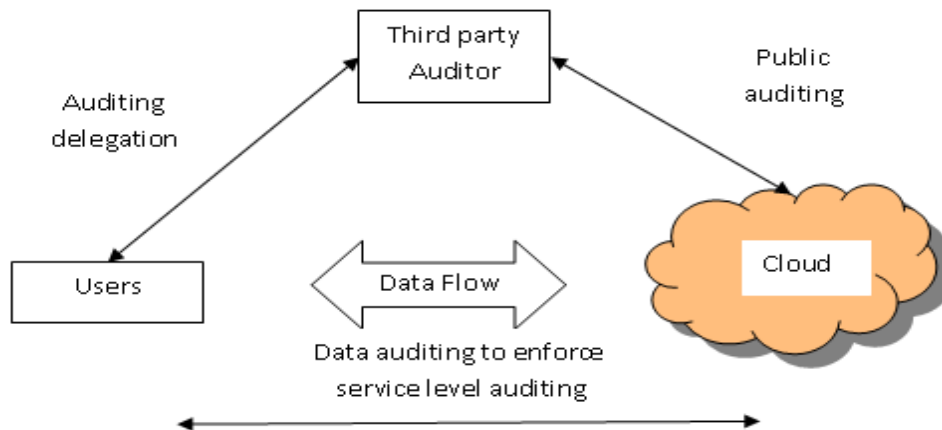
Cloud computing is the delivery information as a service, which shares data resources, software, and data information that are provided to computers as a metered service over a network .

Cloud computing provides data access and data storage resources without requiring cloud users. End users access cloud based applications through a web browser or a light weight desktop or mobile app while the data are stored on servers at a remote location. Cloud application providers strive to provide better service and performance on end-user computers.

II. PROPOSED SYSTEM

In cloud data storage system, user store their data in the cloud. The correctness and availability of the data files [1], [2] stored on the distributed cloud servers must be guaranteed. The key issues is to effectively detect unauthorized data modification and corruption. In order to strike a good balance between error resilience and data dynamics, system explore the algebraic property of our token computation and erasure-coded data, that efficiently support dynamic operation on data blocks. the time, computation data resources, and even the related online burden of users data are saved ,by providing the extension of the proposed main scheme to support third-party auditing. It is well known that erasure-correcting code[4], [6] may be used to tolerate multiple failures in distributed data storage systems. In order to achieve the assurance of data storage correctness and also data error localization simultaneously, our scheme relies on the precomputed verification tokens. The main idea is that before data file distribution, the user pre computes certain number of verification tokens on individual vector. The proposed scheme achieves the integration of storage correctness insurance and data error localization. Error localization is key prerequisite for eliminating errors in storage systems. It is also of critical importance to identify potential threats from external attacks. The system also provide the extension of the proposed main scheme is to support the third-party auditing, where users can safely delegate the data integrity checking tasks to third party auditors and be worry-free to use the cloud storage services.

III. ARCHITECTURE DIAGRAM



3.1. Developing an Cloud model

Initially the basic network model for the cloud data storage is developed in this module. Three different entities can be identified as follows: User: user is the one who stores data in the cloud and relies on the cloud for data storage and data computation, can be either enterprise or individual customers. Cloud Server (CS): is the one, which is managed by cloud service provider (CSP) to provide data storage service and has significant storage space and computation resources. Third-Party Auditor: who are expertise and have the capabilities that users wont have, who is trusted to assess and expose risk of cloud storage services on behalf of the users upon request.

3.2. Implementing the file distribution and the token pre-computation

In this module we use erasure-correcting code to tolerate multiple failures in distributed storage systems. The data file F redundantly across a set of $n = m + k$ distributed servers. An $(m; k)$ Reed-Solomon erasure-correcting code is used to create k redundancy parity vectors from m data vectors in such a way that the original m data vectors can be reconstructed from any m out of the $m + k$ data and parity vectors. By placing each of the $m + k$ vectors on a server, where the original file can survive the failure of any k of the $m + k$ servers without any loss of data, with a space overhead of $k = m$. For support of efficient original file, our file layout is systematic, where the unmodified m data file vectors together with k parity vectors is distributed across $m + k$ different servers. After the file distribution operation precomputation of the token is performed. Token precomputation is the process for assuring the data storage correctness and data error localization simultaneously, our scheme entirely relies on the verification tokens that is precomputed. The main idea is of this project is to precomputes a certain number of short verification tokens on individual vector before file distribution the user $G^{(j)}$ ($j \in \{1; \dots; n\}$), random subset of data blocks is covered by each token.

3.3. Implementation of Correctness Verification and Error Localization

Many previous scheme [3], [5] do not explicitly consider the problem of data error localization. In this module, the system integrate the correctness verification and error localization (misbehaving server identification). The response values from servers for each challenge contain information to locate potential data error(s).

3.4. Implementation of Error Recovery and Third party auditor

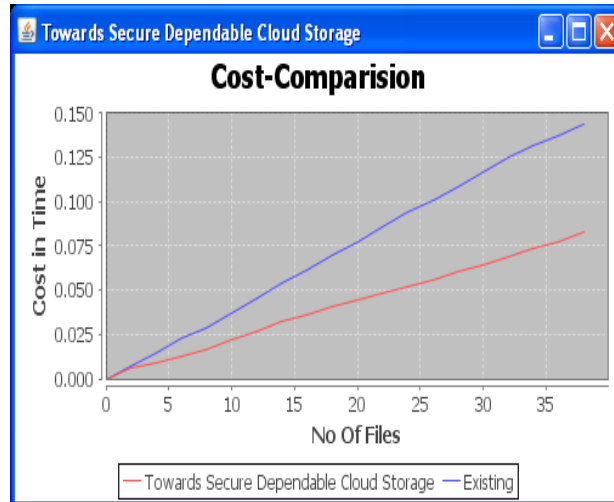
After identifying the misbehaving server from among all other servers we need to recover those files. The user can always ask servers to send back blocks of the r rows specified in the challenge and regenerate the correct blocks by erasure correction, shown in Algorithm, as long as the number of identified misbehaving servers is less than k . The newly recovered blocks can then be redistributed to the misbehaving servers to maintain the correctness of storage.

3.5. Providing dynamic data operation support

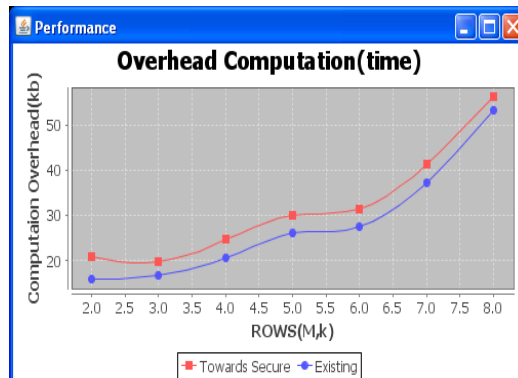
In this module we provide the dynamic data operation support to user [7], [8], [9]. Normally there are four categories of operation available Update operation, delete operation, append and insert operation. In update operation we have to update the existing or already available blocks of data in servers in this operation the user must priory know about the data block which is going to modify or alter. We use the master key to perform that action to update the existing file. In Delete operation first we define the data blocks that are need to remove

from the data server and after remove such file from the server we have to rearrange the remaining data blocks in the storage. The Append and the Insert are the same operation but in append we add new data's to already existing server and the insert operation is we embedding the data for already existing data. Master key is the basic need for all dynamic data support operations performing in data servers.

IV. EVALUATION



The following graph shown in Fig.1 is cost comparison graph in which, number of files ranging from 0 to 35 are taken along x-axis and cost time taken for upload file ranging from 0 to 0.15 minutes are taken along y-axis. It can be inferred from the graph that as like Encryption; Decryption time taken by Reed Solomon Erasure Code is lesser than existing System which indicates proposed system works faster than the existing system.



The following graph shown in Fig.2 is overhead computation graph in which, number of files ranging from 0 to 8 are taken along x-axis and overhead taken for distribute the file ranging from 10 to 50 kb are taken along y-axis. It can be inferred from the graph that as like Encryption; Decryption time taken by Reed Solomon Erasure Code is higher than existing System which indicates proposed system works faster than the existing system.

V. CONCLUSION AND FUTURE WORK

Thus the system investigates the problem of data security in cloud storage of data, which is essentially a distributed data storage system. The system achieve the assurances of cloud data integrity and availability and enforce the quality of dependable cloud storage service for users , by an effective and flexible distributed scheme with explicit dynamic data support, including block update, delete, and append. The system rely on erasure-correcting code in the file distribution preparation to provide redundancy parity vectors and guarantee the data dependability. By utilizing the homomorphic token with distributed verification of erasure code, this scheme achieves the integration of data storage correctness insurance and data error localization, when data corruption has detected during the data storage correctness verification across the distributed servers, it can

almost guarantee the simultaneous identification of the misbehaving server. Considering the time, computation of data resources, and even the related online burden of users, the system also provide the extension of the proposed main scheme to support third-party auditing, where users can safely delegate the integrity checking tasks to thirdparty auditors and be worry-free to use the cloud data storage . by detailed security and extensive results, the system show that proposed scheme is highly efficient and resilient to Byzantine failure, malicious data file modification attack, and even server attacks.

The system ensures the security and dependability for cloud data storage under the aforementioned model. The Analysis shows the proposed scheme is highly efficient and resilient against Byzantine failure; malicious data file modification attack, and even server attacks. The system can enhance work by using Raptor codes is a additional pre-coding on an appropriate LT-Code. In asymptotic settings,a universal Raptor Codes with linear encode/decode time for which the failure probability converges to 1 polynomial fast in input size.

REFERENCES

- [1] Ateniese.G, Burns.R, Curtmola.R, Herring.J, Kissner.L, Peterson.Z, and Song.D, "Provable Data Possession at UntrustedStores," Proc. 14th ACM Conf. Computer and Comm. Security (CCS'07), pp. 598-609, Oct. 2007.
- [2] Bowers.K.D, Juels.A, and Oprea.A, "HAIL: A High-Availability and Integrity Layer for Cloud Storage," Proc. ACM Conf. Computer and Comm. Security (CCS '09), pp. 187-198, 2009.
- [3] Erway.C, Kupcu.A, Papamanthou.C, and Tamassia.R, "Dynamic Provable Data Possession," Proc. 16th ACM.
- [4] Hendricks.J, Ganger.G, and Reiter.M, "Verifying Distributed Erasure-Coded Data," Proc. 26th ACM Symp. Principles of Distributed Computing, pp. 139-146, 2007.
- [5] Juels.A and Kaliski.B.S Jr., "PORs: Proofs of Retrievability for Large Files," Proc. 14th ACM Conf. Computer and Comm. Security (CCS '07), pp. 584-597, Oct. 2007.
- [6] Plank.J.S and Ding.Y, "Note: Correction to the 1997 Tutorial on Reed-Solomon Coding," Technical Report CS-03-504, Univ. of Tennessee, Apr. 2003.
- [7] Schwarz.T and Miller.E.L, "Store, Forget, and Check: Using Algebraic Signatures to Check Remotely Administered Storage," Proc. IEEE Int'l Conf. Distributed Computing Systems (ICDCS '06), pp. 12-12, 2006.
- [8] Wang.Q, Wang.C, Li.J, Ren.K, and Lou.W, "Enabling Public Verifiability and Data Dynamics for Storage Security in Cloud Computing," Proc. 14th European Conf. Research in Computer Security (ESORICS '09), pp. 355-370, 2009.WANG ET AL.: TOWARD SECURE AND DEPENDABLE STORAGE SERVICES IN CLOUD COMPUTING 231
- [9] Wang.C, Wang.Q, Ren.K, and Lou.W, "Privacy-Preserving Public Auditing for Storage Security in Cloud Computing," Proc. IEEE INFOCOM, Mar. 2010. [10] Wang.C, Ren.K, Lou.W, and Li.J, "Towards Publicly Auditable Secure Cloud Data Storage Services," IEEE Network Magazine, vol. 24, no. 4, pp. 19-24, July/Aug. 2010.

Securing Personal Information in Data Mining

¹B. Sreenivasulu, ²A. Sarat Kumar, ³D. Srujan Chandra Reddy

¹Department of CSE, PBRVITS Kavali

²Department of CSE, PBRVITS Kavali

³Assoc. Prof Department of CSE, PBRVITS Kavali

This paper presents few of the frequent authentication and security mechanisms and mechanisms used in several securing personal information in data mining techniques. The paper describes an overview of some of the well known securing personal information (privacy preserve) in data mining, - ID3 for decision tree, association rule mining, EM clustering, frequency mining and Naïve Bayes. Most of these algorithms are usually a modification of a well known data mining algorithm along with some privacy preserving techniques. The paper finally describes the problem of using a model without knowing the model rules on context of passenger classification at the airlines security checkpoint by homeland security. This paper is intended to be a summary and a high level overview of PPDM.

I. INTRODUCTION

Data mining refers to the techniques of extracting rules and patterns from data. It is also commonly known as KDD (Knowledge Discovery from Data). Traditional data mining operates on the data warehouse model of gathering all data into a central site and then running an algorithm against that warehouse. This model works well when the entire data is owned by a single custodian who generates and uses a data mining model without disclosing the results to any third party. However, in a lot of real life application of data mining, privacy concerns may prevent this approach. The first problem might be the fact that certain attributes of the data (SSN for example), or a combination of attributes might leak personal identifiable information. The second problem might be that the data is horizontally split across multiple custodians none of which is allowed to transfer data to the other site. The data might be vertically partitioned in which case, different custodians own different attributes of the data and they have the same sharing restrictions. Finally, the use of the data mining model might have restrictions, - some rules might be restricted, and some rules might lead to individual profiling in ways which are prohibited by law.

Privacy preserving data mining (PPDM) has emerged to address this issue. Most of the techniques for PPDM uses modified version of standard data mining algorithms, where the modifications usually using well known cryptographic techniques ensure the required privacy for the application for which the technique was designed. In most cases, the constraints for PPDM are preserving accuracy of the data and the generated models and the performance of the mining process while maintaining the privacy constraints. The several approaches used by PPDM can be summarized as below:

1. The data is altered before delivering it to the data miner.
2. The data is distributed between two or more sites, which cooperate using a semi-honest protocol to learn global data mining results without revealing any information about the data at their individual sites.
3. While using a model to classify data, the classification results are only revealed to the designated party, who does not learn anything else other than the classification results, but can check for presence of certain rules without revealing the rules.

In this paper, a high level overview of some of the commonly used tools and algorithms for PPDM is presented.

II. SECURE MULTI PARTY COMMUNICATION

Almost all PPDM techniques rely on secure multi party communication protocol. Secure multi party communication is defined as a computation protocol at the end of which no party involved knows anything else except its own inputs the results, i.e. the view of each party during the execution can be effectively simulated by the input and output of the party. In the late 1980s, work on secure multi party communication demonstrated that a wide class of functions can be computed securely under reasonable assumptions without involving a trusted third party. Secure multi party communication has generally concentrated on two models of security. The semi-honest model assumes that each party follows the rule of the protocol, but is free to later use what it sees during execution of the protocol. The malicious model assumes that parties can arbitrarily cheat and such cheating will not compromise either security or the results, i.e. the results from the malicious party will be correct or the malicious party will be detected. Most of the PPDM techniques assume an intermediate model, -

preserving privacy with non-colluding parties. A malicious party may corrupt the results, but will not be able to learn the private data of other parties without colluding with another party. This is a reasonable assumption in most cases.

In the next section I'll present few efficient techniques for privacy preserving computations that can be used to support PPDM.

2.1 Secure Sum

Distributed data mining algorithms often calculate the sum of values from individual sites. Assuming three or more parties and no collusion, the following method securely computes such a sum.

Let $v = \sum_{i=1}^s v_i$ is to be computed for s sites and v is known to lie in the range $[0..N]$. Site 1, designated as the

master site generates a random number R and sends $(R + v_1) \bmod N$ to site 2. For every other site $l = 2, 3, 4 \dots s$, the site receives:

$$V = (R + \sum_{j=1}^{l-1} v_j) \bmod N .$$

Site l computes:

$$(V + v_l) \bmod N = (R + \sum_{j=1}^l v_j) \bmod N$$

This is passed to site $(l+1)$. At the end, site 1 gets:

$$V = (R + \sum_{j=1}^s v_j) \bmod N$$

And knowing R , it can compute the sum v . The method faces an obvious problem if sites collude. Sites $(l-1)$ and $(l+1)$ can compare their inputs and outputs to determine v_l . The method can be extended to work for an honest majority. Each site divides v_l into shares. The sum of each share is computed individually. The path used is permuted for each share such that no site has the same neighbors twice.

2.2 Secure Set Union

Secure set union methods are useful in data mining where each party needs to give rules, frequent itemsets, etc without revealing the owner. This can be implemented efficiently using a commutative encryption technique. An encryption algorithm is commutative if given encryption keys $K_1, K_2, \dots, K_n \in K$, the final encryption of a data M by applying all the keys is the same for any permuted order of the keys. The main idea is that every site encrypts its set and adds it to a global set. Then every site encrypts the items it hasn't encrypted before. At the end of the iteration, the global set will contain items encrypted by every site. Since encryption technique chosen is commutative, the duplicates will encrypt to the same value and can be eliminated from the global set. Finally every site decrypts every item in the global set to get the final union of the individual sets. One addition is to permute the order of the items in the global set to prevent sites from tracking the source of an item. The only additional information each site learns in the case is the number of duplicates for each item, but they cannot find out what the item is.

2.3 Secure Size of Set Intersection

In this case, every party has their own set of items from a common domain. The problem is to securely compute the cardinality/size of the intersection of these sets. The solution to this is the same technique as the secure union using a commutative encryption algorithm. All k parties locally generate their public key-part for a commutative encryption scheme. The decryption key is never used in this protocol. Each party encrypts its items with its key and passes it along to the other parties. On receiving a set of encrypted items, a party encrypts each item and permutes the order before sending it to the next party. This is repeated until every item has been encrypted by every party. Since encryption is commutative, the resulting values from two different sets will be equal if and only if the original values were the same. At the end, we can count the number of values that are present in all of the encrypted item sets. This can be done by any party. None of the parties can find out which of the items are present in the intersection set because of the encryption.

2.4 Scalar Product

Scalar product is a powerful component technique and many data mining problems can be reduced to computing the scalar product of two vectors. Assume two parties P_1 and P_2 each have a vector of cardinality n ,

$X = (x_1, x_2, \dots, x_n)$, $Y = (y_1, y_2, \dots, y_n)$. The problem is to securely compute $\sum_{i=1}^n x_i y_i$. There has been a

lot of research and proposed solution to the 2 party cases, but these cannot be easily extended to the multi party case. The key approach to a possible solution proposed in [3] is to use linear combinations of random numbers to disguise vector elements and then do some computations to remove the effect of these random numbers from the result. Though this method does reveal more information than just the input and the result, it is efficient and suited for large data sizes, thus being useful for data mining.

2.5 Oblivious Transfer

The oblivious transfer protocol is a useful cryptographic tool involving two parties, - the sender and the receiver. The sender's input is a pair (x_0, x_1) and the receiver's input is a bit $\sigma \in \{0,1\}$. The protocol is such that the receiver learns x_σ (and nothing else) and the sender learns nothing. In the semi-honest adversaries, there exist simple and efficient protocols for oblivious transfer.

2.6 Oblivious polynomial evaluation

This is another useful cryptographic tool involving two parties. The sender's input is a polynomial Q of degree k over some finite field F (k is public). The receiver's input is an element $z \in F$. The protocol is such that the receiver learns $Q(z)$ without learning anything else about the polynomial and the sender learns nothing.

In the next section, some common PPDM techniques are described:

III. ANONYMIZING DATA SETS

In many data mining scenarios, access to large amounts of personal data is essential for inferences to be drawn. One approach for preserving privacy in this case it to suppress some of the sensitive data values, as suggested in [5]. This is known as a k -anonymity model which was proposed by Samarati and Sweeney. Suppose we have a table with n tuples and m attributes. Let $k > 1$ is an integer. We wish to release a modified version of this table, where we can suppress the values of certain cells in the table. The objective is to minimize the number of cells suppressed while ensuring that for each tuple in the modified table there are $k-1$ other tuples in the modified table identical to it.

The problem of finding optimized k -anonymized table for any given table instance can be shown to be NP-hard even for binary attributes. There are however $O(k)$ approximation algorithm discussed in [5] for solving this problem. The algorithm is also proven to terminate.

IV. DECISION TREE MINING

In the paper [4], a privacy preserving version of the popular ID3 decision tree algorithm is described. The scenario described is where two parties with database D_1 and D_2 wish to apply the decision tree algorithm on the joint database $D_1 \cup D_2$ without revealing any unnecessary information about their database. The technique described uses secure multi party computation under the semi honest adversary model and attempts to reduce the number of bits communicated between the two parties.

The traditional ID3 algorithm computes a decision tree by choosing at each tree level the best attribute to split on at that level and thus partition the data. The tree building is complete when the data is uniquely partitioned into a single class value or there are no attributes to split on. The selection of best attribute uses information gain theory and selects the attribute that minimizes the entropy of the partitions and thus maximizes the information gain.

In the PPDM scenario, the information gain for every attribute has to be computed jointly over all the database instances without divulging individual site data. We can show that this problem reduces to privately computing $x \ln x$ in a protocol which receives x_1 and x_2 as input where $x_1 + x_2 = x$. This is described in [4].

V. ASSOCIATION RULE MINING

We describe the privacy preserving association rule mining technique for a horizontally partitioned data set across multiple sites. Let $I = \{i_1, i_2, \dots, i_n\}$ be a set of items and $T = \{T_1, T_2, \dots, T_n\}$ be a set of

transactions where each $T_i \subseteq I$. A transaction T_i contains an item set $X \subseteq I$ only if $X \subseteq T_i$. An association rule implication is of the form $X \Rightarrow Y (X \cap Y = \emptyset)$ with support s and confidence c if $s\%$ of the transactions in T contains $X \cup Y$ and $c\%$ of transactions that contain X also contain Y . In a horizontally partitioned database, the transactions are distributed among n sites. The global support count of an item set is the sum of all local support counts. The global confidence of a rule can be expressed in terms of the global support:

$$SUP_g(X) = \sum_{i=1}^n SUP_i(X)$$

$$CONF_g(X \Rightarrow Y) = \frac{SUP_g(X \cup Y)}{SUP_g(X)}$$

The aim of the privacy preserving association rule mining is to find all rules with global support and global confidence higher than the user specified minimum support and confidence. The following steps, utilizing the secure sum and secure set union methods described earlier are used. The basis of the algorithm is the apriori algorithm which uses the (k-1) sized frequent item sets to generate the k sized frequent item sets. The problem of generating size 1 item sets can be easily done with secure computation on the multiple sites.

- ◆ Candidate Set Generation: Intersect the globally frequent item set of size (k-1) with locally frequent (k-1) itemset to get candidates. From these, use the Apriori algorithm to get the candidate k itemsets.
- ◆ Local Pruning: For each X in the local candidate set, scan the local database to compute the support of X. If X is locally frequent, it's included in the locally frequent itemset.
- ◆ Itemset Exchange: Compute a secure union of the large itemsets over all sites.
- ◆ Support Count: Compute a secure sum of the local supports to get the global support.

VI. EM CLUSTERING

Clustering is the technique of grouping data into groups called "clusters" based on the value of the attributes. A well known algorithm for clustering is the EM algorithm which works well for both discrete and continuous attributes. A privacy preserving version of the algorithm in the multi site case with horizontally partitioned data is described below.

Let us assume that the data is one dimensional (single attribute y) and are partitioned across s sites. Each site has

n_i data items ($n = \sum_{l=1}^s n_l$). Let $z_{ij}^{(t)}$ denote the cluster membership for the i th cluster for the j th data point at

the (t)th EM round. In the E step, the values μ_i (mean for cluster i), σ_i^2 (variance for cluster i) and π_i (Estimate of proportion of items i) are computed using the following sum:

$$\sum_{j=1}^n z_{ij}^{(t)} y_j = \sum_{l=1}^s \sum_{j=1}^{n_l} z_{ijl}^{(t)} y_j$$

$$\sum_{j=1}^n z_{ij}^{(t)} = \sum_{l=1}^s \sum_{j=1}^{n_l} z_{ijl}^{(t)}$$

$$\sum_{j=1}^n z_{ij}^{(t)} (y_j - \mu_i^{(t+1)})^2 = \sum_{l=1}^s \sum_{j=1}^{n_l} z_{ijl}^{(t)} (y_j - \mu_i^{(t+1)})^2$$

The second part of the summation in all these cases is local to every site. It's easy to see that sharing this value does not reveal y_i to the other sites. It's also not necessary to share n_i and the inner summation values, but just computing n and the global summation for the values above using the secure sum technique described earlier.

In the M step, the z values can be partitioned and computed locally given the global μ_i , σ_i^2 and π_i . This also does not involve any data sharing across sites.

VII. FREQUENCY MINING

The basic frequency mining problem can be described as follows. There are n customers U_1, U_2, \dots, U_n and each customer has a Boolean value d_i . The problem is to find out the total number of 1s and

Os without knowing the customer values i.e. computing the sum $\sum_{i=1}^n d_i$ without revealing each d_i . We cannot use the secure sum protocol because of the following restrictions.

- Each customer can send only one flow of communication to the miner and then there's no further interaction.
- The customers never communicate between themselves.

The technique presented in [8] uses the additively homomorphic property of a variant of the ElGamal encryption. This is described below:

Let G be a group in which discrete logarithm is hard and let g be a generator in G . Each customer U_i has two

pairs of private/public key pair $(x_i, X_i = g^{x_i})$ and $(y_i, Y_i = g^{y_i})$. The sum $X = \sum_{i=1}^n X_i$ and $Y = \sum_{i=1}^n Y_i$,

along with G and the generator g is known to everyone. Each customer sends to the miner the two values

$m_i = g^{d_i} \cdot X^{y_i}$ and $h_i = Y^{x_i}$. The miner computes $r = \prod_{i=1}^n \frac{m_i}{h_i}$. For the value of d for which $g^d = r$, we can

show that this represents the sum $\sum_{i=1}^n d_i$. Since $0 < d < n$, this is easy to find by encrypt and compare. We can

also that assuming all the keys are distributed properly when the protocol starts, the protocol for mining frequency protects each honest customer's privacy against the miner and up to $(n-2)$ corrupted customers.

VIII. NAÏVE BAYES CLASSIFIER

Naïve Bayes classifiers have been used in many practical applications. They greatly simplify the learning task by assuming that the attributes are independent given the class. They have been used successfully in text classification and medical diagnosis.

Naïve Bayes classification problem can be formulated as follows. Let A_1, A_2, \dots, A_m be m attributes and V be the class attribute. Let each attribute A_i have a domain $\{a_i^1, a_i^2, \dots, a_i^d\}$ and class attribute V has a domain $\{v^1, v^2, \dots, v^d\}$. The data point for the classifier looks like $(a_{j1}, a_{j2}, \dots, a_{jm}, v_j)$. Given a new instance $(a_{j1}, a_{j2}, \dots, a_{jm})$, the most likely class can be found using the equation:

$$v = \arg \max_{v^l \in V} P(v^l) \prod_{i=1}^m P(a_i | v^l)$$

This can be written in terms on number of occurrence # as:

$$v = \arg \max_{v^l \in V} \#(v^l) \prod_{i=1}^m \frac{\#(a_i, v^l)}{\#(v^l)}$$

The goal of the Privacy Preserving Naïve Bayes learner is to learn the Naïve Bayes classifier accurately, but the miner learns nothing about each customer's sensitive data except the knowledge derived from the classifier itself. To learn the classifier, all the miner needs to do is to learn $\#(v^l)$ and $\#(a_i, v^l)$ for each i , each k and each l . Since the occurrence of v^l or the pair (a_i, v^l) can be denoted by a Boolean value, we can use the technique described in Frequency Mining to compute the Naïve Bayes model with the privacy constraints.

IX. USING A MODEL WITHOUT DISCLOSING THE MODEL.

Recent homeland security measures uses data mining models to classify each airline passenger with a security tag. The problem statement comes from following requirements for the system:

- No one learns of the classification result other than the designated party.
- No information other than the classification result will be revealed to the designated party.
- Rules used for classification can be checked for certain condition without revealing the rules.

The problem can be formally stated as follows. Given an instance x from site D with v attributes, we want to classify x according to rule set R provided by site G . The rules $r \in R$ are of the form $\bigcap_{i=1}^v (L_i - > C)$, where each L_i is wither a clause $x_i = a$, or don't care (always true). Using the don't care clause, G can create arbitrary size rules and mask the actual number of clauses in the rule. In addition, D has a set of rules F that are not allows to be used for classification. The protocol will satisfy the following conditions:

- D will not be able to learn any rules in R
- D will be convinced that $F \cap R = \emptyset$
- G will only learn the class value of x

The approach suggested in [2] uses a un-trusted non colluding site, where the only trust placed on the site is that it'll not collude with any of the other sites to violate privacy. Both G and D send synchronized streams of encrypted data and rule clause to site C . The orders of the attributes are scrambled in a way known to D and G only. Each attribute is given two values, - one corresponding to don't care and another it's true value. Each clause also has two values for every attribute. One is an "invalid" value to mask the real value and the other is the actual clause value or the "don't care" value. Site C compares both the values to see if the first or the second match. If yes, then either the attribute is a match or it's a "don't care". If there's a match for every clause in the rule, then the rule is true. To check for $F \cap R = \emptyset$, commutative encryption technique is used and C compares the double encrypted version of the sets.

X. CONCLUSION

As usage of data mining for potential intrusive purposes using personally identifiable information increases, privately using these results will become more important. The above algorithm techniques show that it's possible to ensure privacy without compromising accuracy of results, and has a bound on the computation and the communication cost.

REFERENCES

- [1]. Privacy-preserving Distributed Mining of Association Rules on Horizontally Partitioned Data Murat Kantarcioglu and Chris Clifton, Senior Member, IEEE
- [2]. Assuring Privacy when Big Brother Murat Kantarcioglu Chris Clifton
- [3]. Privacy Preserving Association Rule Mining in Vertically Partitioned Data Jaideep Vaidya & Chris Clifton
- [4]. Privacy Preserving Data Mining Yehuda Lindell & Benny Pinkasy
- [5]. k-anonymity: Algorithm and Hardness, Gagan Aggarwal, Tomas Feder, Stanford University
- [6]. Towards Standardization in Privacy Preserving Data Mining, Stanley R. M. Oliveira and Osmar R Zaiane, University of Alberta, Edmonton, Canada
- [7]. Tools for Privacy Preserving Data Mining, Chris Clifton, Murat Kantarcioglu and Jaideep Vaidya, Purdue University.
- [8]. Privacy Presercing Classification of Customer Data without Loss of Accuracy, Zhiqiang Yang, Sheng Zhong, Rebecca N. Wright.

Study of Strain in Elasto-Plastic Material by X-Ray Diffraction Technique

Prof. M. D. Mehare¹, Prof. N. N. Bhaiswar², Prof. K. S. Shelke³

Applied Physics Department, Priyadarshini Indira Gandhi College of Engineering, Nagpur, Maharashtra,
Department of Mechanical Engineering, Priyadarshini Indira Gandhi College of Engineering, Nagpur,
Maharashtra

Department of Mechanical Engineering, Priyadarshini Indira Gandhi College of Engineering, Nagpur,

ABSTRACT: This research paper highlights the applicability of X-ray diffraction method to evaluate the strain in elasto-plastic material like concrete. The aim of this study is to explore the possibilities of X-Ray diffraction technique in determining strain within the body of any elastoplastic material like concrete. This paper consolidates the calculations of body strain of highly unpredictable elasto-plastic material like concrete.

Keywords: Elastoplastic material, X-ray diffraction, strain.

I. INTRODUCTION

In metals strain is very easily calculated evaluating change in length and original length but case in plastic materials is different. To study strain within body in elastoplastic material is cumbersome job. Rather instrumentation can not be applied in case of unpredictable material like concrete which is heterogeneous and elastoplastic. This paper aims to study the scope of implementation of X-Ray diffraction technique to evaluate strain in concrete. In this paper concrete grade M.20 is taken for X-ray diffraction and 5 grams powder is taken. In this paper 5 grams of two powder samples of 15cm x 15cm x 15cm cubes in unstressed condition (cube not subjected to failure load in compressive testing machine) and stressed condition (cube subjected to failure load in compressive testing machine) are taken and X-ray diffraction is carried out for M-20 grade normal concrete.

II. X-RAY DIFFRACTION GRAPH AND PEAK LIST

2.1 M.20 Unstressed sample:

Anchor Scan Parameters

Dataset Name:	M-20-Unstressed
File name:	H:\X'Pert_Data\Oct 13\15th Oct\M-20-Unstressed.xrdml
Comment:	Configuration=Flat stage, Owner=User-1, Creation date=1/15/2009 8:55:18 AM Goniometer=PW3050/60 (Theta/Theta); Minimum step size 2Theta:0.001; Minimum step size Omega:0.001
Measurement Date / Time:	Sample stage=PW3071/xx Bracket Diffractometer system=XPERT-PRO Measurement program=xrd program, Owner=User-1, Creation date=1/15/2009 9:49:56 AM 10/15/2013 4:51:41 PM
Operator:	ABC
Raw Data Origin:	XRD measurement (*.XRDML)
Scan Axis:	Gonio
Start Position [2Th.]:	5.0044
End Position [2Th.]:	99.9834
Step Size [2Th.]:	0.0170
Scan Step Time [s]:	5.1682
Scan Type:	Continuous
PSD Mode:	Scanning
PSD Length [2Th.]:	2.12
Offset [2Th.]:	0.0000
Divergence Slit Type:	Fixed
Divergence Slit Size [°]:	1.0000
Specimen Length [mm]:	10.00
Measurement Temperature [°C]:	25.00
Anode Material:	Cu
K-Alpha1 [Å]:	1.54060
K-Alpha2 [Å]:	1.54443
K-Beta [Å]:	1.39225
K-A2 / K-A1 Ratio:	0.50000
Generator Settings:	30 mA, 40 kV
Diffractometer Type:	0000000083002110
Diffractometer Number:	0
Goniometer Radius [mm]:	240.00
Dist. Focus-Diverg. Slit [mm]:	100.00
Incident Beam Monochromator:	No
Spinning:	No

2.2 Peak List:

Peak List

Pos. [°2Th.]	Height [cts]	FWHM [°2Th.]	d-spacing[Å]	Rel. Int. [%]
17.9636	93.13	0.1004	4.93809	1.28
20.7871	977.63	0.1171	4.27329	13.48
21.9722	68.26	0.1338	4.04542	0.94
23.0589	122.09	0.2007	3.85716	1.68
24.0698	30.40	0.4015	3.69741	0.42
25.5100	42.42	0.4015	3.49183	0.58
26.5668	7254.31	0.0836	3.35529	100.00
27.3660	447.14	0.0669	3.25909	6.16
29.3672	1225.63	0.1840	3.04140	16.90
30.6241	289.35	0.0669	2.91938	3.99
34.0066	107.39	0.1338	2.63634	1.48
35.9602	107.78	0.2007	2.49747	1.49
36.4285	620.80	0.0669	2.46643	8.56
38.4591	111.17	0.2007	2.34076	1.53
39.3852	528.84	0.0669	2.28783	7.29
40.2112	223.71	0.0502	2.24272	3.08
41.7507	53.73	0.2007	2.16351	0.74
42.3803	276.38	0.0669	2.13282	3.81
43.1493	150.37	0.1673	2.09657	2.07
44.6551	768.35	0.1004	2.02931	10.59
45.7123	150.46	0.0669	1.98481	2.07
47.0766	105.43	0.2007	1.93042	1.45
47.4593	152.88	0.2007	1.91575	2.11
48.4924	136.11	0.2342	1.87732	1.88
50.0845	459.73	0.1020	1.81980	6.34
50.2257	241.77	0.0816	1.81953	3.33
54.8119	238.43	0.0612	1.67350	3.29
54.9546	133.35	0.0612	1.67364	1.84
55.2775	71.06	0.1224	1.66050	0.98
57.4158	67.76	0.3264	1.60364	0.93
58.6429	67.35	0.1224	1.57297	0.93
59.8891	510.83	0.0612	1.54319	7.04
60.0555	254.26	0.0816	1.54313	3.50
60.8803	37.23	0.4896	1.52041	0.51
65.1594	70.85	0.3264	1.43053	0.98
67.6785	183.52	0.1020	1.38328	2.53
68.0779	491.40	0.0816	1.37613	6.77
68.2646	491.03	0.0816	1.37282	6.77
68.4529	132.28	0.0612	1.37291	1.82
72.9589	19.23	1.3056	1.29563	0.27
75.6059	120.23	0.1020	1.25671	1.66
75.8218	92.10	0.0816	1.25679	1.27
78.1617	50.55	0.4080	1.22189	0.70
79.8031	136.78	0.0816	1.20083	1.89
80.0235	76.20	0.1224	1.19808	1.05
81.1619	92.59	0.0816	1.18412	1.28
81.4181	84.21	0.1632	1.18105	1.16
83.8108	80.54	0.1224	1.15331	1.11
85.0514	15.19	0.4896	1.13963	0.21
90.8055	88.57	0.1020	1.08179	1.22
92.8682	17.51	0.4896	1.06309	0.24
94.6207	68.02	0.1224	1.04797	0.94
95.0671	46.71	0.2448	1.04423	0.64
96.2292	54.63	0.1224	1.03468	0.75

2.3 Graphics M.20 stressed sample:

Anchor Scan Parameters

Dataset Name: M-20-stressed
 File name: H:\X'Pert Data\Oct 13\15th Oct\M-20-stressed.xrdml
 Comment: Configuration=Flat stage, Owner=User-1, Creation date=1/15/2009 8:55:18 AM
 Goniometer=PW3050/60 (Theta/Theta); Minimum step size 2Theta:0.001; Minimum step size Omega:0.001
 Sample stage=PW3071/xx Bracket
 Diffractometer system=XPERT-PRO
 Measurement program=xrd program, Owner=User-1, Creation date=1/15/2009 9:49:56 AM

Measurement Date / Time: 10/15/2013 4:40:12 PM
 Operator: ABC
 Raw Data Origin: XRD measurement (*.XRDML)
 Scan Axis: Gonio
 Start Position [°2Th.]: 5.0044
 End Position [°2Th.]: 99.9834
 Step Size [°2Th.]: 0.0170
 Scan Step Time [s]: 5.1682
 Scan Type: Continuous
 PSD Mode: Scanning
 PSD Length [°2Th.]: 2.12
 Offset [°2Th.]: 0.0000
 Divergence Slit Type: Fixed
 Divergence Slit Size [°]: 1.0000
 Specimen Length [mm]: 10.00
 Measurement Temperature [°C]: 25.00
 Anode Material: Cu
 K-Alpha1 [Å]: 1.54060
 K-Alpha2 [Å]: 1.54443
 K-Beta [Å]: 1.39225
 K-A2 / K-A1 Ratio: 0.50000
 Generator Settings: 30 mA, 40 kV
 Diffractometer Type: 0000000083002110
 Diffractometer Number: 0
 Goniometer Radius [mm]: 240.00
 Dist. Focus-Diverg. Slit [mm]: 100.00
 Incident Beam Monochromator: No
 Spinning: No

Peak List					
Pos. [°2 θ .]	Height [cts]	FWHM [°2 θ .]	d-spacing[Å]	Rel.Int. [%]	
11.5645	21.41	1.0706	7.65214	0.36	
13.7225	49.45	0.2007	6.45322	0.82	
18.1827	153.29	0.1004	4.87908	2.54	
20.9784	837.63	0.1004	4.23476	13.89	
23.2095	126.77	0.1338	3.83248	2.10	
23.7271	61.27	0.1004	3.75003	1.02	
24.4821	86.25	0.1004	3.63606	1.43	
25.7221	45.45	0.3346	3.46352	0.75	
26.7827	6030.56	0.0669	3.32873	100.00	
27.1453	260.06	0.0502	3.28508	4.31	
27.5339	1544.98	0.0669	3.23960	25.62	
28.0551	510.18	0.0836	3.18058	8.46	
29.5754	1355.01	0.0836	3.02046	22.47	
30.8945	256.26	0.1004	2.89444	4.25	
32.6720	79.80	0.1004	2.74091	1.32	
34.2250	190.58	0.0669	2.62002	3.16	
36.1688	133.52	0.2342	2.48355	2.21	
36.6768	334.42	0.0669	2.45031	5.55	
39.6046	363.88	0.0669	2.27565	6.03	
40.4476	212.38	0.0502	2.23015	3.52	
41.9522	140.39	0.0669	2.15358	2.33	
50.4180	379.00	0.0612	1.81304	6.28	
50.9634	80.32	0.3264	1.79047	1.33	
55.0168	285.29	0.0816	1.66775	4.73	
55.1672	155.13	0.0612	1.66769	2.57	
55.4590	62.45	0.1224	1.65550	1.04	
57.6249	73.26	0.3264	1.59832	1.21	
58.8522	47.80	0.3264	1.56788	0.79	
60.1090	408.41	0.0816	1.53806	6.77	
60.2722	197.06	0.0816	1.53810	3.27	
64.2298	42.01	0.4896	1.44897	0.70	
67.8861	238.90	0.0816	1.37955	3.96	
68.0793	134.02	0.1224	1.37611	2.22	
68.2899	404.63	0.0612	1.37238	6.71	
68.4788	231.19	0.0816	1.36905	3.83	
73.0223	19.84	1.3056	1.29466	0.33	
73.6183	76.78	0.0816	1.28565	1.27	
75.0889	83.30	0.1224	1.26408	1.38	
75.7790	78.44	0.0816	1.25427	1.30	
77.7923	56.48	0.1632	1.22677	0.94	
79.3161	90.90	0.1224	1.20698	1.51	
80.0398	167.48	0.0816	1.19788	2.78	
80.1969	93.72	0.3264	1.19593	1.55	
81.3277	98.36	0.0612	1.18213	1.63	
81.6017	86.57	0.1632	1.17885	1.44	
83.9691	99.36	0.0816	1.15154	1.65	
90.9624	77.72	0.0816	1.08033	1.29	
94.7783	56.58	0.1224	1.04665	0.94	
96.5044	18.19	0.4896	1.03246	0.30	

2.4 Strain Calculations:

$$d = 1.03246 \text{ \AA} @ 2\theta = 96.5044^\circ$$

$$d_0 = 1.03468 \text{ \AA} @ 2\theta = 96.2292^\circ$$

$$\text{Strain} = (d - d_0) / d_0$$

$$\epsilon = (1.03246 - 1.03468) / 1.03468$$

$$\epsilon = -2.145 \times 10^{-3}$$

III. CONCLUSION

Atomic spacing is more in unstressed condition as compared to atomic spacing in stressed condition at 100% relative intensity. Strain within the body can be very well calculated using simple empirical equation and negative sign indicates that the bond is inter atomic. Strain calculations may prove to be use full in predicting moduli and various other parameters of concrete.

Acknowledgements

Authors would like to acknowledge the support of Prof. N. K. Dhapekar (Head of Civil Engineering Department, Kruti Institute of Technology and Engineering, Raipur, Chhattisgarh) for sharing his valuable data for our research work.

REFERENCES

- [1]. Elements of X-ray diffraction (Second edition) by B. D. Cullity, department of metallurgical engg. and material science, university of Notre Dame.
- [2]. Current applications of X-ray diffraction residual stress measurement by Paul. S. Prevey, Lambda research in ASM international, materials park, OH, 1996, pp 103-110.
- [3]. X-ray diffraction study of the single crystal elastic moduli of Fe up to 30GPa by Sebastien Merkel, Jinflu Shu, Philippe Gillet in journal of geophysical research published on 13 May 2005.
- [4]. www.xpert.com.

Study of Flexible Lift Mechanism for Press Shop

Mr. Sarang Khedkar¹, Prof. B. D. Deshmukh², Prof. G. V. Thakre³,
Mr. Y. V. Mahantare

¹(Department of Production Engg, Y. C. C. E, Nagpur/ RTMNU, Nagpur, India)

²(Department of Production Engg, Y. C. C. E, Nagpur/ RTMNU, Nagpur, India)

ABSTRACT: The industrial sector is one of the important sectors of the Indian economy. The Small Scale Industries (SSI) sector is one of the most vital sectors of the Indian Economy in terms of employment generation, the strong entrepreneurial base it helps to create and its share in production.

The study offers in SSI the press shop, hands-on approach to workplace where material handling table can work effectively considering the space constraint, time constraints, and availability of workers and different postures of workers. It includes the considerations for effective working of the material handling table, layout of the plant with different sections where different operations are performed. Discusses the different stations of press shop where different process such as handling of raw material, cutting of raw material to finished components. Analyses the different problems related to handling of table with their solutions that shows the limitations of presently available material handling table and with objectives. It illustrates the observations carried out for a week showing the loss of time and money. Stimulates new thinking about problems brought about by technological advancements.

Keywords: Down time, Layout, Lifting Mechanism, Machine, Material handling, productivity.

I. INTRODUCTION

Economic development of any nation is totally depends on industries. Industries play an important role in the Indian Economy. A growing industrial sector is crucial to greater economic development and takes in a number of areas as a country develops. Small-scale sector comprises predominantly manufacturing activities. The Small Scale Industries (SSI) sector is one of the most vital sectors of the Indian Economy in terms of employment generation, entrepreneurial base and to increase the production.

II. SELECTIONS OF INDUSTRY

Among all types of industries we selected M/S Asha Industries as it is a small scale industry related with the agriculture equipment which full fills the need of farmers and rural areas.

2.1 M/S ASHA INDUSTRIES PVT. LTD- The products manufactured at Asha Industry are Two-farrow plough, Three-farrow plough, Four-farrow plough, Land Leveler, Medium Duty Cultivator, and Thresher.

2.1.1 PLANT LAYOUT- Plant layout is a systematic and functional arrangement of different departments, machines, equipment, tool and services in an industry to achieve the most efficient utilization of men, machines and materials.



Fig.1 Plant layout

1. Raw material storage section 2. Press shop. 3. Gas profile machine section 4. Drilling machine section 5. Welding and assembly section 6. Painting shop 7.Scrap

2.1.2 PRESS SHOP- The Press shop at a glance

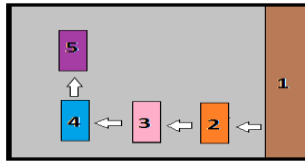


Fig. 2 Press shop

1. Raw Material Storage Section. 2. Material Handling Table. 3. Shearing Machine 4. Finish Product.
5. Bending section

1. Raw Material Storage Section - Raw materials of different sizes are stored in storage section are:

- M.S flat plate, Length: 15 ft Thickness:3mm,4mm,5mm,6mm,8mm,12mm Width: 0.5", 1", 1.5", 2", 4" & 6"
- M.S Round bar size Length: 20 ft. & 30mm diameter
- Angle sizes Length: 18ft. Thickness: 4mm, 6mm Width: 40×40and 30×30

2. Material Handling Table - Material handling table supports the raw material by rolling over it and which can be adjusted vertically as per the requirement of dies which helps to feed the raw material inside shearing machines. Material handling table height is adjusted manually and usually 4 workers are required for it.

3. Shearing Machine - After the raw material placed on table it is feed inside the dies of shearing machine to cut the material in a required length and dies of shearing machine are available in three steps to cut the round bar, flat plate, angle into required length for this operation 2 workers are required.

4. Finish Product - After the shearing operation we get the material in required length. These materials are transfer for further operations in to the different section.

- M.S Flat plate-lengths: 6'', 8'', 10'' & 1ft.
- M.S Round bar-length: 6''.
- Angle length: 5'', 7'', 9'' & 12''.

5. Bending section -The finish products obtained from shearing machine is to be check for alignment and it is to be done on bending machine

2.1.3 VARIATION IN PRODUCTS- As different products are manufactured, they required cut pieces of different sizes of the angle, round bar and flat plate. Raw material are cut into pieces as per the requirement of different section in the layout At what movement which raw material they required, for assembly and different machining process depends on the pieces of raw material which is to be cut on shearing machine. That creates variation in product.

2.2 PROBLEM IDENTIFICATION- Due to the variation in process that causes the problem such as time loss during table adjustment, cutting dies position, Handling of heavy load of table, Uncomfortable posture, Fatigue developed in workers during heavy material handling.



Fig- 3 Cut sees of table

2.3 OBJECTIVES- The objective is to configure all the problems by Developing Flexible Lift Mechanism for Press shop reduces the time loss for changing the height table, Reduce fatigue in workers, increased the production rate, Reduced chances of accident, Reduce the Repeatedly performing tasks downtime to increase the Productivity of Press Machine ultimately to increase the production of organization.

III. LITERATURE REVIEW

Many researchers directly or indirectly have contributed to the area of identified problem. Their work done has been critically studied in literature review and categorizes as down time, Ergonomics, Plant layout, Lifting mechanism, Productivity

Svante Bjorklund, Lennart Ljung (2009) has explained the promising method for estimation of the time-delay in continuous-time linear dynamical systems uses the phase of the all-pass part of a discrete-time model of the system.

Ergonomics is the scientific study of the relationship among the man, the machine and the environment in which he works. According to G.A. Mirka et al. / International Journal of Industrial Ergonomics (2002) The research and design team employed an iterative prototyping process, wherein each ergonomic intervention prototype was subjectively evaluated in the lab by the research team and in the field by furniture workers and the results of these assessments were used to improve on the design of the intervention. Haw S. Jung (2005), he has explained that the study was conducted to develop a prototype of an adjustable table and an adjustable chair for educational institutions, to evaluate its adoptability in accordance with international standards, and to validate the prototype chair by conducting subjective trials. BinShu, ChangshengXu, Dingfang Cheng (2008) in the traditional design process, the design method no effective dynamic technique. It also offers of port machines mainly adopts the static design and has certain value for reference for the dynamic. XiaoliangZheng, Zhongjin Li, Zhengyan Zhang, Taotao Li, Dingfang Chen(2010)-has introduces the way to optimize the rocker-slider mechanism for lifting plat form based on genetic algorithm of excessive objects, aimed at the minimum compression height, the maximum lifting height and the largest cylinder' s axial force. And combined with MATLAB's graph management and interface development function, he has produced a motion simulation for the rocker-slider mechanism for lifting platform.

Productivity is the efficiency in production. V.K. Menon has told that Productivity is the development of an attitude of mind and a constant urge to find better, cheaper, quicker and safe ways of doing a job which may be manufacturing an article or providing a service. Productivity is the balance between all the factors of production that will give the greatest output for smallest efforts.

IV. EXPERIMENTATION/OBSERVATIONS

V. Study to determine the loss due to the problem identified for a weak is summarized in the table. From the observation we calculate the loss in terms of wages and cutting pieces of the component.

Days	Total number of pieces	Actual time (min)	Time loss (min)
1	270	295	125
2	310	340	80
3	279	305	115
4	297	325	95
5	310	340	80
6	279	305	115
Total	1745	1910	610
Average	291	318	102

VI. Table 1- Average loss in pieces and time

Table calculation specifies that firm is investing extra Rs 38700 for the three workers due to the height adjustment of table.

VII. DESIGN & MODELING OF EXISTING LIFTING TABLE

In case of existing work table when the workers are required to adjust the height of work table, they used to call the workers from other workstations to adjust the height of table according to dies position. This method used to disturb the working of other work stations as those workers are engaged in adjustment of table. After the adjustment the row material is brought at work table from raw material storage and kept on table. That

raw material is fed to the shearing machine and pieces are cut that are stored in store bins. Then these finish component are sent to different sections. Weight of table is nearly 78 kg.

Parts of table are Horizontal stripes, Vertical strips, Roller Bars, Nuts& Bolts assembly.

The model of the table is made with the help of Pro-E software.

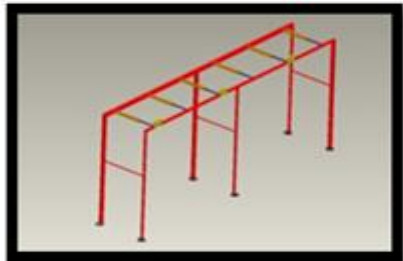
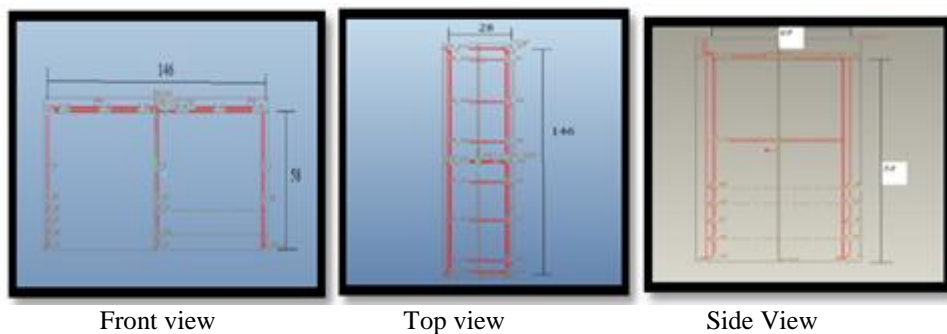


Fig 4 - 3D model of an Existing table.



Front view

Top view

Side View

Fig.19 Model of table (All dimensions are in inches)

VIII. CONCLUSION

Study of project in Industries in press shop carried out where we found that there is certain time and other losses occurring in the functioning of work table and its adjustment it creates the different problems in the process. So study deals with the modification of existing work table to overcome the losses to increase the production rate.

The way, this study gives the overall concept for reduction of losses occurring in the industry to improve the productivity of the industry. The design and modeling of the modified lifting mechanism will be dealing to overcome the existing problem with the help of advancement in the software.

REFERENCES

- [1]. SvanteBjorklund, LennartLjung (2009) an improved phase method for time-delay estimation journal homepage: www.elsevier.com/locate/automatica.
- [2]. S .K. Garg (2009), workshop technology pp. 1-12.
- [3]. G.A. Mirka et al. (2002) Ergonomic interventions for the furniture manufacturing industry. Part-I lift assist devices. International Journal of Industrial Ergonomics 29 (2002) pp 263-273.
- [4]. Hwa S. Jung (2005) A prototype of an adjustable table and adjustable chair for school International Journal of Industrial Ergonomics 35 (2005) pp 955-969.
- [5]. Taho Yang a, Brett A. Peters b, MinganTu (2005) Layout design for flexible manufacturing systems considering single-loop directional flow patternsEuropean Journal of Operational Research 164 (2005) PP 440-455.
- [6]. Bin Shu, ChangshengXu, Dingfang Cheng (2008) Design of the Lifting Mechanism with Virtual Prototyping Technology (2008) pp 384-387.
- [7]. Shubo Xu, Jie Liu, Keke Sun, Peng Liu, Yuanbin Zhang (2010) Study on Modeling Simulation of Long-span Gantry NC Machining CenterStructure,International Conference on Digital Manufacturing & Automation (2010).

Seismic Pounding Effect in Framed Structures

N. N. Gulhane¹, Prof. M. V. Mohod²

¹Post graduate student in structural engineering,

²Department of Civil engineering, Prof. Ram Meghe Institute of Technology and Research Badnera, Sant Gadge Baba Amravati University, Amravati, Maharashtra 444602 India

ABSTRACT: Pounding between adjacent structures is commonly observed phenomenon during major earthquakes which may cause both architectural and structural damages. To satisfy the functional requirements, the adjacent buildings are constructed with equal and unequal heights, which may cause great damage to structures during earthquakes. To mitigate the amount of damage from pounding, the most simplest and effective way is to provide minimum separation distance. To study the effect of structural pounding, a case study has been done on different setback ratios (Area & Height) and to investigate the minimum seismic pounding gap between two adjacent structures by using GAP joint element & non-linear time history analysis.

Keywords: SAP v.14, setback structures, Seismic analysis, gap element

I. INTRODUCTION

Structures are built very close to each other in metropolitan areas where the cost of land is very high. Due to closeness of the structures, they collide with each other when subjected to earthquake or any vibration. This collision of buildings or different parts of the building during any vibration is called pounding which may cause either architectural and structural damage or collapse of the whole structure. This may happen not only in buildings but also in bridges and towers which are constructed close to each other. Although some modern codes have included seismic separation requirement for adjacent structures, large areas of cities in seismically active regions were built before such requirements were introduced. Many investigations have been carried out on pounding damage caused by previous earthquakes. Pounding damage was observed during the 1985 Mexico earthquake, the 1988 Sequenay earthquake in Canada, the 1992 Cairo earthquake, the 1994 Northridge earthquake, the 1995 Kobe earthquake and 1999 Kocaeli earthquake. Significant pounding was observed at sites over 90 km from the epicentre thus indicating the possible catastrophic damage that may occur during future earthquakes having closer epicentres.

II. BUILDING MODELING

For this study 21 story building with a 3m height of each story, Different building geometries Area & Height were taken for the study. These building geometries represent varying degree of irregularity. In 2 D frame structure nine different categories of buildings, ranging 4 bays (in X direction) a bay width 4m and 21 bays in Y direction. In SAP 14 software. three different gap element are provided in building.

TABLE 1

Sr. no.	Description	Specification
1	Number of stories	G+20
2	Building height	63m
3	Bay width in x- direction	4m
4	Size of beam	0.45mx0.45m
5	Size of column	0.45mx0.60m
6	Grade of concrete & steel	M20 & Fe415

TABLE 2

Sr. no.	Along plan area (RA)	Along height (RH)	Gap width (m)
1	RA=25	RH=16/5, 11/10, 6/15	0.05, 0.10, 0.15
2	RA=50	RH=16/5, 11/10, 6/15	0.05, 0.10, 0.15
3	RA=75	RH=16/5, 11/10, 6/15	0.05, 0.10, 0.15

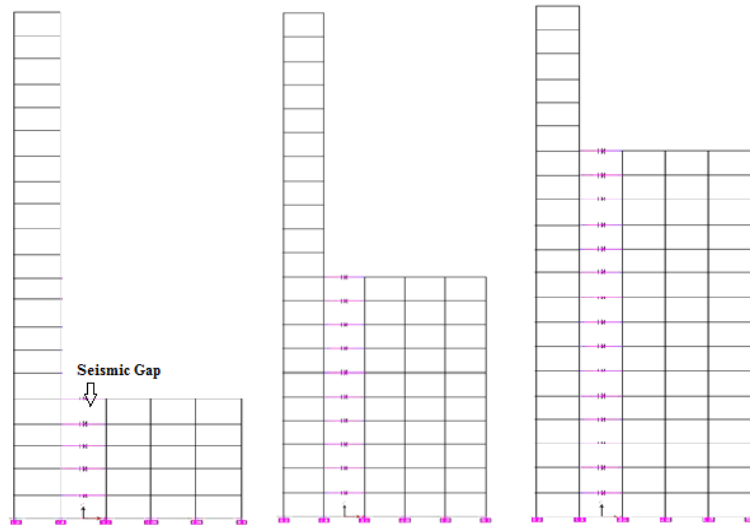


Figure:1 Irregularities In Height i.e. RA=25 and RH=16/5,11/10,6/15

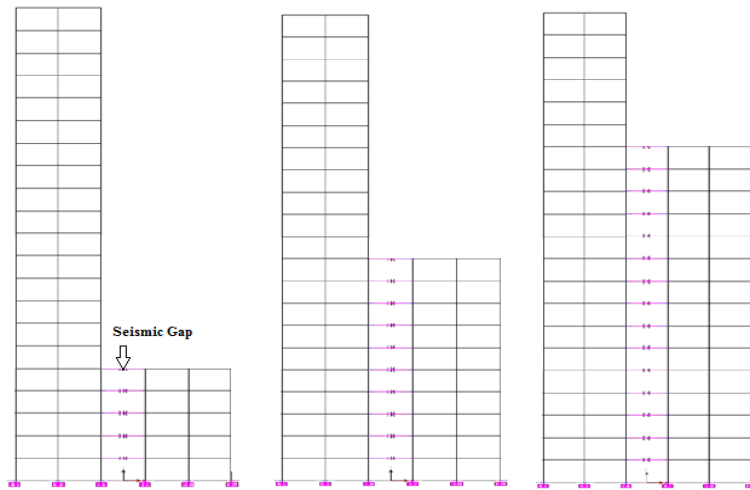


Figure:2 Irregularities In Height i.e. RA=50 and RH=16/5,11/10,6/15

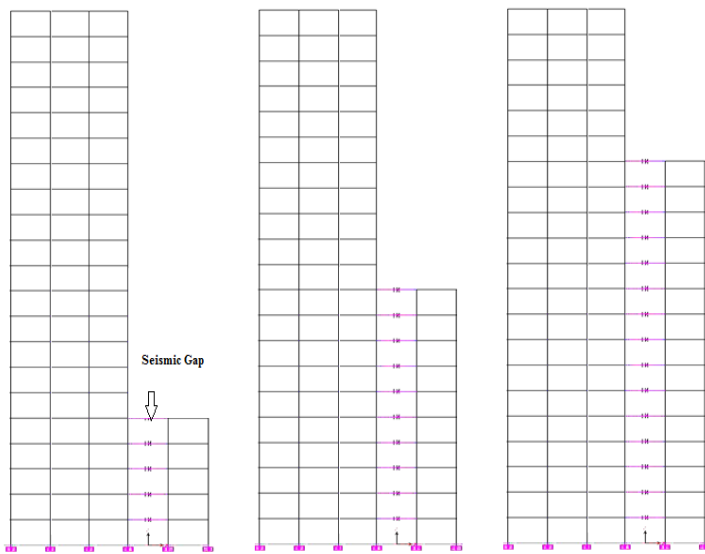


Figure:3 Irregularities In Height i.e. RA=75 and RH=16/5,11/10,6/15

III. RESULTS AND DISCUSSION

For showing variation spectral displacement varies gap width

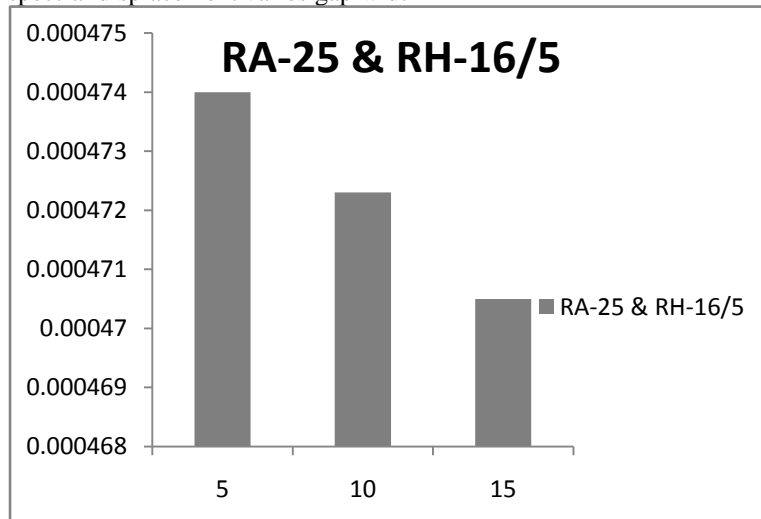


Figure:4 RA=25 and RH=16/5 for gap= 0.05m, 0.10m, 0.15m

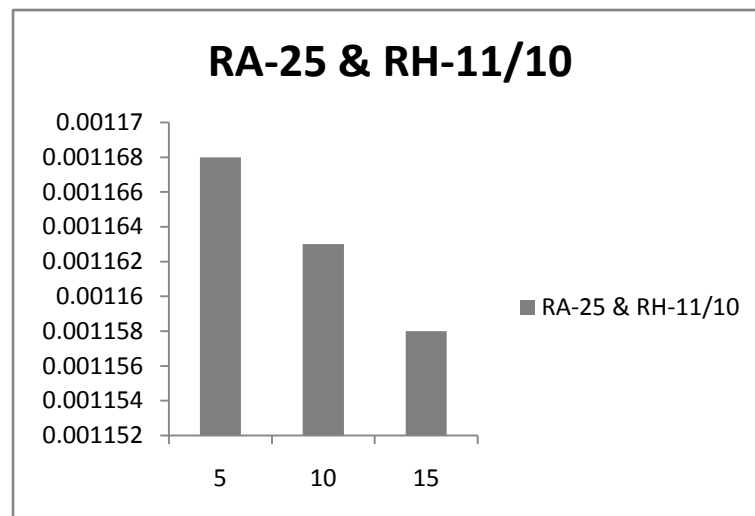


Figure:5 RA=25 and RH=11/10 for gap= 0.05m, 0.10m, 0.15m

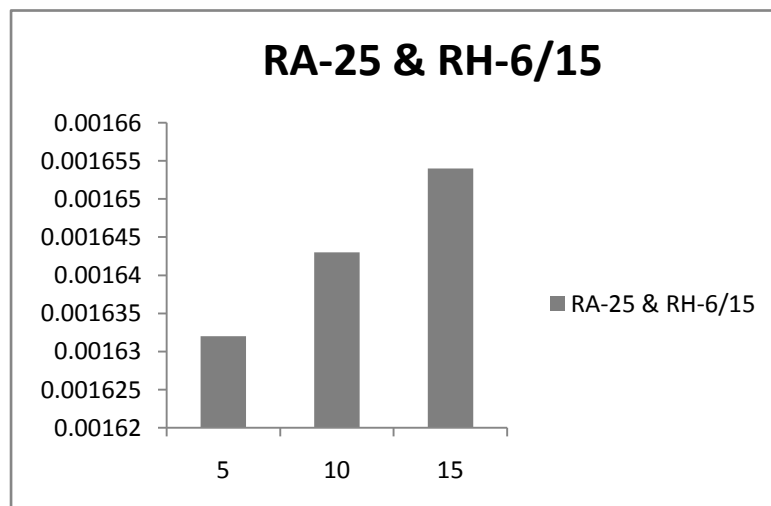


Figure:6 RA=25 and RH=6/15 for gap= 0.05m, 0.10m, 0.15m

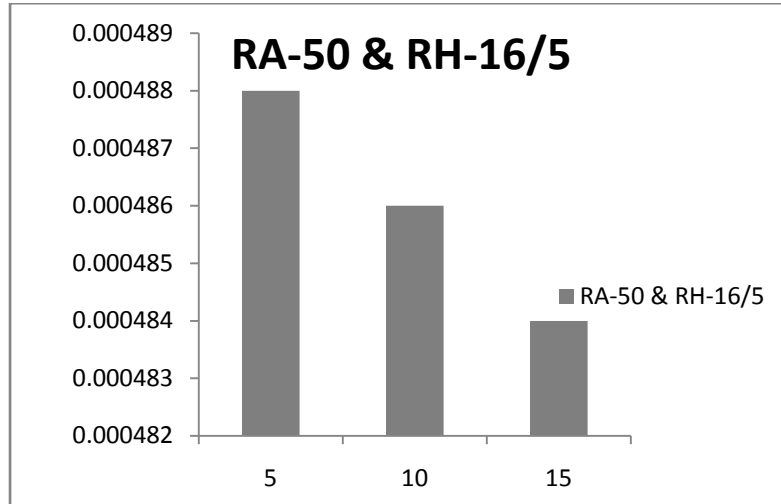


Figure:7 RA=50 and RH=16/5 for gap= 0.05m, 0.10m, 0.15m

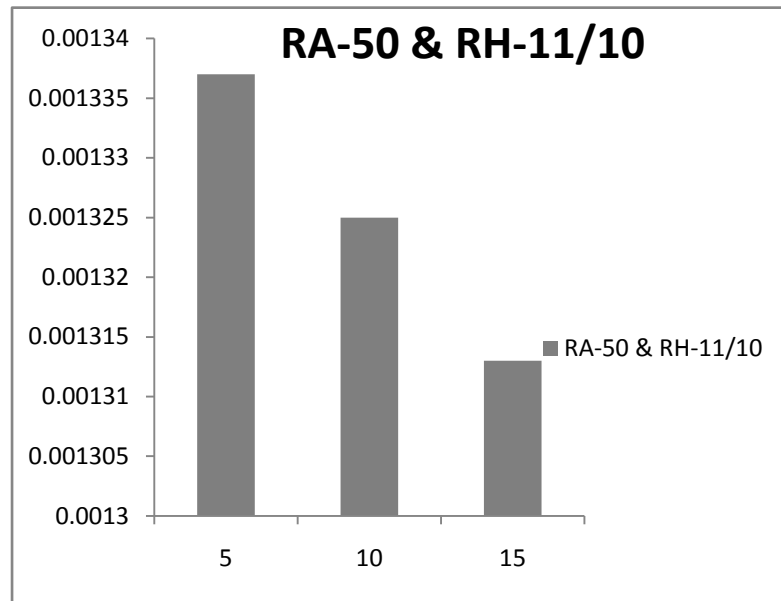


Figure:8 RA=50 and RH=11/10 for gap= 0.05m, 0.10m, 0.15m

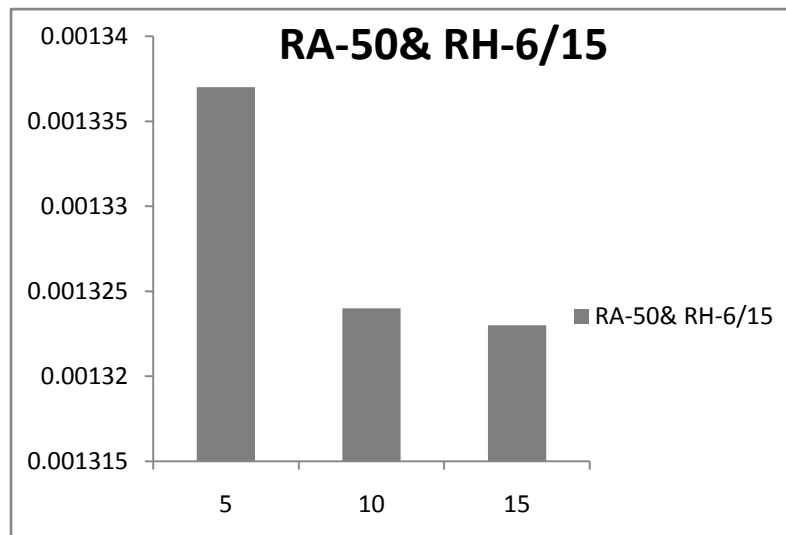


Figure:9 RA=50 and RH=6/15 for gap= 0.05m, 0.10m, 0.15m

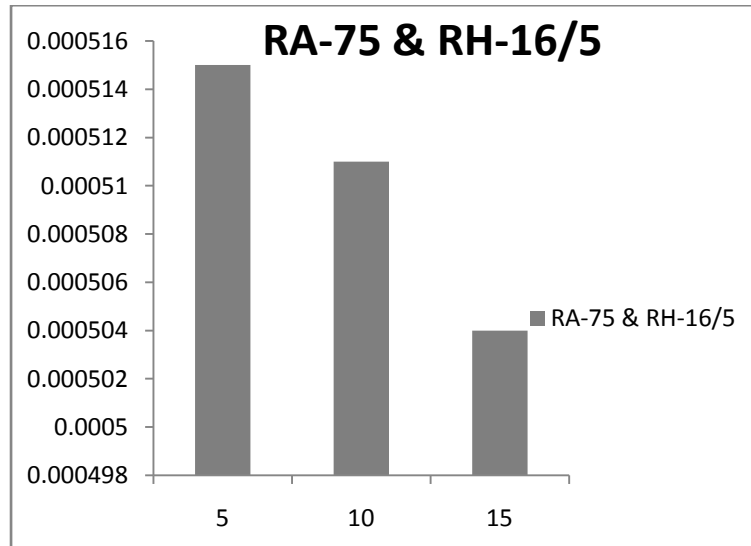


Figure:10 RA=75 and RH=16/5 for gap= 0.05m, 0.10m, 0.15m

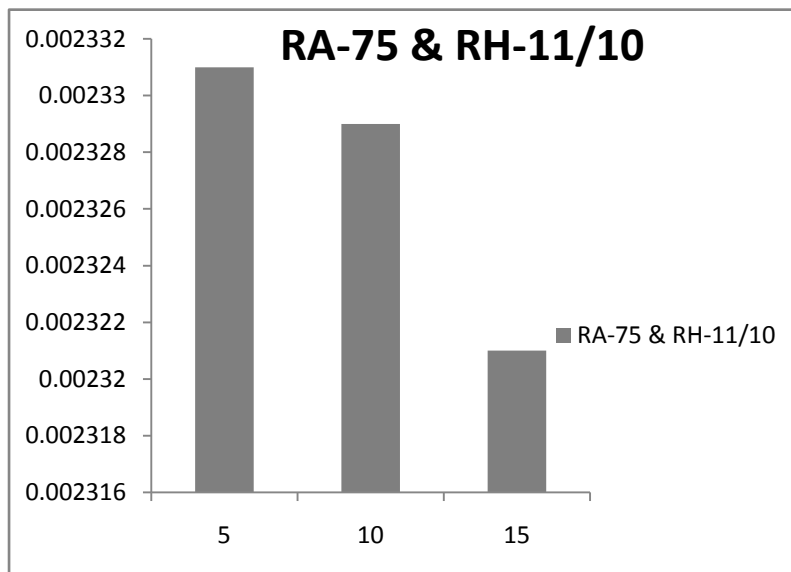


Figure:11 RA=75 and RH=11/10 for gap= 0.05m, 0.10m, 0.15m

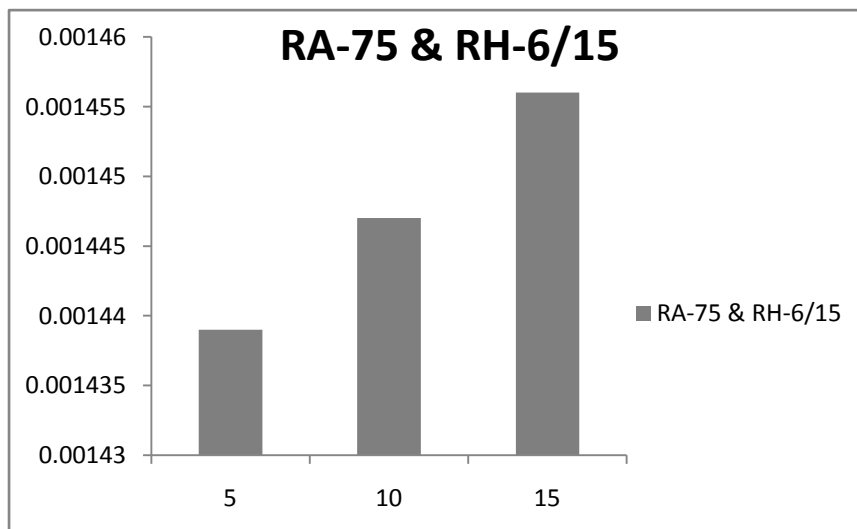


Figure:12 RA=75 and RH=6/15 for gap= 0.05m, 0.10m, 0.15m

Time history results clearly depict the need of seismic gap between adjoining structures. The initial models of RA=25%, RA=75% variation along the height shows the need of seismic gap between the range 5cm to 15cm. whereas for RA=50% and variation along height a seismic gap between 5cm to 10cm is suggested.

IV. CONCLUSIONS

The analytical studies involved design of different building geometries were taken for the study .the building geometries represent varying degree of irregularity or amount of setback.

Following conclusion can be draw from the obtaining result,

- 1) when RA=25,75 and RH=16/5,11/10 in that case response linearly increases then seismic gap width 15 cm have found to be sufficient. RA=25, 75 and RH=6/15 in that case seismic gap width more than 15 cm is needed.
- 2) RA=50 and RH=16/5,11/10 is show similar variation in seismic gap width 15 cm have found to be sufficient. But for RA=50 and RH=6/15 the seismic gap width 10 cm is sufficient.

REFERENCES

- [1]. IS 1893 (Part 1) : 2002 Indian Standard Criteria for Earthquake Resistant Design of Structures, Part 1 General Provisions and Buildings, (Fifth Revision).
- [2]. IS 456 : 2000 Indian Standard Plain and Reinforced Concrete Code of Practice (Fourth Revision)
- [3]. I. J. Sharma “Seismic pounding effect in buildings” Thesis in national institute of technology Rourkela
- [4]. 4.Shehata E.Abdel Raheem Seismic Pounding between Adjacent Building Structures Electronic Journal of Structural Engineering, 6 (2006)
- [5]. H. Shakib and M. pirizade Seismic analysis of setback building by using probabilistic approach method- (ASCE)ST.1943
- [6]. 6.Rajaram Chenna, Pradeep Kumar Ramancharla “Three Dimensional Modeling Of Pounding Between Adjacent Building” Indian Concrete Journal Report No: IIIT/TR/2012/-1
- [7]. 7.Robert Jankowski ” Non-linear Modelling of Earthquake Induced Pounding of Buildings published on ICTAM, 15-21 August 2004, Warsaw, Poland
- [8]. 8. G. L. Cole, R.P.Dhakal, A.J.Carr & D.K. Bull Building pounding state of the art: Identifying structures vulnerable to pounding damage. 2010 NZSEE Conference
- [9]. 9.SAP 2000 Nonlinear Version 14 Software Package.
- [10]. 10. SAP2000 Nonlinear Manuals.
- [11]. 11. SAP Video Tutorial.

Information Technology in Rural India

Y. Srinivas¹, N. Venkatanarayana², A. Sreeram³, J. Vijayasekhar⁴,
G. Yugandhar⁵, M. Rathan Reddy⁵,

¹Department of Information Technology, GITAM University, Hyderabad

²Department of Mathematics, Dr. B. R. Ambedkar Open University, Hyderabad

³Hyderabad Business School, GITAM University, Hyderabad

⁴Department of Mathematics, GITAM University, Hyderabad

⁵Department of Computer Science & Engineering, GITAM University, Hyderabad, India

ABSTRACT: Communication is one of the major components and driving force for the development of rural areas in India. Communication can be done in many ways among them conventionally communication includes electronic media, human communication and in the present days Information technology (IT). Villagers also have their own information needs. They need to know about their village, their districts, natural resources around them, about seasons and monsoons, about market rates of different commodities and about government schemes. They also need to know how much money is being allocated for rural development in their area and how much is being spent. And all these so-called bits of information are related intensely to their lives and livelihood. A connected PC is an effective tool to do all this and much more.

Technological changes further compounded the direction of rural development as Information and communication technology (ICT). It has led to indiscriminate applications and use of ICT in every aspect of information dissemination, management and governance of development. Apart from the development, the introduction of communication in the educational process for open and distance learning is seen as a step towards improving the quality of education and bridging the social and educational gap.

Keywords: Rural Development, ICT.

I. INTRODUCTION

Information technology has become the buzzword in India these days. One hears about it everywhere from stock markets to government corridors across the country. Everybody wants to do something connected with IT be it a school student or a politician. They are looking at IT as the ultimate panacea. The ever-growing media attention on success stories are fuelling this appetite for IT. And within this craze for IT, the focus is on the internet or the World Wide Web. Generally, there is an IT friendly atmosphere in the country. Information Technology is increasingly moving to the core of national competitiveness strategies around the world. Information Technology has given enormous power to individuals with unprecedented access to information and knowledge with important consequences in terms of providing education and access to markets of doing business and social interactions among others. Computers can only provide information, transmit it from one place to another and with the advent of the internet, make communication instant. Approximately 70% of Indian population lives in rural areas. Today rural development is essential for the development of Indian Economy. The role of Information Technology has increased from providing only the Networks to set-up the basis of updated technological programs in rural areas. The rural market of India is showing an impressive growth largely due to changing life style patterns, better communication network and rapidly changing demand structure of consumers of rural area.

II. IMPLEMENTATION OF IT IN RURAL AREAS BY INDIAN GOVT

Fortunately, India took to IT early compared to many other developing countries. The nationwide network of computers set up by the National Informatics Centre took the PC to every district in the country, making government level interaction and communication faster for planners. The internet has now given us an opportunity to take the PC to every village. It has a definite role to play in rural education, health and agriculture. In the Indian situation, a PC need not be a personal computer. It can be a community computer. In the day time, it can be used to educate children at primary and middle level in the village school. In the evening,

the community computer can turn into a "cyber dhaba" for villagers – where they can access web-sites of their choice and get information that they can use.

III. IT IN RURAL SECTOR

In rural sector in underdeveloped countries information Technology include the following namely Education and Health Care.

Education

- Affordable high quality education in rural areas.
- Confidence, speaking flawless English, computer literature students.
- Increased educational awareness in rural societies.
- Estimated growth in education in today is 23.4% and it can be increased to 68.3%



Health Care

- Health care is yet another area where IT can play a major role in rural areas.
- Health care facilities was not good between 1950s and 1980s
- Now Information Technology has improved care, primarily through more timely diagnosis and intervention, reduction of medical errors, and better communication with the care team.
- Doctor or the paramedic staff at the local PHC or sub-PHC can access latest information about health schemes and seek advice from specialists about diseases or ailments they cannot diagnose or treat



IV. ICT IN RURAL DEVELOPMENT

ICTs can be broadly defined as the set of activities that facilitate the capture, storage, processing, transmission and display of information by electronic means. ICTs offer remarkable opportunities for the alleviation of poverty and employment generation. ICTs enhance the opportunities of rural communities by

- Improving their access to market information and lower transaction costs (for poor farmers and traders);
- Increasing efficiency, competitiveness and market access for firms in developing countries.
- Enhancing the ability of developing countries to participate in the global economy and to exploit their comparative advantage in factor costs (particularly skilled labour).
- Health and
- Education.

Furthermore, ICTs promote greater transparency and speed up the decision-making processes of governments, and thus empower rural communities by expanding their use of government services and reduce risks by widening their access to micro-finance. However, barriers to access, high costs and minimal human resources often prevent those living in poverty from reaping the benefits of ICTs. When the private and civil sectors work together as partners, the benefits of ICTs can be greatly enhanced, returns to the community can be improved, and profits can be increased.

V. FACTORS PREVENTING RURAL COMMUNITIES FROM REAPING THE BENEFITS OF ICTS

There are a number of important factors preventing rural communities in developing countries from reaping the benefits of ICTs. Without developing access models that can address these factors, the rural masses will be left far behind urban dwellers, who are closer to digital opportunities. Constraints include:

- Lack of awareness about the benefits of ICTs – despite the growing numbers of people who own a computer and have Internet access, most people in developing countries have little opportunity to connect to the Internet, and therefore are unaware of the socio-economic benefits and stimulus that ICTs can bring to their lives. Because of the absence of demonstration projects in some countries, very limited information is available to assess and to advocate the impact of ICTs on development.
- Lack of access facilities – access facilities include computers and connectivity in rural areas. The cost of computers is still beyond the purchasing power of the majority of individuals in developing countries. The Internet is often far too expensive to be accessible to ordinary citizens and most public service institutions. It is often available only in urban centers, where most Internet service providers (ISPs) have their market.
- Language barriers in using the Internet – these prevent people from familiarizing themselves with the benefits of Internet-based information resources, which invariably require an ability to understand international languages, especially English. As a result, most people in developing countries cannot read and understand most of the Internet content. Another factor is the high illiteracy rate among rural people.
- Lack of local language information products– a lack of suitable information products tailored to the needs and assimilation capacities of rural people in developing countries. In order to better adjust their investment decisions, people need updated information on market prices, new agricultural technologies and methods to raise the quality of their products, adapt to changing climatic conditions or demands of agricultural markets.
- Non-availability of government information online – most countries do not have pro-poor ICT policies and plans to reorient relevant government institutes as electronic service providers to boost rural development.
- Lack of motivation to use information over the Internet – despite connectivity, people will not use ICTs unless they are motivated to do so. The prevailing modality of Internet access requires a certain level of competence from the user that many individuals in developing countries do not have.

Rural development programmes comprises the following:

1. Provision of basic infrastructure facilities in rural areas i.e., schools, roads, drinking water, electrification, etc.
2. Improving agricultural productivity in rural areas.
3. Implementing schemes for the promotion of rural industry, increasing agricultural productivity, rural employment, etc.

VI. E-LEARNING TECHNOLOGIES FOR RURAL INDIA

Computer based training and video based training have been very common for several decades in software industry. Specific software applications have been built and computer based training has been developed for them using easy to use authoring tools.

The student based in rural India will be able to access the content all over the world by using Internet. They can access various e- books and digital libraries from various well-known universities like Stanford, Harvard, etc. Internet will also permit virtual laboratories by which students using laboratory instruments connected to the advanced internet will be able to conduct a laboratory experiment remotely.

VII. NATURAL LANGUAGE INTERFACES

Natural language technology which could be of great use for e-learning. This is a way by which humans can communicate with the machine in a language that is natural to them. Natural language interfaces along with the touch screen technology and voice enabled inputs could be a way by which the National Literacy mission could be achieved through a process of parallel learning and the cycle of literacy followed by computer literacy and usage can be broken.

Ministry of Information Technology is already in several projects such as Bharat Bhasha Kosh, web learning system in Indian languages, Speech synthesis system.

VIII. IT-ENABLED SERVICES IN RURAL INDIA

A. e-Sagu

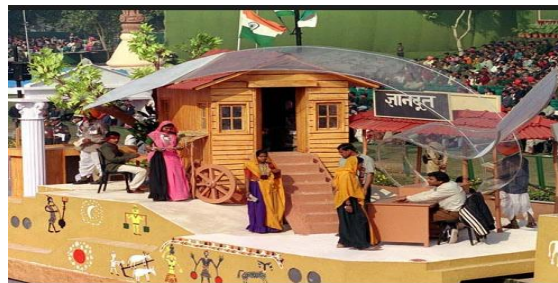
e-Sagu (*Sagu* in Telugu means *cultivation*) is a system which provides Agriculture experts (Scientist's) advice to remote farmers through internet. It was developed at International Institute of Information Technology (IIIT), Hyderabad under supervision of computer science Prof. P. K. Reddy. Reddy realized that the farmers in

rural areas are facing problems and low yields because of non-availability of timely expert advice. He noted that agriculture expertise and knowledge is available in India but there is gap in dissemination of expert advice to the farmers. By using Web Technology and database concepts Reddy's team developed an agricultural expert advice dissemination system. Using it farmers now get quick (about 24 hours or one day), timely and personalized expert advice (consultancy services). This model is very cost effective, scalable, replicable and sufficiently efficient.



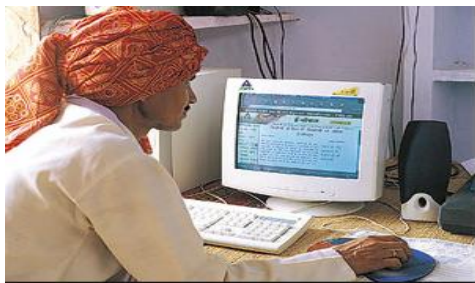
B. Gyandoot

In year 2000, *Gyandoot* (*Gyandoot* in Hindi means Purveyor of knowledge) intranet based information and service delivery project was taken up by Government in Dhar district of Madhya Pradesh in Central India. The network is Govt. owned. This intranet connect 34 rural cyber cafes kiosks called "*Soochanalayas*", each giving service to 10 Gram Panchayats (local government body) and in total serving 30000 populations. Services planned through *gyandoot* are commodity/*mandi* (local market) prices, issuing domicile/caste/income certificate, land holders Land rights certificate and loan pass book.



C. e-Chaupal

e-Chaupal (*Chaupal* in Hindi means *A gathering place*) is an initiative taken up by one of the India's large corporations ITC's International Business Division to give farmers the best price of their agricultural produce by eliminating role of middlemen using a set of Information and Communication Technologies (ICT). *Echaupals* are totally owned and set up by ITC. Typical e-*Chaupal* kiosk consists of a Computer and Internet connection via telephone line or VSAT link.



IX. IMPROVING ACCESS TO MICROFINANCE: SMART CARDS

Microfinance is an important tool for poor people to reduce, mitigate and cope with risk. Computerization, Smart Cards, and software systems providing loan tracking, financial projections and branch management information can reduce costs and help microfinance institutions reach clients more efficiently.

Smart Cards with an embedded microchip containing information on clients' credit histories are helping SKS, a microfinance institution operating in the Medak district of Andhra Pradesh to reduce transaction costs. One of the main problems faced by SKS, which follows the peer-lending model developed by the Grameen Bank, is the high cost of service delivery to the poor. All cash transactions take place at village group

meetings and each transaction takes about 90 seconds per person. Much time is spent not only on paperwork but also discussing terms and conditions and counting coins. Office computerization alone would not bring much time savings because staff would have more free time during the day, but not in the mornings and evenings when people in villages are available for meetings.

Smart Cards have been identified as a solution to the high cost of delivery, because they can lead to gains in efficiency, eliminating paperwork, reducing errors, fraud and meeting time. Potential savings in operations are estimated to be around 18 percent. Once all of SKS operations are conducted with handheld computers, a read-only device will be left in each village for clients to check the information stored on the Smart Cards. Microfinance projects like SKS enable poor people and their micro businesses to gain broader access to financial services.

X. IMPROVING SOCIO-ECONOMIC

One of the key components of improving socio-economic status of people in villages is to ensure that their products find right kind of markets and reach these markets in minimum time without number of middle men involved in it. The reach of IT in rural areas will provide unique opportunities to producers of rural products, agriculture/agro-processing products, rural handicrafts etc. to have direct access to markets. Internet will enable advertising of rural products produced even in the remotest villages to global markets. The agriculture extension worker can access latest information on farm technology and products, and disseminate the same to villages.

XI. CONCLUSION

The empowerment of rural communities is crucial for the development of the rural region. Bringing the people in the rural region in the main stream of digital technologies to access and adopt modern technologies is a major concern now a days. Rural development implies both the economic development of the people and greater social transformation using latest technologies.

REFERENCES

- [1]. Sushmita Mukherjee, Application of ICT in Rural Development: Opportunities and Challenges, *Global Media Journal - Indian Edition. Winter Issue / December 2011, Vol. 2, No.2.*
- [2]. <http://www.slideshare.net/amitjha800/it-in-rural-indiaopportunities-and-challenges#btnNext>
- [3]. http://www.bioinfo.in/uploadfiles/13256528641_1_2_JHPC.pdf
- [4]. <http://itd.ist.unomaha.edu/archives/1.pdf>
- [5]. Cecchini, S. and Raina, M. (2002), "Warana: the case of an Indian rural community adopting ICT", available at: www.iimahd.ernet.in/egov/ifip/apr2002/article3.htm
- [6]. Telecom Regulatory Authority of India (2003), "Consultation paper on accelerating growth of Internet and Broadband penetration", Telecom Regulatory Authority of India, New Delhi, p. 84.

Effect of Cooling Rate on Microstructure of Saw Welded Mild Steel Plate (Grade C 25 as Per IS 1570)

Rahul¹, Harish K Arya², Dr. R K Saxena³

^{1,2,3}Department of Mechanical Engineering

Sant Longowal Institute of Engineering & Technology, Longowal-148106, Punjab India

ABSTRACT: Cooling rate of weldment is depends on the heat input by the welding arc to the weldment. Heat input is controlled by the three variables current, voltage and travel speed. The present experimental study shows the effect of cooling rate on the microstructural changes of weldment, which is mostly responsible for failure of weld. Temperature profile at various cooling rates can help in better understanding and optimisation of submerged arc welding process. Microstructure of HAZ plays important role in strength and durability of weldment and hence by controlling welding parameters we can reduce the risk of weldment failure.

Keywords: Cooling Rate, Current, Microstructure, SAW Welding, Thermocouple, Voltage, Welding

I. INTRODUCTION

With the higher heat input the cooling rate is slower and vice-versa. Microstructure and micro-hardness are depend on the cooling rate, faster the cooling rate fine grains are formed and the hardness is increased and by the slower cooling rate coarse grains are formed and hardness is reduced. Submerged arc welding (SAW) is used for heat input because of high heat input the other processes [1] Heat input is increased with increasing wire feeding speed but increasing welding speed decreases the welding heat input. When heat input increases, the cooling rate decreases for weld metal and increases the volume fraction of tempered martensite and coarsening of the microstructure of weld zone. With increasing the wire feeding speed or preheating temperature, brinell hardness of weldment decreases but effect of welding speed on hardness is reversed to other parameters. When welding speed increases the weld hardness also increases [2].

Equation shows the relation between the welding parameters and heat input.

$$\text{Heat input} = \frac{K \times V \times I \times 60}{S \times 1000} \frac{\text{KJ}}{\text{mm}} \quad (1)$$

Where ‘V’ is arc Voltage in Volts, ‘I’ is welding current in Ampere, and ‘S’ is welding speed in mm/min. ‘K’, the thermal efficiency factor for the welding process, The value of K = 1 is taken here for Submerged arc welding.[3]

Table 1: Specifications of Submerged arc welding machine

Manufacturer	M/S Kanubhai Electrical Pvt. Ltd., Calcutta
Current range	60-1200 Amp
Maximum welding current at 60% duty cycle	1200 Amp
Maximum welding current at 100% duty cycle	900 Amp
Operating voltage	26-44 V
Electrical supply	415

1.1 Base plate

Mild steel plates having size 300×100×12 mm were used in this investigation. The plates were cut into required length with the help of a power hacksaw as shown in Fig: 1

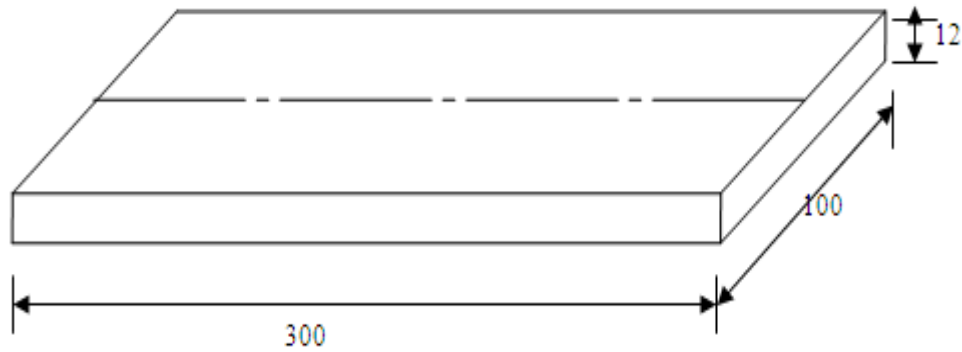


Fig 1: Base plate dimensions (mm)

Table 2: Material composition

Composition of Mild Steel plates					
Element	Carbon	Manganese	Sulphur	Phosphorus	Ferrous
Percentage	0.280	0.533	0.030	0.037	rest.

1.2 Electrode wire

The electrode wire used for the welding was Auto melt Grade - A of 3.15 mm diameter conforming to AWS SFA 5.17, EL-08. [4]

1.3 Flux

An agglomerate flux and crushed slag was used in this investigation. The specification of flux used for welding is AWS 5.17 OK FLUX 10.71 L, F7AZ - EL 8.

II. METHODOLOGY

To study the effect of cooling rate on microhardness the following steps were followed.

- Preparation of base plate
- Identifying the process parameters and their limits.
- Developing the design matrix.
- Conducting the experiments as per the design matrix.
- Measurement of temperature during experimentation.
- Calculating the cooling rate.
- Testing

2.1 Temperature Measurement

For the investigation the K-type thermocouples were used. Type K (chromel–alumel) is the most common general purpose thermocouple. It is inexpensive and available in a wide variety of probes. They are available in the $-200\text{ }^{\circ}\text{C}$ to $+1350\text{ }^{\circ}\text{C}$ range. The range of thermocouples used for experimentation from 1°C to 1200°C . Each thermocouple was connected to the digital meter for the recoding of temperature at same time interval [5]. Four blind holes (each hole was 6 mm deep) were produced to the opposite of weld surface in each plate, for the positioning of thermocouples during welding. First hole was made at the centre of bead and next holes were 1mm apart from its previous hole in perpendicular direction to the bead axis. The dimensions, positioning of holes and actual plate are illustrated in fig: 3.

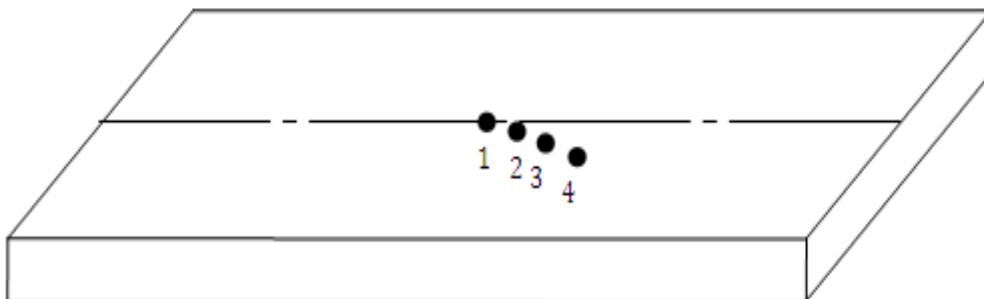


Fig: 2 Thermocouple position

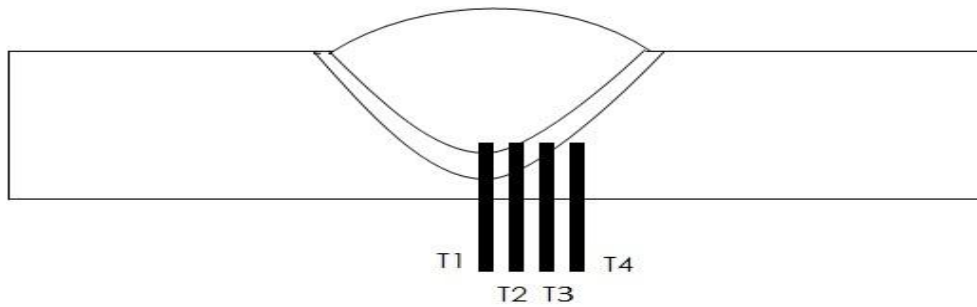


Fig: 3 Insertion of thermocouple

Each hole is 5 mm deep and having 1.5 mm diameter. The holes were drilled by the vertical pillar drilling machine in the machine shop, SLIET, Longowal. 20 plates were prepared for the experimentation.

2.2 Identify the process parameters

Extensive trial runs were carried out to find out the working range of input welding parameters for producing sound welding. By the trial runs following parameters were selected given in table 3

Table 3: Process parameters and their levels

S. No.	Parameters	Units	Symbols	Low Level (-)	High Level (+)
1	Current	Amp	A	325	650
2	Voltage	Volts	V	32	42
3	Welding Speed	mm/min	S	225	425

2.3 Preparation of Design Matrix

After the selection of welding parameters and their levels on the basis of trials the design matrix was prepared [6]. Table 4 shows the design matrix with different heat input.

Table 4: Design matrix

S. No.	Current (A)	Voltage (V)	Welding Speed (m/mm)
1	-	-	-
2	+	-	-
3	-	+	-
4	+	+	-
5	-	-	+
6	+	-	+
7	-	+	+
8	+	+	+

“+” and “-” shows the High and Low levels respectively.

Modeling of process parameters and design of experiments have been done with Design Expert software. Fractional factorial design technique was used for the experimentation. There were three factors and two levels for developing the design matrix, according to the Full Factorial design (2ⁿ) eight set of heat input are designed with different combinations of SAW welding parameters [7].

III. EXPERIMENTATION

The four thermocouples were positioned in to the holes of base plate and weld bead is deposited on the opposite surface to the surface where thermocouples are situated. According to the design matrix eight plates were welded using 3.15 mm diameter conforming to AWS A5.17- 69, EL-08 wire and with the use of fresh flux [8]. Electrode positive reverse polarity was used. A constant potential transformer-rectifier type power source with a current capacity of 1200 amperes at 60% duty cycle and 900 amperes at 100 % duty cycle, an OCV of 32 to 42 volts was used. The complete set of eight trials was repeated twice for the sake of determining the variance of parameters and variance of adequacy for the model. Fig: 4 show the welding setup, base plate and position of thermocouple.

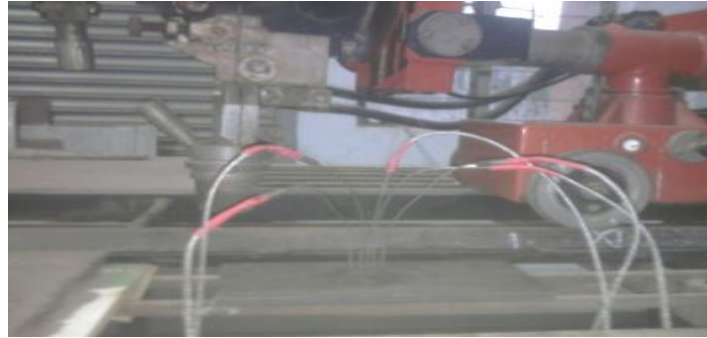


Fig: 4 welding setup, base plate and position of thermocouple

With the help of thermocouple and digital meter the temperature during cooling is recorded at four positions of thermocouple with the interval of 5 seconds. The cross-section view of weld bead with thermocouple is illustrated in figure 5. The temperature is recorded up to 7 minutes. This recorded temperature helps to draw the thermal histories.

3.1 Preparation of test specimen

After welding, transverse section of the weld beads were cut from the middle portion of the plates as specimens as shown in figure 4.6. These specimens were prepared by standard metallurgical polishing methods [9]. After applying the 1000 grade of sand paper the micro hardness was carried out in metallurgy lab, SLIET Longowal.

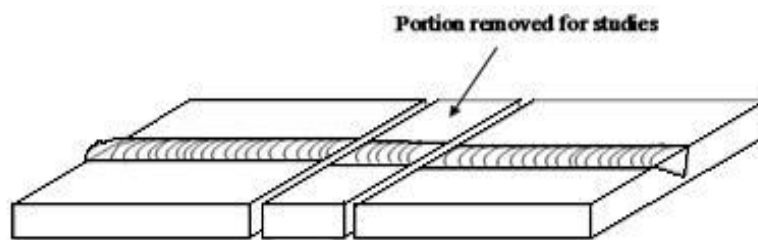


Fig: 5 Removal of specimen from the work piece

IV. RESULT AND DISCUSSION

In the present study, the effect of cooling rate on microstructure of mild steel plate has been investigated. The properties of steel welds are affected by their cooling rates in the 800⁰C to 500⁰C range where the phase transformations important for the evolution of final weld microstructure occur [10]. The effect of cooling rate is not limited to solid state transformations. Cooling rate of weldment is depends on the heat input by the welding arc to the weldment. Heat input is controlled by the three variables Current, Voltage, travel speed. With the higher heat input the cooling rate is slower and vice-versa. The effect of cooling rate on microstructure was investigated [11].

4.1 Cooling rate

Cooling rate is calculated from 800⁰C to 500⁰C, because this temperature range is useful to phase transformation. It is observed that when heat input is increased the cooling rate of weldment is reduced. Cooling rate is calculated by the following equation. Table 5 shows the calculated heat input and cooling rate. Heat input is calculated from welding parameters and cooling rate is calculated from thermal histories.

$$\text{Cooling rate} = \frac{\text{Temp range from } 800^{\circ}\text{C to } 500^{\circ}\text{C}}{\text{Time taken from } 800^{\circ}\text{C to } 500^{\circ}\text{C during cooling}}$$

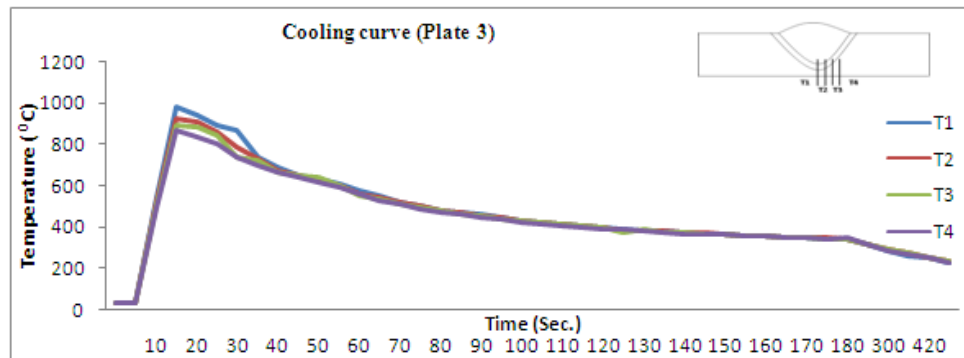
Table 5: Calculated heat input and cooling rate

plate no.	current	voltage	speed	HI in KJ/mm	CR (800-500)
1	325	32	225	2.77	8.5
2	650	32	225	5.54	3.2
3	325	42	225	3.64	6.2
4	650	42	225	7.28	2.5
5	325	32	425	1.46	12.5
6	650	32	425	2.93	8.2
7	325	42	425	1.92	9.5
8	650	42	425	3.85	5.6

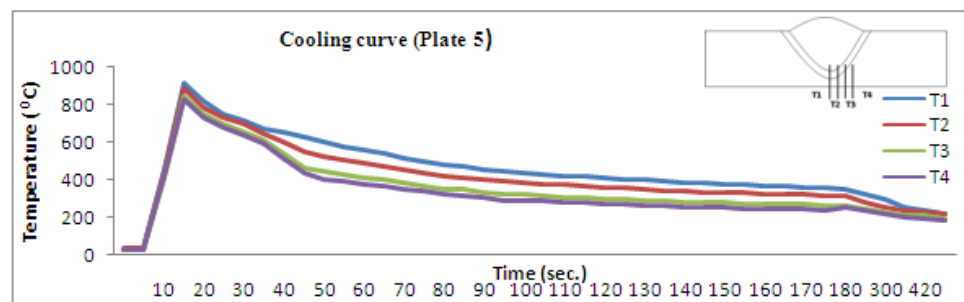
Table 5 illustrates the relation between the heat input and cooling rate of weldment. It is observed that with the increasing in heat input from 1.46 KJ/mm to 7.28 KJ/mm the cooling rate is reduced from 12.5⁰C/sec to 2.5⁰C/sec. so with the reduction in heat input the cooling rate is increased.

4.2 Temperature histories

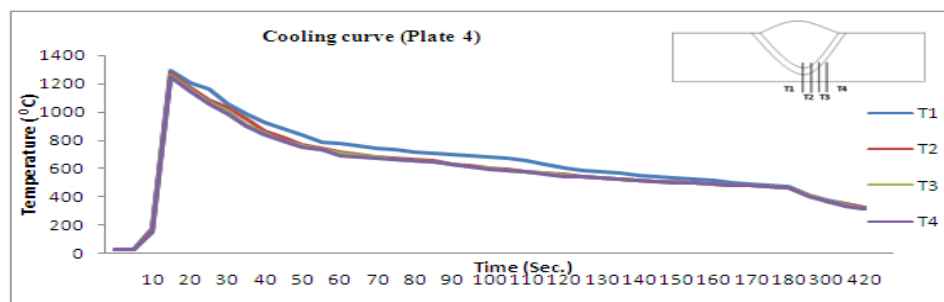
During welding, temperature is measured as a function of time, by thermocouple for different points. These readings of temperature are useful to draw temperature histories. Thermal histories play important role for finding the cooling rate of weldment for different ranges. Fig: 7 shows the temperature history of weldment [12], welded at Low medium and high cooling rates.



(a)



(b)



(c)

Fig: 6 Cooling Curve at (a) Medium (b) High and (c) Low Cooling Rate

V. MICROSTRUCTURE

According to heat input (high, Medium and low heat input) three specimen were selected (plate no. 3,5 & 4) and these specimens were properly polished and etched with 2% Nital solution for 3 seconds, which was followed by investigation of microstructure. Macrostructure is carried out at “7X” and microstructure is conducted at “100X”

Fig: 7 show the macrographs of three different weldments. It is observed from the micrograph that with the increasing heat input and decreasing cooling rate the HAZ area is increased [13].

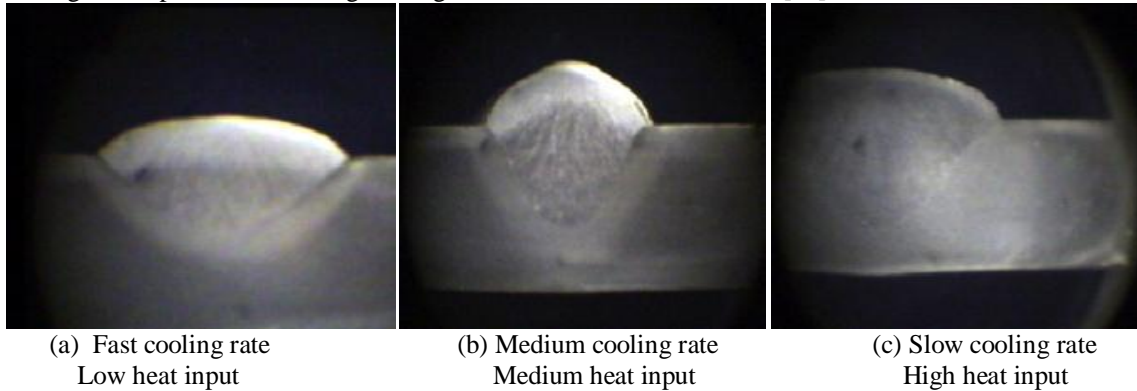
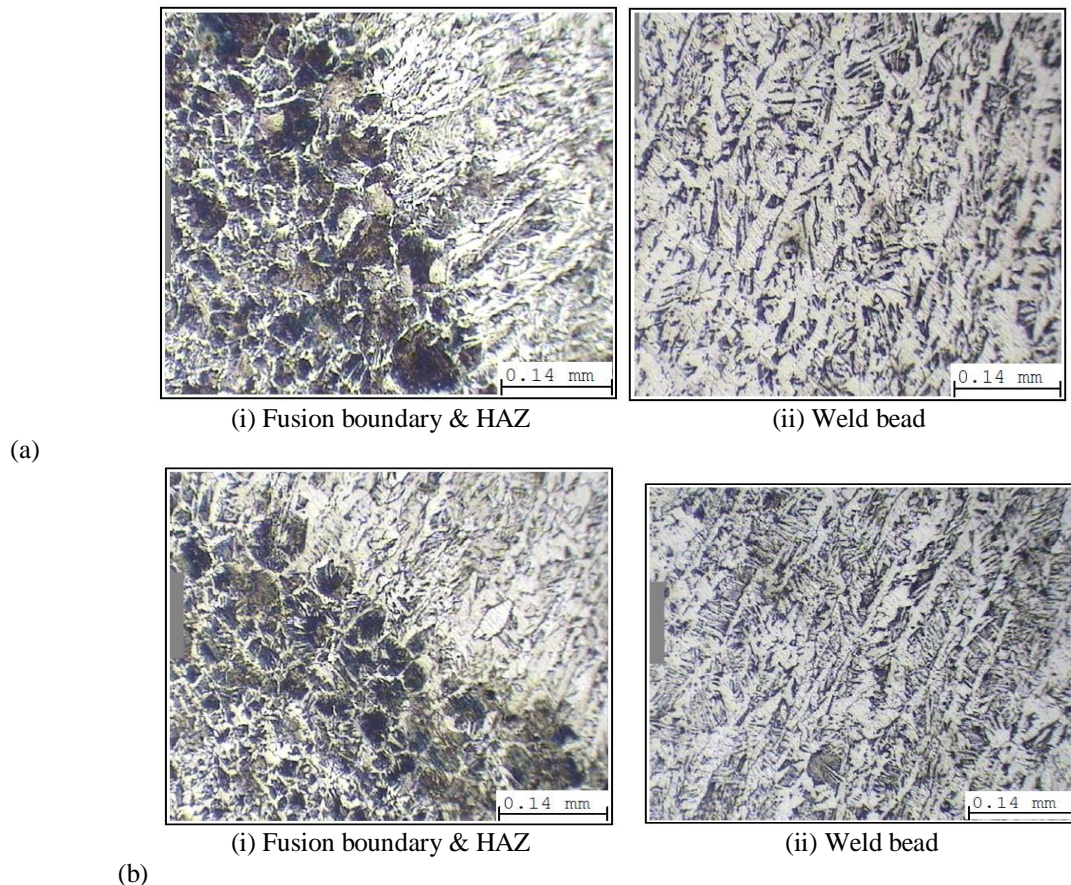
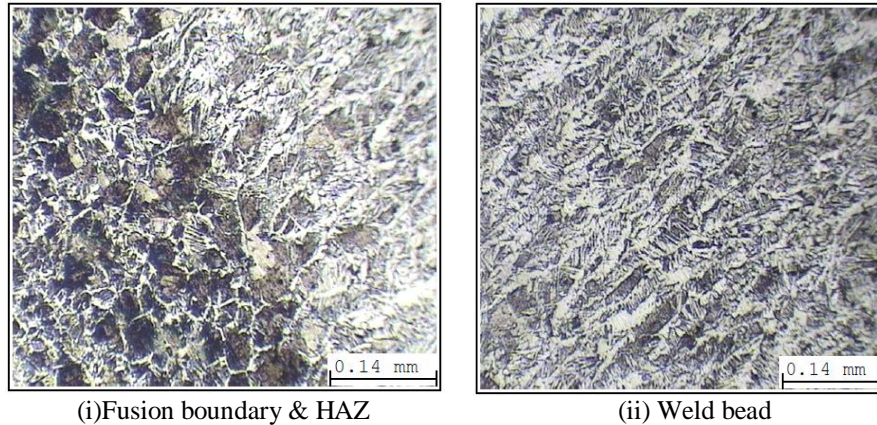


Fig: 7 Macrographs of weldment at different cooling rate and heat input at 7X magnification

Fig: 8 illustrate the micro graph of the weldment with different cooling rate (slow, medium and fast cooling rate). Fig: (i) stands for microstructure of HAZ and figure (ii) stands for the microstructure of weld bead [14]. At the slower cooling rate grains in fusion boundary zone are larger in size as compared to the weldment having Medium and fast cooling rate. By the faster cooling rate finer grains are formed and finer grain produces the higher hardness. Columnar grains are formed in weldment. The larger columnar grains are formed by slow cooling as compared to medium and fast cooling rate. It is also observed that the spacing between dendrites are more in the weldment with slower cooling rate, less spacing between dendrites results the more hardness [15].





(C)

(i) Fusion boundary & HAZ

(ii) Weld bead

Fig: 8 Optical macrographs showing microstructure of [a] Low, (b) Medium and (c) fast cooling rate (100 X magnifications)

VI. CONCLUSION

The following conclusions may obtain from the experiments:

1. The process parameters are directly affect the cooling rate, with the increase of welding Current, voltage and decreasing of welding Speed the cooling rate is decreased and with the decreasing of current, voltage and increasing of welding speed the cooling rate become fast.
2. The grains forms with higher cooling rate are much finer as compare with low cooling rate.
3. The microstructure of base metal with medium heat input is pearlitic/ferritic grain structure with banding at some areas. and in heat affected zone is course as well as very fine grains pearlitic/ferritic structure. And in Weld zone is self cooled pearlitic ferritic structure

REFERENCES

- [1] Kou Sindo. 2003. *Welding Metallurgy* 2nd Edition Published by John Wiley & Sons, Inc., Hoboken, New Jersey.
- [2] Honarbakhsh-Raouf. 2010. Investigation of wire feeding speed, welding speed and preheating temperature on hardness and microstructure of weld in RQT 701-British steel produced by FCAW, *Indian Journal of Science and Technology Vol. 3 No. 5: 0974- 6846*
- [3] Nadkarni S.V. 1988. *Modern arc welding process*, 4th Edition, Oxford & IBH publishing Co. Pvt. Ltd, New Delhi, India
- [4] Parmar R.S. 2010. *Welding process and technology*, 3rd Edition, Khanna publisher, New Delhi, India.
- [5] Attarha M.J. 2011. Study on welding temperature distribution in thin welded plates through experimental measurements and finite element simulation, *Journal of Materials Processing Technology 211: 688–694*
- [6] Douglas C. Montgomery. 2007 *Design and Analysis of Experiments* 7th Edition Published by John Willey & Sons, Inc
- [7] Granovsky Y.V. 1975. *The design of experiments to find optimal conditions*. 1st Edition, Moscow: Mir publishers
- [8] Singh Kulwant, Sahni V, Pandey S. 2009 Slag Recycling in Submerged Arc Welding and its Influence on Chemistry of Weld Metal, *Asian Journal of Chemistry* , Vol. 21, No. 10 , S047-051
- [9] Gunaraj V, Murugan N. 1999. Prediction and comparison of the area of the heat-affected zone for the bead-on-plate and bead-on-joint in submerged arc welding of pipes, *Journal of Materials Processing Technology 95: 246-261*
- [10] Renwick B.G, Patchett B.M. 1976. Operating characteristics of submerged arc process. *Welding Journal, 55:69-76*
- [11] Gery D, Long H, Maropoulos P. 2005 Effects of welding speed, energy input and heat source distribution on temperature variations in butt joint welding, *Materials Processing Technology 167:393–401*
- [12] Mahapatra M.M, Datta G.L, Pradhan B. 2006. Three-dimensional finite element analysis to predict the effect of SAW process parameters on temperature distribution and angular distortions in single-pass butt joints with top and bottom reinforcements, *pressure vessel and piping 83: 721-729*.
- [13] K. pathak, G. L. Datta. 2004. Three-dimensional finite element analysis to predict the different zones of microstructure in submerged arc welding, *Proc. Instn Mech. Engrs, Vol 218 Part B*.
- [14] Kumar S, Shahi A.S. 2011 Effect of heat input on the microstructure and mechanical properties of gas tungsten arc welded AISI 304 stainless steel joints, *Materials and Design 32: 3617–3623*.
- [15] Kolhe P.K, Datta C.K. 2008. Prediction of microstructure and mechanical properties of multipass SAW, *Journal of materials processing technology 197: 241–249*

Design of Shaft Is an Important Tool in Mercerization Machine

J. H. Mokade¹, N. P. Awate²

^{1,2}Department of Mechanical Engineering, G. H. Raisoni College of Engineering, Nagpur Maharashtra, India.

ABSTRACT: Mercerizing is one of part of wet processing technology. It is the special type of treatment. Mercerization is done to get some special properties of the textile materials. In this process, the physical properties of the material get change. The mercerization process essentially consists of treatment of cotton yarn in high concentration caustic soda under tension. If cotton is dipped into a strong alkaline solution such as lithium hydroxide, caustic soda, or potassium hydroxide, the fibers will swell and shrink. If the fibers are placed under tension while in this swollen state and then rinsed with water, the alkali will be removed and a permanent silk-like luster will result. It will be highly desirable to introduce this process in khadi sector which will lead to considerable saving in the dyeing cost. The handling of the hank is in appropriate; disarrangement of the lengths of yarn in one loop can result in different tensions, leading to uneven mercerization due to uneven tension is an unavoidable problem in this methods. This not only reduces productivity, but also results in many yarn-piecing defects during production. In this process tension can be derived by using proper shaft in mercerization machine by measuring the load required to keep the yarn or the fabric at the same length. The latter tension, being a tension intentionally exerted during mercerization, can be considered in three stages, 1) These being during the penetration of the alkaline solution and the swelling, during the fixing of the dimensions 2) Temperature during the treatment, 3) Control of the tension during the different stages is important in the supervision of the mercerizing process. In this process number of hanks are loaded on shaft and rotated for required time. Due to caustic soda treatment, the yarn get swell and length of yarn reduced upto 1/4th, due to continuous rotation of shaft, the load developed on shaft and shaft get bend. These problems may be overcome by designing of optimized shaft in mercerization machine.

Keywords: Mercerization, Mercerizing Machine, caustic soda, Shaft failure, Bending, Mechanical tension.

I. Introduction

Mercerization is the treatment of cotton with a strong caustic alkaline solution in order to improve the luster, hand and other properties, was named after its discoverer, John Mercer, and has been in use for some time. The process of mercerization was developed in 1856, since then it is important in the textile mill sector. Mercerizing is one of part of wet processing technology. It is the special type of treatment. Mercerizing is done for getting some special properties of the textile materials. In which process the physical properties of the material change. Increased dye-uptake, dimensional stability, increased moisture regain, increased reactivity etc. If cotton is dipped into a strong alkaline solution such as lithium hydroxide, caustic soda, or potassium hydroxide, the fibers will swell and shrink. If the fibers are placed under tension while in this swollen state and then rinsed with water, the alkali will be removed and a permanent silk-like structure will result. It will be highly desirable to introduce this process in Khadi sector which will lead to considerable saving in the dyeing cost. In Mercerization machine number of shaft (10-15) arranged in parallel position, these shafts are supported by another shaft which is in parallel position at lower side. The arrangements of all shafts are star arrangement. Initially the yarn is loaded on upper shaft then lower and again on another upper shaft, in this way the shaft rotates continuously for 7 to 8 minute. The hank (yarn) is loaded through the shaft; each hank has a weight around 0.7 to 1.2 kg. These hanks are dipped in caustic soda solution or alkaline sodium hydroxide solution. Due to absorption of caustic soda solution by the yarn, chemical reaction occurs and as results the length of yarn reduces which are turn develops the stress in shaft.

The stress developed in the shaft due to following reasons

1. Length reduction of the yarn
2. The weight of the yarn gradually increased
3. Twisting movement of the shaft due to rotation

During the course of time the bending of the shaft occurs and misalignment of shaft result which in turn has a great adverse effect on the production line, also the misalignment damages the machine and the yarn.

II. Purpose/Need Of Mercerizing

The main changes occurring in the alkaline treatment of cotton are:

1. Solubility in solvents is increased;
2. The length of yarn or area of cloth is reduced;
3. Tensile strength is increased;
4. Absorption of dyestuff is increased;
5. Physical compactness of either cloth or yarn is increased;
6. Water absorption is increased;
7. Reactivity with oxygen (air) is increased;
8. Reactivity of cotton at lower temperatures is increased;
9. Sodium hydroxide (caustic soda) is preferentially absorbed during the process;
10. Luster is increased;
11. Rate of oxidation causing degradation is increased;
12. Removes immature (dead) cotton;
13. Lowers dye cost (up to 40 % on certain colors).

III. Absorption Of The Alkali And Swelling

The cotton hair swells in a strong caustic soda solution, and on viewing the changes in the cross-section that occur during the mercerization process shown in figure, the cross section, originally shaped like a squashed circular pipe, clearly becomes oval-shaped, thus enhancing the luster. The large differences in the swelling that occur due to the concentration of the alkaline solution are relative to the longitudinal shrinkage of the hair.

1. Cross section before mercerization
- 2→5. Swelling process in 18% NaOH
6. Rinsing process after swelling
7. Final state

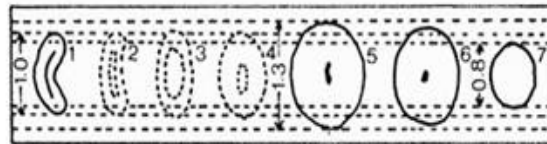


Fig no: 1 Changes in the cross-section of a cotton hair during mercerization

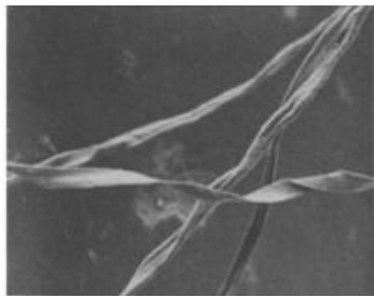


Fig no: 2 Un Mercerized cotton

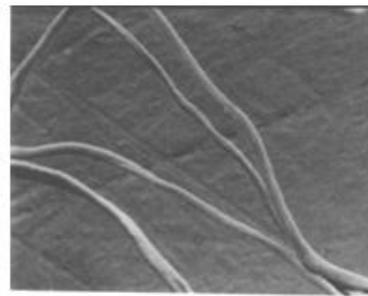


Fig no: 3 Mercerized cotton

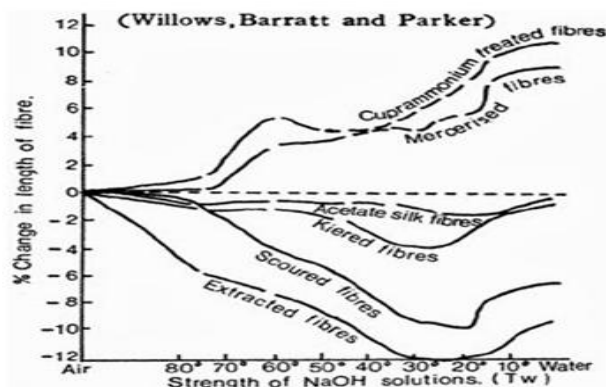


Fig: 4 Change in length of a cotton hair when dipped in decreasing concentrations of alkaline solution (NaOH)

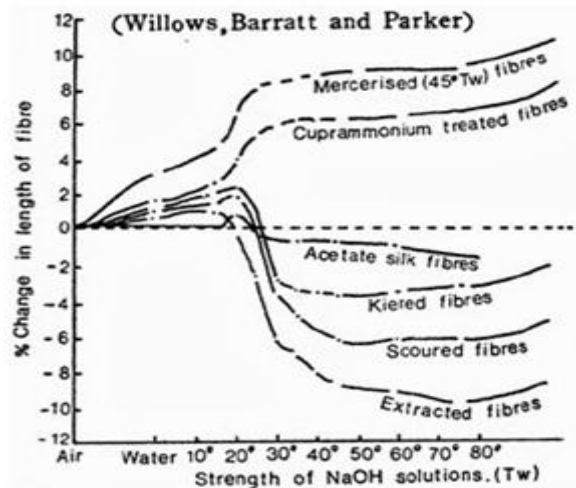


Fig no: 5 Change in length of a cotton hair when dipped in increasing concentrations of alkaline solution (NaOH)

IV. Tension After The Swelling Due To The Alkali

The tension introduced after the swelling of the yarn or the fabric is a mechanical tension exerted to resist the force of the shrinkage of the shrunk yarn or fabric and, by stretching, it fixes the dimensions as required. At this time, the problem in the processing is not the degree of tension required but the amount of stretching. For the generation of a good luster, stretching to the original length before the processing is usually the norm, but stretching beyond the original length will enhance the luster even more. However, stretching is not often beyond the original length of the yarn or the fabric due to the mechanical difficulties and the negative effects on hand and strength.

V. Problem Arises In Mercerization Machine

The winding or the handling of the hank is in appropriate; disarrangement of the lengths of yarn in one loop can result in different tensions, leading to uneven mercerization, which can often result in patchy dyeing. Uneven mercerizing due to uneven tension is an unavoidable problem in current methods of mercerization. While in theory reduction of the amount of yarn in one hank increases the evenness of the mercerization, this not only reduces productivity, but also results in many yarn-piecing defects during production of the weave or knit due to inadequate yarn length. For these reasons, using optimized shaft yarn that has been hank mercerized and then dyed for finishing into solid-color fabrics can result in a barrel effect,

Another problem in hank mercerization is that conventional rinsing after mercerization is insufficient, and without neutralization through separate rinsing with hot water, the remaining alkali can cause problems. While in theory there are no reasons preventing sufficient neutralization through removal of the alkali in this method, complete treatment of batches in hank form a low efficiency, and so not used due to the cost and the level of productivity. Thus, if treatments must be conducted separately by using proper shaft in mercerization machine, Furthermore, handling in hank form is necessary in the scouring and bleaching which follow, as well as in the dyeing, and there is a tendency for the quality of the yarn to deteriorate due to disarrangement of the yarn. Finally, after drying, winding from the hank to a cone or cheese is necessary, and the effort and labor hours needed for this are a major disadvantages. The resulting negative tension can be derived by using proper shaft in mercerization machine measuring the load required to keep the yarn or the fabric at the same length as that before processing, but because this tension cannot be adjusted during mercerization itself, if any adjustments are required, measures must be taken during the design stage of the yarn or the fabric. The latter tension, being a tension intentionally exerted during mercerization, can be considered in three stages,

- A) These being during the penetration of the alkaline solution and the swelling, during the fixing of the dimensions
- B) Temperature during the treatment,
- C) Control of the tension during the different stages is important in the supervision of the mercerizing process.

In this process the hanks are held on shaft. At a time numbers of hanks are loaded on shaft and rotated automatically for required time. Due to caustic soda treatment, the yarn shrinkages and length is reduced. Due to continuous rotation of shaft the load is developed on shaft and shaft get bend. To avoid the bending of shaft, it has important tool to carried out design and analysis of optimized shaft mercerization machine

VI. Need Of Designing Of Mercerization Machine Shaft

As shaft have several types of failure from which bending Failure is have huge impact on mercerization process. We are concentrate on bending failure for design of Mercerization machine shaft.

In the dyeing of cotton, it is well known that if caustic soda is used in vat dyes and other dyes which use caustic soda, the dye's ability to be absorbed will decline, this tendency being especially strong in weak alkaline vat dyes. Caustic soda has an affinity for cellulose fibers, and through routine dyeing experience, it is well known that the removal of caustic soda through rinsing is very difficult when compared with the removal of acid. However, within the range of concentrations of caustic soda generally used in dyeing, the properties and form of cotton does not incur any particular effects, but if the alkaline concentration is gradually increased, they will be affected. Due to the different effects on different yarns, which are a collection of single fibers, or on different knits and wovens a variety of factors have complex cumulative effects, and the basic behavior of cotton exposed to certain alkalis is difficult to ascertain accurately, but clarification has come through using cotton hairs (single cotton fibers). Subsequently, researchers have repeatedly conducted experiments which included quantitative measurements, but the results have lacked consistency. While the reasons for this may be related to experimental procedure or certain errors, essentially, factors involved in the type and the maturation process of natural macro molecules like those in cotton can result in considerable differences in the resulting properties, structure and configuration. In addition to the variations in the responses to alkalis which result from these factors, a precise experimental procedure is difficult to determine, and this can also be considered a factor contributing to the difficulties.

Design and analysis of optimized shaft in machine of mercerization is to minimize the shrinkages in the yarn, increase machining accuracy. The time and capital cost in maintenance can be reduced. The life of machine can be increase, so repair and maintenance charges are minimize. The machine will run smoothly and efficiently so bending of mercerization machine shaft can be avoided.

VII. Significance Of Work

By designing of optimized mercerization machine shaft can control of tension during mercerization. In mercerization process there are two types of tension occur, one produced by the constraining force in opposition to the swelling caused by the twisting of the yarn or the structural density of the yarn when the single fibers which constitute the yarn or the absorb alkaline solution and swell, the other being intentionally exerted on the yarn or fabric during mercerization. The former type of tension occurs due to the relationship between the force of the swelling and the constraining force in opposition to it, and although not certain, as it is due to the force of the swelling, it can be expected to design proper dimension of shaft .

The design of mercerization machine shaft will provide an apparatus for mercerizing the yarn continuously as well as uniformly in caustic soda solution in predetermined quantity under uniform tension in short period of time. This increases the productivity of machine. The fabric produced from mercerized yarn will be dimensionally stable thus reducing the customer complaints of shrinkage of Khadi fabric or garments on washing it will save more dye consumption. By further modification the machine capacity can increase.

REFERENCES

- [1] Liang Heng-chang, Zhou Guo-qing, Liao Bo, Liu Zhi-qiang, Zhou Jin-sheng, Zhao Guang-si, Shang Xiang-yu, Zhang Hou-quan, In-site monitoring and analysis of shaft lining's additional strain in failure and formation grouting, *Procedia Earth and Planetary Science*, 2009, 503–511.
- [2] A. Vaziri, H. Nayeb-Hashemi. A theoretical investigation on the vibrational characteristics and torsional dynamic response of circumferentially cracked turbo-generator shafts, *International Journal of Solids and Structures*, 2006, 4063–4081.
- [3] T. Sean Osis, J.Darren Stefanyshyn. Vibration at the wrist and elbow joints during the golf swing reveals shaft-specific swing kinematics, *Procedia Engineering*, 2010, 2637–2642.
- [4] Jiawei Xiang, YongtengZhong, Xuefeng Chen, Zhengjia He. Crack detection in a shaft by combination of wavelet-based elements and genetic algorithm, *International Journal of Solids and Structures*, 2008, 4782–4795.
- [5] G.S. Zhao, G.Q. Zho , G.R. Zhong, F.P. Zhu H.C. Liang. Analysis of stratum grouting influence on shaft lining stress with the methods of simulation and in site measurements, *Procedia Earth and Planetary Science*, 2009, 497–502.
- [6] Zhou Jie, Zhou Guo-qing , Shang Xiang-yu, Li Ting. Numerical simulation on shaft lining stresses analysis of operating mine with seasonal temperature change, *Procedia Earth and Planetary Science*, 2009, 550–555.
- [7] Wang Yan-sen, Yang Zhi-jiang , Yang Wei-hao. Viscoelastic analysis of interaction between freezing wall and outer shaft wall in freeze sinking, *Procedia Earth and Planetary Science*, 2009, 612–620.
- [8] C. Slater, S.R. Otto and M. Strangwood. The quasi-static and dynamic testing of damping in golf clubs shafts fabricated from carbon fibre composites, *Procedia Engineering*, 2010, 3361–3366.

High Performance MAC Unit for FFT Implementation

Tinju Tresa¹, M. A. Shameem², Sandeep Sreedharan³

¹(M. Tech Vlsi Design, VIT University, Vellore

²(M. Tech Vlsi Design, VIT University, Vellore

³(M. Tech Vlsi Design, VIT University, Vellore

ABSTRACT: In this paper we have proposed an efficient way of implementing a Fast Fourier Transform (FFT) processor using high performance pipelined Multiply and Accumulate (MAC) unit. The multiplication unit is implemented using Modified Radix 4 Booth Multiplier algorithm. The proposed multiplier circuits are based on the modified Booth algorithm and the pipeline technique which are the most widely used to accelerate the multiplication speed. The adder unit is implemented using an area efficient Carry Select Adder (AECSA). As a result we can achieve lower area as compared with that of a normal Carry Select Look ahead Adder (CLSA). The implementation is done using Verilog HDL code. The simulation of the over all design is carried out using NC launch. The synthesis of our design is done using RTL compiler in Cadence. Analysis of the synthesis report shows the design to be of high performance and to be area optimised.

Keywords: Area Efficient CSA, DFT, DIF algorithm, 8point FF, MAC unit, Modified Radix 4 Booth's multiplier, RCA, BEC, ECA.

I. Introduction

The digital signal processing (DSP) is one of the core technologies in multimedia and communication systems. Many application systems based on DSP, especially the recent next generation optical communication systems, require extremely fast processing of a huge amount of digital data. Most of DSP applications such as fast Fourier transform (FFT) require additions and multiplications. Since the multipliers have a significant impact on the performance of the entire system, many high-performance algorithms and architectures have been proposed to accelerate multiplication [4]. The MAC unit determines the speed of the overall system; it always lies in the critical path. Developing high speed MAC is crucial for real time DSP application. Moreover, with the ever-increasing demand for portable electronic products, an electronic component with low power consumption would surely lead the market trend. Therefore, it is needed to design a low-power MAC unit. Many researchers have attempted in designing MAC architecture with high computational performance and low power consumption. In order to improve the speed of the MAC unit, there are two major bottlenecks that need to be considered. The first one is the partial products reduction network that is used in the multiplication block and the second one is the accumulator. Both of these stages require addition of large operands that involve long paths for carry propagation [3]. Various multiplication algorithms such as Booth [5], modified Booth, Braun, Baugh-Wooley have been proposed. The modified Booth algorithm reduces the number of partial products to be generated and is known as the fastest multiplication algorithm. Many researches on the multiplier architectures including array, parallel and pipelined multipliers have been pursued and the pipelining is the most widely used technique to reduce the propagation delays of digital circuits [4]. Much different architecture were proposed for MAC implementation. Li Hsun proposed a low-power Multiplication-Accumulation Computation (MAC) unit using the radix-4 Booth algorithm, by reducing its architectural complexity and minimizing the switching activities [6]. Elgibaly proposed a fast pipelined implementation to lower the MAC architecture's critical delay [7]. Fayed et al. proposed new data merging architecture for high speed multiply accumulate units [8,9] The architecture can be applied on binary trees constructed using 4:2 compressor circuits. Increasing the speed of operation is achieved by taking advantage of the available free input lines of the compressor circuits, which result from the natural parallelogram shape of the generated partial products and using the bits of the accumulated value to fill in these gaps. This results in merging the accumulation operation within the multiplication process. In this paper, we introduce a high speed and area-efficient merged Multiply Accumulate (MAC) Units. The N point sequence FFT is represented using following equation [1]

$$X(k) = \sum_{n=0}^{N-1} x[n]W_N^{nk}; \quad 0 \leq k \leq N-1 \tag{1}$$

The two different Radix 2 algorithms are Decimation in Time DIT and Decimation in Frequency DIF algorithms. In both these algorithms N inputs are divided into two N/2 sequences. In this paper we make use of DIF algorithm because of its improved accuracy and better immunity to noise. For DIF algorithm the output point's frequency is subdivided. The output obtained by this method will be in bit reversed order [1].

Radix-4 Modified Booth algorithm [2] is an efficient algorithm that multiplies two signed numbers using 2's compliment form. The number of partial products is reduced by half for this algorithm. The main bottle-neck of speed is in the addition of partial products. The critical path for the multiplier is on the number of partial products. The partial products generated are added using an area efficient carry select adder [3]. The basic idea of this work is to use Binary to Excess-1 Converter (BEC) instead of RCA with Cin =1 in the regular CSLA to achieve lower area and power consumption [10]–[12]. The main advantage of this BEC logic comes from the lesser number of logic gates than the n-bit Full Adder (FA) structure.

II. Methodology

The most basic computational block involved in the FFT module is a butterfly diagram. The entire process involves $\log_2 N$ stages of decimation, where each stage involves N/2 butterflies of the type shown in the Fig1. below

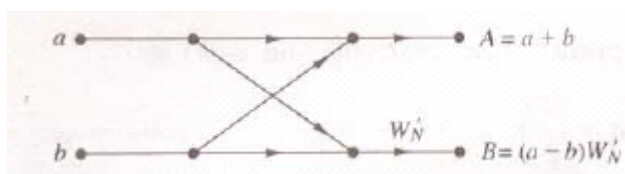


Fig1. Butterfly Diagram

The Fig2. below shows a radix-2 8-point DIF algorithm. The inputs are given by x[n] and the outputs are given as X[n]. The outputs of DIF will be in bit reversed order. It includes three stages.

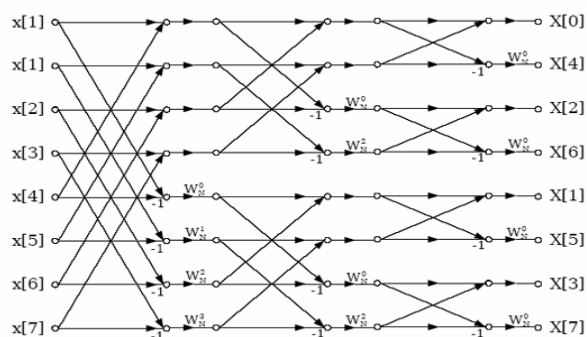


Fig2. Radix-2 8-point DIF algorithm

In the above figure, $W_N = e^{-j2\pi/N}$, is the Twiddle factor. Multiplication is done in two steps, generation of partial products and addition of partial products.

Modified Radix 4 Booth Multiplier Algorithm

Multiplication consists of three steps: 1) the first step to generate the partial products; 2) the second step to add the generated partial products until the last two rows are remained; 3) the third step to compute the final multiplication results by adding the last two rows. The modified Booth algorithm reduces the number of partial products by half in the first step. We used the modified Booth encoding (MBE) scheme proposed in [2]. It is known as the most efficient Booth encoding and decoding scheme. To multiply X by Y using the modified Booth algorithm starts from grouping Y by three bits and encoding into one of $\{-2, -1, 0, 1, 2\}$ Table I shows the rules to generate the encoded signals by MBE scheme. The partial products generated by the modified Booth algorithm are added in parallel using the Wallace tree [1] until the last two rows are remained. The final multiplication results are generated by adding the last two rows.

X_{i+1}	X_i	X_{i-1}	Operation
0	0	0	$0 \times Y$
0	0	1	$1 \times Y$
0	1	0	$1 \times Y$
0	1	1	$2 \times Y$
1	0	0	$-2 \times Y$
1	0	1	$-1 \times Y$
1	1	0	$-1 \times Y$
1	1	1	$0 \times Y$

Table1. Modified

Booth Encoding

Table

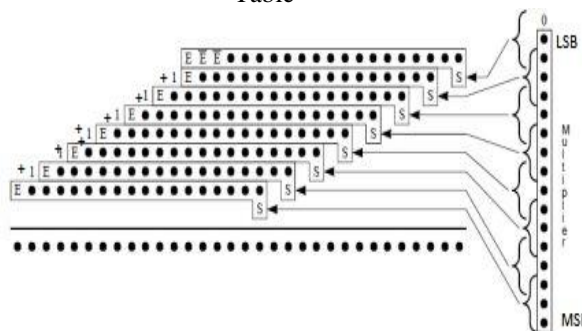


Fig3. Generated Partial Product Scheme

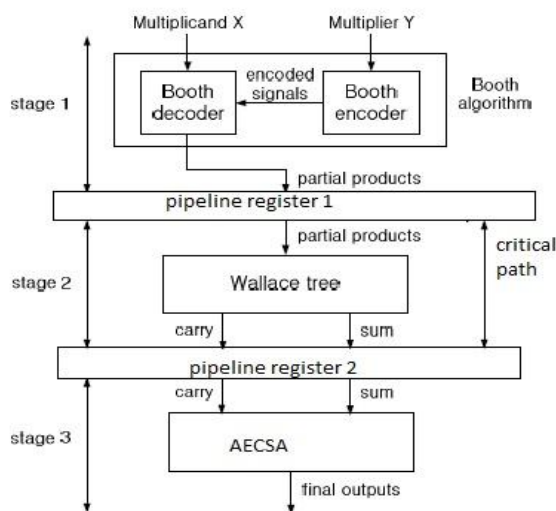


Fig4. Architecture of Modified Booth Multiplier

Fig. 4 shows the architecture of the commonly used modified Booth multiplier. The inputs of the multiplier are multiplicand X and multiplier Y. The Booth encoder encodes input Y and derives the encoded signals and the Booth decoder generates the partial products using the encoded signals and the other input X. The Wallace tree computes the last two rows by adding the generated partial products. The last two rows are added to generate the final multiplication results using an area efficient carry select adder (AECSA).

Area Efficient Carry Select Adder (AECSA)

Carry Select Adder (CSLA) is one of the fastest adders used in many data-processing processors to perform fast arithmetic functions. AECSA is an efficient gate-level modification to significantly reduce the area and power of the CSLA. The delay obtained by this technique will be slightly higher than that of conventional CSLA due to the use of excess one converter since the excess one value will only be calculated after the first sum is generated.

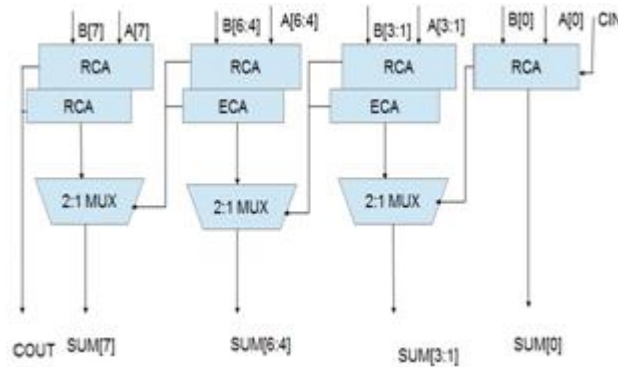


Fig5. AECSA

III. Results and Discussions

MAC unit plays a major role in today’s applications. The major aim of MAC unit is to provide high performance and also to reduce the area overhead in the design. The results show that the design provides a high speed along with reduction in area.

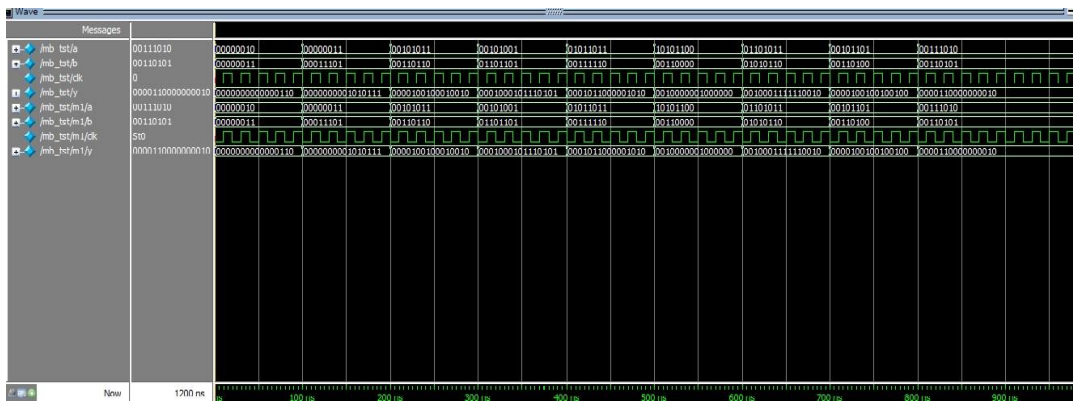


Fig6. Waveform of mac unit

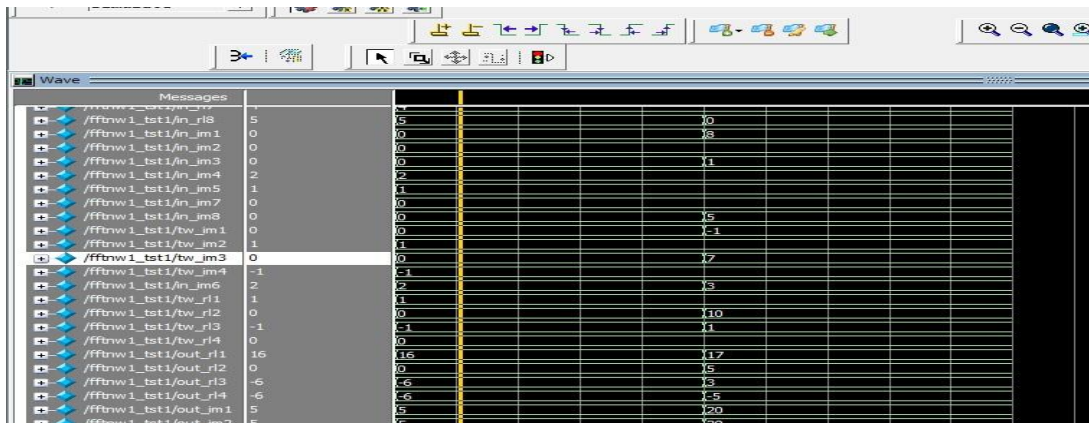


Fig7. Waveform of fft

The synthesis of the design is done using RTL Compiler tool from Cadence. The synthesis is carried out for 45nm technology and the reports show that the design is area and speed optimized. The comparison of area and delay for the different adder architectures are given in the table below

Adder	Delay	Area (μm^2)
CSLA[3]	1.719	991
AECSA	1.879	884

Table2. Comparison of AECSA with CSLA

IV. Conclusion

The proposed paper implements a high performance FFT processor that is both area as well as speed optimized. The area can be effectively reduced by the use of an area efficient CSA [AECSA] only with a slight reduction in speed. This adder unit uses BEC in place of RCA as compared to a normal carry select look ahead adder. The BEC unit consists of lesser number of logic gates and as a result reduces the area of the design.

REFERENCES

- [1] D. G Manolakis and J .G Proakis , Digital Signal Processing , Principles, Algorithms, and applications, Prentice Hall (India) Publications, 3 rd Edition -1998.
- [2] M Ozaki, Y. Adachi, Y. Iwahori, and N. Ishii, Application of fuzzy theory to writer recognition of Chinese characters, International Journal of Modelling and Simulation, 18(2), 1998, 112-116.
- [3] B. Ramkumar and Harish M Kittur, Low-Power and Area-Efficient Carry Select Adder, IEEE Transactions On Very Large Scale Integration (VLSI) Systems, Vol. 20, No. 2, February 2012.
- [4] Soojin Kim and Kyeongsoon Cho , Design of High-speed Modified Booth Multipliers Operating at GHz Ranges, World Academy of Science, Engineering and Technology 37, 2010.
- [5] A. Abdelgawad, Magdy Bayoumi, High Speed and Area-Efficient Multiply Accumulate (MAC) Unit for Digital Signal Processing Applications, IEEE 2007.
- [6] F. Elguibaly, A fast parallel multiplier-accumulator using the modified Booth algorithm, IEEE Trans. Circuits and Systems II: Analog and Digital Signal Processing, vol. 47, pp. 902-098, Sept.2000.
- [7] H. Murakami, et al. A multiplier-accumulator macro for a 45 MIPS embedded RISC processor, IEEE J. Solid-State Circuits, vol. 31, pp.1067-1071, July 1996.
- [8] Ayman Fayed, Walid Elgharbawy, and Magdy Bayoumi, A merged multiply accumulate for high-speed signal processing application, ICASSP IEEE 2004.
- [9] Ayman Fayed , Walid Elgharbawy, and Magdy Bayoumi, A data merging technique for high speed low- power multiply accumulate units, IEEE 2002.
- [10] B. Ramkumar, H.M. Kittur, and P. M. Kannan, ASIC implementation of modified faster carry save adder, Eur. J. Sci. Res., vol. 42, no. 1, pp.53–58, 2010.
- [11] T. Y. Ceiang and M. J. Hsiao, Carry-select adder using single ripple carry adder, Electron. Lett., vol. 34, no. 22, pp. 2101–2103, Oct. 1998.
- [12] Y. Kim and L.-S. Kim, 64-bit carry-select adder with reduced area,Electron. Lett., vol. 37, no. 10, pp. 614–615, May 2001.

Establishing Relations among Various Measures by Using Well Known Inequalities

K. C. Jain¹, Praphull Chhabra²

^{1,2}Department of Mathematics, Malaviya National Institute of Technology Jaipur- 302017 (Rajasthan), INDIA

ABSTRACT: In this paper, we are establishing many interesting and important relations among several divergence measures by using known inequalities. Actually this work is application of well known inequalities in information theory. Except various relations, we tried to get bounds of $N_k^*(P, Q), J_k^*(P, Q), \Delta_k(P, Q), E_k^*(P, Q), S^*(P, Q), L(P, Q), \psi M(P, Q), R_2(P, Q)$ in terms of standard divergence measures. Some relations in terms of Arithmetic Mean $A(P, Q)$, Geometric Mean $G^*(P, Q)$, Harmonic Mean $H(P, Q)$, Heronian Mean $N(P, Q)$, Contra Harmonic Mean $C(P, Q)$, Root Mean Square $S(P, Q)$ and Centroidal Mean $R(P, Q)$, are also obtained.

Mathematics Subject Classification 2000: 62B- 10, 94A17, 26D15

Keywords: Standard Inequalities, Divergence Measures, Convex and Normalized function, Csiszar's Generalized f- Divergence Measure, Seven Standard Means.

I. Introduction

Let $\Gamma_n = \left\{ P = (p_1, p_2, p_3, \dots, p_n) : p_i > 0, \sum_{i=1}^n p_i = 1 \right\}, n \geq 2$ be the set of all complete finite discrete probability distributions. If we take $p_i \geq 0$ for some $i = 1, 2, 3, \dots, n$, then we have to suppose that $0f(0) = 0f\left(\frac{0}{0}\right) = 0$. **Csiszar's f- divergence [1]** is a generalized information divergence measure, which is given by:

$$C_f(P, Q) = \sum_{i=1}^n q_i f\left(\frac{p_i}{q_i}\right) \tag{1}$$

Where $f: (0, \infty) \rightarrow \mathbb{R}$ (set of real no.) is a convex function and $P, Q \in \Gamma_n$. Many known divergences can be obtained from these generalized measures by suitably defining the convex function f .

By (1), we obtain the following divergence measures:

Following measures are due to **(Jain and Srivastava [7])**.

$$E_k^*(P, Q) = \sum_{i=1}^n \frac{(p_i - q_i)^{k+1}}{(p_i q_i)^{\frac{k}{2}}}, k = 1, 3, 5, 7, \dots \tag{2}$$

$$J_k^*(P, Q) = \sum_{i=1}^n \frac{(p_i - q_i)^{k+1}}{(p_i q_i)^{\frac{k}{2}}} \exp\left\{ \frac{(p_i - q_i)^2}{p_i q_i} \right\}, k = 1, 3, 5, 7, \dots \tag{3}$$

Following measures are due to **Kumar P. and others**.

$$S^*(P, Q) = \sum_{i=1}^n \frac{(p_i + q_i)(p_i - q_i)^2}{p_i q_i} \log\left(\frac{p_i + q_i}{2\sqrt{p_i q_i}} \right) \text{ (Kumar P. and Chhina [9])} \tag{4}$$

$$\psi M(P, Q) = \sum_{i=1}^n \frac{(p_i^2 - q_i^2)^2}{2(p_i q_i)^{\frac{3}{2}}} \quad \text{(Kumar P. and Johnson [11])} \quad (5)$$

$$L(P, Q) = \sum_{i=1}^n \frac{(p_i - q_i)^2}{p_i + q_i} \log \left(\frac{p_i + q_i}{2\sqrt{p_i q_i}} \right) \quad \text{(Kumar P. and Hunter [10])} \quad (6)$$

Renyi's second order entropy (Renyi A [12]).

$$R_2(P, Q) = \sum_{i=1}^n \frac{p_i^2}{q_i} \quad (7)$$

Puri and Vineze Divergence Measures (Kafka, Osterreich and Vincze [8]).

$$\Delta_k(P, Q) = \sum_{i=1}^n \frac{|p_i - q_i|^{k+1}}{(p_i + q_i)^k}, \quad k \in (0, \infty) \quad (8)$$

Relative Jensen- Shannon divergence (Sibson [13]).

$$F(P, Q) = \sum_{i=1}^n p_i \log \left(\frac{2 p_i}{p_i + q_i} \right) \quad (9)$$

Relative Arithmetic- Geometric Divergence (Taneja [14]).

$$G(P, Q) = \sum_{i=1}^n \left(\frac{p_i + q_i}{2} \right) \log \left(\frac{p_i + q_i}{2 p_i} \right) \quad (10)$$

Arithmetic- Geometric Mean divergence Measure (Taneja [14]).

$$T(P, Q) = \frac{1}{2} [G(P, Q) + G(Q, P)] = \sum_{i=1}^n \frac{p_i + q_i}{2} \log \left(\frac{p_i + q_i}{2\sqrt{p_i q_i}} \right) \quad (11)$$

Where $G(P, Q)$ is given by (10).

Symmetric Chi- square Divergence (Dragomir, Sunde and Buse [4]).

$$\Psi(P, Q) = \sum_{i=1}^n \frac{(p_i - q_i)^2 (p_i + q_i)}{p_i q_i} \quad (12)$$

Relative J- Divergence (Dragomir, Gluscevic and Pearce [3]).

$$J_R(P, Q) = 2[F(Q, P) + G(Q, P)] = \sum_{i=1}^n (p_i - q_i) \log \left(\frac{p_i + q_i}{2q_i} \right) \quad (13)$$

Where $F(P, Q)$ and $G(P, Q)$ are given by (9) and (10) respectively.

Hellinger Discrimination (Hellinger [5]).

$$h(P, Q) = \frac{1}{2} \sum_{i=1}^n (\sqrt{p_i} - \sqrt{q_i})^2 \quad (14)$$

Triangular Discrimination (Dacunha- Castelle [2]).

$$\Delta(P, Q) = \sum_{i=1}^n \frac{(p_i - q_i)^2}{p_i + q_i} \quad (15)$$

Except above, we obtain the following divergence measures (Due to Jain and Saraswat [6]).

$$N_k^*(P, Q) = \sum_{i=1}^n \frac{(p_i - q_i)^{2k}}{(p_i + q_i)^{2k-1}} \exp \left\{ \frac{(p_i - q_i)^2}{(p_i + q_i)^2} \right\}, \quad k = 1, 2, 3, \dots \quad (16)$$

II. Well Known Inequalities

The following inequalities are famous in literature of pure and applied mathematics, which are important tools to prove many interesting and important results in information theory.

$$1+t \leq e^t \leq 1+t e^t, \quad t > 0 \tag{17}$$

$$\frac{t}{1+t} \leq \log(1+t) \leq t, \quad t > 0 \tag{18}$$

III. Relations Among Various Divergence Measures

Now, we shall obtain bounds of some measures in terms of other divergence measures and many important and interesting relations among several divergence measures by using inequalities (17) and (18) respectively.

Proposition 1: Let $(P, Q) \in \Gamma_n \times \Gamma_n$, then we have the inequalities:

$$N_k^*(P, Q) - N_{k+1}^*(P, Q) \leq \Delta_{2k-1}(P, Q) \tag{19}$$

And $\Delta_{2k+1}(P, Q) \leq N_{k+1}^*(P, Q)$ (20)

Where $k = 1, 2, 3, \dots$, and $N_k^*(P, Q)$, $\Delta_k(P, Q)$ are given by (16) and (8) respectively.

Proof: Put $t = \frac{(p_i - q_i)^2}{(p_i + q_i)^2}$ in inequalities (17), we get

$$1 + \frac{(p_i - q_i)^2}{(p_i + q_i)^2} \leq \exp \frac{(p_i - q_i)^2}{(p_i + q_i)^2} \leq 1 + \frac{(p_i - q_i)^2}{(p_i + q_i)^2} \exp \frac{(p_i - q_i)^2}{(p_i + q_i)^2},$$

now multiply the above expression by $\frac{(p_i - q_i)^{2k}}{(p_i + q_i)^{2k-1}}$, $k = 1, 2, 3, \dots$ and sum over all $i=1, 2, 3, \dots, n$, we get

$$\begin{aligned} \sum_{i=1}^n \frac{(p_i - q_i)^{2k}}{(p_i + q_i)^{2k-1}} + \sum_{i=1}^n \frac{(p_i - q_i)^{2k+2}}{(p_i + q_i)^{2k+1}} &\leq \sum_{i=1}^n \frac{(p_i - q_i)^{2k}}{(p_i + q_i)^{2k-1}} \exp \left\{ \frac{(p_i - q_i)^2}{(p_i + q_i)^2} \right\} \\ &\leq \sum_{i=1}^n \frac{(p_i - q_i)^{2k}}{(p_i + q_i)^{2k-1}} + \sum_{i=1}^n \frac{(p_i - q_i)^{2k+2}}{(p_i + q_i)^{2k+1}} \exp \left\{ \frac{(p_i - q_i)^2}{(p_i + q_i)^2} \right\} \end{aligned}$$

i. e. $\Delta_{2k-1}(P, Q) + \Delta_{2k+1}(P, Q) \leq N_k^*(P, Q) \leq \Delta_{2k-1}(P, Q) + N_{k+1}^*(P, Q)$ (21)

From second and third part of (21), we get inequality (19) and from first and third part, we get (20).

Now at $k=1, 2, 3 \dots$ we get the followings [from inequalities (19) and (20)]:

At $k=1$ $\Rightarrow N_1^*(P, Q) - N_2^*(P, Q) \leq \Delta_1(P, Q)$ and $\{\because \Delta_1(P, Q) = \Delta(P, Q)\}$ (22)

$$\Delta_3(P, Q) \leq N_2^*(P, Q)$$

At $k=2$ $\Rightarrow N_2^*(P, Q) - N_3^*(P, Q) \leq \Delta_3(P, Q)$ and

$$\Delta_5(P, Q) \leq N_3^*(P, Q)$$

At $k=3$ $\Rightarrow N_3^*(P, Q) - N_4^*(P, Q) \leq \Delta_5(P, Q)$ and

$$\Delta_7(P, Q) \leq N_4^*(P, Q) \text{ and so on...}$$

Proposition 2: Let $(P, Q) \in \Gamma_n \times \Gamma_n$, then we have the inequalities:

$$J_k^*(P, Q) - J_{k+2}^*(P, Q) \leq E_k^*(P, Q) \tag{23}$$

And $E_{k+2}^*(P, Q) \leq J_{k+2}^*(P, Q)$ (24)

Where $k = 1, 3, 5, \dots$, and $E_k^*(P, Q)$, $J_k^*(P, Q)$ are given by (2) and (3) respectively.

Proof: Put $t = \frac{(p_i - q_i)^2}{p_i q_i}$ in inequalities (17), we get

$$1 + \frac{(p_i - q_i)^2}{(p_i q_i)} \leq \exp \frac{(p_i - q_i)^2}{(p_i q_i)} \leq 1 + \frac{(p_i - q_i)^2}{(p_i q_i)} \exp \frac{(p_i - q_i)^2}{(p_i q_i)},$$

Now multiply the above expression by $\frac{(p_i - q_i)^{k+1}}{(p_i q_i)^{k/2}}$, $k = 1, 3, 5, \dots$ and sum over all $i=1, 2, 3, \dots, n$, we get

$$\begin{aligned} \sum_{i=1}^n \frac{(p_i - q_i)^{k+1}}{(p_i q_i)^{k/2}} + \sum_{i=1}^n \frac{(p_i - q_i)^{k+3}}{(p_i q_i)^{\frac{k}{2}+1}} &\leq \sum_{i=1}^n \frac{(p_i - q_i)^{k+1}}{(p_i q_i)^{k/2}} \exp \left\{ \frac{(p_i - q_i)^2}{(p_i q_i)} \right\} \\ &\leq \sum_{i=1}^n \frac{(p_i - q_i)^{k+1}}{(p_i q_i)^{k/2}} + \sum_{i=1}^n \frac{(p_i - q_i)^{k+3}}{(p_i q_i)^{\frac{k}{2}+1}} \exp \left\{ \frac{(p_i - q_i)^2}{(p_i q_i)} \right\} \end{aligned}$$

i. e. $E_k^*(P, Q) + E_{k+2}^*(P, Q) \leq J_k^*(P, Q) \leq E_k^*(P, Q) + J_{k+2}^*(P, Q)$ (25)

From second and third part of (25), we get inequality (23) and from first and third part, we get (24).

Now at $k=1, 3, 5 \dots$ we get the followings [from inequalities (23) and (24)]:

At $k=1 \Rightarrow J_1^*(P, Q) - J_3^*(P, Q) \leq E_1^*(P, Q)$ and

$$E_3^*(P, Q) \leq J_3^*(P, Q)$$

At $k=3 \Rightarrow J_3^*(P, Q) - J_5^*(P, Q) \leq E_3^*(P, Q)$ and

$$E_5^*(P, Q) \leq J_5^*(P, Q) \text{ and so on...}$$

Except these, from first and second part of the inequalities (25), we can easily see that

$$E_1^*(P, Q) \leq J_1^*(P, Q) \tag{26}$$

Proposition 3: Let $(P, Q) \in \Gamma_n \times \Gamma_n$, then we have the inequalities:

$$\psi(P, Q) - 2E_1^*(P, Q) \leq S^*(P, Q) \tag{27}$$

And $S^*(P, Q) + \psi(P, Q) \leq \psi M(P, Q)$ (28)

Where $\psi(P, Q)$, $E_1^*(P, Q)$, $S^*(P, Q)$ and $\psi M(P, Q)$ are given by (12), (2), (4) and (5) respectively.

Proof: Put $t = \frac{(\sqrt{p_i} - \sqrt{q_i})^2}{2\sqrt{p_i q_i}}$ in inequalities (18), we get

$$\frac{\frac{(\sqrt{p_i} - \sqrt{q_i})^2}{2\sqrt{p_i q_i}}}{1 + \frac{(\sqrt{p_i} - \sqrt{q_i})^2}{2\sqrt{p_i q_i}}} \leq \log \left(1 + \frac{(\sqrt{p_i} - \sqrt{q_i})^2}{2\sqrt{p_i q_i}} \right) \leq \frac{(\sqrt{p_i} - \sqrt{q_i})^2}{2\sqrt{p_i q_i}}$$

i. e. $\frac{p_i + q_i - 2\sqrt{p_i q_i}}{p_i + q_i} \leq \log \left(\frac{p_i + q_i}{2\sqrt{p_i q_i}} \right) \leq \frac{p_i + q_i - 2\sqrt{p_i q_i}}{2\sqrt{p_i q_i}}$

Now multiply the above expression by $\frac{(p_i + q_i)(p_i - q_i)^2}{p_i q_i}$ and sum over all $i=1, 2, 3 \dots n$, we get

$$\sum_{i=1}^n \frac{(p_i + q_i)(p_i - q_i)^2}{p_i q_i} \frac{p_i + q_i - 2\sqrt{p_i q_i}}{p_i + q_i} \leq \sum_{i=1}^n \frac{(p_i + q_i)(p_i - q_i)^2}{p_i q_i} \log \left(\frac{p_i + q_i}{2\sqrt{p_i q_i}} \right)$$

$$\leq \sum_{i=1}^n \frac{(p_i + q_i)(p_i - q_i)^2}{p_i q_i} \frac{p_i + q_i - 2\sqrt{p_i q_i}}{2\sqrt{p_i q_i}}$$

i.e.

$$\sum_{i=1}^n \frac{(p_i - q_i)^2 (p_i + q_i)}{p_i q_i} - 2 \sum_{i=1}^n \frac{(p_i - q_i)^2}{\sqrt{p_i q_i}} \leq S^*(P, Q) \leq \sum_{i=1}^n \frac{(p_i^2 - q_i^2)^2}{2(p_i q_i)^{\frac{3}{2}}} - \sum_{i=1}^n \frac{(p_i - q_i)^2 (p_i + q_i)}{p_i q_i}$$

i. e. $\psi(P, Q) - 2E_1^*(P, Q) \leq S^*(P, Q) \leq \psi M(P, Q) - \psi(P, Q)$ (29)

From first and second part of (29), we get inequality (27) and from second and third part, we get (28).
Except these, if we add (27) and (28), we get the following

$$2\psi(P, Q) \leq \psi M(P, Q) + 2E_1^*(P, Q) \tag{30}$$

From second and third part of the inequalities (29), we can easily see that

$$S^*(P, Q) \leq \psi M(P, Q) \tag{31}$$

By taking both (27) and (31), we can write

$$\psi(P, Q) - 2E_1^*(P, Q) \leq S^*(P, Q) \leq \psi M(P, Q) \tag{32}$$

Proposition 4: Let $(P, Q) \in \Gamma_n \times \Gamma_n$, then we have the inequalities:

$$L(P, Q) + \Delta(P, Q) \leq \frac{1}{2} E_1^*(P, Q) \tag{33}$$

And $\Delta(P, Q) \leq L(P, Q) + 2 \sum_{i=1}^n \frac{\sqrt{p_i q_i} (p_i - q_i)^2}{(p_i + q_i)^2}$ (34)

Where $L(P, Q)$, $E_1^*(P, Q)$, $\Delta(P, Q)$ are given by (6), (2) and (15) respectively.

Proof: Put $t = \frac{(\sqrt{p_i} - \sqrt{q_i})^2}{2\sqrt{p_i q_i}}$ in inequalities (18), we get

$$\frac{p_i + q_i - 2\sqrt{p_i q_i}}{p_i + q_i} \leq \log \left(\frac{p_i + q_i}{2\sqrt{p_i q_i}} \right) \leq \frac{p_i + q_i - 2\sqrt{p_i q_i}}{2\sqrt{p_i q_i}}$$

Now multiply the above expression by $\frac{(p_i - q_i)^2}{p_i + q_i}$ and sum over all $i=1, 2, 3 \dots n$, we get

$$\sum_{i=1}^n \frac{(p_i - q_i)^2}{p_i + q_i} \frac{p_i + q_i - 2\sqrt{p_i q_i}}{p_i + q_i} \leq \sum_{i=1}^n \frac{(p_i - q_i)^2}{p_i + q_i} \log \left(\frac{p_i + q_i}{2\sqrt{p_i q_i}} \right) \leq \sum_{i=1}^n \frac{(p_i - q_i)^2}{p_i + q_i} \frac{p_i + q_i - 2\sqrt{p_i q_i}}{2\sqrt{p_i q_i}}$$

i. e. $\sum_{i=1}^n \frac{(p_i - q_i)^2}{p_i + q_i} - 2 \sum_{i=1}^n \frac{\sqrt{p_i q_i} (p_i - q_i)^2}{(p_i + q_i)^2} \leq L(P, Q) \leq \frac{1}{2} \sum_{i=1}^n \frac{(p_i - q_i)^2}{\sqrt{p_i q_i}} - \sum_{i=1}^n \frac{(p_i - q_i)^2}{p_i + q_i}$

i. e. $\Delta(P, Q) - 2 \sum_{i=1}^n \frac{\sqrt{p_i q_i} (p_i - q_i)^2}{(p_i + q_i)^2} \leq L(P, Q) \leq \frac{1}{2} E_1^*(P, Q) - \Delta(P, Q)$ (35)

From second and third part of (35), we get inequality (33) and from first and second part, we get (34).
 From inequality (33), we can easily see that

$$\Delta(P, Q) \leq \frac{1}{2} E_1^*(P, Q) \tag{36}$$

Proposition 5: Let $(P, Q) \in \Gamma_n \times \Gamma_n$ and $\sum_{i=1}^n p_i = \sum_{i=1}^n q_i = 1$, then we have the inequalities:

$$A(P, Q) \leq h(P, Q) \leq T(P, Q) \tag{37}$$

$$A(P, Q) + h(P, Q) \leq \frac{1}{4} \sum_{i=1}^n \frac{(p_i + q_i)^2}{\sqrt{p_i q_i}} \tag{38}$$

And
$$A(P, Q) + T(P, Q) \leq \frac{1}{4} \sum_{i=1}^n \frac{(p_i + q_i)^2}{\sqrt{p_i q_i}} \tag{39}$$

Where $T(P, Q)$, $h(P, Q)$ are given by (11) and (14) respectively and $A(P, Q) = \sum_{i=1}^n \frac{p_i + q_i}{2} = 1$ is well known Arithmetic Mean Divergence.

Proof: Put $t = \frac{(\sqrt{p_i} - \sqrt{q_i})^2}{2\sqrt{p_i q_i}}$ in inequalities (18), we get

$$\frac{p_i + q_i - 2\sqrt{p_i q_i}}{p_i + q_i} \leq \log \left(\frac{p_i + q_i}{2\sqrt{p_i q_i}} \right) \leq \frac{p_i + q_i - 2\sqrt{p_i q_i}}{2\sqrt{p_i q_i}}$$

Now multiply the above expression by $\frac{p_i + q_i}{2}$ and sum over all $i=1, 2, 3, \dots, n$, we get

$$\sum_{i=1}^n \frac{(p_i + q_i)}{2} \frac{p_i + q_i - 2\sqrt{p_i q_i}}{p_i + q_i} \leq \sum_{i=1}^n \frac{(p_i + q_i)}{2} \log \left(\frac{p_i + q_i}{2\sqrt{p_i q_i}} \right) \leq \sum_{i=1}^n \frac{(p_i + q_i)}{2} \frac{p_i + q_i - 2\sqrt{p_i q_i}}{2\sqrt{p_i q_i}}$$

i. e.
$$\sum_{i=1}^n \frac{p_i + q_i - 2\sqrt{p_i q_i}}{2} \leq T(P, Q) \leq \sum_{i=1}^n \frac{(p_i + q_i)^2}{4\sqrt{p_i q_i}} - 1$$

i. e.
$$\sum_{i=1}^n \frac{(\sqrt{p_i} - \sqrt{q_i})^2}{2} \leq T(P, Q) \leq \sum_{i=1}^n \frac{(p_i + q_i)^2}{4\sqrt{p_i q_i}} - 1$$

i. e.
$$h(P, Q) \leq T(P, Q) \leq \sum_{i=1}^n \frac{(p_i + q_i)^2}{4\sqrt{p_i q_i}} - 1 \tag{40}$$

From first and third part of (40), we get inequality (38) and from second and third part, we get (39).
 Except these, from (38) and (40), we can easily see the followings

$$A(P, Q) \leq \frac{1}{4} \sum_{i=1}^n \frac{(p_i + q_i)^2}{\sqrt{p_i q_i}} \tag{41}$$

$$h(P, Q) \leq \frac{1}{4} \sum_{i=1}^n \frac{(p_i + q_i)^2}{\sqrt{p_i q_i}} \tag{42}$$

And
$$h(P, Q) \leq T(P, Q) \tag{43}$$

Now do (41)-(42), we get

$$A(P, Q) - h(P, Q) \leq 0 \Rightarrow A(P, Q) \leq h(P, Q) \tag{44}$$

By taking both (43) and (44), we get the inequalities (37).

Proposition 6: Let $(P, Q) \in \Gamma_n \times \Gamma_n$ and $\sum_{i=1}^n p_i = \sum_{i=1}^n q_i = 1$, then we have the inequalities:

$$G(Q, P) \geq \frac{1}{2} - \log 2 \tag{45}$$

And $\log 2 + G(Q, P) \leq \frac{1}{2} [R_2(P, Q) + 1]$ (46)

Where $R_2(P, Q)$, $G(Q, P)$ are given by (7) and (10) respectively.

Proof: Put $t = \frac{p_i}{q_i}$ in inequalities (18), we get

$$\frac{p_i}{p_i + q_i} \leq \log \left(\frac{p_i + q_i}{q_i} \right) \leq \frac{p_i}{q_i}$$

Now multiply the above expression by $\frac{p_i + q_i}{2}$ and sum over all $i=1, 2, 3 \dots n$, we get

$$\sum_{i=1}^n \frac{p_i + q_i}{2} \frac{p_i}{p_i + q_i} \leq \sum_{i=1}^n \frac{p_i + q_i}{2} \log \left(\frac{2 p_i + q_i}{2 q_i} \right) \leq \sum_{i=1}^n \frac{p_i + q_i}{2} \frac{p_i}{q_i}$$

i. e. $\sum_{i=1}^n \frac{p_i}{2} \leq \log 2 \sum_{i=1}^n \frac{p_i + q_i}{2} + \sum_{i=1}^n \frac{p_i + q_i}{2} \log \left(\frac{p_i + q_i}{2 q_i} \right) \leq \sum_{i=1}^n \frac{p_i^2}{2 q_i} + \sum_{i=1}^n \frac{p_i}{2}$

i. e. $\frac{1}{2} \leq \log 2 + G(Q, P) \leq \frac{1}{2} [R_2(P, Q) + 1]$ (47)

From first and second part of (47), we get inequality (45) and from second and third part, we get (46).

Proposition 7: Let $(P, Q) \in \Gamma_n \times \Gamma_n$ and $\sum_{i=1}^n p_i = \sum_{i=1}^n q_i = 1$, then we have the inequalities:

$$\log 2 - F(P, Q) \leq A(P, Q) \tag{48}$$

And $\frac{1}{2} H(P, Q) + F(P, Q) \leq \log 2$ (49)

Where $F(P, Q)$ is given by (9), $A(P, Q) = \sum_{i=1}^n \frac{p_i + q_i}{2} = 1$ and $H(P, Q) = \sum_{i=1}^n \frac{2 p_i q_i}{p_i + q_i}$ are Arithmetic Mean and Harmonic Mean Divergences respectively.

Proof: Put $t = \frac{p_i}{q_i}$ in inequalities (18), we get

$$\frac{p_i}{p_i + q_i} \leq \log \left(\frac{p_i + q_i}{q_i} \right) \leq \frac{p_i}{q_i}$$

Now multiply the above expression by $2 q_i$ and sum over all $i=1, 2, 3 \dots n$, we get

$$\sum_{i=1}^n 2 q_i \frac{p_i}{p_i + q_i} \leq \sum_{i=1}^n 2 q_i \log \left(\frac{2 p_i + q_i}{2 q_i} \right) \leq \sum_{i=1}^n 2 q_i \frac{p_i}{q_i}$$

i. e. $H(P, Q) \leq 2 \log 2 \sum_{i=1}^n q_i - 2 \sum_{i=1}^n q_i \log \left(\frac{2 q_i}{p_i + q_i} \right) \leq 2 \sum_{i=1}^n p_i$

i. e. $H(P, Q) \leq 2 \log 2 - 2F(Q, P) \leq 2$

After interchanging P and Q, we get the following

$$H(P, Q) \leq 2 \log 2 - 2F(P, Q) \leq 2 \tag{50}$$

from second and third part of (50), we get inequality (48) and from first and second part, we get (49).

Some Relations:

$$\because H(P, Q) \leq G^*(P, Q) \leq N(P, Q) \leq A(P, Q) \leq R(P, Q) \leq S(P, Q) \leq C(P, Q) \text{ (Taneja [15]).} \tag{51}$$

The above inequalities (51) is a famous relation among seven means, where $H(P, Q), G^*(P, Q), N(P, Q), A(P, Q), R(P, Q), S(P, Q), C(P, Q)$ are mentioned in abstract.

Now we can get some other important relations among various divergences with the help of above inequalities, these are as follows.

❖ from (37) and (51), we get

$$H(P, Q) \leq G^*(P, Q) \leq N(P, Q) \leq A(P, Q) \leq h(P, Q) \leq T(P, Q) \tag{52}$$

❖ from (48) and (51), we get

$$\log 2 - F(P, Q) \leq A(P, Q) \leq R(P, Q) \leq S(P, Q) \leq C(P, Q) \tag{53}$$

❖ from (37) and (48), we get

$$\log 2 - F(P, Q) \leq A(P, Q) \leq h(P, Q) \leq T(P, Q) \tag{54}$$

❖ do (46) - (48), we get

$$G(Q, P) + F(Q, P) \leq \frac{1}{2} [R_2(P, Q) + 1] - A(P, Q)$$

i. e. $2A(P, Q) + 2[G(Q, P) + F(Q, P)] \leq R_2(P, Q) + 1$

i. e. $2A(P, Q) + J_R(P, Q) \leq R_2(P, Q) + 1 \tag{55}$

❖ from (22), (26) and (36), we get

$$N_1^*(P, Q) - N_2^*(P, Q) \leq \Delta(P, Q) \leq \frac{1}{2} E_1^*(P, Q) \leq \frac{1}{2} J_1^*(P, Q) \tag{56}$$

❖ from (22) and (23), we get

$$N_1^*(P, Q) - N_2^*(P, Q) \leq \Delta(P, Q) \leq \frac{1}{2} E_1^*(P, Q) - L(P, Q) \tag{57}$$

REFERENCES

- [1]. Csiszar I., Information type measures of differences of probability distribution and indirect observations, *Studia Math. Hungarica*, 2(1967), 299-318.
- [2]. Dacunha- Castelle D., *Ecole d'Ete de Probabilites de Saint-Flour VII-1977*, Berlin, Heidelberg, New York: Springer, 1978.
- [3]. Dragomir S.S., Gluscevic V. and Pearce C.E.M, Approximation for the Csiszar f-divergence via midpoint inequalities, in *inequality theory and applications - Y.J. Cho, J.K. Kim and S.S. Dragomir (Eds.)*, Nova Science Publishers, Inc., Huntington, New York, Vol. 1, 2001, pp. 139-154.
- [4]. Dragomir S.S., Sunde J. and Buse C., "New inequalities for Jeffreys divergence measure", *Tamusi Oxford Journal of Mathematical Sciences*, 16(2) (2000), 295-309.
- [5]. Hellinger E., *Neue begrundung der theorie der quadratischen formen von unendlichen vielen veranderlichen*, J. Rein.Aug. Math., 136(1909), 210-271.
- [6]. Jain K.C. and Saraswat R. N., Series of information divergence measures using new f- divergences, convex properties and inequalities, *International Journal of Modern Engineering Research (IJMER)*, vol. 2(2012), pp- 3226-3231.
- [7]. Jain K.C. and Srivastava A., On symmetric information divergence measures of Csiszar's f- divergence class, *Journal of Applied Mathematics, Statistics and Informatics (JAMSI)*, 3 (2007), no.1, pp- 85- 102.
- [8]. Kafka P., Osterreicher F. and Vincze I., On powers of f- divergence defining a distance, *Studia Sci. Math. Hungar.*, 26 (1991), 415-422.
- [9]. Kumar P. and Chhina S., A symmetric information divergence measure of the Csiszar's f-divergence class and its bounds, *Computers and Mathematics with Applications*, 49(2005),575-588.
- [10]. Kumar P. and Hunter L., On an information divergence measure and information inequalities, *Carpathian Journal of Mathematics*, 20(1) (2004), 51-66.

- [11]. Kumar P. and Johnson A., On a symmetric divergence measure and information inequalities, *Journal of Inequalities in Pure and Applied Mathematics*, 6(3) (2005), Article 65, 1-13.
- [12]. Renyi A., On measures of entropy and information, *Proc. 4th Berkeley Symposium on Math. Statist. and Prob.*, 1(1961), 547-561.
- [13]. Sibson R., Information radius, *Z. Wahrs. Undverw. Geb.*, (14) (1969),149-160.
- [14]. Taneja I.J., New developments in generalized information measures, Chapter in: *Advances in Imaging and Electron Physics*, Ed. P.W. Hawkes, 91(1995), 37-135.
- [15]. Taneja, I.J. Inequalities having seven means and proportionality relations, 2012. Available online: <http://arxiv.org/abs/1203.2288/> (accessed on 7 April 2013).



International Journal of Modern Engineering Research (IJMER)

Volume : 4 Issue : 1 (Version-2)

ISSN : 2249-6645

January - 2014

Contents :

Wheel Speed Signal Time-Frequency Transform and Tire Pressure Monitoring System Design <i>Wang Liqiang, Meng Hui, Han Zongqi</i>	01-08
Effect of Injection Pressure on Ignition Delay and Combustion Duration of Diesel Engine with Biodiesel (Jatropha Oil) and Its Blends <i>Mr. Alireza Valipour</i>	09-14
Enhancing the Control of Iraqi Power System Using FACTS Devices and Renewable Energy with Matlab Simulation <i>Er. Mohammed Hamed Yasen, Prof. (Dr.) A. K. Bhardwaj, Er. Surya Prakash</i>	15-23
Life Cycle Assessment in a Cold Rolling Mill Manufacturing Industry in India-A Review <i>Vishal Y. Bhise, Ajay Kashikar</i>	24-29
A Study of Performance and Emissions of Diesel Engine Fuelled With Blends of Cotton Seed Oil Methyl Ester and Petro-Diesel <i>Dr. C. Solaimuthu, Dr. S. Chitra, Prof. P. Rajasekaran, G. Jagadeeshkumar, P. C. Pradeep, N. Raqibudeen, M. Vikram</i>	30-34
Transmission Error in Gear <i>Deepak Malviya, Dr. Pushpendra Kumar Sharma</i>	35-37
Detection of DC Voltage Fault in SRM Drives Using K-Means Clustering and Classification with SVM <i>V. S. Chandrika, A. Ebenezer Jeyakumar</i>	38-42
Design, Analytical Analysis, Instrumentation and Flow Simulation of Sub-Sonic Open Circuit Wind Tunnel Model <i>Tomar Vishvendra Singh, Sangwan Vipul, Singh Shaktiman, Singh Raj Kumar, Agrawal Jubin</i>	43-52
Secure Multi-Owner Group Signature Based Secure M-Health Records in Cloud <i>B. Anitha, V. Udhaya Kumar</i>	53-57
Studies Of Influence on Multiwalled Carbon Nanotubes (MWCNT's) Reinforced Epoxy Based Composites <i>Mahesh V. M., B. K. Muralidhara, Raji George</i>	58-63

Wheel Speed Signal Time-Frequency Transform and Tire Pressure Monitoring System Design

Wang Liqiang¹, Meng Hui², Han Zongqi³

¹(College of Vehicle and Energy Engineering, Yanshan University, China)

²(College of Electrical Engineering, Yanshan University, China)

³(College of Vehicle and Energy Engineering, Yanshan University, China)

ABSTRACT: This article designed a tire pressure monitoring system with time-frequency conversion function, the system can convert wheel speed time signal into frequency signal, can filter in the frequency domain to obtain pure wheel speed signal, and use it to determine tire pressure. This article described the wheel speed signal sampling frequency calculation methods, filter mode selection methods, Fast Fourier Transform (FFT) and Inverse Fast Fourier Transform (IFFT) algorithm and its implementation within the microcontroller, and the implementation of frequency domain filtering within the microcontroller. We designed the tire pressure monitoring system based on XC2336A microcontroller; vehicle road test showed that after the time-frequency conversion, the tire pressure monitoring system can effectively improve the monitoring accuracy at a high speed.

Keywords: Tire Pressure Monitor, Time-frequency Conversion, Sample Frequency, FFT/IFFT

I. Introduction

Tire is the only parts contact with the road when a car in moving process and the tire pressure is an important parameter^[1] directly related to the car driving performance and the safety. Tire Pressure Monitoring System (TPMS) is an ideal device to maintain the tire pressure to be normal. Accordance to the working principle, TPMS can be divided into Direct and Indirect categories. Direct TPMS can accurately monitor the tire pressure, but because of its complex structure, so many alters on the wheels, installation difficulties, high price and other shortcomings, it is only used in a few advanced cars. Indirect TPMS can infer the level of tire pressure indirectly by collecting and processing the ABS wheel speed sensor signal, calculating and analyzing the rolling radius of the wheels, wheel speed, and tire deformation parameters. Because of its simple structure, low cost, easy to implement, the Indirect TPMS has attracted much more attention. However, in the existing indirect TPMS, when the speed is bigger than 100km / h, since the incretion of the noise of wheel speed signal, signal processing methods are simple; the monitoring accuracy is reduced significantly.

This article provided indirect TPMS with a more pure wheel speed signal which went through the time-frequency conversion and filtering. The road test showed that after video conversion, the tire pressure monitoring system can effectively improve the monitoring accuracy at a high speed.

II. Sampling Cycle, Acquisition Cycle And The Definition Of Monitoring Cycle

Acquisition cycle is an interval for a system to determine a tire pressure. If each acquisition cycle performs wheel speed signal acquisition for only once, by memory limitation of the selected microcontroller, each wheel speed signal acquisition can not collect too much wheel speed signal; by the limited accuracy of tire pressure monitoring and alarm, the number of wheel speed signal pluses used to determine tire pressure can not be too small. Therefore, each acquisition cycle is divided into ten sampling periods, so that the wheel speed signal of each sampling period does not exceed microcontroller memory; add the number of pulses of ten sampling period to determine the tire pressure so that tire pressure detection alarm accuracy can not be affected by the small pulse number.

The number of calculation pulses for each sampling period will produce ± 1 pulse error^[2]. so the maximum error of ten sampling period namely a collection cycle is ± 10 , it does not affect the judgment of tire pressure.

Monitoring cycle is the time interval to determine whether to alarm. A monitoring cycle consists of five acquisition cycles, the cycle decides whether to alarm according to the judgments of these five system acquisition cycles on the tire pressure. After each new acquisition cycle generated, we discard the earliest recorded data, so that we can ensure each monitoring cycle contains only the five most recently recorded pulse data.

III. Tire Speed Signal Sampling Frequency And Filter Mode

3.1 determine of the number of speed signal samples

Real vehicle experiments shows that, to determine the tire pressure that is an acquisition cycle, each wheel takes about 5000 pulses, if we take 5120 pulses, and then four wheels require a total of $5120 \times 4 = 20480$ wheel speed signal pulses. The sampling period is one tenth of the acquisition cycle, that is each sample periods needs to collect $20480/10 = 2048$ pulses. Assuming the sampling frequency is 4 times of the wheel speed signal frequency, so that each sampling period needs to collect $2048 \times 4 = 8192$ wheel speed signal. During the Fast Fourier Transform (FFT) process, each wheel speed signal consists of the real and imaginary parts of two integer variables, each integer variable consists of two bytes, then the FFT process requires namely 32K RAM, in this article the model of selected SCM is SAF-XC2336A-56F80L of the Infineon company, the chip RAM is 50K, which meets the requirements.

3.2 determine of the wheel speed signal sampling frequency

In each sampling period, the sampling frequency is determined by the output of the wheel speed signal frequency. Diameter of the rolling tires :

$$D = (L \times H) \times 2 + d \times 25.4 \quad (1)$$

Wherein, D is the wheel diameter, L is the tire width, H is the aspect ratio, d is the diameter of the hub. The wheel speed signal output frequency is:

$$f_1 = \frac{V \times Z}{\pi \times D} \quad (2)$$

Wherein, V is the vehicle speed, Z is the ring gear teeth of the wheel speed sensor. Take JETTA models as an example, the tire model is 185/60R14, wheel speed sensor ring gear teeth Z is 40, when the vehicle speed is 20km / h, the sensor output signal frequency is 122HZ, speed is 200km / h, the sensor output signal is 1220Hz

By the limitation of microcontroller memory, the number of wheel speed signal collected by each sampling period is fixed, if the sampling frequency is constant, the number of pulses collected at 200km / h is the tenth of number collected at 20km / h. When setting the sampling frequency, if we determine the frequency according to the output frequency of wheel speed signal at a high speed, the sampling frequency is too large, resulting in the number of pulses collected in the low speed is too small, and the measurement accuracy of tire pressure monitoring is reduced. If we determine according to the output frequency of the low wheel speed signal, the sampling frequency is too small, it can not meet the sampling theorem at high speed, leading to the distortion of the signal collected.

This article presents a frequency collection method which can change frequency automatically according to the wheel speed. Wheel speed signal acquisition is carried out in the real-time interrupt function, at the end of each sampling period, 4 paragraph wheel speed signals can be obtained. Set the real-time interrupt interval as t_1 , the number of real-time interrupt of each sampling period is N. SO the sampling time for each sampling period can be calculated is:

$$T = N \times t_1 \quad (3)$$

At the end of sampling, the number of pulse of 4 paragraph wheel speed signals can be calculated, according to the cycle method [2] the wheel speed at this time can be calculated for:

$$V = \frac{(n_1 + n_2 + n_3 + n_4) \pi D}{4 Z T} \quad (4)$$

Wherein, n_1 、 n_2 、 n_3 、 n_4 are the number of pulses of four wheels during each sampling period. The interval of each sampling cycle times is very short; it can be assumed that the wheel speed variation for the next sampling period is not big. The interval of next sampling period real-time interrupt can be steted based on the calculated wheel speed. Set the expectation numbers of pulses collected is n_0 , the real-time interrupt interval is:

$$t_1 = \frac{n_0 \pi D}{4 Z N V} \quad (5)$$

Thus, the number of pulses for each sampling period is similar. Thus, according to the previous wheel speed of sampling period to determine the sampling frequency of the next cycle, can not only ensure the number of pulses for each sampling period be too small to affect the measurement accuracy of tire pressure monitoring, but also can prevent signal distortion.

3.3 filter mode selection

When the wheel speed is 100km / h or less, the interference of wheel speed signal is very small, the clutter can be good removed by a hardware filter and software filtering is unnecessary. Meanwhile, in order to ensure the tire pressure of indirect TPMS can detect when the vehicle is started (at this point the speed is low), In order to minimize low speed detection cycle as much as possible, which also requires no further software filtering at low speed. Before filtering the software each sample period selects the filter mode according to the wheel speed calculated when setting the frequency sample. If the wheel speed is greater than 100km / h, then the collected wheel speed signal will be software filtered. If the wheel speed is less than 100km / h, then software filtering is no longer carried out, directly calculate the number of pulses.

IV. SCM Software Filtering

The wheel speed signal collected through fast Fourier transformed (FFT) converted into frequency domain signal, then be filtered, and finally through inverse fast Fourier transform (IFFT) converted into time domain signals.

4.1 FFT and IFFT algorithm principle

The idea of FFT algorithm is: continually decomposing the long sequence of DFT into short sequences of the DFT, and using the periodicity and symmetry of rotation factor to reduce the number of calculations of DFT.

Set the length of sequence $X(n)$ is N , and satisfying: M is a natural number, The sequence $X(n)$ is divided into $x_1(n)$, $x_2(n)$ two sequences by n is odd or even, with $2N/2$ point DFT to complete a N -point DFT calculations:

$$\begin{cases} x_1(r) = x_1(2r) \\ x_2(r) = x_1(2r + 1) \end{cases} \quad (6)$$

Wherein $r = 0, 1, 2, \dots, N/2-1$, substituted into DFT conversion formula:

$$X(k) = DFT[x(n)] = \sum_{n=0}^{N-1} x(n)W_N^{nk} \quad (7)$$

Among them $0 \leq k \leq N-1$, W_N^{nk} is the rotation factor, we have:

$$X(k) = \sum_{r=0}^{N/2-1} x_1(r)W_N^{2rk} + W_N^k \sum_{r=0}^{N/2-1} x_2(r)W_N^{2rk} \quad (8)$$

Since the rotation factor:

$$W_N^{2n} = e^{-j\frac{2\pi}{N}2n} = e^{-j\frac{2\pi}{N/2}n} = W_{N/2}^n \quad (9)$$

Substituted into (8), we obtain:

$$X(k) = X_1(k) + W_N^k X_2(k) \quad (10)$$

Since the cycle of $X_1(k)$ and $X_2(k)$ is $N/2$, and $X(k)$ can be expressed as:

$$\begin{cases} X(k) = X_1(k) + W_N^k X_2(k) \\ X(k + N/2) = X_1(k) - W_N^k X_2(k) \end{cases} \quad (11)$$

Wherein, $k = 0, 1, \dots, N/2-1$. So that the N -point DFT is decomposed into two $N/2$ point DFT. Break down $x_1(r)$ and $x_2(r)$ continually by odd or even. This decomposition continues until it can no longer be decomposed.

4.2 FFT and IFFT algorithm implemented in the microcontroller

FFT and IFFT algorithm achieved in the microcontroller mainly consider the real-time of system and the microcontroller RAM limitation. Experimental results show that when the length of sequence $X(n)$ N is 8192, with the microcontroller clock frequency 80MHz, It takes about 600ms for FFT / IFFT, namely tire pressure detection system detects the time of the tire lack of gas is delayed by 600ms, which has little effect to the tire pressure detection systems.

Therefore FFT / IFFT algorithm achieved within microcontroller mainly considered the RAM limitation.

In order to achieve FFT/IFFT algorithm within microcontroller, we use the following three ways to save RAM needed by the FFT algorithm.

(1) The sequence of length $N = 2M$ point FFT, has a total of M -class butterfly computation. At the same level,

the two input data of each butterfly is only useful for the butterfly itself. After calculating a butterfly, the output data resulted can be stored in storage unit immediately, which is occupied by original input data. After M-class operation, the original input data stored in N memory cells may be sequentially stored in the output data of the N values. Such using the same storage unit stores the butterfly calculated input and output data, can save more storage space.

(2) In the FFT algorithm, we can see from the Euler equation:

$$W_N^r = e^{-j2\pi r/N} = \cos(2\pi r/N) - j \sin(2\pi r/N) \quad (12)$$

When W_N^r is multiplied, we should make the corresponding sin and cos calculation. In programming, one method is to attribute each step directly. From the symmetry of the rotation factor, during calculation we should define $N / 2$ variables to memorize, this takes more RAM, and slow the computing speed [3]. Another method is to calculate W_N^r in advance, the values are stored in the ROM, which is equivalent to set up a sine and cosine function table. This will not only improve the operation speed, and also save the RAM space. Considering indirect TPMS wheel speed signals collected have already occupied a larger RAM, this article adopts the second way to save RAM space.

(3) when performing wheel speed signal acquisition, the data through the A/D conversion is not the actual wheel speed voltage signal, but needs to be multiplied by a constant, and then transferred into a voltage signal expressed by a decimal, so we should use floating point type of data to storage, float data in MCU will occupy 4 bytes, which occupied too many bytes. Therefore, during the A/D conversion, we no longer calculate the voltage signal, but directly use the integer data after A/D conversion for FFT and filtering, the integer data type only occupy 2 bytes, it saves the chip RAM and does not affect filtering results.

4.3 frequency domain filtering implementation in single-chip within

After FFT conversion, the real wheel speed signal energy amplitude increased, while the amplitude of noise energy decreased. In the frequency domain, "filtering" process is to keep the real amplitude of the signal energy, to attenuate the amplitude of the noise energy component. Set after the FFT transform, wheel speed signal sequence of each frequency component and the corresponding energy amplitude of the series are shown in Table 1.

Table 1 frequency of the signal with the corresponding energy value

Frequency f	f_0	f_1	...	f_m	...	f_n
Energy Amplitude Y	Y_0	Y_1	...	Y_{max}	...	Y_n

Before filtering we must first determine the highest energy value Y_{max} and corresponding center frequency f_m . Shown in Fig4.

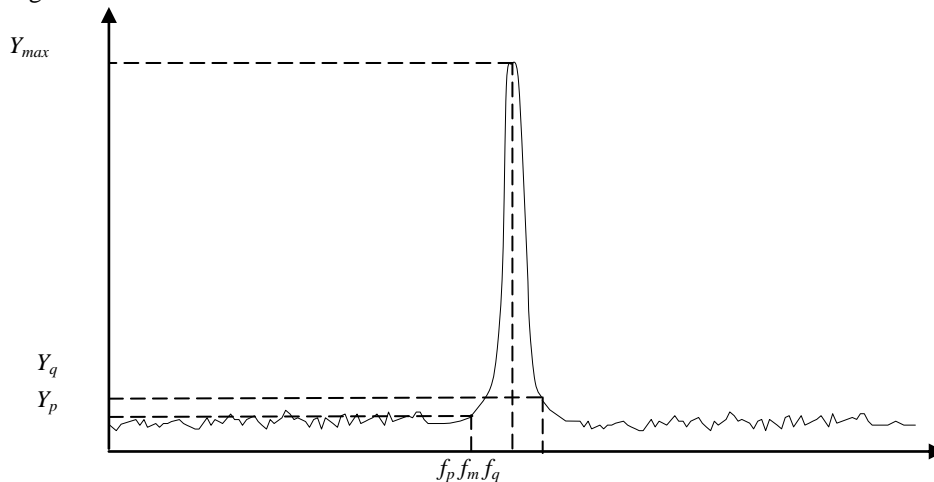


Figure 4 the division of filter frequency bands

The output frequency of wheel speed signal is approximately equal to the center frequency f_m ; we can estimate the center frequency by using frequency of the wheel speed signal which is calculated when setting the sampling frequency. Since the wheel speed of the wheel speed signal acquisition cycle is not fixed, and the

wheel speed calculated by the cycle method has some error [2], so the wheel speed signal output frequency is not equal to the center frequency f_m , but must in the vicinity of the center frequency. So when we looking for the highest energy value Y_{max} , is not required to calculate the maximum energy amplitude of the overall situation, just calculate the local maximum near the wheel speed signal output frequency. After determining the center frequency f_m , it is required to determine the "binding site" of the wheel speed signal and the noise f_p and f_q , shown in Figure 4. f_p and f_q are determined by the coefficients of the signal / noise amplitude ratio a and b :

$$\begin{cases} f_p = f_m/a \\ f_q = f_m/b \end{cases} \quad (12)$$

Signal to noise ratio coefficient is obtained by experiment. Finally respectively fit both sides of the binding sites secondary:

$$\begin{aligned} [Y_0, Y_1, \dots, Y_p] &= F_1[f_0, f_1, \dots, f_p] \\ [Y_q, Y_{q+1}, \dots, Y_n] &= F_2[f_q, f_{q+1}, \dots, f_n] \end{aligned} \quad (13)$$

After fitting Substitute the data into the frequency value, obtaining the corresponding energy amplitude. Fit the corresponding spectrum shown in Fig.3, of which the vehicle speed is 160Km / h. After fitting, the spectral curve and the IFFT time-domain graph are respectively restored in Fig.5 and Fig.6.

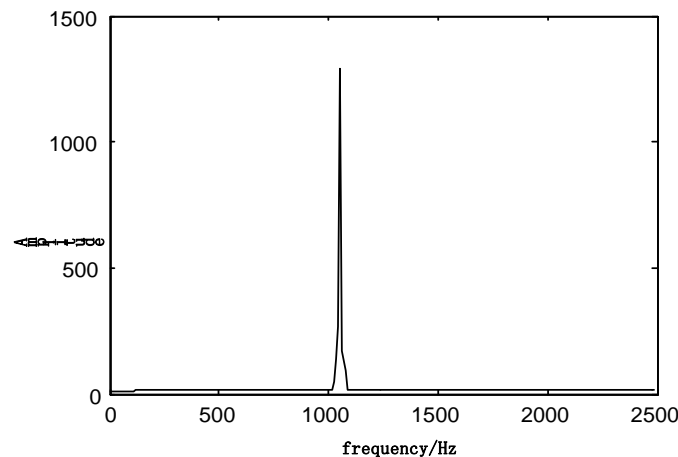


Figure 5 the frequency domain spectrum after treatment

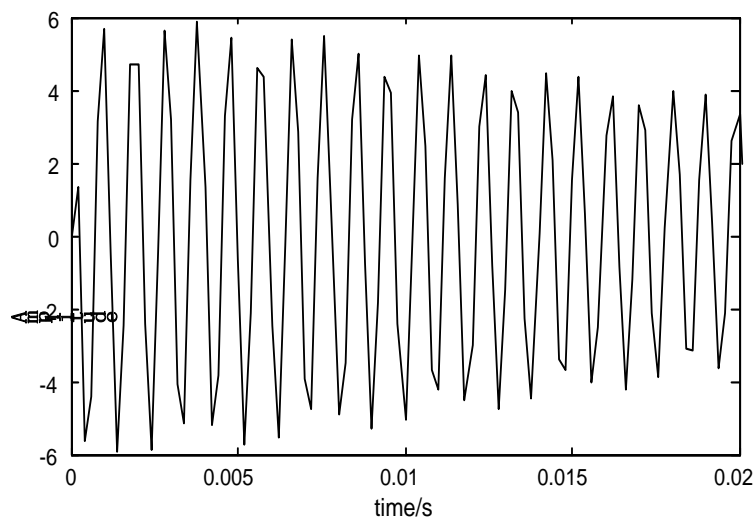


Figure 6 the IFFT time domain graph after the inverse transform

Comparing Fig.3 with Fig.12, it can be seen that the wheel speed signal after filtering can eliminating the noise basically.

V. Design Of Tire Pressure Monitoring System

5.1 hardware design of tire pressure monitoring system

System consists of wheel speed signal input module, a central processing module, abnormal tire pressure alarm module and serial communication module. Shown in Fig.7,

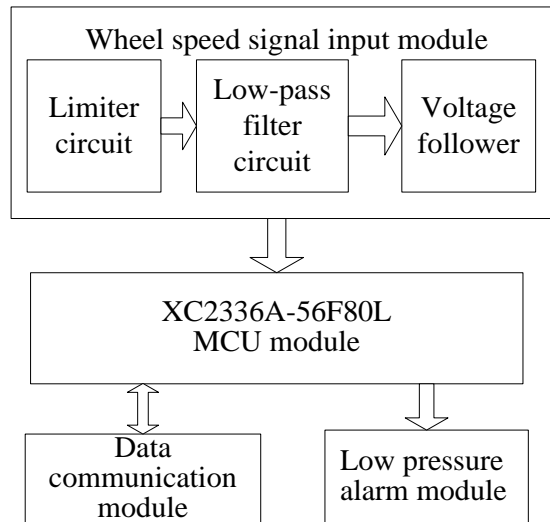


Figure 7 system component modules

When using a magnetic wheel speed sensor, in order to prevent the voltage of wheel speed signal exceeds the tolerance range of microcontroller, we must reduced voltage after a limiter circuit.

After the limiter circuit, the wheel speed signal to be filter out portion of the noise in the signal through the filter circuit. In order to prevent signal acquisition affects ECU, the wheel speed signal after processing should go through the voltage follower to be isolated. Final design is completed and the in or out of the wheel speed signal module circuit is shown in Fig.8.

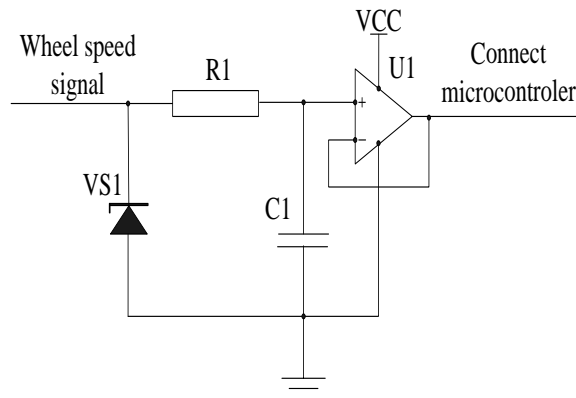


Figure 8 speed signal input module

Wherein the Zener diode VS1 formed the limiter circuit. R1 and C1 form a low-pass filter circuit, U1 is a voltage follower.

System uses XC2336A asynchronous / synchronous serial interface USIC0, achieving the bidirectional communication between PC and microcontroller. Abnormal tire pressure alarm module consists of a buzzer and a fault light.

5.2 Tire pressure monitoring system programming

Tire pressure monitoring system flow chart as shown below:

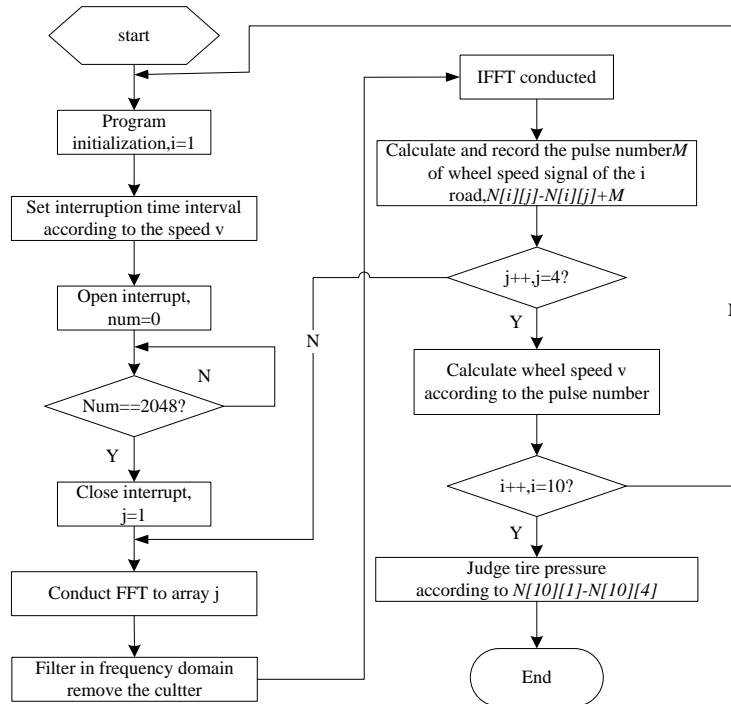


Figure 9

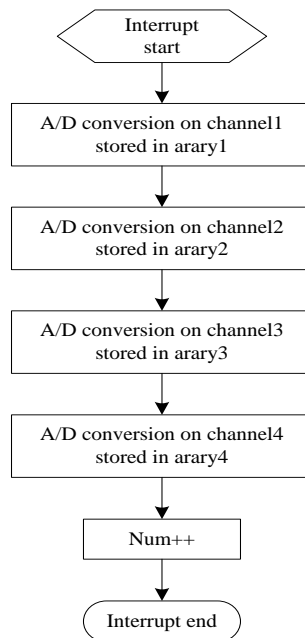


Figure 10

5.3 abnormal tire pressure warning module

In this paper the alarm module designed two level thresholds and three level alarm modes according to reference^[4]. In each monitoring cycle, the system calculated 5 relative errors and 5 absolute errors according to the number of pulses of five acquisition cycles, a total of ten data. Systems can determine if the tire pressure is abnormal based on the number of times these 10 data exceeds to the threshold value. Assume that the number of alarm which is more than one level is X, more than two levels is Y, then the alarm conditions and alarm manner are shown in Table 2.

Table 2 alarm conditions and manner

Alarm type	Alarm condition	Sound alarm method
Level one alarm	$X \geq 6$	Frequency 1.0Hz
Level two alarm	$X \geq 8$ and $Y \geq 4$	Frequency 0.5Hz
Level three alarm	$X = 10$ and $Y \geq 8$	Continous beep
Error	$X < Y$	Fault light on

VI. Road Comparison Test

We installed a tire pressure monitoring system with software filtering function and another tire pressure monitoring system with no software filtering function on the same sedan to take a comparison test. During the experiment, two systems always use the same wheel speed signal. The test tire model is 185/70R14. When tested coefficients of the ratio of signal / noise amplitude a and b are respectively set to 1.05 and 0.95, i.e. $f_p = f_m / a = 0.95f_m$, $f_q = f_m / b = 1.05f_m$. In the first test, four tire pressures is normal, which is 0.25MPa; in the second test the left rear tire pressure was reduced to 0.15MPa, the remaining three rounds were unchanged. Tests were respectively finished under 120km / h, 140km / h, and 160km / h four kinds of speed. During the test the number of alarm which is more than one level X and which is more than two levels Y, were transferred to a PC via the serial port for analysis comparing, the test results are shown below.

Table 3 alarm condition of tire pressure monitoring system with no software filtering feature

Vehicle speed	Tire pressure normal			Left rear tire pressure(0.15Mpa)		
	X	Y	Alarm	X	Y	Alarm
120km/h	1	0	No	7	0	Level one
140km/h	3	0	No	9	2	Level one
160km/h	7	0	Level one	10	6	Level Two

Table 4 alarm condition of tire pressure monitoring system with software filtering feature

Vehicle Speed	Tire pressure normal			Left rear tire pressure 0.15MPa		
	X	Y	Alarm	X	Y	Alarm
120km/h	0	0	No	7	0	Level one
140km/h	0	0	No	7	0	Level One
160km/h	1	0	No	8	0	Level one

Comparison Table 3 with Table4 ,we can concluded that at high speed the tire pressure monitoring system with no filtering software was easy to produce false or wrong reports, and filtered with a tire pressure monitoring system software basically eliminate this situation, and the tire pressure monitoring system with a filtered software can basically eliminate this situation.

VII. Conclusions

Wheel speed signal after FFT transformation filtered in the "frequency domain", and then after IFFT transformation converted to the time domain, the interference signal is substantially eliminated. Road comparison test proved that the tire pressure monitored by the tire pressure monitoring system with the time-frequency conversion function is more accurate, especially when a car at high speed, it can effectively eliminate the noise caused by false or wrong reports.

Acknowledgements

This work was financially supported by the National Natural Science Foundation (51175450), Hebei Province Natural Science Foundation (E2012203046).

References

- [1]. Zheng Anwen. Basic characteristics and preventive measures of highway traffic accidents[J]. *Highway and Transportation Research*, 2002, 19(4): 110-112.
- [2]. Li Pu, Song Jian, Yu Liangyao. ABS wheel speed signal interference processing method [J]. *Automotive Technology*, 2001(5): 15-18.
- [3]. Li xinshe, Yi yaxing, Li Zhongke etc. The twiddle factor generation algorithm research in FFT[J]. *Aeronautical Computing Technology*, 2000, 30(3): 19-20.
- [4]. Han zongQi, Song Jian, Su dandan, etc. Abnormal tire pressure warning system design based on the rolling radius [J]. *Automotive Engineering*, 2008, 30(8): 721-724.

Effect of Injection Pressure on Ignition Delay and Combustion Duration of Diesel Engine with Biodiesel (Jatropha Oil) and Its Blends

Mr. Alireza Valipour

Department of Mechanical Engineering, Aligarh Muslim University, India

ABSTRACT : This paper discusses the combustion characteristics of jatropha methyl ester (further biodiesel) in direct injection diesel engine with injection pressure range from 100 bar to 300 bar and variation of ambient air pressure from 5 bar to 25 bar. The experiments were carried out in a constant volume combustion chamber under conditions similar to the real engine condition using a single holepintle nozzle for the various blends i.e., B20 and B40 and the results were compared with the neat diesel. The combustion characteristics such as ignition delay and combustion duration were computed. The results showed that for all test fuels the reduction in ignition delay increases with the increase in injection pressure during all ambient air pressure. Analysis of combustion characteristics also shows that the combustion durations of JME were more than diesel fuel but with the increase in injection pressure from 100 to 300 bar leads to reduction in combustion duration.

Keywords: Jatropha, Biodiesel, Ignition Delay, Combustion Duration

I. Introduction

Diesel engine has gained the name and fame in serving the society in many ways. Its main attractions are ruggedness in construction, simplicity in operation and ease of maintenance. The performance and emission characteristics of diesel engines depends on various factors like fuel quantity injected, fuel injection timing, fuel injection pressure, shape of combustion chamber, position and size of injection nozzle hole, fuel spray pattern, air swirl etc. The fuel injection system in a direct injection diesel engine is to achieve a high degree of atomization for better penetration of fuel in order to utilize the full air charge and to promote the evaporation in a very short time and to achieve higher combustion efficiency. The fuel injection pressure in a standard diesel engine is in the range of 200 to 1700 atm depending on the engine size and type of combustion system employed [1]. Due to the better fuel economy diesel engines have been widely used in automotive area. However, the limited reserve of fossil fuel and deteriorating environment have made scientists seek to alternative fuels for diesel while keeping the high efficiency of diesel engine. Since last decades researchers around the world have been trying to find new alternative fuels that are available, technically feasible, economically viable and environmentally acceptable [2]. One of the promising alternative fuel considered for diesel engine is “biodiesel”. With recent increases in petroleum prices and uncertainties concerning petroleum availability, there is renewed interest in vegetable oil fuels for Diesel engines. Biodiesel is non-explosive, biodegradable, non-flammable, renewable, non-toxic as well as environment friendly. It has similar properties with diesel fuel. Biodiesel is alky esters of fatty acids and can be obtained by employing the transesterification treatment of vegetable oils, animal fats, waste cooking oils. Vegetable oil can be obtained from both edible (palm oil, rapseed oil, coconut oil etc) and non-edible (jatropha, neem,jojobaetc) oil sources [3].

II. Literature Survey

Till today several biodiesel fuels for CI engines have been investigated. Most investigations show that the use of biodiesel results in lower emissions (except NO_x) and better combustion [4]. Pramanik (2003) has investigated the use of Jatropha oil blends with diesel fuel in direct injection diesel engine. It has been reported that 50 % of Jatropha oil blends can be substituted for diesel fuel in CI engine. It has been reported that the Jatropha oil exhibited higher specific fuel consumption and lower exhaust gas temperatures compared to diesel fuel. Szybist et al., (2007) have reported that the injection and ignition process can be altered significantly by biodiesels and their blends. An increase in the ignition delay period and combustion duration with both jatropha oil and its esters with lower heat release rates were noticed compared to diesel fuel. Tapan K. Gogoi, Shovana Talukdar, Debendra C. Baruah have analyzed the performance and combustion characteristics of 10%,

20%, 30% and 40% blending of Koroch Seed Oil Methyl Ester (KSOME) and Jatropha Methyl Ester (JME) with diesel as fuels in a diesel engine. They reported that the ignition delay was less and the combustion duration was more for the JME blends as compared to the KSOME blends. They have found that the ignition delay period for the KSOME and JME blends was less as compared to the diesel fuel. M.Senthil Kumar, A.Kerihuel, J.Bellettre and M.tazerouthave used preheated animal fat as fuel in single cylinder direct injection diesel engine developing a power output of 2.8 kW at 1500 rev/min. Experiments are conducted at the fuel inlet temperatures of 30, 40, 50, 60 and 70°C. They reported that animal fat at low temperature results in higher ignition delay and combustion duration than diesel. Preheated animal fat shows reduced ignition delay and combustion duration.

III. Biodiesel Production Processes for Combustion Study

3.1 Process flow chart

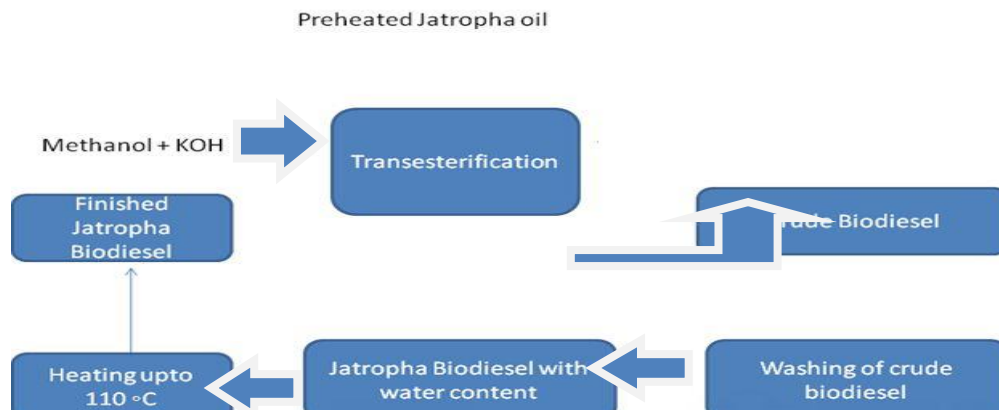


Figure1: Diagram of Jatropha Biodiesel Production (FFA less than 2.5%)

This experiment has been performed to evaluate performance of mechanical stirring method of biodiesel production in terms of yield (%) and time.

Experiment has been performed with the following steps:

1. Jatropha oil (4 Kg) is taken in a beaker and filtered it to remove impurities. The raw oil is heated up to 110 °C in order to remove water content of oil to avoid soap formation. This oil is allowed to cool up to 55 °C temperatures for the reaction to take place.
2. Now methanol (CH₃OH) is taken with a molar ratio of (1:6) and catalyst (KOH) is taken as (1%) by wt of oil. The mixture of methanol & KOH stirred until KOH dissolved into methanol.
3. Then Jatropha oil mixed in to the mixture of methanol & KOH.
4. Whole mixture stirred for 1 hr with the help of magnetic stirrer.
5. For better reaction, temperature of mixture kept into the range of 50°C to 60 °C because methanol boiling point is 65 °C.
6. When reaction is completed the beaker is kept for the separation. Glycerol has higher sp- weight therefore it settles down at bottom. It will take 2 to 3 hrs.
7. After separation methyl ester (biodiesel) contains only catalyst KOH in form of impurity.
8. KOH harmful for diesel engine therefore it must be separate out into the biodiesel. Water washing process use for removing KOH in biodiesel. In the process water (at 55 °C) mixed in to separate methyl ester and left for settling down. KOH dissolved in to water and separated to biodiesel.
9. Excess water removed by heating the biodiesel up to 120 °C.

3.2 Description of Test Fuels:

The fuels used in this study include conventional diesel and blends of jatropha biodiesel. The blended fuels contain 20% and 40% by volume of jatropha biodiesel which are identified as B20 and B40 fuels. The biodiesel used in our experiments was produced from Jatropha oil. The major properties of the fuels are measured in petrochemical lab of the college. These properties are listed in the TABLE below. The properties with * are adopted from Sunil Kumar et.al [5].

Table I: Properties of Tested Fuels

Fuel	Viscosity, C.stokes at 40 °C	Lower heating value (MJ/kg) *	Flash Point (°C) FP	Density (kg/l) ρ	Cetane Number *
Diesel	4.2	42	155	0.83	49
Jatropha biodiesel	5.2	34.2	185	0.88	51

IV. Experimental Apparatus and Procedure

The investigations on the combustion characteristics were conducted on a Direct Injection Constant Volume Combustion Chamber (DI-CVCC). Combustion Chamber in present study is stainless steel cylindrical tank having a 54.2 mm length, 95 mm diameter and 7.5 mm thickness. A pintle type nozzle is fitted on the head of the combustion chamber (right hand side). The combustion chamber used in present study is a closed type chamber so that the pressure developed inside the combustion chamber is very high as required in present study. The photo sensor is attached to the combustion chamber to detect the event of start of combustion, on the storage oscilloscope. The rise time of photo sensor for present study is 5 μ sec. For detecting the event of combustion, the borosil glass window which the photo sensor is installed in front of it is attached on left hand side of combustion chamber. When fuel is injected into the combustion chamber with the help of fuel injection system, there is a pressure change takes place inside the fuel line. This pressure change is sensed by the piezo-electric crystal and display this signal on the screen of oscilloscope. Heating elements or coils act as a heater. One of them is fitted inside the combustion chamber so that hot surface combustion of fuel and air mixture takes place inside the chamber and other is fitted around the combustion chamber for increasing the surface temperature. Maximum temperature of heating coils for present study is 1400°C. The oscilloscope used in present experimental setup is a digital storage two channel oscilloscope (RIGOL DS 1102, 100 MHz, 1GSa/s). On one channel it shows the fuel injection process and on the other channel it shows the combustion process. The ignition delay can easily be measured on the screen of oscilloscope by noting the difference between start of injection and start of combustion on adjusting the timescale and further it can be investigate to analyse the combustion duration.

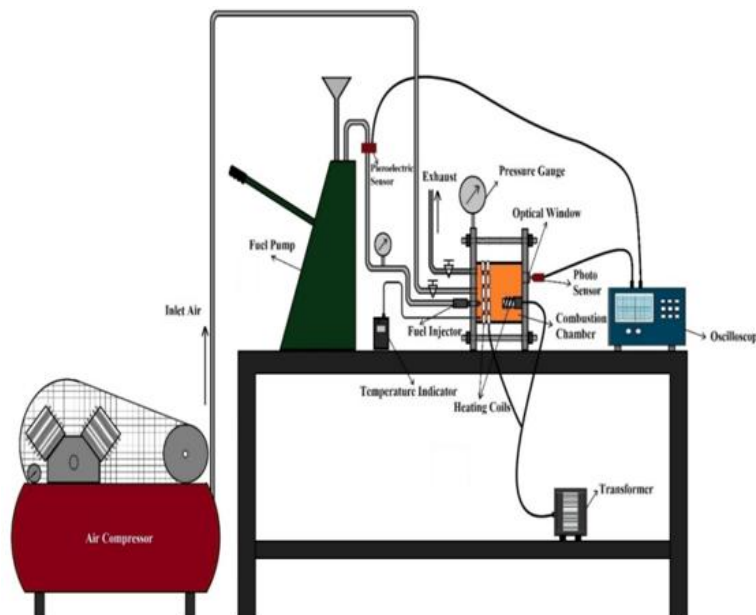


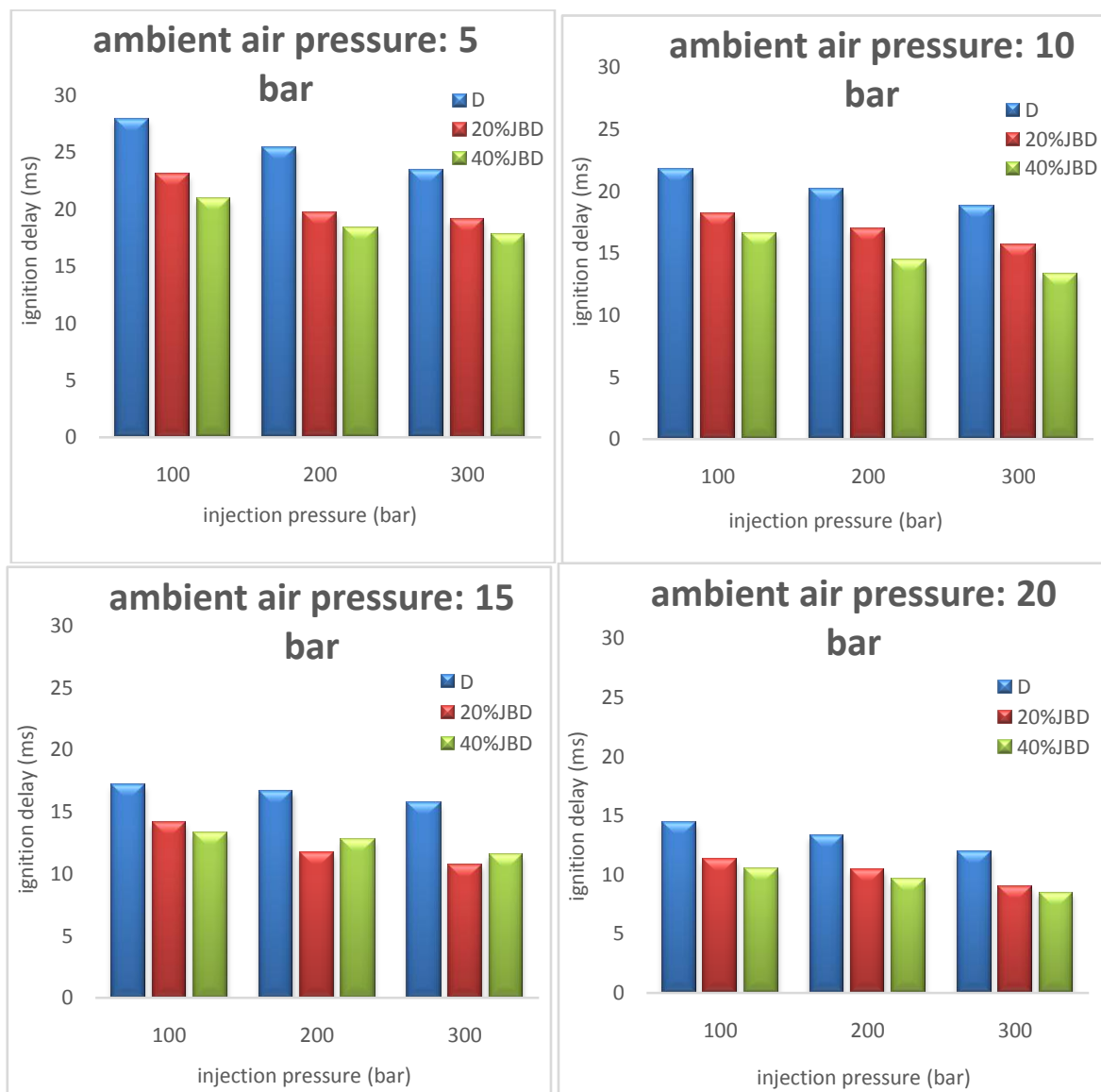
Figure2: Block Diagram of the Experimental Setup

V. Results and Discussion

5.1 Effect of Injection Pressure on Ignition Delay of Jatropha Biodiesel Blended Diesel in Different Ambient Air Pressure:

The variation of ignition delay period with different injection pressures for different cylinder pressures is plotted in Fig.3. Ignition delay is the period between the start of fuel injection into the combustion chamber and the start of combustion. The effect of injection pressure ranging from 100 to 300MPa on the ignition characteristics of biodiesel fuel spray using direct injection system was investigated. Observations demonstrate

that high-pressure injection affects engine ignition and combustion. An increase in injection pressure leads to reduced ignition delay time. When fuel injection pressure is low, fuel particle diameters will enlarge and ignition delay period during the combustion will increase. This situation leads to inefficient combustion in the engine. When the injection pressure is increased fuel particle diameters will become small. The mixing of fuel and air becomes better during ignition delay period. The ignition delay period of the tested fuels decreases with increasing cylinder pressure and fuel injection pressure. Among all the tested injection pressures, minimum ignition delay period of 6.32 ms is observed at 300 bar jatropha biodiesel operation and 27.92 ms is observed at 100 bar diesel operation. The reduction in ignition delay period of jatropha biodiesel is mainly due to higher cetanenumber . From Fig.3, it is observed that the increase in injection pressure from 100 to 300 bar leads to better atomization and proper mixing of fuel with air, there by reduction in ignition delay is achieved at all cylinder pressure . It can be observed from figure that the effect of cylinder pressure on ignition delay is more dominant than injection pressure. . If the injection pressure is too high ignition delay become shorter. So, possibilities of homogeneous mixing decrease and combustion efficiency falls down. Therefore, smoke is formed at exhaust of engine [6].



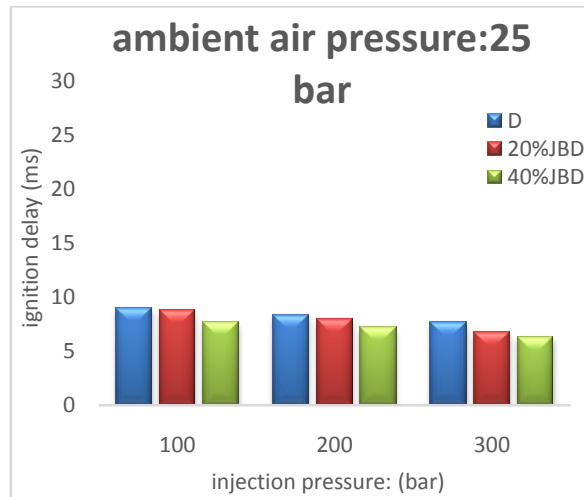
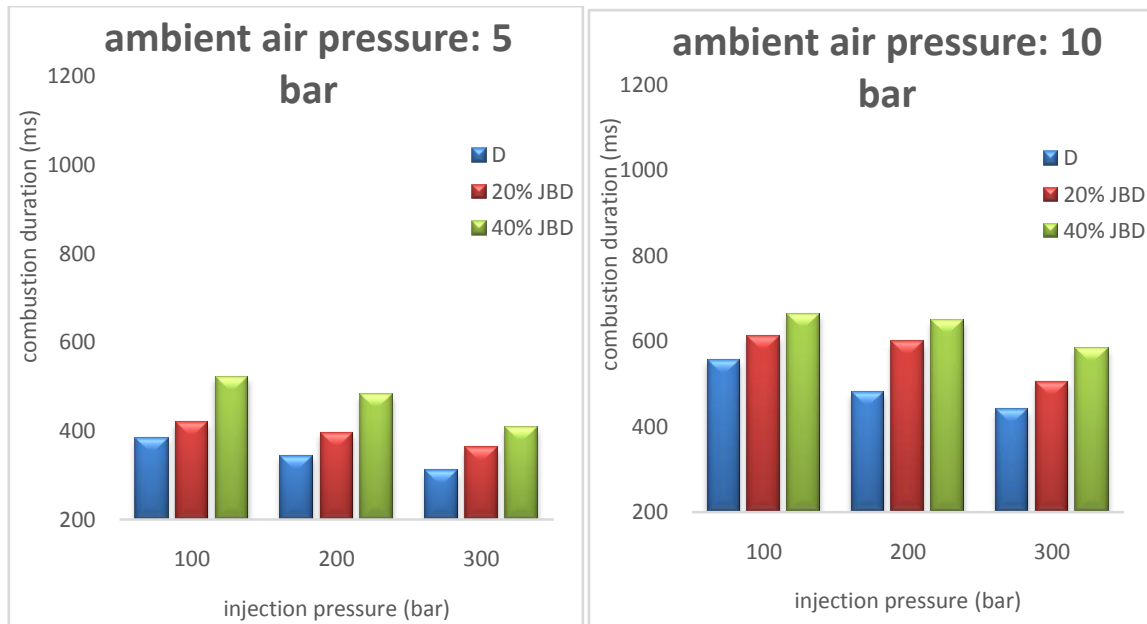


Figure 3: Variation of Ignition Delay of JBD Blends Diesel with Different Injection Pressure

5.2 Effect of Injection Pressure on Combustion Duration of Jatropha Biodiesel Blended Diesel in Different Ambient Air Pressure:

Observations demonstrate that injection pressure affects engine ignition and combustion. Combustion duration of a diesel engine can be defined as the time interval from the start of heat release to the end of heat release [7]. The fuel penetration distance become longer and the mixture formation of the fuel and air was improved when the combustion duration became shorter as the injection pressure became higher [8]. Fig.4 shows the combustion duration for diesel and the various jatropha biodiesel blends(20% and 40%) with different cylinder pressure (5, 10, 15, 20 and 25 bar) and 100, 200 and 300 bar injection pressure respectively. It was seen that, the combustion durations of JBD were more than diesel fuel but with the increase in injection pressure from 100 to 300 bar leads to reduction in combustion duration. Higher combustion duration was obtained with JBD40 at 100 bar injection pressure (1037 ms) compared to neat diesel fuel (310 ms at 300 bar injection pressure). This is may be due to the injection of more amount of JBD40 than diesel fuel. Higher duration of combustion with respect to JBD20 and JBD40 could be due to earlier start of combustion and relatively longer diffusion combustion for these blends.



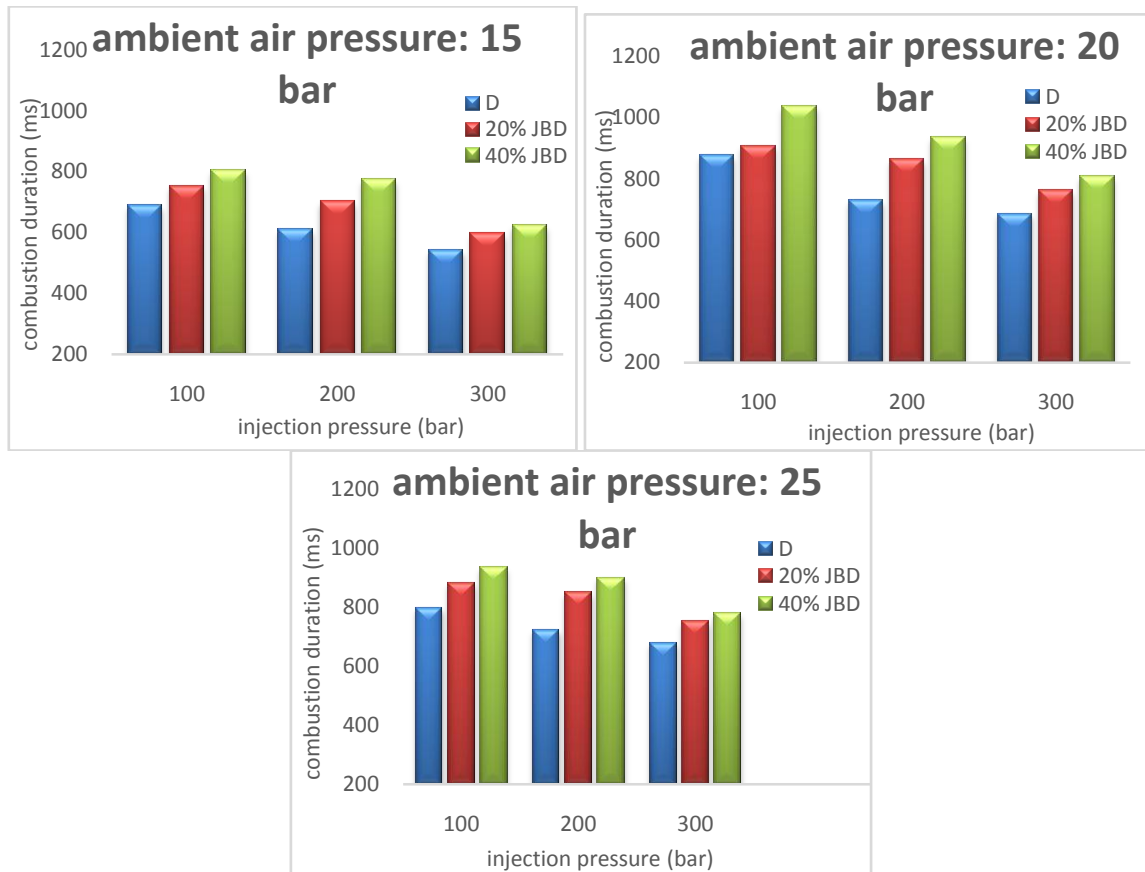


Figure 4: Variation of Combustion Duration of JBD Blends Diesel with Different Injection Pressure

VI. Conclusion

The purpose of the present work was to study experimentally the effect of injection pressure (100 to 300 bar) on combustion characteristics of jatropha biodiesel blended with diesel fuel (20% and 40%) in direct injection constant volume combustion chamber.

The conclusions drawn from the present study are the following points:

- Ignition delay decreases with the increase in injection pressure and ambient air pressure for all tested fuel.
- JBD has the shorter ignition delay which is prolonged with increasing biodiesel content in the blends.
- The combustion durations of JBD were more than diesel fuel but with the increase in injection pressure from 100 to 300 bar leads to reduction in combustion duration.

References

- [1] Heywood, J.B., "Internal Combustion Engine Fundamentals" (McGraw-Hill, Singapore, ISBN 0-07-100499-8, 1988).
- [2] Liaquat AM, Kalam MA, Masjuki HH and Jayed MH. (2010). "Potential Emission Reduction in Road Transport Sector using Biofuel in Developing Countries", Atmos Environ, 2010;44:3869-77.
- [3] Mufijur M, Masjuki HH, Kalam MA, Hazrat MA, Liaquat AM and Shahabuddin M. (2012). "Prospects of Biodiesel from Jatropha in Malaysia", Renew Sust. Energy Rev. 2012;16:5007-20.
- [4] Spataru A and Romig C. (1995). "Emissions and Engine Performance from blends of Soya and CanoaMethyle Ester with ARB#2 Diesel in a DCC6V92TAMUI Engine", SAE Paper No.952388, Warrendale, PA: SAE International.
- [5] Kumar S, Chaube A and Kumar SH. "Critical review of jatropha biodiesel promotion policies in India".
- [6] Celikten I. (2003)"An Experimental Investigation of the effect of the Injection Pressure on Engine Performance and Exhaust Emission in Indirect Injection Diesel Engine", Applied Thermal Engineering, 2003; 23: 2051-2060.
- [7] Sahoo P.K and Das L.M. (2009)." Combustion Analysis of Jatropha, Karanja and Polanga based Biodiesel as Fuel in a Diesel Engine", Fuel 88, pp. 994-999.
- [8] Lee SW, Tanaka D, Kusaka J and Daisho Y. (2002)"Effects of Diesel Fuel Characteristics on Spray and Combustion in a Diesel Engine". JSAE Review. 2002; 23: 407-414.

Enhancing the Control of Iraqi Power System Using FACTS Devices and Renewable Energy with Matlab Simulation

Er. Mohammed Hamed Yasen¹, Prof (Dr.) A. K. Bhardwaj²
Er. Surya Prakash³

¹(Iraqi Ministry of Electricity/Operation & Control Directorate/The control center of the northern , Iraq +Sam Higginbottom Institute of Agriculture Technology & Sciences, Deemed University, Allahabad, Uttar Pradesh, India)

²(Associate Professor, Department of Electrical Engineering, Sam Higginbottom Institute of Agriculture Technology & Sciences, Deemed University, Allahabad, Uttar Pradesh, India,

³(Assistant Professor, Department of Electrical Engineering, Sam Higginbottom Institute of Agriculture Technology & Sciences, Deemed University, Allahabad, Uttar Pradesh, India,

ABSTRACT: Many Research and Study it is searched to resolve problems of a Power System by best Methods. In this work design Iraqi Electrical Power System contents (25 Bus bars- 400 kilo volt) and Resolve many problem in Electrical Power System, Such as Voltage ripple, Frequency Swing and Unstability Electrical Power System. By using FACTS Devices it is Distribution Static Synchronize Compensator (STATCOM) and (D – STATCOM) resolve Voltage Sag, Swill and reach to Voltage Stability, by injection Reactive Power also response Time about (25ms). Using Renewable Energy it is Wind Turbine (WT) for resolve Demand increase with Clean Energy, Environment-Friendly and Free Energy under MatLab Program Simulation.

Keywords: Iraq, FACTS, Renewable Energy, Control, Power System, MatLab.

I. Introduction

Power quality is certainly a major concern in the present era. It becomes especially important with the insertion of sophisticated devices, whose performance is very sensitive to the quality of power supply. A Power quality problem is an occurrence manifested as a nonstandard voltage, current or frequency that results in a failure or a miss-operation of end user equipment's. Modern industrial processes are mainly based on electronic devices such as PLC's, power electronic devices, drives etc., and since their controls are sensitive to disturbances such as voltage sag, swell and harmonics, voltage sag is most important power quality problems It contributes more than 80% of power quality (PQ) problems that exist in power systems, and more concern problems faced by many industries and utilities. [1]. by definition, voltage sag is an rms (root mean square) reduction in the AC voltage at the power frequency, for duration from a half-cycle to a few seconds. Voltage sag is caused by a fault in the utility system, a fault within the customer's facility or a large increase of the load current, like starting a motor or transformer energizing. Typical faults are single-phase or multiple-phase short circuits, which leads to high currents. The high current results in a voltage drop over the network impedance. Voltage sags are not tolerated by sensitive equipment's used in modern industrial plants such as process controllers; programmable logic controllers (PLC), adjustable speed drive (ASD) and robotics. Various methods have been applied to reduce or mitigate voltage sags. The conventional methods are by using capacitor banks, introduction of new parallel feeders and by installing uninterruptible power supplies (UPS). However, the PQ problems are not solved completely due to uncontrollable reactive power compensation and high costs of new feeders and UPS. The D-STATCOM has emerged as a promising device to provide not only for voltage sags mitigation but a host of other power quality solutions such as voltage stabilization, flicker suppression, power factor correction and harmonic control.

1.1 Configuration of D-Statcom

The basic electronic block of the D-STATCOM is the voltage source inverter that converts an input dc voltage into a three-phase output voltage at fundamental frequency. These voltages are in phase and coupled with the ac system through the reactance of the coupling transformer. Suitable adjustment of the phase and

magnitude of the D-STATCOM output voltages allows effective control of active and reactive power exchanges between the D-STATCOM and the ac system. Fig 1 shows the schematic of D-STATCOM. The D-STATCOM employs an inverter to convert the DC link voltage V_{dc} on the capacitor to a voltage source of adjustable magnitude and phase. Therefore the D-STATCOM can be treated as a voltage-controlled source. Figure 1 shows a single phase equivalent of the Statcom. A voltage source inverter produces a set of three phase voltages, V_i , that are in phase with the system voltage, V_s . small reactance, X_c , is used to link the compensator voltage to the power system. When $V_i > V_s$, a reactive current, i_c , is produced that leads V_s and when $V_i < V_s$, the current lags V_s .

IRNet Transactions on Electrical and Electronics Engineering 97 Design And Simulation Studies of D-Statcom for Voltage Sag, Swell Mitigation

Inductance L and resistance R which represent the equivalent circuit elements of the step-down transformer and the inverter will be the main component of the D-STATCOM. The voltage V_i is the effective output voltage of the D-STATCOM and δ is the power angle. The reactive power output of the D-STATCOM inductive or capacitive depending can be either on the operation mode of the D-STATCOM. Referring to figure 1, the controller of the D-STATCOM is used to operate the inverter in such a way that the phase angle between the inverter voltage and the line voltage is dynamically adjusted so that the D-STATCOM generates or absorbs the desired VAR at the point of connection. The phase of the output voltage of the thyristor-based inverter, V_i , is controlled in the same way as the distribution system voltage, V_s . Figure 2 shows the three basic operation modes of the D-STATCOM output current, I , which varies depending upon V_i . If V_i is equal to V_s , the reactive power is zero and the D-STATCOM does not generate or absorb reactive power. When V_i is greater than V_s , the D-STATCOM shows an inductive reactance connected at its terminal. The current, I , flows through the transformer reactance from the D-STATCOM to the ac system, and the device generates capacitive reactive power. If V_s is greater than V_i , the D-STATCOM shows the system as a capacitive reactance. Then the current flows from the ac system to the D-STATCOM, resulting in the device absorbing inductive reactive power. [2]

1.2 Wind Turbine:

Researchers have begun to show that a floating axis wind turbine (FAWT) could in fact generate cheaper energy than the more standard offshore horizontal axis wind turbine (HAWT).

As shown in the image above, there are several types of floating wind turbines available, but researchers from the Korea Advanced Institute of Science and Technology and University of Tokyo have showed that the installed cost per rated power of the floating axis wind turbine (FAWT) is 50% and 57% of those in the referenced HAWT (horizontal axis wind turbine) and guyed VAWT (vertical axis wind turbine) configurations, respectively.

On top of that, the estimated cost of the electricity produced in a FAWT-style farm would be approximately 25% lower than that of the base HAWT.

The researchers published their results in the journal *Environmental Letters* and outlined the major merits of FAWT:

- (1) The float supports the weight of the turbine and most of its axial load. The bearing rollers swivel like swivel casters of a desk chair. It allows relative heave motion of the rotating float to the bearing mechanism so that only the thrust force of the turbine is on the bearing mechanism. The thrust force of a wind turbine is less than 1/10 of the weight of the VAWT mechanism.
- (2) Power output from the turbine is obtained from torque of the rotating float by rollers contacting on the cylindrical surface of the float. Since the drive train is not in a limited space like the nacelle of a HAWT or the shaft of a VAWT, restrictions on the weight and size of the mechanism are lighter than those in other turbine concepts.
- (3) Non-rigid support of the turbine axis avoids concentration of the load. Since the weight and bending moment of the turbine are not directly on the drive train, the configuration leads to lighter structural requirements. Gyroscopic moment of the turbine and the float stabilizes the direction of the turbine axis in wind fluctuation.
- (4) FAWTs inherit the simple mechanism and low maintenance cost of VAWTs.
- (5) Installation of FAWTs does not require floating cranes and other specifically designed service vessels.

“We have to reassess the costs of renewable energy and explore new possibilities of energy generation which can be substituted for a part of the present share of nuclear power,” the authors write. “In Japan, wind power is one of the prospective candidates. However, in Japan, flat land and shallow water area available for the construction of new wind farms is very limited. Therefore, there is an urgent need for low-cost offshore wind turbines that are applicable to deep water regions.”

The authors are well aware that their hopes may run into difficulties and unknown challenges, but they are confident that the FAWT will help them find a way to create low-cost offshore wind power. [4]

1.2.1-Wind Turbine Types and Characteristics:

- 1-Variable speed and fixed speed
- 2-Pitch and stall control

The vertical and horizontal axis turbines are explained below and for the others three types the links are in the menu aside. It is also added the next sub-section, wind turbine components, to enhance understanding of the text.

Vertical and horizontal axis wind turbines

The wind turbines may be generally categorized in two types: vertical axis and horizontal axis. The vertical axis is named also “Darrieus” in honor to its inventor Georges Darrieus. Its key advantage is that they do not need an orientation mechanism due to their use of the wind flow from any direction and its main disadvantage is a low power coefficient. Additionally, most of the vertical axis turbines are not built for high power capacity because they are installed at ground level where the wind flow is low. Therefore, this webpage will not explain more about the vertical axis wind turbines and will focus on the horizontal axis ones.

In the case of horizontal wind turbines they may contain one or more blades. The number of blades has to deal with the coefficient of power (Cp) that is basically the electricity produced by a wind turbine divided by the total energy available from the wind (better explained in this link). Furthermore, a higher CP is obtained with three blades as shown in the graph above on the right. Nevertheless, for higher wind speed one or two blades would have a higher CP.

The axis represented in the graph at the top on the right are Tip-speed ratio (λ) and the rotor power coefficient (CPR), axis x and y. The Tip-speed ratio is the rotational speed of the blades ($\omega \cdot r$) divided by the wind speed. [5]

1.2.2- How a Wind Turbine Produces Energy?

The solar energy along with earth rotation makes dissimilar air heating which in turn creates wind. The warmer air mass near to the equator is lighter than the cold air mass and tends to go to the North and South Pole creating wind flows. Moreover, by the movement of the earth and its tilt there are other incredible effects are produced, such as Coriolis. By watching the previous video if we consider the ball as an air mass, we can understand the components of wind movement in its total.

Still, there are other aspects to be concerned when it comes to the wind flow e.g. the roughness and topography of the land and atmospheric stability, which will be commented in the section measurement of wind.

To explain a wind turbine let's consider it the opposite of a regular home fan. The regular home fan uses: an electric motor, blades, and electricity in order to produce wind. As the opposite the wind turbine uses: an electric generator, blades, and wind in order to produce electricity. The wind turbine uses the wind flow that strikes the blades, and using the principles of torque or rotational force it produces electricity. The energy that winds produces relies on 3 aspects:

- Air density
- The rotor area
- Wind speed

To explain the wind power generated from a wind turbine it is important to remember the mechanical classic.

The kinetic energy, in this case wind power (P), that as we all know is equal to half of the mass (m) per speed (v) squared.

$$P = \frac{1}{2} * m * v^2$$

And therefore, if we consider the air mass as equal to the density (ρ) per superficial area (S) per wind speed (v)

$$M = \rho * S * v$$

And later substitute the mass into the equation of kinetic energy the result is that wind power is proportional to the swept area from the wind turbine rotor and in cubic relation with the wind speed

$$P = \frac{1}{2} * \rho * S * v^3$$

Nevertheless, the maximum energy that may be obtained by wind is 59% according to the Betz's law (not taking into consideration the electrical losses). [6].

1.2.3-Variable speed and fixed speed

There are two types of speeds that should not be mistaken with each other, the rotor speed (RPM) and the wind speed (m/s). All wind turbines will work until they reach a certain wind speed otherwise they will work as a motor similar to a house fan, withdrawing electricity from the grid. After reaching the minimum level of wind speed (start-up speed) the brakes are released and the rotor accelerates; however, when the maximum wind speed is reached (cut-out speed) the rotor stops by stall or pitch control (mentioned in subsection pitch and stall control)

In the case of fixed speed, first the rotor accelerates until it reaches a fixed number of RPM, and later the wind turbine is connected to the grid and supplies power. The wind turbine remains connected to the grid at a fixed speed regardless of the wind speed, and changes the power supply through the principles of torque in the blades (the blades angle position) until the cut-out speed is reached and it is when the wind turbine stops.

On the other hand, wind turbine that uses variable speed connects to the grid and supplies power at different rotor speed (RPM). It is to say that the speed of the rotor is matched to the wind speed and along with the blade angle effects the power supplied which creates a maximum efficiency. Therefore, the rotor can be connected to the grid at low speeds during light winds and would increase its power proportionally to wind speed.

Finally, an example is shown that you can find in this link (page 4) and also a more detailed explanation. A small turbine rotor is operating at 40 rpm and the wind speed is 3 meters per second (m/s) producing less than 1 kilowatt of power. If the wind suddenly increases at 6 m/s but the machine is using fixed speed and the rotor remains at 40 rpm the machine will produce between one and two kW; in the case of variable speed the wind turbine will produce between three and four kilowatts. [7]

1.2.4- Pith and Stall Control:

The stall and pitch regulation control works to limit the rotor power in high operational wind flows.

Stall control may be passive or active. Passive stall control is when the blades are attached to the hub at fixed angle. The blades are aerodynamically designed in such manner that when the wind flow exceeds the cut-out speed, the blades start to stall and thus the power production decreases. One advantage of passive control is that moving parts inside the rotor are avoided. In the case of active stall control there is an inclination of the blades, similar to pitch control, but only in low wind speeds, to improve efficiency. On the contrary, at high wind speeds which may damage the generators the position of the blades is the same as in the passive stall control so as to stop the movement of the rotor.

On the other hand, in the pitch power control electronic sensors are used to monitor the output of power. Supposing that the level of power is exceeded the blades are turned or pitched out of the wind. Additionally, when there are low wind speeds the blades are pitched back to catch the wind at an optimal angle.

Figure (9) Section of (WT)

Literature Review

MejalyAlkhazragy (2008)This paper presents a brief description of Lyapunov's direct method, and Demonstrates its efficiency with respect to previous indirect step by step method, in order to compute the stability of electromechanically power system. The practical advantages of this direct method of analysis are:

(i) Rapid solution.

(ii) Ability to compute the degree of stability.

(iii) For computing the critical clearing time integrate the faulted equation, until $V=V1$.

The basic concepts and the mathematical formulation of the method are Summarized. Practical test system are used to demonstrate the superior Efficiency of the method relative to step by step method. [8]

Cristian Dragoş Dumitru (2010) The paper presents the modeling of a solar-wind-hydroelectric hybrid system in Matlab/Simulink environment. The application is useful for analysis and simulation of a real hybrid solar-wind-hydroelectric system connected to a public grid. Application is built on modular architecture to facilitate easy study of each component module influence. Blocks like wind model, solar model, hydroelectric model, energy

II. Result And Discussion

M-FILE CODE1

This is MatLab M-file Code for get the voltage of Iraqi Power System with FACTS devices and with Renewable Energy:-

This Code by MatLab Programmable language.

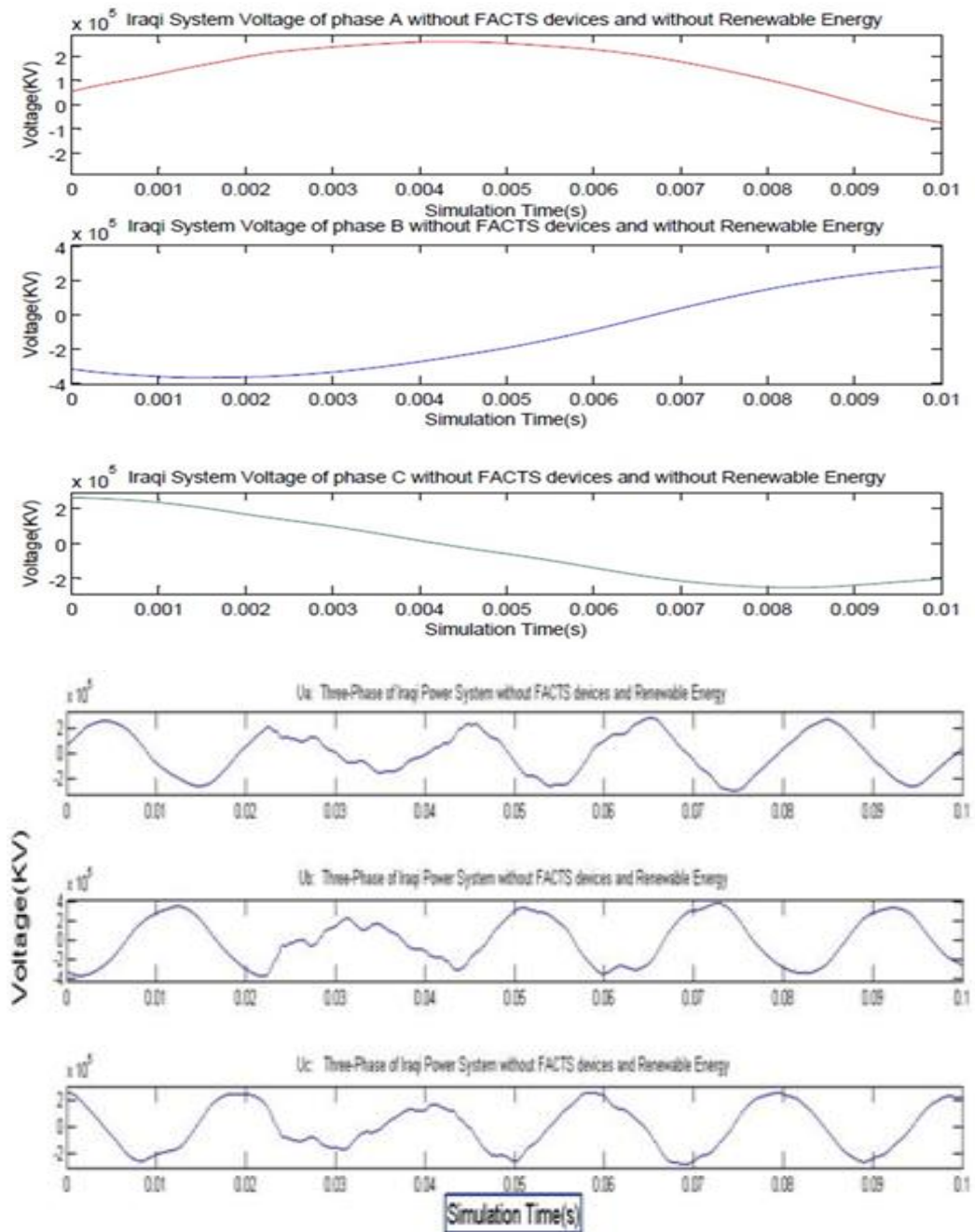
START PROGRAM

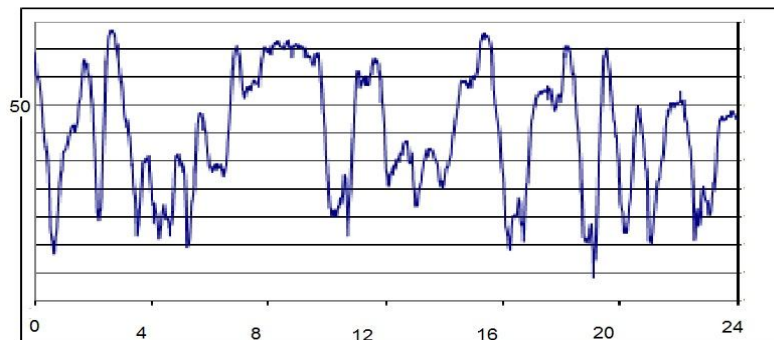
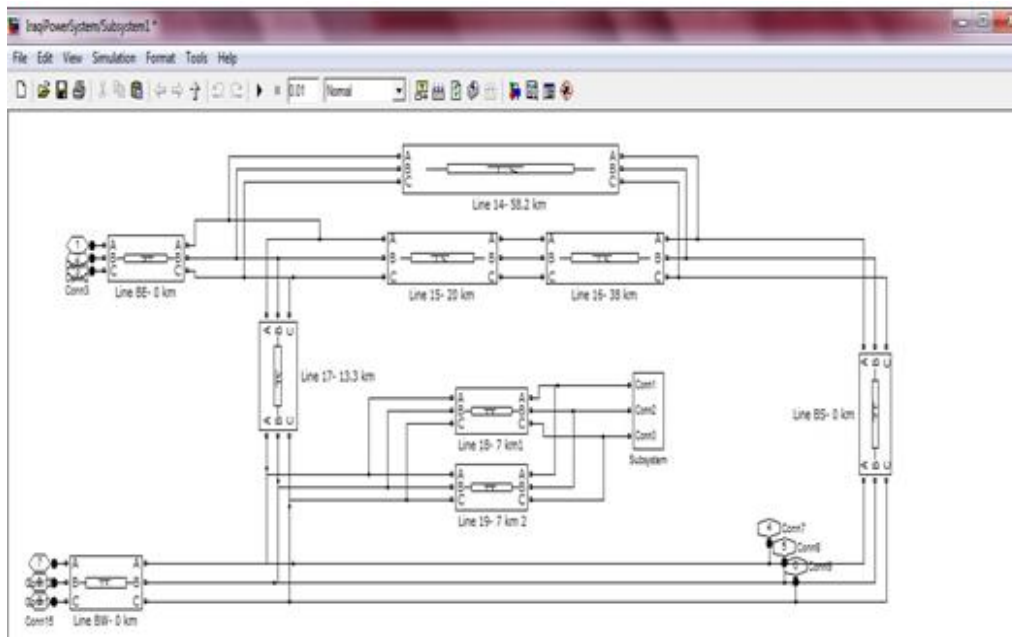
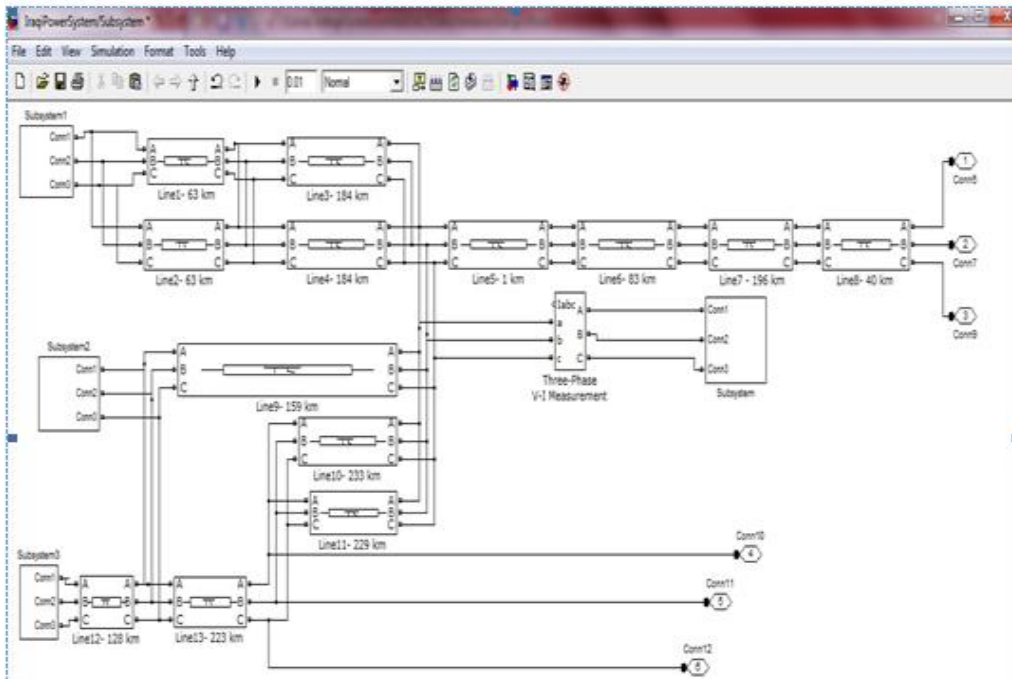
```
function createfigure(X1, Y1, Y2, Y3)
```

```
%CREATEFIGURE(X1,Y1,Y2,Y3)
```

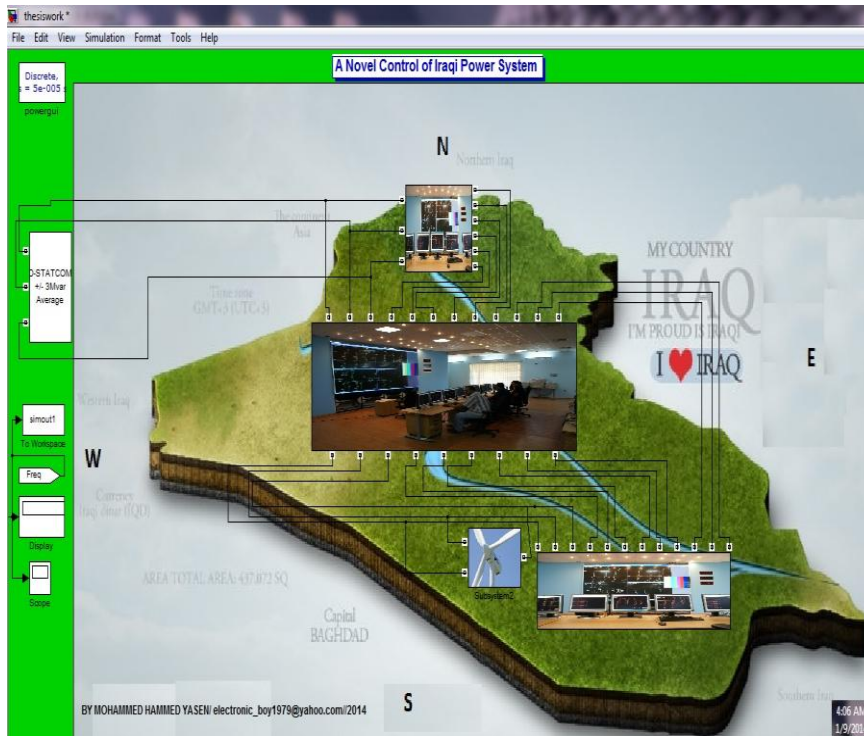
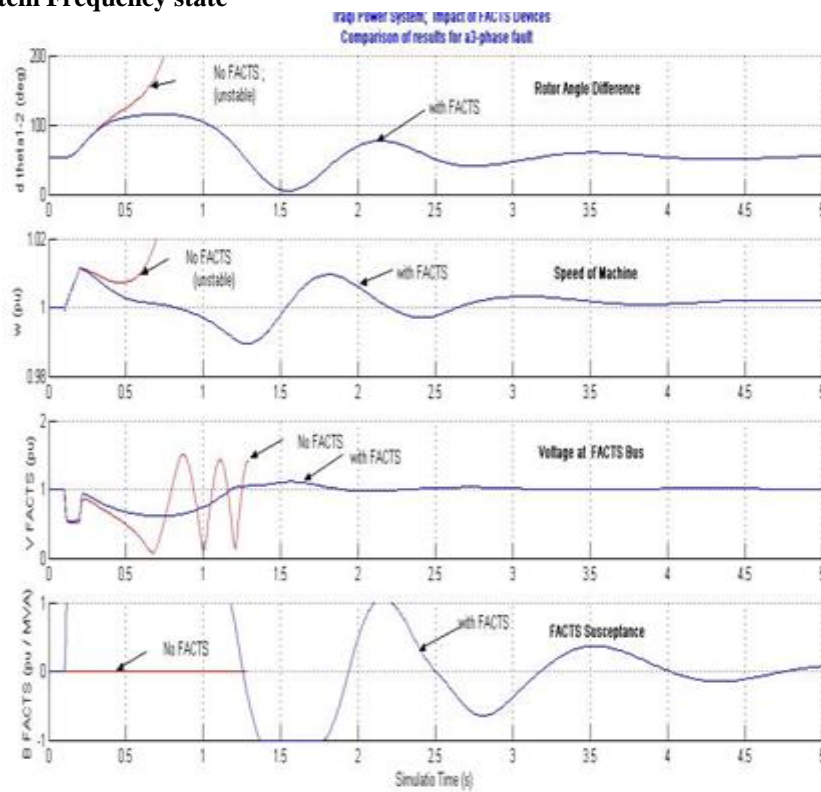
```
% X1: vector of x data
% Y1: vector of y data
% Y2: vector of y data
% Y3: vector of y data
% Auto-generated by MATLAB on 08-Jan-2014 07:22:31
% Create figure
figure1 = figure('NumberTitle','off',...
    'Name','Simulation result for : Multimeter',...
    'IntegerHandle','off');
% Create subplot
subplot1 = subplot(3,1,1,'Parent',figure1);
% Uncomment the following line to preserve the X-limits of the axes
% xlim(subplot1,[0 0.01]);
% Uncomment the following line to preserve the Y-limits of the axes
% ylim(subplot1,[-286833.85846247 286833.85846247]);
box(subplot1,'on');
hold(subplot1,'all');
% Create plot
plot(X1,Y1,'Parent',subplot1,'Color',[1 0 0]);
% Create xlabel
xlabel('Simulation Time(s)');
% Create ylabel
ylabel('Voltage(KV)');
% Create title
title('Iraqi System Voltage of phase A without FACTS devices and without Renewable Energy');
% Create subplot
subplot2 = subplot(3,1,2,'Parent',figure1);
% Uncomment the following line to preserve the X-limits of the axes
% xlim(subplot2,[0 0.01]);
% Uncomment the following line to preserve the Y-limits of the axes
% ylim(subplot2,[-404371.40804379 404371.40804379]);
box(subplot2,'on');
hold(subplot2,'all');
% Create plot
plot(X1,Y2,'Parent',subplot2);
% Create xlabel
xlabel('Simulation Time(s)');
% Create ylabel
ylabel('Voltage(KV)');
% Create title
title('Iraqi System Voltage of phase B without FACTS devices and without Renewable Energy');
% Create subplot
subplot3 = subplot(3,1,3,'Parent',figure1);
% Uncomment the following line to preserve the X-limits of the axes
% xlim(subplot3,[0 0.01]);
% Uncomment the following line to preserve the Y-limits of the axes
% ylim(subplot3,[-288366.691663778 288366.691663778]);
box(subplot3,'on');
hold(subplot3,'all');
% Create xlabel
xlabel('Simulation Time(s)');
% Create ylabel
ylabel('Voltage(KV)');
% Create title
title('Iraqi System Voltage of phase C without FACTS devices and without Renewable Energy');
END PROGRAM
```

III. Figures And Tables





Iraqi Power System Frequency state



IV. Conclusion

This thesis it is found that the Iraqi power system has many troubles, like Voltage unstable, Frequency Swing, power system operation is many time reach to unstable. And in this work try to resolve the Iraqi Power System problems.. to solve the Frequency Swing connected the Renewable Energy Power plants. In this Work used Wind Turbine and connected in Iraqi Southern Region because many Research found the South of Iraq has high speed wind to reach (5 to 9 m/s) and can use to generation.

Acknowledgements

To God for everything
To my parents for their support
To my family for their patience
To my country for his blood being lost every day
To my Ministry for their support to me
To all my professors
To each of the supported me

References

- [1] Dugan, Roger C.; McGranaghan, Mark F.; Beaty, H Wayne. "Electrical Power Systems Quality". McGraw Hill Companies, Inc. 1996.
- [2] D.R.Patil & Komal K.Madhale "Design and Simulation Studies of D-StatcomFor Voltage Sag, Swell Mitigation" IRNet Transactions on Electrical and Electronics Engineering.2012.
- [3] <http://www.financial-innovation.com/compensator/performance-analysis-of-d-statcom-compensator9.html>.2013.
- [4] Environmental Research Letters via Energy Matters, http://techzoho.blogspot.in/2011/12/latest-from-cleantechnica_28.html. 2013.
- [5] <http://renewableenergyin.wix.com/latin-america#!wind-turbines-types-and-charach>.2013.
- [6] <http://renewableenergyin.wix.com/latin-america#!how-a-wind-turbine-produces-energy>.2013.
- [7] http://www.mccsemi.com/up_pdf/applications/Small%20Type%20Wind%20Turbine%20Generator.pdf /generator types. 2013.
- [8] Mejaly Alkhazragy, "USING MATLAB PROGRAM IN SIMULATION OF POWERSYSTEM STABILITY BY LYAPUNOV'S DIRECT METHOD", Journal of Electrical Technical ,2008.
- [9] Cristian Dragoş Dumitru, Adrian Gligor, "MODELING AND SIMULATION OF RENEWABLE HYBRID POWER SYSTEM USING MATLAB/SIMULINK ENVIRONMENT",Scientific Bulletin of the „PetruMaior” University of TârguMureş Vol. 7 (XXIV), no. 2, ISSN 1841-9267 .2010.
- [10] Chetan E. Morkhade, Bhushan S. Rakhonde, "Improvement in Voltage Profile using FACT Device", International Journal of Scientific & Engineering Research, Volume 4, Issue 6, June-2013
- [11] Ravi Kumar Hada1, Sarfaraz Nawaz2, "Optimal location of shunt FACT devices for Power flow control in power System", International Journal of Engineering Research & Technology (IJERT) , Vol. 1 Issue 5, July – 2013.
- [12] MOHAMMED HAMMED YASEN, "Enhanced Control of Power System by Using Smart Grid and Possibility of Applying it in Iraq", International Journal of Soft Computing and Engineering (IJSCE) ISSN: 2231-2307, Volume-3, Issue-1, March 2013.

Author 'S Details

	Er. MOHAMMED HAMMED YASEN Belongs to Kirkuk/Iraq DOB is 18/12/1979, Received his Bachelor of engineering degree from Kirkuk collage Technology (Iraq) in 2007, at this time he is M.Tech. Student in SHIATS /Electrical and Electronic Engineering (Power System), His field of interest includes power system operation & control, Artificial Intelligent control Load forecasting, Power Electronics and Energy management system.
	Dr. A. K. Bhardwaj Belongs to Noida. He received his B.Tech in Electrical Engineering from JMI University, M.Tech from IIT Delhi and Ph.D. from SHIATS Deemed University, Allahabad. Presently he is working as Associate Prof.in the department of Electrical and Electronics Engineering, SHIATS-Deemed University Allahabad. His field of interest includes Load forecasting, Power Electronics and Energy management system.
	Er. Surya Prakash Belongs to Allahabad, DOB is 01.05.1971, Received his Bachelor of Engineering degree from The Institution of Engineers (India) in 2003, He obtained his M.Tech. In Electrical Engg. (Power System) from KNIT, Sultanpur. UP-India in 2009. Presently he is Pursuing Ph. D in Electrical Engg. (Power System). SSET, SHIATS (Formerly Allahabad Agriculture Institute, Allahabad-India). His field of interest includes power system operation & control, Artificial Intelligent control.

Life Cycle Assessment in a Cold Rolling Mill Manufacturing Industry in India-A Review

Vishal Y. Bhise¹, Ajay Kashikar²

¹(Research Fellow-Master of Engineering, Dept. of Mechanical Engg., LTCOE, Navi Mumbai, India)

²(Asst. Professor, Dept. of Mechanical Engg., LTCOE, Navi Mumbai, India)

ABSTRACT: The life cycle phases of rolls of cold rolling mill consist of extraction of raw material, manufacturing, use and recycling. During each phase of life it consumes several inputs in the form of resources like energy, material, water etc and emit outputs in the form of air, water & solid emissions which creates the heavy environmental burden and leads to global warming potential, acidification, eutrophication etc. This paper gives the brief information about the history of LCA, views and definitions of Indian and foreign authors, method of data collection, formulation of questions to identify goal and scope, formulation of the inventory, categorization of impacts and their evaluation. The paper mainly focuses on the methodology used for assessment which enables to measure the environmental performance of an individual product as well as overall performance of the firm which leads the company towards the journey of sustainable development.

Keywords: Life cycle assessment, Life cycle inventory, Input-output models, Environmental impacts, Life cycle performance indicators, Life cycle decision making, Recycle modelling, LCA softwares.

I. Introduction

In the today's world of greener economy and sustainably conscious society, It has become significant for industries to focus on minimization of the environmental impacts of products, occurred due to various operations performed for it's creation. The influence of implementation of environmental policies framed by various worldwide organizations and government bodies, the industries look forward for the sustainable manufacturing. The current trend of zero emission has forced the industries to produce less harmful and eco-friendly products to sustain in the competitive market and to gain the higher market share & customer faith. In order to achieve this it is significant to evaluate the environmental performance of manufacturing firms. Therefore, professionals find the Life cycle assessment as one of the highly efficient tool which is used to evaluate the environmental impact of a product during its whole life cycle. Further, the aggregation of all products impacts can give the total environmental impact of the manufacturing firm.

In 1969, the first initiative about reducing the environmental impact was taken by Coka-Cola. They realized the impacts of beverage tin. In order to cope up the situation they combinely formed a team with local authorities to collect the aluminium tins and recycled them instead of using the primary raw material every time. As a result, they reduced the energy conservation by 90%.

During 1970's some policies were formed which used to focus only on single state of products life, such as production of a single problem such as waste water. Due to focusing on a single issue the another burdons were getting ignored, as a result these policies were ineffective. However, their main objective was to change the attitude of people towards the business and environment.

In 1979, The Society of Environmental Toxicology and Chemistry was founded. Basically, it was a non-profit professional society with objectives to promote the various approaches for solving the environmental issues and to implement & regulate the government policies of environment.

In the 1980's the lifecycle assessment became a vital tool to identify the behavior of a product throughout it's life cycle to assess the environmental impact of product. Also, in late 1989, The 'PE International' launched a Life cycle assessment software tool into the market, which consist of database of several economic sectors to assess the environmental impact of product as well as industry sectors.

In 1993, The international standard organization involved the professionals from Society of Environmental Toxicology and Chemistry (SETAC) to standardize the LCA procedure . First, they standardize

the 'Principles and Framework' in 1997 in the form of ISO 14040. Further in year 2006, they reviewed & complied it and finally brought ISO 14044 life cycle assessment 'guidelines & requirements'.

In year 2002, Society of Environmental Toxicology and Chemistry (SETAC), United Nations Environmental Program (UNEP), professionals & experts from government authorities, industries came together to jointly promote the life cycle assessment method all over the globe.

In 2012, The European commission joint research center's 'Institute For Environmental & Sustainability' published the International reference life cycle database in the form of handbook for various economic sectors of industries within the framework and guidelines of ISO 14040 and ISO 14044 life cycle assessment standards[16]

II. Life Cycle Assessment

Life cycle assessment is a tool to evaluate the environmental consequences of a Product/Project or activity throughout its entire life from extraction of raw material, use of material, disposal and it's composition back to the element. The sum of all those phases is the life cycle of a product. The LCA enables to track and monitor the environmental impact of products over the entire life and to recognize the factors of environmental impacts

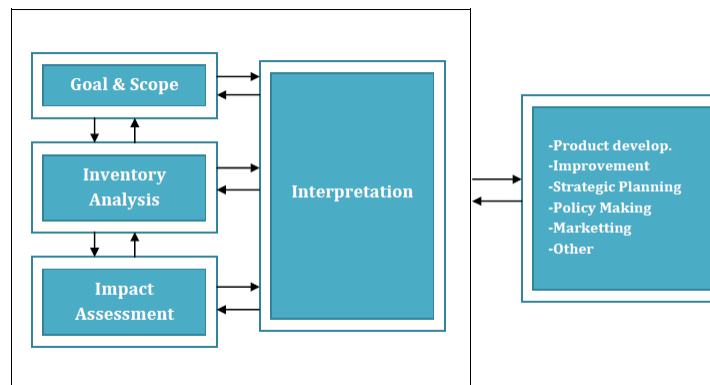


Figure 1. Life Cycle Assessment Framework (Source: ISO, 2006)

Cassiano Moro Piekarski defined, " Life cycle assessment is an entrepreneurial tool for firms to achieve sustainable results through of renewed vision about business management and green innovations" [3]. Arun kumar defined LCA " as a systematic analytical method to identify, evaluate and minimize the environmental impacts of a product through every step of it's life from transformation of raw materials into useful products and the final disposal of all products and it's byproducts" [2]. Stephen Finnegan, defined " LCA as a technique used for carrying out quantitative analysis of the environmental aspects of a product or service over its entire life cycle that allows for analysis of environmental aspects of a product and provides an assessment of the potential impacts on the environment" [6]. Darko Milankovic described " LCA as a basis for establishing an environmental policy and is generally used to guide the clean production, development of green production, and the environmental harmonization design" [4]. LCA Expert Jim Fava and N. Dasilva defines, " the LCA is a tool which assess the impacts of product on environment and human health through the life cycle of product, process and activity and enable the practitioners to model the entire product system." [15]

The life cycle assessment has its applications in various functions of organization. In Product development process, the LCA is used in decision making, planning and implementation of product development projects [3]. Yang & Chen, used the LCA tool for the development of eco-friendly products and evaluated the environmental performance of product during it's design stage [17]. In Improvement process the LCA helps to evaluate the environmental impacts of material and processes therefore, one can identify the harmful materials and the processes which can be replaced by another one having lesser or zero impact. In Strategic planning the LCA has the application in the design of supply chain in which the life cycle indicators are incorporated into the green supply chain building. The evaluation and identification of environmental burdens helps to frame the environmental policies in the manufacturing organization. In marketing the LCA have the application to develop a green marketing strategy based on the recyclability and reuse of the product. [3]

III. Literature Review

The process of finding out the various life cycle impact areas, their analysis & interpretation, current practices & case studies and databases requires a exhaustive literature review of the authors who have made the

research in the concerned area. Reputed journals from Science Direct and others were selected for literature survey. Articles, handbooks of national and international government authorities and reference books from year 2000 to 2013 were taken into account. Keywords like “Life cycle assessment, Life cycle inventory, Input-output models, Environmental impacts, Life cycle performance indicators , Life cycle decision making, Recycling models, LCA databases & softwares” were given more importance in literature study. About 2/3rd of research papers belongs to the year between 2010-2013. The below Pie chart shows the year wise distribution of literature review.

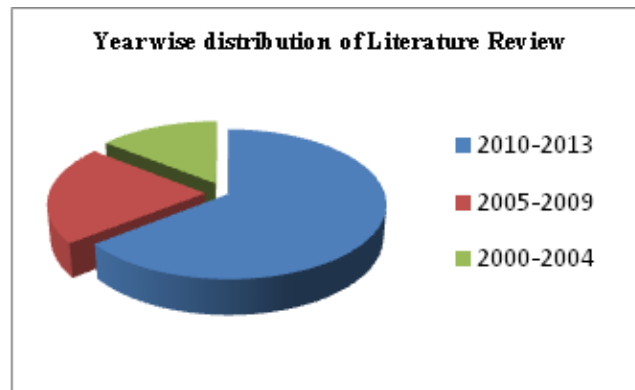


Figure 2. Year wise distribution of Literature Review

IV. Methodology

From last decade the efforts towards the development of LCA methodology has increased throughout the globe for the evaluation of the environmental performance based on the life cycle assessment of product. The International standard organization has developed and standardize the methodology for LCA across the world in the form of ISO 14040 series (ISO, 2006a & ISO, 2006b) [18] [19]. Following are the stages & techniques through which the life cycle of rolls throughout the life cycle is achieved.

1. Goal and Scope –

This phase consist of identification of the problem, scope and boundaries of the analysis. In order to achieve this the relevant questions and their answers are formulated which gives clear idea of the intended application. Following are some questions and their relevant answers to identify the goal and scope of this research.

- *On Which Product the research is to be carried out and why?*

The research is to be carried out on Rolls of cold rolling mill. The fast growth of manufacturing sector worldwide has created business opportunities but concurrently increased substantial environmental problems also. The burdens of air emissions, waste material, depleting resources occur at all stages of a product’s life cycle. Awareness about environmental protection is growing all over the globe. Therefore, it is very important to assess the environmental performance of a product throughout the life cycle of it’s various phases, so that from obtained results, the manufacturers can take the decisions related to material selection, process selection, and type of energy to be fed.

The Rolls of cold rolling mill are subjected to high compressive and torsional stresses. As a result, the rolls brakes/cracks at a point where the diameter suddenly reduces, as the stress concentration is higher at that point. It cannot be reused by applying welding or any other process and has to scrapped. Hence, new manufacturing of rolls is required to fulfill the need. This new manufacturing creates the heavy environmental and human health burden through extraction of raw material, manufacturing process, use phase and recycling which consumes several inputs and emits outputs in the form of resources and emissions respectively. This burden can be reduced by evaluating the environmental performance of product and accordingly taking the corrective actions in selection of energy use, material and processes.

- *What is the material of Rolls of cold rolling mill?*
Alloy Steel. (Contents: C, Si, Mn, P&S, Cr, Mo, Ni)
- *What are basic inputs (Resources) and outputs (Emissions) of rolls during it’s life cycle?*
Basic Inputs: Material, electricity, non-renewable fuels, water etc.
Basic Outputs: Usable product, airborne emission, solid wastes, water effluents and other releases.
- *What is the boundary of this Research?*

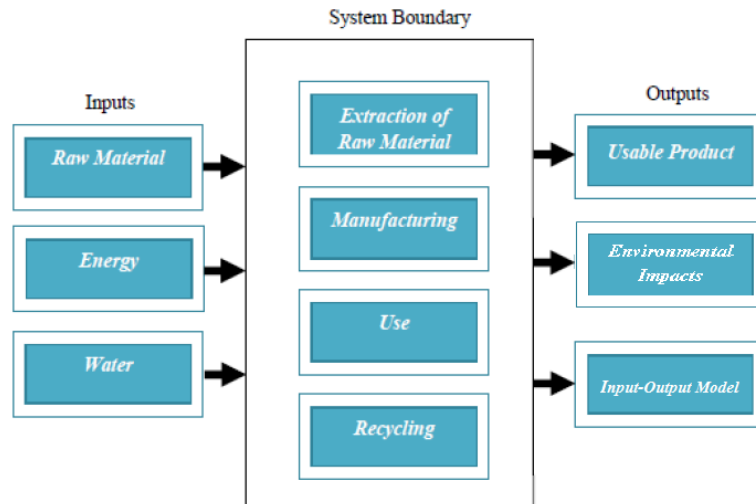


Figure 3. Boundary of Assessment (Source: World steel Association 2011)

The assessment is limited to the rolls of cold rolling mill only. Further, the impacts produced by rolls in LCA study are considered during extraction of raw material, manufacturing, use phase and recycling. In order to keep the analysis traceable, this LCA limit the scope of analysis only for the major inputs at each stage. In case all the minor inputs are to be taken into account then one has to approach different suppliers, which will lead to high cost, time and issues related to variable data. As a result, the LCA cannot deliver the expected results and becomes highly complex. From the above fig.3 we can understand the boundaries of this research.

- *In what way the input output model throughout the lifecycle can be formed?*

The rolls of cold rolling mill are assessed during the extraction of raw material, manufacturing, use phase and recycling. The inputs and outputs during each unit process are quantified and are evaluated for each phase of its life cycle with the help of GaBi software. From the fig. below we can understand the basic input-output model.

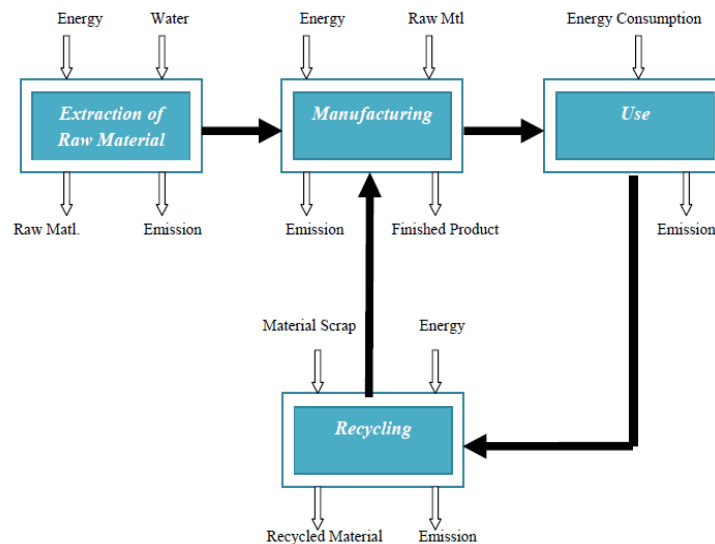


Figure 4. Input-Output model (Source: Tom N.Lighthart,2012)

2. Data Collection –

The data for raw material extraction and recycling phase is obtained from several national and international public databases, resource directory of European Reference Life Cycle Database (ELCD), International Reference Life Cycle Data System (ILCD), LCT forum, softwares tool GaBi , journal papers for variety of material/products and basic services that are needed in every LCA. [9] [20]

The data for manufacturing phase is obtained by actual self observations & calculations and conducting interviews of managers, engineers & workmen at factory, while the data for use phase is obtained from customers/end users of company by conducting interviews and addressing them a set of questionnaires.

3. Life Cycle Inventory –

The detail description of Life cycle inventory (LCI) has given in the ISO 14041 standards [2]. This is the most important phase and forms the base for LCA. Life cycle inventory deals with the development of the product system. The rolls during its life phase undergoes to extraction of raw material, manufacturing, use phase and recycling. During, each phase the product system requires several inputs in the form of resources like material, energy, water etc and outputs in the form of emissions & wastes like CO₂, SO₂, NO_x etc which creates heavy burden on environment as well as on human health. Therefore, in this phase at each unit process the inputs and outputs of a product system are quantified. The process comprises of identification of the flows at input as well as output side and their respective quantitative data are obtained in relation to the functional unit. The functional unit is the reference unit of the measurement that quantifies the performance of the outflows of the product system. The main objective of inventory analysis is to perform mass and energy balances to quantify the material, energy and emission balances. Finally, the results of the inventory analysis is often a long list with disparate entries such as carbon dioxide, nitrogen oxide, chloromethane, mercury etc. [7] [10]

4. Life Cycle Impact Assessment –

The detail description of Life cycle impact assessment (LCIA) has given in the ISO 14042 standards. Impact assessment consist of classification, characterisation, normalisation and weighting. In classification various environmental impacts are classified into impact categories like Global warming potential, Acidification potential, Eutrophication potential, Ozone layer depletion potential, Abiotic depletion elements, Abiotic depletion fossil, Freshwater aquatic ecotoxicity potential, Human toxicity potential, Marine aquatic ecotoxicity potential, Petrochem.ozone creation potential, Terrestrial ecotoxicity potential. The characterisation involves evaluation of the magnitude of the impacts under each impact category by converting the quantities under each category into equivalent quantities of a reference impact (e.g. methane into an equivalent amount of CO₂ under the global warming category) which gives one single impact indicator for each impact category. Further, optionally characterisation results may be normalised in order to relate the results to a reference value such as annual global or European extent of each impact. Finally, a weighting step may be performed in which priority weights are assigned to the characterisation or normalisation results and which may give one final score for each alternate product system [2] [4].

5. Interpretation –

The detail description of life cycle impact assessment (LCIA) has given in the ISO 14043 standards. It is the last stage of life cycle assessment where a final judgement and decision is outspoken, consist of identification, quantification, data check and evaluation of the information from the results of previous phases of life cycle inventory and life cycle impact assessment. It mainly deals with the meaning and robustness of the information obtained and processed in the previous phases, comprises of comparisons with previously published LCA studies on similar product, uncertainty, sensitivity analysis, data checks and external comments. The ultimate outcome of this phase is the identification of the conclusions and recommendations. [2] [8]

V. Conclusion

The life cycle assessment tool with an appropriate methodology alongwith the use of GaBi software tool enables to develop an input–output model of the product system for the rolls. The model works as a map which shows the flows to and from the system and their respective magnitude. The assessment enables to take the corrective actions in selection of material, energy use and the processes which imparts less harm to the environment and human health. Besides, LCA tool helps the management in strategic planning, product development, marketing and improvement. The same methodology can be applied to other products as well, and the aggregation of environmental performance of all products gives the overall environmental performance of the firm which helps the company in framing internal environmental policies accordingly. The environmental consciousness about the products, enables to take the competitive advantage, gain higher market share, obtain customer faith and good reputation in society.

References

- [1]. James W. Levis, [2013] A generalized multistage optimization modeling framework for life cycle assessment – based integrated solid waste management, *International journal of sustainable Resources, Conservation and Recycling*, Vol. 73 (2013) pp.211– 228
- [2]. Arun Kumar [2013], Methodology used for life cycle assessment of electrical generation through coal – fired thermal power plants in India- A Review, *International Journal of Emerging Technology and Advanced Engineering* Volume 3, Special Issue 3: ICERTSD 2013, Feb 2013, pages 545-548
- [3]. Cassiano Moro Piekarski [2013], Life cycle assessment as entrepreneurial tool for business management and green innovations, *Journal of Technology Management & Innovation*, 2013, Vol.8, Issue 1.
- [4]. Darko Milankovic, Brainsilav Milanovic [2013], Life cycle assessment of an intermodal steel building unit, *RMZ*2013|Vol.60| pp.67-72
- [5]. S.J. McLaren [2013], Scoping of Life cycle assessment studies: A missed opportunity? The 6th International Conference on Life Cycle Management in Gothenburg 2013.
- [6]. Stephen Finnegan [2013], Life Cycle Assessment and its role in improving decision making for sustainable development, *Engineering Education for Sustainable Development*, Cambridge, UK. September 22 – 25, 2013
- [7]. Tom N Lightart and Toon, M.M Ansems, [2012] Modelling of Recycling in LCA, Available from <http://www.intechopen.com/books/post-consumer-waste-recycling-and-optimal-production/modelling-of-recycling-in-lca>
- [8]. M.Karpagam, Geetha Jaikumar, [2012] A Book on Green Management, Ane Books Pvt. Ltd.
- [9]. Javier Sanfeliix [2012] The Enhanced LCA resources Directory: A tool aimed at improving life cycle thinking practices, *International journal of life cycle assessment*.
- [10]. Goran Finnvedan, Michael Hauschild [2009], Recent developments in life cycle assessment, *Journal of Environmental Management*, page 1-21.
- [11]. Ken Alston [2008], Cradle to Cradle Design Initiatives: Lessons and opportunities for preventions through design (PtD), *Journal of Safety Research*, Vol. 39, 135-136.
- [12]. Satish Joshi [2000], Product Environmental life cycle assessment using input output techniques, *Journal of Industrial Ecology*, Vol.3, Number 2&3.
- [13]. United Nations Environment Programme [2002], Life Cycle Initiative homepage. <<http://www.uneptie.org/pc/sustain/lcinitiative/home.htm>>
- [14]. World Steel Association [2011], Life Cycle assessment methodology report, 1-88.
- [15]. N.dasilva, J.Fava [2009], Framework for a Life Cycle Assessment, Communications & Society Program, The Aspen Institute.
- [16]. Life cycle assessment [1997], A guide to approaches, experiences and information sources, *Environmental Issues Series* no.6.
- [17]. Yang, C.J., Chen, J. L. [2012]. Forecasting the design of ecoproducts by integrating TRIZ evolution patterns with CBR and Simple LCA methods. *Expert Systems with Applications*, 39, (3), 2884–2892.
- [18]. ISO, 2006a. ISO 14040 International Standard. In: *Environmental Management – Life Cycle Assessment – Principles and Framework*. International Organisation for Standardization, Geneva, Switzerland.
- [19]. ISO, 2006b. ISO 14044 International Standard. In: *Environmental Management – Life Cycle Assessment – Requirements and Guidelines*. International Organisation for Standardisation, Geneva, Switzerland
- [20]. International Reference Life Cycle Data System [2012], Towards more sustainable production and consumption for a resource-efficient Europe, JRC reference report.

A Study of Performance and Emissions of Diesel Engine Fuelled With Blends of Cotton Seed Oil Methyl Ester and Petro-Diesel

Dr. C. Solaimuthu¹, Dr. S. Chitra², Prof. P. Rajasekaran³, G. Jagadeeshkumar, P. C. Pradeep, N. Raqibudeen, M. Vikram⁴

¹Professor cum Director (Research), Department of Mechanical Engineering, Er. Perumal Manimekalai College of Engineering, Hosur – 635 117, Tamil Nadu, India

²Principal, Er. Perumal Manimekalai College of Engineering, Hosur – 635 117, Tamil Nadu, India

³Assistant Professor and Head, Department of Mechanical Engineering, Er. Perumal Manimekalai College of Engineering, Hosur – 635 117, Tamil Nadu, India

⁴U.G Scholars, Department of Mechanical Engineering, Er. Perumal Manimekalai College of Engineering, Hosur – 635 117, Tamil Nadu, India

ABSTRACT: The engine performance and emission characteristics of Cotton Seed oil biodiesel (Cotton Seed Oil Methyl Ester) and its blends with petro-diesel are presented. The engine tests are conducted on a 4-Stroke Tangentially Vertical (TV1) single cylinder kirloskar 1500 rpm water cooled direct injection diesel engine with eddy current dynamometer at nozzle opening pressure 230 bar with standard static injection timing of 23° bTDC maintained as constant throughout the experiment under steady state conditions at full load condition. From the test results, it could be observed that the B25 blend gives optimum performance like higher brake thermal efficiency lower specific fuel consumption and lower emissions like lower in smoke density and oxides of nitrogen. The research findings show that B25 gives lowest emissions which make it a good alternative fuel to operate diesel locomotives without any modification in existing diesel engine.

Keywords: Cotton Seed Oil; Biodiesel; Nozzle Opening Pressure; Static Injection Timing; Performance; Combustion; Emissions

I. Introduction

Researchers of internal combustion engine group have always focused towards engine performance and emission control in economical and environmental aspects. Diesel engine which is being used in various sectors like transportation, railways and agriculture has high thermal efficiency durability and reliability of usage. India being an agricultural country, producing a large variety of vegetables, a thorough and wide investigation is required to find an appropriate vegetable to produce biodiesel. This research attempts to use radish seed oil to investigate its suitability as a biodiesel as radish seed oil has cetane number as close to that of neat diesel fuel. In the forthcoming decades, the eco-friendly and vital biofuels will serve as an alternative for conventional petroleum fuel which will be under hectic shortage. A brief literature review of research work carried out by various researchers is presented below. The cotton seed oil methyl ester gives optimum performance compared to neem oil methyl ester [1]. The performance and emission control characteristics of various biofuels have been carried out [2, 3]. Vegetable oil as a suitable alternate fuel for compression ignition engine is in its pure form or blended with petroleum diesel. Moreover biodiesel is better than diesel based on some of its physical properties like sulfur content, flash point, aerometric content and biodegradability [4]. The diesel engine operation was carried out with 1,4 dioxine- ethanol-diesel blends on diesel engines with and without thermal barrier coating. The blend ratio of 70% diesel, 20% ethanol and 10% dioxane blend gives better performance and lower emissions [5]. The operation was carried out on a DI diesel engine fuelled with pure Mahua oil methyl ester (B100) and neat diesel (B0). The B100 gives the lower emissions as compared with B0 [6]. The report of the biodiesel preparation was done and discussed its performance and emission characteristics of diesel engine with B0 and B100 fuel. The Mahua Oil Methyl Ester (B100) burn more efficiently than diesel (B0) and the emissions of B100 is lower than that of B0 [7]. The neat Marotti Oil Methyl Ester (MOME) gives lower emissions like hydrocarbon and oxides of nitrogen as compared to neat diesel for all load conditions [8]. From the previous studies, it could be observed that most of the studies are mainly related to the performance and emission characteristics of diesel engine using biodiesel as fuel. In this paper an analysis of four stroke TV single cylinder

DI with different nozzle opening pressures of 230 bar and with a constant static injection timing of 23° bTDC at full load condition of the diesel engine with eddy current dynamometer using B0, B25, B50, B75 and B100 as fuel is presented.

II. Materials And Methods

2.1 Characterization of the Oil

The properties of the oil were first measured to determine if pretreatment is necessary or not before alkaline transesterification. It was found that the free fatty acid value of the oil is 0.23% of NaOH by volume which is high for direct alkaline transesterification as it can react with the catalyst to form soap which can inhibit methyl ester yield. The water content is 10% which is a little bit too high for uninhibited transesterification hence the oil is heated to 110° C and held constant for 30 minutes to allow some of the water to evaporate.

2.2 Transesterification Procedure

Generally, vegetable oils contain fatty acids (palmitic, stearic, oleic, linoleic, lignoceric, eicosenoic, arachidic and behenic). Of these cotton seed oil contains the saturated fatty acids palmitic (hexadecanoic acid) and stearic (octadecanoic acid) and the unsaturated acids oleic (octadec-9-enoic acid) and linoleic (9,12-octadecadienoic acid). The cotton seed oil is commercially available in the local market and used as the raw material. Transesterification process is the reaction between a triglyceride and alcohol in the presence of a catalyst to produce glycerol and ester. To complete the transesterification process stoichiometrically, 3:1 molar ratio of alcohol to triglycerides is needed. However, in practice, higher ratio of alcohol to oil ratio is generally employed to obtain biodiesel of low viscosity and high conversion. Among all alcohols that can be used in the transesterification process are methanol, ethanol, propanol and butanol. Methanol and ethanol are widely used and especially methanol because of its low cost. Vegetable oil is made to react with methanol in the presence of catalyst which produces mixture of alkyl ester and glycerol. This oil can be produced by a base catalyst process. Cotton seed oil is transesterified using methanol as reagent and NaOH as catalysts, to yield biodiesel (Cotton Seed Oil Methyl Ester).

III. Experimental Setup And Procedure

Experiments have been conducted on a 4 stroke, kirloskar, Tangentially Vertical single cylinder (TV1) direct injection (DI) diesel engine developing power output of 5.2 kW at 1500 rpm connected with water cooled eddy current dynamometer.

IV. Results And Discussion

4.1 Specific Fuel Consumption (SFC)

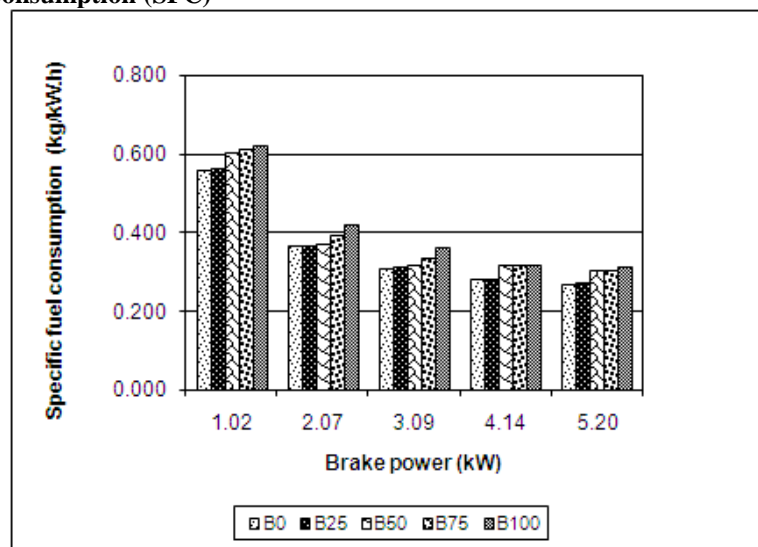


Figure 1: Specific Fuel Consumption vs Brake Power

The variation in specific fuel consumption for B100 to B0 is shown in Figure 1. From this figure, it is seen that the B0 and B25 give lowest specific fuel consumption of 0.54 and 0.29 kg/kWh respectively for both the fuel at no load and full load. However, the B100 gives the highest specific fuel consumption of 0.64 and

0.32 kg/kWh respectively at no load and full load. For B100, the percentage increase in specific fuel consumption at no load and full load is 11.39% and 16.23% respectively as compared to B0 and B25. The same trend is observed for all blends of fuel. The Specific fuel consumption decreases with the increase in load for all blends of fuel. However, at each load B0 and B25 have the lowest specific fuel consumption and these increase with the blend value. This is due to comparatively higher viscosity and lower calorific value. This is due to increase in fuel quantity with increase in load which causes better utilisation of air leading to better combustion. At no load, diesel engines operate with very lean mixture.

4.2 Brake Thermal Efficiency (BTE)

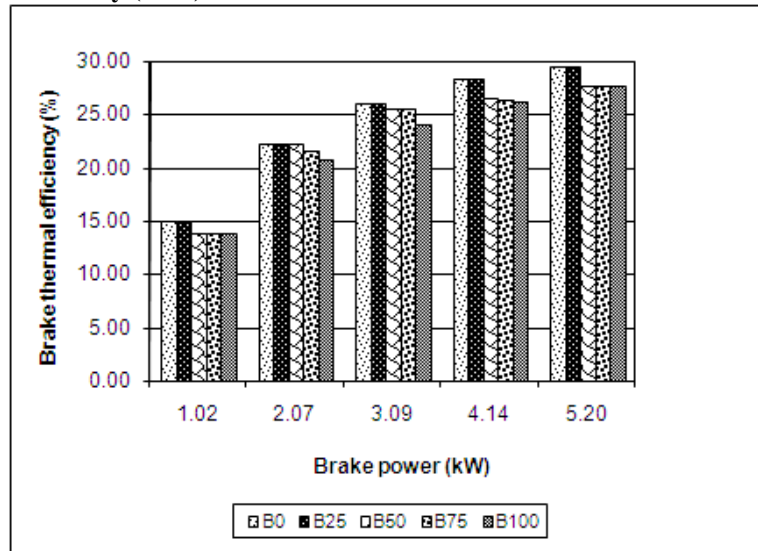


Figure 2: Brake Thermal Efficiency vs Brake Power

Figure 2 shows variation of brake thermal efficiency with respect to brake power for B100 to B0. As can be seen, B0 and B25 have almost the same maximum brake thermal efficiency of 14.72% and 29.34% for both the fuel at no load and full load condition, respectively. It may be noted that at all loads, B100 gives lower brake thermal efficiency. At no load and full load, the brake thermal efficiency for B100 is 7.35% and 6.35% is lower compared to B0 and B25 fuel. The same trend is observed for all blends of fuel. The Brake thermal efficiency depends on heating value and specific gravity. The combination of heating value and mass flow rate indicate energy input to the engine. This energy input to the engine in case of B50, B75 and B100 are more compared to neat diesel. This may be the reason to have lower brake thermal efficiency for all blends of fuel as compared with B0.

4.3 Smoke Density (SD)

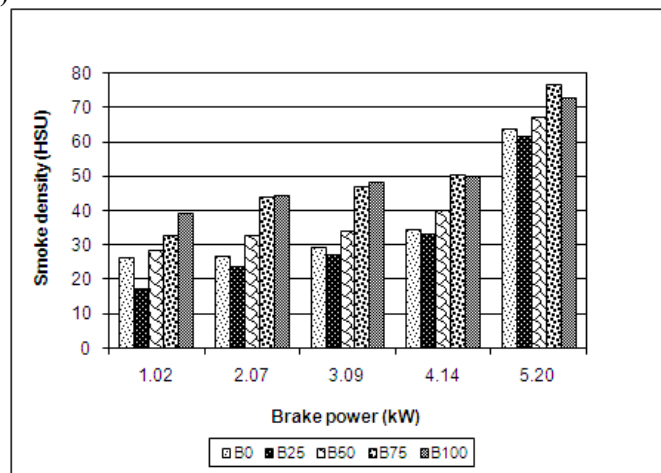


Figure 3: Smoke Density vs Brake Power

Figure 3 shows the variation of smoke density over the complete load range. It can be seen from figure 3 that for all blends including neat diesel the smoke density increases with load. This is to be expected, because in diesel engine which is a quality governed engine, the combustion depends upon the local air fuel ratio. Increase in load at constant speed is achieved by increasing the fuel quantity. It is evident that at no load, B25 has the lowest smoke density of 16.5 HSU, whereas B100 has the highest smoke density of 38.3. It is interesting to note that B25 emits lower smoke compared to neat diesel (B0). This may be due to the chemistry of fuel blend which may promise conducive atmosphere for lower smoke density for B25 compared to B0. Further at no load, the engine is operating at very lean mixture. As the load is increased from no load to 75% there is only gradual increase in smoke density. However, the smoke density for B25 is lower than B0 over their load range for the reasons explained above B75 and B100 are almost bunching together in this load range. It can also be seen from Figure 3, as the load increases from 75 to 100%, there is a steep rise in the smoke density for all the blends, as well as neat diesel. This is to be expected because more fuel is injected into the engine to take care of the load. As the engine is running at constant speed of 1500 rpm, there is less time for complete combustion to take place which can cause an increase in smoke density.

4.4 Oxides of Nitrogen (NO_x)

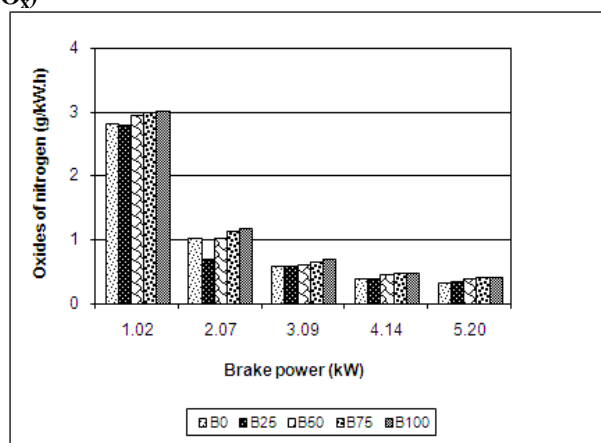


Figure 4: Oxides of Nitrogen vs Brake Power

The variation in NO_x for B100 to B0 is shown in Figure 4. It is evident that the maximum NO_x (g/kWh) is 3.34 for B100 whereas for B0 is 2.53 at no load. At full load, the maximum NO_x of 0.45 for B100 whereas for B0 it is 0.36. The variation in NO_x at full load is higher at no load condition of B100 as compared with B0 fuel. At full load, the percentage reduction in NO_x for B100 is 8.45% as compared with B0 whereas at no load the variation in NO_x is 2.45%. However, the B75 blend gives better reduction in NO_x as compared with B0, B25, B50 and B100 at full load condition. The percentage reduction in NO_x for B75 is 9.56% as compared to B0 fuel at full load condition of the engine whereas at no load, the percentage reduction in NO_x is 4.54% for B75. The percentage reduction in NO_x for B100 is 1.14% as compared to B75 fuel. This is due to decrease in exhaust gas temperature. It is well known that vegetable based fuel contains a small amount of nitrogen. This contributes towards the NO_x production.

V. Conclusions And Recommendations

From this study, it could be concluded that the B25 gives optimum performance and lower emissions of SD and NO_x. Finally, it is concluded that B25 could be used as a viable alternative fuel to operate four-stroke tangentially vertical single cylinder direct injection diesel engine with nozzle opening pressure of 230 bar and static injection timing of 23° bTDC, thereby saving 25% of the precious petro-diesel fuel.

Acknowledgement

The authors have thanked the Chairman **Er. P. Perumal**, Secretary **Shri. P. Kumar** and Trustee **Smt. P. Mallar** of Er. Perumal Manimekalai College of Engineering, Hosur, Tamil Nadu, India for providing the support and encouragement for investigating the Performance of Diesel Engine at I.C Engines Laboratory, Department Mechanical Engineering.

References

- [1] K Dilip Kumar and P. Ravindra Kumar, Experimental Investigation of Cotton Seed Oil and Neem Methyl Esters as Biodiesel on CI Engine, *International Journal of Modern Engineering Research*, 2(4), 2012, 1741-1746.
- [2] Hanbey Hazar, and Huseyin Aydin, Performance and emission evaluation of a CI engine fuelled with preheated raw rapeseed oil (RRO) – Diesel blends. *Applied Energy* 87, 2010, 786-790.
- [3] Deepak Agarwal, and Avinash Kumar Agarwal, Performance and emissions characteristic of Jatropha oil (preheated and blends) in a direct injection compression ignition engine. *Applied Thermal Engineering*, 27, 2007, 2314- 2323.
- [4] Syed Ameer Basha, K. Raja Gopal, and S. Jebaraj, A review on biodiesel production, combustion, emissions and performance. *Renewable and Sustainable Energy Reviews* 13, 2009, 1628-1634.
- [5] C Sundarraj, S. Arul, S. Sendilvelan, and C.G Saravanan, Performance analysis of 1,4 dioxine-ethanol-diesel blends on diesel engines with and without thermal barrier coating, *Thermal Science*, 14, 2010, 979-988.
- [6] N Saravanan, G. Nagarajan, S. Puhan, Experimental investigation on a DI diesel engine fuelled with Madhuca Indica ester and diesel blend, *Biomass and Bioenergy*, 34, 2010, 838-843.
- [7] S Puhan, N. Vedaraman, G. Sankaranarayanan, V. Boppana and B. Ram, Performance and emission study of Mahua oil (madhuca indica oil) ethyl ester in a 4-S natural aspirated direct injection diesel engine, *Renewable Energy*, 30, 2005, 1269-1278.
- [8] R Karthikeyan, Dr. C. Solaimuthu, and N. Balakrishnan, A Study of Performance and Emissions of Diesel Engine fuelled with neat Diesel and neat *Hydnocarpus Pentandra* biodiesel, *IOSR Journal of Mechanical and Civil Engineering*, 10(2), 2013, 53-57.

Transmission Error in Gear

Deepak Malviya¹, Dr. Pushpendra Kumar Sharma²

¹(Deepak Malviya, scholar student of Mechanical department, NRI-IST, Bhopal, India)

²(Dr. Pushpendra Kumar Sharma, Head & Guide of Mechanical Department, NRI-IST Bhopal, India)

ABSTRACT: The power transmission by the gears is mostly used in the industries, automobile gearbox, robotics office automation etc. and this is possible mostly by the gearing. Gearing is one of the most critical components in mechanical power transmission systems. Transmission error is to be one of the main contributors to noise and vibration in gear set. This paper aim is to know about the gear "Transmission error". Transmission error is considered to be an important excitation mechanism for gear noise and vibration. The definition of transmission error is "the difference between the actual position of the output gear and the position it would occupy if the gear drive were perfectly conjugate". The gear transmission error that widely occurs in the actual gear system which arise because of irregular shape tool geometry imperfect mounting misalignment of two gear and so on. The influence of transmission error cannot be determined by investigating the gears only.

I. Introduction

Gearing transmissions have a long history dating back since the time of the first engineering systems. Their practical usage in the present day modern engineering system is enormous. In accordance with a contemporary development of mechanical engineering techniques ever growing requirements and working specifications. Along with modern high speed manufacturing industry development, gear are used widely in many applications ranging from automotive transmission to robot and aerospace engines. Different kinds of metallic gears are currently being manufactured for various industrial purposes. Seventy-four percent of them are spur gears, fifteen percent helical, five percent worm, four percent bevel, and the others are either epicyclical or internal gears. The main purpose of gear mechanisms is to transmit rotation and torque between axes. The gear is a machine element that has intrigued many engineers because of numerous technological problems arises in a complete mesh cycle. If the gears were perfectly rigid and no geometrical errors or modifications were present, the gears would result in a constant speed at the output shaft. The assumption of no friction leads to that the gears would transmit the torque perfectly, which means that a constant torque at the output shaft. No force variations would exist and hence no vibrations and no noise could be created. Of course, in reality, there are geometrical errors, deflections and friction present, and accordingly, gears sometimes create noise to such an extent that it becomes a problem. Transmission error occurs when a traditional non-modified gear drive is operated under assembly errors. Transmission error is the rotation delay between driving and driven gear caused by the disturbances of inevitable random noise factors such as elastic deformation, manufacturing error, alignment error in assembly.

II. Transmission Error

Theoretically, for two gears with perfect involutes and an infinite stiffness, the rotation of the output gear would be a function of the input rotation and the gear ratio. A constant rotation of the input shaft would therefore result in a constant rotation of output shaft. Due to both intended shape modifications and unintended modifications, such as manufacturing errors, gears will be a motion error of the output gear relative to the input gear.

The transmission error and mesh stiffness variation is often considered to be the primary excitation of gear noise and a minimization of the transmission error is believed to minimise noise. The definition of transmission error is "the difference between the actual position of the output gear and the position it occupy if the gear drive were perfectly conjugate". The transmission error can be measured statically or dynamically, unloaded or loaded shown in the table.

		Load (Torque)	
		Low	High
Speed	Low	Static unloaded	Static Loaded
	High	Dynamic Unloaded	Dynamic Loaded

III. Static Transmission Error

The main source of excitation in gearboxes is generated by the meshing process. Researchers usually assume that transmission error and variation in gear mesh stiffness are responsible of noise radiated by the gearbox. The transmission error characteristics depend on the instantaneous situations of the meshing tooth pairs. Under load at very low speed (static transmission error), these situations result from tooth deflections and manufacturing errors.

Under operating conditions, the mesh stiffness variation (due to variations in the length of contact line and tooth deflections) and the excitation located at teeth mesh point generate dynamic mesh force which is transmitted to the housing through shafts and bearings. Noise radiated by the gearbox is closely related to the vibratory level of the housing.

Predicting the static transmission error is a necessary condition to reduce noise radiated from the gearbox. Various researchers deals with estimation of static transmission error and mesh stiffness variations of gears. They are worked based on a 3D finite element analysis of tooth deflections, using two different modelling and solvers.

Two methods are used to solve the static equilibrium of the gear pair, in order to estimate load distribution and static transmission error, for a set of successive positions of the driving wheel. Different modelling of a generic gear pair have been built in order to analyse the effect of wheel body deformation and interactions between adjacent loaded teeth. They have found satisfied results.

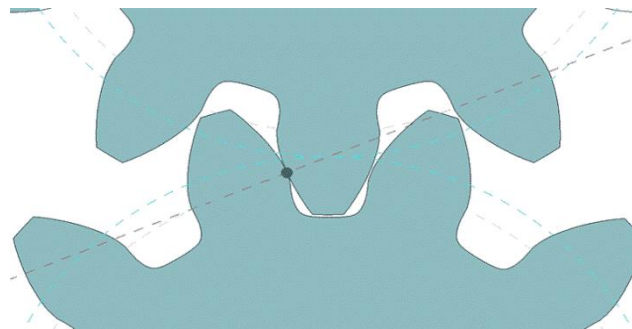


Figure-1

IV. Dynamic Transmission Error

The most relevant transmission error measurements for noise and vibration predictions are probably the dynamic. When measuring dynamic transmission error, the gears should be in the gearbox, because the dynamical properties of the system consisting of gears, shaft, bearings and casing are important. Dynamic transmission error is taken as the parameter for the modelling of noise in geared transmission. In the last two decades there is plenty of work has been concentrating on modelling of the dynamic transmission error for spur and helical gears and representing the influence of the dynamic transmission errors on the level of noise in the geared transmission. Lately, there have been several experiments conducted in order to isolate particular noise effects like noise, meshing action noise and backlash noise simply by measuring the dynamic transmission error. For different analysis purpose, there are several modelling choices such as a simple dynamic factor model, compliance tooth model, torsional model, and geared rotor dynamic model. Using the free vibration analysis critical parameters such as natural frequencies and vibration modes that are essential for almost all dynamic investigations can be calculated.

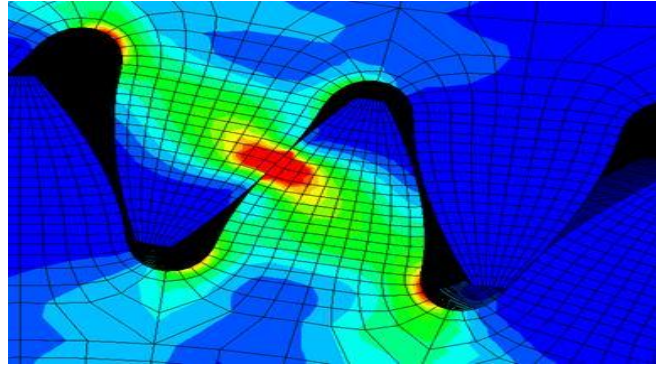


Figure-2

V. Conclusion

The contribution of this paper work presented here can be summarized as follows the aim of the work is highlight factors to generate the transmission errors in gears and its adverse effect on the gearing. There are various points consider to cause of transmission error is generate in gearing. First problem is very common do not proper mountings of gears for conjugate action, manufacturing error during operation such as milling of gears, hobbing of gears etc., tooth mesh stiffness and load variation on the gears. These problems to radiate noise and vibrations during operating condition of gears. In this paper to review literary, various papers to overcome the transmission error and its effect. Thus the static transmission error overcome by the proper mountings of gears for proper meshing and the dynamic transmission error overcome by the modelling of the gears on FEM.

Aknowledgement

The auther wishes to acknowledge the project guide Dr. Pushendra Kumar Sharma, Head of Department Nri-ist Bhopal, India, for their continual guidance.

REFERENCES

- [1] Dr. Raghu Kumar research paper on "Transmission Error on Spur Gear".
- [2] Volvo Construction Equipment components ABSE-631 85 Eskilstuna, Sweden "Gear Noise and Vibration-A Literature Survey".
- [3] Evgeny Podzharov "Static and Dynamic Transmission Error in Spur Fears".
- [4] Mats Henriksson "On Noise Generation and Dynamic Transmission Error of Gears" Department of Aeronautical and Vehical Engineering.
- [5] Vera Nikolic "Dynamic Model for the Stress and Strain State Analysis of Spur Gear Transmission".
- [6] Emmauel RIGAUD "Modelling And Analysis Of Static Transmission Error-Effect Of Wheel Body Deformation And Interactions Between Adjacent Loaded Teeth"

Detection of DC Voltage Fault in SRM Drives Using K-Means Clustering and Classification with SVM

V. S. Chandrika¹, A. Ebenezer Jeyakumar²

¹(Department of EEE, P.S.V. College of Engineering and Technology, Krishnagiri Dt., Tamilnadu, India

²(Sri Ramakrishna Engineering College, Coimbatore, Tamilnadu, India

ABSTRACT: This paper presents a new method of detection of DC voltage fault in SRM drives based on K Means Clustering technique. Also the range of fault is classified using Support Vector Machines (SVM). Switched reluctance motors are very popular in these days, because of ease in manufacturing and operation. Though an electronic circuit can detect the fault like under voltage and over voltage but, the classification cannot be done effectively with electronic circuitry. More over an intelligent method can easily identify the fault and classify and hence the root cause of the fault may be guessed and rectified using this method of classification. The information used to include this intelligence in the system are just torque waveforms. Moreover, the early detection minimizes the faulty operation time and ensures the plant stability and saves the life of motor too. Hence a system to detect such fault under a simulation model has been proposed in this study.

Keywords: K Means Clustering, SRM (Switched Reluctance Motor), SVM (Support Vector Machines)

I. Introduction

The applications of SRM in aircraft and industrial automations applications are enormous and need a perfect flaw free operation to obtain the required electrical and mechanical outputs from the motor [1]. The absence of rotor windings and permanent magnets in rotor makes the manufacturing of SRM easy and hence the SRM is very popular in market based on commercial aspects too. The special feature of SRM is that, a particular phase of SRM is not influenced by the other phase and is very negligible. Hence, the motor continues to rotate even at faulty conditions but it might not produce the exact required output parameters based on mechanical aspects. So, early detection of the faults in SRM is mandatory. The salient pole configuration of the SRM is responsible for ripples in torque, anyhow that can be minimized using the works in [2]. The major issue with faulty operation is that, though the motor continues to rotate, the mechanical forces become imbalanced and the mechanical power decrease proportional to the number of phases disconnected from the circuit.

Open circuit faults have not been given much importance in earlier literatures except [1]. Open circuit can be easily identified with the presence or absence of the phase current. A typical electronic circuit would do it. But the circuit fails to classify the faults if the numbers of faults are more and more over the time instant of fault occurrence is never known with circuit based detection. In addition to the above said draw backs of circuit based detection, the circuits needs the sensors which are likely to fail. Also the number sensors to be used is proportional to the number of phases, which considerably increases the cost of the system. Hence a processor based intelligent device may be suitable at these circumstances.

Fault tolerant systems are abundant in market, in which the motor can continue with its operation even at faulty conditions like, open, short and phase to phase shorts as given in [3]. This study would be a main source for all other further AI based fault detection systems. But such models were unable to classify the various faults, so remedial action could not be taken against the faults. The authors of this study feel that apart from the fault detection, fault classification becomes essential in order to impart intelligence to the machines. As in [4] certain works had been done using fuzzy controller to stabilize the SRM. The papers [1], [5], [6], [7] and [8], discusses about the various power converters and faults likely to occur and methods to detect the faults. To the best of the author's knowledge, clustering algorithms and SVM based classification techniques had not been used in SRM fault detection.

This study has been organized as follows: Section II, describes the concept of K means clustering techniques, Section III deals with SVM classification techniques, Section IV discusses about the proposed method and the simulation outputs are discussed in section V.

II. K-Means Clustering

Clustering is a method of grouping similar data into various groups based on the amplitude of the data points. This is an iterative scheme to find the local minimal solution. This clustering method has been clearly shown in [9]. Optimal placement of the center at centroid is the technique behind this algorithm. Let us suppose that N numbers of data points are the outcome of an experiment. These data points are clustered into K number of clusters, with each cluster consisting the number of elements which depends on the value of the data points. Mathematical investigation of k means algorithms is beyond the scope of this study. In our work, the feature vectors for detecting the DC voltage fault is extracted from using this k means clustering. The corresponding waveforms and results are shown in section V.

III. Support Vector Machine Based Classification

The basic idea behind the SVM classification technique is to identify the class of the input test vectors. This is a supervised learning algorithm, where the training vectors are used to train the system to map these training vectors in a space with clear gaps between them using some standard kernel functions and the input test vectors are mapped on to the same space to predict the possible class. The choice of the kernel functions have been discussed in [1]. Given some training data D, a set of n points of the form:

$$D = \{(x_i, y_i) | x_i \in \mathbb{R}^p, y_i \in \{-1, 1\}\}_i^n = 1 \quad (1)$$

Where, y_i is either belonging to the class 1 or class-1, which means the class which the point x_i belongs. Each x_i is a p-dimensional real vector. While classifying, it is essential to find the maximum possible margin hyper plane that segments the data sets having $y_i = 1$ from those data sets having $y_i = -1$. So any hyper plane can be written as data sets X satisfying maximum possible margin hyperplane and margins for an SVM trained with samples from two classes. Samples exactly on the margins are called the support vectors:

$$W \cdot X - b = 0 \quad (2)$$

Where \cdot denotes the dot product and is the normal vector to the hyper plane. The term $b/\|w\|$ determines the offset of the hyper plane from the origin along the normal vector W. In case, the training data sets are linearly separable, then two hyper planes can be constructed in such a way that they group the data sets and there are no points between them and then tried to increase the distance among them. The region surrounded by them is called "margin".

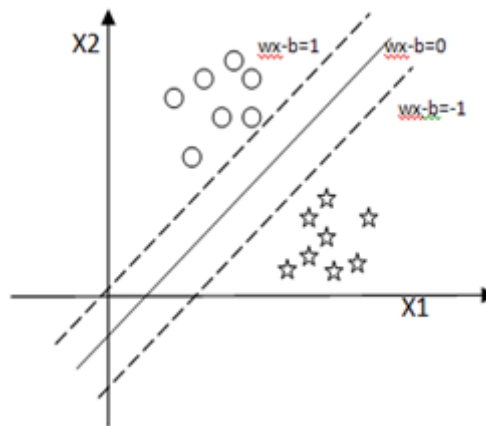


Figure 1: SVM Scenario

These hyper planes can be described by the equations:

$$w \cdot x - b = 1 \quad (3)$$

and

$$w \cdot x - b = -1 \quad (4)$$

Fig. 1 shows the process of how two data sets (one represented by circles and the other set by stars) are classified in two different regions while a linear kernel is used for classification. In the testing phase, the data points x_i are separated using the following constraints $w \cdot x_i - b \geq 1$ for x_i of the first class or $w \cdot x_i - b \leq -1$ for x_i of the second class.

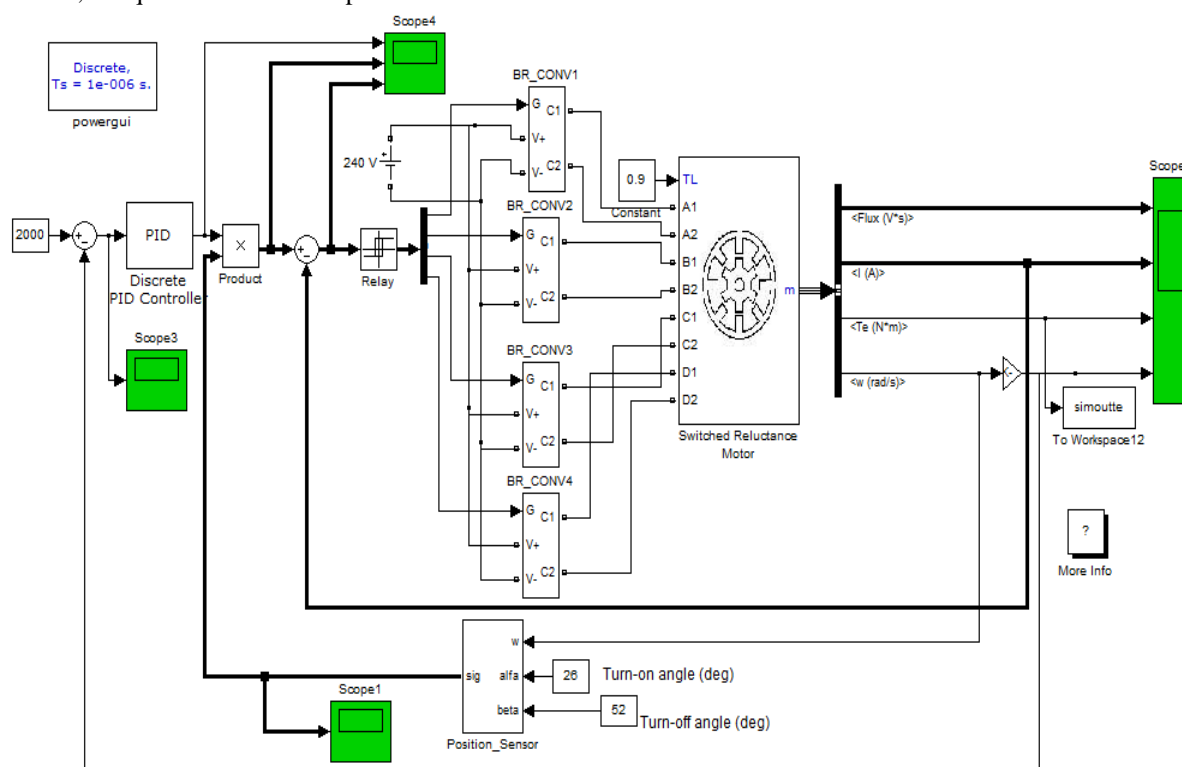
IV. Proposed Fault Detection Method

There exist two types of motoring operation based on the health of motors, Normal operation and faulty operation. These modes of operation are well discussed in [1]. The major contribution in this study is to detect

the dc voltage fault and classify it. This method of detecting the fault is achieved through an efficient method of feature selection and classification. DC voltage shift directly reflects in the magnitude of the torque ripples hence the range of torque ripples can be used to detect the range of DC voltage. These online values of torque data is clustered and features are classified to find the voltage fault. This method is very useful when the electrical drive circuit is far away from the worksite of the motor. The DC voltage faults usually create a flux to deviate from its healthy condition. These flux values are clustered to find the mean value of the data points and number of data points in each class. This is done using k means clustering. These clustered values are classified using Support Vector Machines (SVM).

V. Simulation And Outputs

Fig. 2 shows the simulation model of the proposed fault detection method for DC voltage fault. First the SRM drive is simulated at healthy condition and the corresponding Flux, Stator current, Torque variations and Speed outputs are obtained. Then the DC voltage faults are created and the same parameters, Flux, Stator current, Torque variations and Speed are shown.



DC voltage Fault detection in Current-controlled 8/6 Switched Reluctance Motor drive

Figure 2: Simulation model of SRM

5.1. Healthy Conditions

A Matlab simulink model of the SRM drive with 8/6 configuration has been designed and simulated with all the switches at perfect healthy conditions. The parameters have been shown at steady state. Load torque is set as 0.9. Fig. 3 shows the output of the healthy SRM drive with a speed of 2000 rpm ,where it can be noted that, the torque ripples have an offset of 9 N-m . The parameters like, Flux, Stator current, Torque variations and Speed are shown.

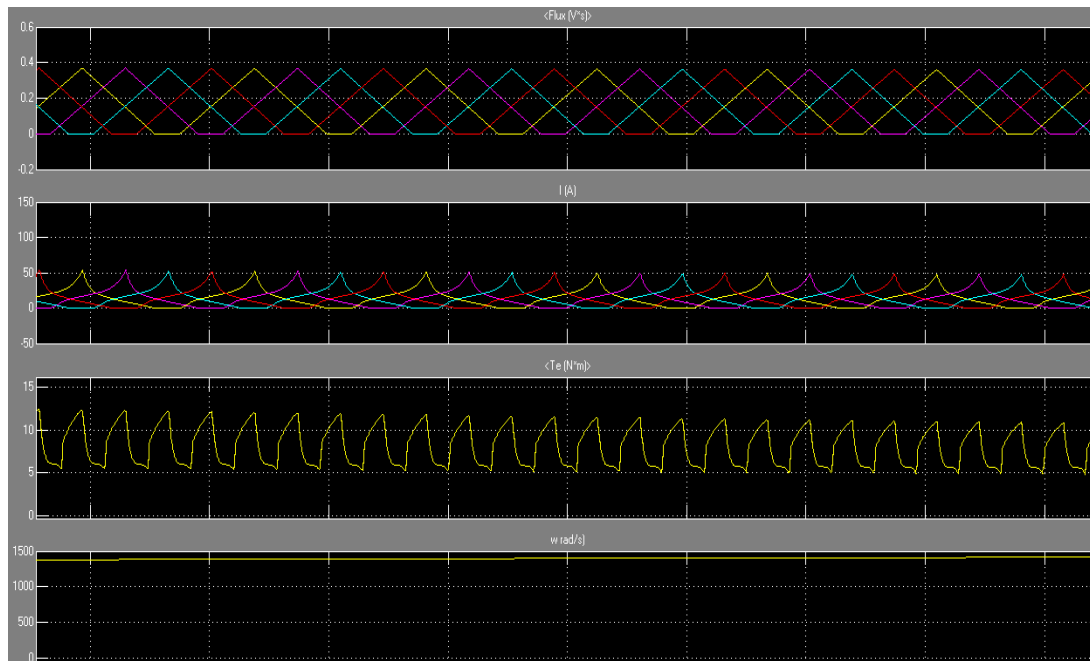


Figure 3: Steady state waveforms of flux, current, torque and speed at healthy conditions

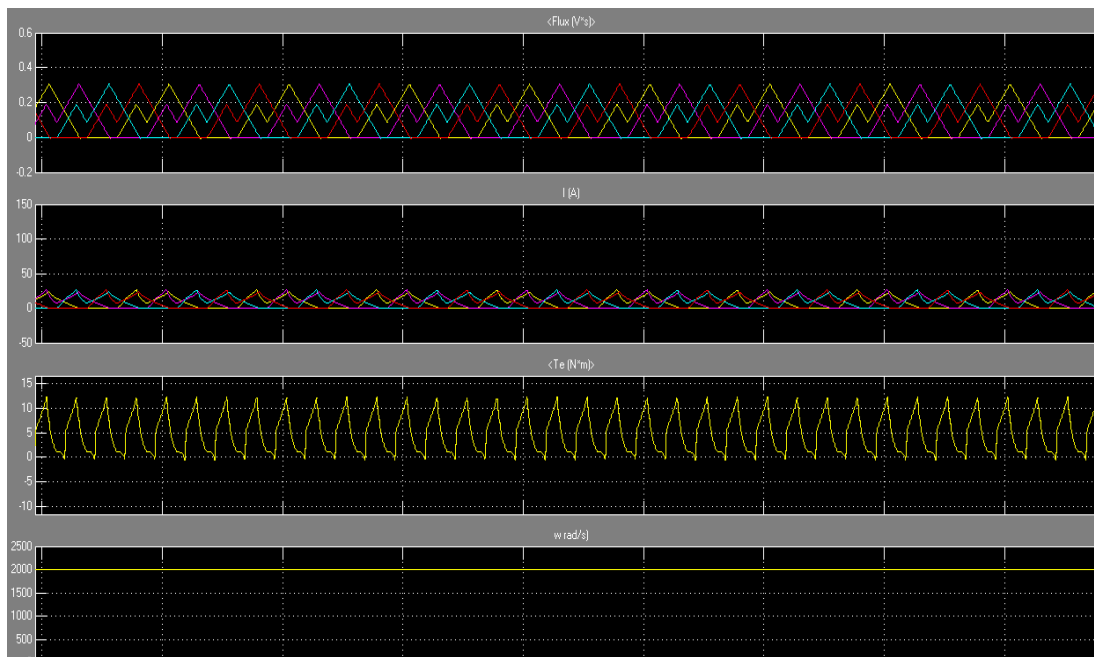


Fig. 4. Waveforms of flux, current, torque and speed at dc voltage fault

5.2 DC Voltage Fault Conditions

DC voltage fault is nothing but, a variation in the DC link voltage which is to be inverted further to apply for stator coils. This reduction or increase in DC will reflect in dc offset of ripples in torques, the offset in the captured waveform is around 5 N-m. So the major task is to follow the torque waveforms. This method is very suitable to detect the faults when the control circuit and the motor is at a distant place. In this DC voltage faults, $k = 10$ is chosen to cluster the torque wave-forms. Two voltage conditions of 240 V, a full rated voltage and 120V, half of the rated voltages were applied to excite the SRM. Based on the number of elements in cluster, Classification using SVM is performed to identify the DC bus fault. The faulty torque waveforms at $V=120$ volts is shown are shown in the Fig. 4.

VI. Conclusion

In this study, a K - Means clustering based method to detect the DC voltage fault in SRM and classification based on SVM has been implemented. Hence, earlier detection of DC voltage faults increases the life time of the SRM. Implementation of this simulation as a real time system requires a high speed processor to perform all mathematical calculations along with high speed Analog to digital converters at online. The future extension of this work may be concentrated on multiple DC levels of the input voltage, and the major merit in our work is that this method can be applied to any type of motors.

Acknowledgements

Our thanks to the support extended by the P.S.V College of Engineering and Technology, Krishnagiri.

REFERENCES

- [1]. Natália, S. Gameiro and Antonio J. Marques Cardoso, 2012. A New method for power converter fault diagnosis in SRM drives. *IEEE Trans. Industry Applic.*, 48: 653-662. DOI: 10.1109/TIA.2011.2180876
- [2]. Xue, X. D., K.W.E. Cheng and S.L. Ho, 2009. Optimization and evaluation of torque-sharing functions for torque ripple minimization in switched reluctance motor drives. *IEEE Trans. Power Electron.*, 24: 2076-2090. DOI: 10.1109/TPEL.2009.2019581
- [3]. Sivakumar, M. and R.M.S. Parvathi, 2013. Particle swarm and neural network approach for fault clearing of multilevel inverters. *American Journal of Applied Science*, 10: 579-595. DOI: 10.3844/ajassp.2013.579.595
- [4]. Paramasivam, S. and R. Arumugam, 2004. Real Time Hybrid Controller Implementation for Switched Reluctance Motor Drive, *American Journal of Applied Science*, 1: 284-294. DOI: 10.3844/ajassp.2004.284.294
- [5]. Schinnerl, B. and D. Gerling, 2009. Analysis of winding failure of switched reluctance motors. *Proceedings of the IEEE International Electric Machines and Drives Conference*, May 3-6, IEEE Xplore Press, Miami, FL, pp: 738-743. DOI: 10.1109/IEMDC.2009.5075287
- [6]. Gameiro, N.S. and M.A.J. Cardoso, 2010. Power converter fault diagnosis in SRM drives based on the dc bus current analysis. *19th International Conference on Electrical Machines*, Sept. 6-8, IEEE Xplore Press, Rome, pp: 1-6. DOI: 10.1109/ICELMACH.2010.5608258
- [7]. Terec, R., I. Bentia, M. Ruba, L. Szabó and P. Rafajdus, 2011. Effects of winding faults on the switched reluctance machine's working performances. *Proceedings of the 3rd IEEE International Symposium on Logistics and Industrial Informatics*, Aug. 25-27, IEEE Xplore Press, Budapest, pp: 143-148. DOI: 10.1109/LINDI.2011.6031137
- [8]. Miremadi, A., H. Torkaman and A. Siadatan, 2013. Maximum current point tracking for stator winding short circuits diagnosis in switched reluctance motor. *Proceedings of the 4th Power Electronics, Drive Systems and Technologies Conference*, Feb. 13-14, IEEE Xplore Press, Tehran, pp: 83-87. DOI: 10.1109/PEDSTC.2013.6506678
- [9]. Shanmugam, N., A.B. Suryanarayana, S. TSB, D. Chandrashekar and C.N. Manjunath, 2011. A novel approach to medical image segmentation. *Journal of Computer Science*, 7: 657-663. DOI: 10.3844/jcssp.2011.657.663
- [10]. Gomathi, M. and P. Thangaraj, 2010. A computer aided diagnosis system for lung cancer detection using support vector machine. *American Journal of Applied Science*, 7: 1532-1538. DOI: 10.3844/ajassp.2010.1532.1538

Design, Analytical Analysis, Instrumentation and Flow Simulation of Sub-Sonic Open Circuit Wind Tunnel Model

Tomar Vishvendra Singh¹, Sangwan Vipul², Singh Shaktiman³,
Singh Raj Kumar⁴, Agrawal Jubin⁵

^{1,2,3,4}Department of Mechanical Engineering, Delhi Technological University, Delhi, 110042, India

⁵Department of Mechanical Engineering, ABES-IT, Ghaziabad, 201009, India

ABSTRACT: The Wind Tunnel is well known for its enormous amount of potential in Civil, Environmental, Automobile and Aeronautical applications. In today's world, Everyone's main focus is to save time, material and money which have compelled us to opt for the experimental testing on scale models, before the final product is to be shaped. The Wind Tunnel is one such platform, which provides us the appropriate desired environment conditions around the model scaled to the compatible dimensions. Therefore, to develop the favorable conditions, the design of the tunnel plays the foremost role in its proper functioning. In this paper, knowing the intricacy of the tunnel's requirements, A Sub-Sonic Open Circuit Wind Tunnel (SOWT) Model is developed and simulated, having a Mach Number (M) of 0.15. The guiding dimensions taken for the Test Chamber are: Length (L_T) = 45cm, Height (H_T) = 18cm and Width (W_T) = 24cm with maximum operating speed to be 50m/s. Using these, the secondary design parameters were estimated and the design is finalized. Moreover, the instrumentation of the Tunnel including Data Acquisition Systems (DAQs) is reviewed.

Keywords: Sub Sonic Open Circuit Wind Tunnel, Mach number, Boundary Layer Modeling Parameters, Model Testing and Simulation.

I. Introduction

Today, the wind tunnel is an indispensable part of development of modern aircraft, automobile etc as no one would contemplate committing an advanced design without first measuring its stability, lift and drag properties. The utility of the wind tunnel is obvious, but it was not the first aerodynamic test device. The quest to measure drag and various aspects of aviation theory started with the very first advancement in aviation with the introduction to whirling arm. The whirling arm apparatus (4 feet long) was developed by Benjamin Robins (1707-1751), a brilliant English mathematician. It spun by a falling weight acting on a pulley and spindle arrangement having velocities of only a few feet per second at the arm tip (top speeds ranging from 3 to 6 m/s). The large amount of turbulence posed serious problems in front of experimenters like in determination of the true relative velocity between the model and air. Also, it was difficult to mount the instruments and measure the small forces exerted on the model when it was spinning at high speeds. Francis Herbert Wenham (1824–1908), a council member of the Aeronautical Society of Great Britain, addressed the issue by inventing, designing and operating the first enclosed wind tunnel in 1871. After some of the experimental studies, it was found that lift-to-drag ratios were very high as such wings could support substantial loads, making powered flight which seemed much more attainable than previously thought possible. Further research work revealed the effect of what is now known as aspect ratio: long, narrow wings, like those on modern gliders, provided much more lift than stubby wings with the same areas [1-3].

Wilbur Wright (1867-1912) and Orville Wright (1871-1948) built their first flying machine in August 1899 and then their first unpowered manned glider in 1900. However, the glider was generating far less lift and more drag than they expected. They developed a simple experiment using natural winds to compare the relative lifting forces of flat and cambered surfaces. Then they built an aerodynamic balance that showed unambiguously, which test airfoil (among the two being tested) can develop more lift. Thus for the first time "Wind Tunnel without Walls" was subjected to test. It confirmed the accepted aerodynamic design tables that they were using, were seriously in error. This helped them in rectification of the wing area, airfoil curvature. During the experimental work, they reached at conclusion that without synthesizing a well equipped wind tunnel they could not continue their work anymore as such they developed the wind tunnel in its true sense and helped themselves to trigger the flight! [1, 4]

Wind tunnels are designed for a specific purpose and speed range. Therefore, there are different types of wind tunnels and several different ways to classify wind tunnels. On the basis of Speed Regime developed in the test section relative to the speed of sound (Mach Number 'M'), Wind Tunnels are classified as subsonic ($M < 0.8$), transonic ($0.8 < M < 1.2$), supersonic ($1.2 < M < 5.0$), hypersonic ($M > 5.0$). On the basis of Tunnel Geometry, Wind tunnels are classified as Closed Circuit Wind tunnel (CCWT) and Open Circuit Wind Tunnel (OCWT) (Fig. 1). A wind tunnel that is closed and re-circulates the air through the test section is called a Closed Circuit Wind Tunnel. A wind tunnel that is open on both ends and draws air from the atmosphere into the test section is called an Open Circuit Wind Tunnel [5, 6].

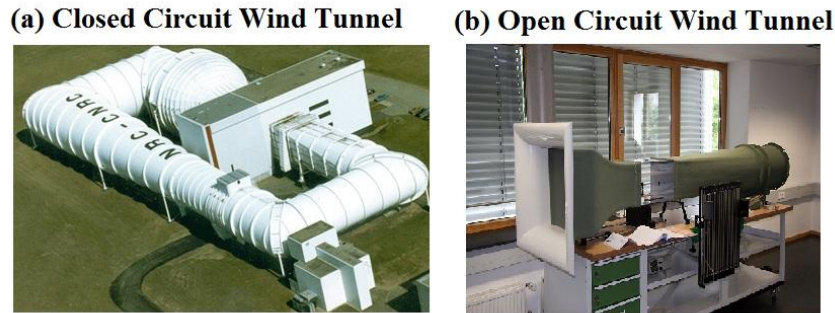


Fig. 1: Classification of Wind Tunnels on the basis of Tunnel Geometry as (a) Closed Circuit Wind Tunnel and (b) Open Circuit Wind

The OCWTs Models are used to investigate the different automotive designs by testing on scale models of cars, trucks etc. Airflow over a vehicle determines the drag forces, which in turn affects the vehicle's performance and efficiency. The three basic forces are lift, drag, and side force as measured in an axis system referenced to the direction of the vehicle. The concept of Lift and Drag can be understood with the help of airfoil. The airfoil long in the direction perpendicular to the plane of the drawing and the flow can be considered as two dimensional. The airfoil is tilted with respect to the (undisturbed) flow direction, defined by the angle of attack (AOA). The force experienced by airfoil is F_R . Decomposing the force F_R into components F_L and F_D {Given by (1) and (2)} perpendicular and parallel to the flow direction. F_L is termed as lift force and F_D is termed as drag force, the resistance to be balanced by the propulsion force generated by the engines (Fig. 2). The expressions for Lift and Drag Forces are as follows:

$$F_L = 0.5 C_L \rho A_1 u^2 \quad \dots(1)$$

$$F_D = 0.5 C_D \rho A_2 u^2 \quad \dots(2)$$

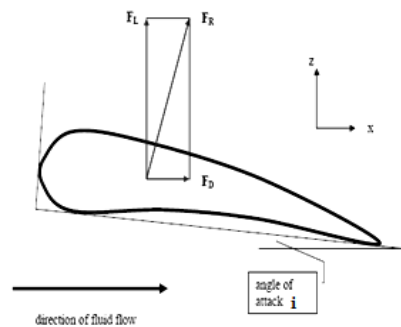


Fig. 2: Lift and Drag Forces on Airfoil subjected to fluid flow

The designer of an airplane tries to maximize C_L and to minimize C_D . C_L and C_D are dependent on the angle of attack. Usually the C_L drops sharply and C_D increases strongly at $i = 15^\circ$ (approx.) [7].

Wind tunnels have been used widely to simulate airflow about complete aircraft, specific aircraft components, and to conduct fundamental research concerning flow phenomena related to flight for over a century. Wind tunnels are made in different shapes and sizes, from just 30 cm long to large enough to contain a passenger airplane. The various sorts of Wind Tunnels find potential applications in estimation of pollution dispersion level near the building, investigation of wind-driven rain and building envelop, various aspects of wind loading on roofs and wind effects on towers and bridges. In Wind Engineering, wind tunnel tests are used

to measure the velocity around, and forces or pressures upon structures. Very tall buildings, buildings with unusual or complicated shapes (such as a tall building with a parabolic or a hyperbolic shape), cable suspension bridges or cable stayed bridges are analyzed in specialized atmospheric boundary layer wind tunnels. The basic idea behind all wind tunnels is universal. Depending upon the situations like thermal and hydraulic testing, it generates uniform air flows with low turbulence intensity. The aerodynamic principles of the wind tunnel work equally on watercraft, except the water is more viscous and so sets greater forces on the object being tested. External flow tunnels are used to study the external flow through the chassis climatic tunnels and used to evaluate the performance of door systems, braking systems etc. under various climatic conditions. Aero-acoustic tunnels are used in the studies of noise generated by flow and its suppression. Wind tunnel tests are also performed to measuring the air movement of the fans, Turbine Blades, Propellers etc at a specific pressure exactly [3, 8-12].

A lot of research work have been accomplished to optimize the Wind Tunnel Design and still to make it better at various levels depending upon the situations research work is still in progress. Peter et al. in their work, focused on the wind tunnel test section flow quality and its application to a numerical CCWT by studying the effects of various variables for its evaluation [8]. Diana et al. evaluated the design criteria that supported the choice of the original solution for potential application of a new large wind tunnel in Civil, Environmental and Aeronautical aspects and discussed the feasibility of a plant on the basis of experimental analysis on a 1:9 scale model [13]. Lohan [14] focused on the design and application of LSWTs having well-defined, controllable, uniform flow of air for experimental and design validation purposes. Senol and Cinar with the help of Flow Simulation Fluent 6.0 program corrected the earlier developed design of a suction-type SOWT by simulating it in computer environment [15]. Eckert et al. discussed some Aerodynamic design guidelines and computer program for estimation of SSWT performance [16]. The enormous amount of research work and experiments undertaken in wind tunnels and their importance for human life motivated the high demands that are posed on optimum design level for Wind Tunnels against the minimum cost with optimum output. This paper deals with the Sub-Sonic Open Circuit Wind Tunnel (SOWT) with negligible effect of compressibility. Following the research works and significant guidelines related to design consideration, the design for SOWT Model is developed. The Mach Number of 0.15 allows it to use for aerodynamics tests and performance of some scale models having speeds around 150 km/hr.

II. Design of Sub Sonic Open Circuit Wind Tunnel Model

The Wind tunnels cannot be perfect simulations of environmental conditions, but up to some extent they can be treated as ideal to surrounding conditions. The degree to which they are flawed is measured with the help of Reynolds Number. The SSWTs are designed to provide a well-defined, controllable, uniform flow of air for experimental and design validation purposes. These tunnels when applied as open circuit cannot be used where a very high accuracy level and precise results are required due to their inability to control air flow up to a large extent. However, with proper designs and controlled instrumentation, these tunnels can be made to produce accurate results within close limit to practical value. The major advantage associated with this tunnel is its Set-Up and Maintenance Cost, which is very small as compared to CCWT. The leading manufacturer of automobiles use the OCWTs for the Drag and performance estimation of the vehicles as with current technology & designs, these tunnels are giving results quite close to practical values under proper calibrations.

The OCWT (Fig. 3) consists of five basic parts, which are (From front to back) the Settling Chamber, the Contraction Cone, the Test Section, the Diffuser and the Drive Section. The Settling Chamber is at the very front of the wind tunnel and is made up of screens and honeycomb-shaped mesh, which straighten out the air and reduce turbulence. The Contraction Cone forces a large volume of air through a small opening in order to increase the wind velocity in the tunnel, as there is gradual decrease in area. The Test Section is the place where a model is mounted on sensors. The Diffuser is at the end of the Test Section and keeps the air running smoothly as it goes toward the back. It also increases in volume in order to slow the air down as it exits the tunnel. The Drive Section is at the very back of the wind tunnel, and it is where the fan is housed and draws air into the wind tunnel by blowing air out of it and hence reduces turbulence along with greater control of the airflow through the tunnel. The decisive characteristic of wind tunnels lies in the flow quality inside the test chamber and the overall performances.

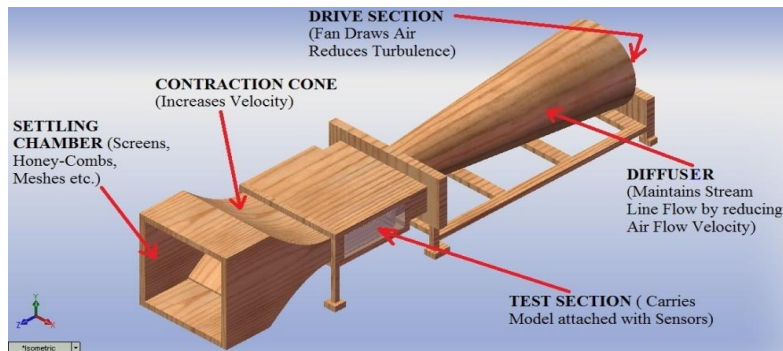


Fig. 3: Isometric View of Sub-Sonic Open Circuit Wind Tunnel Model developed Solid-Works

Three main criteria that are commonly used to define them are: maximum achievable speed, flow uniformity and turbulence level. Hence in general, the design aim of a wind tunnel is to get a controlled flow in the test chamber, achieving the necessary flow performance and quality parameters. The main specifications for a wind tunnel are the dimensions of the test section and the desired maximum operating speed. Also, it is crucial to avoid flow separation close to the walls of the contraction zone. In the subsequent sections, the design of each of the component of the Wind Tunnel is developed one by one, from the design of the Test Chamber to the Diffuser.

2.1 Test Chamber Design

The test chamber (Fig. 4) is the most delicate part of the tunnel and is also called as “The Heart of the Wind Tunnel” as it is the region for experimental study, carrying the scale model, sensors etc along with the controlled flow. Its size must be defined according to the wind tunnel main specifications, which also include the operating speed and desired flow quality. Its size and operating speed determine the maximum size of the models and the maximum achievable Reynolds number. In most of the cases, its cross-section is square in shape and its area should be decided according to the scale model which is going to be tested. The equivalent frontal area of the model should not be higher than 10% of the test chamber cross-sectional area. The width to height ratio adopted for 3-D Tests is 4:3. The Test Section Assembly is composed of the Test Section (Plexiglas) to avoid pressure loss and the Test Section Base (wooden stand and sensor mounts) [14-19].

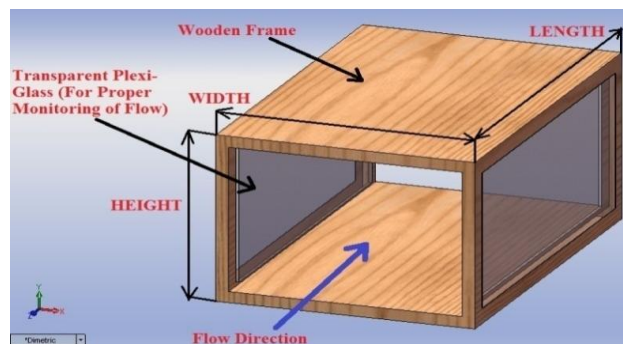


Fig. 4: Dimetric View of The Test Chamber developed using Solid-Works.

2.2 Contraction Cone Design

The Contraction Cone is the most important part in the design of a Wind Tunnel as it has the highest impact on the Test Chamber flow quality. It accelerates the flow from the Settling Chamber to the Test Chamber as such also known as ‘Nozzle’. It also helps in reduction of flow turbulence and non-uniformities in the test chamber. The flow acceleration and non-uniformity attenuations mainly depend on the ratio of cross-section area of inlet to that of exit, termed as contraction ratio (N). Theoretically, the value of N should be as large as possible but it has an upper limit as it strongly influences the overall wind tunnel dimensions and hence its cost. For the Wind Tunnels used in civil or industrial applications, a contractions ratio between 4.0 and 6.0 may be sufficient reducing the flow turbulence and non-uniformities levels to the order of 2.0%, which is acceptable for many applications. Further with just one screen placed in the settling chamber it reduces to 0.5%. Even this is a very reasonable value for some aeronautical purposes.

$$N \text{ (Contraction Ratio)} = \frac{\text{Area at entry of C.C.}}{\text{Area at exit of C.C.}} \dots(3)$$

The second characteristic of the contraction cone is its shape, taking into account that the contraction is rather smooth. For this 1-D (One-Dimensional) approach to the flow analysis is applied to determine the pressure gradient along it. The important point of consideration is the pressure distribution on the contraction walls, as if it has some regions with adverse pressure gradient, it may produce local boundary layer separation which can increase the turbulence level considerably, resulting in poor flow quality in the test chamber. The solution to this is to make the ratio of the radius of curvature to the flow width about the same at each end. But at the upstream end the radius of curvature cannot be too large as it leads to slow acceleration and therefore increased rate of growth of boundary-layer thickness which causes centrifugal instability in the tunnels having laminar flow. The contraction semi-angles: $\alpha/2$ and $\beta/2$ are taken to be in the order of 12° , this causes the contraction cone to possess a reasonable length and a good fluid dynamic behavior. Bradshaw et al. recommended two segments of third degree polynomial curves for deciding the exact curve (Fig. 5) for the Contraction Cone [14-20]. The polynomials are:

$$y = a_W + b_W X + c_W X^2 + d_W X^3 \dots(4)$$

$$y = a_N + b_N X + c_N X^2 + d_N X^3 \dots(5)$$

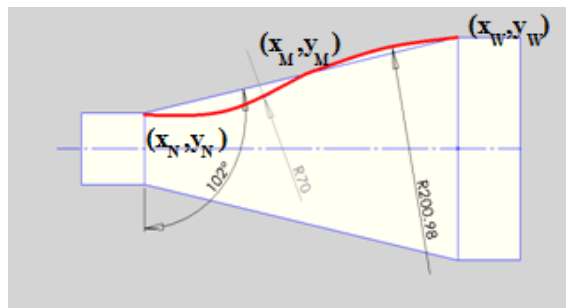


Fig. 5: Fitting Polynomial for the Contraction Cone Curve developed using Solid-Works

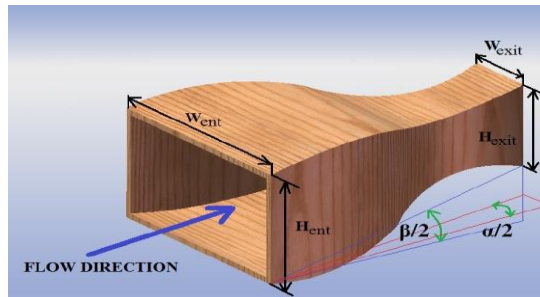


Fig. 6: Isometric View of The Contraction Cone developed using Solid-Works

The Contraction Cone developed using the above curve (Fig. 6) doesn't allow boundary layer to separate and keep boundary layer thickness within certain limit. It provides the favorable flow to the Test Chamber.

2.3 Settling Chamber Design

The Settling Chamber (Fig. 7) is the very first region designed to provide controlled high quality flow to the Contraction Cone by attenuating the various flow components responsible for turbulence. To develop high quality flow some devices like screens and honeycombs etc are installed to increase the flow uniformity and to reduce the turbulence level at the entrance of the contraction cone. They produce a relatively high total pressure loss. Honeycomb is very efficient at reducing the lateral turbulence, as the flow pass through long and narrow pipes. But the problem with Honeycombs is, it introduces axial turbulence of the size equal to its diameter which restrains the thickness of the honeycomb. To tackle this problem, Screens are introduced as they reduce longitudinal turbulence very efficiently. In this case, the problem is that in the Contraction Cone the lateral turbulence is less attenuated than the longitudinal one. Hence, to obtain better flow characteristics, a combination of Honeycombs and Screens is used. This configuration requires the honeycomb to be located upstream of 1 or 2 screens [14-21].

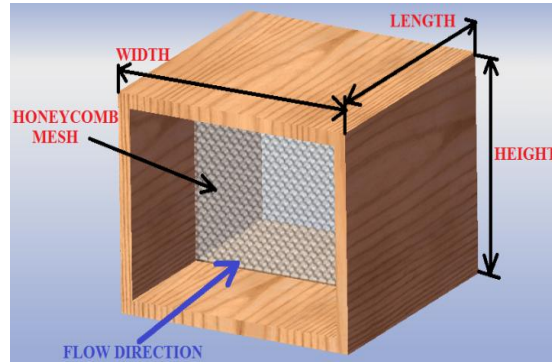


Fig. 7: Isometric View of The Settling Chamber developed using Solid-Works

2.4 Diffuser Design

The Diffuser (Fig. 8) plays an important role in controlling the flow quality inside the Test Chamber by avoiding the flow detachment as in case of flow detachment; the pressure pulsation is transmitted upstream into the test chamber, resulting in pressure and velocity non-uniformities. To avoid flow detachment, the maximum semi-opening angle in the diffuser has to be smaller than 3.5° [14-21].

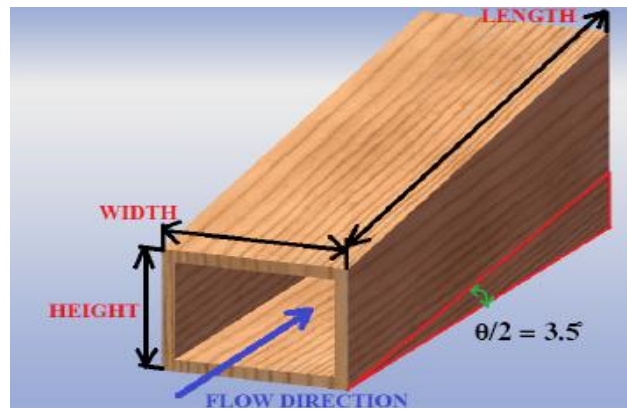


Fig. 8. Dimetric View of The Diffuser developed using Solid-Works.

III. Analysis of Sub Sonic Open Circuit Wind Tunnel Model

The Primary Design Parameters for the overall design of the Wind Tunnel include Test chamber dimensions i.e. Width (W_T), Height (H_T) and length (L_T). With the help of these parameters cross-sectional area of the Test Chamber can be calculated as $A_T = W_T \cdot H_T$. The hydraulic diameter is given by the relation [14-21]:

$$D_T = \frac{2 W_T H_T}{(W_T + H_T)} \quad \dots(6)$$

The Contraction ratio (N) is taken 5 for the Wind Tunnel with Mach number ($M=0.15$), having Maximum operating speed (V_T) to be 50 m/s. These Design variables can be summarized in the Table. 1. The dimensions for the Test Section are $W_T = 24\text{cm}$, $H_T = 18\text{cm}$, $L_T = 45\text{cm}$ and the V_T is taken to be 50m/s which gives us the Mach Number (M) to be 0.15. So, The Designing of all other parts is done based on these dimensions with $N = 5$. The semi angle in the Contraction Cone ($\alpha/2$) is taken as 12° and the semi angle in the Diffuser ($\theta/2$) is taken as 3.5° . The non dimensional lengths for the Settling Chamber (l_s) and Diffuser (l_D), for Sub-Sonic Open Circuit Flow, are taken as 0.5 and 3.2 respectively. The calculated parameters are displayed in Table. 2. And the final design for this analytical analysis is represented by (Fig. 9). The total length of the SOWT is:

$$L_{WT} = L_S + L_C + L_T + L_D \quad \dots(7)$$

$$L_{WT} = 26.83 + 45 + 69.78 + 76.80 = 218\text{cm}$$

Hence, L_{WT} is equal to **218cm**.

Table. 1: The primary and secondary design parameters required for designing of SOWT Model

PRIMARY DESIGN PARAMETERS	SECONDARY DESIGN PARAMETERS
TEST CHAMBER WIDTH (W_T)	SEMI ANGLE IN CONTRACTION CONE ($\alpha/2$)
TEST CHAMBER HEIGHT (H_T)	SEMI ANGLE IN DIFFUSER ($\theta/2$)
TEST CHAMBER LENGTH (H_T)	SETTLING CHAMBER NON DIMENSIONAL LENGTH (L_S)
CONTRACTION RATIO (N)	DIFFUSER NON DIMENSIONAL LENGTH (L_D)
MAXIMUM OPERATING SPEED (V_T)	SETTLING CHAMBER LENGTH (L_S)
MACH NUMBER (M)	CONTRACTION CONE LENGTH (L_C)
	DIFFUSER LENGTH (L_D)

Table. 2: Secondary design Parameters of SOWT Model

Secondary Parameters	Expressions	Values
Cross-Sectional Area of the Test Chamber (A_T)	$A_T = W_T H_T$	432 cm ²
Hydraulic Diameter of the Test Chamber (D_T)	$D_T = \frac{2W_T H_T}{W_T + H_T}$	20.57 cm
Length of The Contraction Cone (L_C)	$L_C = \frac{(\sqrt{N} - 1) W_T}{2 \tan(\alpha/2)}$	69.78 cm
Length of The Settling Chamber (L_S)	$L_S = \sqrt{N} W_T I_S$	26.83 cm
Length of The Diffuser (L_D)	$L_D = W_T I_D$	76.80 cm

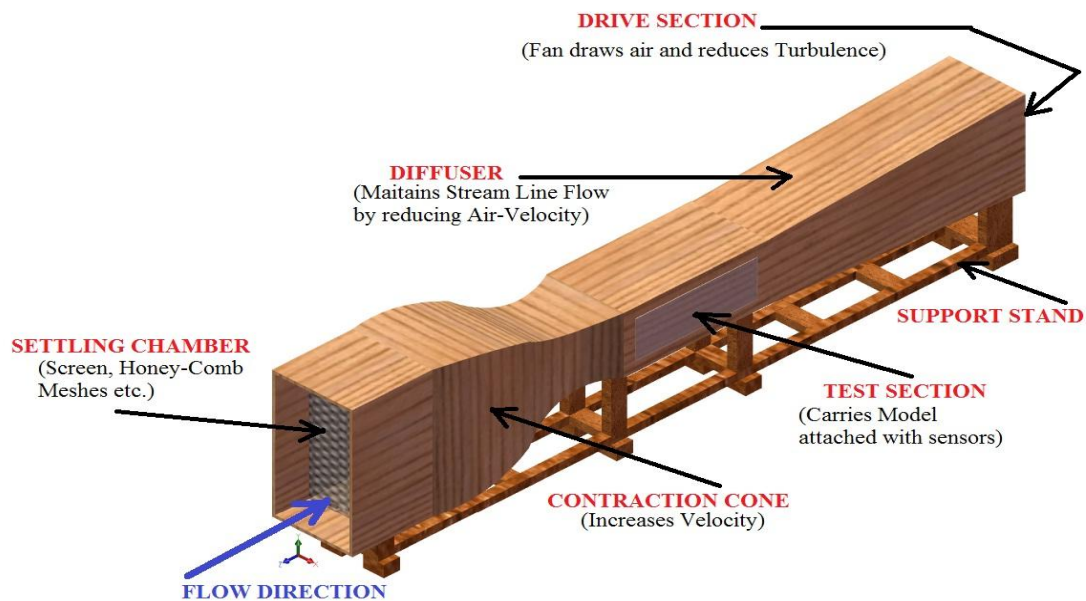


Fig. 9: Isometric View of the complete model of SOWT developed using Solid-Works

IV. Instrumentation of Sub Sonic Open Circuit Wind Tunnel Model

The instrumentation of wind tunnel emphasizes on the various instruments and Data Acquisition Systems (DAQs) required by a tunnel for its proper functioning, Pressure and Flow measuring ability, Flow Visualization and Image Acquisition. In the instrumentation of the tunnel, Standard data acquisition (DAQ), Motion Control, and Image Capture hardware play a very crucial role. Data acquisition is the process of sampling signals that measure real world physical conditions and converting the resulting samples into digital numeric values that can be manipulated by a computer. Data acquisition systems convert analog waveforms into digital values for processing. The various components of data acquisition systems are Sensors (convert physical parameters to electrical signals), Signal conditioning circuitry (convert sensor signals into a form that can be converted to digital values) and Analog-to-Digital converters (convert conditioned sensor signals to digital

values). Further, various operations can be integrated to the system including Flow Visualization with Image Acquisition, Multipoint differential pressure scanning, Hot Wire Anemometry, Force and Moment measurement using internal balances, Roll, Pitch and Yaw angle measurements, and Noise and Temperature measurements.

For Pressure and Flow Measurements, measuring devices coupled with DAQs like LabVIEW and pressure scanners etc. can be used. Similarly for Force and Moment Measurements, Six-component Strain Gauge Balances can be applied. And for Flow Visualization and Image Acquisition, light sheets using Argon-ion lasers with CCD cameras and recording system can be used to capture and analyze the exact trajectory of flow particles, even sometimes incorporating IMAQ hardware and software (IMAQ vision). With such a proper design and proper instrumentation, a wind tunnel can be used for Full-model tests with sting support mechanism, Half-model testing with external balance, Two-dimensional model testing, Ground effect simulation with moving belt, Gust and cross wind simulation, Aero-acoustic testing etc. For a Wind Tunnel with $M < 0.3$, the instrumentation required is not so much complex but still it requires attention for getting accurate and precise results [22-26].

V. Simulation of Sub Sonic Open Circuit Wind Tunnel Model

Solid-Works Flow-Express is a first pass qualitative flow analysis tool which gives insight into water or air flow inside the Solid-Works model. Using this, the simulation is carried out. The constants and assumptions used in the simulation study are tabulated as (Table. 3):

Table. 3: The constants and various parameters determining the environment conditions for the simulation of SOWT Model.

CONSTANTS AND VARIOUS PARAMETERS	VALUES
Inlet Pressure	100890 Pa
Outlet Pressure	100000 Pa
External Ambient Temperature	293.20° K
Gas Constant	287 J/kg ² K
Kinematic Viscosity	1.714 x 10 ⁻⁵ Kg/m-s
Acceleration due to gravity	9.81 m/s ⁻²
Air Density	1.2251 kg/m ³
Entrance Speed	11.335 m/s

The flow velocity simulation of the designed Wind Tunnel have been performed (using particle flow visualization) under the above mentioned environment conditions (Fig. 10). Also, the variation of flow velocity against the length of the tunnel is obtained. Fig. 11 shows the flow speed changes within the wind tunnel. The lowest flow speed is occurred at the surfaces of the entrance section, at the corners joining the settling chamber and the contraction cone, and the diffuser exit. Flow speed accelerates while passing through the contraction and it reaches the highest required value (49.118 m/s \approx 50 m/s) in the test chamber. Also the flow rate increases throughout the contraction and remains constant throughout the test chamber. Flow rate gradually decreases as air exits from the test chamber and enters into the diffuser. Further, at the diffuser exit, it reaches the same value with the wind tunnel entrance.

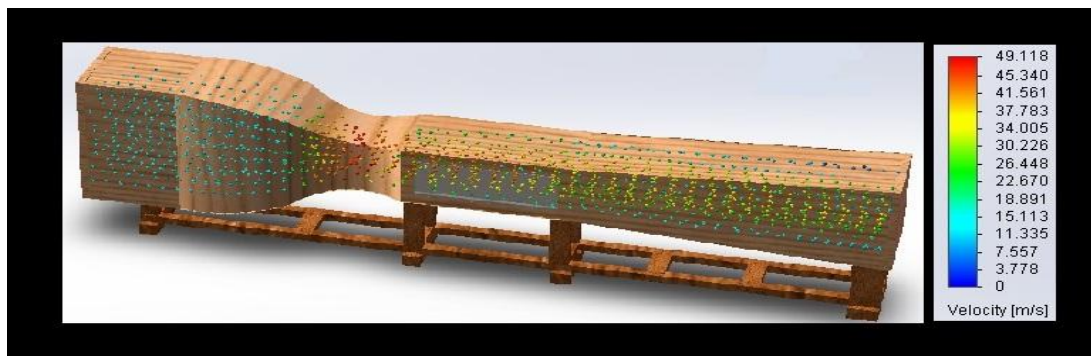


Fig. 10: Particle Flow Visualization of Air as fluid inside the SOWT, illustrating Velocity variation along the length of the Tunnel

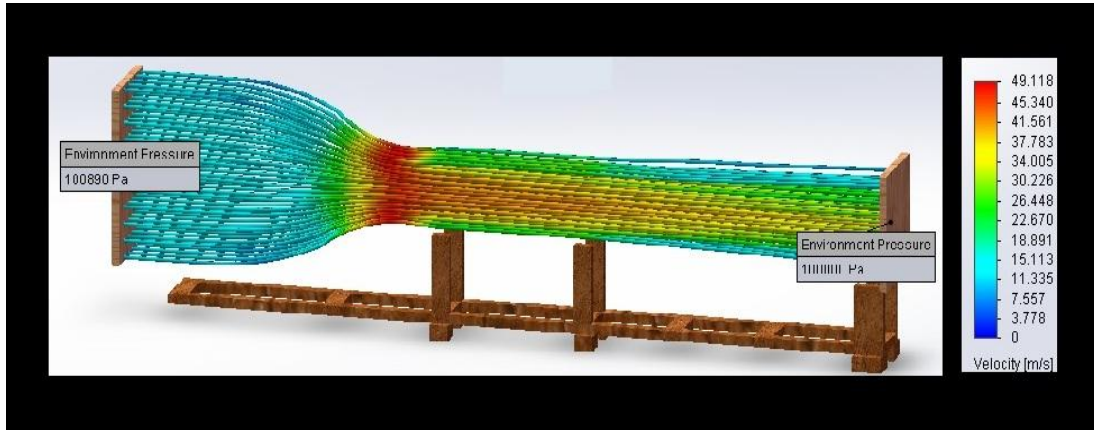


Fig. 11: Flow Velocity Variation of Air as fluid inside the SOWT along the length of the Tunnel

The graphic of static pressure distribution and velocity changes throughout the wind tunnel is shown in Fig. 12. The static pressure on the edges of the entrance section is the maximum value (100890 Pa.). It can be said that a major turbulence and counter pressure zone are created at these points. Static pressure values are closed to the each others at the settling chamber ($x=2.5$ ft.) and the diffuser exit ($x=7$ ft.). A bit of static pressure drop is occurred in the middle zone of the contraction cone. The pressure is reached to the lowest value at the test chamber exit. Since the static pressure changes are very small throughout the test chamber, it can be said that there is not any boundary layer thickening along the test chamber walls and the air flow quality is good.

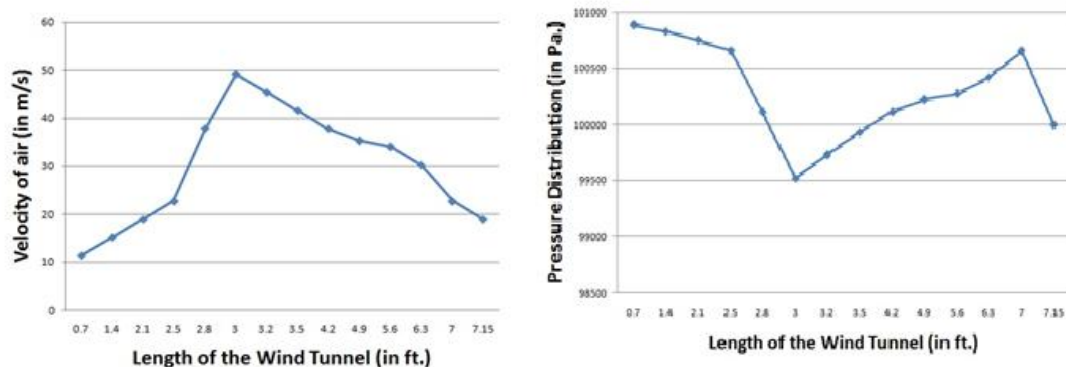


Fig. 12: Flow Velocity Variation (Quantitatively) and Pressure Distribution (Quantitatively) of Air as fluid inside the SOWT along the length of the Tunnel

VI. Conclusion

The design of Low Cost SOWT model has been generated. The main considerations like Boundary Layer Separation, Controlled Air Flow Quality, Turbulence Intensity, Stream Line Flow, Cost-Effectiveness, Design Ease and Mach Number ($M = 0.15$) etc were taken into the account and accordingly the model is designed. The primary design parameters of the Test Chamber were taken as the baseline and following the design guidelines, the secondary design parameters for approximately 220 cm tunnel were calculated. The Contraction Cone and the Test Chamber section were given special attention as they have direct influence on the scale model testing and the data generated. A brief insight is given to the instrumentation segment of the tunnel, especially to the various measurements and DAQs that are still playing their part in research and development concerning the various wind tunnel applications. The Velocity Variations and Static Pressure changes throughout this model were simulated. Moreover, the quantitative variation of Velocity and Pressure is plotted against the tunnel's length. With the final design, the maximum operating speed obtained at the test chamber is 49.12 m/s, quite close to desired value 50 m/s. The air flow obtained is of smooth quality with no boundary layer thickening process at the Test Chamber. Thus, the final SOWT Model design obtained can be used wherever the maximum operating velocity required is 50 m/s or 180 km/h, which generally is the case with the automobiles at high speeds.

References

- [1]. Dodson, MG (2005), An Historical and Applied Aerodynamic Study of the Wright Brothers, Wind Tunnel Test Program and Application to Successful Manned Flight, US Naval Academy Technical Report, USNA-334.
- [2]. Whirling Arms and the First Wind Tunnels, Wind Tunnels of NASA by Donald D. Baals and William R. Corliss, (Searched on Sept 1, 2013) <http://www.grc.nasa.gov/WWW/k12/WindTunnel/history.html>.
- [3]. History, Origins of Wind Tunnel, NASA Aeronautics and Space Administration, http://en.wikipedia.org/wiki/Wind_tunnel (Searched on Sept 1, 2013).
- [4]. Wright Brothers, National Memorial, Wind Tunnel Tests 1901, (Searched on Sept 1, 2013) http://www.cr.nps.gov/history/online_books/hh/34/hh34i.htm.
- [5]. Types of Wind Tunnels, NASA Aeronautics and Space Administration, (Searched on Sept 1, 2013) <http://www.grc.nasa.gov/WWW/k12/airplane/tuntype.html>.
- [6]. Science Buddies: How to Build a Subsonic Wind Tunnel (Searched on Sept 1, 2013) <http://www.sciencebuddies.org/science-fair-projects/wind-tunnel-toc.shtml>.
- [7]. A Textbook of Fluid Mechanics and Hydraulic Machines, Dr. R. K. Bansal, Laxmi Publications Pvt. Ltd., New Delhi, Forces on Submerged Bodies, Page No. 657-659.
- [8]. Peter Moonen, Bert Blocken, Jan Carmeliet, Indicators for the evaluation of wind tunnel test section flow quality and application to a numerical closed-circuit wind tunnel, *Journal of Wind Engineering and Industrial Aerodynamics* 95 (2007) 1289–1314.
- [9]. Aly Mousaad, Alberto Zasso and Ferruccio Resta (2011), On the dynamics of a very slender building under winds: response reduction using MR dampers with lever mechanism, *The Structural Design of Tall and Special Buildings*.
- [10]. Windless Wind Tunnels for High Altitude Tests, *Popular Mechanics*, February 1952, Page No-105.
- [11]. J.E. Cermak, Wind tunnel for the study of turbulence in the atmospheric surface layer, Final Report Air Force Cambridge Center, Air Research and Development Command, Bedford, MA (Contract AF 19(604)-1706), 1958, 36 pages.
- [12]. R.E. Whitbread, The measurement of non-steady wind forces on small-scale building models, in: *Proceedings of the fourth International Conference on Wind Effects on Buildings and Structures*, Heathrow, England, 1975, pages-567–574.
- [13]. G. Diana, S. De Ponte, M. Falco, A. Zasso, A new large wind tunnel for civil-environmental and aeronautical applications, *Journal of Wind Engineering and Industrial Aerodynamics* 74-76 (1998) 553-565.
- [14]. John Lohan, PhD, Article on Design and Applications of Low Speed Wind Tunnels, Department of Mechanical and Industrial Engineering, Galway-Mayo Institute of Technology (GMIT), Dublin Road, Galway, Ireland.
- [15]. Serhat Senol, Ali Cinar, Design and Flow Simulation of an Open Circuit Wind Tunnel, *EnginSoft International Conference 2009 1st-2nd Oct. 2009*.
- [16]. Eckert W. T, Mort K. W, & Jope J, Aerodynamic design guidelines and computer program for estimation of subsonic wind tunnel performance, NASA technical note / D-8243, NASA Washington, (1976).
- [17]. Maskell, E. C. A theory of the blockage effects on bluff bodies and stalled wings in a closed wind tunnel, R. & M. 3400, November, (1963).
- [18]. The Royal Aeronautical Society. Wind tunnels and wind tunnel test techniques, Royal Aeronautical Society London, (1992).
- [19]. Mehta, R. D, & Bradshaw, P. Design Rules for Small Low-Speed Wind Tunnels, *Aero. Journal*, (Royal Aeronautical Society), (1979), 73, 443.
- [20]. Borger G. G., The optimization of wind tunnel contractions for the subsonic range, NASA Technical Translation / F-16899, NASA Washington, (1976).
- [21]. Scheiman, J. Considerations for the installation of honeycomb and screens to reduce wind-tunnel turbulence, NASA Technical Memorandum / 81868, NASA Washington, (1981).
- [22]. Gorlin, S. M, & Slezinger, I. I. Wind tunnels and their instrumentation, *Israel Program for Scientific Translations Jerusalem*, (1966).
- [23]. Data Acquisition, (Searched on Sept 15, 2013) http://en.wikipedia.org/wiki/Data_acquisition.
- [24]. Kamal Poddar, Sanjay Gupta, Instrumentation for National Wind Tunnel Facility, IIT Kanpur.
- [25]. Barlow, J. B, Rae, W. H, & Pope, A. Low-speed wind tunnel testing, John Wiley & Sons New York, (1999).
- [26]. Sub-Sonic Wind Tunnels and Instrumentation, www.aerolab.com, 301-776-6585 Laurel, Maryland, USA.

Secure Multi-Owner Group Signature Based Secure M-Health Records in Cloud

B. Anitha¹, V. Udhaya Kumar²

¹M.Tech Student Department of Computer Science and Engineering PRIST University Pondicherry, India

²Assistant professor Department of Computer Science and Engineering PRIST University Pondicherry, India

ABSTRACT: Cloud-assisted mobile health monitoring, which applies the prevailing mobile communications and cloud computing technologies to provide feedback decision support, has been considered as a revolutionary approach to improving the quality of healthcare service while lowering the healthcare cost. Unfortunately, it also poses a serious risk on both clients' privacy and intellectual property of monitoring service providers which could deter the wide adoption of mHealth technology. Paper is to address this important problem and design a cloud assisted privacy preserving mobile health monitoring system to protect the privacy of the involved parties and their data. Moreover, the outsourcing decryption technique and a newly proposed key private proxy re-encryption are adapted to shift the computational complexity of the involved parties to the cloud without compromising clients' privacy and service providers' intellectual property. Finally, our security and performance analysis demonstrates the effectiveness of our proposed design.

Keywords: MHealth, monitoring, decryption

I. Introduction

We design a cloud-assisted mobile health monitoring system (CAM). We first identify the design problems on privacy preservation and then provide our solutions. To ease the understanding, we start with the basic scheme so that we can identify the possible privacy breaches. We then provide an improved scheme by addressing the identified privacy problems. The resulting improved scheme allows the mobile health service provider (the company) to be offline after the setup stage and enables it to deliver its data or programs to the cloud securely. To reduce clients' decryption complexity, we incorporate the recently proposed outsourcing decryption technique into the underlying multi-dimensional range queries system to shift clients' computational complexity to the cloud without revealing any information on either clients' query input or the decrypted decision to the cloud. To relieve the computational complexity on the company's side, which is proportional to the number of clients, we propose a further improvement, leading to our final scheme. It is based on a new variant of key private proxy re-encryption scheme, in which the company only needs to accomplish encryption once at the setup phase while shifting the rest computational tasks to the cloud without compromising privacy, further reducing the computational and communication burden on clients and the cloud.

II. Problem Definition

Major problem in addressing security and privacy is the computational workload involved with the cryptographic techniques. With the presence of cloud computing facilities, it will be wise to shift intensive computations to cloud servers from resource-constrained mobile devices. However, how to achieve this effectively without compromising privacy and security becomes a great challenge, which should be carefully investigated.

The problem becomes especially trickier for cloud assisted mobile health systems because we need not only to guarantee the privacy of clients' input health data, but also that of the output decision results from both cloud servers and healthcare service providers (which will be referred to as the company in the subsequent development).

III. Problem Description

We first identify the design problems on privacy preservation and then provide our solutions. To ease the understanding, we start with the basic scheme so that we can identify the possible privacy breaches. We then provide an improved scheme by addressing the identified privacy problems. The resulting improved scheme allows the mobile health service provider (the company) to be offline after the setup stage and enables it to

deliver its data or programs to the cloud securely. To reduce clients' decryption complexity, we incorporate the recently proposed outsourcing decryption technique into the underlying multi-dimensional range queries system to shift clients' computational complexity to the cloud without revealing any information on either clients' query input or the decrypted decision to the cloud.

IV. Feasibility Study

Feasibility analysis tells how the present system is compatible with the resource present with developing team. The objective is to determine quickly at the minimum expense how to solve a problem. The following feasibility studies are conducted to the feasibility of proposed system.

The feasibility study is term in three ways as followed:

- Technical feasibility
- Behavioral feasibility
- Economical feasibility

A. Technical Feasibility

Technical feasibility center on the computer system (hardware, software etc.) and to what extend it can support the proposed system. This system uses ASP.NET with c# as front end and SQL as back end. Since the system needs much user interface, the design and implementation can be done.

B. Behavioral Feasibility

The annotation overhead is very small. So that the performance of the fully automatic static verification is acceptable, and that the performance overhead of the runtime checking is limit. So this system is operationally feasible.

C. Economic Feasibility

The current project is economically feasible because the project duration is 6 months and the man power is one. All the necessary hardware and software are provided in the organization.

The basic COCOMO estimation:

A development project is sized at 3.7 KLOC.

The basic COCOMO equation for effort (E) in staff-months(SM) is:

Effort(SM) = 2.4(KLOC) 1.05 = 2.4(3.7)1.05 = 2.4(3.885) = 9.324 staff-months.

Development time (TDEV): TDEV = 2.5(SM) 0.38 = 2.5(9.324)0.38 = 2.5(3.54312) = 6 months.

The average number of staff members(S):

Staff = Effort / TDEV = 10 staff-months / 6 months = 1.5 staff members on average.

The productivity rate (P):

Productivity = Size / Effort = 3700 LOC / 9.324 staff-months = 396 LOC/staff-months

So the implementation of the project is no so costlier and the system is economically feasible.

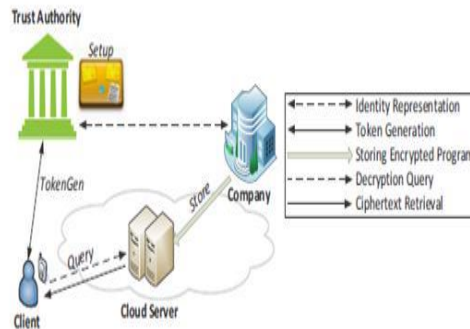
V. Proposed System

In this paper, we design a cloud-assisted mobile health monitoring system (CAM). We first identify the design problems on privacy preservation and then provide our solutions. We then provide an improved scheme by addressing the identified privacy problems. The resulting improved scheme allows the mobile health service provider (the company) to be offline after the setup stage and enables it to deliver its data or programs to the cloud securely. To reduce clients' decryption complexity, we incorporate the recently proposed outsourcing decryption technique into the underlying multi-dimensional range queries system to shift clients' computational complexity to the cloud without revealing any information on either clients' query input or the decrypted decision to the cloud. It is based on a new variant of key private proxy re-encryption scheme, in which the company only needs to accomplish encryption once at the setup phase while shifting the rest computational tasks to the cloud without compromising privacy.

VI. System Architecture

The company stores its encrypted monitoring data or program (branching program) in the cloud. Individual clients collect their medical data and store them in their mobile devices, which then transform the data into attribute vectors. The attribute vectors are delivered as inputs to the monitoring program in the cloud through a mobile (or smart) phone. TA is responsible for distributing private keys to clients and collecting service fees from clients according to a certain business model such as "pay-peruse" model. TA can be

considered as a collaborator or a management agent for a company (or several companies) and thus shares certain level of mutual business interest with the company.

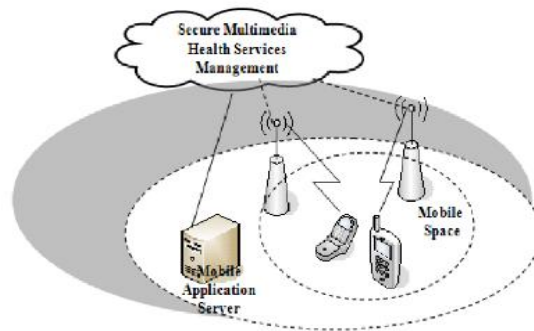


At the initial phase, TA runs the Setup phase and publishes the system parameters. Then, the company first characterizes the flow chart of an mobile health monitoring program as a branching program which is encrypted under the respective directed branching tree. Then the company will deliver the resulting cipher text and its company index to the cloud, which corresponds to the Store algorithm in the context. When a client wishes to query the cloud for a certain mobile health monitoring program, the i-th client and TA run the Token Gen algorithm. The client sends the company index to TA, and then inputs its private query (which is the attribute vector representing the collected health data) and TA inputs the master secret to the algorithm. The client obtains the token corresponding to its query input while TA gets no useful information on the individual query.

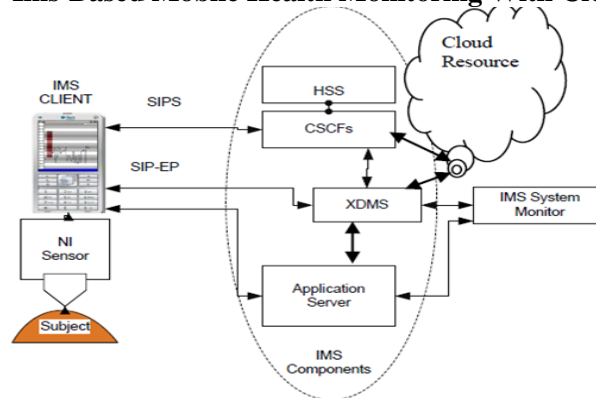
At the last phase, the client delivers the token for its query to the cloud, which runs the Query phase. The cloud completes the major computationally intensive task for the client's decryption and returns the partially decrypted cipher text to the client. The client then completes the remaining decryption task after receiving the partially decrypted cipher text and obtains its decryption result, which corresponds to the decision from the monitoring program on the client's input. The cloud obtains no useful information on either the client's private query input or decryption result after running the Query phase.

VII. Data Flow Diagram

A data flow diagram is graphical tool used to describe and analyze movement of data through a system.



VIII. Ims-Based Mobile Health Monitoring With Cloud Support



A. Outsourcing Decryption

The basic CAM has the following security weaknesses. First, the identity representation set for a client's attribute vector v is known to TA, and hence TA can easily infer the client's private attribute vector. Second, the client cannot protect his privacy from the cloud either because the cloud can easily find out the identity representation for the private key sk_{vi} , $i \in [1, n]$ by running identity test in MDRQ. The cloud can simply encrypt a random message under any attribute value v' until it can use $sk_{v'}$ to successfully decrypt the cipher text, which means there is a match between $v' = v_i$ and hence it successfully finds out v_i . Third, neither can the data privacy of the company be guaranteed since the identity representation of the respective range is revealed to the cloud whenever the decryption is successful due to the match revealing property (see Sec. II-D3) of MDRQ. The cloud can finally find out the company's branching program since it has the private keys of all the system users.

To rectify these weaknesses in the basic CAM, we provide the following improvement in this module. The high level idea is as follows: in order to avoid leaking the attribute vector to TA, the client obviously submits his attribute vectors to TA so that he can obtain the respective private keys without letting TA get any useful information on his private vector. The client runs the outsourcing decryption of MDRQ to ensure the cloud completes the major workload while obtaining no useful information on his private keys. On the other hand, the company will permute and randomize its data using homomorphism encryption² and MDRQ so that neither the cloud nor a client can get any useful information on its private information on branching program after a single query. Meanwhile, the company is also required to include the randomness in the randomization step in the encryption sent to TA to ensure that TA can successfully generate tokens for clients.

B. Healthcare

Feature of Mobile Health All the major health failure problem classification to this page.

a. Login

i. Login the all authorized administrator user to login and give diagnosis the patient.

ii. Registration

iii. User Directory

iv. User Treatment Commands

v. User Profile

b. Privacy Block

In this Module, security tools and offers the necessary modifications to meet our design needs.

c. Bilinear Pairing:

Bilinear pairing is crucial to our design, which would further serve as the building block of the proposed CAM.

d. Homomorphic Encryption:

Another technique we will use for oblivious transfer protocol is homomorphic encryption, which is widely used as an underlying tool for constructing secure protocols. CAM adopts a semantically secure additively homomorphic public-key encryption technique.

C. Mobile Health Information

The proposed re-encryption scheme incorporates the outsourcing decryption so that the other security and efficiency characteristics in the final CAM should be inherited here. By using our newly-proposed key private proxy re-encryption, we are design our highly efficient CAM with full Privacy in this module.

D. Cloud user

We create a local Cloud and provide priced abundant storage services. The users can upload their data in the cloud. We develop this module, where the cloud storage can be made secure. However, the cloud is not fully trusted by users since the CSPs are very likely to be outside of the cloud users' trusted domain. Similar to we assume that the cloud server is honest but curious. That is, the cloud server will not maliciously delete or modify user data due to the protection of data auditing schemes, but will try to learn the content of the stored data and the identities of cloud users.

E. Group Manager

Group manager takes charge of followings,

1. System parameters generation,
2. User registration,
3. User revocation, and
4. Revealing the real identity of a dispute data owner.

Therefore, we assume that the group manager is fully trusted by the other parties. The Group manager is the admin. The group manager has the logs of each and every process in the cloud. The group manager is responsible for user registration and also user revocation too.

F. Group Member

Group members are a set of registered users that will

1. Store their private data into the cloud server and
2. Share them with others in the group.

Note that, the group membership is dynamically changed, due to the staff resignation and new employee participation in the company. The group member has the ownership of changing the files in the group. Whoever in the group can view the files which are uploaded in their group and also modify it. The group meme

G. File Security

- Encrypting the data file.
- File stored in the cloud can be deleted by either the group manager or the data owner. (i.e., the member who uploaded the file into the server).

H. Group Signature

A group signature scheme allows any member of the group to sign messages while keeping the identity secret from verifiers. Besides, the designated group manager can reveal the identity of the signature's originator when a dispute occurs, which is denoted as traceability.

I. User Revocation

User revocation is performed by the group manager via a public available revocation list (RL), based on which group members can encrypt their data files and ensure the confidentiality against the revoked users.

XI. CONCLUSION

In this paper, we design a cloud-assisted privacy preserving mobile health monitoring system, called CAM, which can effectively protect the privacy of clients and the intellectual property of mobile health service providers. To protect the clients' privacy, we apply the anonymous Boneh-Franklin identity based encryption (IBE) in medical diagnostic branching programs. To reduce the decryption complexity due to the use of IBE, we apply recently proposed decryption outsourcing with privacy protection to shift clients' pairing computation to the cloud server. To protect m Health service providers' programs, we expand the branching program tree by using the random permutation and randomize the decision thresholds used at the decision branching nodes. Finally, to enable resource constrained small companies to participate in mobile health business.

REFERENCES

- [1]. [1] P. Mohan, D. Marin, S. Sultan, and A. Deen, "Medinet: personalizing the self-care process for patients with diabetes and cardiovascular disease using mobile telephony," in Engineering in Medicine and Biology Society, 2008. EMBS 2008. 30th Annual International Conference of the IEEE. IEEE, 2008, pp. 755–758.
- [2]. [2] A. Tanas, M. Little, P. McSharry, and L. Ramig, "Accurate telemonitoring of parkinson's disease progression by noninvasive speech tests," Biomedical Engineering, IEEE Transactions on, vol. 57, no. 4, pp. 884– 893, 2010.
- [3]. [3] G. Clifford and D. Clifton, "Wireless technology in disease management and medicine," Annual Review of Medicine, vol. 63, pp. 479–492, 2012.
- [4]. [4] L. Ponemon Institute, "Americans' opinions on healthcare privacy, available: <http://tinyurl.com/4atsdlj>," 2010.
- [5]. [5] A. V. Dhukaram, C. Baber, L. Elloumi, B.-J. Van Beijnum, and P. D. Stefanis, "End-user perception towards pervasive cardiac healthcare services: Benefits, acceptance, adoption, risks, security, privacy and trust," in Pervasive Health, 2011, pp. 478–484.
- [6]. [6] M. Delgado, "The evolution of health care it: Are current U.S. privacy policies ready for the clouds?" in SERVICES, 2011, pp. 371–378.
- [7]. [7] N. Singer, "When 2+ 2 equals a privacy question," New York Times, 2009.

Studies Of Influence on Multiwalled Carbon Nanotubes (MWCNT's) Reinforced Epoxy Based Composites

Mahesh V. M.¹, B. K. Muralidhara², Raji George³

¹ Asst. Professor, Dept. of Mechanical Engg., M.S.Ramaiah Institute of Technology, Bangalore-560054

² Professor, Dept. of Mechanical Engg., University Visvesvaraya College of Engineering, Bangalore-560001

³ Professor, Dept. of Mechanical Engg., M.S.Ramaiah Institute of Technology, Bangalore-560054.

ABSTRACT: In the present work, the Multiwalled Carbon Nanotube reinforced epoxy composites are fabricated with different weight fraction of the reinforcement and are subjected to hardness test as well as compression test. The mechanical properties of these composites are investigated and found possess increase in hardness test and young's modulus with increased weight fraction of the reinforcement compared to the based matrix fabricated using the same process.

Keywords: Epoxy resin, hardner, multiwalled carbon nanotube, nanocomposites.

I. Introduction

Carbon nano-tubes is the form of carbon, multiwalled carbon nanotubes (MWCNT's) is rolled to a tubular shape with multiple layers. MWCNT's are to revolutionize several fields in mechanical and electrical engineering. This are a major component of nanotechnology. MWCNT have a wide range of unexplored potential applications in various technological areas antistatic behavior such as fuel filler caps, automotive fuel lines, fuel filter housings, fuel hoses, etc., housings such as mobile phones, coatings etc., Mechanical strengths such as electrostatic paintings, adhesives, aircraft parts, sports goods, coatings etc., electrical components, etc., Epoxy-based composite materials are being used as structural components not only in weight sensitive aerospace industry, but also in the marine, armor, automobile, railways, structural engineering to their excellent high-adhesion, low-weight, and good chemical/corrosion-resistance.

Over the years, many attempts have made to modify epoxy by adding either rubber particles or fillers to improve the matrix-dominated composite properties. The addition of rubber particles improves the fracture toughness of epoxy, but decreases its Young's modulus and strength. The addition of fillers, improves the Young's modulus and strength of epoxy.

These properties would enable us the exact application for which the specimens can be tailor-made. Applications are of conductive polymers & composites in electronic & automobile products, as sensors & instruments in applications like microscope probe tips, gas leak detectors, electromagnetic shielding sporting goods(tennis racket), as conductive coatings in printed circuit board, as catalysts in petrochemical applications, as textiles and fibers, in lithium ion batteries, lamps, semiconducting materials, advanced ceramics, microwave antennas, medical implants, drug delivery, aerospace etc.

II. Experimental section

2.1 Methods of Synthesizing MWCNT

The oldest method for the carbon nanotube production is the electric arc discharge. This technique was used already in the early sixties by R. Bacon for the synthesis of carbon fibers called whiskers. The same technique was adapted in 1990 by Kratschmer and Huffman to produce fullerenes in good yields, and later on this method was improved and applied for the synthesis of multiwall (MWNT) and single wall (SWNT) carbon nanotubes. Other methods such as the laser evaporation/ablation and chemical vapour deposition (CVD) were also successfully examined in the production of carbon nanotubes. The laser evaporation process is technically similar to the arc discharge method. The difference between these two methods is in the quality and purity of the obtained products. However, the arc discharge and the different types of CVD are the most promising and utilized techniques in the large scale production of carbon nanotubes and related materials. Here, we use Arc Discharge method.

2.1.1 Arc Discharge Method:

Nanotubes were observed in 1991 in the carbon soot of graphite electrodes during an arc discharge, by using a current of 100 amps that was intended to produce fullerenes. However the first macroscopic production of carbon nanotubes was made in 1992 by two researchers at NEC's Fundamental Research Laboratory. The method used was the same as in 1991. During process, carbon contained in negative electrode sublimates because of high-discharge temperatures. Because nanotubes were initially discovered using this technique, it has been the most widely used method of nanotube synthesis.

The yield for this method is up to 30% by weight and it produces both single-walled and multi-walled nanotubes with lengths of up to 50 micrometers with few structural defects.

The arc discharge technique generally involves the use of two high-purity graphite electrodes. The anode is either pure graphite or contains metals. In the latter case, the metals are mixed with the graphite powder and introduced in a hole made in the anode center. The electrodes are momentarily brought into contact and an arc is struck. The synthesis is carried out at low pressure (30-130 torr or 500 torr) in controlled atmosphere composed of inert and/or reactant gas. The distance between the electrodes is reduced until the flowing of a current (50–150 A).

The temperature in the inter-electrode zone is so high that carbon sublimates from the positive electrode (anode) that is consumed. A constant gap between the anode and cathode is maintained by adjusting the position of the anode. A plasma is formed between the electrodes. The plasma can be stabilized for a long reaction time by controlling the distance between the electrodes by means of the voltage (25–40 V) control. The reaction time varies from 30–60 seconds to 2–10 minutes.

2.2 Preparation of MWCNT/Epoxy Composite

2.2.1 Material

The polymer matrix consisted of bisphenol-A-based epoxy resin (Araldite GY LY556) with an amine-based hardener (Aradur HY 917), obtained from Huntsman Advanced Materials and Ethanol was the chosen solvent. Multi-walled carbon nanotubes produced by arc discharge were supplied by NANOSHELL Wilmington DE USA and its purity was higher than 98% (information taken from the supplier data sheet).

2.2.2 Preparation

MWCNT was mixed with ethanol and sonicated for 15 minutes in a beaker. The sonication helps disperse the nanoparticles uniformly and reduce lumps, thus countering the Vander wall's forces set up. This procedure helps us in getting fine grained MWCNT. The above mixture (MWCNT & ethanol) is heated on an electric heater to evaporate ethanol in the same beaker. Care must be taken to not heat the MWCNT above 75°C. MWCNT taken in amounts of 0.25%, 0.5%, 0.75%, 1%, 1.25%, 1.5%, 1.75% and 2% weight fraction, epoxy resin and hardener were taken in appropriate weight standards (composition), with respect to the mould used. Only MWCNT and epoxy resin were thoroughly mixed for 30 minutes using sonicator. The sonication is carried out in a water bath thereby lowering the undesired heat which polymerizes the epoxy fluid. The sonication helps to disperse the nanoparticles uniformly throughout the epoxy polymer matrix. Hardener was added to the above mixture (MWCNT & epoxy resin) 10:1 and stirred for 5 minutes with a stirrer. The mixture is pre-heated in an electric oven up to 45°C after adding the hardener. The mixture is heated in a controlled environment in an electric oven and then poured into the die and placed in a Petri dish. It is kept in an atmospheric condition for 12 hrs to cure.

2.3 Characterization

XRD graphs of the samples were taken and thus the components of the samples were determined and verified. The phase purity of the MWCNT and epoxy resin were characterized by X-ray diffraction (XRD) on a X-ray Diffractometer with Cu K α radiation ($k = 1.5418 \text{ \AA}$). The powdered samples of MWCNT and its composites (MWCNT/epoxy) were pressed into an appropriate glass mold with a pit for XRD characterization

III. Results and Discussion

3.1 Rockwell hardness test

The specimen was prepared according to the ASTM standard ASTM785.

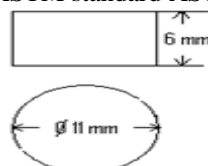
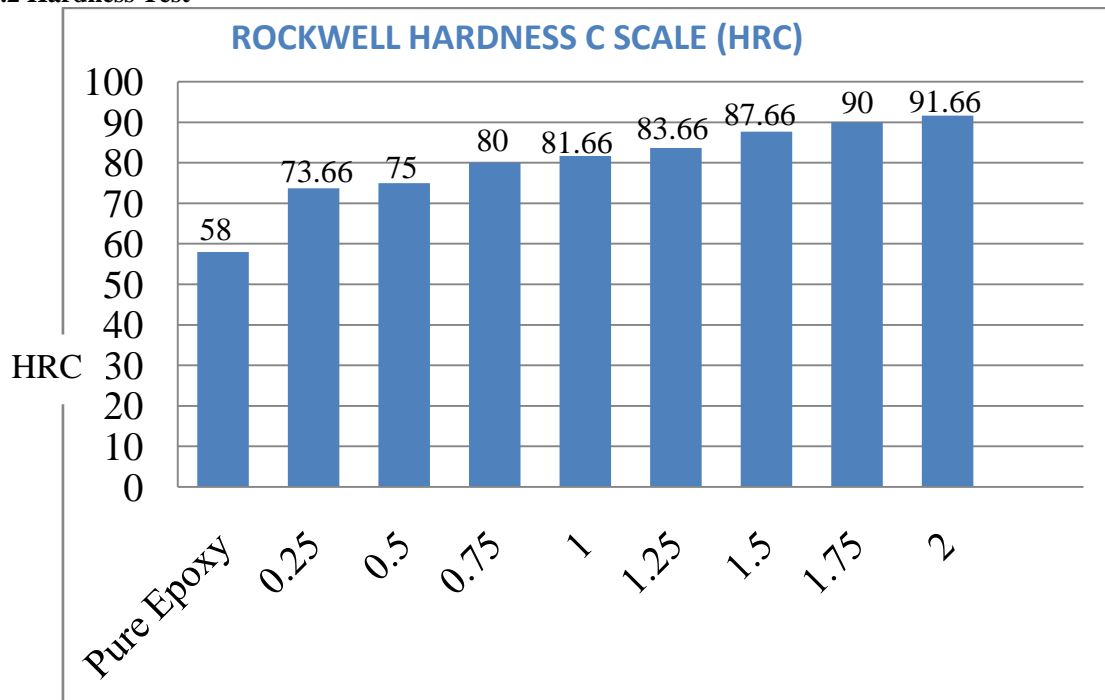


Figure 1: Specimen Dimension

3.2 Hardness Test



Graph.1 : % age of MultiWalled Carbon NanoTube

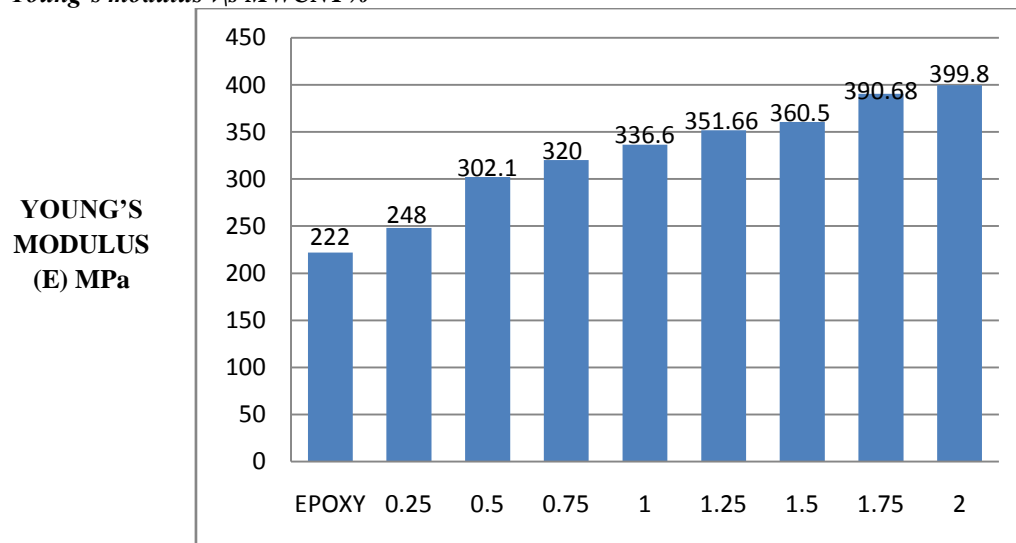
Graph-1 shows that as the percentage of multiwalled carbon tube increases, the hardness also increases.

3.3 Compression test

The specimen was prepared according to the ASTM standard ASTM695.

Each sample was a round solid cylinder with dimensions of length 40mm and diameter 15.5mm. The Load v/s Deflection and Stress v/s Strain graphs were obtained and hence Young's Modulus was determined for each of the samples. The bar graph of Young's moduli versus samples containing certain weight percentages of MWCNT's is as shown below.

Young's modulus v/s MWCNT%



Graph.2: Variation of Young's modulus for different %age of MWCNT

3.4 XRD Graphs

XRD Graphs of the polymer composite samples containing 0.25%, 0.75%, 1.25% and 2% by weight of MWCNT were taken to verify the composition of the prepared samples and are shown in below fig.2, fig.3, fig.4 and fig.5

XRD GRAPHS

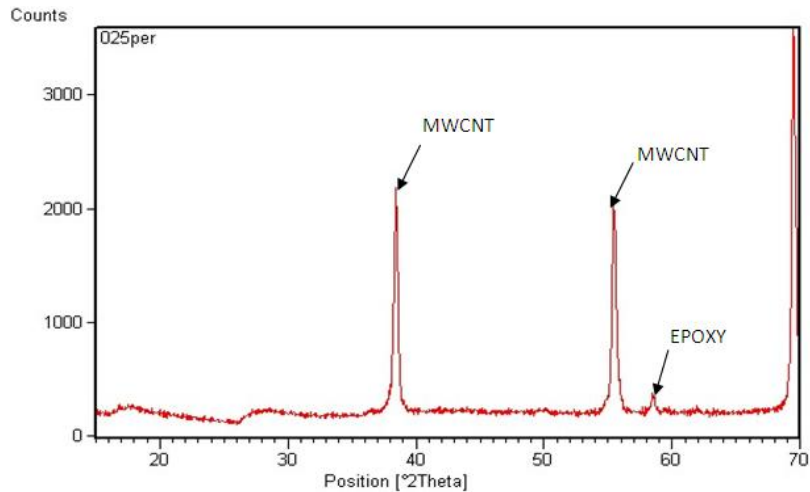


Fig.2 : 0.25 % MWCNT-Epoxy Composite

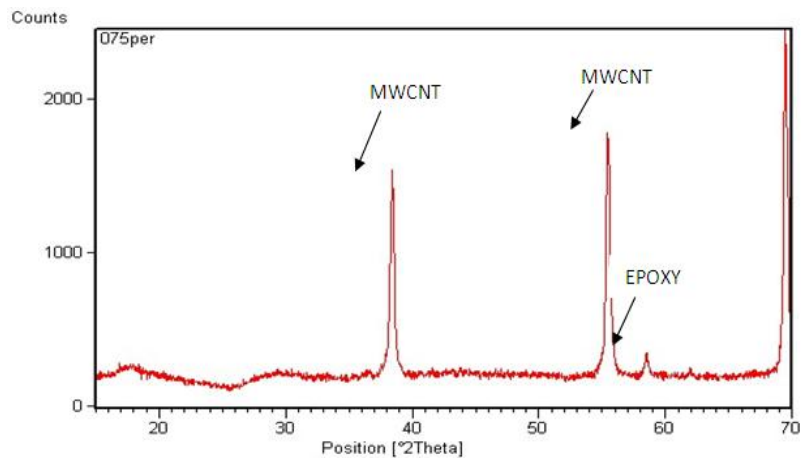


Fig.3: 0.75 % MWCNT-Epoxy Composite

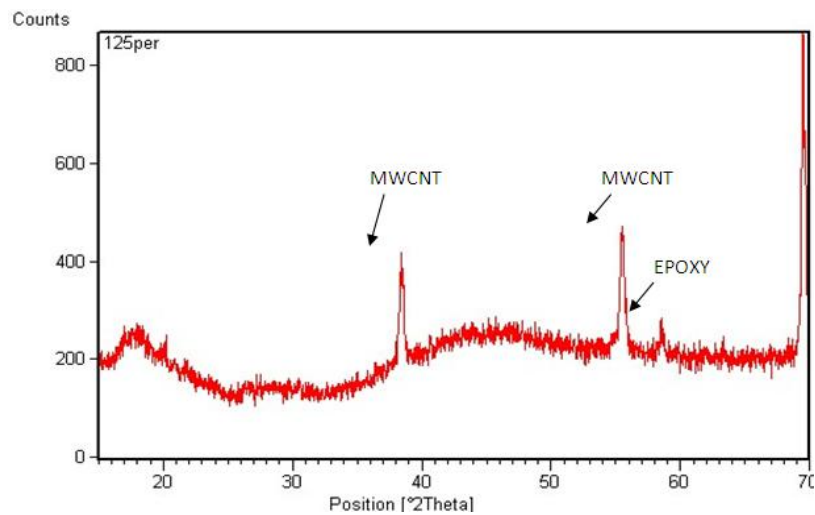


Fig.4: 1.25 % MWCNT-Epoxy Composite

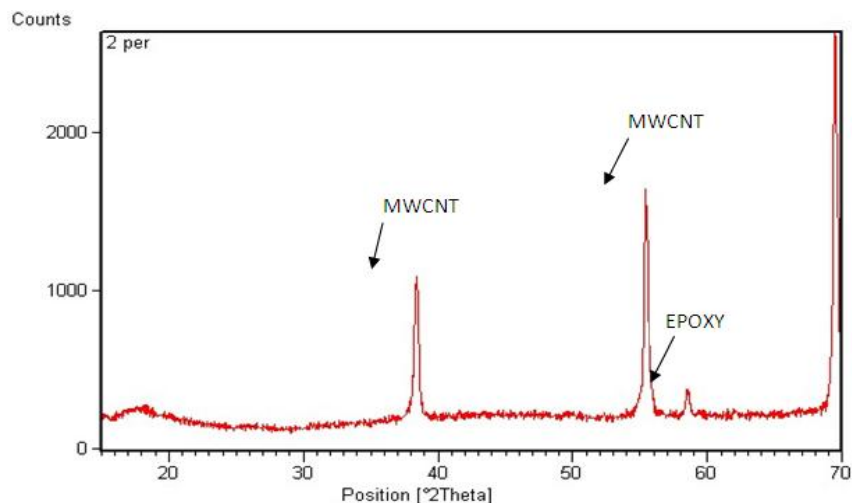


Fig.5: 2 % MWCNT-Epoxy Composite

IV. Conclusion

The MWCNT/epoxy nanocomposites have been fabricated and the reinforcing effect of MWCNT been investigated for enhancing the mechanical properties of the epoxy resin. It is shown that the blending of MWCNT a proper content of 0.25 wt.% into the epoxy matrix can simultaneously enhance the compression strength, Young's modulus and Hardness strength. The composite compression and hardness strengths reach the maximum with an improvement of 0.5%, 0.75%, 1.25%, 1.50%, 1.75% and 2.0% for the compression strength and hardness strength respectively. These are explained mainly in terms of the MWCNT–epoxy interfacial bonding at room temperature and the dispersion of MWCNT in the epoxy matrix. Consequently, MWCNT is a promising nano-modifier for enhancing the mechanical properties of epoxy resins.

REFERENCES

- [1] A Allonius, S Bai. Mechanical and electrical properties of a MWNT/epoxy composite. *Composite science and technology* 62(2002) 1993-1998
- [2] Sabyasachi Gangulia,* , Ajit K. Roy, David P. Andersonb, Improved thermal conductivity for chemically functionalized exfoliated graphite/epoxy composites. *Carbon*46 (2008) 806-817. Mohamed Abdalla, Derrick Dean, Pamela Robinson, and Elijah Nyairo. Cure behavior of epoxy/MWCNT nanocomposites: The effect of nanotube surface modification. *Polymer* 49(2008) 3310-3317. Mohamed Abdalla a, Derrick Dean a,* , David Adibempe b, Elijah Nyairo c, Pamela Robinson d. The effect of interfacial chemistry on molecular mobility and morphology of multiwalled carbon nanotubes epoxy nanocomposite. *Polymer* 48(2007) 5662-5670.
- [3] Pascal Hubert, Kamal Adhikari, , James Meredith, Srikari Vengallatore, Benoit Simard. Synthesis and Characterization of carbon nano tube reinforced epoxy and elastic modulus. *Composite science and technology* 69(2009) 2274-2280. YU Hsuan Liao, Olivier Tondin, and Chuck Zhang Investigation of the dispersion process of MWNTs/SC-15 epoxy resin composites. *Material science and engineering A* 385(2004) 175-181
- [4] F H Gojny, MHW Wichmann, K Schtule. Carbon nano tube-reinforced epoxy composites: enhanced stiffness and fracture toughness at low nano tube content. *Composite science and technology* 64 (2004) 2363-2371.
- [5] David H Wang, Sangwooki Sihm and Ajit K Roy. Nano composites based on vapor-grown carbon nano fibres and an epoxy Functionalization, preparation and characterization. *European polymer journal* 46(2010) 1404-1416.
- [6] I.M.Low, C.Shi. Vickers Indentation Responses of Epoxy Polymers. *Journal of material science letters* 17(1998) 1181-1183.
- [7] Christian p.deck, Gregg s.b. Mckee and Kenneth s. Vecchio. Synthesis Optimization and Characterization of Multiwalled Carbon Nanotubes. *Journal of electronic materials* vol35, no2 (2006).
- [8] Peng-Cheng Ma, Naveed A.Siddiqui, Gad Marom, Jang-Kyo Kim. Dispersion And Functionalization Of Carbon Nanotubes For Polymer-Based Nanocomposites. *Composite part A* 41(2010) 1345-1367.
- [9] Yuanxin Zhou, Farhana Pervin, Lance Lewis, Shaik Jeelani. Fabrication And Characterization Of Carbon/Epoxy Composites Mixed With Multi-Walled Carbon Nanotubes. *Material science and engineering A*475 (2008) 157-165.
- [10] Kin-Tak Lau, San-Qiang Shi, Li-Min Zhou and Hui-Mint Cheng. Micro-Hardness and Flexural Properties Of Randomly-Oriented Carbon Nanotubes Composites. *Journal of composite material* vol37, no4/2003.
- [11] Carole A. Cooper, Diana Ravich, David Lips, Joerg Mayer, H.Daniel Wagner. Distribution and Alignment Of Carbon Nanotubes And Nanofibrils In A Polymer Matrix. *Composite science and technology* 62(2002) 1105-1112.
- [12] Hsu-Chiang Kuan, Chen-Chi M.Ma, Wei-Ping Chang, Siu-Ming Yuen, Hsin-Ho Wu, Tzong-Ming Lee Synthesis, Thermal, Mechanical And Rheological Properties Of Multiwalled Carbon Nanotubes/Waterborne Polyurethane Nanocomposite. *Composite science and technology* 65(2005) 1703-1710.

- [13] Hiroaki Miyagawa, Lawrence T. Drzal. Thermo-Physical and Impact Properties Of Epoxy Nanocomposites Reinforced by Single-Wall Carbon Nanotubes. *Polymer* 45(2004) 5163-5170. Kin-Tak Lau, Mei Tu. Chun-ki lam, Hoi-Yan Cheung, Fen-Lin Sheng, Hu-Lin Li. Thermal And Mechanical Properties Of Single-Walled Carbon Nanotube Bundle-Reinforced Epoxy Nanocomposites: The Role of Solvent for Nanotube Dispersion. *Composite science and technology* 65(2005) 719-725.
- [14] Florian H. Gojny, Malte H.G.Wichmann, Bodo Fiedler, Karl Schulte. Influence Of Different Carbon Nanotubes On The Mechanical Properties Of Epoxy Matrix Composites-A Comparative Study. *Composite science and technology* 65(2005) 2300-2313.
- [15] Y.X.Zhou, P.X.Wu, Z-Y.Cheng, J.Ingram, S.Jeelani. Improvement In Electrical, Thermal And Mechanical Properties Of Epoxy By Filling Carbon Nanotube. *Express polymer letters* vol2 no 1 (2008) 40-48.
- [16] F.H.Gojny, M.H.G.Wichmann, U.Kopke, B.Fiedler, K.Schulte. Carbon Nanotubes-Reinforced Epoxy-Composites: Enhanced Stiffness And Fracture Toughness At Low Nanotube Content. *Composites science and technology* 64(2004) 2363-2371.
- [17] Kai yang, Mingyuan Gu, Yiping Guo, Xifeng Pan, Guohong Mu. Effects of carbon nanotube functionalization on the mechanical and thermal properties of epoxy composites. *Polymer* 47(2009) 1723-1737.